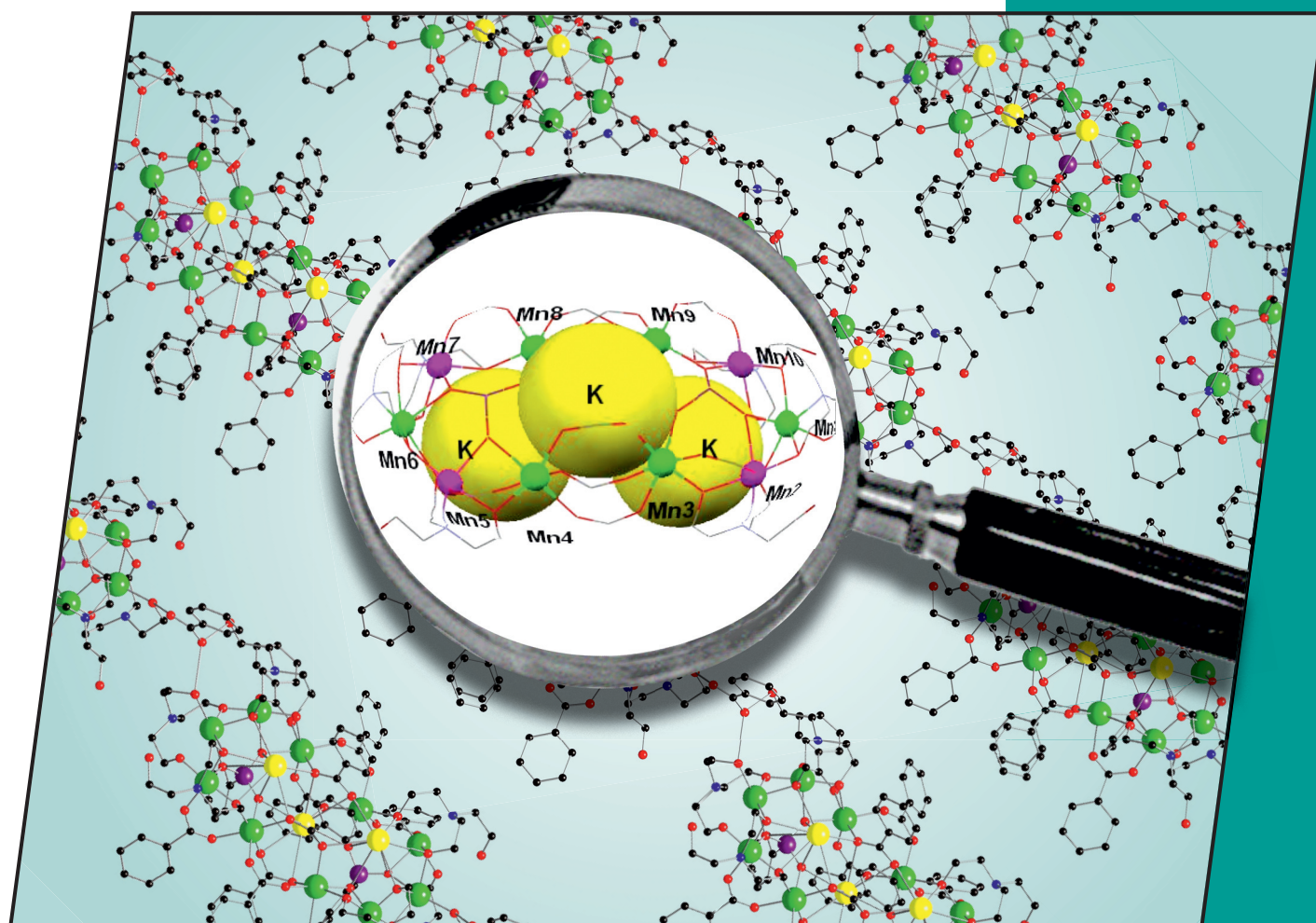


20/2010
2nd July Issue

EurJIC
European Journal of
Inorganic Chemistry



Cover Picture

Catherine Dendrinou-Samara, Richard E. P. Winpenny et al.
Non-Oxido Mixed-Valence $Mn^{II}_6 Mn^{III}_4$ Cluster

Microreview

Boniface P. T. Fokwa
Transition-Metal-Rich Borides – Crystal Structures and Magnetic Properties

 **WILEY-VCH**

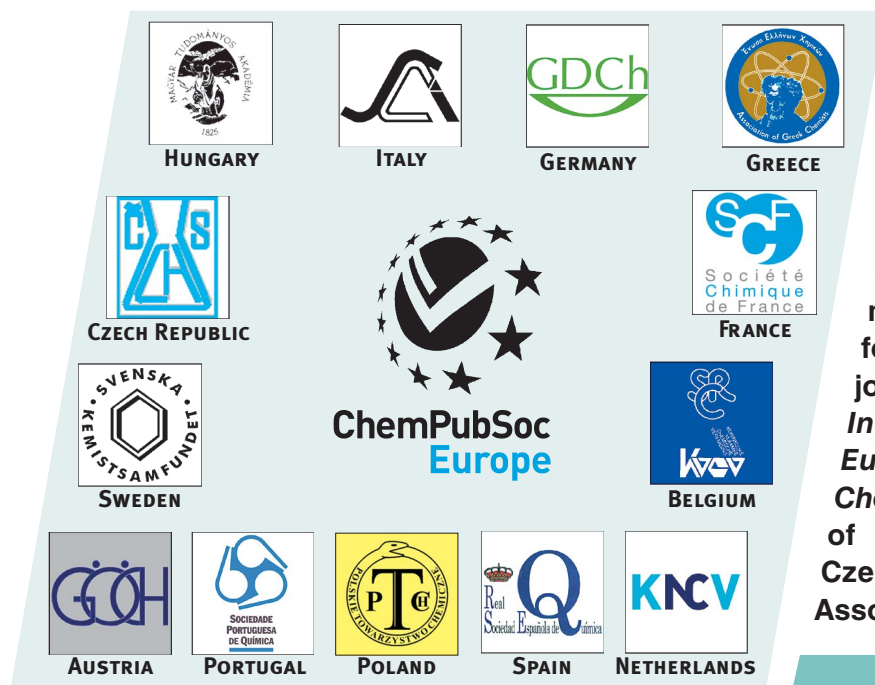
www.eurjic.org

EJICFK (20) 3061–3232 (2010) · ISSN 1434-1948 · No. 20/2010

A Journal of



ChemPubSoc
Europe

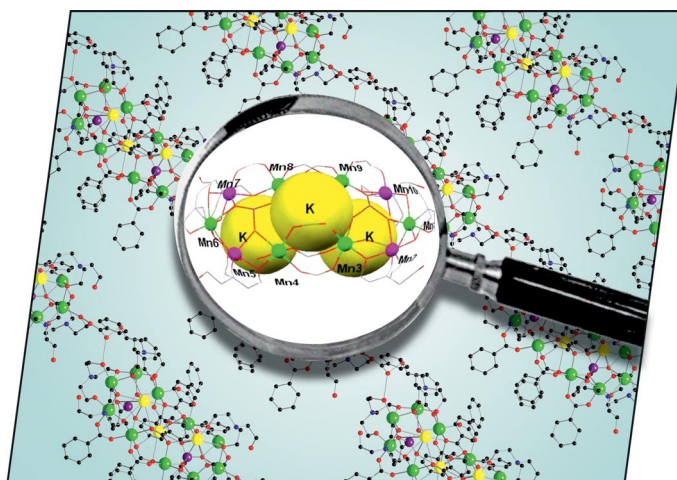


EurJIC is co-owned by 11 societies of ChemPubSoc Europe, a union of European chemical societies for the purpose of publishing high-quality science. All owners merged their national journals to form two leading chemistry journals, the *European Journal of Inorganic Chemistry* and the *European Journal of Organic Chemistry*. Three further members of ChemPubSoc Europe (Austria, Czech Republic and Sweden) are Associates of the two journals.

Other ChemPubSoc Europe journals are *Chemistry – A European Journal*, *ChemBioChem*, *ChemPhysChem*, *ChemMedChem*, *ChemSusChem* and *ChemCatChem*.

COVER PICTURE

The cover picture shows a mixed-valence $\{\text{Mn}_{10}\}$ cage, which can be regarded as an analogue of 24-metallacrown-10. The cage is a host for three potassium ions and crystallises as a cation; benzoate anions link the cages into a 1D polymer within the crystal. Details are discussed in the article by C. Dendrinou-Samara, R. E. P. Winpenny et al. on p. 3097ff. The authors thank Mrs. A. Samara for the artwork of the cover picture.





On these pages, we feature a selection of the excellent work that has recently been published in our sister journals. If you are reading these pages on a

computer, click on any of the items to read the full article. Otherwise please see the DOIs for easy online access through Wiley InterScience.

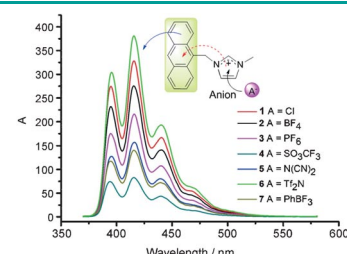


Functionalized Ionic Liquids

Z. Fei, D.-R. Zhu, X. Yang, L. Meng, Q. Lu, W. H. Ang, R. Scopelliti, C. G. Hartinger, P. J. Dyson*

An Internal Fluorescent Probe Based on Anthracene to Evaluate Cation–Anion Interactions in Imidazolium Salts

Cation–anion interactions: An anthracene moiety that has been incorporated into an imidazolium unit acts as an internal probe revealing insights into cation–anion interactions in the solid state and in solution (see graphic).



Chem. Eur. J.
DOI: 10.1002/chem.201000253

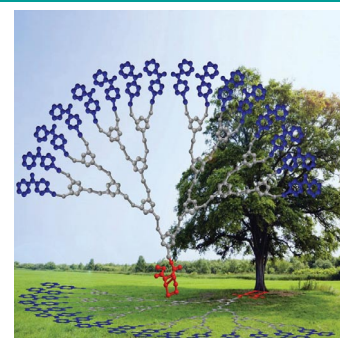


Energy Transfer

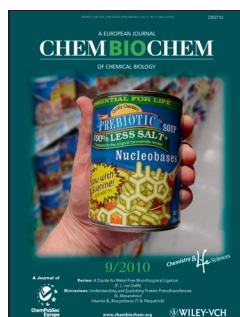
Y. Zeng, Y.-Y. Li, J. Chen,* G. Yang,* Y. Li*

Dendrimers: A Mimic Natural Light-Harvesting System

Passed on through the generations: Dendrimers are well-defined tree-like macromolecules having numerous chain ends all emanating from a single core, which make them mimics of natural light-harvesting systems. Recent developments of light-harvesting dendrimers will be discussed in this article, focusing on their energy transfer and electron transfer properties.



Chem. Asian J.
DOI: 10.1002/asia.200900653

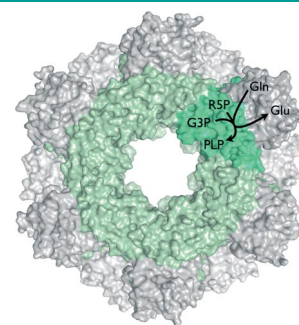


Vitamins

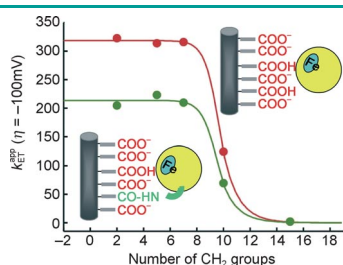
T. B. Fitzpatrick,* C. Moccand, C. Roux

Vitamin B₆ Biosynthesis: Charting the Mechanistic Landscape

Enzyme of the rings: Vitamin B₆ biosynthesis through the DXP-independent route is catalyzed by PLP synthase. The enzyme utilizes ribose 5-phosphate, glyceraldehyde 3-phosphate and ammonia to synthesize the cofactor form of the vitamin, pyridoxal 5'-phosphate (PLP). This review provides the emerging mechanistic details of this remarkable Pdx1:Pdx2 glutamine amidotransferase complex.



ChemBioChem
DOI: 10.1002/cbic.201000084



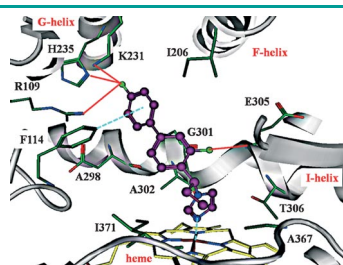
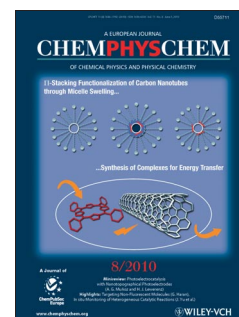
ChemPhysChem
DOI: 10.1002/cphc.200900966

Electron Transfer

H. K. Ly, M. A. Marti, D. F. Martin, D. Alvarez-Paggi, W. Meister, A. Kranich, I. M. Weidinger, P. Hildebrandt,* D. H. Murgida*

Thermal Fluctuations Determine the Electron-Transfer Rates of Cytochrome c in Electrostatic and Covalent Complexes

Interfacial electron-transfer processes of cytochrome c covalently or electrostatically bound to electrodes coated with self-assembled monolayers (SAMs) of ω -functionalized alkanethiols are studied by time-resolved surface-enhanced resonance Raman spectroscopy and molecular dynamics simulations (see picture).



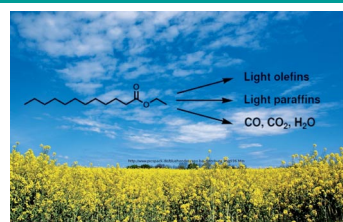
ChemMedChem
DOI: 10.1002/cmdc.201000065

Antitumor Agents

Q. Hu, M. Negri, S. Olgen, R. W. Hartmann*

The Role of Fluorine Substitution in Biphenyl Methylene Imidazole-Type CYP17 Inhibitors for the Treatment of Prostate Carcinoma

CYP17 inhibition is a promising approach for the treatment of prostate cancer. Modification of biphenyl methylene imidazoles by fluorine substitution significantly increases the inhibitory potency of this compound class and prolongs plasma half-life. Compound **9** (ball-and-stick structure) was found to be a potent CYP17 inhibitor ($IC_{50} = 131$ nM) with good pharmacokinetic properties.



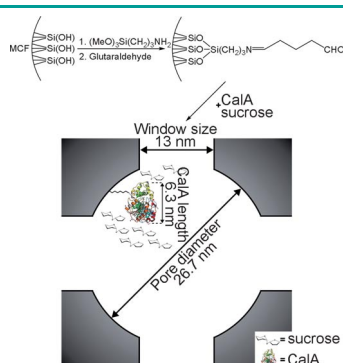
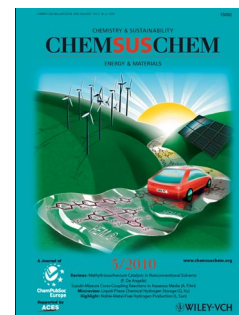
ChemSusChem
DOI: 10.1002/cssc.200900234

Biorenewables

O. Busse, K. Räuchle, W. Reschetilowski*

Hydrocracking of Ethyl Laurate on Bifunctional Micro-/Mesoporous Zeolite Catalysts

Olefins from biomass: Metal-modified micro- and mesoporous composite materials are promising catalyst systems for the conversion of ethyl laurate, as a model compound for vegetable oils. The selectivity to light olefins can be enhanced up to 60 wt %.



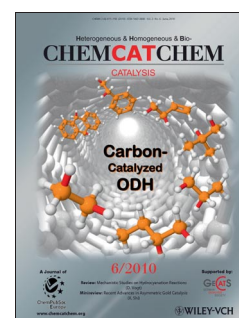
ChemCatChem
DOI: 10.1002/cctc.201000027

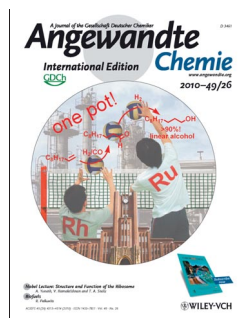
Supported Enzymes

M. Shakeri, K. Engström, A. G. Sandström, J.-E. Bäckvall*

Highly Enantioselective Resolution of β -Amino Esters by *Candida antarctica* Lipase A Immobilized in Mesocellular Foam: Application to Dynamic Kinetic Resolution.

***Candida antarctica* lipase A (CALA)** immobilized in functionalized mesocellular foam (MCF) in the presence of sucrose facilitated a dramatic increase in enantioselectivity for the kinetic resolution (KR) of representative β -amino esters. The temperature of optimum activity of CALA shifted from 20–30 °C to 80–90 °C on immobilization in the MCF. Combination of the immobilized CALA with a ruthenium complex allowed dynamic KR at 90 °C.



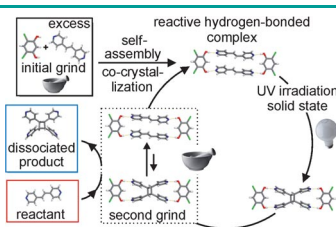


Supramolecular Catalysis

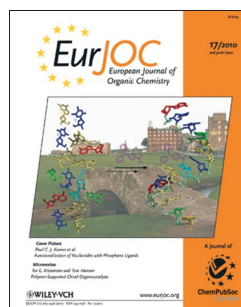
A. N. Sokolov, D.-K. Bučar, J. Baltrusaitis, S. X. Gu,
L. R. MacGillivray*

Supramolecular Catalysis in the Organic Solid State through Dry Grinding

Chemical mechanics: Hydrogen-bond-driven self-assembly and mechanochemistry are used to facilitate supramolecular catalysis in the solid state. Mortar-and-pestle grinding proves to be an efficient means to achieve co-crystal formation and turnover using a physical mixture composed of an olefin and catalytic amounts of a ditopic template (see scheme).



Angew. Chem. Int. Ed.
DOI: 10.1002/anie.201000874

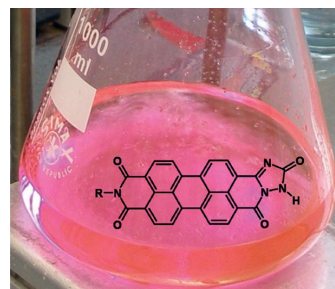


Red Fluorescence

H. Langhals,* T. Pust

Axially Extended Perylene Dyes

Perylenecarboxylic anhydride imides were condensed with semi-carbazide and thiosemicarbazide to obtain strongly red-fluorescent triazolinone and triazolinthione derivatives, respectively, suitable for nucleophilic labelling. A Schönberg reaction of the latter with diazoalkanes allowed the synthesis of spirothiiranes.



Eur. J. Org. Chem.
DOI: 10.1002/ejoc.201000230

New Journal

Heterogeneous, Homogeneous and BioCatalysis

www.chemcatchem.org

FREE ONLINE ACCESS

In 2010 for all users from institutions that have registered

Ask your librarian to register for complimentary online access TODAY

www.interscience.wiley.com/newjournals

Founding Societies:

A journal of

Transition-Metal-Rich Borides – Fascinating Crystal Structures and Magnetic Properties

Boniface P. T. Fokwa*[a]

Keywords: Transition metals / Boron / Structure elucidation / Density functional calculations / Magnetic properties

The ability to design and predict new phases in solid-state chemistry remains a challenge. However, experiment and theory have been working together in the last decade to find new phases with targeted magnetic properties in the family of transition-metal-rich borides. These studies were very successful for boride phases crystallizing with the $\text{Ti}_3\text{Co}_5\text{B}_2$ structure type. Furthermore, strong variations of the magnetic properties in some series of compounds as a function of the number of valence electrons were observed experimentally and explained by using density functional theory calcu-

lations. The $\text{Zn}_{11}\text{Rh}_{18}\text{B}_8$ and Th_7Fe_3 structure types have also produced many magnetically ordered phases, whereas the new $\text{Ti}_{1.6}\text{Os}_{1.4}\text{RuB}_2$ and $\text{Ti}_{1+x}\text{Rh}_{2-x+y}\text{Ir}_{3-y}\text{B}_2$ structure types have the potential to produce new materials with interesting magnetic properties. The large family of perovskite boride phases has welcomed new members whose structures enable the ordering of boron atoms and vacancies. Renewed interest has been observed for boride phases crystallizing with the Cr_{23}C_6 -type structure, whose magnetic properties were mainly studied before the nineties.

1 Introduction

Most research efforts in current solid-state chemistry are concerned with the design and prediction of new structures and materials. In general it is difficult to design a phase a priori.^[1] However, progress has been considerable, and we have many cases in which “materials design” is actually possible, for example, simple isoelectronic elemental substitutions, the intercalation of species into solids, the synthesis of coordination solids based on solid-state structures. Nevertheless, in most cases the ability to broadly design and predict new phases remains a challenge.^[2]

When it comes to the use of solid-state materials, the solid-state age does not show any sign of stopping at the present time. In the second half of the 20th century, micro-electronic chips with million transistors, solar photovoltaics and all solid-state lighting, cell phones, displays, data storage and retrieval benefit from the exciting properties of

solid-state materials. Magnetic compounds of course play a central role in our increasingly demanding information society. Therefore, it would be of great help to be able to rationally synthesize new magnetic compounds with predicted magnetic properties. However, this is far from being achievable, because of the complex nature of magnetism itself. In fact, even today, it remains difficult to understand why some materials are magnetically ordered whereas others are not. Nevertheless, some theoretical signposts, based on calculation techniques borrowed from solid-state quantum physics and chemical bonding concepts rooted in molecular quantum chemistry, have been introduced some years ago for the rational design of antiferromagnets and ferromagnets in some complex transition-metal borides.^[3] Borides are already playing a role in our modern world with applications such as hard materials (e.g. TiB_2),^[4] superconducting materials (MgB_2),^[5] and permanent magnets ($\text{Nd}_2\text{Fe}_{14}\text{B}$).^[6]

This work is devoted to a branch of solid-state chemistry that enables the use of both experiment and theory to study new structural and magnetic characteristics of transition-metal-rich borides. In general, itinerant magnetism (if compared with molecular magnetism) has not been extensively

[a] Institute of Inorganic Chemistry, RWTH Aachen University, 52056 Aachen, Germany
Fax: +49-241-8092642
E-mail: Boniface.fokwa@ac.rwth-aachen.de
Homepage: www.ssc.rwth-aachen.de/fokwa



Boniface P. T. Fokwa received his B.S. from the University of Yaounde I in 1998 and his D.E.A. the following year also from the same University. He then moved to Germany in 1999 to the University of Technology in Dresden, where he received his Ph.D. in 2003 under the supervision of Professors Peter Böttcher and Michael Ruck. Thereafter, he joined the group of Professor Richard Dronskowski at RWTH Aachen University, where he recently completed his habilitation. The research efforts of his group focus on experimental and theoretical solid-state chemistry, with a specific emphasis on structure–property relationships in metal-rich borides. He has received a fellowship (2004–2006) from the “Deutsche Forschungsgemeinschaft” (German Science Foundation).

studied, and the family of transition-metal-rich borides is no exception. However, systematic studies with the aim of achieving some targeted magnetic properties in a given structural family may help to enhance already known properties or find unforeseen ones. Very often, drastic changes of the magnetic properties (in isotypic phases) are achieved by modifying the magnetically active element. A different strategy is followed in this work; the magnetic properties of transition-metal-rich borides are experimentally and theoretically studied as a function of the number of valence electrons (VE) alone (the magnetically active element remaining unchanged), for a given series of isotypic compounds. In addition, theory [density functional theory (DFT)] and experiment have been used in a synergistic way to explain some unexpected structural or magnetic phenomena on the one side, and to discover new phases with potentially interesting magnetic properties on the other.

2 Borides Containing Chains of a Magnetically Active Element

2.1 Crystal Chemistry of $\text{Ti}_3\text{Co}_5\text{B}_2$ -Type Phases

$\text{Ti}_3\text{Co}_5\text{B}_2$ (space group $P4/mbm$, no. 127)^[7] is one of the most prolific structure types within the metal-rich boride family, as more than fifty isotypic phases have already been discovered: ternaries ($\text{A}_3\text{T}_5\text{B}_2$), quaternaries ($\text{A}_2\text{MT}_5\text{B}_2$), and quinary ($\text{A}_2\text{MT}_{5-n}\text{T}'_n\text{B}_2$).^[8–11] A large variety of elements have been used in the process: main group elements (Be, B, Mg–P, Ga–As), 3d (Sc–Zn), 4d (Nb, Ru, Rh), and 5d (Hf, Ta, Ir) transition metals.

The ternary phases, with the general formula $\text{A}_3\text{T}_5\text{B}_2$, are ordered substitutional variants of the $\text{Ti}_3\text{Co}_5\text{B}_2$ structure type, where A (Mg, Sc, Ti, Nb, Hf, Ta) represents the largest element and is pentagonal- and tetragonal-prismatically coordinated by the electron-rich but smaller T (Co, Ru, Rh, Ir) atoms, whereas the boron atom is trigonal-prismatically coordinated by the T atoms. The prisms are face-connected, building a three-dimensional network (Figure 1, left).

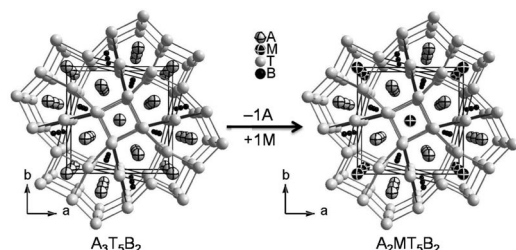


Figure 1. Perspective views along the [001] direction of the crystal structures of the ternary phases $\text{A}_3\text{T}_5\text{B}_2$ (left, e.g. $\text{Sc}_3\text{Rh}_5\text{B}_2$) and of the quaternary phases $\text{A}_2\text{MT}_5\text{B}_2$ (right, e.g. $\text{Sc}_2\text{FeRh}_5\text{B}_2$).

The ordered quaternary substitutional variants are obtained after substitution of the tetragonal-prismatically coordinated A atoms by smaller elements M (Be, Al–P, Ti–Zn, Ga–As). A perspective view of the structure of these quaternary phases ($\text{A}_2\text{MT}_5\text{B}_2$) along [001] is shown in

Figure 1 (right). It has to be mentioned that some arsenic- and phosphorus-deficient phases were also reported ($\text{Mg}_2\text{As}_{0.9}\text{Rh}_5\text{B}_2$ and $\text{Mg}_2\text{P}_{0.9}\text{Rh}_5\text{B}_2$).^[10] Other quaternary, partially ordered phases are obtained when some T atoms are substituted in the ternaries $\text{A}_3\text{T}_5\text{B}_2$, which leads to $\text{A}_3\text{T}_{5-x}\text{T}'_x\text{B}_2$ phases. This type of substitution was successful for the newly synthesized $\text{Ti}_{3-x}\text{Ru}_{5-y}\text{Ir}_y\text{B}_{2+x}$ complex solid solution. The member with $x = 1$ has the particularity that boron is found not only in the usual trigonal prisms but also for the first time in the tetragonal prisms.^[12a]

Quinary ($\text{A}_2\text{MT}_{5-n}\text{T}'_n\text{B}_2$) phases are achieved by substituting some T atoms (e.g. Ru) in the quaternary $\text{A}_2\text{MT}_5\text{B}_2$ by one-electron-richer T' atoms (e.g. Rh). So far, $\text{Sc}_2\text{MnRu}_2\text{Rh}_3\text{B}_2$ ^[3] and the two series of compounds $\text{Sc}_2\text{FeRu}_{5-n}\text{Rh}_n\text{B}_2$ ($n = 0–5$)^[13] and $\text{Ti}_2\text{FeRu}_{5-n}\text{Rh}_n\text{B}_2$ ($n = 1–5$)^[14] were obtained. In these quinarys, the ruthenium and rhodium atoms are assumed to be statistically distributed at their two available sites (8j and 2c), because they cannot be distinguished by X-ray diffraction methods (they differ from each other just by a single electron). Substituting rhodium in $\text{Ti}_2\text{FeRu}_{5-n}\text{Rh}_n\text{B}_2$ by the electron-richer congener iridium enables the study of the site preference and the distribution of ruthenium and iridium atoms in these two sites. In fact, the coordination environment is different for the two sites, the 2c site sitting in the smaller polyhedron. The obtained new series $\text{Ti}_2\text{FeRu}_{5-n}\text{Ir}_n\text{B}_2$ ($n = 1–4$) has the same structure type as the others and, as expected, a site-preferential substitution is observed: Although both elements are mixed in each Wyckoff site, ruthenium prefers the 2c Wyckoff site, whereas iridium sits preferentially on 8j.^[12b]

Of particular interest are quaternary and quinary phases containing a magnetically active element (Cr–Ni), because they may induce magnetic ordering in the respective phases. As stated above, the magnetically active atoms are found in the tetragonal prisms (8j site), and the fact that the prisms are face-connected enables significant interaction between neighboring atoms in the [001] direction, thus leading to chains with intrachain distances of exactly the lattice parameter c (ca. 3.0 Å), whereas interchain distances are more than two times longer (ca. 6.6 Å), indicating rather weak interaction between the chains (Figure 2).

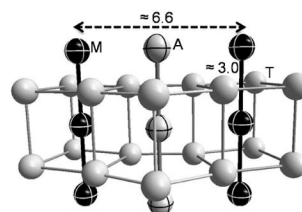


Figure 2. Part of the crystal structure of the $\text{A}_2\text{MT}_5\text{B}_2$ phases showing the intrachain and interchain M–M interactions (M = magnetically active element).

Such chains of a magnetically active element have been the subject of intense studies within the nonmetallic (salt-like) compounds (e.g. in ref.^[15]). However, little was known on the magnetic properties of their metallic counterparts,

although Weinert et al. showed in 1983 by electronic structure calculations that one-dimensional metallic iron and nickel lattices give rise to magnetic moments and exchange interactions comparable to those found in the bulk.^[16] The discovery of the above-mentioned first quaternary phases of the $\text{Ti}_3\text{Co}_5\text{B}_2$ structure type by Jung et al. in 1990^[8a] then enabled the study of the magnetism induced by such a low-dimensional substructure of a magnetically active element.

2.2 Magnetic Properties of $\text{Ti}_3\text{Co}_5\text{B}_2$ -Type Phases

Magnetic studies by Jung et al. have revealed evidence for antiferromagnetic (e.g. $\text{Mg}_2\text{MnRh}_5\text{B}_2$, $T_N = 3\text{ K}$, $\theta = -130\text{ K}$), metamagnetic ($\text{Sc}_2\text{MnRh}_5\text{B}_2$, $T_N = 130\text{ K}$, $\theta = 270\text{ K}$), and ferromagnetic (e.g. $\text{Sc}_2\text{FeRh}_5\text{B}_2$ with $T_C = 450\text{ K}$) ordering,^[8–10] where T_N , T_C , and θ are the Néel temperature, the Curie temperature, and the Weiss constant, respectively. Theoretical calculations by Dronskowski et al. predicted the phases with 62 valence electrons (VE) [e.g. $\text{Mg}_2\text{MnRh}_5\text{B}_2$, 62 VE = $2 \times 2\text{ (Mg)} + 1 \times 7\text{ (Mn)} + 5 \times 9\text{ (Rh)} + 2 \times 3\text{ (B)}$] to be antiferromagnets and those with 65 VE (e.g. $\text{Sc}_2\text{FeRh}_5\text{B}_2$) to be ferromagnets.^[3] Systematic studies of the magnetic properties as a function of the number of VE in these phases were then carried out, because nothing could safely be predicted below the 62 VE limit, for the 62–65 VE regime, and above 65 VE.

2.2.1 From Antiferromagnetism to Ferromagnetism in $\text{Sc}_2\text{FeRu}_{5-n}\text{Rh}_n\text{B}_2$

The series of compounds $\text{Sc}_2\text{FeRu}_{5-n}\text{Rh}_n\text{B}_2$ ($0 \leq n \leq 5$) was studied both experimentally and theoretically. This series allows for a synthetic scan of adequate candidates for the investigation of the range $60 \leq \text{VE} \leq 65$, in particular, as they differ from each other exclusively in the Ru/Rh ratio, they seem ideal for the chemical tuning of the VE.^[13] Furthermore, electronic structure calculations on this series help to understand the nature of magnetic coupling in this series, in particular the influence of 4d–3d Rh/Ru–Fe interactions on the total effective coupling of the Fe atoms as compared to the 3d–3d Fe–Fe interactions.^[17]

At high temperatures, the magnetic susceptibilities of the characterized^[8–10] intermetallics $\text{Sc}_2\text{FeRu}_5\text{B}_2$ (60 VE) and $\text{Sc}_2\text{FeRu}_3\text{Rh}_2\text{B}_2$ (62 VE) obey the Curie–Weiss law $\chi_m =$

$C/(T - \theta)$. The experimentally obtained Curie constants $C = 2.4 \times 10^{-5}\text{ m}^3\text{ K mol}^{-1}$ and $C = 2.5 \times 10^{-5}\text{ m}^3\text{ K mol}^{-1}$ correspond to paramagnetic moments $\mu = 3.9\text{ }\mu_B$ and $4.0\text{ }\mu_B$ and Weiss constants of $\theta = -995\text{ K}$ and -90 K , respectively, indicating much stronger antiferromagnetic Fe–Fe interactions for the former. The overall high-temperature behavior for $\text{Sc}_2\text{FeRu}_4\text{RhB}_2$ (61 VE) also points to considerable antiferromagnetic Fe–Fe interactions, although no Curie–Weiss behavior was observed. This finding becomes obvious by comparing the μ_{eff} data [for the definition see footnote (b) of Table 1], namely $\mu_{\text{eff}} = 2.1, 3.2$, and 3.6 at 400 K for the systems with 60, 61, and 62 VE, respectively (Table 1). In this series, the 61 VE compound takes up the intermediate position. The μ_{eff} vs. T curves for the 60, 61, and 62 VE phases (Figure 3) clearly reveal a decrease in the antiferromagnetic exchange interactions as the VE count increases; the incremental step is more pronounced from 60 to 61 VE than from 61 to 62 VE. In other words, the antiferromagnetic Fe–Fe interactions weaken when the VE count increases from 60 to 62.^[13]

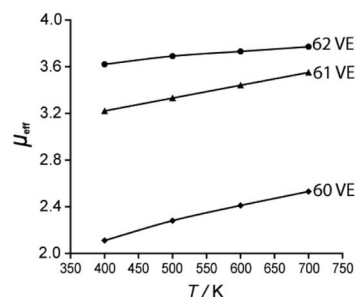


Figure 3. Effective magnetic moment vs. temperature for $\text{Sc}_2\text{FeRu}_5\text{B}_2$ (60 VE), $\text{Sc}_2\text{FeRu}_4\text{RhB}_2$ (61 VE), and $\text{Sc}_2\text{FeRu}_3\text{Rh}_2\text{B}_2$ (62 VE).

Further increasing VE from 62 to 63 changes the Weiss constant dramatically from -90 K to $+375\text{ K}$, thereby inducing a change in the nature of the magnetic ordering and leading to a ferromagnet with a Curie temperature $T_C \approx 300\text{ K}$. Further increments of VE by one and two electrons strengthen the ferromagnetic behavior even more. For 64 and 65 VE, T_C increases to 350 K (Figure 4) and 450 K , and μ_a increases to $3.1\text{ }\mu_B$ and $3.3\text{ }\mu_B$ respectively (Table 2). Hence the Fe–Fe ferromagnetic interactions increase significantly between 63 and 65 VE with an increase in the number of valence electrons.

Table 1. Magnetic quantities for the compound series $\text{Sc}_2\text{FeRu}_{5-n}\text{Rh}_n\text{B}_2$ ($0 \leq n \leq 5$).

n	VE	AF, F	$T_N, T_C/\text{K}$	$\mu_a^{[a]}/\mu_B$	$\mu_{\text{eff}}^{[b]}(400\text{ K})$	$\mu^{[c]}/\mu_B$	θ/K	Range /K	Ref.
0	60	AF	ca. 13 (T_N)	–	2.1	3.9	–995	500–770	[8]
1	61	AF	ca. 10 (T_N)	0.08	3.2	no Curie–Weiss behavior			[13]
2	62	AF	–	–	3.6	4.0	–90	100–400	[3]
3	63	F	ca. 300 (T_C)	3	–	4.2	375	500–800	[13]
4	64	F	ca. 350 (T_C)	3.1	no Curie–Weiss behavior				[13]
5	65	F	ca. 450 (T_C)	3.3	no Curie–Weiss behavior				[10]

[a] μ_a : atomic magnetic dipole moment at 4 K and $B_0 = 5\text{ T}$. [b] μ_{eff} : effective Bohr magneton number; $\chi_m = \mu_0 \frac{N_A \mu_B^2}{3k_B T} \mu_{\text{eff}}^2$; $\mu_{\text{eff}} = 797.74(\chi_m T)^{1/2}$ (SI units). [c] μ : permanent paramagnetic moment calculated from the Curie constant C .

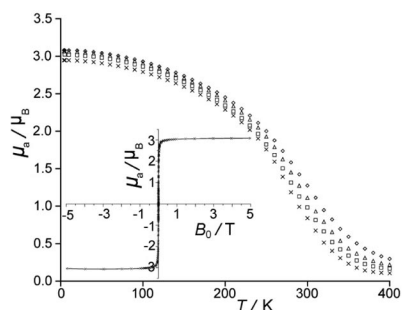


Figure 4. Magnetization vs. temperature for $\text{Sc}_2\text{FeRuRh}_4\text{B}_2$ (64 VE) at various applied fields: $B_0 = 2$ T ($\diamond\diamond\diamond$), 1 T ($\triangle\triangle\triangle$), 0.5 T ($\square\square\square$), and 0.2 T ($\times\times\times$). Inset: Hysteresis loop at 4.5 K.

Table 2. Magnetic quantities for the compound series $\text{Ti}_2\text{FeRu}_{5-n}\text{Rh}_n\text{B}_2$ ($1 \leq n \leq 5$).

n	VE	$\theta^{[a]}$ / K	$\mu^{[b]}$ / μ_B	CW range / K	T_C / K	$\mu_a^{[c]}$ / μ_B	$H_C^{[d]}$ / kA m^{-1}
5	67	+200	5.1	≥ 250	ca. 208	2.3	0.9
4	66	no CW behavior until 400 K			≥ 350	3.1	2.4
3	65	no CW behavior until 400 K			≥ 350	2.2	1.6
2	64	+230	5.0	≥ 300	ca. 285	1.7	10.3
1	63	+175	3.7	≥ 250	ca. 220	0.6	23.9

[a] θ : Weiss constant determined from Curie–Weiss (CW) straight lines in χ_m^{-1} vs. T plots. [b] μ : permanent paramagnetic moment calculated from the Curie constant C by using $\mu = 797.74C^{1/2}$. [c] μ_a : atomic magnetic dipole moment at 5 K and $B_0 = 4.5$ T, $\mu_a = M_m/N_A$, measured in Bohr magnetons (μ_B) (M_m : magnetization per mol, N_A : Avogadro's number). [d] H_c : coercivity obtained from the hysteresis loops recorded at $-4.5 \leq B_0 \leq 4.5$ T and 5 K.

To conclude, with an increasing VE count from 60 to 65, the series $\text{Sc}_2\text{FeRu}_{5-n}\text{Rh}_n\text{B}_2$ ($0 \leq n \leq 5$) exhibits a clear trend from antiferromagnetism to ferromagnetism. This result was also correctly reproduced by first-principles density functional calculations of the ground-state magnetic ordering and exchange-interaction parameters.

A DFT-based crystal orbital Hamilton population (COHP) analysis made it possible to understand, from a chemical perspective, the nature of the magnetic behavior in the quaternary intermetallic borides $\text{A}_2\text{MT}_5\text{B}_2$.^[3] Ferromagnets have 65 valence electrons per formula unit (e.g. $\text{Sc}_2\text{FeRh}_5\text{B}_2$), the Fermi level falling within M–M antibonding states, whereas antiferromagnets, for example, $\text{Mg}_2\text{MnRh}_5\text{B}_2$, have 62 valence electrons, where the Fermi level falls within M–M nonbonding states (Figure 5a). These findings eventually allowed further experimental search for new ferromagnets and antiferromagnets and successfully led to the discovery of both $\text{Sc}_2\text{MnRu}_2\text{Rh}_3\text{B}_2$ and $\text{Sc}_2\text{FeRu}_3\text{Rh}_2\text{B}_2$.^[3,8] These two isotypic compounds both contain 62 valence electrons and, as predicted, both are itinerant antiferromagnets. Figure 5b illustrates the course of the effective exchange coupling parameter, J_0 , for the T site as a function of the number of valence electrons per formula unit for the $\text{Sc}_2\text{FeRu}_{5-n}\text{Rh}_n\text{B}_2$ series, a parameter which was calculated within a rigid-band model specifically.^[17] This dependence provides a relevant description of the stability of ferromagnetic and antiferromagnetic order in these phases. Clearly, the different valence electron

counts make $\text{Sc}_2\text{FeRh}_5\text{B}_2$ a ferromagnet and $\text{Sc}_2\text{FeRu}_5\text{B}_2$ an antiferromagnet. The crossover between antiferromagnetic and ferromagnetic ordering is achieved at a valence electron count between 62 and 63 electrons; below this number, antiferromagnetic ordering is preferred, which is in perfect agreement with the COHP picture (Figure 5a) and the experiment described above.

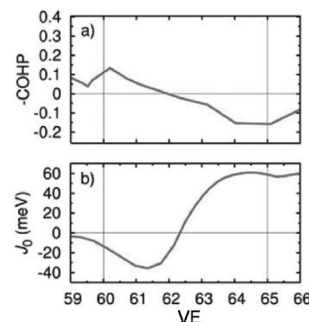


Figure 5. (a) Variation of Fe–Fe–COHP values with the number of valence electrons (VE) per formula unit for the $\text{Sc}_2\text{FeRu}_{5-n}\text{Rh}_n\text{B}_2$ series based on a calculation of nonmagnetic $\text{Sc}_2\text{FeRh}_5\text{B}_2$. (b) Effective exchange coupling parameter, J_0 , as a function of VE for the Fe site based on ferromagnetic $\text{Sc}_2\text{FeRh}_5\text{B}_2$. Vertical lines indicate E_F (Fermi level) values for $\text{Sc}_2\text{FeRh}_5\text{B}_2$ (65 electrons) and $\text{Sc}_2\text{FeRu}_5\text{B}_2$ (60 electrons), respectively.

2.2.2 One-Electron-Step Evolution from Soft to Semi-Hard Magnets in $\text{Ti}_2\text{FeRu}_{5-n}\text{Rh}_n\text{B}_2$

DFT calculations on the $\text{Sc}_2\text{FeRu}_{5-n}\text{Rh}_n\text{B}_2$ series reveal that the contributions of scandium and boron to the magnetic properties are negligible. Nonetheless, it would be interesting to see which influence an additional electron on the scandium site (replacing scandium with titanium) may have on the magnetic properties. The resulting compound series $\text{Ti}_2\text{FeRu}_{5-n}\text{Rh}_n\text{B}_2$ was successfully synthesized for $n = 1$ –5 (VE = 63, 64–67),^[14] and the obtained lattice parameters (a and c) vary in opposite directions, leading to little volume change. This series enables the investigation of phases with more than 65 VE: The phases $\text{Ti}_2\text{FeRuRh}_4\text{B}_2$ (66 VE) and $\text{Ti}_2\text{FeRh}_5\text{B}_2$ (67 VE) are both ferromagnetically ordered with Curie temperatures higher than 200 K and have μ_a values (at an applied field of 4.5 T at 5 K) of 3.1 μ_B and 2.3 μ_B , respectively. Overall in the series, μ_a increases from 0.6 μ_B (63 VE) to a maximum of 3.1 μ_B (66 VE) and then decreases to 2.3 μ_B (67 VE) (Table 2).

Magnetic materials are classified, on the basis of their coercive field strength, into hard (very large hysteresis loop with coercive field $H_c > 30$ kA/m) and soft (very narrow hysteresis loop, $H_c < 1$ kA/m). A group of semi-hard magnetic materials with coercive fields lying in the intervening range has also gained some importance.^[18–20] The best hard magnetic materials (at room temperature) known to date are the metal-rich borides with the general formula $(\text{RE})_2\text{Fe}_{14}\text{B}$ (RE = rare earth element) having extremely high coercive fields ($H_c > 600$ kA/m).^[21] The presence of a rare earth element is fundamental for the achievement of this hard magnetic property. In fact, materials containing only magnetically active transition metals (i.e. without any

rare earth metal) as magnetic centers often show soft magnetic properties, reminiscent of the very soft magnetic transition elements (Fe, Co, Ni) and some of their alloys.^[22] Transition-metal borides containing these magnetically active transition metals make no exception (e.g. the technologically important iron borides are soft ferromagnets).^[23] To the best of my knowledge, all ferromagnetic transition-metal borides characterized so far are soft. The trend was also verified in all ferromagnetic complex borides $A_2M'T_5B_2$ ($Ti_3Co_5B_2$ structure type).^[8]

The ferromagnets of the $Sc_2FeRu_{5-n}Rh_nB_2$ compound series ($n = 3-5$, VE = 63–65) are, according to their very small coercive field ($H_c < 1$ kA/m, see for example inset of Figure 4), classified as soft ferromagnetic materials. A substitution of scandium by titanium in this series leads to the phases $Ti_2FeRu_{5-n}Rh_nB_2$ ($n = 3-5$, VE = 65–67). Among these new ferromagnets, only the phase with the highest VE (67) has an H_c value (0.9 kA m^{-1}) lower than 1 kA m^{-1} , the two others (VE = 65 and 66) exhibit H_c values (2.4 and 1.6 kA m^{-1}) significantly higher than 1 kA m^{-1} . This enlargement of the hysteresis loop (Figure 6) is solely attributed to the additional electrons added after substituting scandium by titanium (note that both are not magnetically active). Decreasing VE further to 64 and 63 dramatically increases H_c , which reaches 10.3 kA m^{-1} at 64 VE, then 23.9 kA m^{-1} at 63 VE (Figure 6 and Table 2). Therefore, a clear trend is observed in the $Ti_2FeRu_{5-n}Rh_nB_2$ series: An evolution from soft to semi-hard ferromagnetic materials is obtained when VE decreases from 67 to 63.^[14]

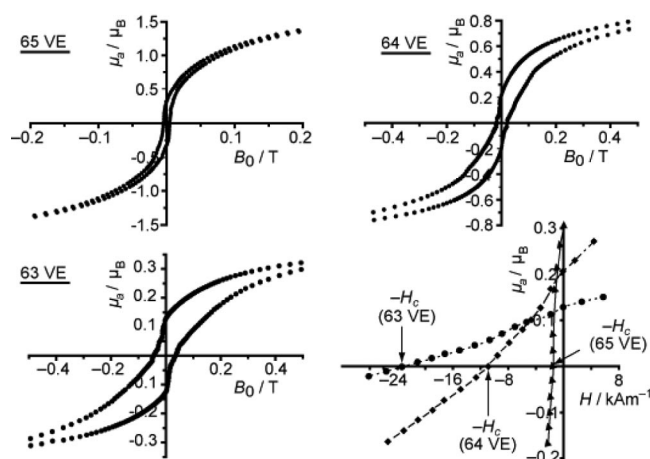


Figure 6. Central parts of the hysteresis loops μ_a vs. B_0 [recorded at 5 K and $-4.5 \leq B_0 \leq 4.5$ T] in the $Ti_2FeRu_{5-n}Rh_nB_2$ series showing their enlargement with decreasing number of valence electron (VE) from 65 to 63. Bottom right: enlarged left parts of these hysteresis loops showing the increase in coercivity H_c with decreasing VE.

This finding opens a new direction in the research of novel magnetic materials not only in the field of transition-metal-rich borides, but in the entire family of magnetic intermetallics: In this family, the need to enhance the coercivity of a given magnetic material may be achieved by the substitution of a magnetically “silent” element by titanium.

2.2.3 Slater–Pauling Behavior and Prediction of Other Magnetic $M_2M'Ru_{5-n}Rh_nB_2$ Series

From the results given above, the magnetic properties of both the $Sc_2FeRu_{5-n}Rh_nB_2$ and the $Ti_2FeRu_{5-n}Rh_nB_2$ series can be divided in two ranges depending on the number of VE: In the range between 60 and 62 VE, antiferromagnets are found, whereas ferromagnets are observed between 63 and 67 VE (Tables 1 and 2). In the antiferromagnetic range, continuous decreasing antiferromagnetic interactions are observed, whereas in the ferromagnetic range the ferromagnetic interactions increase up to 66 VE and then decrease.

On a theoretical point of view, first-principles density functional calculations were used to characterize four series of phases with the general composition $M_2M'Ru_{5-n}Rh_nB_2$. The result shows that the variation in saturation magnetic moment with valence-electron count follows a Slater–Pauling curve, a maximum moment occurring typically at 66 valence electrons (Table 3), as observed experimentally in the $Ti_2FeRu_{5-n}Rh_nB_2$ series (Table 2). Two of the series, $Sc_2CoRu_{5-n}Rh_nB_2$ and $Nb_2FeRu_{5-n}Rh_nB_2$, are promising candidates yet to be synthesized, and the highest moments were predicted in the Nb series.^[24]

Table 3. Theoretically predicted^[24] (VASP-GGA) and experimentally determined saturation magnetic moments in Bohr magnetons (μ_B), for different compositions of the $M_2M'Ru_{5-n}Rh_nB_2$ series at different number of valence electron (VE). The highest moment is obtained at 66 VE regardless of the series (highlighted column).

VE	63	64	65	66	67	68	69
$Sc_2FeRu_{5-n}Rh_nB_2$	3.5/ 3.0	4.1/ 3.1	4.3/ 3.3				
$Sc_2CoRu_{5-n}Rh_nB_2^{[a]}$	2.5	2.7	2.8	3.0			
$Ti_2FeRu_{5-n}Rh_nB_2$	3.1/ 0.6 ^[b]	3.8/ 1.7 ^[b]	4.3/ 2.2 ^[b]	4.4/ 3.1 ^[b]	4.0/ 2.3 ^[b]		
$Ti_2CoRu_{5-n}Rh_nB_2^{[a]}$	1.9	2.3	2.8	3.1	3.1	2.6	
$Nb_2FeRu_{5-n}Rh_nB_2^{[a]}$		3.4	4.1	4.5	4.3	4.3	4.0

[a] Predicted series yet to be synthesized. [b] Hysteresis is not saturated at $B_0 = 4.5$ T and $T = 5$ K.

3 Borides Containing Ladders of a Magnetically Active Element

3.1 Crystal Chemistry of $Zn_{11}Rh_{18}B_8$ -Type Phases

As demonstrated in the previous section, the $Ti_3Co_5B_2$ structure type, which accommodates chains of magnetically active elements, has spawned new compounds with a wide range of magnetic ordering: antiferromagnetism, metamagnetism, and ferromagnetism. Similar chains, composed of a magnetically active element, have also been observed in other transition-metal borides, $Zn_{10}MRh_{18}B_8$ ($M = Mn, Fe, Co, Ni$), with a $Zn_{11}Rh_{18}B_8$ -type structure (space group $P4/mbm$, no. 127), which is related to the aforementioned structure type (Figure 7a). The main difference between the two structure types is the additional presence of elongated hexagonal prisms in the $Zn_{11}Rh_{18}B_8$ -type structure, the consequence being a near doubling of the lattice parameter a while c remains unchanged. In these phases, the elongated hexagonal prisms are centered by dumbbells of zinc atoms.

To date, the magnetic properties of $\text{Zn}_{10}\text{MRh}_{18}\text{B}_8$ phases have not been published.^[25] Recently, a new quaternary substitutional variant of the $\text{Zn}_{11}\text{Rh}_{18}\text{B}_8$ structure type was discovered: $\text{Ti}_9\text{Fe}_2\text{Ru}_{18}\text{B}_8$ (Figure 7b).^[26] The particularity of this new complex boride is the presence of well-separated chains of iron dumbbells (Figure 7b, right). Such a ladder substructure had not been previously reported for a 3d magnetically active element (Cr, Mn, Fe, Co, Ni) in intermetallic compounds but does occur in the ionic compound AFe_2S_3 ($\text{A} = \text{K}, \text{Rb}, \text{Cs}$).^[27] It is, therefore, a substructure with numerous challenges and possibilities for magnetic structure, where it is expected that short-range magnetic ordering (in the dumbbell) competes with long-range ones (between the dumbbells).

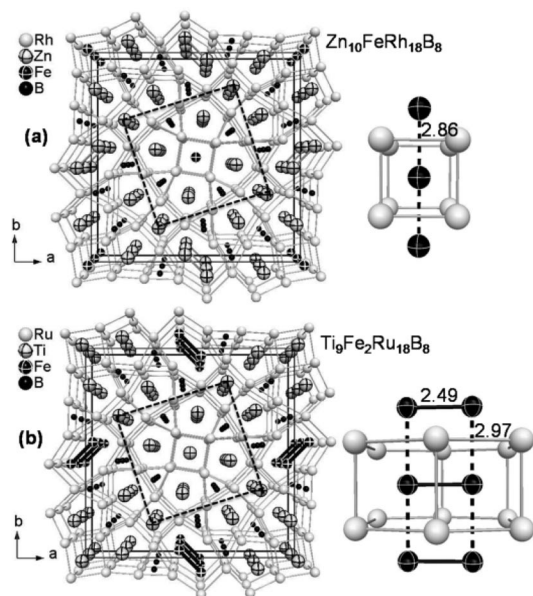


Figure 7. (a) Perspective view along [001] of the crystal structure of $\text{Zn}_{10}\text{FeRh}_{18}\text{B}_8$ (top left) and tetragonal prism of Rh atoms accommodating the Fe atom (top right). (b) Perspective view along [001] of the crystal structure of $\text{Ti}_9\text{Fe}_2\text{Ru}_{18}\text{B}_8$ (bottom left) and elongated hexagonal prism of Ru atoms encapsulating the Fe_2 dumbbell (bottom right); the dotted lines indicate the unit cell of the $\text{Ti}_3\text{Co}_5\text{B}_2$ -type structure. Significant Fe–Fe distances (in Å) are noted.

In the $\text{Zn}_{11}\text{Rh}_{18}\text{B}_8$ -type structure, iron atoms exhibit different local structures after replacing either zinc in $\text{Zn}_{11}\text{Rh}_{18}\text{B}_8$ or titanium in a hypothetical “ $\text{Ti}_{11}\text{Ru}_{18}\text{B}_8$ ”. In this structure type, both zinc and titanium atoms occupy tetragonal, pentagonal, and elongated hexagonal prisms of rhodium or ruthenium atoms, respectively, the elongated hexagonal prisms accommodating two atoms (as “dumbbells”). In terms of volume, one-half of the elongated hexagonal prism, that is, the volume accommodating only one atom of the dumbbell, is smaller than a single pentagonal prism but larger than a tetragonal prism. Consequently, if atomic size factors are influential for the stability of these compounds, substituting zinc and titanium by iron in $\text{Zn}_{11}\text{Rh}_{18}\text{B}_8$ and “ $\text{Ti}_{11}\text{Ru}_{18}\text{B}_8$ ”, respectively, should give the same result, since both zinc (atomic radius, $r_a = 1.31 \text{ Å}$) and titanium ($r_a = 1.38 \text{ Å}$) have clearly larger atomic radii than

iron ($r_a = 1.25 \text{ Å}$). However, different substitution patterns emerge: $\text{Zn}_{10}\text{FeRh}_{18}\text{B}_8$ finds iron replacing zinc atoms in the smallest tetragonal prism, as expected from size considerations; whereas in $\text{Ti}_9\text{Fe}_2\text{Ru}_{18}\text{B}_8$, iron has replaced titanium preferentially and unexpectedly in the elongated hexagonal prisms. Therefore, electronic factors should play a key role in understanding the substitutional preference of titanium by iron in hypothetical “ $\text{Ti}_{11}\text{Ru}_{18}\text{B}_8$ ” leading to $\text{Ti}_9\text{Fe}_2\text{Ru}_{18}\text{B}_8$. The synthesis of “ $\text{Ti}_{11}\text{Ru}_{18}\text{B}_8$ ”, if achievable, may offer a better understanding of the above-mentioned substitution preference. However, the tentative synthesis of “ $\text{Ti}_{11}\text{Ru}_{18}\text{B}_8$ ” leads to the phase $\text{Ti}_{10}\text{Ru}_{19}\text{B}_8$ instead, which is better described as a component of the $\text{Ti}_{11-x}\text{Ru}_{18+x}\text{B}_8$ solid solution, because a phase width was observed during the investigations.^[28]

By comparing $\text{Zn}_{11}\text{Rh}_{18}\text{B}_8$ with $\text{Ti}_{10}\text{Ru}_{19}\text{B}_8$ it becomes clear why different substitution patterns occur en route to the quaternaries $\text{Zn}_{10}\text{FeRh}_{18}\text{B}_8$ and $\text{Ti}_9\text{Fe}_2\text{Ru}_{18}\text{B}_8$. In the two ternary phases, zinc and titanium are present at the same sites with the exception of the $4h$ site, where Zn_2 and $(\text{Ti}/\text{Ru})_2$ dumbbells are found. In fact, all tetragonal and pentagonal prisms present in $\text{Zn}_{11}\text{Rh}_{18}\text{B}_8$ and $\text{Ti}_{10}\text{Ru}_{19}\text{B}_8$ (built up by rhodium and ruthenium, respectively) are centered by zinc or titanium, respectively, although both prisms are the smallest and the largest available for the two elements. The middle-sized prism (half the elongated hexagonal prism) is also centered as expected by zinc in $\text{Zn}_{11}\text{Rh}_{18}\text{B}_8$ but not by titanium alone (mixed with ruthenium) in $\text{Ti}_{10}\text{Ru}_{19}\text{B}_8$. The fact that titanium can only fill the $4h$ site together with the electron-rich but smaller ruthenium is the proof that this site needs more valence electrons than the four available for titanium. Therefore, the synthesis of the stoichiometric quaternary derivatives “ $\text{Ti}_9\text{M}_2\text{Ru}_{18}\text{B}_8$ ” ($\text{M} = \text{Cr}–\text{Zn}$) should be possible, because at this $4h$ site more valence electrons will be available from the M elements relative to titanium. Indeed these phases are all achievable,^[29] and they are isotypic with $\text{Ti}_9\text{Fe}_2\text{Ru}_{18}\text{B}_8$. On the contrary, the synthesis of stoichiometric “ $\text{Ti}_9\text{Sc}_2\text{Ru}_{18}\text{B}_8$ ” should not be possible. The VE-driven site preference observed in the Ti-based phases, particularly for the $4h$ site, is the main difference relative to the Zn-based phases of the $\text{Zn}_{11}\text{Rh}_{18}\text{B}_8$ structure type. It is also the main reason why stoichiometric “ $\text{Ti}_{11}\text{Ru}_{18}\text{B}_8$ ” is not accessible experimentally. Attempts to synthesize the $\text{Zn}_{10}\text{FeRh}_{18}\text{B}_8$ -related “ $\text{Ti}_{10}\text{FeRu}_{18}\text{B}_8$ ” also failed, as expected.^[12a]

The bonding situation was studied in detail for $\text{Ti}_9\text{Fe}_2\text{Ru}_{18}\text{B}_8$ phase by COHP bonding analysis, which shows that Ru–B and Ti–Ru contacts are responsible for the structural robustness while Fe–Fe interactions influence the magnetic behavior.

Because the distances observed in all isotypic $\text{Ti}_9\text{M}_2\text{Ru}_{18}\text{B}_8$ phases are in the expected ranges (comparable to those observed in $\text{Ti}_9\text{Fe}_2\text{Ru}_{18}\text{B}_8$), it is expected that the same leading interactions prevail in these phases. Like in $\text{Ti}_9\text{Fe}_2\text{Ru}_{18}\text{B}_8$, the COHP curves of all phases indicate that Ru–B and Ru–Ti orbital interactions are optimized: bonding orbitals are filled; antibonding orbitals are empty. Ru–M, M–M and Ru–Ru contacts show antibonding character

around the Fermi level. This COHP analysis suggests that it is the heteroatomic Ru–B and Ru–Ti bonds that create the structural stability of these phases.

In the $\text{Ti}_9\text{M}_2\text{Ru}_{18}\text{B}_8$ ($\text{M} = \text{Mn–Cu}$) series, the Ru–B, Ru–Ti, and Ru–Ru contacts are VE-independent, because their respective integral crystal orbital Hamiltonian population (ICOHP) values remain nearly constant, whereas the M-containing distances, Ru–M and M–M, are strongly VE-dependent: The ICOHP values of the M–M interatomic distances increase rapidly from -2.22 eV (Cr–Cr) to -0.87 eV (Cu–Cu) with increasing VE number from 216 to 226, and those of Ru–M interactions vary in the same manner but from -1.48 eV (Cr–Ru) to -1.01 eV (Cu–Ru) (Figure 8).

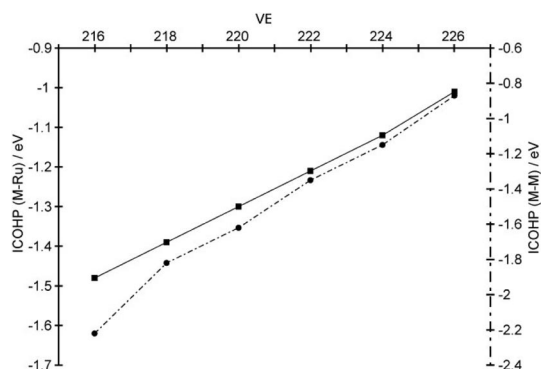


Figure 8. Plots of the ICOHP values of M–M and M–Ru bonds as a function of the number of valence electrons (VE) in the $\text{Ti}_9\text{M}_2\text{Ru}_{18}\text{B}_8$ ($\text{M} = \text{Cr, Mn, Fe, Co, Ni}$ and Cu) series.

A closer examination of the crystal structure of $\text{Ti}_9\text{Fe}_2\text{Ru}_{18}\text{B}_8$ reveals the presence of chains of titanium atoms (ca. 3 Å from the iron ladders), which, if substituted by chains of a magnetically active element, will induce magnetic interactions between both substructures. Theoretical density of states (DOS) of $\text{Ti}_9\text{Fe}_2\text{Ru}_{18}\text{B}_8$ strengthens this idea, because a pseudogap was found at approximately 0.5 eV above the Fermi level,^[26] which indicates that the structure of $\text{Ti}_9\text{Fe}_2\text{Ru}_{18}\text{B}_8$ may even be more stabilized by some additional valence electrons. Therefore, a substitution of titanium by any of the magnetically active elements (Cr, Mn, Fe, Co, Ni) may be possible, because this process enhances the number of valence electrons. Indeed, single phases $\text{Ti}_8\text{M}_3\text{Ru}_{18}\text{B}_8$ ($\text{M} = \text{Fe, Co}$) have been successfully

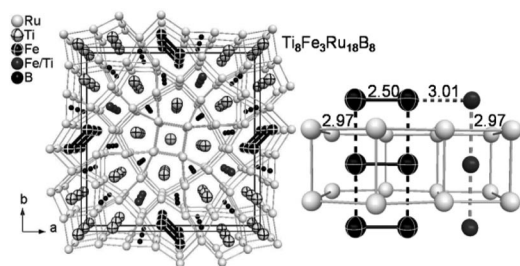


Figure 9. Perspective view along [001] of the crystal structure of $\text{Ti}_8\text{Fe}_3\text{Ru}_{18}\text{B}_8$ (left) and part of it showing interactions between the Fe ladder and the Ti/Fe chain (right): all distances are given in Å.

synthesized, and the remaining phases ($\text{M} = \text{Cr, Mn, Ni}$) were obtained with at least 80% yield. Single-crystal structure analysis of $\text{Ti}_8\text{Fe}_3\text{Ru}_{18}\text{B}_8$ reveals that all available tetragonal prisms are centered by a mixture of titanium and iron atoms (Figure 9). This model was then successfully applied in the Rietveld refinements of all phases.^[12a]

3.2 Magnetic Properties of $\text{Ti}_9\text{M}_2\text{Ru}_{18}\text{B}_8$ ($\text{M} = \text{Cr–Ni}$)

As stated above, COHP bonding analysis indicates that the Fe–Fe interactions influence the magnetic behavior. In fact, ferromagnetic order is predicted by the COHP analysis of the Fe–Fe interactions within the structure of $\text{Ti}_9\text{Fe}_2\text{Ru}_{18}\text{B}_8$: Antibonding Fe–Fe interactions, which are observed at the Fermi level, point towards a potential instability of the system with respect to spin polarization. Given a sufficient exchange splitting, a redistribution of the electron spins to establish a net magnetization of the system may annihilate antibonding interactions and lower the total energy (Figure 10).^[26] This effect takes place here, as the observed antibonding interactions at the Fermi level in the Fe–Fe COHP curve for the “nonmagnetic” case disappear upon splitting into majority and minority spin bands after spin polarization.

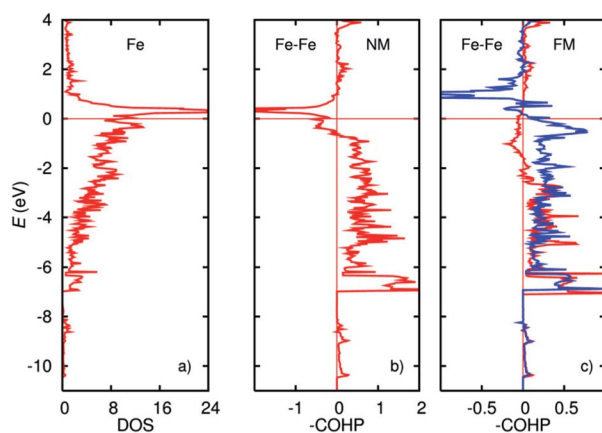


Figure 10. Partial DOS of Fe atoms (a) and COHP curves for Fe–Fe bonds in $\text{Ti}_9\text{Fe}_2\text{Ru}_{18}\text{B}_8$, (b) for the non-spin-polarized case and (c) for the spin-polarized case (showing majority and minority spin bands). The Fermi level is the energy reference. NM: nonmagnetic, FM: ferromagnetic.

According to the variation of the atomic magnetic dipole moment (μ_a) vs. applied field, a relatively small field of 0.05 T at 5 K is required to induce a μ_a value of $0.3 \mu_B$. Upon increasing the field, μ_a rapidly increases, doubling in value for an applied field of 1.2 T, but remaining unsaturated, reaching a value of $1.2 \mu_B$, up to a field of 7 T, the highest field measured (Figure 11). As there is only one iron site in the structure, $\text{Ti}_9\text{Fe}_2\text{Ru}_{18}\text{B}_8$ is a ferromagnet exhibiting spontaneous magnetization below a Curie temperature (T_C) of approximately 200 K.^[26]

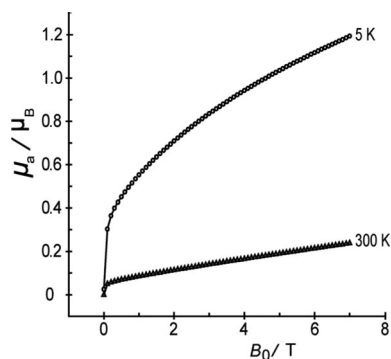


Figure 11. Atomic magnetic dipole moment (μ_a) vs. applied field at 5 K and 300 K for $\text{Ti}_9\text{Fe}_2\text{Ru}_{18}\text{B}_8$.

Ferromagnetic coupling between Fe atoms in the Fe_2 dumbbell with such a short Fe–Fe distance (2.49 Å) may seem surprising. However, the site symmetry of this dimer is D_{2h} (mmm) in the crystal. A molecular orbital analysis of an Fe_2 dimer in this site symmetry suggests that the ferromagnetic coupling within the dumbbell could be the result of Hund's rule for a half-filled, nearly degenerate pair of Fe–Fe π^* molecular orbitals. Figure 12 illustrates the results of molecular orbital calculations on a neutral Fe_2 dimer (in the intermetallic compound, there is very little net charge transfer, just a redistribution of orbital occupations). In the gas-phase Fe_2 molecule (point group $D_{\infty h}$), the HOMOs are the half-filled, doubly degenerate π^* orbitals. In the crystal under D_{2h} site symmetry, all degeneracies are strictly broken and hybridization can occur within the Fe–Fe σ and δ bonding/antibonding orbitals, but not with the π bonding/antibonding orbitals. Therefore, the π^* orbitals remain nearly degenerate and half-filled. According to Hund's rule, the most stable electronic configuration will be a spin triplet. Therefore, another interpretation of the observed ferromagnetism in $\text{Ti}_9\text{Fe}_2\text{Ru}_{18}\text{B}_8$ is ferromagnetically coupled Fe_2 spin triplet dimers. Consequently, ferromagnetic coupling along the c axis arises from spin polarization of the conduction bands, because these Fe–Fe orbital interactions are strongly antibonding at the Fermi level in the nonmagnetic case. Ferromagnetic coupling within the Fe_2 dimer arises by having a half-filled, nearly degenerate pair of orbitals.

The occurrence of ferromagnetism in a boride containing mainly ruthenium atoms ($\text{Ti}_9\text{Fe}_2\text{Ru}_{18}\text{B}_8$) is new in the family of transition-metal borides. In fact, most borides synthesized and characterized to date, and containing mostly ruthenium, are antiferromagnets (e.g. $\text{Sc}_2\text{FeRu}_5\text{B}_2$ and $\text{Sc}_2\text{MnRu}_5\text{B}_2$), in contrast to those containing mainly rhodium that tend to build more ferromagnets than antiferromagnets (section 2.2). Therefore, the unexpected presence of ferromagnetism in $\text{Ti}_9\text{Fe}_2\text{Ru}_{18}\text{B}_8$ may be solely attributed to the novel iron ladder found in this compound.

Preliminary magnetic investigations on the isotypic $\text{Ti}_9\text{M}_2\text{Ru}_{18}\text{B}_8$ ($\text{M} = \text{Cr}, \text{Mn}, \text{Co}, \text{Ni}$) phases indicate a very different behavior relative to the ferromagnet $\text{Ti}_9\text{Fe}_2\text{Ru}_{18}\text{B}_8$. Their overall magnetic behavior (at $T > 5$ K) points toward a mixture of Pauli and temperature-independent paramag-

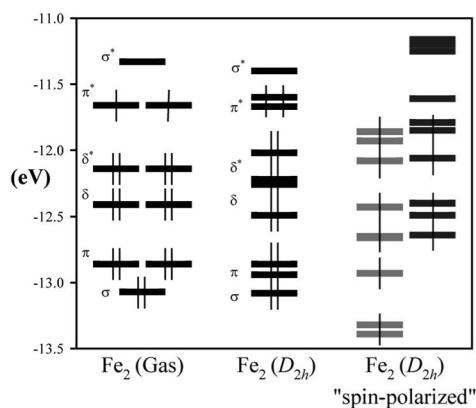


Figure 12. Molecular orbital diagrams for (left) Fe_2 in the gas phase ($D_{\infty h}$), (middle) Fe_2 in D_{2h} symmetry of the $\text{Ti}_9\text{Fe}_2\text{Ru}_{18}\text{B}_8$ crystal, and (right) Fe_2 in D_{2h} symmetry with applied spin polarization. Occupied levels are indicated.

netism.^[12a] However, DFT calculations on the $\text{Ti}_9\text{Co}_2\text{Ru}_{18}\text{B}_8$ and $\text{Ti}_9\text{Ni}_2\text{Ru}_{18}\text{B}_8$ phases indicate a stable ferromagnetic ground state for the Co phase but confirm the paramagnetic state for the Ni case.^[17b] Magnetic measurements at low applied fields and lower temperatures are still needed to fully characterize these phases.

4 Borides with Th_7Fe_3 -Type Structure

The Th_7Fe_3 structure type (space group $P6_3mc$, no. 186)^[30] has attracted some research interest mainly in the physics community. The reason lies in the wide range of exciting properties that originate from this noncentrosymmetric structure: for example, hydrogenation of superconducting Th_7Fe_3 leading to ferromagnetic $\text{Th}_7\text{Fe}_3\text{H}_{30}$,^[31] giant magnetoresistance (GMR) in Th_7Rh_3 ,^[32] or ferromagnetic transition at about 334 K in Gd_7Pd_3 ,^[33] just to name a few. Although many transition-metal borides have been reported, which also crystallize with this structure type, they did not attract much attention like their isotypic intermetallic counterparts. For example only Ru_7B_3 has recently (2009) been studied by two research groups, who simultaneously confirmed its superconducting properties already discovered 46 years ago.^[34] However, is magnetic ordering also achievable in this class of boride?

4.1 Crystal Chemistry of Th_7Fe_3 -Type Boride Phases

A couple of binary transition-metal borides were synthesized and described in the Th_7Fe_3 structure type more than four decades ago: Ru_7B_3 ,^[35] Rh_7B_3 , Re_7B_3 ,^[36] and Tc_7B_3 .^[37] Although the synthesis of the ternary compound $\text{Re}_5\text{W}_2\text{B}_3$ has also been reported, its structure has not been determined in detail yet. In the early seventies, some ternary borides of rhenium were also reported in this structure type: $\text{Co}_{0.77}\text{Re}_{6.23}\text{B}_3$,^[38] $\text{Hf}_{0.77}\text{Re}_{6.23}\text{B}_3$,^[39] $\text{Ni}_{0.5}\text{Re}_{6.5}\text{B}_3$,^[40] and $\text{Ta}_{1.2}\text{Re}_{5.8}\text{B}_3$.^[41] They were structurally characterized by X-ray powder diffraction, assuming that the two metals are statistically distributed all over the three available sites.

FeRh_6B_3 was the first well-characterized ternary compound in this family of borides.^[42] Its structure is characterized by two important features: there are boron-centered trigonal prisms built up by rhodium and M ($M \approx 2/3 \text{ Rh} + 1/3 \text{ Fe}$) and empty octahedral Rh_6 clusters (Figure 13). Three trigonal prisms share one edge and are thus interconnected to each other through their vertices. This unit is then connected to other units composed of three trigonal prisms through their edges to form a three-dimensional network. The octahedral Rh_6 clusters are linked to each other through their faces to form a one-dimensional channel along the [001] direction, perpendicular to the layer of trigonal prisms. In fact, there are three different rhodium positions in this structure [Rh1, M (Rh2 and Fe), and Rh3]. Rh1 builds the octahedral Rh_6 clusters, M is part of the three-dimensional network of interconnected triangles, whereas Rh3 is only connected to the other atoms. The reason why the substitution of rhodium in the binary Rh_7B_3 by iron takes place preferentially at just one rhodium site (Rh2) is to be found in the polyhedral nature around the rhodium atoms. In fact, the Th_7Fe_3 structure type hosts three different polyhedra around the thorium (rhodium, in our case) atoms, but only one is decisively smaller than the others. In the case of FeRh_6B_3 , the iron atom prefers the smallest coordination sphere, because iron is 0.1 Å smaller than rhodium. In other words, iron would prefer to build bonds that are nearer to those usually observed in its elemental structures (e.g. 2.55 Å in $\gamma\text{-Fe}$); therefore, the distances which will preferably accommodate iron are the M–M distances (average 2.67 Å) that are decisively shorter than the other Rh–Rh distances (average 2.77 Å).^[42]

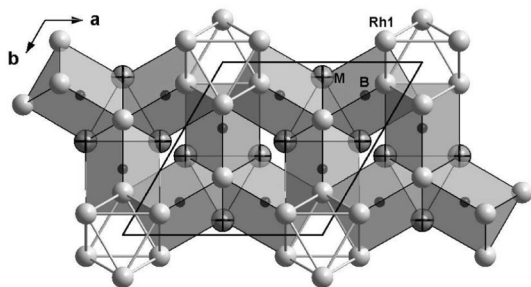


Figure 13. Projection of the structure of FeRh_6B_3 along [001]. $\text{B}(\text{Rh}_4\text{M}_2)$ trigonal prisms ($M \approx 2/3 \text{ Rh} + 1/3 \text{ Fe}$) and octahedral Rh_6 clusters are highlighted.

The situation becomes very different if we remove some electrons from the system, by replacing rhodium with ruthenium, thereby lowering the number of valence electrons from 71 VE in FeRh_6B_3 to 65 VE in “ FeRu_6B_3 ”. As a result, broader peaks are observed in the powder diffractogram of “ FeRu_6B_3 ”, which suggests a phase width. This was confirmed by single-crystal analyses on two single crystals, which yielded the compositions $\text{Fe}_x\text{Ru}_{7-x}\text{B}_3$ ($x = 0.5, 0.8$). These analyses also demonstrate that the substitution of iron by ruthenium preferentially takes place at two (not only one, like in the rhodium case) of the available three sites, as only the ruthenium atom (Ru1) that builds the octa-

hedral Ru_6 clusters is not substituted by iron (Figure 14). Although the iron content in the Ru2 site (17% for $x = 0.5$ and 23% for $x = 0.8$) is higher than that in the Ru3 site (4% for $x = 0.5$ and 10% for $x = 0.8$), an increase in the amount of iron at the Ru3 site also correlates with a similar increase at the Ru2 site. In other words, the preference of iron for both the Ru2 and the Ru3 sites is quite similar, with only a minute advantage for the Ru2 site, which is very different from the situation of the rhodium-containing phase, where the site preference is much more pronounced. Despite the fact that there is a Ru/Rh substitution by iron, the quantitative differences from the rhodium-containing phases are so distinct that the geometrical explanation given for the preferred substitution in the case of FeRh_6B_3 is *not* strictly transferable to $\text{Fe}_x\text{Ru}_{7-x}\text{B}_3$ ($0 < x < 1$), and electronic reasons must play an important role.^[43]

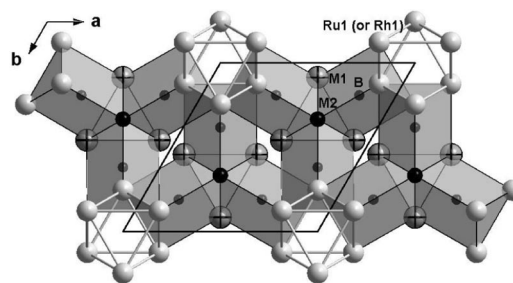


Figure 14. Projection of the crystal structure of the compounds $\text{Fe}_x\text{Rh}_{7-x}\text{B}_3$ ($1 < x \leq 1.3$) and $\text{Fe}_x\text{Ru}_{7-x}\text{B}_3$ ($0.5 < x < 1$) along [001]. $\text{B}[\text{Rh}_3\text{M}_1(\text{M}_2)_2]$ trigonal prisms and octahedral $(\text{Rh1 or Ru1})_6$ clusters are highlighted. $\text{M1} = \text{Ru2 (or Rh2)} + \text{Fe}$ and $\text{M2} = \text{Ru3 (or Rh3)} + \text{Fe}$.

Upon substituting more than one ruthenium atom by iron from the Ru_7B_3 composition, the powder X-ray intensities become even broader such that it seems unlikely to synthesize single-phase products in this system, probably because of the competition observed for the two sites (2b and 6c) when iron substitutes ruthenium. Therefore, the homogeneity range for $\text{Fe}_x\text{Ru}_{7-x}\text{B}_3$ cannot be studied in detail, because not only the iron-rich phases but also the iron-poor phases are present at any synthetic target with $x \geq 1$. The situation is different for Rh_7B_3 when more than one iron substitutes rhodium. These investigations reveal that a maximum of 41% rhodium can be substituted by iron at the Rh2 site, whereas not more than 7% rhodium can be replaced at the Rh3 site, and no rhodium substitution whatsoever is observed for Rh1, leading to the solid solution $\text{Fe}_x\text{Rh}_{7-x}\text{B}_3$ with $x \leq 1.3$.

A suitable composition, which may be obtained as a single phase in $\text{Fe}_x\text{Ru}_{7-x}\text{B}_3$ solid solution, is $\text{Fe}_{0.5}\text{Ru}_{6.5}\text{B}_3$ (65 VE), because nearly all substituted iron atoms are on the Ru2 site as only 4% of iron was found at the Ru3 site. Indeed, $\text{Fe}_{0.5}\text{Ru}_{6.5}\text{B}_3$ could be achieved as a single phase. Furthermore, the $\text{M}'_{0.5}\text{Ru}_{6.5}\text{B}_3$ ($\text{M}' = \text{Cr, Mn, Co, Ni}$; 64, 65.5, 66, 66.5 VE) series were also successfully synthesized. Rietveld refinements reveal impurities of the intermetallic phase $\text{Ru}_{0.93}\text{M}'_{0.07}$ in phases with $\text{M}' = \text{Cr, Mn, Ni}$, whereas a single-phase product was obtained in the case of

$\text{Co}_{0.5}\text{Ru}_{6.5}\text{B}_3$.^[44] Single-crystal structure analyses reveal that no manganese is present at the Ru3 site in $\text{Mn}_{0.5}\text{Ru}_{6.5}\text{B}_3$, which indicates that $\text{Mn}_{0.5}\text{Ru}_{6.5}\text{B}_3$ adopts the FeRh_6B_3 structure model. This situation is different from that of the isotypic Fe- and Ni-based phases: In these two cases, both the Ru2 and Ru3 sites accommodate the M' element. However, it is expected that a preferential substitution of Ru by M' also takes place at the Ru2 site alone in the $\text{M}'_x\text{Ru}_{7-x}\text{B}_3$ ($\text{M}' = \text{Cr, Fe, Co, Ni}$) phases at lower M' content ($0 < x < 0.5$). Therefore, the site preference in the Ru-based phases is similar to the one observed in the Rh-based ones, the difference lying only in the range in which a particular model is adopted. In the $\text{Fe}_x\text{Rh}_{7-x}\text{B}_3$ phases,^[42,43] only one of three possible sites is preferentially occupied by iron when $x \leq 1$, whereas the same situation is observed in $\text{Mn}_x\text{Ru}_{7-x}\text{B}_3$ but for $x \leq 0.5$ and should also be expected in $\text{M}'_x\text{Ru}_{7-x}\text{B}_3$ ($\text{M}' = \text{Cr, Fe, Co, Ni}$) but only for $x < 0.5$.

4.2 Magnetic Properties of FeRh_6B_3 and $\text{M}_{0.5}\text{Ru}_{6.5}\text{B}_3$ ($\text{M} = \text{Fe, Cr, Mn, Co, Ni}$)

4.2.1 FeRh_6B_3 : The First Ferromagnetic Boride of Th_7Fe_3 -Type Structure

FeRh_6B_3 is a ferromagnet exhibiting spontaneous magnetization below a Curie temperature (T_C) of approximately 225 K. Figure 15 shows the hysteresis loop of FeRh_6B_3 at 5 K and an enlarged part of it showing a small remanence and a coercive field $H_C = 1.99 \text{ kA m}^{-1}$ lying in the range ($1\text{--}30 \text{ kA m}^{-1}$) of semi-hard magnetic materials.^[45]

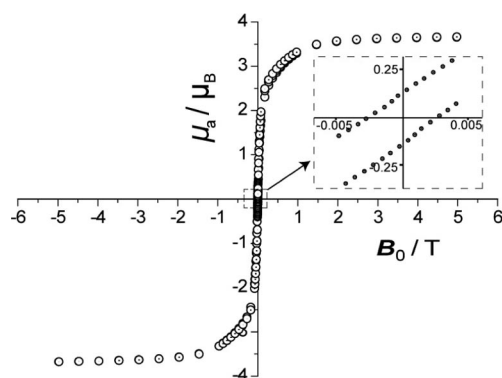


Figure 15. Hysteresis loop of FeRh_6B_3 at 5 K. Inset: enlarged part of the hysteresis showing the coercive field and the remanence.

Electronic structure calculations were also performed on FeRh_6B_3 using the linear muffin-tin orbital (LMTO) method, in its tight-binding representation to determine its ground-state magnetic ordering.^[45] These calculations confirmed the ferromagnetic ground state with an indirect coupling of the magnetic moments (located at the iron site) via the rhodium atoms. This type of indirect coupling was already found in the Rh-rich ferromagnetic phases of the $\text{Sc}_2\text{FeRu}_{5-n}\text{Rh}_n\text{B}_2$ series (section 2.2). The calculated magnetic saturation moment for FeRh_6B_3 is $4.02 \mu_B$. The local moment for iron is $2.78 \mu_B$, with a small average moment for rhodium ($0.22 \mu_B$). FeRh_6B_3 therefore reinforces the

trend already observed for borides of the $\text{Ti}_3\text{Co}_5\text{B}_2$ structure type containing rhodium as the main component (section 2.2) and showing leading ferromagnetic interactions.

4.2.2 Weakly Ferrimagnetic $\text{Fe}_{0.5}\text{Ru}_{6.5}\text{B}_3$ and Paramagnetic $\text{M}_{0.5}\text{Ru}_{6.5}\text{B}_3$ ($\text{M} = \text{Cr, Mn, Co, Ni}$)

As already seen in sections 2 and 3, nearly all transition-metal-rich borides containing ruthenium as the main component show strong antiferromagnetic interactions, with the exception of $\text{Ti}_9\text{Fe}_2\text{Ru}_{18}\text{B}_8$, in which ferromagnetic interactions are observed. A plot of the atomic magnetic dipole moment (μ_a) vs. applied field in $\text{Fe}_{0.5}\text{Ru}_{6.5}\text{B}_3$ reveals that a field of 0.03 T at 5 K produces only a very small magnetic moment of $0.01 \mu_B$ and even at 5 T only a moment of $0.3 \mu_B$ is obtained. Therefore, considerable but weak ferromagnetic interactions are present in this phase below a very low Curie temperature of only 5 K. On the other hand, the effective magnetic moment (μ_{eff}) vs. temperature curve (Figure 16) resembles those plotted for the antiferromagnets $\text{Sc}_2\text{FeRu}_5\text{B}_2$ (60 VE), $\text{Sc}_2\text{FeRu}_4\text{RhB}_2$ (61 VE), and $\text{Sc}_2\text{FeRu}_3\text{Rh}_2\text{B}_2$ (62 VE) (Figure 3), indicating that strong antiferromagnetic interactions are also present. The presence of both ferromagnetic and antiferromagnetic interactions in $\text{Fe}_{0.5}\text{Ru}_{6.5}\text{B}_3$ suggests that this phase orders ferrimagnetically below 5 K. This is further supported by the fact that iron is found at two independent crystallographic sites with different occupations in the crystal structure of $\text{Fe}_{0.5}\text{Ru}_{6.5}\text{B}_3$.

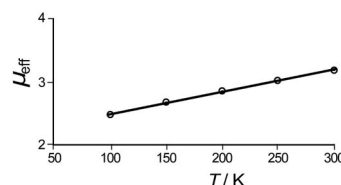


Figure 16. Effective magnetic moment vs. temperature for $\text{Fe}_{0.5}\text{Ru}_{6.5}\text{B}_3$.

The isotypic $\text{M}_{0.5}\text{Ru}_{6.5}\text{B}_3$ ($\text{M} = \text{Cr, Mn, Co, Ni}$) phases are all paramagnets: the Cr-, Co-, and Ni-based phases are Pauli paramagnets, whereas the Mn-based phase shows a mixture of temperature-dependent and Pauli paramagnetism. The obtained temperature-independent molar susceptibilities (χ_m) are $1.0 \times 10^{-8} \text{ m}^3 \text{ mol}^{-1}$ ($\text{Cr}_{0.5}\text{Ru}_{6.5}\text{B}_3$, 64 VE), $2.2 \times 10^{-8} \text{ m}^3 \text{ mol}^{-1}$ ($\text{Co}_{0.5}\text{Ru}_{6.5}\text{B}_3$, 65.5 VE), and $3.8 \times 10^{-8} \text{ m}^3 \text{ mol}^{-1}$ for ($\text{Ni}_{0.5}\text{Ru}_{6.5}\text{B}_3$, 66 VE). A clear VE-dependence of this constant molar susceptibility is observed in these paramagnets: χ_m increases with increasing VE count in the $\text{M}_{0.5}\text{Ru}_{6.5}\text{B}_3$ ($\text{M} = \text{Cr, Mn, Co, Ni}$) series, that of $\text{Mn}_{0.5}\text{Ru}_{6.5}\text{B}_3$ phase makes an exception but still remains in the same range as the others. These values are also comparable to the one found for the transition-metal-rich boride $\text{Sc}_2\text{NiIr}_5\text{B}_2$ ($2 \times 10^{-8} \text{ m}^3 \text{ mol}^{-1}$).^[9]

5 New Structure Types with Potentially Interesting Magnetic Properties Containing B_4 Units

The crystal structures of metal-rich borides usually contain isolated boron atoms (as seen in the previous sections),

but often the boron atoms tend to build homonuclear bonds, leading to the formation of boron fragments or chains.^[11] The tendency of boron to form small B-units even in metal-rich borides is indeed governed by the paucity of electron-donating properties of the metal partners. Boron compensates the lack of electrons by making B–B bonds.

The most common boron fragment found in metal-rich borides is a dumbbell (boron pair). Moreover, *cis-trans* chain-like B₆ fragments occur in Rh₃B_{2-x},^[46] linear B₄ chain fragments were found in Rh₅B₄,^[47] *trans zigzag* B₄ fragments were observed in Mo₂IrB₂,^[48] *cis zigzag* B₄ fragments were observed in the β-phase of Cr₂IrB₂,^[49] whereas B₄ tetrahedra^[50] were observed in some borides of the Cr₂₃C₆-type structure (section 7). Given the diversity of B₄ fragments observed, one had to wait until the year 2006 to discover the first trigonal planar B₄ unit in Ti_{1.6}Os_{1.4}RuB₂,^[51] although nearly all boron layers and even the boron chain present in Ru₁₁B₈ can be thought of as being constructed from a trigonal planar B₄ fragment.^[52] Such a boron “missing link” in terms of structure had never been reported before, neither in borides nor in other intermetallic phases. However, two examples of a related trigonal planar unit were found for the elements *silicon* and *germanium* in the Zintl phases Li₁₂Si₇ and M_{5+x}Mg_{18-x}E₁₃ (M = Sr, Ba; E = Si, Ge),^[53,54] but usually the observed X₄ units (X = any element) in other ionic compounds are *not* trigonal planar. For example, As₄⁴⁻ or Sb₄⁴⁻ *squares* are found in arsenides and antimonides, respectively,^[55] and even in the very rich structural chemistry of polysulfides, the S₄²⁻ units are *zigzag-like*.^[56] A trigonal planar arrangement, however, is commonly found by combining at least two elements (XY₃), for example, the boron trihalogenides BZ₃ (Z = F, Cl, Br, I) or the complex ions BO₃³⁻, BN₃⁶⁻, and CO₃²⁻, which are all trigonal planar. The following subsections are devoted to the crystal chemistry of boride phases containing not only the rare trigonal planar B₄ unit but also phases accommodating the more common *zigzag* B₄ fragment. The potential of these phases to produce new magnetic materials is also discussed.

5.1 Trigonal Planar B₄ Units in Ti_{1.6}Os_{1.4}RuB₂-Type Phases

5.1.1 The Ti_{1.6}Os_{1.4}RuB₂ Structure Type

Ti_{1.6}Os_{1.4}RuB₂ could be synthesized from the elements by using about 50% excess osmium. Its crystal structure, determined by single-crystal X-ray diffraction, is of a new type [*a* = 8.8554(14) Å, *c* = 3.0336(7) Å, space group *P*6̄2*m*, no. 189]. It is composed of two alternating layers stacked along the *c* axis (Figure 17): The first layer contains the M1 atoms (69% Os + 31% Ti) and the trigonal planar B₄ fragments (containing B1 and B2 atoms), whereas the second layer is filled with ruthenium atoms, M2 atoms (96% Ti + 4% Os), and isolated boron atoms (B3). Although the two layers exhibit mixed atomic positions (M1 and M2) by osmium and titanium, there is an obvious site-preferential tendency: The osmium atoms mainly enter the layer at *z* =

1/2, whereas the titanium atoms are mostly found in the layer at *z* = 0. The two layers are interconnected, mainly by M1–M1, M1–Ru, and Ru–Ru bonds, thereby generating the coordination environments around the boron atom and the M2 atoms (Figure 17).

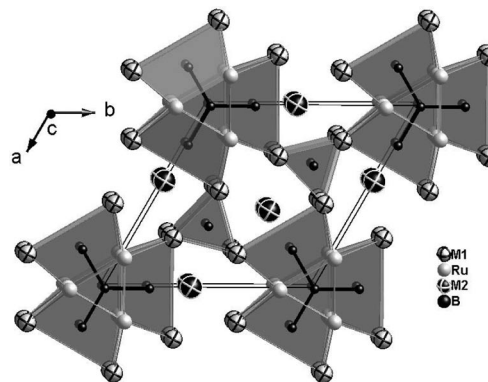


Figure 17. Projection of the crystal structure of Ti_{1.6}Os_{1.4}RuB₂ along [001]. Boron-centered trigonal prisms are highlighted: M1 = 69% Os + 31% Ti, M2 = 96% Ti + 4% Os.

There are three interesting features seen in the structure of Ti_{1.6}Os_{1.4}RuB₂ (Figure 18): one-dimensional M2 (96% Ti + 4% Os) chains, one-dimensional strings of face-sharing empty tetrahedral and square-pyramidal clusters, and, most importantly, the already mentioned trigonal planar B₄ fragments.

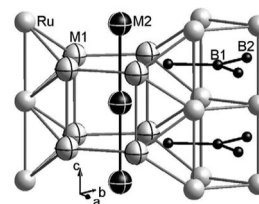


Figure 18. The three structural features of Ti_{1.6}Os_{1.4}RuB₂: one-dimensional strings of face-sharing empty tetrahedral and square-pyramidal (Ru/M1)₆ clusters (left part) running along [001], one-dimensional chains of M2 atoms, also running along [001], and the trigonal planar B₄ units: M1 = 69% Os + 31% Ti, M2 = 96% Ti + 4% Os.

The interatomic distances in the structure of Ti_{1.6}Os_{1.4}RuB₂ compare quite well with those already found in transition-metal borides reported in the previous sections. COHP bonding analyses have indicated that the metal–boron interactions (Os–B, Ru–B, Ti–B) are the strongest in the structure as observed for other transition-metal-rich borides. However, they experience a strong competition from the B–B interactions in this new structure type.

The B1–B2 distance (1.89 Å) is just 0.07 Å larger than the average distance observed in α-boron (ca. 1.82 Å). The COHP analysis shows very strong B–B bonding interactions up to the Fermi level (Figure 19, right), with an energy integral (ICOHP) of –3.13 eV/bond, a value not far from the one calculated for the B–B interaction in the boron layer of TiB₂ (ICOHP = –4.04 eV/bond).^[57] The analysis further

shows that the B–B bond can host even more electron density, because there are virtual bonding levels in the conduction band.

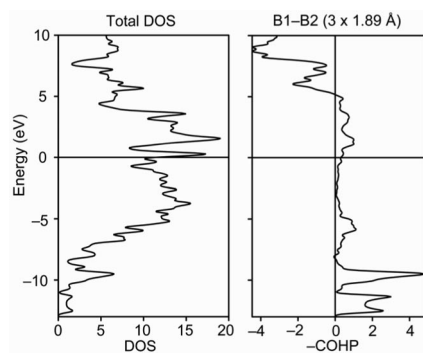


Figure 19. Theoretical density of states (DOS) of $\text{Ti}_{1.6}\text{Os}_{1.4}\text{RuB}_2$ and COHP bonding analysis of the B1–B2 interactions; the Fermi level has been set to the energy zero. Reproduced from ref.^[51] with permission of The Royal Society of Chemistry.

Because of the finite DOS at the Fermi level (Figure 19, left), the phase is predicted to be a metal, as expected, and the slightly lowered DOS just above the Fermi edge also indicates that this very structure type may accommodate additional electrons. Despite this suggestion, it is still not clear which element in the structure may be substituted by another one having more electrons. Such information is nonetheless useful for the discovery of new compounds with the same structure type or to even target a specific property such as magnetism, in order to find new magnetic materials belonging to this structure type. We may follow the example of the $\text{Ti}_3\text{Co}_5\text{B}_2$ -type structure, which has produced many magnetic materials: for example, Sc chains were substituted by Fe chains in $\text{Sc}_3\text{Rh}_5\text{B}_2$ to produce the strong ferromagnet $\text{Sc}_2\text{FeRh}_5\text{B}_2$ (section 2, Table 1). It is worthwhile noting that the one-dimensional M2 chain (96% Ti + 4% Os) found here has also been observed for all 3d elements in related phases (with $\text{Ti}_3\text{Co}_5\text{B}_2$ and $\text{Zn}_{11}\text{Rh}_{18}\text{B}_8$ structure types, see sections 2 and 3). In all three cases, the intrachain metal distances are almost the same (ca. 3.0 Å). However, the interchain distances come out smaller (4.6 Å) for $\text{Ti}_{1.6}\text{Os}_{1.4}\text{RuB}_2$ than for the compounds of the $\text{Ti}_3\text{Co}_5\text{B}_2$ type (ca. 6.6 Å) and $\text{Zn}_{11}\text{Rh}_{18}\text{B}_8$ type (ca. 12.5 Å). Nonetheless, it is very well possible that substituting M2 by a magnetically active element (such as Cr, Mn, Fe, Co, Ni) could have the same consequence on the magnetic behavior of these hypothetical phases as for those of the $\text{Ti}_3\text{Co}_5\text{B}_2$ structure type where itinerant magnetic ordering has been observed.

5.1.2 Ternary and Quinary Phases with $\text{Ti}_{1.6}\text{Os}_{1.4}\text{RuB}_2$ -Type Structure

The importance of osmium for phases with $\text{Ti}_{1.6}\text{Os}_{1.4}\text{RuB}_2$ -type structure was further tested by substituting ruthenium by another osmium atom, which led to the ternary $\text{Ti}_{1.6}\text{Os}_{2.4}\text{B}_2$ having the same number of valence electrons.^[58] In contrast to the quaternary $\text{Ti}_{1.6}\text{Os}_{1.4}\text{RuB}_2$ phase, in which the titanium site is mixed with a small

amount of osmium, the ternary $\text{Ti}_{1.6}\text{Os}_{2.4}\text{B}_2$ did not show any osmium at the titanium site. Thus, the resulting titanium chains resemble those present in $\text{Ti}_3\text{Co}_5\text{B}_2$, which were substituted by a magnetically active element (M') to produce the substitutional variants $\text{M}_2\text{M}'\text{T}_5\text{B}_2$ showing exciting magnetic properties (antiferromagnetism, metamagnetism, and ferromagnetism). Since these properties are mainly attributed to the M'-chains, which have nearly the same intrachain distance (ca. 3.0 Å) as the titanium chain in $\text{Ti}_{1.6}\text{Os}_{2.4}\text{B}_2$, a similar substitution of titanium in $\text{Ti}_{1.6}\text{Os}_{2.4}\text{B}_2$ by a magnetically active element (e.g. iron) may also lead to interesting magnetic properties. Nonetheless, experimental efforts so far allow for the substitution of only 7% of titanium in $\text{Ti}_{1.6}\text{Os}_{2.4}\text{B}_2$ by iron, so the compound was not investigated any further.

In view of the knowledge from the section 2, it is very probable that a phase containing iron chains (or iron/titanium chains) and rhodium atoms (not ruthenium) may order ferromagnetically. One third of the titanium in “ $\text{TiOs}_2\text{RhB}_2$ ” was successfully substituted by iron. Two single crystals yielded the formulas $\text{Ti}_{0.67}\text{Fe}_{0.33}\text{Os}_2\text{RhB}_2$ and $\text{Ti}_{0.75}\text{Fe}_{0.25}\text{Os}_2\text{RhB}_2$, indicating a phase width and the solid solution $\text{Ti}_{1-x}\text{Fe}_x\text{Os}_2\text{RhB}_2$.^[58] In contrast to the quaternary $\text{Ti}_{1.6}\text{Os}_{1.4}\text{RuB}_2$, no mixed occupancy was observed at the osmium and rhodium sites in the new quinary iron-containing phases, which indicates that they are more ordered than the quaternary phase.^[58] As expected, the crystals of the solid solution $\text{Ti}_{1-x}\text{Fe}_x\text{Os}_2\text{RhB}_2$ ($0 < x < 0.5$) are strongly attracted by the external magnetic field of a bar magnet. This preliminary observation needs to be confirmed prior to the synthesis of larger crystals for magnetic measurements. These measurements cannot be done on powder samples, because, at this stage, phase-pure powder samples could not be synthesized.

5.2 An Unexpected New Structure Type Related to the $\text{Ti}_{1.6}\text{Os}_{1.4}\text{RuB}_2$ Type

All phases with $\text{Ti}_{1.6}\text{Os}_{1.4}\text{RuB}_2$ structure type were synthesized from the elements by using an excess of osmium, indicating that they melt incongruently. But why is an excess of osmium only (not the other metals) so important to these syntheses? A substitution of osmium by an element having more electrons (in accordance with the DOS prediction) may provide an answer to this question. Iridium is the direct neighbor of osmium in the periodic table having one electron more, thus iridium may be the ideal candidate for this substitution. The syntheses of “ $\text{Ti}_{1.6}\text{Ir}_{1.4}\text{RuB}_2$ ” and “ $\text{TiIr}_2\text{RuB}_2$ ” could not be achieved in the $\text{Ti}_{1.6}\text{Os}_{1.4}\text{RuB}_2$ structure type, because phases with $\text{Ti}_3\text{Co}_5\text{B}_2$ -type structure were identified in the multiphase powder diffractograms as main components. In the next synthesis, the number of valence electrons was increased by substituting ruthenium with rhodium, leading to “ $\text{Ti}_{1.6}\text{Ir}_{1.4}\text{RhB}_2$ ” and “ $\text{TiIr}_2\text{RhB}_2$ ” starting compositions. Neither $\text{Ti}_{1.6}\text{Os}_{1.4}\text{RuB}_2$ nor $\text{Ti}_3\text{Co}_5\text{B}_2$ -type structures were observed. From the diffractograms, only iridium could be assigned and many

peaks remained unidentified. Luckily, some single crystals of a new phase were obtained.^[59] Its crystal structure (Figure 20) is strongly related to the $\text{Ti}_{1.6}\text{Os}_{1.4}\text{RuB}_2$ structure type.

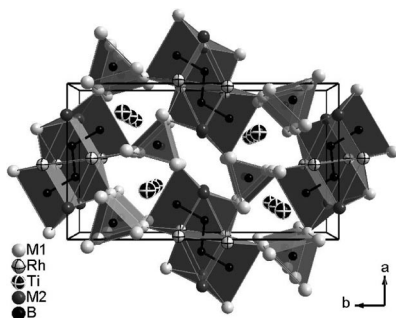


Figure 20. Projection of the structure of $\text{Ti}_{1.7}\text{Os}_{2.4}\text{Rh}_{1.9}\text{B}_3$ along [001]. Boron-centered trigonal prisms are highlighted: M1 = 65% Ir + 35% Rh, M2 = 68% Ti + 32% Rh.

The new phase (around 10%) was found in the form of single crystals while searching for “ $\text{TiIr}_2\text{RhB}_2$ ”, and the reaction yield could be improved up to 60% by using an excess of Ir: This excess is the first similarity between the new structure and the $\text{Ti}_{1.6}\text{Os}_{1.4}\text{RuB}_2$ structure type. The refined compositions from two single crystals are $\text{Ti}_{1.7}\text{Rh}_{2.4}\text{Ir}_{1.9}\text{B}_3$ and $\text{Ti}_{1.9}\text{Ir}_{2.0}\text{Rh}_{2.1}\text{B}_3$, which indicates that the obtained phase is actually a complex solid solution of the general type $\text{Ti}_{1+x}\text{Rh}_{2-x+y}\text{Ir}_{3-y}\text{B}_2$, because rhodium is found to mix with both titanium and iridium at different sites (Figure 20). The structure is strongly related to the $\text{Ti}_{1+x}\text{Os}_{2-x}\text{RuB}_2$ type. Both contain one-dimensional Ti chains with nearly the same intrachain and interchain distances, empty face-sharing clusters, and B_4 fragments with comparable B–B distances but different shapes. The B_4 fragments present in $\text{Ti}_{1.6}\text{Os}_{1.4}\text{RuB}_2$ type structures are trigonal-planar but they adopt the most common zigzag-like shape in the new solid solutions $\text{Ti}_{1+x}\text{Rh}_{2-x+y}\text{Ir}_{3-y}\text{B}_2$. Therefore, the main difference between the two structures is the different shapes of the B_4 fragments.^[59]

For this structure type, too, it is well possible that substituting the titanium chain by a chain of a magnetically active element (e.g. iron) could have the same consequence for the magnetic behavior of the hypothetical compounds as for those of the previous structure types, which were found to behave as itinerant magnets.

6 New Transition-Metal Borides with Double-Perovskite-Like Crystal Structures

Among the large family of perovskites, a group of cubic intermetallic perovskites with the general formula AM_3X ,^[11] where A and M are metals and X is B, C, or N, have drawn a great deal of attention lately due to their interesting physical properties.^[60–63] YRh_3B possesses the hardness value of 8 GPa,^[64] while YRh_3B ^[65] and MgNi_3C ^[66] are superconductors with transition tempera-

tures of 0.8 and 8 K, respectively. They all crystallize with the simple cubic perovskite structure in the space group $Fm\bar{3}m$ (no. 221).

6.1 $\text{Ti}_2\text{Rh}_6\text{B}$: The First Boride with a Double-Perovskite-Like Structure

In recent years, a large number of ternary and quaternary rhodium borides have been synthesized and structurally characterized. Some of them crystallize with a simple cubic perovskite-like structure. The crystal structure of the series $\text{RE}\text{T}_3\text{B}_{1-x}$ (RE = Sc, La, rare-earth element, T = Ni, Rh, $0 < x \leq 1$)^[67–70] has been described as a normal cubic perovskite, whereas $\text{SnRh}_3\text{B}_{1-x}$ ($x \approx 0.2$)^[71] crystallizes with the filled U_3Si structure type, a distorted variant of the cubic perovskite. No superstructure reflections were observed for these normal cubic perovskite phases during the X-ray diffraction experiments. This would have lead to some ordering of the boron site and possibly a change in the chemical formula. For example, many compounds are described with only half of the expected boron content, for example, $\text{ScRh}_3\text{B}_{0.5}$ and $\text{ScNi}_3\text{B}_{0.5}$. Superstructure reflections were observed for the first time in the powder diffraction and single-crystal X-ray diffraction data of $\text{Ti}_2\text{Rh}_6\text{B}$,^[72] which is the first transition-metal boride with a double-perovskite-like structure (Figure 21).

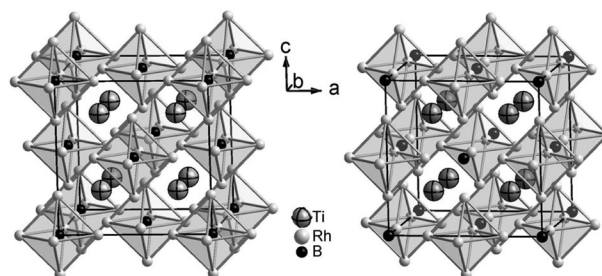


Figure 21. Left: Perspective view of the structure of $\text{Ti}_2\text{Rh}_6\text{B}$ emphasizing the BRh_6 octahedra. Right: The same view but highlighting the empty octahedral Rh_6 clusters.

In the crystal structure of $\text{Ti}_2\text{Rh}_6\text{B}$ (space group $Fm\bar{3}m$, no. 225), titanium occupies the Wyckoff position $8c$ and is surrounded by twelve rhodium atoms at 2.76 \AA to form a cuboctahedron. Rhodium occupies the position $24e$ and is surrounded by four titanium atoms and eight other rhodium atoms to also form a cuboctahedron, but here one quadratic face of the cuboctahedron is centered by a boron atom. Boron lies at position $4e$ and is octahedrally surrounded by six rhodium atoms. There is no crystallographic indication of any substitutional disorder.

The crystal structure of $\text{Ti}_2\text{Rh}_6\text{B}$ can be described as a double perovskite, $\text{A}_2\text{BB}'\text{O}_6$, in which the A site is occupied by titanium, the B site by boron, the O site by rhodium but the B' site is vacant. As shown in Figure 21 (left), isolated BRh_6 octahedra adopt the motif of a face-centered cubic structure. The resulting octahedral sites are vacant, which leads to the formation of Rh_6 clusters (highlighted in Fig-

ure 21, right), and both entities are linked with each other through their corner rhodium atoms.

The chemical bonding in $\text{Ti}_2\text{Rh}_6\text{B}$ was investigated by LMTO band structure calculations. The DOS in the valence region exhibits significant rhodium character, titanium levels contributing slightly from -10 eV up to the Fermi level (Figure 22a). Because of the nonvanishing DOS at the Fermi level, the phase is predicted to be a metal, as expected for this intermetallic compound. According to COHP bonding analysis (Figure 22b–d), the strongest bonding interaction is found for the B–Rh bonds, and this is in accord with the short B–Rh distance of 2.02 Å, which is even shorter than the sum of the covalent radii (2.07 Å). A similar interatomic distance (2.04 Å) was also found in the perovskite phase ScRh_3B .^[67] There are also strong Ti–Rh interactions, which do not come unexpectedly, taking into account the short (2.77 Å) bond that resembles the metallic distance for coordination number (CN) 12 (2.79 Å, ref.^[73]) and the one present in binary Rh_3Ti (2.70 Å, ref.^[74]).

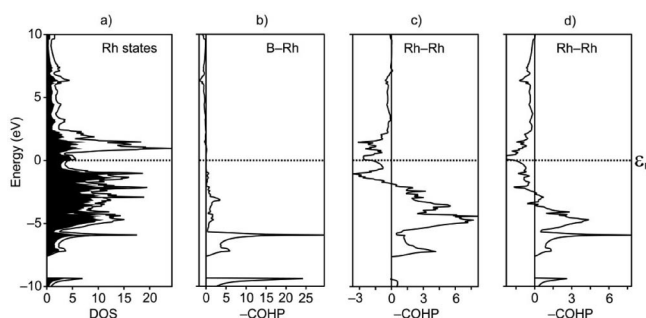


Figure 22. (a) Total and Rh-projected (black area) DOS for $\text{Ti}_2\text{Rh}_6\text{B}$; COHP curves for (b) the B–Rh bond, (c) the Rh–Rh bonds in the Rh_6 cluster (2.68 Å), and (d) the Rh–Rh bonds in the BRh_6 octahedron (2.85 Å).

With respect to the Rh–Rh interactions, there are two types to consider. First, one finds twelve short Rh–Rh contacts of 2.68 Å in the empty Rh_6 cluster and, second, there are other twelve but wider Rh–Rh contacts of 2.85 Å in the filled BRh_6 units. The analysis (Figure 22c and d) evidences a net bonding effect for both, but the energy integral (ICOHP) for the empty Rh_6 cluster is more than two times as large as the one of filled BRh_6 units. The BRh_6 octahedron is very much weakened, because too much electron density has gone into the B–Rh bond. For completeness, we note that the length of the short Rh–Rh contact (2.68 Å and strongly bonding) is equal to the metallic Rh distance for CN 12 (2.68 Å, ref.^[73]) but shorter than the observed average value (2.75 Å) in Rh_6 cluster complexes^[74] and slightly longer than the calculated metallic distance (2.63 Å) of an octahedral Rh_6 cluster.^[75] Ti–Ti bonding interactions are not present.

Coming back to Figure 22c and d, the antibonding Rh–Rh interactions observed at the Fermi level point towards a potential instability of the system with respect to spin polarization. Given a sufficient exchange splitting, a redistribution of the spins and a magnetization of the system may annihilate antibonding interactions and lower the total

energy, as observed in section 2. For the 4d element Rh, this effect does not take place here because any introduced magnetic moment vanishes for $\text{Ti}_2\text{Rh}_6\text{B}$ upon iterating to self consistency, leaving the phase with a zero net moment.^[72] This theoretical finding further corroborates prior theoretical calculations performed on the octahedral Rh_6 cluster.^[75] Experimentally, magnetism was only observed for free Rh_n clusters with $9 \leq n \leq 34$.^[76]

6.2 $\text{Zr}_2\text{Ir}_6\text{B}$ with an Eightfold Superstructure of $\text{ZrIr}_3\text{B}_{0.5}$

$\text{Ti}_2\text{Rh}_6\text{B}$ (reported above) is the first phase in which a boron ordering was observed due to the presence of the $\frac{1}{2} \frac{1}{2} \frac{1}{2}$ -type superstructure reflections in both X-ray single crystal and powder diffraction data. However, electron diffraction patterns have also revealed the presence of the same type of superstructure reflections together with some satellite ones in CeRh_3B_x ($0.4 \leq x \leq 0.5$)^[77] and ScRh_3B_x ($0.5 \leq x \leq 0.75$)^[78] phases. These findings indicate that the structures of these nonstoichiometric perovskite borides are actually only the average structures. Even in $\text{CePd}_3\text{B}_{0.13}$, the eightfold superstructure ($\text{Ce}_8\text{Pd}_{24}\text{Sb}$ -type^[79]) found in related $\text{Ce}_8\text{Pd}_{24}\text{M}$ ($8 \times \text{CePd}_3\text{M}_{0.13}$) phases ($\text{M} = \text{Al}, \text{Ga}, \text{In}, \text{Ge}, \text{Sn}, \text{Pb}$) was not observed.^[80] ZrIr_3B_x ($0 < x \leq 0.5$) compounds synthesized in the late seventies^[81] make no exception, as they were structurally described also as simple cubic perovskites (Figure 23, left). However, high-quality powder samples and single crystals, for the composition with $x = 0.5$, could be synthesized recently, and X-ray diffraction data show the $\frac{1}{2} \frac{1}{2} \frac{1}{2}$ -type superstructure reflections.^[82] $\text{Zr}_2\text{Ir}_6\text{B}$ (Figure 23, right) is isotypic to $\text{Ti}_2\text{Rh}_6\text{B}$ described above, and its crystal structure represents an eightfold superstructure of the reported $\text{ZrIr}_3\text{B}_{0.5}$. Because the transition metals in both phases belong pairwise (Ti/Zr pair and Rh/Ir pair) to the same groups in the periodic table, their electronic properties are qualitatively very similar. However, a pseudogap, not observed in $\text{Ti}_2\text{Rh}_6\text{B}$, is found at approximately 1 eV above the Fermi level of $\text{Zr}_2\text{Ir}_6\text{B}$. DOS predicts $\text{Zr}_2\text{Ir}_6\text{B}$ to be a metallic conductor, as expected.

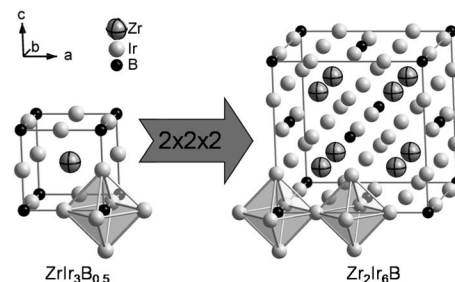


Figure 23. Eightfold superstructure transformation of $\text{ZrIr}_3\text{B}_{0.5}$ into $\text{Zr}_2\text{Ir}_6\text{B}$. Boron-filled and empty Ir_6 octahedra are highlighted.

The element substitutions from $\text{Ti}_2\text{Rh}_6\text{B}$ en route to $\text{Zr}_2\text{Ir}_6\text{B}$ have induced an increase in the unit cell volume of $\text{Zr}_2\text{Ir}_6\text{B}$ of roughly 32 Å³ relative to that of $\text{Ti}_2\text{Rh}_6\text{B}$. Two different types of substitutions may also be imagined with these elements, namely a combination of 3d with 5d or 4d

with 4d transition metals, leading to the hypothetical “Ti₂Ir₆B” and “Zr₂Rh₆B” phases, respectively, whose volumes should lie between those of Ti₂Rh₆B and Zr₂Ir₆B. The authors who discovered ZrIr₃B_x (0 < x ≤ 0.5) also synthesized ZrRh₃B_x (0 < x ≤ 1),^[81] but the corresponding “TiIr₃B_x” phase is still unknown. It is well possible that the same superstructure reflections observed in Zr₂Ir₆B and Ti₂Rh₆B can also be found in a high-quality diffraction pattern of ZrRh₃B_{0.5}, which will then induce its formulation as “Zr₂Rh₆B”. In fact, the structure of all intermetallic boride phases crystallizing with the simple cubic perovskite structure should be revised. However, obtaining high-quality powder or single-crystal diffraction data is the prerequisite for the observation of these very small superstructure reflections.

7 Transition-Metal Borides with Cr₂₃C₆-Type Crystal Structure

7.1 Crystal Chemistry

Metal-rich borides crystallizing with the Cr₂₃C₆-type crystal structure represent the largest group in this boride family (see Table 4 for some stable examples). These borides are mostly attractive, because of their good mechanical hardness and their soft ferromagnetic properties.

In fact, the crystal structure of Cr₂₃C₆ (space group *Fm* $\bar{3}$ *m*, Cr on 48*h*, 32*f*, 8*c*, and 4*a*; C on 24*e*) enables multiple substitution paths at the metal positions when carbon is substituted by boron (Figure 24a). In the boride systems, substitutions by at least one metal seems to be a stabilizing factor, because until today no binary boride with Cr₂₃B₆ structure type has been reported to exist in thermodynamic equilibrium. However, the formation of metastable binary borides Fe₂₃B₆, Co₂₃B₆,^[83] and Ni₂₃B₆^[84] was reported, and recently a Co₂₃B₆ single crystal was obtained from a Co–In–B alloy.^[85] Interestingly, a large range of M' elements (M' = main group element, transition metal, lanthanoid element)^[86,87] helps to stabilize the binaries M₂₃B₆, thereby leading to two groups of ordered ternary phases. Depending on the size of the substituting M' element, different sites are affected by the substitution: When the M' element

Table 4. Stable boride phases with Cr₂₃B₆-type (space group *Fm* $\bar{3}$ *m*) or related structures.

M ₂₁ (M _{1-x} M' _x) ₂ B ₆ (mostly ordered)	
M	M'
Co	In, Sb; ^[87a] Ga, Sn; ^[87b] Ge; ^[87c] Sc; ^[87a,87d] Cr; ^[87e] Zr, Hf; ^[87a] Ta; ^[87b,87f] Mo, W; ^[87a] U ^[87e]
Ni	Ca, Sn, Ge; ^[87b] In; ^[87b,87g] Sb; ^[87a] Sc; ^[87d] Ce, Lu, Tm, Yb, Er; ^[87e] Ho; ^[87h] U ^[87a]
M ₂₀ M' ₂ (M _{1-x} M' _x)B ₆ (mostly ordered)	
M	M'
Co	Ti, Nb, V; ^[87a] Mg, Al ^[49,87b]
Ni	Li; ^[87i] Zr, Hf, Ti; ^[87a] Nb, Ta; ^[87e,87b] V; ^[87a] Zn, Al, Ga ^[87b]
(M _{1-x} M' _x) ₂₃ B ₆ (strongly disordered)	
M	M'
Mn	Co; ^[87j] Ni; ^[87b] Fe ^[87k] with x = 1.2–13.8
Re	Mn, Fe, Co, Ni ^[87d] with x = 1.4–20
Ir	Cr, Mn, Co, Fe ^[87l] with x = 7.6–13
Ru	Nb, Ta (x ≈ 19) ^[87l]
(M _{1-x} M' _x) ₂₁ M _{2-y} B _{6+4y}	
M	M'
Ni	Al (x = 1, y = 2) ^[50]
Co	Ir (x = 8.9, y = 1.125) partial ordering ^[85]
	Ir (x = 7.56, y = 1) full ordering (space group <i>F</i> $\bar{4}$ 3 <i>m</i>) ^[86]

is larger than M, it occupies predominantly the atomic site with the highest coordination number (site 8*c*, CN = 16), thereby leading to the formula M₂₁M'₂B₆; with increasing M' content, the M' atoms may additionally enter site 4*a* (CN = 12) to give the formula M₂₀M'₃B₆ (Figure 24a). Moreover, mixtures of the two metals are often observed, so that the aforementioned two general formulas become M₂₁(M_{1-x}M'_x)₂B₆ and M₂₀M'₂(M_{1-x}M'_x)B₆, respectively. With decreasing differences in atomic radii, the statistical distribution of M (Cr, Fe, Mn, Co) and M' (Ir, Re) on atomic sites 48*h* and 38*f* is observed, thereby displaying extended homogeneous regions and leading to the general formula (M_{1-x}M'_x)₂₃B₆.^[85,86]

In some boride systems, additional boron atoms have been observed, which leads to the general formula (M_{1-x}M'_x)₂₁M_{2-y}B_{6+4y} (y = 1–2): for example, Ni₂₀AlB₁₄,^[50] Co_{12.3}Ir_{8.9}B_{10.5},^[85] and Co_{13.60}Ir_{7.56}B₁₀.^[86] In the

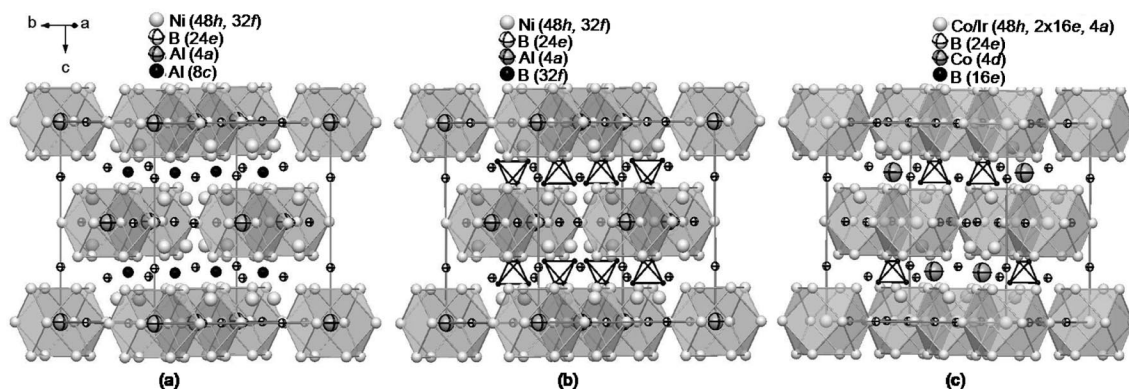


Figure 24. Crystal structures of Ni₂₀Al₃B₆ (a) and the boron-rich phases Ni₂₀AlB₁₄ (b) and Co_{13.60}Ir_{7.56}B₁₀ (c) projected nearly along [110]. Al on 8*c* in (a) is totally substituted by B₄ tetrahedra in (b), but only one half is substituted by B₄ tetrahedra in (c) and the other half contains only a small amount (16%) of cobalt.

first structural model for these phases, the greater boron content has been explained by partial or total replacement of metal atoms at the $8c$ site by B_4 tetrahedra (boron atoms at $32f$),^[50,85] thus maintaining the $Fm\bar{3}m$ space group (no. 225, centrosymmetric) and $Cr_{23}C_6$ -type structure. A full boron substitution at this site, that is, with $y = 2$ (two boron tetrahedra substitute two M' atoms), leads to the formula $(M_{1-x}M'_x)_{21}B_{14}$, for which $Ni_{20}AlB_{14}$ (Figure 24b) is the only structurally characterized representative.^[50] For $y < 2$, a random substitution has to be assumed, if the structure type is to be maintained, a situation proposed, for example, in the structure of $Co_{12.3}Ir_{8.9}B_{10.5}$.^[85] A low-symmetry variant (space group $F\bar{4}3m$ no. 216, non-centrosymmetric) of the $Cr_{23}C_6$ -type structure was proposed recently for $(Co_{0.64}Ir_{0.36})_{21}Co_{0.16}B_{10}$.^[86] At lower symmetry, the $8c$ site splits into two sites ($4c$ and $4d$), of which the $4c$ site stays empty but $4d$ is partially filled with cobalt. Similarly, the $32f$ site splits into two $16e$ sites, of which only one is occupied by boron atoms (B_4 -tetrahedron). This structure model exhibits full atom order separating M' (Co3) atoms and B_4 -tetrahedra in individual sites $4d$ (partially occupied by Co3 atoms) and $16e$ (completely filled by boron atoms), avoiding random replacements (Figure 24c). A crystallographic group-subgroup relation indicates that the low-symmetry variant is a *translationengleiche*, nonisomorphic maximal subgroup of index 2 of $Fm\bar{3}m$.^[86]

7.2 Soft Ferromagnetic Borides with $Cr_{23}C_6$ -Type Structure

The magnetic properties in metal-rich borides of the $Cr_{23}C_6$ -type structure have been extensively studied mainly for phases containing cobalt as main component,^[88] although a few systems without cobalt have also been studied.^[87g,89] These phases usually order ferromagnetically at very high Curie temperatures (T_C often above room temperature): $Co_{20}Al_3B_6$, for example, is a ferromagnet below 403 K.^[88d] Substituting Co by another magnetically active 3d metal leading to the alloys $(Co_{1-x}Fe_x)_{20}Al_3B_6$ and $(Co_{1-x}Ni_x)_{20}Al_3B_6$ increases T_C in the Fe case up to approximately 800 K (at a Co/Fe ratio of 50:50), but in the Ni case, T_C first increases until a maximum (at a Co/Ni ratio of 85:15) is reached, then decreases until approximately 100 K. Furthermore, the magnetic saturation moment follows exactly the same path in both cases. No plausible explanation has been given by the authors, and theoretical calculations are needed here to really understand these behaviors, at least that of the magnetic moment, which can nowadays be calculated with a very good accuracy, as shown in previous sections of this work.

Another important aspect of the ferromagnetic materials of this structure type is their soft nature. In fact, as shown for example in $In_2Ni_{21}B_6$,^[87g] their hysteresis loops have very small coercive fields, but their usually high magnetic permeability combined with the equally high mechanical hardness and appropriate brittleness has prompted scientists in the late seventies to propose them as good candidates for magnetic transducing heads.^[88e] Most magnetic

properties of these phases have been studied before the nineties, although the potential for applications have been already recognized in the late sixties. This is probably due to the competition proposed in the form of the very good mechanical hardness they also have. However, the complexity of their compositions (as shown above) and the strong disorder observed in some crystal structures surely complicate the interpretation of the magnetic properties and make theoretical calculations very challenging. Another important aspect is the synthesis, which is generally not straightforward, and many phases have been discovered from a different starting composition.

8 Synthesis of Transition-Metal-Rich Borides

The synthetic methods for solid-state chemistry include direct combination (high-temperature approaches), syntheses from fluxes and melts, hydrothermal syntheses, and syntheses from solutions. Because of the very low diffusion coefficients in solids, the traditional solid-state synthesis requires high thermal activation. In this method, reactants are weighed in a specific ratio, ground together, pressed into a pellet, and heated to high temperatures. The temperatures needed to facilitate solid-state diffusion and reaction between grains often require, particularly with refractory transition-metal-rich borides, the use of specialized furnaces operating at least at 1500 K, arc welders, RF induction heating. Therefore, this high-temperature route is the method of choice to synthesize transition-metal-rich borides.

9 Conclusions

For the most part of this microreview, experiment and theory have been used in a synergistic way to study the relationship between crystal structure and magnetic properties in various transition-metal-rich borides.

Besides the predicted antiferromagnetism for phases of $Ti_3Co_5B_3$ -type structure having 62 valence electrons (VE) and ferromagnetism for those with 65 VE, a classification of this family of borides in two groups has been established: the first group with VE below 63 shows predominantly antiferromagnetic interactions, whereas the second having at least 63 VE shows predominantly ferromagnetic interactions. Furthermore, antiferromagnetic interactions decrease as ferromagnetic ones increase until a maximum is reached at 66 VE, before the ferromagnetic interactions decrease again. In this study, titanium, actually considered to be magnetically inactive, has a tremendous influence on the hysteresis loops of these phases, as its substitution for scandium has led to the discovery of the first semi-hard ferromagnets of the entire family of transition-metal-rich borides.

The $Zn_{11}Rh_{18}B_8$ -type structure has produced two exciting series of quaternary phases, $Zn_{10}MRh_{18}B_8$ and $Ti_9M_2Ru_{18}B_8$. In the former, size considerations are mainly responsible for the stabilization of the expected phase by M, whereas mainly electronic reasons are predominant in

the latter. In addition, $\text{Ti}_{10}\text{Ru}_{19}\text{B}_8$, the first ternary phase in the Ti–Ru–B system, was decisive in understanding the VE-dependence of the M site in $\text{Ti}_9\text{M}_2\text{Ru}_{18}\text{B}_8$ phases. Furthermore, the presence of iron ladders in $\text{Ti}_9\text{Fe}_2\text{Ru}_{18}\text{B}_8$ has produced the first ferromagnetic boride containing ruthenium as the main component.

In the structural family of borides with Th_7Fe_3 -type structure, many ternary borides have been structurally well characterized recently: A strong site preference is observed when substituting either rhodium or ruthenium by a magnetically active element; this has led not only to the first ferromagnet (FeRh_6B_3) but also to the first ferrimagnet ($\text{Fe}_{0.5}\text{Ru}_{6.5}\text{B}_3$) of this structure type.

Two new structure types, $\text{Ti}_{1.6}\text{Os}_{1.4}\text{RuB}_2$ and $\text{Ti}_{1+x}\text{Rh}_{2-x+y}\text{Ir}_{3-y}\text{B}_2$, have the potential to produce new materials with interesting magnetic properties, because of the presence in their crystal structures of titanium chains, which may be substituted by chains of a magnetically active element as proven in $\text{Ti}_{1-x}\text{Fe}_x\text{Os}_{1.4}\text{RhB}_2$. Furthermore $\text{Ti}_{1.6}\text{Os}_{1.4}\text{RuB}_2$ -type crystal structures contain the first reported trigonal planar B_4 units, whereas the solid solutions $\text{Ti}_{1+x}\text{Rh}_{2-x+y}\text{Ir}_{3-y}\text{B}_2$ contain the more common *zigzag* B_4 units.

In the perovskite boride family, two phases crystallizing with double-perovskite-like structures were discovered. Their structures show boron ordering, in strong contrast to the reported disordered borides crystallizing with a simple cubic crystal structure. Furthermore, the discovery of superstructure and satellite reflections in some other phases in this family by electron diffraction indicates that all the reported disordered structures have to be revised.

The difficulty to achieve single-phase transition-metal boride products in the Cr_{23}C_6 -type structure has hindered the study of magnetic properties in this group of phases to its full potential. However, the phases studied show strong ferromagnetic interactions and are soft magnets. Furthermore, this structure type has also produced (in some few cases) B_4 units; unlike those reported above, they are B_4 tetrahedra.

Acknowledgments

The author would like to thank past and present members of his group, who have contributed to this work, especially the Ph.D. candidates P. R. N. Misse, C. Goerens, and M. Hermus. Professor R. Dronskowski is gratefully acknowledged for his tremendous support during the habilitation period in his group. The author would also like to thank his DFG-NSF collaborator, Professor G. J. Miller, and his group members for their valuable contributions. Mr. K. Kruse, Ms. R. Zaunbrecher, and Dr. P. Müller are acknowledged for their support during various experiments. Finally, thanks to Deutsche Forschungsgemeinschaft (DFG), Verband der Chemischen Industrie (VCI), and Umicore for financial support during the last few years.

[1] F. J. DiSalvo, *Pure Appl. Chem.* **2000**, 72, 1799.

[2] M. O'Keeffe, M. Eddaoudi, H. Li, T. Reineke, O. M. Yaghi, *J. Solid State Chem.* **2000**, 152, 3.

- [3] a) R. Dronskowski, K. Korczak, H. Lueken, W. Jung, *Angew. Chem.* **2002**, 114, 2638; *Angew. Chem. Int. Ed.* **2002**, 41, 2528; b) R. Dronskowski, *Computational Chemistry of Solid State Materials*, Wiley-VCH, Weinheim, New York, **2005**.
- [4] P. Schwartzkopf, R. Kieffer, *Refractory Hard Metals: Borides, Carbides, Nitrides and Silicides*, Macmillan, New York, **1953**.
- [5] J. Nagamatsu, N. Nakagawa, T. Muranaka, Y. Zenitani, J. Akimitsu, *Nature* **2001**, 410, 63.
- [6] J. F. Herbst, *Rev. Mod. Phys.* **1991**, 63, 819898.
- [7] Yu. B. Kuz'ma, Y. P. Yarmolyuk, *Zh. Strukt. Khim.* **1971**, 12, 458.
- [8] a) W. Jung, J. Schiffer, *Z. Anorg. Allg. Chem.* **1990**, 581, 135; b) E. A. Nagelschmitz, Dissertation, University of Cologne, **1995**; c) R. Feiten, Dissertation, RWTH Aachen University, **1996**.
- [9] E. A. Nagelschmitz, W. Jung, *Chem. Mater.* **1998**, 10, 3189.
- [10] E. A. Nagelschmitz, W. Jung, R. Feiten, P. Müller, H. Lueken, *Z. Anorg. Allg. Chem.* **2001**, 627, 523.
- [11] P. Villars, K. Cenzual, *Pearson's Crystal Structure Database for Inorganic Compounds* (on CD-ROM), Version 1.0, Materials Park, OH, USA, **2007/8**.
- [12] a) B. P. T. Fokwa, Habilitation Thesis, RWTH Aachen University, **2009**; b) M. Hermus, B. P. T. Fokwa, manuscript in preparation.
- [13] B. P. T. Fokwa, H. Lueken, R. Dronskowski, *Chem. Eur. J.* **2007**, 13, 6040.
- [14] B. P. T. Fokwa, H. Lueken, R. Dronskowski, manuscript in preparation.
- [15] W. Massa, J. Pebler, F. Hahn, D. Babel, *Organic and Inorganic Low-Dimensional Crystalline Materials*, NATO ASI Series, Plenum Press, New York, **1987**.
- [16] M. Weinert, A. J. Freeman, *J. Magn. Magn. Mater.* **1983**, 38, 23.
- [17] a) G. Samolyuk, B. P. T. Fokwa, R. Dronskowski, G. J. Miller, *Phys. Rev. B* **2007**, 76, 094404; b) G. D. Samolyuk, G. J. Miller, *J. Comput. Chem.* **2008**, 29, 2177.
- [18] R. L. Carlin, *Magnetochemistry*, Springer, Berlin, Heidelberg, **1986**.
- [19] S. Chikazumi, *Physics of Ferromagnetism*, Clarendon, Oxford, **1997**.
- [20] H. Lueken, *Magnetochemie*, Teubner, Stuttgart, **1999**.
- [21] J. F. Herbst, *Rev. Mod. Phys.* **1991**, 63, 819898.
- [22] J. M. D. Coey, *J. Magn. Magn. Mater.* **1999**, 196–197, 1.
- [23] a) V. I. Matkovich, *Boron and Refractory Borides*, Springer, Berlin, **1977**; b) Y. Li, E. Tevaarwerk, R. P. H. Chang, *Chem. Mater.* **2006**, 18, 2552.
- [24] J. Burghaus, R. Dronskowski, G. J. Miller, *J. Solid State Chem.* **2009**, 10, 2613.
- [25] U. Eibenstein, W. Jung, *Z. Anorg. Allg. Chem.* **1998**, 624, 802.
- [26] B. P. T. Fokwa, G. D. Samolyuk, G. J. Miller, R. Dronskowski, *Inorg. Chem.* **2008**, 47, 2113.
- [27] R. H. Mitchell, K. C. Ross, E. G. Potter, *J. Solid State Chem.* **2004**, 177, 1867.
- [28] B. P. T. Fokwa, *Z. Anorg. Allg. Chem.* **2009**, 635, 2258.
- [29] B. P. T. Fokwa, C. Goerens, M. Gilleßen, *Z. Kristallogr.* **2010**, 225, 180–186.
- [30] J. V. Florio, N. C. Baenziger, R. E. Rundle, *Acta Crystallogr.* **1956**, 9, 367.
- [31] E. B. Boltich, S. K. Malik, T. Takeshita, *Solid State Commun.* **1978**, 28, 359.
- [32] K. Sengupta, K. K. Iyer, E. V. Sampathkumaran, *Solid State Commun.* **2006**, 139, 351.
- [33] E. Talik, M. Klimczak, R. Troc, J. Kusz, W. Hofmeister, A. Winiarski, *J. Alloys Compd.* **2008**, 460, 1.
- [34] a) B. T. Matthias, T. H. Geballe, V. B. Compton, *Rev. Mod. Phys.* **1963**, 35, 1; b) L. Fang, H. Yang, X. Zhu, G. Mu, Z.-S. Wang, L. Shan, C. Ren, H.-H. Wen, *Phys. Rev. B* **2009**, 79, 144509; c) N. Kase, J. Akimitsu, *J. Phys. Soc. Jpn.* **2009**, 78, 044710.
- [35] B. Aronsson, *Acta Chem. Scand.* **1959**, 13, 109.

- [36] B. Aronsson, E. Stenberg, J. Aselius, *Acta Chem. Scand.* **1960**, 14, 733.
- [37] W. Trzebiatowski, J. Rudzinski, *J. Less-Common Met.* **1964**, 6, 244.
- [38] Y. B. Kuz'ma, M. V. Chepiga, *Inorg. Mater.* **1973**, 9, 1505.
- [39] Y. B. Kuz'ma, V. I. Lakh, B. I. Stadnyk, D. A. Kovalyk, *Sov. Powder Metall. Met. Ceram.* **1970**, 9, 1003.
- [40] M. V. Chepyha, *Visn. L'viv. Derzh. Univ. (Ser. Khim.)* **1972**, 14.
- [41] Y. B. Kuz'ma, V. I. Lakh, B. I. Stadnyk, N. F. Chaban, *Dopov. Akad. Nauk Ukr. RSR (Ser. A)* **1971**, 849.
- [42] B. P. T. Fokwa, R. Dronskowski, *Z. Anorg. Allg. Chem.* **2005**, 631, 2478.
- [43] B. P. T. Fokwa, R. Dronskowski, *J. Alloys Compd.* **2007**, 428, 84.
- [44] P. R. N. Misse, B. P. T. Fokwa, *Z. Anorg. Allg. Chem.* **2010**, 636, 1013–1017.
- [45] B. P. T. Fokwa, P. R. N. Misse, M. Gilleßen, manuscript in preparation.
- [46] P. Salamakha, O. Sologub, C. Rizzoli, A. P. Goncalves, M. Almeida, *J. Solid State Chem.* **2004**, 177, 4237.
- [47] B. Norlang, L. Tergenius, I. Westman, *J. Less-Common Met.* **1981**, 82, 303.
- [48] P. Rogl, H. Nowotny, *J. Less-Common Met.* **1978**, 61, 39.
- [49] D. Kotzot, M. Ade, H. Hillebrecht, *Solid State Sci.* **2008**, 10, 2921.
- [50] H. Hillebrecht, M. Ade, *Angew. Chem.* **1998**, 110, 981; *Angew. Chem. Int. Ed.* **1998**, 37, 935.
- [51] B. P. T. Fokwa, J. von Appen, R. Dronskowski, *Chem. Commun.* **2006**, 4419.
- [52] J. Aselius, *Acta Chem. Scand.* **1960**, 14, 2169.
- [53] H. G. von Schnering, R. Nesper, J. Curda, K. F. Tebbe, *Angew. Chem. Int. Ed. Engl.* **1980**, 19, 1033.
- [54] R. Nesper, S. Wengert, F. Zurcher, A. Currao, *Chem. Eur. J.* **1999**, 5, 3382.
- [55] G. A. Papoian, R. Hoffmann, *Angew. Chem. Int. Ed.* **2000**, 39, 2408.
- [56] H. Fukuoka, R. Suga, K. Komaguchi, S. Yamanaka, M. Shiotani, *Inorg. Chem.* **2004**, 43, 5780.
- [57] B. P. T. Fokwa, P. R. N. Misse, M. Gilleßen, R. Dronskowski, *J. Alloys Compd.* **2010**, 483, 339.
- [58] B. P. T. Fokwa, R. Dronskowski, *Z. Anorg. Allg. Chem.* **2008**, 634, 1955.
- [59] B. P. T. Fokwa, manuscript in preparation.
- [60] P. Rogl, L. Delong, *J. Less-Common Met.* **1983**, 91, 97.
- [61] H. Takei, T. Shishido, *J. Less-Common Met.* **1984**, 97, 223.
- [62] R. E. Schaak, M. Avdeev, W.-L. Lee, G. Lawes, H. W. Zandbergen, J. D. Jorgensen, N. P. Ong, A. P. Ramirez, R. J. Cava, *J. Solid State Chem.* **2004**, 177, 1244.
- [63] D. Music, J. M. Schneider, *Appl. Phys. Lett.* **2006**, 88, 031914.
- [64] T. Shishido, J. Ye, K. Kudou, S. Okada, K. Obara, T. Sugawara, M. Oku, K. Wagatsuma, H. Horiuchi, T. Fukuda, *J. Alloys Compd.* **1999**, 291, 52.
- [65] H. Takei, N. Kobayashi, H. Yamauchi, T. Shishido, T. Fukase, *J. Less-Common Met.* **1986**, 125, 233.
- [66] T. He, Q. Huang, A. P. Ramirez, Y. Wang, K. A. Regan, N. Rogado, M. A. Hayward, M. K. Haas, J. S. Slusky, K. Inumara, H. W. Zandbergen, N. P. Ong, R. J. Cava, *Nature* **2001**, 411, 54.
- [67] a) T. Shishido, J.-H. Ye, K. Kudou, S. Okada, K. Obara, T. Sugawara, M. Oku, K. Wagatsuma, H. Horiuchi, T. Fukuda, *J. Alloys Compd.* **1999**, 291, 52; b) T. Shishido, J.-H. Ye, S. Okada, K. Kudou, T. Sasaki, S. Isida, T. Naka, M. Oku, I. Higashi, H. Kishi, H. Horiuchi, T. Fukuda, *J. Alloys Compd.* **2000**, 309, 107; c) T. Shishido, K. Kudou, T. Sasaki, S. Okada, J. Ye, K. Iizumi, A. Nomura, T. Sugawara, K. Obara, M. Tanaka, S. Kohiki, Y. Kawazoe, K. Nakajima, M. Oku, *J. Alloys Compd.* **2004**, 383, 294.
- [68] H. Takei, T. Shishido, *J. Less-Common Met.* **1984**, 97, 223.
- [69] R. B. King, *J. Solid State Chem.* **1987**, 71, 233.
- [70] M. Oku, T. Shishido, T. Shinohara, Q. Sun, Y. Kawazoe, K. Nakajima, K. Wagatsuma, *J. Solid State Chem.* **2004**, 177, 457.
- [71] W. Klünter, W. Jung, *Z. Anorg. Allg. Chem.* **1996**, 622, 2099.
- [72] B. P. T. Fokwa, R. Dronskowski, *Z. Kristallogr.* **2006**, 221, 445.
- [73] L. Pauling, *J. Am. Chem. Soc.* **1947**, 69, 542.
- [74] a) D. H. Farrar, E. V. Grachova, A. Lough, C. Patirana, A. J. Poe, S. P. Tunik, *J. Chem. Soc., Dalton Trans.* **2001**, 13, 2015; b) M. J. Ingleson, M. F. Mahon, P. R. Raithby, A. S. Weller, *J. Am. Chem. Soc.* **2004**, 126, 4784; c) P. J. Dyson, J. S. McIndoe, *Angew. Chem. Int. Ed.* **2004**, 43, 6028.
- [75] Z.-Q. Li, J.-Z. Yu, K. Ohno, Y. Kawazoe, *J. Phys.: Condens. Matter* **1995**, 7, 47.
- [76] A. J. Cox, J. G. Louderback, S. E. Apsel, L. A. Bloomfield, *Phys. Rev. B* **1994**, 49, 12295.
- [77] K. Yubuta, A. Nomura, T. Yamamura, T. Shishido, *J. Alloys Compd.* **2008**, 451, 301.
- [78] K. Yubuta, A. Nomura, K. Nakajima, T. Shishido, *J. Alloys Compd.* **2009**, 471, 341.
- [79] R. A. Gordon, F. J. DiSalvo, *Z. Naturforsch., Teil B* **1996**, 51, 52.
- [80] C. D. W. Jones, R. A. Gordon, B. K. Cho, F. J. DiSalvo, J. S. Kim, G. R. Stewart, *Physica B* **1999**, 262, 284.
- [81] P. Rogl, H. Nowotny, *J. Less-Common Met.* **1979**, 67, 41.
- [82] M. Hermus, B. P. T. Fokwa, *J. Solid State Chem.* **2010**, 183, 784.
- [83] V. F. Bashev, I. S. Miroshnichenko, G. A. Sergeev, *Inorg. Mater.* **1981**, 17, 1206.
- [84] L. Battezzati, C. Antonione, M. Baricco, *J. Alloys Compd.* **1997**, 247, 164.
- [85] D. Kotzot, M. Ade, H. Hillebrecht, *J. Solid State Chem.* **2009**, 182, 538.
- [86] O. Sologub, P. Rogl, G. Giester, *Intermetallics* **2010**, 18, 694–701.
- [87] a) E. Ganglberger, H. Nowotny, F. Benesovsky, *Monatsh. Chem.* **1965**, 96, 1144; b) H. H. Stadelmeier in *Developments in the Structural Chemistry of Alloy Phases* (Ed.: B. C. Giessen), Plenum Press, New York, **1969**, vol. 1, pp. 141–180; c) E. Fruchart, R. Fruchart, *C. R. Acad. Sci. Paris* **1964**, 258, 3032; d) E. Ganglberger, H. Nowotny, F. Benesovsky, *Monatsh. Chem.* **1966**, 97, 101; e) B. Yu. Kuz'ma, *Crystal Chemistry of Borides*, Vyshcha Shkola, Lvov, **1983**; f) W. Steurer, P. Rogl, H. Nowotny, *Monatsh. Chem.* **1979**, 110, 791; g) Th. Adelsberger, M. Jansen, *Z. Anorg. Allg. Chem.* **1999**, 625, 438; h) I. B. Hubych, *Visnyk Lviv. Univers.* **1991**, 31, 5; i) W. Jung, *Z. Kristallogr.* **1980**, 151, 113; j) P. Rogl in *Inorganic Reactions and Methods* (Eds.: J. J. Zuckerman, A. P. Hagen), John Wiley & Sons, New York, **1991**, vol. 13, pp. 85–167; k) G. Pradelli, C. Gianoglia, E. Quadrini, *Met. Ital.* **1975**, 67, 21; l) P. Rogl, H. Nowotny, *Monatsh. Chem.* **1973**, 104, 1325.
- [88] a) L. T. Jordan, R. K. Mathur, K. R. Brose, H. H. Stadelmaier, *Z. Metallkd.* **1981**, 72, 782; b) K. H. J. Buschow, P. G. van Engen, R. Jongebreur, *J. Magn. Magn. Mater.* **1983**, 38, 1; c) H. Hirota, A. Yanase, *J. Phys. Soc. Jpn.* **1965**, 20, 1960; d) H. Hirota, *J. Phys. Soc. Jpn.* **1967**, 23, 512; e) H. Hirota, Y. Tawara, Y. Komatsu, *Jpn. J. Appl. Phys.* **1969**, 8, 962.
- [89] R. Sobczak, *Monatsh. Chem.* **1974**, 105, 1071.

Received: February 2, 2010
Published Online: June 10, 2010

2,4,6-Triacetylphlorogucinol as Threefold Symmetric Bridging Ligand: Synthesis, Structure and Magnetic Properties of the Copper Complex

Eike T. Spielberg^[a] and Winfried Plass^{*[a]}

Keywords: Copper / Bridging ligands / Magnetic properties / Stacking interactions / Tritopic ligands

It is shown that 2,4,6-triacetylphlorogucinol (H_3tapg) can be utilized as C_3 -symmetric tritopic bridging ligand, that can be regarded as an annulated threefold acetylacetonate. Together with 2-[bis(2-hydroxyethyl)amino]ethylamine (H_2bhea) as capping ligand the corresponding trinuclear copper complex $[Cu_3(tapg)(H_2bhea)_3](ClO_4)_3$ has been synthesized as

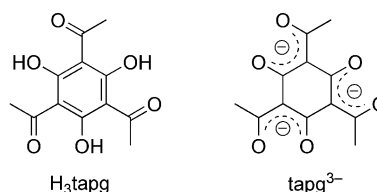
the first example. The compound crystallizes in the trigonal space group $R3c$ with the complex cation located on a threefold rotation axis. Magnetic measurements reveal a ferromagnetic coupling between the copper centers, which are transmitted through the bridging $tapg^{3-}$ ligand by a spin-polarization mechanism.

Introduction

Polynuclear transition-metal complexes have attracted considerable attention because of their relevance to magnetically coupled active sites in metalloproteins and their potential applications as magnetic materials.^[1] Although polytopic ligands play an important role in supramolecular chemistry and crystal engineering,^[2] threefold symmetric organic frameworks have been less employed.^[3]

In molecular magnetism symmetry plays a major role. The overlap of orbitals and hence the exchange interactions between the magnetic centers crucially depend on symmetry.^[4] In particular threefold symmetric systems possess favorable properties related to phenomena like single-molecule magnets (SMMs)^[5] and spin frustration.^[6] Nevertheless, tritopic ligands inducing strict C_3 symmetry onto the resulting complex molecule are rather scarce and to the best of our knowledge limited to Schiff-base ligands based on derivatives of triaminoguanidine^[7] and phloroglucinol.^[8] In case of copper complexes the phloroglucinol-based ligands are capable to transmit ferromagnetic exchange interactions via spin-polarization mechanism. However, assembly of *meta*-phenylene-bridged transition metal complexes is not a conclusive recipe to construct high-spin molecules as opposing spin-delocalization and spin-polarization effects are operative in such systems.^[9]

Herein we report the synthesis of a trinuclear copper complex as the first example of a transition metal compound with 2,4,6-triacetylphlorogucinol (H_3tapg ; Scheme 1) as threefold bridging ligand, which in its deprotonated form can be considered as an annulated threefold acetylacetonate based on a benzene core.



Scheme 1. 2,4,6-Triacetylphlorogucinol (H_3tapg).

Results and Discussion

The stepwise synthesis utilizing H_3tapg as a threefold symmetry inducing ligand together with 2-[bis(2-hydroxyethyl)amino]ethylamine (H_2bhea) as capping coligand affords the trinuclear copper complex $[Cu_3(tapg)(H_2bhea)_3](ClO_4)_3$ (**1**) as blue crystalline compound. At first the copper precursor containing the coligand is prepared by adding an ethanolic solution of H_2bhea to an ethanolic solution of copper perchlorate hexahydrate. In a second step this precursor complex is treated in acetonitrile solution with the H_3tapg ligand together with stoichiometric amounts of triethylamine to facilitate deprotonation. For prolonged reaction times the initially blue reaction solution turns green, probably caused by a coordination induced Schiff-base formation between the primary amine of the H_2bhea coligand and the carbonyl group of $tapg^{3-}$ core ligand. To avoid condensation reaction, a fast crystallization procedure is crucial. By vapor diffusion of diethyl ether into the acetonitrile solution needles with hexagonal basal plane are obtained within a few hours. The chemical constitution of **1** has been confirmed by analytical and spectroscopic data.

The complex **1** crystallizes in the trigonal space group $R3c$ together with one acetonitrile molecule as solvent of crystallization. In Figure 1 the structure of the complex cation $[Cu_3(tapg)(H_2bhea)_3]^{3+}$ and the atom numbering scheme are given along with selected bond lengths and

[a] Institut für Anorganische und Analytische Chemie, Friedrich-Schiller-Universität Jena, Carl-Zeiss-Promenade 10, 07743 Jena, Germany
Fax: +49-3641-948132
E-mail: sekr.plass@uni-jena.de

angles. The molecular structure shows that the three copper ions are bridged by the tritopic tapg^{3-} ligand with copper–copper distances of 725 pm. Each copper ion is coordinated by one phenolic (O1) and one acetyl oxygen atom (O2) from the bridging ligand. The equatorial coordination plane is completed by two nitrogen atoms (N1 and N2) of the H_2bhea capping ligand. The two hydroxy groups (O3 and O4) of the capping ligand are occupying the axial positions of the elongated octahedron. The observed bond lengths are typical for a Jahn–Teller distorted copper(II) ion, with the axial bonds about 50 pm elongated with respect to those of the equatorial plane. The least-squares plane given by the equatorial donor atoms at the copper center (N1, N2, O1, and O2) is tilted by about 15° with respect to the central aromatic ring of the tapg^{3-} ligand, leading to a slightly bowl-shaped arrangement. A similar distortion has also been observed for the complexes of so-called tripesalen ligands,^[8] which are Schiff-base derivatives of the H_3tapg core ligand. The equatorial planes of the copper coordination spheres within the molecular cation are tilted against each other by about 25° . The observed equivalence of the C–O (126 pm) and C–C (143 pm) bond lengths within the tapg^{3-} ligand are clearly indicative of its chelating nature as annulated threefold acetylacetonate core ligand (cf. Figure 1). This is in contrast to the alternating bond lengths observed for the protonated free H_3tapg ligand.^[10]

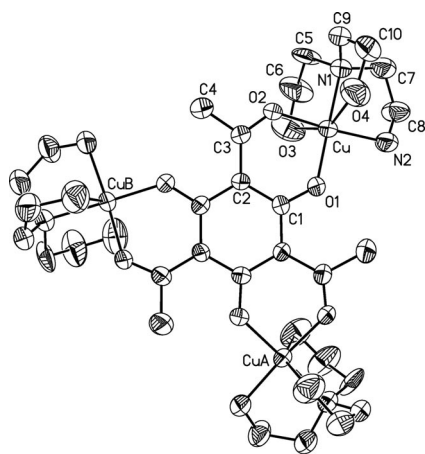


Figure 1. Molecular structure of the complex cation $[\text{Cu}_3(\text{tapg})-(\text{H}_2\text{bhea})_3]^{3+}$ in crystals of $1 \cdot \text{CH}_3\text{CN}$. Hydrogen atoms are omitted for clarity, only one set of the disordered positions for the chelate ring containing O3 is displayed, thermal ellipsoids are drawn at the 50% probability level. Selected bond lengths [pm]: Cu–O1 189.2(3), Cu–O2 192.0(3), Cu–N2 199.8(4), Cu–N1 203.9(4), Cu–O3 237.8(15), Cu–O4 250.8(5), O1–C1 1.274(4), O2–C3 1.257(5), C1–C2 1.438(5), C2–C3 1.431(5), C1–C2A 1.432(5). Selected angles [$^\circ$]: O1–Cu–O2 89.19(13), O1–Cu–O3 98.7(3), O1–Cu–O4 102.10(16), O1–Cu–N1 178.70(17), O1–Cu–N2 93.39(15), O2–Cu–O3 80.7(4), O2–Cu–O4 80.54(17), O2–Cu–N1 91.96(15), O2–Cu–N2 173.6(2), O3–Cu–O4 151.7(4), O3–Cu–N1 80.9(3), O3–Cu–N2 104.7(4), O4–Cu–N1 78.70(17), O4–Cu–N2 93.2(2), N1–Cu–N2 85.53(16).

The cationic trinuclear complexes are stacked along crystallographic threefold rotation axis with a twist angle of 18.2° and alternating chirality of the complex units, but the same orientation of the bowl-shaped units with respect to the rotation axis. The resulting crystal packing is illustrated

in Figure 2. Within the stacks the bowl-shaped complex cations are separated by about 695 pm, whereas the stacks are separated by a distance of about 1500 pm. As a consequence the shortest intermolecular copper–copper distances are about 708 pm. Along the stacks hydrogen-bonding interactions are observed between the complex cations as depicted in Figure 3. The perchlorate counterions are located in the space between the bowl-shaped complex cations and form hydrogen bonds to the primary amino group (N1) and one of the hydroxy groups (O4) of the H_2bhea capping ligands (Figure 3).

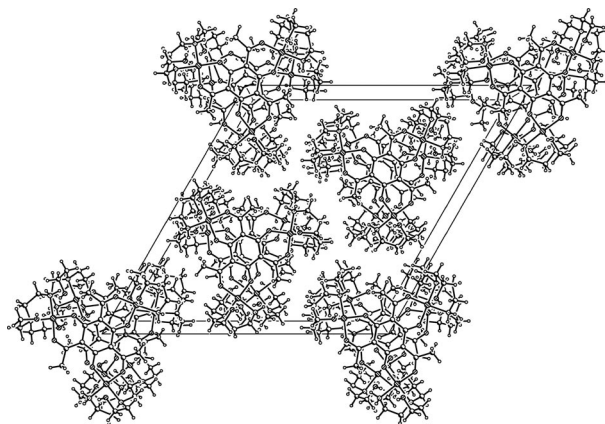


Figure 2. View of the packing of the complex cations $[\text{Cu}_3(\text{tapg})-(\text{H}_2\text{bhea})_3]^{3+}$ in crystals of $1 \cdot \text{CH}_3\text{CN}$ along the $[001]$ direction. The perchlorate counterions and the acetonitrile molecules are omitted for clarity.

The temperature dependence of the magnetization data has been measured on powdered samples of the trinuclear compound $1 \cdot \text{CH}_3\text{CN}$ in the temperature range from 2 to 300 K. These data are shown in Figure 4 as temperature dependent plots of χ_M and $\chi_M T$, where χ_M is the molar paramagnetic susceptibility. At higher temperatures the linear dependence of the $\chi_M T$ values is indicative of temperature-independent paramagnetic contributions. Whereas below 45 K the $\chi_M T$ values increase indicating ferromagnetic coupling between the three copper centers.

Due to the C_3 symmetry of the molecular system, which is imposed by the tapg^{3-} ligand, an equilateral triangle with only one exchange coupling constant J_{CuCu} can be used to describe the interactions between the copper centers leading to the Heisenberg Hamiltonian shown in Equation (1). The resulting analytical expression for $\chi_M T$ derived for three $S = 1/2$ centers is given in Equation (2).^[11] Where g_{Cu} is the average gyromagnetic factor of the copper centers, θ the mean field parameter, J_{CuCu} the isotropic coupling constants, and χ_{TIP} the temperature-independent paramagnetism.

$$\hat{H} = -J_{\text{CuCu}} (\hat{S}_{\text{Cu1}} \hat{S}_{\text{Cu2}} + \hat{S}_{\text{Cu1}} \hat{S}_{\text{Cu3}} + \hat{S}_{\text{Cu2}} \hat{S}_{\text{Cu3}}) \quad (1)$$

$$\chi_M T = \frac{N \beta^2 g_{\text{Cu}}^2 T}{4k(T - \theta)} \frac{1 + 5 \exp[3J_{\text{CuCu}} / 2kT]}{1 + \exp[3J_{\text{CuCu}} / 2kT]} + \chi_{\text{TIP}} T \quad (2)$$

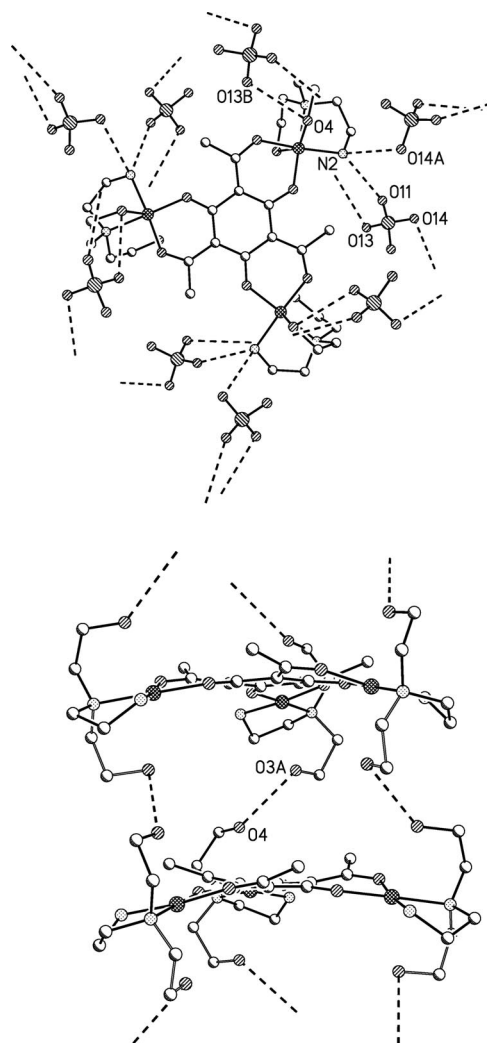


Figure 3. Representation of the hydrogen-bonding interactions of the complex cation $[\text{Cu}_3(\text{tapg})(\text{H}_2\text{bhea})_3]^{3+}$ with the perchlorate counterions (top) and neighboring complex cations along the stack (bottom) in crystals of **1**·CH₃CN. Hydrogen atoms are omitted for clarity, only one set of the disordered atoms is shown, broken lines represent hydrogen bonds. Pertinent distances [pm]: N2...O11 292.8(11), N2...O14A 311.4(14), O4...O13B 315(2), O3A...O4 308.5(16).

The best fit of the experimental susceptibility data to Equation (2) yields the parameters $g_{\text{Cu}} = 2.1031(6)$, $J_{\text{CuCu}} = +1.10(4) \text{ cm}^{-1}$, $\chi_{\text{TIP}} = 00018(1) \text{ cm}^3 \text{ mol}^{-1}$, and $\theta = -0.51 \text{ K}$ with a final coefficient of determination of $R^2 = 0.98892$ and is depicted in Figure 4. The observed ferromagnetic exchange coupling is consistent with a spin-polarization mechanism based on the bowl-shaped distortion of the complex unit and well within the range reported for trinuclear copper systems based on the so-called triplesalen ligands.^[8]

For these triplesalen ligands it has been reported, that the folding at the hinge given by the two equatorial donor atoms of the central aromatic core (for **1**: O1 and O2) results in a non-orthogonal overlap of the p_z orbitals of these oxygen donors with the magnetic $d_{x^2-y^2}$ orbital at the copper center and therefore enables a direct delocalization of spin-

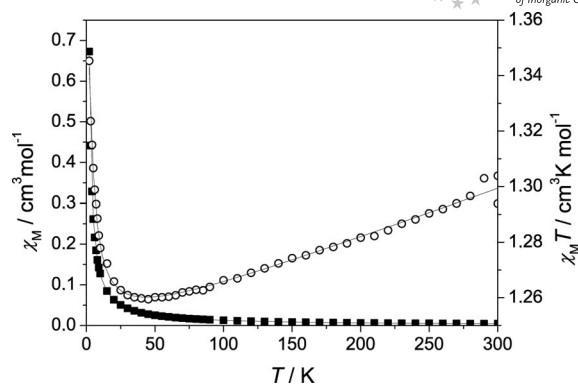


Figure 4. Temperature dependence of χ_M (black squares) and $\chi_M T$ (empty circles) measured on powder samples of **1**·CH₃CN. The solid lines represent the simulation with the parameters given in the text.

density into the p_z orbitals of the bridging ligand. Consequently this hinge folding is a crucial factor for the size of the observed exchange coupling mediated in such systems.^[8] Larger folding angles are found to favor larger ferromagnetic coupling between the copper centers. This is consistent with the rather moderate bowl-shaped distortion observed for the complex unit in **1** showing an actual folding angle at the hinge of 12.7° . Nevertheless, also the nature of the donor atoms in the equatorial coordination plane have to be considered with respect to their influence on the strength of the copper–phenolate bond. In this context also the observed behavior of the H₃tapg ligand as an annulated threefold acetylacetonate is to be emphasized, as this can facilitate an efficient interaction between the copper centers and the bridging core ligand.

Although the intermolecular copper–copper distances along the hydrogen-bonded stack (cf. Figure 3) are somewhat shorter than the intramolecular ones (708 and 725 pm, respectively), a relevant magnetic exchange interaction cannot be expected due to the relative orientation of the magnetic orbitals with respect to the OH...O hydrogen bonds.^[12]

Conclusions

We have presented the synthesis of a trinuclear copper complex with 2,4,6-triacetylphlorogucinol as C_3 -symmetric bridging ligand. This is the first example of a transition metal complex with this annulated threefold acetylacetonate core ligand. Moreover, this is a rare case for which the threefold symmetry of the bridging ligand is transferred into the resulting crystal structure, here leading to the trigonal space group $R3c$. The bridging ligand facilitates ferromagnetic exchange interactions between the copper centers.

Experimental Section

General Remarks: The ligands 2,4,6-triacetylphlorogucinol (H₃tapg)^[13] and 2-[bis(2-hydroxyethyl)amino]ethylamine (H₂bhea)^[14] were prepared according to reported procedures. All chemicals were used as received without further purification. IR spectra were

recorded on a Bruker IFS55/Equinox spectrometer on samples prepared as KBr pellets. Raman spectra were measured with the Bruker IFS55/Equinox spectrometer equipped with FRA 106/S Raman unit on neat solid samples. Mass spectra were recorded on a Bruker MAT SSQ 710 instrument utilizing electron spray ionization and observation in positive mode. Elemental analyses (C, H, N) were carried out on Leco CHNS-932 and El Vario III elemental analyzers. Magnetic susceptibilities were measured on a Quantum Design MPMSR-5S-SQUID magnetometer in the range from 2 to 300 K with an applied field of 2000 Oe. Diamagnetic corrections were estimated according to Pascal's constants.

[Cu₃(tapg)(H₂bhea)₃](ClO₄)₃·CH₃CN: A solution of 2-[bis(2-hydroxyethyl)amino]ethylamine (H₂bhea) (44.6 mg, 0.3 mmol) in 2 mL ethanol was added to a solution of Cu(ClO₄)₂·6H₂O (111.3 mg, 0.3 mmol) in 2 mL ethanol. The volatiles are removed under a continuous flow of nitrogen. The obtained blue viscous oil is dissolved in 2 mL acetonitrile and a solution of 2,4,6-triethylphloroglucinol (25.8 mg, 0.1 mmol) and triethylamine (43.2 μL, 0.3 mmol) in 2 mL of acetonitrile is added resulting in a deep blue solution. Long hexagonal needles suitable for X-ray diffraction could be obtained at room temperature by fast vapor diffusion of diethyl ether into the acetonitrile solution within a few hours; yield 83.9 mg (0.07 mmol, 70%). C₃₂H₆₀Cl₃Cu₃N₇O₂₄ (1223.98): calcd. C 31.40, H 4.94, N 8.01; found C 31.08, H 5.07, N 7.84. Selected IR data (KBr): $\tilde{\nu}$ = 3435 (νOH), 3340 (ν_{as}NH₂), 3287 (ν_sNH₂), 2974 (ν_{as}CH₂, CH₃), 2932 (ν_sCH₃), 2897 (ν_sCH₂), 2255 (νC≡N), 1553 (νC=C_{arom}), 1461 (δCH₂), 1380 (δCH₃), 1091 (ν_sClO₄) cm⁻¹. Selected Raman data (50 mW, 100 scans): $\tilde{\nu}$ = 2902 (ν_sCH₃), 2864 (ν_sCH₂), 1546 (νC=C_{arom}), 1463 (δCH₂), 1379 (δCH₃), 933 (ν_sClO₄) cm⁻¹. MS-ESI positive (CH₃CN+MeOH): *m/z* (%) = 1082 (4) {[Cu₃(tapg)(H₂bhea)₃](ClO₄)₂ + 2H}⁺, 771 (19) {[Cu₂(Htapg)(H₂bhea)₂](ClO₄)₂}⁺, 462 (100) [Cu(H₂tapg)(H₂bhea)]⁺. UV/Vis (CH₃CN): λ_{max} (ε, M⁻¹cm⁻¹) = 623 (187), 232 (43300), 224 (19800) nm.

X-ray Crystallographic Study for [Cu₃(tapg)(H₂bhea)₃](ClO₄)₃·CH₃CN: C₃₂H₆₀Cl₃Cu₃N₇O₂₄, *M_r* = 1223.84 g mol⁻¹, trigonal space group *R*3c, *a* = 24.9693(4), *c* = 13.9097(3) pm, *V* = 7510.4(2)·10⁶ pm³, *Z* = 6, μ(Mo-*K*_α) = 1.510 mm⁻¹, *d*_{calc} = 1.624 g·cm⁻³, 16894 reflections measured with a Nonius KappaCCD diffractometer at 183(2) K in the 2.89 to 27.49° theta range. The structure was solved by direct methods and subsequently refined against *F*² with the SHELXL-97 program^[15] utilizing 308 parameters and 55 restraints. The final solution converged at *R*₁ = 0.0404, *wR*₂ = 0.1023 for 3308 observed reflections with *I* > 2σ(*I*) and *R*₁ = 0.0488, *wR*₂ = 0.1087 for the total number of 3795 unique reflections with a goodness-of-fit on *F*² of 1.073 and a Flack parameter of -0.011(19).

All non-hydrogen atoms were refined with anisotropic displacement parameters, except those of the disordered acetonitrile molecule. All hydrogen atoms were placed at calculated positions and refined as riding atoms with isotropic displacement parameters. For one of the hydroxy ethyl chelate rings of the H₂bhea ligand a disorder at a ratio of 1:1 over two crystallographic positions is observed. A similar situation is found for the perchlorate counterion which is also disordered over two positions in a 1:1 ratio. The additional molecule of acetonitrile per trinuclear complex found in the crystal structure is strongly disordered around the threefold rotation axis in the cavity above and below the aromatic core fragment. The relevant carbon and nitrogen atoms were refined with isotropic dis-

placement parameters and the corresponding hydrogen atoms have not been included. Due to the highly disordered electron density in this region of the crystal structure the refinement was only possible with appropriate restraints. The largest positive and negative residual Fourier peaks after the refinement were equal to 0.41 and -0.34, respectively.

CCDC-770566 contains the supplementary crystallographic data for this paper. These data can be obtained free of charge from the Cambridge Crystallographic Data Centre via www.ccdc.cam.ac.uk/data_request/cif.

Acknowledgments

We thank the Deutsche Forschungsgemeinschaft (DFG) (Priority Program: Molecular Magnetism) for financial support. E. T. S. gratefully acknowledges scholarships by the Carl-Zeiss-Stiftung and the Jenaer Graduiertenakademie.

- [1] a) R. H. Holm, P. Kennepohl, E. I. Solomon, *Chem. Rev.* **1996**, 96, 2239; b) J. S. Miller, M. Drillon (Eds.), *Magnetism: Molecules to Materials*, vol. I–V, Wiley-VCH, Weinheim, **2001–2005**; c) O. Kahn, *Acc. Chem. Res.* **2000**, 33, 647; d) W. Plass, *Chem. Unserer Zeit* **1998**, 32, 323; e) D. Gatteschi, R. Sessoli, J. Villain, *Molecular Nanomagnets*, Oxford University Press, Oxford, **2006**.
- [2] a) S. Kitagawa, R. Kitaura, S.-I. Noro, *Angew. Chem. Int. Ed.* **2004**, 43, 2334; b) B. Moulton, M. Zaworotko, *Chem. Rev.* **2001**, 101, 1629.
- [3] a) P. J. Lusby, P. Müller, S. J. Pike, A. M. Z. Slawin, *J. Am. Chem. Soc.* **2009**, 131, 16398; b) A. E. Ion, E. T. Spielberg, H. Görls, W. Plass, *Inorg. Chim. Acta* **2007**, 360, 3925; c) M. J. Prushan, N. K. Privette, M. Zeller, A. D. Hunter, S. Lofland, S. D. Preite, *Inorg. Chem. Commun.* **2007**, 10, 631; d) A. Zharkouskaya, A. Buchholz, W. Plass, *Eur. J. Inorg. Chem.* **2005**, 4875; e) A. Zharkouskaya, H. Görls, G. Vaughan, W. Plass, *Inorg. Chem. Commun.* **2005**, 8, 1145; f) M. Pasqu, F. Lloret, N. Avarvari, M. Julve, M. Andruh, *Inorg. Chem.* **2004**, 43, 5189; g) J. Leveque, C. Moucheron, A. Kirsch-De Mesmaeker, F. Loiseau, S. Serroni, F. Puntoriero, S. Campagna, H. Nierengarten, A. Van Dorselaerc, *Chem. Commun.* **2004**, 878; h) B. Conerney, P. Jensen, P. Kruger, C. MacGloinn, *Chem. Commun.* **2003**, 1274.
- [4] O. Kahn, *Angew. Chem. Int. Ed. Engl.* **1985**, 24, 834.
- [5] D. Gatteschi, R. Sessoli, *Angew. Chem. Int. Ed.* **2003**, 42, 268.
- [6] J. Yoon, E. I. Solomon, *Coord. Chem. Rev.* **2007**, 251, 379.
- [7] W. Plass, *Coord. Chem. Rev.* **2009**, 253, 2286.
- [8] T. Glaser, H. Theil, M. Heidemeier, *C. R. Chim.* **2008**, 11, 1121.
- [9] a) D. Plaul, A. Buchholz, H. Görls, W. Plass, *Polyhedron* **2007**, 26, 4581; b) D. Plaul, D. Geibig, H. Görls, W. Plass, *Polyhedron* **2009**, 28, 1982.
- [10] P. E. Hansen, S. Bolvig, K. Wozniak, *J. Mol. Struct.* **2005**, 749, 155.
- [11] O. Kahn, *Molecular Magnetism*, Wiley-VCH, Weinheim, **1993**.
- [12] W. Plass, A. Pohlmann, J. Rautengarten, *Angew. Chem. Int. Ed.* **2001**, 40, 4207.
- [13] S. R. Gupta, K. K. Malik, T. R. Seshadri, *Ind. J. Chem.* **1968**, 6, 481.
- [14] W. Plass, *Z. Anorg. Allg. Chem.* **1994**, 620, 1635.
- [15] G. Sheldrick, *SHELXS-97 and SHELXL-97*, University of Göttingen, **1997**.

Received: March 27, 2010
Published Online: June 2, 2010

Non-Oxido Mixed-Valence $\text{Mn}^{\text{II}}_6\text{Mn}^{\text{III}}_4$ Cluster with Benzoate, Triethanolamine and Phosphonate Bridging Ligands

Catherine Dendrinou-Samara,^{*,[a]} Christopher A. Muryn,^[b] Floriana Tuna,^[b] and Richard E. P. Winpenny^{*,[b]}

Keywords: Manganese / Cluster compounds / Antiferromagnetic behaviour / Tripodal ligands / Mixed-valent compounds

The synthesis, structure and magnetic properties of a new non-oxido mixed-valence decanuclear heterometallic manganese cluster $[\text{K}_3\text{Mn}_{10}(\text{PhCOO})_{10}(\text{PhPO}_3)_2(\text{Htea})_6](\text{PhCOO})\cdot 6\text{MeCN}]_n$ (**1**), where Htea^{2-} is the dianion of triethanolamine, is reported. Compound **1** can be regarded as an analogue of 24-metallacrown-10, acting as a host for three potassium ions. The resulting $\{\text{Mn}_{10}\}$ cage crystallises as a cation; benzoate anions link the cages into a 1D polymer within the crys-

tal. Direct current magnetic susceptibility measurements were collected at temperatures between 1.8 and 300 K and applied magnetic fields of 1 and 10 kG. The room-temperature value is very close to the spin-only value of $38.25 \text{ cm}^3 \text{ mol}^{-1} \text{ K}$ expected for an Mn_{10} -cage repeat unit comprising six Mn^{II} and four Mn^{III} ions. At 2 K and 70 kG the magnetisation reaches a value of $19.5 \text{ N}\mu_{\text{B}}$, suggesting a ground state larger than $S = 10$.

Introduction

Manganese metallacrowns^[1] exhibit cyclic structures analogous to crown ethers, as they encapsulate guest ions or molecules; this observation has led to the proposal that they could function as cation, anion or ionic recognition agents.^[2] Normally, manganese metallacrowns have two bridging heteroatoms between metal atoms and are restricted to analogues of 12-crown-4, 15-crown-5 and 18-crown-6. Technically, some other cyclic structures have been described as metallacrowns, for example, the class of heteropolyanions.^[3] These molecules have only one bridging atom between metal atoms as 12-metallacrown-6, where the ring involves single-atom hydroxide and alkoxide bridges between Fe^{III} or Mn^{III} ions and an alkali metal cation encapsulated in the centre.^[4] Many wheel-shaped structures of the first-row transition metals are described,^[5] whereas in manganese chemistry they are not so common. However, larger cyclic structures with manganese are also known. These include the huge ring $[\text{Mn}_{84}\text{O}_{72}(\text{O}_2\text{CMe})_{78}(\text{OMe})_{24}(\text{OH})_6(\text{MeOH})_{12}(\text{H}_2\text{O})_{42}]$ reported by Christou and co-workers;^[6] $[\text{Mn}^{\text{IV}}_6\text{Mn}^{\text{II}}_{18}(\text{bpy})_{24}(\text{O}_2\text{CMe})_6(\text{N}_3)_6(\text{tmp})_{12}]^{12+}$ [bpy = bipyridine; $\text{H}_3\text{tmp} = 1,1,1\text{-tris}(\text{hydroxymethyl})\text{propane}$], where acetate bridges link triangular subunits to form a wheel structure;^[7] five rings involving carboxylates and ethanolamine ligands: $[\text{Mn}^{\text{III}}_6\text{Mn}^{\text{II}}_6(\text{O}_2\text{CMe})_{14}(\text{mdea})_8]$

(mdea = *N*-methyldiethanolamine),^[8] $[\text{Mn}^{\text{III}}_4\text{Mn}^{\text{II}}_4(\text{O}_2\text{CCH}_2\text{tBu})_{12}(\text{teaH})_4]$,^[9] $[\text{Mn}^{\text{III}}_8\text{Mn}^{\text{II}}_8(\text{O}_2\text{CMe})_{16}(\text{teaH})_{12}]$,^[9] $[\text{Mn}^{\text{III}}_8\text{Mn}^{\text{II}}_8(\text{O}_2\text{CCH}(\text{CMe})_2)_{16}(\text{teaH})_{12}]$ ^[10] and $[\text{Mn}^{\text{III}}_8\text{Mn}^{\text{II}}_8(\text{O}_2\text{CCH}_3)_8(\text{O}_2\text{CnPr})_8(\text{teaH})_{12}]$ ^[10] (teaH₃ = triethanolamine); and two metalladiazamacrocycles, $[\text{Mn}^{\text{III}}_{10}(\text{2-dmpshz})_{10}(\text{py})_{10}]$ [2-dmpshz = *N*-(2,2-dimethylpropanoyl)-salicylohydrazide] and $[\text{Mn}^{\text{III}}_{10}(\text{bzshz})_{10}(\text{MeOH})_{10}]$ (bzshz = *N*-phenylsalicylohydrazide), with an $[\text{Mn}_{10}(\mu\text{-NN})_{10}]^{20+}$ core and a spin ground state of $S = 2$ in both cases.^[11,12]

We have used a mixture of carboxylates, phosphonates and triethanolamine ligands in the synthesis of new polynuclear manganese complexes. In this report, we present a decanuclear heterometallic manganese cluster, $\{[\text{K}_3\text{Mn}_{10}(\text{PhCOO})_{10}(\text{PhPO}_3)_2(\text{Htea})_6](\text{PhCOO})\cdot 6\text{MeCN}]_n$ (**1**), showing a cyclic structure, which binds three potassium ions within the ring. Compound **1** can be regarded as a metallacrown, an analogue of 24-metallacrown-10 acting as a host for three potassium ions. The resulting cage crystallises as a cation, and benzoate anions link the cages into a 1D polymer within the crystal. The magnetic properties of **1** are also reported.

Results and Discussion

The molecular structure of $\{[\text{K}_3\text{Mn}_{10}(\text{PhCOO})_{10}(\text{PhPO}_3)_2(\text{Htea})_6](\text{PhCOO})\cdot 6\text{MeCN}]_n$ (**1**) (Figure 1) has no crystallographic symmetry. The $\{\text{Mn}_{10}\}$ cluster has a planar cyclic core comprising six Mn^{II} and four Mn^{III} ions. Assignment of oxidation states was determined by inspection of metric parameters and confirmed by bond-valence sum analysis developed by Brown and Thorp and co-workers.^[13]

[a] Department of Chemistry, Aristotle University of Thessaloniki, 54124 Thessaloniki, Greece
E-mail: samkat@chem.auth.gr

[b] School of Chemistry, The University of Manchester, Oxford Road, Manchester M13 9PL, UK
Fax: +44-161-275-4616

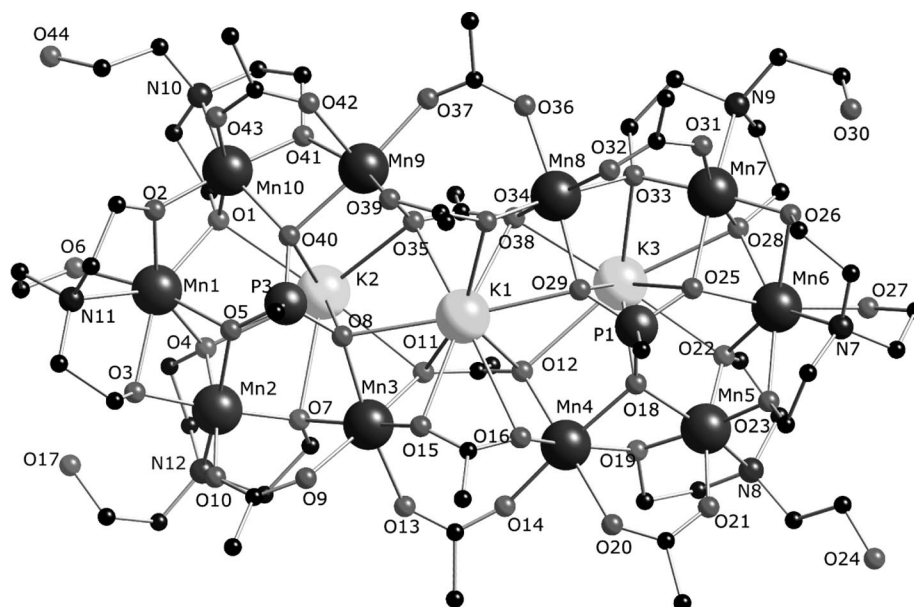


Figure 1. The crystal structure of **1**. Phenyl rings of ligands, hydrogen atoms and solvate molecules are excluded for clarity.

The decametallic core is approximately planar, and arranged with two parallel lines of four Mn sites: Mn2, Mn3, Mn4 and Mn5 on one side, and Mn7, Mn8, Mn9 and Mn10 on the other. The Mn2...Mn3...Mn4, Mn3...Mn4...Mn5, Mn7...Mn8...Mn9 and Mn8...Mn9...Mn10 angles are approximately 160°. The cyclic structure is completed by Mn1 and Mn6, and the Mn10...Mn1...Mn2 and Mn5...Mn6...Mn7 angles are approximately 120°. In some ways this resembles the double-horseshoes of chromium(III) reported by Timco et al.,^[14] the two {Mn₅} horseshoes contain Mn3, Mn2, Mn1, Mn10, and Mn9, and Mn4, Mn5, Mn6, Mn7 and Mn8, respectively.

The metal-metal edges of this very irregular decagon fall into five groups. Firstly, two edges, Mn1...Mn2 and Mn6...Mn7, are bridged by two alkoxide oxygen atoms and an oxygen atom from phosphonate (e.g., O3, O4 and O5 bridge Mn1...Mn2). Secondly, the two edges Mn1...Mn10 and Mn5...Mn6 are bridged by two alkoxides (e.g., O1 and O2 bridge Mn1...Mn10). Thirdly, the two edges Mn2...Mn3 and Mn7...Mn8 are bridged by a single alkoxide oxygen atom and a 2.11 (Harris notation^[15]) bridging carboxylate. Fourthly, the edges Mn4...Mn5 and Mn9...Mn10 are bridged by an alkoxide oxygen atom, a phosphonate oxygen atom and a 2.11 bridging benzoate. Finally, the edges Mn3...Mn4 and Mn8...Mn9 are each bridged by three carboxylates.

There are three types of chemically distinct manganese sites (selected bond lengths are given in Table 1):

(i) Mn1 and Mn6 are in a +2 oxidation state and are seven-coordinate, with an NO₆ donor set and average Mn–O/N distances of 2.273 Å and 2.265 Å, respectively. Each centre binds to a tetrachelate double deprotonated triethanolamine group Htea^{2−} through O2, O6, O3, N11 and O23, O26, O27, N7, respectively, and one μ₂-oxygen atom (O5

Table 1. Selected bond lengths for compound **1**.

Mn ^{II} O ₆ N			
Mn1–O2 _(triol)	2.152(3)	Mn6–O23 _(triol)	2.149(3)
Mn1–O1 _(triol)	2.236(3)	Mn6–O27 _(triol)	2.198(4)
Mn1–O4 _(triol)	2.248(3)	Mn6–O28 _(triol)	2.217(3)
Mn1–O6 _(triol)	2.279(4)	Mn6–O22 _(triol)	2.249(3)
Mn1–O3 _(triol)	2.342(3)	Mn6–O26 _(triol)	2.431(3)
Mn1–O5 _(phosp)	2.232(3)	Mn6–O25 _(phosp)	2.223(3)
Mn1–N11	2.426(4)	Mn6–N7	2.391(4)
Mn ^{III} O ₅ N			
Mn2–O7 _(triol)	1.903(3)	Mn10–O2 _(triol)	1.905(3)
Mn2–O4 _(triol)	1.919(3)	Mn10–O41 _(triol)	1.907(3)
Mn2–O3 _(triol)	1.924(3)	Mn10–O43 _(triol)	1.927(3)
Mn2–O10 _(triol)	1.948(3)	Mn10–O1 _(triol)	1.928(3)
Mn2–O5 _(phosp)	2.257(3)	Mn10–O40 _(phosp)	2.205(3)
Mn2–N12	2.378(4)	Mn10–N10	2.394(4)
Mn5–O23 _(triol)	1.890(3)	Mn7–O33 _(triol)	1.907(3)
Mn5–O19 _(triol)	1.910(3)	Mn7–O26 _(triol)	1.913(3)
Mn5–O22 _(triol)	1.919(3)	Mn7–O28 _(triol)	1.925(3)
Mn5–O21 _(triol)	1.954(3)	Mn7–O31 _(triol)	1.940(3)
Mn5–O18 _(phosp)	2.212(3)	Mn7–O25 _(phosp)	2.234(3)
Mn5–N8	2.391(4)	Mn7–N9	2.346(4)
Mn ^{II} O ₆			
Mn3–O13 _(carbox)	2.127(3)	Mn9–O39 _(carbox)	2.116(4)
Mn3–O15 _(carbox)	2.146(3)	Mn9–O37 _(carbox)	2.131(3)
Mn3–O11 _(carbox)	2.260(3)	Mn9–O35 _(carbox)	2.183(3)
Mn3–O9 _(carbox)	2.192(3)	Mn9–O42 _(carbox)	2.260(3)
Mn3–O7 _(triol)	2.141(3)	Mn9–O41 _(triol)	2.177(3)
Mn3–O8 _(phosp)	2.160(3)	Mn9–O40 _(phosp)	2.237(3)
Mn4–O14 _(carbox)	2.105(3)	Mn8–O38 _(carbox)	2.111(4)
Mn4–O16 _(carbox)	2.109(3)	Mn8–O36 _(carbox)	2.121(3)
Mn4–O16 _(carbox)	2.251(3)	Mn8–O34 _(carbox)	2.242(3)
Mn4–O20 _(carbox)	2.171(3)	Mn8–O32 _(carbox)	2.200(3)
Mn4–O19 _(triol)	2.177(3)	Mn8–O33 _(triol)	2.156(3)
Mn4–O18 _(phosp)	2.205(3)	Mn8–O29 _(phosp)	2.153(3)

and O25, respectively) of the phosphonates. The coordination spheres are completed by O1, O4 and O28, O22 from neighbouring Htea^{2−} groups.

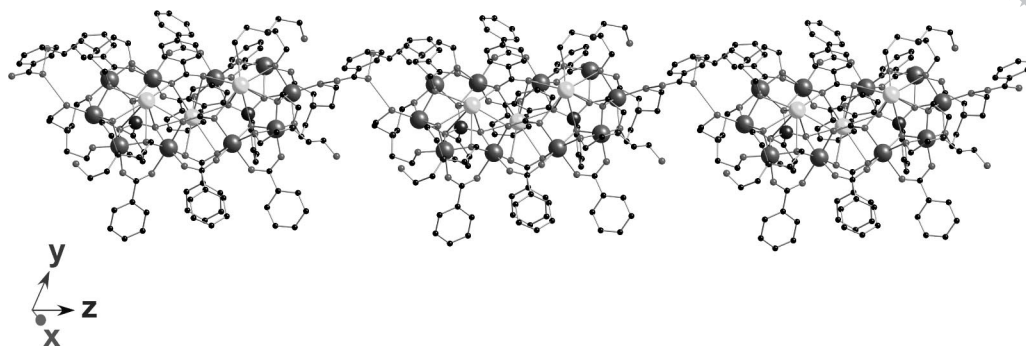


Figure 2. The 1D chain of units of **1** within the crystal, linked by benzoate counterions.

(ii) The Mn2 and Mn5 sites on one side and Mn10 and Mn7 sites on the other are in a +3 oxidation state and are six-coordinate with an NO_5 donor set. All these sites have distorted octahedral coordination with typical Jahn–Teller elongation. The basal plane of each comprises one oxygen atom from a bridging benzoate (O10 for Mn2; O21 for Mn5; O31 for Mn7; O43 for Mn10), one from a tetradentate Htea^{2-} (O3 for Mn2; O23 for Mn5; O26 for Mn7; O2 for Mn10) and two from a tridentate Htea^{2-} (O4, O7 for Mn2; O19, O22 for Mn5; O28, O33 for Mn7; O1, O41 for Mn10). The average bond lengths of the basal planes are: for Mn2, 1.923; for Mn5, 1.918; for Mn7, 1.921; and for Mn10, 1.916 Å. The apical positions are occupied by nitrogen atoms from the tridentate Htea^{2-} groups [Mn2–N12 2.378(4), Mn5–N8 2.391(4), Mn7–N9 2.346(4), Mn10–N10 2.394(4) Å] and oxygen atoms from phosphonate ligands [Mn2–O5 2.257(3), Mn5–O18 2.212(3), Mn7–O25 2.234(3), Mn10–O40 2.205(3) Å].

(iii) The third group contains Mn3, Mn4, Mn9 and Mn8, and these manganese centres are in a +2 oxidation state and are bound to six oxygen donor atoms. Four oxygen atoms are provided by bridging benzoates (O9, O11, O13, O15 for Mn3; O12, O14, O16, O20 for Mn4; O35, O37, O39, O42 for Mn9; O32, O34, O36, O38 for Mn8), one oxygen atom comes from a phosphonate (O8 for Mn3; O18 for Mn4; O40 for Mn9; O29 for Mn8) and one from a tridentate chelate Htea^{2-} (O7 for Mn3; O19 for Mn4; O41 for Mn9; O33 for Mn8). Bond lengths fall into the following ranges: for Mn3, 2.127(3)–2.260(3) Å; for Mn4, 2.105(3)–2.251(3) Å; for Mn8, 2.111(4)–2.242(3) Å; and for Mn9, 2.116(4) Å–2.260(3) Å.

The average $\text{Mn}^{\text{II}}\cdots\text{Mn}^{\text{III}}$ interatomic distances in the structure are 3.22 Å, significantly shorter than the $\text{Mn}^{\text{II}}\cdots\text{Mn}^{\text{II}}$ contacts, which have an average of 4.38 Å. Three potassium ions are found within the metallocrown; all these sites are nine-coordinate; K1 lies within the plane of the metallocrown, whereas K2 lies 0.314 Å above the plane, and K3 is 0.064 Å below the plane.

The phosphonates show the 5.221 binding mode (Harris notation^[15]). Four of the double deprotonated triethanolamines (Htea^{2-}) act as 5.2201 ligands, whereas two of them act as 6.2211. All benzoates are in a bidentate fashion 2.11.

The crystal structure also contains deprotonated benzoates in the lattice, which bridge the $\{\text{Mn}_{10}\}$ cage through three hydrogen bonds creating a 1D polymeric structure along the c axis, as shown in Figure 2. The benzoate oxygen atoms, O45 and O46, of the lattice are involved in strong intermolecular H-bonding; O45 H-bonds to one of the free alcohol arms of a tridentate triethanolamine ligand ($\text{O45}\cdots\text{O44}$ 2.78 Å) and also to the terminal tetradentate triethanolamine ($\text{O45}\cdots\text{O6}$ 2.74 Å). The second benzoate oxygen atom, O46, H-bonds to a terminal tetradentate triethanolamine of the next $\{\text{Mn}_{10}\}$ cage ($\text{O46}\cdots\text{O27'}$ 2.59 Å), creating a polymeric 1D structure parallel to the c axis. Furthermore, intramolecular interactions occur between the other two free alcohol arms of tridentate triethanolamine ligands, O30 and O17, with terminal tetradentate oxygen atoms on triethanolamine ligands in neighbouring chains (O26 and O3, respectively) ($\text{O30}\cdots\text{O26}$ 2.70, $\text{O17}\cdots\text{O3}$ 2.68 Å). This H-bonding network allows the $\{\text{Mn}_{10}\}$ cage to pack in a rather efficient and compact manner and is due to the flexibility of the triethanolamine ligand. Analogous extended H-bonding was also seen in the previously reported $[\text{Mn}_{16}]$ wheels,^[9,10] where Htea^{2-} was used as the constructing ligand.

Magnetic Studies

The magnetic susceptibility of compound **1** was measured in the 1.8–300 K temperature range at 1 and 10 kG external fields. $\chi_{\text{M}}T$ (χ_{M} is the molar paramagnetic susceptibility) decreases smoothly from 37.6 $\text{cm}^3\text{mol}^{-1}\text{K}$ at 300 K (Figure 3) to about 17.8 $\text{cm}^3\text{mol}^{-1}\text{K}$ at 10 K, before dropping more rapidly to reach 8.4 $\text{cm}^3\text{mol}^{-1}\text{K}$ at 2 K in a 10 kG magnetic field or 12.7 $\text{cm}^3\text{mol}^{-1}\text{K}$ in a 1 kG magnetic field. The room-temperature value is very close to the spin-only value of 38.25 $\text{cm}^3\text{mol}^{-1}\text{K}$ (assuming $g = 2$) expected for an Mn_{10} -cage repeat unit comprising six Mn^{II} ($S = 5/2$) and four Mn^{III} ($S = 2$) ions. The decrease of $\chi_{\text{M}}T$ upon cooling suggests dominant antiferromagnetic exchange, whereas the field dependence of $\chi_{\text{M}}T$ at low temperatures can be attributed to zero-field splitting and/or Zeeman-level depopulation effects. Fitting the data with the

Curie–Weiss law [$\chi = C/(T - \theta)$] in the temperature region 20–300 K affords parameters of $C = 39.7 \text{ cm}^3 \text{ mol}^{-1} \text{ K}$ and $\theta = -18.2 \text{ K}$. Given the size of the structure and hence the matrices required for calculations, no attempt was made to model the susceptibility data.

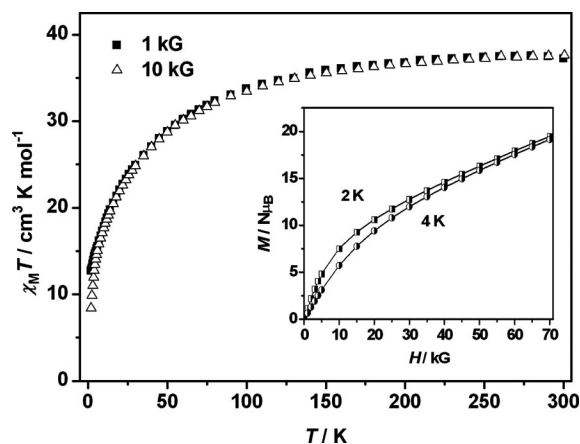


Figure 3. The magnetic susceptibility (χ_m) behaviour of **1**; temperature plotted as the product $\chi_m T$ vs. T . Inset: magnetisation of **1** with field at 2 and 4 K.

The isothermal M versus H curves recorded at 2 and 4 K (inset Figure 3) show a continuous increase of the magnetisation with increasing magnetic field, indicating a strong anisotropy of either the material or population, at large enough applied dc fields, of low-lying excited states with S values larger than that of the ground state. The magnetisation reaches a value of $19.5 N\mu_B$ at 2 K and 70 kG, which would suggest a ground state larger than $S = 10$. However, such a large ground-state spin is not supported by the low-temperature low-field susceptibility data, which rather indicate a smaller spin value of 4 or 5. This situation is frequently encountered in molecular clusters with a large percentage of Mn^{II} ions, because of the small exchange coupling promoted by the Mn^{II} ions, which often leads to a plethora of low-lying excited states close in energy to the ground state.^[16] At high magnetic fields, such spin states can cross in energy below the lowest-lying spin ground state, thus affecting the S value of the ground state.

Conclusions

By combining two tripodal ligands of different natures, triethanolamine and phosphonates, with manganese benzoate, a new structural motif resulted. Complex **1** can be regarded as a 24-membered metallacrown with 6 Mn^{II} and 4 Mn^{III} atoms accommodating three potassium ions in its cavity. The resulting $\{\text{Mn}_{10}\}$ cage can be prepared in higher yield through a solvothermal procedure. Its utility as host to three potassium ions suggests that these molecular species may be allowed to distinguish between different guests, and this is under investigation.

Experimental Section

General: All reagents, metal salts and ligands were used as obtained from Aldrich. All chemicals and solvents were reagent grade.

Synthesis A: Benzoic acid (1.0 g, 8.0 mmol) in MeOH (10 mL) was treated with KMnO_4 (0.1 g, 0.6 mmol) for 1 h. After 1 h, a suspension of PhPO_3H_2 (0.1 g, 0.6 mmol) and triethanolamine (1.0 mL, 7.50 mmol) in MeCN (30 mL) was added. The solution was stirred vigorously for 3 h and then filtered. During the reaction the solution became light brown in colour. The filtrate was concentrated to about 15 mL and left for slow concentration. Orange-brown crystals of **1** grew from the filtrate after 2 d. Yield ca. 45% (based on potassium permanganate). $\text{C}_{137}\text{H}_{161}\text{K}_3\text{Mn}_{10}\text{N}_{12}\text{O}_{46}\text{P}_2$ (3440.42); calcd. C 47.83, H 4.72, K 3.41, N 4.89; found C 47.52, H 4.13, K 3.2, N 4.70.

Synthesis B: Complex **1** was also isolated by using a solvothermal procedure. Benzoic acid (1.0 g, 8.0 mmol) in MeOH (10 mL) was treated with KMnO_4 (0.1 g, 0.6 mmol) for 1 h to give a brown solid. This was collected by filtration, dried and then heated in a Teflon-lined autoclave at 150 °C for 12 h with a suspension of PhPO_3H_2 (0.1 g, 0.6 mmol) and triethanolamine (1.0 mL, 7.50 mmol) in MeCN (8 mL). After slow cooling (1°C min^{-1}) to room temperature, the resulting red solution was filtered and left for slow concentration. The next day, the solution turned light brown, and, after 1 d, orange-brown crystals of **1** [yield ca. 60% (based on potassium permanganate)] grew as clarified from a single-crystal X-ray diffraction study. $\text{C}_{137}\text{H}_{161}\text{K}_3\text{Mn}_{10}\text{N}_{12}\text{O}_{46}\text{P}_2$ (3440.42); calcd. C 47.83, H 4.72, K 3.41, N 4.89; found C 48.02, H 4.55, K 3.2, N 4.70. Sample purity was additionally confirmed by powder X-ray diffraction.

Structure Determination: Data were collected with an Oxford Xcalibur CCD diffractometer (Mo- K_α , $\lambda = 0.71069 \text{ \AA}$). The selected crystal was mounted on the tip of a glass pin by using Paratone-N oil and placed in the cold flow (100 K) produced by an Oxford Cryocooling device.^[17] A complete hemisphere of data was collected by using ω -scans (0.3° , 30 s/frame). Integrated intensities were obtained with SAINT+,^[16] and they were corrected for ab-

Table 2. Crystallographic data and refinement details for compound **1**.

Empirical formula	$\text{C}_{137}\text{H}_{161}\text{K}_3\text{Mn}_{10}\text{N}_{12}\text{O}_{46}\text{P}_2$
M_r	3440.42
Crystal system	triclinic
Space group	$P\bar{1}$
a [Å]	19.5969(6)
b [Å]	20.5821(5)
c [Å]	22.4782(5)
α [°]	67.087(2)
β [°]	75.780(2)
γ [°]	66.902(3)
V [Å ³]	7635.3(3)
T [K]	100(2)
Z	2
Crystal size [mm]	$0.30 \times 0.25 \times 0.03$
$\rho_{\text{calcd.}}$ [g cm ⁻³]	1.496
Crystal colour and shape	brown plate
Radiation	Mo- K_α
λ [Å]	0.71073
Independent reflections	25707
Reflections with $I > 2\sigma(I)$	16789
Parameters	1919
Restraints	24
R_1, wR_2	$R_1 = 0.0490, wR_2 = 0.1309$
Goodness of fit	1.027

sorption by using SADABS.^[18] Structure solution and refinement were performed with the SHELX-package.^[18] The structure was solved by direct methods and completed by iterative cycles of ΔF syntheses and full-matrix least-squares refinement against F^2 . Crystal data are given in Table 2. CCDC-757459 (for **1**) contains the supplementary crystallographic data for this paper. These data can be obtained free of charge from The Cambridge Crystallographic Data Centre via www.ccdc.cam.ac.uk/data_request/cif.

Magnetic Measurements: Magnetic measurements were performed on polycrystalline samples restrained in eicosane with a Quantum Design MPMS-XL SQUID magnetometer equipped with a 7 T magnet. Data were corrected for the diamagnetism of the compounds by using Pascal constants and for the diamagnetic contributions of the sample holder and eicosane by measurement. Direct current measurements were collected at temperatures between 1.8 and 300 K and applied magnetic fields of 1 and 10 kG.

Acknowledgments

This work was supported by the Engineering and Physical Sciences Research Council (EPSRC-UK) and the European Commission "Network of Excellence" MAGMANet. R. E. P. W. is grateful to the Royal Society for a Wolfson Merit Award.

- [1] a) V. L. Pecoraro, A. J. Stemmler, B. R. Gibney, J. J. Bodwin, H. Wang, J. W. Kampf, A. Barwinski, *Prog. Inorg. Chem.* **1997**, *45*, 83–177; b) J. J. Bodwin, A. D. Cutland, R. G. Malkani, V. L. Pecoraro, *Coord. Chem. Rev.* **2001**, *216–217*, 489–512; c) G. Mezei, C. M. Zaleski, V. L. Pecoraro, *Chem. Rev.* **2007**, *107*, 3933–5003.
- [2] a) C. Dendrinou-Samara, M. Alexiou, C. J. Zaleski, J. W. Kampf, E. Depperman, D. P. Kessissoglou, M. L. Kirk, V. L. Pecoraro, *J. Am. Chem. Soc.* **2005**, *127*, 12862–12872; b) C. Dendrinou-Samara, C. M. Zaleski, A. Evagorou, J. W. Kampf, V. L. Pecoraro, D. P. Kessissoglou, *Chem. Commun.* **2003**, 2668–2669; c) C. Dendrinou-Samara, G. Psomas, L. Iordanidis, V. Tangoulis, D. P. Kessissoglou, *Chem. Eur. J.* **2001**, *7*, 5041–5051; d) T. Afrati, C. Dendrinou-Samara, C. P. Raptopoulou, A. Terzis, V. Tangoulis, D. P. Kessissoglou, *Angew. Chem. Int. Ed.* **2002**, *41*, 2148–2150; e) C. Dendrinou-Samara, M. Alexiou, C. M. Zaleski, J. W. Kampf, M. L. Kirk, D. P. Kessissoglou, V. L. Pecoraro, *Angew. Chem. Int. Ed.* **2003**, *42*, 3763–3766.
- [3] a) H. Barrow, D. A. Brown, N. W. Alcock, H. J. Clase, M. G. H. Wallbridge, *J. Chem. Soc., Chem. Commun.* **1995**, 1231; b) C. D. Chandler, C. Roger, M. J. Hampden-Smith, *Chem. Rev.* **1993**, *93*, 1205.
- [4] a) G. L. Abbati, A. Cornia, A. C. Fabretti, A. Caneschi, D. Gatteschi, *Inorg. Chem.* **1998**, *37*, 1430–1431; b) G. L. Abbati, A. Cornia, A. C. Fabretti, W. Malavasi, L. Schenetti, A. Caneschi, D. Gatteschi, *Inorg. Chem.* **1997**, *36*, 6443–6446.
- [5] See for example: a) A. Dolbecq, F. Secheresse, *Adv. Inorg. Chem.* **2002**, *53*, 1; b) E. J. L. McInnes, S. Piligkos, G. A. Timco, R. E. P. Winpenny, *Coord. Chem. Rev.* **2005**, *249*, 2577.
- [6] A. J. Tasiopoulos, A. Vinslava, W. Wernsdorfer, K. A. Abboud, G. Christou, *Angew. Chem. Int. Ed.* **2004**, *43*, 2117–2121.
- [7] R. T. W. Scott, C. J. Milios, A. Vinslava, D. Lifford, S. Parsons, W. Wernsdorfer, G. Christou, E. K. Brechin, *Dalton Trans.* **2006**, 3161–3163.
- [8] D. Foguet-Albiol, T. A. O'Brien, W. Wernsdorfer, B. Moulton, M. J. Zaworotko, K. A. Abboud, G. Christou, *Angew. Chem.* **2005**, *117*, 919–923; *Angew. Chem. Int. Ed.* **2005**, *44*, 897–901.
- [9] M. Murugesu, W. Wernsdorfer, K. A. Abboud, G. Christou, *Angew. Chem. Int. Ed.* **2005**, *44*, 892–896.
- [10] S. J. Shah, C. M. Ramsey, K. J. Heroux, J. R. O'Brien, A. D. DiPasquale, A. L. Rheingold, E. del Baeco, D. N. Hendrickson, *Inorg. Chem.* **2008**, *47*, 6245–6253.
- [11] R. P. John, K. Lee, B. J. Kim, B. J. Suh, H. Rhee, M. S. Lah, *Inorg. Chem.* **2005**, *44*, 7109–7121.
- [12] S.-X. Liu, S. Lin, B.-Z. Lin, C.-C. Lin, J.-Q. Huang, *Angew. Chem. Int. Ed.* **2001**, *40*, 1084–1087.
- [13] a) I. D. Brown, K. W. Wu, *Acta Crystallogr., Sect. B* **1976**, *32*, 1957; b) H. H. Thorp, *Inorg. Chem.* **1992**, *31*, 1585–1588.
- [14] L. P. Engelhardt, C. A. Muryn, R. G. Pritchard, G. A. Timco, F. Tuna, R. E. P. Winpenny, *Angew. Chem. Int. Ed.* **2008**, *47*, 924–927.
- [15] Harris notation describes the binding mode as $[X_Y Y_2 Y_3 \cdots Y_n]$, where X is the overall number of metal atoms bound by the whole ligand, and each value of Y refers to the number of metal atoms attached to the different donor atoms. The ordering of Y is listed by the Cahn–Ingold–Prelog priority rules, hence O before N: R. A. Coxall, S. G. Harris, D. K. Henderson, S. Parsons, P. A. Tasker, R. E. P. Winpenny, *J. Chem. Soc., Dalton Trans.* **2000**, 2349–2356.
- [16] S. L. Langley, K. J. Berry, B. Moubaraki, K. S. Murray, *Dalton Trans.* **2009**, 973–982.
- [17] J. Cosier, A. M. Glazer, *J. Appl. Crystallogr.* **1986**, *19*, 105–107.
- [18] Bruker Analytical X-ray Systems, *SHELX-PC Package*, Madison, WI, **1998**.

Received: December 18, 2009
Published Online: March 11, 2010

Trapped in a Complex: the 1,2,4,5-Tetrakis(tetramethylguanidino)benzene Radical Cation (ttmgb^{•+}) with a Bisallylic Structure

Christine Trumm,^[a] Olaf Hübner,^[a] Elisabeth Kaifer,^[a] and Hans-Jörg Himmel^{*[a]}

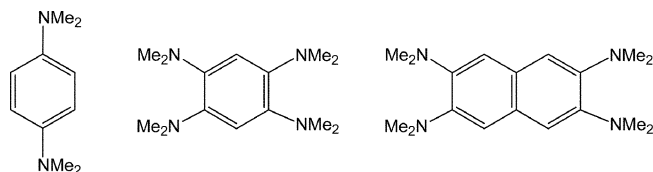
Keywords: Copper / Redox chemistry / Radical ions

In this work we follow the reaction of the strong electron donor 1,2,4,5-tetrakis(tetramethylguanidino)benzene (ttmgb) with Cu^{II} nitrate. Three binuclear Cu^{II} complexes were isolated as products of this reaction. Depending on the reaction conditions, especially the molar ratio of the two reactants, the ttmgb ligand in these complexes is neutral, mono- or dicationic. All three complexes were structurally characterized. In addition to the experimental studies, quantum chemical cal-

culations were carried out, which, in combination with experimental magnetic (SQUID) curves, especially shed light on the magnetic superexchange. The binuclear Cu^{II} complex of the ttmgb radical cation represents a three-spin system. The SQUID magnetic data as well as the results of quantum chemical calculations indicate strong ferromagnetic copper-ligand coupling.

Introduction

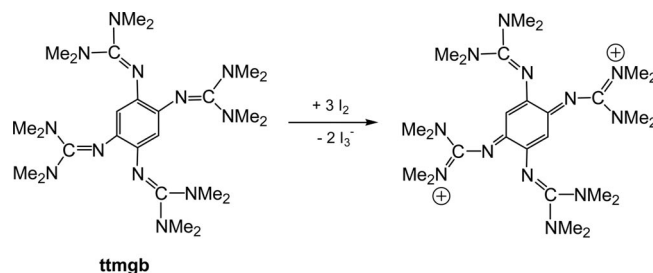
Amino-substituted aromatic systems were shown to be electron donor compounds (see Scheme 1 for three representatives). The colourful salts obtained upon one-electron-oxidation of 1,4-bis(dimethylamino)benzene (see Scheme 1) are known already for more than 100 years,^[1] and oxidation reactions of this organic electron donor are still intensively studied.^[2] Staab et al. reported on the synthesis and oxidation of 1,2,4,5-tetrakis(dimethylamino)benzene^[3] and 2,3,6,7-tetrakis(dimethylamino)naphthalene^[4] and also recorded EPR and ENDOR spectra for the radical cations of both compounds.^[5]



Scheme 1. Some amino-functionalized aromatic compounds which were shown to be electron donors.

Guanidines are much stronger bases than amines.^[6] Therefore by replacing the amino groups by guanidino groups one should obtain superior electron donors. Guanidino groups have a further important advantage over amino groups. Hence aromatic compounds in which a second dialkylamino group is located in ortho position to a first one

are sterically crowded and barely suitable as chelating ligands. On the other hand, the steric situation around the imino N atoms of guanidino groups is relatively relaxed so that the corresponding guanidino compounds are versatile chelating ligands. We recently reported on the synthesis and properties of the strong electron donor ttmgb [1,2,4,5-tetrakis(tetramethylguanidino)benzene].^[7–9] Oxidation, e.g. with I₂,^[7] leads to the dication [ttmgb]²⁺ (see Scheme 2) under removal of two of the aromatic π -electrons. Although this process should involve the radical monocation [ttmgb]^{•+} as an intermediate, we were not able to isolate or detect this species. The CV curves display a single two-electron-oxidation wave and EPR experiments with equimolar mixtures of the neutral ttmgb and the dication [ttmgb]²⁺ gave no evidence for the presence of the radical cation. In the following we reacted ttmgb with a number of electron acceptors including late-transition metal ions which were shown to form binuclear metal complexes with the neutral or dicationic ttmgb as bridging ligand.^[10] However, the monocation was not observed in these experiments. Herein we report on new experiments in this direction which finally led to the isolation of the monocation, stabilized in a binuclear Cu^{II} complex.



Scheme 2.

[a] Anorganisch-Chemisches Institut, Ruprecht-Karls-Universität Heidelberg, Im Neuenheimer Feld 270, 69120 Heidelberg, Germany
Fax: +49-6221-545707
E-mail: hans-jorg.himmel@aci.uni-heidelberg.de
Supporting information for this article is available on the WWW under <http://dx.doi.org/10.1002/ejic.201000118>.

Results and Discussion

Synthesis and Structural Characterization

Reaction of ttmgb with $\text{Cu}(\text{NO}_3)_2$ in a 1:5.7 molar ratio proceeded as described by the overall formula given in Scheme 3. Elemental Cu was formed, and the single product isolated from the solution turned out to be the salt $[\{\text{Cu}(\text{NO}_3)_2\}_2(\text{ttmgb})][\text{Cu}(\text{NO}_3)_4]$, **1**. Its molecular structure as derived from single-crystal X-ray diffraction is visualized in Figure 1.^[11] The C–C bond lengths within the C_6 ring as well as the C–N distances in **1** clearly confirm oxidation of the ttmgb ligand. Two of the C–C distances within the C_6 ring (C1–C2 and C4–C5) are with 150.5(5) and 149.8(5) pm significantly larger than the others, which fall within the range 137.3(5)–139.9(5) pm (see Table S1 in the Supporting Information for a list of structural parameters). For comparison, the corresponding distances in ttmgb vary only between 139.8–140.9 pm.^[7] The bond lengths from the C atoms of the C_6 ring to the guanidino N atoms amount to 131.3–135.6 pm in **1**. The imino C=N double bond lengths increase from 128.8/129.1 pm in ttmgb^[7] to 138.5(4)–141.2(5) pm in **1**. These changes argue for significant delocalization of the two positive charges. The Cu–O distances cover the range 197.2(3)–199.7(3) pm. The Cu^{II} ion of the $[\text{Cu}(\text{NO}_3)_4]^{2-}$ anion is square-planar coordinated, and the shortest distance $\text{Cu}\cdots\text{O}$ to one of the nitrate units in the dicationic unit measures 357.8(3) pm.

In subsequent experiments the reaction conditions were slightly changed (see Exp. Sect.), and as a consequence another product was obtained. A few crystals of this product were grown from CH_3CN and turned out to consist of the neutral binuclear Cu^{II} complex $[\{(\text{NO}_3)_2\text{Cu}\}_2(\text{ttmgb})]$, **2**.^[11] It could be assumed that **2** represents the first intermediate in the course of the redox reaction between the Cu^{II} ions and the ttmgb electron donor. Because of the intermediate character of **2** we were unfortunately not able to obtain **2** in larger amounts. The compound is not a thermodynamically stable product of the reaction in solution, but is stabilized through precipitation. When crystals of **2** were dissolved in CH_3CN or acetone, decomposition was observed (for instance by IR spectroscopy), in the course of which **1** is formed. Nevertheless, some details of the molecular structure of **2** should be discussed briefly (see Figure 2 for an illustration of its molecular structure). First, the C–C bond

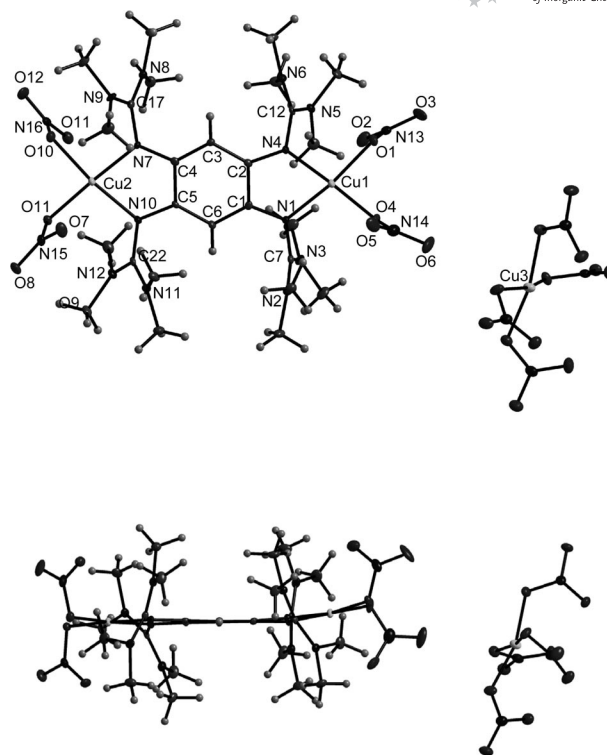


Figure 1. Illustration of the molecular structure of **1**. Thermal ellipsoids are drawn at the 50% probability level.

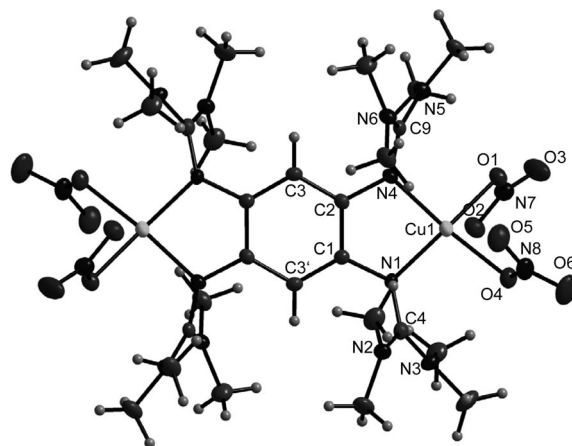
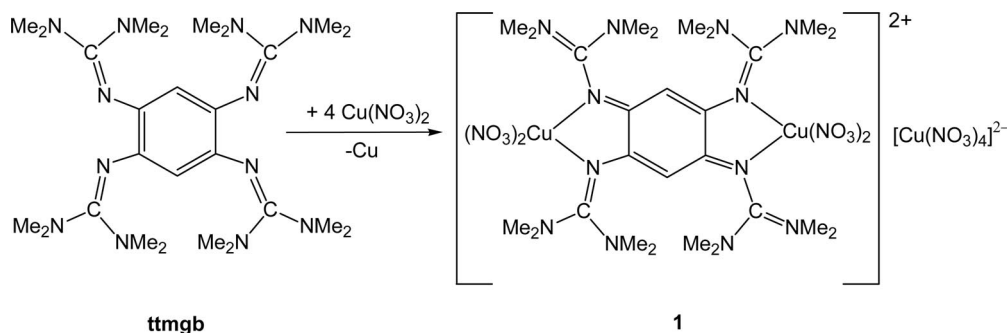


Figure 2. Molecular structure of **2**. Thermal ellipsoids are drawn at the 50% probability level.



Scheme 3.

lengths within the C₆ ring are within the range 138.9(4)–140.4(4) pm, indicating an intact aromatic system (see also Table S2 in the Supporting Information). The average Cu–N distance is shorter in **2** (196.6 pm) than in **1** (197.3 pm). This can be explained by the better donor capacity of neutral ttmgb (as present in **2**) compared with [ttmgb]²⁺ (as present in **1**). The imino N=C bond lengths (N1–C4 and N4–C9) within the ttmgb unit in **2** (133.3(3) and 134.6(3) pm) are relatively short.

Thus the experiments led to the isolation of what might be the first (and thermodynamically highly unstable) intermediate of the redox-process, namely complex **2** with a still neutral ttmgb unit, and also the final end-product, complex **1** with a dicationic ttmgb unit, but not of the likely intermediate species featuring the radical cation of ttmgb. In a next series of experiments we lowered systematically the metal/ligand ratio. When the reaction was carried out with 2.8 equiv. of the Cu^{II} salt, a new product was obtained and the glass vessel got coated with a thin layer of elemental Cu. The new product was crystallized from acetone solutions and turned out to be the salt [{(NO₃)₂Cu}₂(ttmgb)]⁺NO₃[−], **3** (see Scheme 4 and Figure 3).^[11] Complex **3** features finally the long sought-after radical cation ttmgb^{•+}, trapped in a binuclear Cu^{II} complex. In agreement with a bisallyl-type structure, two of the C–C distances in the C₆ ring (C1–C2 and C4–C5) are elongated (to 145.6 pm) with respect to neutral ttmgb, while the four other distances are significantly shorter (139.2–139.8 pm). A list of structural parameters is provided in the Supporting Information (Table S3, see also Table S4 and Figure S1 for a structural comparison of compounds **1**, **2** and **3**). The bisallyl form in this derivative of the C₆H₆^{•+} cation is stabilized over the quinoid form by the presence of the four guanidino groups. The parent radical cation C₆H₆^{•+} was the subject of intense research work, both experimentally in the gas-phase and inert-gas matrices^[12] as well as theoretically.^[13] Due to the Jahn–Teller effect, the structure should deviate from D_{6h} symmetry. However, this effect can lead to either a quinoid or a bisallyl (*anti*-quinoid) structure, with elongation of either four or two bonds, respectively. The energy difference between both forms is extremely small. Very recently, Seppelt et al. succeeded in the isolation and structural characterization through X-ray diffraction of C₆F₆^{•+}Sb₂F₁₁[−] and

C₆F₆^{•+}Os₂F₁₁[−].^[14] Interestingly, the solid state of these salts features the radical cation in both the quinoid and the bisallyl (or *anti*-quinoid) isomeric forms.

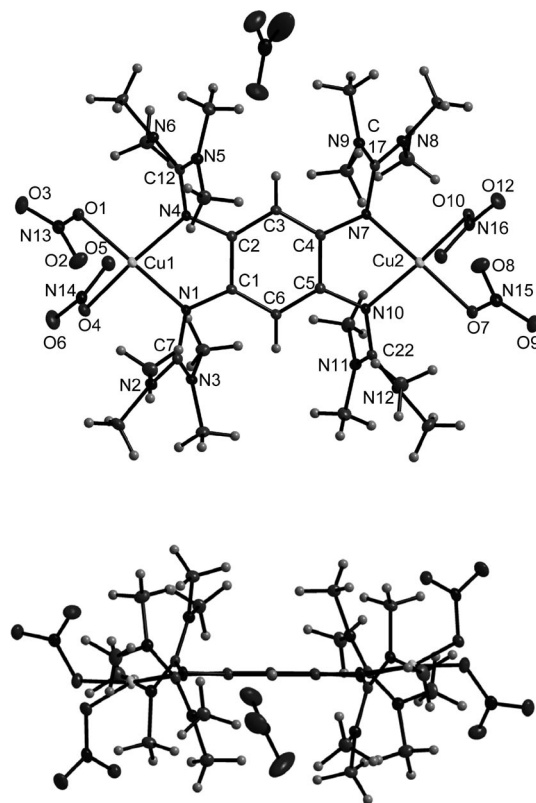
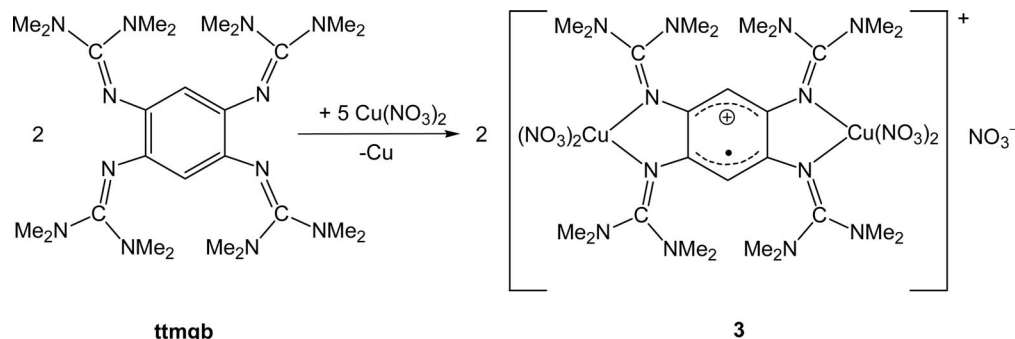


Figure 3. Molecular structure of **3**. Thermal ellipsoids are drawn at the 50% probability level.

Molecular Magnetism

The χT vs. T plot as derived from the SQUID magnetic data recorded for complex **1** is displayed in Figure 4. The form of the curve immediately argues for weak antiferromagnetic coupling. The $\chi T - T$ curve can be fitted with Equation (1) (in which TIP represents the temperature-independent paramagnetism, and g_{12} and g_3 are the g values for the cationic and anionic part, respectively). With values



Scheme 4.

of 2.0 and 2.1 for g_{12} and g_3 , the fit returned $J/k = -19.7$ K, $\Theta = -0.53$ K and $\text{TIP} = 0.9$ memu mol $^{-1}$.^[15] The two Cu^{II} centers in the complex dication of **1** are thus weakly antiferromagnetically coupled. For **1** in its electronic ground state S equals 1/2 (due to the presence of the $[\text{Cu}(\text{NO}_3)_4]^{2-}$ anion).

$$\chi T = \frac{N_A \mu_B^2}{k} \cdot \frac{T}{(T - \Theta)} \cdot \left(\frac{2g_{12}^2}{3 + \exp\left(\frac{-2J}{kT}\right)} + \frac{g_3^2}{4} \right) + \text{TIP} \cdot T \quad (1)$$

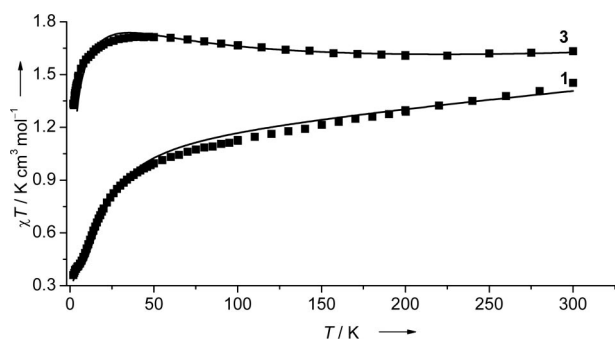


Figure 4. χT vs. T plots as derived from SQUID magnetic measurements for **1** (at 500 Oe) and for **3** (at 1000 Oe). The solid line results from a curve fit (see text).

Complex **3** is an example of a three-spin system with two spins residing on the metal atoms and one spin on the ttmgb^+ unit. Hybrid systems with stable radical cations were synthesized previously, e.g. with nitroxides^[16] or verdazyl derivatives,^[17] and trinuclear Cu^{II} complexes have also been studied.^[18] The $\chi T - T$ plot based on the SQUID data is shown in Figure 4. With decreasing temperature, the χT value passes a maximum of 1.71 K cm 3 mol $^{-1}$ at ca. 40 K. This behaviour is characteristic for ferromagnetic coupling. The system with three spins localized at different centers in principle is characterized by three coupling constants. But because of the symmetry, the coupling between the central ligand and each of the Cu centers should be equal. Therefore, the system was described by two constants, J (coupling between the ligand and Cu) and J' (coupling between the Cu centers), and the spin Hamiltonian \mathbf{H} was formulated according to Equation (2). The dependence of χT from the temperature T is then given by Equation (3) (in which the parameters Θ and TIP were added). The fit was accomplished with g_A and g_B values fixed at a value of 1.98. With $\Theta = -1.8$ K and $\text{TIP} = 0.87$ memu mol $^{-1}$, we obtained $J/k = +159$ K and $J'/k = -30$ K. These values can only be considered as rough estimates. The analysis clearly confirms the presence of considerable ferromagnetic coupling between the electrons of the Cu^{II} and the radical ligand unit and weak antiferromagnetic coupling between the electrons on the Cu^{II} ions.

$$\mathbf{H} = -2J(S_{\text{Cu1}} \cdot S_{\text{ttmgb}} + S_{\text{Cu2}} \cdot S_{\text{ttmgb}}) - 2J'S_{\text{Cu1}} \cdot S_{\text{Cu2}} \quad (2)$$

$$\chi T = \left(\frac{N_A \mu_B^2 T}{4k(T - \Theta)} \right) \cdot \frac{g_a^2 + g_b^2 \exp\left(\frac{2(J - J')}{kT}\right) + \frac{5}{2}(g_a + g_b)^2 \exp\left(\frac{3J}{kT}\right)}{1 + \exp\left(\frac{2(J - J')}{kT}\right) + 2 \exp\left(\frac{3J}{kT}\right)} + \text{TIP} \cdot T \quad (3)$$

Quantum Chemical Calculations

First we carried out quantum chemical calculations [B3LYP/SV(P)] on the free ttmgb^{+} radical cation. As in **3**, a bisallyl-type structure resulted with bond lengths of 140.7 pm for C2–C3, C3–C4, C1–C6 and C5–C6 and of 146.8 pm for C1–C2 and C4–C5. These values are very close to the experimentally determined ones for **3**. The distances C1–N1, C2–N4, C4–N7 and C5–N10 were calculated to be 135.7 pm, in pleasing agreement to the experimental values of 136.4(2)–137.5(2) pm in **3**. On the other hand, as anticipated, coordination of the Cu^{II} ions changes the C=N double bond lengths [experimental values in the range 136.7(2)–137.7(2) pm in **3**, but calculated value of 130.7 pm in free ttmgb^{+}]. Part a and b of Figure 5 display

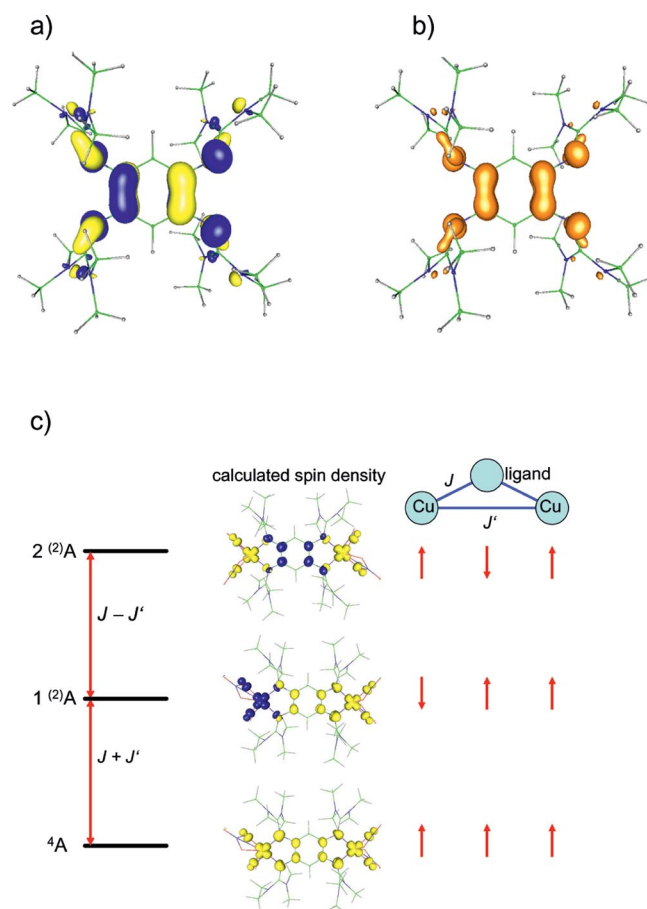


Figure 5. a) Isodensity plot of the SOMO orbitals, and b) spin density in the free ttmgb^{+} radical cation (from B3LYP/SV(P) calculations). c) Spin densities of the different broken-symmetry states and the high-spin state of **3**, as well as the energy levels of the associated states of the Ising Hamiltonian. The broken-symmetry states are not eigenfunctions of the S^2 operator but only of the S_z operator. To indicate this, the multiplicity of the term symbol is given in parentheses.

isodensity plots of the SOMO orbital and the spin density of the free ttmgb^{+} radical cation. It resembles one of the degenerate HOMO orbitals of benzene, the only difference being that some electron density is also located on the imino N atoms of the guanidino groups.

To complete the investigation, quantum chemical calculations based on density functional theory were performed for the complex in its three charge states: $[\{\text{Cu}(\text{NO}_3)_2\}_2(\text{ttmgb})]^{0/+2+}$. The lowest state of $[\{\text{Cu}(\text{NO}_3)_2\}_2(\text{ttmgb})]^{2+}$ is the broken symmetry state (where the spins of the two centers point to opposite directions). But the high-spin ^3A term is calculated to be higher in energy by only 0.13 kJ mol^{-1} . This transforms into a value for the spin coupling constant $J/k = -15.2 \text{ K}$ ($\mathbf{H} = -2 J \mathbf{S}_1 \mathbf{S}_2$) that is in pleasing agreement with the value derived from the SQUID measurements for **1** (see above). The structures of both terms are virtually identical. For two of the bonds of the aromatic ring (the C1–C2 and the C4–C5 bond) the considerably longer value for the distance of 151.7 pm is found, whereas the remaining distances amount to twice 139.8 and twice 141.2 pm, in agreement with the crystal structure that features the two values of 150.5 pm and 149.8 pm and four values between 137.3 and 139.9 pm. For the four C=N imino bonds the values are twice 138.5 and twice 139.5 pm, also matching very well the crystal structure results between 138.5 and 141.2 pm. Hence, the calculations corroborate the experimental results.

Also for the neutral species, the lowest state is the broken symmetry state, and the ^3A term exhibits an energy higher by only 0.11 kJ mol^{-1} . Both states have virtually identical structures. The splitting corresponds to a value of $J/k = -13.6 \text{ K}$. As for the neutral, the structure optimized by DF calculations is in close agreement with the experimental data for **2**. The values for C–C bond lengths of the benzene ring amount to twice 141.9 pm and four times 140.4 pm, close to the observed results between 138.9 and 140.4, and the imino bond lengths have values of 133.2 pm, close to the experimental results of 133.3 and 134.6 pm.

For the singly charged species (monocation of **3**), the lowest-lying term in energy is calculated to be the high-spin ^4A term. Broken symmetry terms with an inverted spin either at one of the Cu centers or at the bridging ligand are found to lie 1.52 and 3.25 kJ mol^{-1} higher, respectively (see Figure 5, c). As for the neutral and doubly charged systems, the structures of the different terms are very similar. For the ^4A ground term, the structure has two longer C–C distances of 146.2 pm and four shorter C–C distances of twice 140.0 and twice 140.7 pm, a result again in close agreement with the crystal structure values of **3** (145.6 pm and 139.2–139.8 pm). The same applies to the imino bond lengths calculated to 135.5 pm, a value between the results for the neutral and the dication. Values for the coupling constants have been determined for the structure optimized by the B3LYP calculations. For the optimized structure of the ^4A term, the calculation yields values for J/k and J'/k of 201.1 K and -11.4 K . Hence, the splitting in energy of the lowest states of $[\{\text{Cu}(\text{NO}_3)_2\}_2(\text{ttmgb})]^+$ is dominated by the “ferromagnetic” coupling of the adjacent spins, whereas the coupling

between the spins of the Cu centers has the same small magnitude as within the neutral or doubly ionized system. This leads to the energetic order shown in part c of Figure 5. The calculations are in reasonable agreement with the results of the magnetic curve analysis.

Conclusions

This work deals with redox chemistry of the organic electron donor 1,2,4,5-tetrakis(tetramethylguanidino)benzene. We show for the first time that not only products of two- but also of one-electron oxidation of this molecule can be isolated. The radical cation can be trapped in a binuclear Cu^{II} complex, which represents a three-spin system. The results of an analysis of the magnetic SQUID data as well as quantum chemical calculations indicate strong ferromagnetic copper-ligand coupling in this complex. In ongoing work we seek to shed more light on the mechanisms of this and similar redox processes of GFAs (guanidino-functionalized aromatic compounds). Matrix isolation experiments are planned to obtain reactive intermediates of model redox reactions. Experiments are also under way to use complex **3** as transfer reagent for the ttmgb^{+} radical cation, which presumably cannot be synthesized without protection by complexation. Finally, we currently explore the possibility of using these complexes as building blocks for magnetic spin-coupled materials.

Experimental Section

General: All synthetic work was carried out using standard Schlenk techniques. The synthesis of the ttmgb ligand was carried out as described previously.^[7] IR spectra were recorded with a Bruker Vertex 80v spectrometer. A Perkin–Elmer Lambda 19 spectrometer was used to record UV/Vis spectra.

$[\{\text{Cu}(\text{NO}_3)_2\}_2(\text{ttmgb})][\text{Cu}(\text{NO}_3)_4]$ (1**). Route A:** To a solution of ttmgb (252.3 mg, $475.4 \mu\text{mol}$) in 250 mL of acetone $\text{Cu}(\text{NO}_3)_2 \cdot 3\text{H}_2\text{O}$ (512.3 mg, $2731.5 \mu\text{mol}$) was added. The purple reaction mixture was stirred for 1 h at 40°C and subsequently allowed to cool down to room temp. Dark crystals of **1** were obtained in about 12 h; yield 398.5 mg (69% with respect to the ttmgb).

Route B: $\text{Cu}(\text{NO}_3)_2 \cdot 3\text{H}_2\text{O}$ (55 mg, $293.3 \mu\text{mol}$), dissolved in 5 mL acetone, was added to a suspension of ttmgb (25 mg, $47.1 \mu\text{mol}$) in 5 mL of acetone. The purple reaction mixture was stirred for 5 min. A dark precipitate appeared. The solution was filtered and the filtrate condensed to a volume of 2 mL. After 2 d dark crystals of **1** were obtained. The product was washed with acetone. $\text{C}_{26}\text{H}_{50}\text{Cu}_3\text{N}_{20}\text{O}_{24}$ (1217.43): calcd. C 25.65, H 4.14, N 23.01, Cu 15.66, O 31.54; found C 26.13, H 4.46, N 21.87. IR (CsI): $\tilde{\nu} = 2934$ (w), 1616 (m), 1495 (s), 1361 (vs), 1311 (vs), 1172 (w), 1011 (m), 833 (m), 746 (w), 593 (m) cm^{-1} . UV/Vis (CH_3CN , $c = 2.244 \times 10^{-5} \text{ mol L}^{-1}$): λ_{max} (ϵ) = 209 (113592), 276 (22873), 406 (26944). MS (FAB): m/z (%): 655 (24) $[\text{Cu}_2(\text{ttmgb})]$, 593 (20) $[\text{Cu}(\text{ttmgb})]$, 532 (100) $[(\text{ttmgb})\text{H}]^+$, 531 (51) $[\text{ttmgb}]$, 487 (28) $[(\text{ttmgb})\text{H}]^+ - \text{HN}(\text{CH}_3)_2$, 460 (60) $[\text{C}_{16}\text{H}_{28}\text{Cu}_2\text{N}_8]$, 442 (19) $[(\text{ttmgb})\text{H}]^+ - 2 \text{HN}(\text{CH}_3)_2$, 417 (60) $[(\text{ttmgb})\text{H}]^+ - \text{N}(\text{CH}_3)_2\text{CN}]$. Crystal data for $1 \cdot \text{Me}_2\text{CO}$: $\text{C}_{29}\text{H}_{56}\text{Cu}_3\text{N}_{20}\text{O}_{25}$, $M_r = 1275.56$, $0.40 \times 0.30 \times 0.30 \text{ mm}^3$, orthorhombic, space group $P2(1)2(1)2(1)$, $a = 13.493(3)$, $b = 17.638(4)$, $c = 21.297(4) \text{ \AA}$, $V = 5068.5(18) \text{ \AA}^3$,

$Z = 4$, $d_{\text{calc}} = 1.672 \text{ Mg m}^{-3}$, Mo- K_{α} radiation (graphite-monochromated, $\lambda = 0.71073 \text{ \AA}$), $T = 200 \text{ K}$, $\theta_{\text{range}} 1.50$ to 30.08° . Reflections measured: 83419, independent: 14844, $R_{\text{int}} = 0.0888$. Final R indices [$I > 2\sigma(I)$]: $R_1 = 0.0497$, $wR_2 = 0.1105$.

[{Cu(NO₃)₂}₂(ttmgb)] (2): A solution of ttmgb (7.9 mg, 14.9 μmol) in 2 mL of acetonitrile was prepared, then Cu(NO₃)₂·3H₂O (14.7 mg, 78.4 μmol) was added. The colour of the solution turned to deep green, after 1 d a deep-green precipitate had formed. This precipitate was dissolved in 10 mL of acetonitrile leading to a purple solution. Dark crystals of **2** appeared after removal of half of the solvent in vacuo. 4.0 mg of product (30%) was obtained, a sufficient amount of substance to record IR and UV/Vis spectra and to analyse the structure by X-ray diffraction; the crystallisation procedure could not be reproduced. IR (CsI): $\tilde{\nu} = 2932 \text{ (w)}$, 1616 (m) , 1568 (m) , 1519 (s) , 1397 (vs) , 1361 (vs) , 1315 (s) , 1288 (s) , 1180 (w) , 1026 (w) , 897 (w) , 812 (w) cm^{-1} . UV/Vis (CH₃CN, $c = 1.34 \times 10^{-5} \text{ mol L}^{-1}$): λ_{max} (ϵ) = 210 (119797), 280 (24482), 426 (32060). Crystal data for **2**: C₂₆H₅₀Cu₂N₁₆O₁₂, $M_r = 905.87$, $0.25 \times 0.18 \times 0.15 \text{ mm}^3$, orthorhombic, space group $Pbca$, $a = 15.355(3)$, $b = 13.210(3)$, $c = 19.852(4) \text{ \AA}$, $V = 4026.8(15) \text{ \AA}^3$, $Z = 4$, $d_{\text{calc.}} = 1.494 \text{ Mg m}^{-3}$, Mo- K_{α} radiation (graphite-monochromated, $\lambda = 0.71073 \text{ \AA}$), $T = 200 \text{ K}$, $\theta_{\text{range}} 2.05$ to 30.10° . Reflections measured: 11806, independent: 5901, $R_{\text{int}} = 0.0593$. Final R indices [$I > 2\sigma(I)$]: $R_1 = 0.0484$, $wR_2 = 0.1543$.

[{Cu(NO₃)₂}₂(ttmgb)](NO₃) (3): First 24.0 mg (45.2 μmol) ttmgb are dissolved in 25 mL acetone. Then 23.8 mg (126.9 μmol) Cu(NO₃)₂·3H₂O are added. The purple reaction mixture is stirred for a period of 1 h at 40°C and subsequently slowly cooled down to room temp. Dark crystals of **3** are formed overnight; yield 12.3 mg (28% with respect to the ttmgb). C₂₆H₅₀Cu₂N₁₇O₁₅ (967.87)·Me₂CO·H₂O: calcd. C 33.36, H 5.56, Cu 12.17, N 22.81, O 26.05; found C 33.66, H 5.56, N 22.35. IR (CsI): $\tilde{\nu} = 2964 \text{ (w)}$, 1608 (m) , 1567 (m) , 1520 (s) , 1476 (s) , 1400 (vs) , 1283 (vs) , 1262 (vs) , 1097 (vs) , 1019 (vs) , 855 (w) , 803 (vs) , 702 (w) cm^{-1} . UV/Vis (CH₃CN, $c = 1.32 \times 10^{-5} \text{ mol L}^{-1}$): λ_{max} (ϵ) = 211 (70632), 276 (13417), 416 (14748). MS (FAB): m/z (%): 906 (6) [(Cu(NO₃)₂)₂-(ttmgb)]⁺, 655 (27) [Cu₂(ttmgb) – H]⁺, 530 (49) [ttmgb]⁺, 461 (62) [C₁₆H₂₉Cu₂N₈]⁺. Crystal data for **3**·2Me₂CO·0.25H₂O, C₃₂H₆₂Cu₂N₁₇O_{17.25}, $M_r = 1088.07$, $0.50 \times 0.30 \times 0.30 \text{ mm}^3$, monoclinic, space group $P2_1/c$, $a = 22.966(5)$, $b = 10.171(2)$, $c = 23.201(5) \text{ \AA}$, $\beta = 115.96(3)^{\circ}$, $V = 4872.6(17) \text{ \AA}^3$, $Z = 4$, $d_{\text{calc.}} = 1.483 \text{ Mg m}^{-3}$, Mo- K_{α} radiation (graphite-monochromated, $\lambda = 0.71073 \text{ \AA}$), $T = 200 \text{ K}$, $\theta_{\text{range}} 1.76$ to 30.04° . Reflections measured: 27841, independent: 14261, $R_{\text{int}} = 0.0310$. Final R indices [$I > 2\sigma(I)$]: $R_1 = 0.0421$, $wR_2 = 0.1215$.

Details of the X-ray Crystallographic Studies: Suitable crystals were taken directly out of the mother liquor, immersed in perfluorinated polyether oil, and fixed on top of a glass capillary. Measurements were made on a Nonius-Kappa CCD diffractometer with low-temperature unit using graphite-monochromated Mo- K_{α} radiation. The temperature was set to 100 K. The data collected were processed using the standard Nonius software.^[19] All calculations were performed using the SHELXT-PLUS software package. Structures were solved by direct methods with the SHELXS-97 program and refined with the SHELXL-97 program.^[20,21] Graphical handling of the structural data during solution and refinement was performed with XPLA.^[22] Atomic coordinates and anisotropic thermal parameters of non-hydrogen atoms were refined by full-matrix least-squares calculations.

Details of the Quantum Chemical Calculations: Density-functional calculations were performed with the program package TURBO-MOLE^[23] using the B3LYP functional^[24] in combination with the

def2-SV(P) basis set.^[25] For the numerical integration grid “m4” was used. SCF energies were converged to 1×10^{-7} Hartree. The molecular structures were optimized, converging the maximum gradient to 1×10^{-4} Hartree/Bohr. The neutral and the doubly positively charged complexes are characterized by two unpaired electrons, residing on the two Cu centers. Due to the Heisenberg spin coupling they give rise to two low-lying terms. The energy splitting of these terms is calculated within the broken symmetry framework according to the work of Noodleman.^[26] The singly charged complex possesses three unpaired electrons that are localized at the two Cu centers and the aromatic system of the ttmgb ligand. Again, the spin coupling between the electrons leads to different low-lying terms. The broken symmetry solutions for the complex are approximately eigenstates of an Ising Hamiltonian. Therefore, estimates of the spin coupling constants can be obtained by simply equating the broken symmetry solutions with the Ising eigenstates. We follow in this respect the work of Fliegl et al.^[27]

Supporting Information (see also the footnote on the first page of this article): Tables with selected structural parameters for **1**, **2** and **3** (Tables S1–S3), comparison between some structural parameters of the three molecules (Table S4), overlap of the three molecules to illustrate the changes in the guanidino group conformation (Figure S1).

Acknowledgments

The authors gratefully acknowledge continuous financial support by the Deutsche Forschungsgemeinschaft (DFG).

- a) C. Wurster, *Ber. Dtsch. Chem. Ges.* **1879**, 12, 522–528; C. Wurster, *Ber. Dtsch. Chem. Ges.* **1879**, 12, 2071–2072; b) C. Wurster, E. Schobig, *Ber. Dtsch. Chem. Ges.* **1879**, 12, 1807–1813; c) R. Kuhn, H. Katz, *Z. Angew. Chem.* **1933**, 46, 478–479.
- See, for example: a) A. D. Clegg, N. V. Rees, O. V. Klymenko, B. A. Coles, R. G. Compton, *ChemPhysChem* **2004**, 5, 1234–1240; b) G. Grampp, A.-M. Kelterer, S. Landgraf, M. Sacher, D. Niethammer, J. P. Telo, R. M. B. Dias, A. J. S. C. Vieira, *Monatsh. Chem.* **2005**, 136, 519–536; c) N. E. Gruhn, N. A. Marcías-Ruvalcaba, D. H. Evans, *J. Phys. Chem. A* **2006**, 110, 5650–5655.
- a) K. Elbl, C. Krieger, H. A. Staab, *Angew. Chem.* **1986**, 98, 1024–1026; *Angew. Chem. Int. Ed. Engl.* **1986**, 25, 1023; b) H. A. Staab, K. Elbl, C. Krieger, *Tetrahedron Lett.* **1986**, 27, 5719–5722.
- K. Elbl-Weiser, C. Krieger, H. A. Staab, *Angew. Chem.* **1990**, 102, 183–185; *Angew. Chem. Int. Ed. Engl.* **1990**, 29, 211–213.
- K. Elbl-Weiser, F. A. Neugebauer, H. A. Staab, *Tetrahedron Lett.* **1989**, 30, 6161–6164.
- R. Schwesinger, *Nachr. Chem. Tech. Lab.* **1990**, 38, 1214–1226; and references given therein.
- A. Peters, E. Kaifer, H.-J. Himmel, *Eur. J. Org. Chem.* **2008**, 5907–5914.
- D. Emeljanenko, A. Peters, N. Wagner, J. Beck, E. Kaifer, H.-J. Himmel, *Eur. J. Inorg. Chem.* **2010**, 1839–1846.
- We denote such strong electron donors consisting of aromates functionalized by several guanidino groups GFAs (guanidino-functionalized aromatics).
- a) A. Peters, C. Trumm, M. Reinmuth, D. Emeljanenko, E. Kaifer, H.-J. Himmel, *Eur. J. Inorg. Chem.* **2009**, 3791–3800; b) V. Vitske, C. König, O. Hübner, E. Kaifer, H.-J. Himmel, *Eur. J. Inorg. Chem.* **2010**, 115–126.
- CCDC-744641 (for **1**), -744642 (for **2**), -744643 (for **3**) contain the supplementary crystallographic data for this paper. These data can be obtained free of charge from The Cambridge

- Crystallographic Data Centre via www.ccdc.cam.ac.uk/data_request/cif.
- [12] See, for example, for recent experimental studies: a) R. M. Kadam, Y. Itagaki, N. P. Benetis, A. Lund, R. Erickson, M. Huber, W. Hilczner, *Phys. Chem. Chem. Phys.* **1999**, *1*, 4967–4974; b) R. G. Satink, H. Piest, G. von Helden, G. Meijer, *J. Chem. Phys.* **1999**, *111*, 10750–10753; c) V. I. Feldman, F. Sukhov, A. Orlov, R. Kadam, Y. Itagaki, A. Lund, *Phys. Chem. Chem. Phys.* **2000**, *2*, 29–35.
- [13] See, for example, for recent theoretical studies: a) B. E. Applegate, T. A. Miller, *J. Chem. Phys.* **2002**, *117*, 10654–10674; b) K. Tokunaga, T. Sato, K. Tanaka, *J. Chem. Phys.* **2006**, *124*, 154303–1–10; c) K. F. Hall, A. M. Tokmachev, M. J. Bearpark, M. Boggio-Pasqua, M. A. Robb, *J. Chem. Phys.* **2007**, *127*, 134111–1–11.
- [14] H. Shorafa, D. Mollenhauer, B. Paulus, K. Seppelt, *Angew. Chem.* **2009**, *121*, 5959–5961; *Angew. Chem. Int. Ed.* **2009**, *48*, 5845–5847.
- [15] The R_2 value for the fit is 0.9934.
- [16] a) H. O. Stumpf, L. Ouahab, Y. Pei, D. Grandjean, O. Kahn, *Science* **1993**, *261*, 447–449; b) K. Inoue, H. Iwamura, *J. Am. Chem. Soc.* **1994**, *116*, 3173–3174.
- [17] T. M. Barclay, R. G. Hicks, M. T. Lemaire, L. K. Thompson, *Inorg. Chem.* **2001**, *40*, 5581–5584.
- [18] See, for example: R. Veit, J.-J. Girerd, O. Kahn, F. Robert, Y. Jeannin, *Inorg. Chem.* **1986**, *25*, 4175–4180.
- [19] DENZO-SMN, Data processing software, Nonius **1998**; <http://www.nonius.com>.
- [20] a) G. M. Sheldrick, *SHELXS-97, Program for Crystal Structure Solution*, University of Göttingen, **1997**; <http://shelx.uni-ac.gwdg.de/SHELX/index.html>; b) G. M. Sheldrick, *SHELXL-97, Program for Crystal Structure Refinement*, University of Göttingen, **1997**; <http://shelx.uni-ac.gwdg.de/SHELX/index.html>.
- [21] *International Tables for X-ray Crystallography*, vol. 4, Kynoch Press, Birmingham, UK, **1974**.
- [22] L. Zsolnai, G. Huttner, *XPMA*, University of Heidelberg, **1994**; <http://www.uni-heidelberg.de/institute/fak12/AC/huttner/software/software.html>.
- [23] a) R. Ahlrichs, M. Bär, M. Häser, H. Horn, C. Kölmel, *Chem. Phys. Lett.* **1989**, *162*, 165–169; b) O. Treutler, R. Ahlrichs, *J. Chem. Phys.* **1995**, *102*, 346–354.
- [24] a) P. J. Stephens, F. J. Devlin, C. F. Chabalowski, M. J. Frisch, *J. Phys. Chem.* **1994**, *98*, 11623–11627; b) A. D. Becke, *J. Chem. Phys.* **1993**, *98*, 5648–5652; c) C. Lee, W. Yang, R. G. Parr, *Phys. Rev. B* **1988**, *37*, 785–789.
- [25] F. Weigend, R. Ahlrichs, *Phys. Chem. Chem. Phys.* **2005**, *7*, 3297–3305.
- [26] L. Noodleman, *J. Chem. Phys.* **1981**, *74*, 5737–5743.
- [27] H. Fliegl, K. Fink, W. Klopper, C. E. Anson, A. K. Powell, R. Clérac, *Phys. Chem. Chem. Phys.* **2009**, *11*, 3900–3909.

Received: February 2, 2010

Published Online: May 27, 2010

Synthesis, Crystal Structure, DNA Binding, and Hydrolytic Cleavage Activity of a Manganese(II) Complex

Jing Qian,^[a,b] Xiao-Fang Ma,^[c] Hai-Zhen Xu,^[a] Jin-Lei Tian,^{*,[b]} Jing Shang,^[a] Yuan Zhang,^[a] and Shi-Ping Yan^{*,[b]}

Keywords: Manganese / Bridging ligands / Magnetic properties / DNA cleavage / Hydrolytic cleavage / Structure elucidation

A new trinuclear manganese(II) complex $\{[\text{MnCl}(\text{bpma})_2]_2\text{[Mn}(\mu\text{-Cl})_4(\text{H}_2\text{O})_2]\}\cdot\text{CH}_3\text{CN}$ (**1**) [bpma = *N,N*-bis(2-pyridylmethyl)methylamine] has been synthesized and structurally characterized by X-ray crystallography. The variable temperature-dependent susceptibility measurement (2–300 K) of **1** reveals a weak antiferromagnetic interaction between the manganese ions through the dichlorido bridging ligands, with $J = -0.46 \text{ cm}^{-1}$, $g = 1.99$. The electrospray ionization mass spectrum of **1** in solution indicates that the dinu-

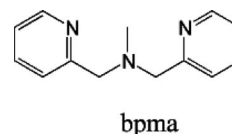
clear $[\text{Mn}_2(\text{bpma})_2\text{Cl}_2(\text{H}_2\text{O})(\text{OH})]^+$ ion is the active species. In the absence of a reducing agent, supercoiled plasmid DNA cleavage by the active species was performed and its hydrolytic mechanism was demonstrated with radical scavengers, anaerobic reaction, and T4 ligase. The pseudo-Michaelis–Menten kinetic parameters (k_{cat} , K_{M}) were calculated to be 1.11 h^{-1} and $6.65 \times 10^{-4} \text{ M}$ for the dinuclear species.

Introduction

Metal-based artificial nucleases are of current interest in nucleic acid chemistry for their diverse applications like footprinting and sequence-specific binding to nucleic acids, and as new structural probes and therapeutic agents.^[1–10] Chemical nucleases present some advantages over conventional enzymatic nucleases in that they are smaller in size and thus can reach more sterically hindered regions of a macromolecule. Many of these utilize the redox properties of the metal and dioxygen to produce reactive oxygen species that oxidize DNA, thereby yielding direct strand scission or base modification.^[11] Hydrolytic degradation of DNA by nuclease enzymes is an important biological reaction in which metal ions play a central role in mediating such cleavage pathways.^[12] Nucleic acid cleavage in a redox manner will permit the manipulation of gene expression and the development of gene therapies. Additionally, the biomimetic hydrolysis of nucleic acids is of increasing importance in biotechnology and medicine.^[13]

In the past few years we have undertaken studies that involve the preparation and structural characterization of transition-metal binuclear/polynuclear complexes.^[14,15] Recently we have begun to explore the nuclease activity of

binuclear/polynuclear complexes.^[16–18] In an attempt to obtain more insight into the selectivity and efficiency of DNA recognized and cleaved by different complexes, herein we have synthesized and characterized a dichlorido-bridged trinuclear manganese(II) complex of the bpma ligand, namely, $\{[\text{MnCl}(\text{bpma})_2]_2\text{[Mn}(\mu\text{-Cl})_4(\text{H}_2\text{O})_2]\}\cdot\text{CH}_3\text{CN}$ (**1**) (Scheme 1). A detailed study of the magnetic properties was also carried out. Variable-temperature magnetic susceptibility studies (2–300 K) showed the existence of antiferromagnetic coupling between the manganese(II) ions in complex **1**. The electrospray ionization mass spectrum of **1** in solution indicates that the dinuclear $[\text{Mn}_2(\text{bpma})_2\text{Cl}_2(\text{H}_2\text{O})(\text{OH})]^+$ ion is the active species. In addition, we have examined the DNA binding ability of the dinuclear ion by using UV absorption, fluorescent spectroscopy methods, and a DNA cleavage study performed using an agarose gel assay to indicate the ability of the dinuclear complex ion to cleave plasmid supercoiled circular pBR322 DNA (SC) into its nicked circular (NC) form as well as linear (L) form without addition of external oxidative and/or reductive agents. This revealed that the mechanism of DNA cleavage of the dinuclear ion is a hydrolytic pathway.



Scheme 1. Structure of ligand (bpma).

[a] College of Chemistry & Life Science, Tianjin Normal University, 300387, Tianjin, P. R. China

[b] Department of Chemistry, Nankai University, 300071, Tianjin, P. R. China

[c] College of Basic Medicine Science, Zhengzhou University, Zhengzhou 450001, P. R. China

Supporting information for this article is available on the WWW under <http://dx.doi.org/10.1002/ejic.200901231>.

Results and Discussion

Crystal Structure of 1

The structure of **1** was characterized by single-crystal X-ray crystallography. Its crystal structure consists of a trinuclear $\{[\text{MnCl}(\text{bpma})]_2[\text{Mn}(\mu\text{-Cl})_4(\text{H}_2\text{O})_2]\} \cdot \text{CH}_3\text{CN}$ molecule and CH_3CN molecules. In each trinuclear cluster, there are two crystallographically distinct Mn atoms, and the three Mn^{II} atoms are in a linear form linked by four Cl^- atoms with $\text{Mn1} \cdots \text{Mn2}$ distances of 3.663 Å and with two bpma ligands as terminal ligands. The central metal center (Mn2) is located on a crystallographic inversion center and thus the trinuclear cluster adopts a linear structure. Figure 1 shows the trinuclear entity of complex **1** with the atomic numbering scheme. Selected bond lengths and angles are listed in Table 1.

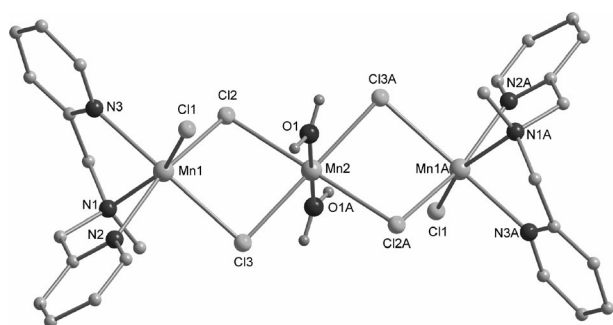


Figure 1. The molecular structure of **1** showing the atom-labeling scheme adopted. Hydrogen atoms and CH_3CN are omitted for clarity.

Table 1. Selected bond lengths and angles of **1**.

Bond lengths [Å]			
Mn1–N1	2.344(2)	Mn1–Cl1	2.463(8)
Mn1–N2	2.238(2)	Mn1–Cl2	2.550(8)
Mn1–N3	2.300(2)	Mn1–Cl3	2.583(8)
Mn2–O1	2.211(19)	Mn2–Cl3	2.511(7)
Mn2–Cl2	2.5687(7)	Mn1–Mn2	3.663(5)
Bond angles [°]			
N2–Mn1–N3	100.48(7)	N2–Mn1–N1	73.96(7)
N3–Mn1–N1	72.18(8)	N2–Mn1–Cl1	92.55(6)
N3–Mn1–Cl1	94.19(6)	N1–Mn1–Cl1	158.20(6)
N2–Mn1–Cl2	163.71(6)	N3–Mn1–Cl2	88.26(5)
N1–Mn1–Cl2	96.06(5)	Cl1–Mn1–Cl2	100.55(3)
N2–Mn1–Cl3	85.06(6)	N3–Mn1–Cl3	167.28(6)
N1–Mn1–Cl3	98.75(6)	Cl1–Mn1–Cl3	97.01(3)
Cl2–Mn1–Cl3	83.79(2)	O1–Mn2–Cl2	93.31(6)
O1–Mn2–Cl3	90.30(6)	Mn2–Cl3–Mn1	91.94(2)
Cl3–Mn2–Cl2	84.87(2)	Mn1–Cl2–Mn2	91.39(2)

The central and terminal manganese(II) ions (Mn1 and Mn1A) are nonequivalent. The central Mn2 ion has a distorted octahedral geometry with the MnO_2Cl_4 chromophore. The basal plane is defined by the four bridging chloride ions (Cl2 , Cl3 , Cl2A , and Cl3A). The apical position is occupied by two coordinated H_2O molecules (O1 and O1A). The Cl2 , Cl2A , Cl3 , Cl3A , and Mn2 ions are strictly coplanar; the bond angles of Cl2–Mn2–Cl3 and Cl2–Mn2–

Cl3A are 84.87 and 95.13°, respectively. The two bridging bond lengths of Mn2–Cl2 and Mn2–Cl3 are slightly different (2.569/2.511 Å).

Two terminal manganese atoms, Mn1 and Mn1A , are equivalent due to the inversion center passing through the central Mn2 atom. $\text{Mn1}(\text{Mn1A})$ has a distorted octahedral geometry with N_2Cl_2 defining the basal plane and NCl (N3 and Cl3) occupying the apical positions. The adjacent manganese centers are bridged by two chloride ions that lead to an Mn_2Cl_2 diamond core [$\text{Mn1–Cl2–Mn2} = 91.39(2)^\circ$, $\text{Mn1–Cl3–Mn2} = 91.94(2)^\circ$], and the bond lengths of Mn1–Cl2 and Mn1–Cl3 are slightly different (2.550/2.583 Å), both of which are longer than the terminal Mn1–Cl1 bond length (2.463 Å). All these structural features are similar to those of other structurally characterized $\text{Mn}^{\text{II}}\text{Mn}^{\text{II}}$ di- μ -chlorido complexes.^[19] The $\text{Mn1} \cdots \text{Mn2}$ distance in **1** is 3.663 Å, which is longer than the distance (3.56 Å) observed in the trinuclear complex $[\text{LMn}(\mu\text{-Cl})_2\text{Mn}(\text{thf})_2(\mu\text{-Cl})_2\text{MnL}]$ [$\text{L} = \text{HC}(\text{CMeNAr})_2$, $\text{Ar} = 2,6\text{-iPr}_2\text{C}_6\text{H}_3$]^[20] and also slightly longer than the distance (3.636 Å) in the $[\text{Mn}_3(\text{bdt})_2\text{Cl}_2(\text{def})_6]$ ($\text{bdt}^{2-} = 1,4\text{-benzeneditetrazolate}$; $\text{def} = N,N\text{-diethylformamide}$).^[21]

Magnetic Properties of 1

The magnetic properties of **1**, in the form of an $\chi_{\text{M}}T$ versus T plot, are shown in Figure 2. At room temperature $\chi_{\text{M}}T$ is equal to $12.78 \text{ cm}^3 \text{ mol}^{-1} \text{ K}$, which is slightly lower than the spin-only value of $13.12 \text{ cm}^3 \text{ mol}^{-1} \text{ K}$, a value that corresponds to that expected for a three-spin isolated $S = 5/2$ ground-state system with a g value of around 2.0. As the temperature is lowered, $\chi_{\text{M}}T$ decreases gradually down to $4.08 \text{ cm}^3 \text{ mol}^{-1} \text{ K}$ at 1.8 K, indicative of the presence of antiferromagnetic coupling between Mn^{II} ions through the chloride routes. From 80–300 K, the magnetic data can be better fitted to a Curie–Weiss law with $C = 13.1 \text{ cm}^3 \text{ mol}^{-1} \text{ K}$ and $\theta = -5.84 \text{ K}$, which also indicated a weak antiferromagnetic interaction between the three Mn^{II} ions in **1**. Taking into account the structure of the isolated and linear Mn^{II} trimer units in **1**, and assuming that the exchange coupling within the cluster is isotropic and that there is no interaction between the two terminal Mn^{II} ions, the Heisenberg Hamiltonian for the trimer system can be written as: $\hat{H} = -J(\hat{S}_1\hat{S}_2 + \hat{S}_2\hat{S}_3)$. By application of Van Vleck's equation,^[22] a theoretical expression for the molar susceptibility (χ_{M}) may be derived as follows:

$$\chi_{\text{M}} = \frac{Ng^2\beta^2}{3kT} \left(\frac{3F_1}{4F_2} \right)$$

where $F_1 = 680e^{27.5x} + 455(e^{20x} + e^{25x}) + 286(e^{13.5x} + e^{18.5x} + e^{22.5x}) + 165(e^{8x} + e^{13x} + e^{17x} + e^{20x}) + 84(e^{3.5x} + e^{8.5x} + e^{12.5x} + e^{15.5x} + e^{17.5x}) + 35(e^{15x} + e^{5x} + e^{9x} + e^{12x} + e^{14x}) + 10(e^{2.5x} + e^{6.5x} + e^{9.5x} + e^{11.5x}) + (e^{5x} + e^{8x}) + 35$; $F_2 = 8e^{27.5x} + 7(e^{20x} + e^{25x}) + 6(e^{13.5x} + e^{18.5x} + e^{22.5x}) + 5(e^{8x} + e^{13x} + e^{17x} + e^{20x}) + 4(e^{3.5x} + e^{8.5x} + e^{12.5x} + e^{15.5x} + e^{17.5x}) + 3(e^{15x} + e^{5x} + e^{9x} + e^{12x} + e^{14x}) + 2(e^{2.5x} + e^{6.5x} + e^{9.5x} + e^{11.5x}) + (e^{5x} + e^{8x}) + 3$; and $x = J/(kT)$.

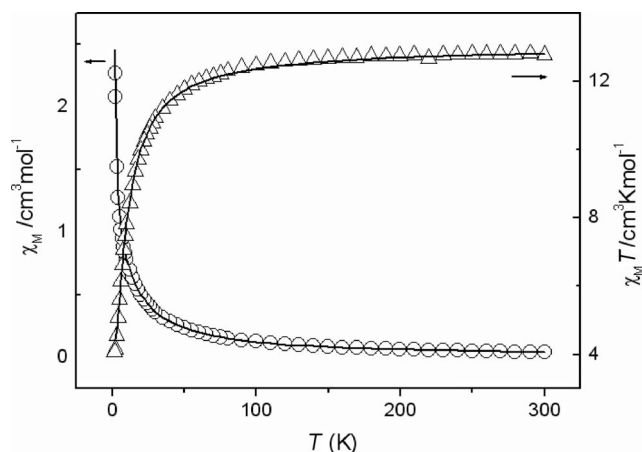


Figure 2. Plots of χ_M (open circle) and $\chi_M T$ (open triangle) versus T for **1**. The solid lines are theoretical fits.

Least-squares fitting of the experimental results led to the best-fit parameters of $J = -0.46 \text{ cm}^{-1}$, $g = 1.99$. An agreement factor defined as $R = \Sigma(\chi_{\text{obsd.}} - \chi_{\text{calcd.}})^2 / \Sigma\chi_{\text{obsd.}}^2$ was 2.84×10^{-3} . The negative J value indicates antiferromagnetic coupling between the Mn^{II} ions, which is consistent with some similar linear Mn^{II} trimers.^[23]

Solution Properties of **1**

Complex **1** exhibits a good solubility in 5% $\text{C}_2\text{H}_5\text{OH}$ aqueous solution [5 mM tris(hydroxymethyl)aminomethane (Tris)-HCl/NaCl buffer, pH 7.2], which facilitates investigation of its behavior in aqueous solutions. The species distribution of **1** in aqueous solution was measured by the ESI-MS method. The electrospray ionization mass spectrum in positive mode (ESI^+) gives three peaks at $m/z = 643.032$ [$\text{Mn}_2(\text{bpma})_2\text{Cl}_3$] $^+$, 665.099 [$\text{Mn}_2(\text{bpma})_2\text{Cl}_2(\text{OH})(\text{H}_2\text{O})$] + $0.5 \text{ C}_2\text{H}_5\text{OH}$] $^+$, 689.143 [$\text{Mn}_2(\text{bpma})_2\text{Cl}_3$ + $\text{C}_2\text{H}_5\text{OH}$] $^+$ (Figure S1 in the Supporting Information), which is derived from the trinuclear complex; which is to say, the trinuclear manganese compound dissolved to form binuclear manganese species in solution.

DNA Binding Properties

DNA binding is a critical step for subsequent cleavage. Therefore, prior to investigation of the nuclease activities of this complex, the binding properties of the binuclear manganese species with DNA were examined using various techniques.

UV Titration

The binuclear manganese species were titrated with varying concentrations of calf thymus (CT)-DNA and the change in the absorption spectral profile of it at different concentrations of DNA is shown in Figure 3. Upon addition of an increasing amount CT-DNA to the 5% $\text{C}_2\text{H}_5\text{OH}$ aqueous solution of **1** (pH 7.2), a 52.3% hypo-

chromism and slight redshift (6 nm) could be detected in the UV spectra by monitoring the change in the absorption intensity of the spectral band at 266 nm (π - π^* transition band).^[24] Although this is not definitive proof, hypochromism and redshifts observed for other complexes in the presence of CT-DNA are often taken as a sign of an intercalative binding mode in which stacking interactions between the aromatic chromophore of the complex and the base pairs of DNA modulate the absorption characteristics of the metal complexes.^[25–28] The value of the intrinsic binding constants ($K_b = 1.37 \times 10^4$) for the binuclear ion was determined by regression analysis.^[29] The value obtained is lower by around 100 times than those reported for typical classical intercalators [e.g., ethidium bromide (EB)-DNA, ca. 10^6 M^{-1}],^[30,31] about an order lower than those of the affinities of intercalators that contain similar planar ligands.^[25–28] The lower K_b value observed for the present complex implies that it does not intercalate very strongly or deeply between the DNA base pairs. So we propose that the lower redshifts observed in the UV spectra are due to the partial intercalation of the pyridyl ring.

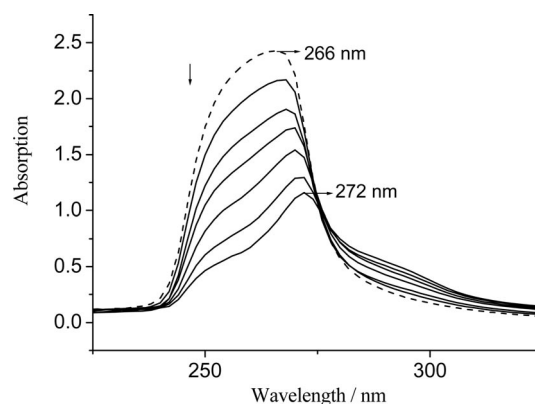


Figure 3. Absorption spectrum of binuclear complex ($6.3 \times 10^{-5} \text{ M}$) in the absence (dashed line) and presence (solid line) with increasing amounts of CT-DNA (0 – $3.81 \times 10^{-4} \text{ M}$) at room temperature in 5 mM Tris-HCl/NaCl buffer (pH 7.2).

Fluorescence Spectral Studies

As the binuclear manganese complexes are nonemissive, a relative binding study with EB-CT-DNA was carried out with a view to exploring the binding mode. EB emits intense fluorescent light in the presence of DNA due to its strong intercalation between the adjacent DNA base pairs, and the enhanced fluorescence could be quenched by the addition of another molecule.^[32] Such a binding result suggests that the complex displaces DNA-bound EB and binds to DNA at the intercalation sites with almost the same affinity. The relative binding propensity of the binuclear manganese complex to CT-DNA was determined from the comparison of the slopes of the lines in the fluorescence intensity versus complex concentration plots.^[33] Figure 4 shows the plot of I_0/I , in which I_0 and I represent the fluorescence intensities in the absence and presence of the complex, respectively,

versus the concentration of the complex. The apparent binding constant (K_{app}) was calculated from the equation $K_{\text{EB}}[\text{EB}] = K_{\text{app}}[\text{complex}]$, in which the complex concentration was the value at a 50% reduction of the fluorescence intensity of EB and $K_{\text{EB}} = 1.0 \times 10^7 \text{ M}^{-1}$ ($[\text{EB}] = 4.0 \text{ }\mu\text{M}$). The binding constant of the classical intercalator and metalintercalator was along the order of 10^7 M^{-1} .^[34] The apparent binding constant (K_{app}) value for the binuclear manganese species is $4.3 \times 10^4 \text{ M}^{-1}$, thus indicating that the interaction of it with DNA is a moderate intercalative mode. The value obtained suggests that the EB molecule is replaced by the binuclear manganese species, which is consistent with the above spectral results that suggest partial intercalation of the pyridyl ring in the ligand, which facilitates DNA binding.

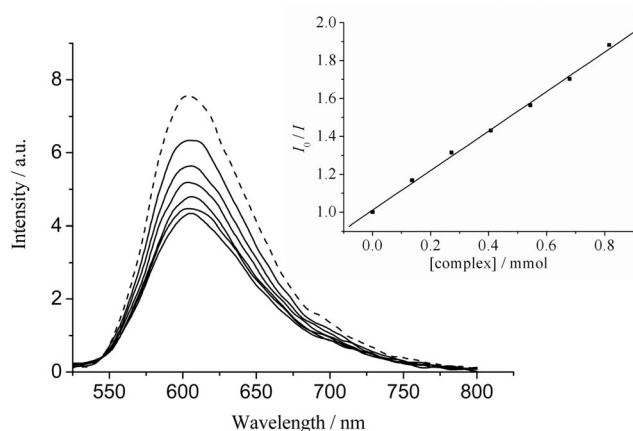


Figure 4. Fluorescence emission spectra of the EB-CT-DNA system in the absence (dashed line) and presence (solid lines) of binuclear complex ($0\text{--}3 \times 10^{-3} \text{ M}$). Inset: the plot of I_0/I versus the complex concentration.

DNA Cleavage by the Binuclear Complexes

The ability of the binuclear complexes to cleave DNA was assayed with the aid of gel electrophoresis on supercoiled pBR322 plasmid DNA as a substrate in a medium of 50 mM Tris-HCl/18 mM NaCl buffer (pH 7.2) in the absence of an external agent. When circular plasmid DNA is analyzed by electrophoresis, the fastest migration will be observed for the supercoiled form (form I). If one strand is cleaved, the supercoiled form will relax to produce a slower-moving nicked circular form (form II). If both strands are cleaved, a linear form (form III) will be generated that migrates between form I and form II.

Effect of Complex Concentration on Plasmid DNA Cleavage

Firstly, the concentration-dependent DNA cleavage by the complex was performed. The activity of the binuclear complex was assessed by the conversion of DNA from form I to form II and form III. Figure 5 shows that the results of gel electrophoretic separations of plasmid pBR322 DNA

induced by increasing the concentration of the binuclear complex and manganese salt in the absence of an external agent at pH 7.2 (50 mM Tris-HCl/NaCl buffer) and 37 °C. Upon increasing the concentration of the complex, the amount of form I decreased gradually and the amount of forms II and III increased, but the manganese salt is not visible. At the same time, under aerobic conditions, when the concentration of the binuclear complex reached 0.18 mM the linear form III was visible in the gel (lane 4). The percentage of linear and nicked DNA molecules observed with Mn complex increased along with an increase in the concentration; however, the supercoiled DNA is degraded by 80% at a concentration of 2.16 mM (lane 6). It is clear that the degradation of pBR322 DNA is highly dependent on the concentration of binuclear complex used. The linear form III was observed in this case, revealing a double-strand DNA cleavage. It has been widely accepted that the metal-bound hydroxyl species (LM-OH) in enzymes or their models are the active species in the hydration of the phosphate backbone. For **1**, the ESI mass spectrum indicates three binuclear species, however, the $[\text{Mn}_2(\text{bpma})_2\text{Cl}_2(\text{H}_2\text{O})(\text{OH})]^+$ species is most likely the active one. For the other two binuclear species, coordinated Cl^- anions may be replaced by water molecules and further lead to the formation of hydroxyl-coordinated binuclear species.

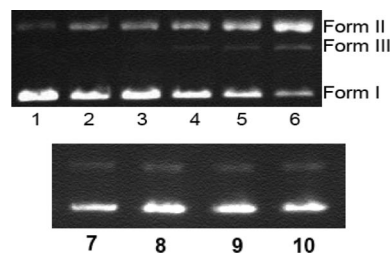


Figure 5. Gel electrophoresis diagrams showing the cleavage of pBR322 DNA ($0.2 \text{ }\mu\text{g}$, $33 \text{ }\mu\text{M}$) at different complex concentrations in 50 mM Tris-HCl/NaCl buffer (pH 7.2) at 37 °C, for 6 h. Lane 1: DNA control (6 h); lanes 2–6: DNA + binuclear complex (0.018, 0.072, 0.18, 0.72, and 2.16 mM, respectively); lane 7: DNA control; lanes 8–10: DNA + MnCl_2 (0.05, 0.25, 1.25 mM, respectively).

Effects of Reaction Time on Plasmid DNA Cleavage

The time-dependent cleavage of DNA by the binuclear complex was also studied under similar conditions. As the reaction time was increased, the amounts of forms II and III increased and form I gradually disappeared. The results show that the binuclear complex can effectively cleave the pBR322 plasmid DNA without the addition of external agents, and cleavage of DNA by the binuclear complex is dependent on the reaction time (shown in Figure 6). From these experimental results, we find that the plots for the appearance of form II as well as the disappearance of form I follow pseudo-first-order kinetic profiles and fit well to a single-exponential decay curve, which is consistent with the general model for enzyme-catalyzed reactions.^[35] By fitting the experimental data with first-order consecutive kinetic equations, the rate constants, $k_{\text{obs}} = 2.87 \times 10^{-4} \text{ s}^{-1}$ for the

conversion of supercoiled to nicked DNA are obtained for the binuclear complex. The cleavage efficiency depends both on the complex concentration and on the reaction time. Figures 5 and 6 clearly show that the cleavage mediated by the binuclear complex produced a double-strand cleavage on the DNA, whereby the linear form appears before the supercoiled form (form I) has been completely converted into the linear form.

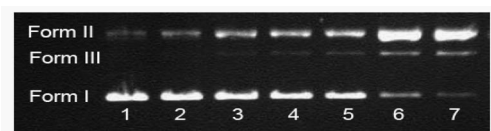


Figure 6. Time courses of pBR322 DNA cleavage (0.2 μg , 33 μM) by the binuclear complex at pH 7.2 and 37 $^{\circ}\text{C}$: Lane 1: DNA control; lanes 2–7: DNA + 1.45 mM binuclear complex (0.25, 1, 4, 8, 21, and 23 h, respectively).

Effects of Radical Scavengers on Plasmid DNA Cleavage

To verify if reactive oxygen species (ROS) may be formed in the DNA cleavage reaction, DNA cleavage experiments were carried out in the presence of a hydroxyl radical scavenger (DMSO),^[36] a superoxide scavenger [superoxide dismutase (SOD)],^[37] a singlet oxygen quencher (L-histidine),^[38] a peroxide scavenger (catalase), and a chelating agent [ethylenediaminetetraacetic acid (EDTA)] under physiological conditions. As shown in Figure 7, no obvious inhibitions are observed in the presence of DMSO, L-histidine, catalase, and SOD, the results rule out the possibility of DNA cleavage by a hydroxyl radical, peroxide, singlet oxygen, and superoxide. EDTA can efficiently inhibit DNA cleavage, indicating that the Mn^{II} complex plays a key role in the cleavage. To clarify other aspects of the mechanism, groove binders such as methyl green (a major-groove binder) and/or SYBR Green (a minor-groove binder) can also be used. The addition of SYBR Green and methyl green hardly inhibited DNA cleavage, which suggests that the complex did not interact through the grooves.

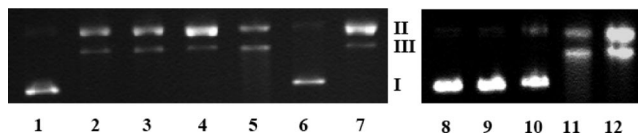


Figure 7. Gel electrophoresis diagrams showing the cleavage of pBR322 DNA (30 μM) by the binuclear complex (3.62 mM, 2 h) in the presence of different additives at pH 7.2 and 37 $^{\circ}\text{C}$: Lane 1: DNA control; lane 2: DNA + complex; lanes 3–7: DNA + complex + (DMSO, L-histidine, SOD, EDTA, catalase, respectively); lane 8: DNA control; lane 9: DNA + methyl green (0.05 mM); lane 10: DNA + SYBR Green (10 μM); lane 11: DNA + complex + methyl green (0.05 mM); lane 12: DNA + complex + SYBR Green (10 μM).

To clarify whether O_2 in air is responsible for the DNA cleavage by the complex, it is necessary to perform the cleavage experiment under anaerobic conditions. The binuclear complex still cleaved pBR322 plasmid DNA under an-

aerobic conditions; this can be seen in Figure 8. The results indicated that O_2 was not an indispensable cofactor for DNA scission. On the basis of the above observation, we make the hypothesis that the examined complex may be capable of promoting DNA cleavage through a hydrolytic mechanism.

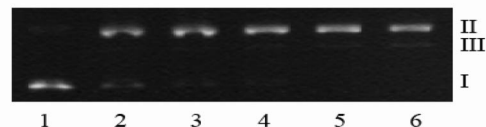


Figure 8. Anaerobic cleavage of supercoiled plasmid DNA (30 μM) by the binuclear complex incubated for 6.5 h at pH 7.2 and 18 $^{\circ}\text{C}$ under anaerobic conditions. Lane 1: DNA control; lanes 2–6: DNA + complex (0.652, 1.956, 2.608, 3.26, and 4.564 min).

T4 Ligation Experiment

Direct evidence of DNA hydrolysis was further obtained from ligation experiments of the linear DNA cleavage products generated by the binuclear complex (Figure 9). To explore the effects of molecular oxygen on the degradation of DNA by the binuclear complex, the reaction was also performed under anaerobic conditions. A gel fragment of the linear DNA was cut off from a low-melting-point agarose gel and subjected to the DNA recovery system. The recovered linear DNA was subjected to an overnight ligation reaction with T4 DNA ligase. The result after electrophoresis shows that the linear DNA fragments cleaved by the binuclear complex can be re-ligated by T4 ligase. Hence, this result implied that the process of DNA cleavage by the binuclear complex occurs by means of a hydrolytic path.

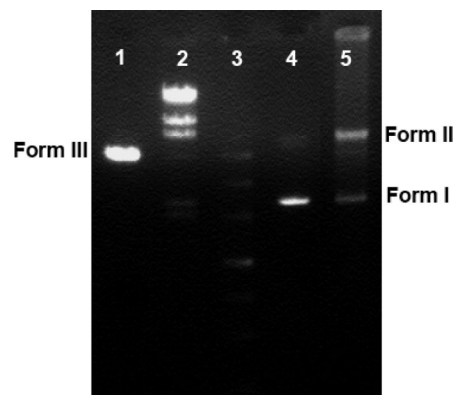


Figure 9. Agarose gel electrophoresis for ligation of linearized pBR322 DNA: lane 1: pBR322 DNA linearized by the complex without T4 ligase; lane 2: $\lambda\text{HindIII}$ DNA markers; lane 3: DNA markers; lane 4: DNA control; lane 5: pBR322 DNA linearized by the complex with T4 ligase.

The Pseudo-Michaelis–Menten Kinetics of DNA Cleavage

The cleavage reaction of supercoiled plasmid DNA into nicked and linear DNA by the complex was carried out in

the absence of an external agent. The decrease of form I was fitted to a single-exponential decay curve (pseudo-first-order kinetics) by use of Equation (1) or (2), where y_0 is the initial percentage of a form of DNA, y is the percentage of a specific form of DNA at time t , a is the percentage of uncleaved DNA, and k_{obs} is the hydrolysis rate, or apparent rate constant.

$$y = (y_0 - a) \exp(-k_{\text{obs}}x) + a \quad (1)$$

$$y = (100 - y_0)[1 - \exp(-k_{\text{obs}}x)] \quad (2)$$

To determine the hydrolytic cleavage rate, the kinetic aspect of the hydrolytic DNA cleavage has been investigated. Reactions were carried out under pseudo-Michaelis–Menten conditions by using various concentrations of complex. Based on the plots of k_{obs} versus concentration of complex (Figure 10), the pseudo-Michaelis–Menten kinetic parameters (k_{cat} and K_{M}) were calculated to be 1.11 h^{-1} and $6.65 \times 10^{-4} \text{ M}$, respectively, for the binuclear manganese species.

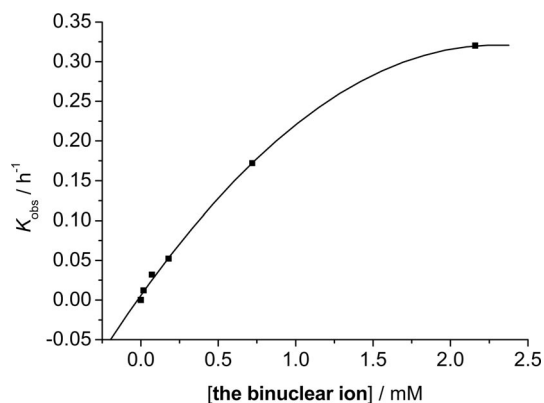


Figure 10. Plot showing the saturation kinetics for the cleavage of plasmid pBR322DNA with different complex concentrations of the binuclear ion at 37 °C in Tris-HCl/NaCl buffer (pH 7.2).

Conclusion

In summary, although chlorido-bridged complexes have been reported previously, we have shown how they are attractive in terms of their structure and magnetism. Our work provides a linear sandwich-like trinuclear unit designed and characterized to serve as a nuclease mimic. Unexpectedly, the species was a dinuclear cation in solution. DNA cleavage promoted by the dinuclear cation was demonstrated to occur by a hydrolytic path under anaerobic conditions, and the result was supported by a T4 ligase experiment.

Experimental Section

General: All reagents and chemicals were from commercial sources and used without further purification. Solvents used in this research were purified by following standard procedures. The bpma ligand was prepared by following a literature method.^[39] Plasmid

pBR322 DNA, agarose, ethidium bromide (EB), and calf thymus (CT) DNA were from Sigma. Tris-HCl buffer solution was prepared using deionized sonicated triple-distilled water.

Elemental analyses (C, H, and N) were performed on a Perkin–Elmer 240 CHN elemental analyzer. The infrared, electronic, and fluorescence spectroscopic data were obtained using a Bruker TENOR 27 spectrophotometer, Jasco-UV-570 spectrometer, and MPF-4 fluorescence spectrophotometer, respectively. The Gel Imaging and Documentation DigiDoc-It System (UVI, England) were assessed using Labworks Imaging and Analysis Software (UVI, England).

[MnCl(bpma)]₂[Mn(μ-Cl)₄(H₂O)₂]·CH₃CN (1**):** Complex **1** was obtained by the reaction of MnCl₂ with bpma in acetonitrile/water at ambient temperature and crystallized by slow evaporation of the solution. The reaction of ligand *N,N*-bis(2-pyridylmethyl)ethylamine (bpea) (0.200 g, 0.88 mmol) and MnCl₂ (0.110 g, 0.88 mmol) in a water/ethanolic mixture to afford the dimeric complex [(bpea)Mn(μ-Cl)₂]₂ has been reported elsewhere.^[19] However, the similar reaction of bpma (0.188 g, 0.88 mmol) and MnCl₂ (0.110 g, 0.88 mmol) in an acetonitrile/water mixture unexpectedly resulted in the formation of **1** in good yield, although a ratio of 1:1 of the starting materials was employed; yield 38%. C₂₈H₃₇Cl₆Mn₃N₇O₂ (881.16): calcd. C 38.13, H 4.20, N 11.12; found C 38.61, H 4.04, N 11.56. FTIR (KBr): $\tilde{\nu}$ = 1604 (s), 1571 (m), 1481 (s), 1444 (s), 1414 (w), 1386 (m), 1353 (s), 1314 (m), 1297 (m), 1224 (w), 1186 (w), 1159 (s), 1116 (m), 1104 (m), 1052 (w), 1020 (s), 989 (w), 894 (w), 865 (w), 766 (s), 730 (w), 641 (m), 412 (m) cm⁻¹. UV/Vis: λ = 266 (π – π^*), 310 nm (n– π).

X-ray Crystallographic Procedure: Suitable single crystals with approximate dimensions were used for X-ray diffraction analyses by mounting the sample on the tip of a glass fiber in air. Crystallographic data for **1** are shown in Table 2. Data were collected on a Bruker APEX-II CCD diffractometer with Mo- K_{α} radiation (λ = 0.71073 Å) at 294(2) K. The structures were solved by direct methods using the program SHELXS-97 and refined anisotropically with full-matrix least-squares on F^2 using SHELXL-97.^[40] All non-hydrogen atoms were refined anisotropically and all the hydrogen

Table 2. Crystallographic data for **1**.

Formula	C ₁₄ H _{18.50} Cl ₃ Mn _{1.50} N _{3.50} O
M_r	440.58
Crystal system	monoclinic
Space group	$P2_1/n$
a [Å]	11.171(18)
b [Å]	13.703(2)
c [Å]	12.322(19)
α [°]	90
β [°]	96.474(3)
γ [°]	90
V [Å ³]	1874.2(5)
Z	4
Calculated density [mg m ⁻³]	1.561
Absorption coefficient [mm ⁻¹]	1.459
$F(000)$	894
Crystal size [mm ³]	0.32 × 0.28 × 0.22
θ Range for data collection [°]	2.23 to 26.39
Limiting indices, h, k, l	–13 to 13, –16 to 17, –15 to 11
Reflections collected	10360
Independent reflections [$R(\text{int})$]	3811(0.0339)
Goodness-of-fit on F^2	1.042
R_1/wR_2 [$I > 2\sigma(I)$]	0.0329/0.0777
R_1/wR_2 (all data)	0.0541/0.0874
Largest diff. peak [e Å ⁻³]	0.307/–0.372

atoms were generated geometrically. Molecular graphics were drawn with the program package Diamond.

CCDC-602624 contains the supplementary crystallographic data for **1**. These data can be obtained free of charge from The Cambridge Crystallographic Data Centre via www.ccdc.cam.ac.uk/data_request/cif.

DNA Binding Experiments: By using the electronic absorption spectral method, the relative bindings of the title complex to CT-DNA were studied in 5 mM Tris-HCl/NaCl buffer at pH 7.2. The solution of CT-DNA gave a ratio of UV absorbance at 260 and 280 nm, A_{260}/A_{280} , of 1.89, indicating that the DNA was sufficiently free of protein.^[41] The CT-DNA stock solutions of 5 mM were prepared in Tris-HCl/NaCl buffer, pH 7.2 (stored at 4 °C and used within 4 d after their preparation). The concentration of CT-DNA was determined from its absorption intensity at 260 nm with a molar extinction coefficient of $6600 \text{ M}^{-1} \text{ cm}^{-1}$.^[42]

By using the fluorescence spectral method, the relative bindings of the complex to CT-DNA were studied with an EB-bound CT-DNA solution in 5 mM Tris-HCl/NaCl buffer (pH 7.2). The excitation wavelength was fixed at 510 nm and the emission range was adjusted before measurements. Fluorescence intensities at 602 nm were measured at different complex concentrations.^[43]

DNA Cleavage Experiments: Cleavage of supercoiled pBR322 DNA by the title complex was studied by agarose gel electrophoresis. The reaction was carried out by mixing SC DNA (30 μM ; 4 μL), complex solution (2 μL), 50 mM Tris-HCl/NaCl buffer (pH 7.2; 4 μL) to yield a total volume of 10 μL . The sample was incubated at 37 °C, followed by the addition to 2 μL the loading buffer containing 0.25% Bromphenol Blue, 50% glycerol, 0.61% Tris, and the solution was finally loaded on 1% agarose gel containing $1.0 \mu\text{g mL}^{-1}$ ethidium bromide. Electrophoresis was carried out for 4 h at 70 V in Tris-boric-EDTA (TBE) buffer (45 mM Tris, 45 mM H_3BO_3 , 1 mM EDTA, pH 8.3). Bands were visualized by UV light and photographed. The extent of cleavage of the SC DNA was determined by measuring the intensities of the bands using the Gel Documentation System.^[44] Supercoiled plasmid DNA values were corrected by a factor of 1.22, based on an average literature estimate of lowered binding of ethidium.^[45]

Anaerobic Reaction: Deoxygenated solutions were prepared by four freeze–pump–thaw cycles. Before the final two cycles, the solutions were equilibrated with argon to aid in the deoxygenation process. The deoxygenated solutions were stored under an argon atmosphere prior to use. Reaction mixtures were prepared in the glove box by the addition of the appropriate volumes of stock solutions to the reaction tubes. The reactions were initiated by quick centrifugation, incubated at room temperature, and quenched by the addition to the loading buffer in the glove box. All other conditions were the same as those listed for the aerobic cleavage reactions.

DNA Cleavage Mechanism Experiments: These reactions were carried out by adding scavengers of 1 mM dimethyl sulfoxide (DMSO), 200 Unit mL^{-1} SOD, 0.1 M EDTA, and 25 mM L-histidine to SC DNA to separate samples. Cleavage was initiated by the addition of the complex and quenched with loading buffer (2 μL). Further analysis was carried out by using the standard method given above.

Enzymatic Re-Ligation: After incubation of pBR322 DNA with 300 mM **1** for 24 h at 37 °C, the cleavage product, that is, the linear form, was purified by using a DNA Gel Extraction Kit. The ligation reaction of the linearized plasmid was performed as follows: a mixture of T4 ligase (15 units; 3 μL), 10 \times ligation buffer (3 μL), 1 mM adenosine triphosphate (ATP; 1 μL), 50% (w/v) polyethylene glycol PEG4000 (3 μL), and the solution containing the DNA

cleavage fragment linearized by the binuclear manganese species (20 μL) were incubated for 72 h at 16 °C. Afterwards, the ligation products were electrophoresed, stained, and imaged.

Supporting Information (see also the footnote on the first page of this article): Electrospray mass spectra and isotope distribution patterns for **1**.

Acknowledgments

Financial support from the National Natural Science Foundation of China (grant no. 20771063), Tianjin Educational Committee Foundation (grant no. 20070606), and the PhD Science Foundation of Tianjin Normal University (grant no. 52LX28) are gratefully acknowledged.

- [1] D. S. Sigman, *Acc. Chem. Res.* **1986**, *19*, 180–186; D. S. Sigman, T. W. Bruice, A. Mazumder, C. L. Sutton, *Acc. Chem. Res.* **1993**, *26*, 98–104; D. S. Sigman, A. Mazumder, D. M. Perrin, *Chem. Rev.* **1993**, *93*, 2295–2316.
- [2] L. K. J. Boerner, J. M. Zaleski, *Curr. Opin. Chem. Biol.* **2005**, *9*, 135–144.
- [3] K. E. Erkkila, D. T. Odom, J. K. Barton, *Chem. Rev.* **1999**, *99*, 2777–2796.
- [4] H. T. Chifotides, K. R. Dunbar, *Acc. Chem. Res.* **2005**, *38*, 146–156.
- [5] W. K. Pogozelski, T. D. Tullius, *Chem. Rev.* **1998**, *98*, 1089–1107.
- [6] C. J. Burrows, J. G. Muller, *Chem. Rev.* **1998**, *98*, 1109–1151.
- [7] D. R. McMillin, K. M. McNett, *Chem. Rev.* **1998**, *98*, 1201–1219.
- [8] J. A. Cowan, *Curr. Opin. Chem. Biol.* **2001**, *5*, 634–642; E. L. Hegg, J. N. Burstyn, *Coord. Chem. Rev.* **1998**, *173*, 133–165; S. E. Wolkenberg, D. L. Boger, *Chem. Rev.* **2002**, *102*, 2477–2495; S. J. Franklin, *Curr. Opin. Chem. Biol.* **2001**, *5*, 201–208.
- [9] G. Pratviel, J. Bernadou, B. Meunier, *Angew. Chem. Int. Ed. Engl.* **1995**, *34*, 746–769.
- [10] J. Reedijk, *J. Inorg. Biochem.* **2001**, *86*, 89.
- [11] M. G. Alvarez, G. Alzueta, J. Borrás, B. Macías, A. Castiñeiras, *Inorg. Chem.* **2003**, *42*, 2992–2998.
- [12] A. Sreedhara, J. A. Cowan, *J. Biol. Inorg. Chem.* **2001**, *6*, 337–347; A. Radzicka, R. Wolfenden, *Science* **1995**, *267*, 90–93; K. M. Deck, T. A. Tseng, J. N. Burstyn, *Inorg. Chem.* **2002**, *41*, 669–677.
- [13] E. M. Boon, J. L. Kisko, J. K. Barton, *Method Enzymol.* **2002**, *353*, 506–522; C. L. Liu, M. Wang, T. Zhang, H. Sun, *Coord. Chem. Rev.* **2004**, *248*, 147–168.
- [14] J. Qian, J. L. Tian, W. Gu, S. Gao, X. Liu, S. P. Yan, J. Ribas, D. Z. Liao, P. Cheng, *Dalton Trans.* **2008**, 6948–6952.
- [15] H. D. Bian, W. Gu, J. Y. Xu, F. Bian, S. P. Yan, D. Z. Liao, Z. H. Jiang, P. Cheng, *Inorg. Chem.* **2003**, *42*, 4265–4267.
- [16] J. Qian, W. Gu, H. Liu, F. X. Gao, L. Feng, S. P. Yan, D. Z. Liao, P. Cheng, *Dalton Trans.* **2007**, 1060–1066.
- [17] D. D. Li, J. L. Tian, Y. Y. Kou, F. P. Huang, G. J. Chen, W. Gu, X. Liu, D. Z. Liao, P. Cheng, S. P. Yan, *Dalton Trans.* **2009**, 3574–3583.
- [18] Y. Y. Kou, J. L. Tian, D. D. Li, W. Gu, X. Liu, S. P. Yan, D. Z. Liao, P. Cheng, *Dalton Trans.* **2009**, 2374–2382.
- [19] I. Romero, M. N. Collomb, A. Deronzier, A. Llobet, E. Perret, J. Pécaut, L. L. Pape, J. M. Latour, *Eur. J. Inorg. Chem.* **2001**, 69–72.
- [20] J. F. Chai, H. P. Zhu, H. W. Roesky, Z. Yang, V. Jancik, R. H. Irmer, H. G. Schmidt, M. Noltemeyer, *Organometallics* **2004**, *23*, 5003–5006.
- [21] M. Dincă, A. F. Yu, J. R. Long, *J. Am. Chem. Soc.* **2006**, *128*, 8904–8913.
- [22] K. F. Hsu, S. L. Wang, *Inorg. Chem.* **2000**, *39*, 1773–1778.

- [23] X. M. Lu, P. Z. Li, X. T. Wang, S. Gao, X. J. Wang, L. Zhou, C. S. Liu, X. N. Sui, J. H. Feng, Y. H. Deng, Q. H. Jin, J. Liu, N. Liu, J. P. Lian, *Polyhedron* **2008**, *27*, 3669–3673.
- [24] C. V. Kumar, J. K. Barton, N. J. Turio, *J. Am. Chem. Soc.* **1985**, *107*, 5518–5523.
- [25] E. Y. Stemp, L. Weiner, I. Sagi, R. A. Yellin, A. Shanzer, *J. Inorg. Biochem.* **2004**, *98*, 1750–1756.
- [26] M. S. Deshpande, A. A. Kumbhar, A. S. Kumbhar, *Inorg. Chem.* **2007**, *46*, 5450–5452.
- [27] R. M. Hartshorn, J. K. Barton, *J. Am. Chem. Soc.* **1992**, *114*, 5919–5925.
- [28] Q. X. Zhen, B. H. Ye, Q. L. Zhang, J. G. Liu, H. Li, L. N. Ji, L. Wang, *J. Inorg. Biochem.* **1999**, *76*, 47–53.
- [29] A. Wolfe, G. H. Shimer, T. Meehan, *Biochemistry* **1987**, *26*, 6392–6396.
- [30] K. G. Strothkamp, R. E. Strothkamp, *J. Chem. Educ.* **1994**, *71*, 77–79.
- [31] J. B. Le Pecq, C. Paoletti, *J. Mol. Biol.* **1967**, *27*, 87–106.
- [32] J. R. Lakowicz, G. Weber, *Biochemistry* **1973**, *12*, 4161–4170; H. Li, X. Y. Le, D. W. Pang, H. Deng, Z. H. Xu, Z. H. Lin, *J. Inorg. Biochem.* **2005**, *99*, 2240–2247.
- [33] J. Bermadou, G. Pratviel, F. Bennis, M. Girardet, B. Meunier, *Biochemistry* **1989**, *28*, 7268–7275.
- [34] M. Cory, D. D. McKee, J. Kagan, D. W. Henry, J. A. Miller, *J. Am. Chem. Soc.* **1985**, *107*, 2528–2536.
- [35] J. J. Li, R. Geyer, W. Tan, *Prog. Nucleic Acid Res. Mol. Biol.* **2000**, *28*, e52.
- [36] O. I. Aruoma, B. Halliwell, M. Dizdaroğlu, *J. Biol. Chem.* **1989**, *264*, 13024–13028.
- [37] K. Yamamoto, S. Kawanishi, *J. Biol. Chem.* **1989**, *264*, 15435–15440.
- [38] R. Nilsson, P. B. Merkel, D. R. Keams, *Photochem. Photobiol.* **1972**, *16*, 117–124.
- [39] K. B. Jensen, C. J. McKenzie, O. Simonsen, H. Toftlund, A. Hazell, *Inorg. Chim. Acta* **1997**, *257*, 163–172.
- [40] *SHELXTL 6.10*, Bruker Analytical Instrumentation, Madison, WI, USA, **2000**.
- [41] J. Marmur, *J. Mol. Biol.* **1961**, *3*, 208–218.
- [42] M. E. Reichmann, S. A. Rice, C. A. Thomas, P. Doty, *J. Am. Chem. Soc.* **1954**, *76*, 3047–3053.
- [43] B. C. Baguley, M. LeBret, *Biochemistry* **1984**, *23*, 937–943; J. R. Lakowicz, G. Weber, *Biochemistry* **1973**, *12*, 4161–4170.
- [44] J. Bermadou, G. Pratviel, F. Bennis, M. Girardet, B. Meunier, *Biochemistry* **1989**, *28*, 7268–7275.
- [45] R. P. Hertzberg, P. B. Dervan, *J. Am. Chem. Soc.* **1982**, *104*, 313–315.

Received: December 21, 2009

Published Online: May 27, 2010

Unexpected Oxidative Dimerisations of a Cyclopentadienyl-Phosphane – Formation of Unprecedented, Structurally Remarkable Phosphacyclic Compounds

Crispin Lichtenberg,^[a] Michael Elffertding,^[a] and Jörg Sundermeyer*^[a]

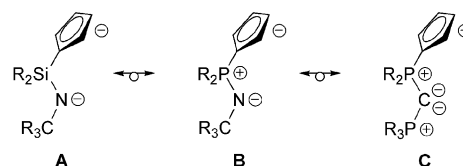
Keywords: Phosphorus heterocycles / Phosphanes / Spiro compounds / Isolobal relationship / Oxidative dimerisation

The reactions of $\text{Me}_2\text{PCp}^\#$ (**1**) ($\text{Cp}^\# = \text{C}_5\text{HMe}_4$) with $\text{Ph}_3\text{PCH}_2\text{X}^+ \text{X}^-$ ($\text{X} = \text{Cl}, \text{Br}, \text{I}$) and diiodomethane as potential electrophiles have been investigated. Unexpectedly, in all four cases unprecedented oxidative dimerisations of the cyclopentadienylphosphane **1** have been observed. In the reactions with the phosphonium salts, an ionic group 15 analogue of octamethyl-tetrahydro-*s*-indacene with different counterions X^- has been obtained (**5–7**) as a result of X^+ transfer

and H^+ elimination. In the reaction of **1** with diiodomethane a fourfold anellated, partially unsaturated, heterocyclic compound **9** exhibiting two spiro carbon centres, which are directly linked, was formed, presumably as a result of iodine radical transfer. Both of the novel phosphorus heterocycles have been characterised by means of single crystal XRD analysis.

Introduction

Constrained geometry complexes (CGCs) have been established as a class of catalysts for olefin polymerisation, since they were first described in the early 1990s.^[1] The pronounced characteristic of these catalytic systems is their ability to incorporate higher olefins into a polymer chain.^[2] In this respect they were found to be superior to ansa-metallocenes, which represent a closely related class of polymerisation catalysts. Dianions derived from cyclopentadienylsilylamines are the archetypes of ligands for the synthesis of CGCs (**A**, Scheme 1).^[3] These are isoelectronic (and isolobal) to monoanionic ligands of type **B** (Scheme 1), which have therefore been in the focus of our research interest. We recently reported a convenient synthetic approach to a variety of *P*-amino-cyclopentadienylidene-phosphoranes,^[4] which are protonated forms of type **B** ligands, and their use for the complexation of lanthanides.^[5] The series of isoelectronic ligands for the synthesis of CGCs can be extended to monoanions **C** (Scheme 1). The protonated forms of type **C** ligands can formally be described as cyclopentadienyl-carbodiphosphoranes, a class of compounds which is unknown to the literature and which we set out to synthesise. In this paper we would like to describe an unusual unprecedented reaction pattern of a cyclopentadienylphosphane which we observed during our studies concerning a possible access to type **C** ligands.



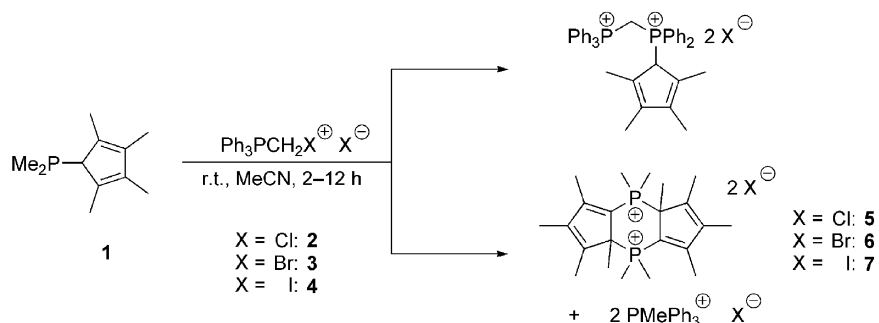
Scheme 1. Three examples of isoelectronic ligands for the synthesis of constrained geometry complexes; R = alkyl, aryl.

Results and Discussion

Formation of a 4,8-Diphospha-tetrahydro-*s*-indacene

Hexaphenylcarbodiphosphorane^[6] is the most investigated representative of the class of parent carbodiphosphoranes $\text{R}_3\text{P}-\text{C}-\text{PR}_3$. In analogy to a well established synthetic route to this molecule^[7] the reaction of a cyclopentadienylphosphane with halomethyltriphenyl-phosphonium salts (**2–4**) as electrophiles was studied. Unexpectedly, the outcome of this reaction was not an overall nucleophilic displacement of a halogen substituent by a phosphane moiety (upper part, Scheme 2), but an oxidative dimerisation of the cyclopentadienylphosphane **1** (lower part, Scheme 2) yielding the products **5–7**. The dication of the bisphosphonium salts **5–7** exhibits *Ci*-symmetry leading to isochrony of six pairs of methyl groups in the ^1H NMR spectra and one pair of phosphorus atoms in the ^{31}P NMR spectra. The low solubility of the dimers **5–7** in common solvents did not allow for interpretable ^{13}C NMR spectra to be obtained. The molecular structure of the dication being part of the substances discussed here was unambiguously established via X-ray analysis of **7** (Figure 1). This dication is a group

[a] Fachbereich Chemie der Philipps-Universität Marburg, Hans-Meerwein-Str., 35032 Marburg, Germany
Fax: +49-6421 2828917
E-mail: jsu@staff.uni-marburg.de



Scheme 2. Planned (upper part) and observed (lower part) outcome of the reaction of cyclopentadienylphosphane **1** with halomethyltriphenylphosphonium salts **2–4**; $\text{PMePh}_3^+ \text{X}^-$ was isolated in the case of X = I as a stoichiometric side product.

15 derivative of a molecule with a tetrahydro-*s*-indacene core and is isolobal to the known group 14 parent compound (**D**, Scheme 3).^[8a] A group 16 derivative has also

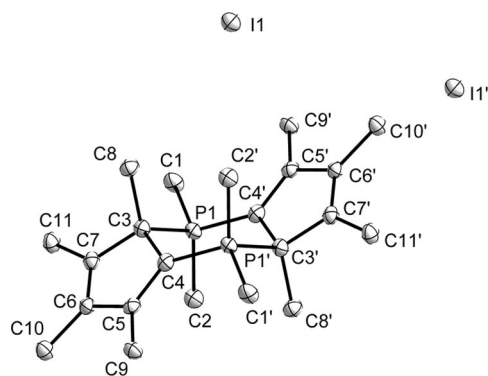
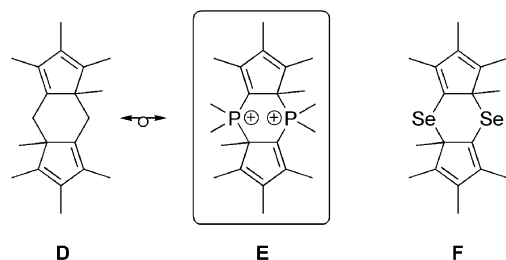


Figure 1. Molecular structure of **7**; the thermal ellipsoids are drawn at the 50% probability level. Hydrogen atoms are omitted for clarity. Two molecules of DMSO per formula unit are present in the crystal structure; they do not interact with **7** and are therefore not shown. Selected bond lengths [Å], distances [Å], bond angles [°] and dihedral angles [°]: P1–C1 1.786(3), P1–C2 1.784(3), P1–C3 1.843(4), P1–C4' 1.768(3), C3–C4 1.537(4), C4–C5 1.362(4), C5–C6 1.469(4), C6–C7 1.349(4), C7–C3 1.507(3), plane(C4, C5, C6, C7)–C3 0.000(3), C1–P1–C2 108.2(1), C1–P1–C3 108.5(1), C1–P1–C4' 112.7(1), C2–P1–C3 109.2(1), C2–P1–C4' 112.5(1), C3–P1–C4' 105.6(1), P1–C3–C4 106.3(2), C3–C4–P1' 122.0(2), plane(C3, C4, C5, C6, C7)–plane(C3', C4', C5', C6', C7') 0.0(1).



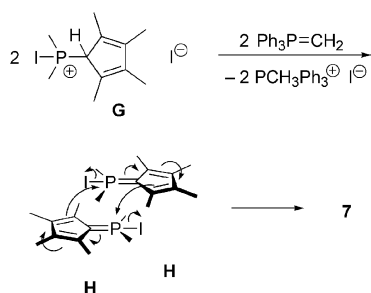
Scheme 3. Isolobal relationship between 1,2,3,3a,5,6,7,7a-octa-methyl-3a,4,7a,8-tetrahydro-*s*-indacene (**D**, left) and a group 15 analogue (**E**, middle), which the molecular structures have been established by X-ray analyses. A group 16 analogue (**F**, right) has also been characterised via X-ray analysis.

been described (**F**, Scheme 3).^[8b] Being only the second example of such a group 15 derivative^[9] and the first one to be characterised via X-ray analysis it represents the missing link between substances of type **D** and type **F**.

In the molecular structure of **7** the six-membered heterocycle is found to be in a slightly distorted chair conformation. Deviations of bond angles [105.6(1)–122.0(2)°] from an idealised six-membered carbon ring can be ascribed to the incorporation of two heteroatoms and two sp^2 -hybridised carbon atoms into the cycle as well as to the annellation of two pentacycles. These annellated cyclopentadienyl rings are parallel, indicated by an interplanar (C_5)–(C_5') angle of 0.0(1)°, and exhibit two distinct double bonds. They are essentially planar as the distance between the best plane of four sp^2 carbon atoms and the sp^3 carbon atom (C3) is as small as 0.000(3) Å. The P–C bonds in **7** range from 1.768(3) to 1.843(4) Å, which points at the differences of the involved carbon atoms with respect to hybridisation and incorporation into a ring system. The characteristics described above are in good agreement with those found in type **D** and **F** compounds (Scheme 3) with one exception. This is that deviations of bond angles in the six-membered ring from an idealised carbon hexacycle are much smaller in the case of **D** as there are no heteroatoms involved.

Mechanistic aspects of the reactions leading to the formation of the bisphosphonium salts **5–7**, which are the main products in all three cases, shall briefly be discussed. Three different kinds of elementary reactions are undergone in each of these syntheses. (i) Selectivity and yield of the reactions increase with the atomic number of the halogen atoms in the reactants **2–4**. Having in mind that based on the HSAB principle phosphanes represent soft bases and the softness of halogen cations increases with their atomic number,^[10] an X^+ abstraction (X = Cl, Br, I) from the halo-methyltriphenylphosphonium salts **2–4** is a plausible initiating reaction step. Accordingly, a *P*-halo-cyclopentadienylphosphonium salt (**G**, Scheme 4) and triphenylmethylenephosphorane, a non charged leaving group, are formed as intermediates. An elementary reaction of this kind should be undergone two times per formula unit, as both phosphorus atoms in the products **5–7** exhibit a formal oxidation state of +V. When the reaction leading to product **7** (X = I) was carried out at lower temperatures, indirect

spectroscopic evidence for the appearance of triphenylmethylenephosphorane, the plausible intermediate formed from oxidant **4** upon loss of I^+ and I^- , could be found (for details see Exp. Sect.). Attempts to isolate supposed intermediate **G** in pure form proved to be unsuccessful. This was ascribed to the fact that isomers of **G** can be formed via [1,5]-sigmatropic shifts of the proton bound to the cyclopentadienyl ring and to the fact that this CH-acid is prone to be deprotonated by the base triphenylmethylenephosphorane present. Attempts to independently synthesise **G** by reaction of phosphane **1** with X^+ donors such as iodine, *N*-bromosuccinimide or hexachloroethane at low reaction temperatures proved to be unsuccessful as they are less selective, probably due to direct halogenation at the cyclopentadienyl substituent. (ii) From the molecular structure of the products it can easily be deduced that the proton which was bound to the cyclopentadienyl-ring in reactant **1** has been abstracted in the course of the reaction. Triphenylmethylenephosphorane, the formation and indirect detection of which is described in (i), can act as a Brønsted base.^[11] The corresponding protonated form, the phosphonium salt $\text{MePPh}_3^+ \text{I}^-$, was isolated and characterised in the case of **7**. Overall, this acid-base reaction must be undergone twice and in agreement with these stoichiometric considerations, two equivalents of $\text{MePPh}_3^+ \text{I}^-$ were isolated. With intermediate **G** acting as the Brønsted acid **H** would be generated as an intermediate (Scheme 4). (iii) In order to achieve the formation of the products **5–7**, a six-membered heterocycle must be generated. A nucleophilic displacement of the halogen atom in assumed intermediate **H** is a plausible reaction step, which must be undergone twice. This is equivalent with a dimerisation of **H**.^[12] So the oxidative dimerisation of **1** leading to the formation of the bisphosphonium salts **5–7** is a complex sequence of reactions including at least six elementary reactions of three different kinds. A plausible reaction mechanism, which is in agreement with (i)–(iii), is shown in Scheme 4. The key reaction step is the dimerisation of the proposed intermediate **H**, which does not necessarily have to proceed in a concerted fashion (as depicted in Scheme 4 for space-saving reasons) but could also follow a stepwise mechanism.



Scheme 4. Proposed mechanism for the oxidative dimerisation of **1** yielding the bisphosphonium salts **5–7** (shown for **7**). The dimerisation of supposed intermediate **H**, formed by deprotonation of intermediate **G**, is the key step in this mechanism.^[12]

Evidence of $\text{Br}\cdots\text{Br}^-$ Contacts in $\text{Ph}_3\text{PCH}_2\text{Br}^+ \text{Br}^-$ (**3**)

The abstraction of an iodine cation from the phosphonium salt **4** as an initiating reaction step in the formation of the dimer **7** is in accordance with the fact that **4** exhibits an electrophilic iodine atom and $\text{I}\cdots\text{I}^-$ contacts in solid state.^[13] The tendency for such symmetric halogen \cdots halogen $^-$ contacts to be formed decreases with the atomic number of the halogen atoms involved.^[14] In order to find stronger evidence of an X^+ abstraction as the initial reaction step in the dimerisations described here, the phosphonium bromide **3** was characterised by means of X-ray analysis (Figure 2). Indeed, this compound also exhibits $\text{Br}\cdots\text{Br}$ contacts in solid state indicated by a $\text{Br1}-\text{Br2}$ distance of 3.568(1) Å, which is 4% below the doubled value of the van der Waals radius of bromine.^[15] The $\text{Br2}-\text{Br1}-\text{C1}$ unit exhibits a bond angle of 175.4(1)° revealing an interaction of nucleophilic bromide Br2 with the electrophile, the $\sigma^*_{\text{C1}-\text{Br1}}$ orbital (LUMO), respectively. Accordingly, the $\text{C1}-\text{Br1}$ bond is slightly lengthened.^[16] A $\text{C}-\text{H}\cdots\text{Br}^-$ contact is found in the crystal structure of the phosphonium bromide **3** as an additional secondary interaction.

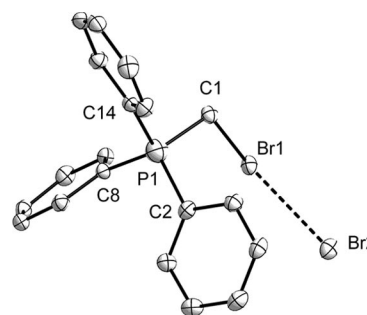
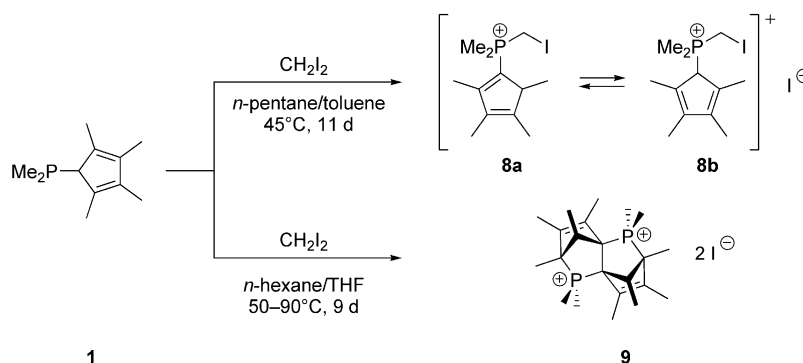


Figure 2. Molecular structure of $\text{Ph}_3\text{PCH}_2\text{Br}^+ \text{Br}^-$ (**3**); the thermal ellipsoids are drawn at the 50% probability level. Hydrogen atoms are omitted for clarity. Selected bond lengths [Å] and angles [°]: $\text{Br1}-\text{Br2}$ 3.568(1), $\text{Br1}-\text{C1}$ 1.948(2), $\text{P1}-\text{C1}$ 1.804(2), $\text{P1}-\text{C2}$ 1.792(4), $\text{P1}-\text{C8}$ 1.787(2), $\text{P1}-\text{C14}$ 1.785(2), $\text{Br2}-\text{Br1}-\text{C1}$ 175.4(1).

The $\text{Br}\cdots\text{Br}^-$ contact in **3** provides further evidence that sterically hindered halomethylphosphonium cations are susceptible to a nucleophilic attack at the part of the $\sigma^*_{\text{C-X}}$ orbital which is located at the halogen and not at the carbon atom explaining why **3** acts as halogen $^+$ and not carbenium transfer agent.

Formation of a Fourfold Anellated, Phosphacyclic Dispiro Compound

Driven by the initial motivation of our studies to find a synthetic approach to type **C** ligands (Scheme 1), the (cyclopentadienyl)(iodomethyl)phosphonium iodide **8** was prepared as a potential target for *P*-nucleophiles. This synthesis was achieved by reaction of cyclopentadienylphosphane **1** with diiodomethane (see upper part of Scheme 5). The desired product was obtained as a mixture of the isomers **8a** and **8b** in a 58:42 ratio. When the phosphonium iodide **8** is solvated in DMSO this ratio increases up to 67:33 in favour of the isomer **8a** over a period of one day, after



Scheme 5. Nucleophilic substitution reaction (upper part) and oxidative dimerisation (lower part) of cyclopentadienylphosphane **1**.

which this ratio was found to be constant. The structures of these substances were established by means of 2D NMR measurements (COSY, HMQC, HMBC) in addition to the usual 1D NMR experiments.

Under only slightly different reaction conditions (*n*-hexane/THF, 50–90 °C, 9 d) **9** was obtained as a completely unexpected side product of this reaction (lower part, Scheme 5).

In this case, diiodomethane does not act as an electrophile but as an iodine radical donor. Whereas variations of the ratio of tetrahydrofuran in the solvent mixture did not have a significant impact on the outcome of the experiment, an elevation of the reaction temperature and reaction time led to an increase in the selectivity towards **9**. Under optimised reaction conditions the formation of the heterocyclic compound **9** was achieved with a selectivity of 30%. **8a** and **8b** were also observed as well as a fourth substance with a composition $[\text{CH}_2(\text{PMe}_2\text{Cp}^\#)_2]\text{I}_2$ ($\text{Cp}^\# = \text{C}_5\text{HMe}_4$) tentatively assigned on the basis of high resolution ESI mass spectra. After several crystallisations, small amounts of the phosphonium iodide **9** could be obtained in an analytically pure form. Six pairs of methyl groups, five pairs of endocyclic carbon atoms and the two phosphorus atoms of this substance are isochronal. This indicates that the dication of the bisphosphonium salt **9** shows C_2 -symmetry in solution. The molecular structure of **9** was indubitably established by X-ray analysis (Figure 3). In solid state **9** exhibits non-crystallographic C_1 symmetry. Like the phosphonium salts **5–7**, it originates from an oxidative dimerisation of the cyclopentadienylphosphane **1**. The unexpected product **9** is a fourfold anellated, partially unsaturated, heterocyclic compound. Two spiro centres, which are directly linked, are incorporated into this cyclic framework. The combination of these features makes this bisphosphonium iodide unique in its structural characteristics. They also lead to a high degree of ring strain within the dication, which is the dominating property of this molecule. This leads to strong deviations of most of the bond lengths and angles from values which would be expected for unstrained systems. The most remarkable examples of this are found around the two spiro centres, C1 and C12. The C–C bond linking these atoms is stretched to 1.626(4) Å. The bond angles at both spiro centers range from 99.5(1) to 124.4(1)°

covering a spectrum of about 25°. The highest values of these bond angles around the sp^3 carbon atoms C1 and C12 even exceed 120° which are ideally expected for bond angles with sp^2 carbon atoms in the central position. Structural elements which are further apart from the two spiro centres are still affected by the ring strain, but to a lesser extent. The endocyclic bonds in the dication of **9** (apart from C1–C12, which was discussed above) are with few exceptions slightly stretched. In the crystal structure of the bisphosphonium iodide **9** there is also a secondary binding interac-

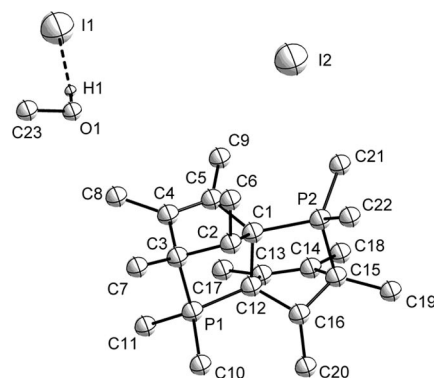
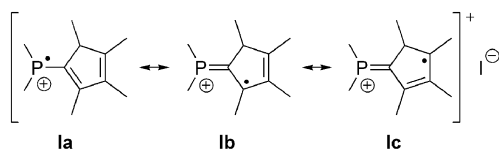


Figure 3. Molecular structure of the bisphosphonium iodide **9**; thermal ellipsoids are shown at the 50% probability level. Hydrogen atoms except for H1 are omitted for clarity. Two molecules of methanol are incorporated into the crystal structure of **9**. One of these is disordered, does not interact with **9** and is therefore not shown. Selected bond lengths [Å] and angles [°]: C1–C12 1.626(4), P1–C3 1.835(3), P1–C10 1.783(3), P1–C11 1.783(3), P1–C12 1.832(2), P2–C1 1.842(2), P2–C15 1.837(3), P2–C21 1.784(2), P2–C22 1.785(2), C1–C2 1.562(2), C2–C3 1.557(3), C3–C4 1.528(3), C4–C5 1.338(2), C5–C1 1.539(3), C12–C13 1.537(2), C13–C14 1.337(3), C14–C15 1.525(3), C15–C16 1.552(3), C16–C12 1.549(3), H1–I1 2.623(41), P1–C12–C1 100.2(1), P1–C12–C13 124.6(1), P1–C12–C16 116.5(1), C1–C12–C13 106.9(2), C1–C12–C16 106.0(2), P2–C1–C2 117.7(1), P2–C1–C5 124.4(1), P2–C1–C12 99.5(1), C2–C1–C12 105.3(3), C5–C1–C12 107.6(2), C3–P1–C10 109.1(1), C3–P1–C11 113.9(1), C3–P1–C12 95.7(1), C10–P1–C11 107.5(1), C10–P1–C12 113.5(1), C11–P1–C12 116.8(1), C1–P2–C15 95.6(1), C1–P2–C21 118.6(1), C1–P2–C22 112.6(1), C15–P2–C21 111.0(1), C15–P2–C22 112.4(1), C21–P2–C22 106.5(1), C1–C2–C3 95.8(2), C2–C3–C4 100.6(2), C3–C4–C5 109.8(2), C4–C5–C1 107.3(2), C5–C1–C2 100.7(2), C12–C13–C14 107.2(2), C13–C14–C15 109.5(2), C14–C15–C16 101.3(2), C15–C16–C12 95.9(2), C16–C12–C13 101.2(2), O1–H1–I1 179.1(35).

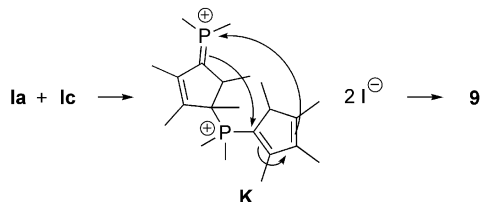
tion. This is an $\text{H}\cdots\text{I}^-$ contact, in which the hydrogen atom belongs to the hydroxy group of a solvent molecule (MeOH). The hydrogen bond $\text{H1}\cdots\text{I1}$ exhibits a length of 2.623(41) Å, which is more than 17% below the sum of the van der Waals radii^[15] and an $\text{O1}\cdots\text{H1}\cdots\text{I1}$ bond angle of 179.1(35)°.

Mechanistic considerations concerning the formation of the bisphosphonium iodide **9** shall be discussed in brief. The chemical formula of the product, $(\text{PMe}_2\text{Cp}^\#)_2\text{I}$, indicates that overall an iodine radical addition to the cyclopentadienyl-phosphane **1** followed by a dimerisation of the resulting radical intermediate has taken place. Such an iodine radical transfer to the cyclopentadienylphosphane **1** would result in the formation of intermediate **I** with resonance formulae **Ia**, **Ib** and **Ic** shown in Scheme 6. Product **9** is a dimer of **I**.



Scheme 6. Resonance structures of supposed intermediate **Ia**, **Ib** and **Ic** (formed probably as P–I contact ion pairs) as result of an iodine radical interaction with the cyclopentadienylphosphane **1**.

It is important to note that **Ia** represents an electrophilic radical, whereas **Ib** and **Ic** are nucleophilic radicals. Dimerisation of radical **Ia** with sterically less hindered **Ic** would generate **K** as an intermediate (Scheme 7). Two intramolecular P–C bond formations in transient **K**, probably via a polar mechanism, would lead to isolated product **9**.



Scheme 7. Proposed stepwise mechanism for the formation of **9** via intermediate **K**, which would be formed by dimerisation of the radical intermediate **I**.

Conclusions

Four cases of unexpected oxidative dimerisations of the cyclopentadienylphosphane $\text{Me}_2\text{PCp}^\#$ (**1**) ($\text{Cp}^\# = \text{C}_5\text{HMe}_4$) have been reported. In sharp contrast to known reactions of $\text{Ph}_3\text{PCH}_2\text{X}^+ \text{X}^-$ ($\text{X} = \text{Cl}, \text{Br}, \text{I}$) with PPh_3 , the former phosphonium salts act as halogen⁺ (not carbenium ion) transfer agents towards phosphane **1**. In a second reaction step the resulting leaving group triphenylmethylenephosphorane acts as a Brønsted base leading to a formal H^+ by I^+ exchange. A group-15 analogue of octamethyl-tetrahydro-*s*-indacene with X^- counterions is the final reaction product in each of these reactions. The first example of an X-ray analysis of such a heterocyclic compound is reported.

Mechanistic aspects of these reactions have been investigated and an X^+ abstraction from the electrophile and oxidising agent by cyclopentadienylphosphane **1** has been established as the initiating reaction step. In the fourth example of an oxidative dimerisation of cyclopentadienylphosphane **1** diiodomethane is acting as oxidising agent, presumably via iodine radical instead of a carbon electrophile transfer leading to expected **8a,b**. The unexpected product **9** of this reaction has been characterised by X-ray analysis and exhibits highly remarkable structural features. It is a fourfold anellated, partially unsaturated, heterocyclic compound with two spiro carbon centres, which are directly linked to each other.

Experimental Section

General: All experimental procedures were carried out in an atmosphere of purified argon or nitrogen using standard Schlenk techniques or a glovebox. The solvents used were dried and degassed according to standard protocols. Chemicals were purchased from Alfa Aesar, Aldrich or Merck and used without further purification. PClMe_2 ,^[17] $\text{LiCp}^\#$ ^[18] ($\text{Cp}^\# = \text{C}_5\text{HMe}_4$), $\text{PPh}_3\text{CH}_2\text{X}^+ \text{X}^-$ ($\text{X} = \text{Cl}$,^[19] Br ,^[20] I ^[21]) and PPh_3CH_2 ^[22] were synthesised according to literature procedures. NMR measurements were performed using a Bruker AVANCE 300, DRX 400 or DRX 500 spectrometer at 25 °C. Elemental analyses were carried out at the Analytical Laboratory of the Department of Chemistry, Philipps University of Marburg. ESI mass spectra were recorded using a Finnigan TSQ 700 instrument.

$\text{PMe}_2\text{Cp}^\#$ (1**): Method A:** A solution of Me_2PCl (364 mg, 3.77 mmol) in toluene (2.25 mL) was added to a suspension of $\text{LiCp}^\#$ (507 mg, 3.96 mmol) in *n*-pentane/diethyl ether (1:1) (24 mL) at 0 °C. The reaction mixture was warmed up to room temperature over 17 h, after which the volume of the liquid phase was reduced to half in vacuo at 0 °C. The solid was separated by filtration and washed with *n*-pentane (3×8 mL). The colourless filtrate was used as a source of the phosphane **1** in one of the following reactions. **Method B:** See method A, but neat *n*-pentane was used as a solvent. Moreover, the volume of the liquid phase was not reduced to half in vacuo prior to filtration. **Method C:** See method A, but *n*-hexane/tetrahydrofuran (2:1) was used as a solvent mixture. –78 °C was chosen as the initial reaction temperature instead of 0 °C.

Isolation of $\text{PMe}_2\text{Cp}^\#$ (1**):**^[23] **1** was prepared according to method A. Removal of all volatiles under reduced pressure at 0 °C yielded a colourless oil which was then dried in vacuo; yield 557 mg (81 %). **1** was isolated as a mixture of three isomers.

Dimethyl(2,3,4,5-tetramethylcyclopenta-2,4-dienyl)phosphane (1a**, 75 %):** ¹H NMR (300.1 MHz, C_6D_6): $\delta = 0.84$ (d, $^2J_{\text{HP}} = 5.0$ Hz, 6 H, PMe_2), 1.73 (s, 6 H, 3,4- CpMe_2), 1.93 (s, 6 H, 2,5- CpMe_2), 2.80 (br. s, 1 H, 1- CpH) ppm. ¹³C NMR (75.5 MHz, C_6D_6): $\delta = 9.5$ (d, $^1J_{\text{CP}} = 19.4$ Hz, PMe_2), 11.2 (s, 3,4- CpMe_2), 14.3 (d, $^3J_{\text{CP}} = 8.3$ Hz, 2,5- CpMe_2), 57.9 (d, $^1J_{\text{CP}} = 22.7$ Hz, 1- Cp), 134.1 (d, $^2J_{\text{CP}} = 2.3$ Hz, 2,5- Cp), 136.2 (d, $^3J_{\text{CP}} = 2.7$ Hz, 3,4- Cp) ppm. ³¹P NMR (121.5 MHz, C_6D_6): $\delta = -37.1$ ppm.

Dimethyl(2,3,4,5-tetramethylcyclopenta-1,3-dienyl)phosphane (1b**, 15 %):** ¹H NMR (300.1 MHz, C_6D_6): $\delta = 1.08$ (d, $^3J_{\text{HH}} = 7.6$ Hz, 3 H, 5- CpMe), 1.18 (d, $^2J_{\text{HP}} = 3.6$ Hz, 3 H, $\text{PMe}^{1/2}$), 1.19 (d, $^2J_{\text{HP}} = 3.5$ Hz, 3 H, $\text{PMe}^{2/1}$), 1.65 (s, 3 H, 3- CpMe), 1.73 (3 H, 4- CpMe , overlapped by the resonance due to 3,4- CpMe_2 of **1a**), 2.09 (s, 3 H,

2-CpMe) 2.80 (1 H, 5-CpH, overlapped by the resonance due to 1-CpH of **1a**) ppm. ^{13}C NMR (75 MHz, C_6D_6): δ = 11.0 (s, 3-CpMe), 11.0 (s, 4-CpMe), 13.4 (d, $^1J_{\text{CP}}$ = 26.7 Hz, PMe $^{1/2}$), 13.5 (d, $^1J_{\text{CP}}$ = 27.7 Hz, PMe $^{2/1}$), 13.9 (d, $^3J_{\text{CP}}$ = 5.9 Hz, 2-CpMe), 15.8 (d, $^3J_{\text{CP}}$ = 1.5 Hz, 5-CpMe), 52.2 (d, $^2J_{\text{CP}}$ = 4.3 Hz, 5-Cp) ppm. Resonances arising from four C atoms being part of the five-membered ring could not be detected due to the low ratio of this isomer. ^{31}P NMR (121.5 MHz, C_6D_6): δ = -67.3 ppm.

Dimethyl(1,2,3,4-tetramethylcyclopenta-2,4-dienyl)phosphane (1c, 10%): ^1H NMR (300.1 MHz, C_6D_6): δ = 0.50 (d, $^2J_{\text{HP}}$ = 4.5 Hz, 3 H, PMe $^{1/2}$), 0.84 (d, $^2J_{\text{HP}}$ = 4.9 Hz, 3 H, PMe $^{2/1}$), 1.23 (d, $^3J_{\text{HP}}$ = 14.6 Hz, 3 H, 1-CpMe), 1.68 (s, 3 H, 3-CpMe), 1.82 (s, 3 H, 2-CpMe), 1.86 (s, 3 H, 4-CpMe), 5.77 (br. s, 1 H, 5-CpH) ppm. ^{13}C NMR (75.5 MHz, C_6D_6): δ = 8.5 (d, $^1J_{\text{CP}}$ = 18.1 Hz, PMe $^{1/2}$), 10.9 (s, 2-CpMe, partially overlapped by the resonances due to 3-CpMe and 4-CpMe of **1b**), 11.3 (d, $^1J_{\text{CP}}$ = 19.8 Hz, PMe $^{2/1}$, partially overlapped by 3,4-CpMe $_2$ von **1a**), 13.8 (s, 4-CpMe, partially overlapped by the resonance due to 2-CpMe of **1b**), 17.2 (d, $^2J_{\text{CP}}$ = 19.9 Hz, 1-CpMe) 53.9 (d, $^1J_{\text{CP}}$ = 17.8 Hz, 1-Cp) 132.0 (d, $^2J_{\text{CP}}$ = 3.1 Hz, 5-Cp) ppm. Resonances due to four C atoms of **1c** could not be detected due to the low ratio of this isomer. ^{31}P NMR (121.5 MHz, C_6D_6): δ = -25.9 ppm.

[PMe $_2$ (C $_5$ Me $_4$) $_2$ X $_2$ (5, X = Cl; 6, X = Br; 7, X = I): A solution of PMe $_2$ Cp $^\#$ (**1**), was prepared according to method A. The solvent was removed in vacuo at 0 °C to give a colourless oil, which was dissolved in acetonitrile (15 mL) and slowly added to a suspension of Ph $_3$ PCH $_2$ X $^+$ X $^-$ (X = Cl: 1.05 g, 3.02 mmol; X = Br: 1.32 g, 3.03 mmol; X = I: 1.60 g, 3.02 mmol) in acetonitrile (20 mL). The reaction mixture was allowed to stir for an appropriate time span (X = Cl: 12 h, X = Br, I: 2 h). After that the white solid was filtered off, washed with acetonitrile (3 \times 4 mL) and diethyl ether (3 \times 4 mL) and dried in vacuo.

5·2 MeCN (X = Cl): Yield 413 mg (53%), ESI-MS: exact mass calcd. for C $_{22}$ H $_{35}$ P $_2^{2+}$: m/z = 361.2209, found m/z (%) = 361.2215(9) [(M - 2 Cl $^-$ - H $^+$) $^+$]. C $_{22}$ H $_{36}$ P $_2^{2+}$: m/z = 181.1141, found m/z (%) = 181.1140 (100) [(M - 2 Cl $^-$) $^{2+}$]. C $_{26}$ H $_{42}$ Cl $_2$ N $_2$ P $_2$ (515.48): calcd. C 60.58, H 8.21, N 5.43, found C 60.66, H 8.42, N 5.18. ^1H NMR (300.1 MHz, [D $_6$]DMSO): δ = 1.52 (d, $^2J_{\text{HP}}$ = 17.6 Hz, 3 H, PMe), 1.74 (d, $^2J_{\text{HP}}$ = 13.6 Hz, 3 H, PMe), 1.95 [d, $^{4/5}J_{\text{HP}}$ = 1.7 Hz, 3 H, C(sp 2)Me], 2.13 [s, 3 H, C(sp 2)Me], 2.39 [s, 3 H, C(sp 2)Me], 2.58 [d, $^3J_{\text{HP}}$ = 13.9 Hz, 3 H, C(sp 3)Me] ppm. ^{31}P NMR (121.5 MHz, [D $_6$]DMSO): δ = 26.7 ppm.

6·2 MeCN (X = Br): Yield 494 mg (54%), ESI-MS: exact mass calcd. for C $_{22}$ H $_{35}$ P $_2^{2+}$: m/z = 361.2209, found m/z (%) = 361.2218 (5) [(M - 2 Br $^-$ - H $^+$) $^+$]. C $_{22}$ H $_{36}$ P $_2^{2+}$: m/z = 181.1141, found m/z (%) = 181.1140 (100) [(M - 2 Br $^-$) $^{2+}$]. C $_{26}$ H $_{42}$ Br $_2$ N $_2$ P $_2$ (604.38): calcd. C 51.67, H 7.00, N 4.64, found C 51.87, H 6.65, N 5.03. ^1H NMR (300.1 MHz, [D $_6$]DMSO): δ = 1.51 (d, $^2J_{\text{HP}}$ = 17.6 Hz, 3 H, PMe), 1.72 (d, $^2J_{\text{HP}}$ = 13.6 Hz, 3 H, PMe), 1.95 [s, 3 H, C(sp 2)Me], 2.13 [s, 3 H, C(sp 2)Me], 2.38 [s, 3 H, C(sp 2)Me], 2.55 [d, $^3J_{\text{HP}}$ = 13.8 Hz, 3 H, C(sp 3)Me] ppm. ^{31}P NMR (121.5 MHz, [D $_6$]DMSO): δ = 26.7 ppm.

7 (X = I): Yield 651 mg (70%), ESI-MS: exact mass calcd. for C $_{22}$ H $_{35}$ P $_2^{2+}$: m/z = 361.2209, found m/z (%) = 361.2216 (5) [(M - 2 I $^-$ - H $^+$) $^+$]. C $_{22}$ H $_{36}$ P $_2^{2+}$: m/z = 181.1141, found m/z (%) = 181.1140 (100) [(M - 2 I $^-$) $^{2+}$]. C $_{24}$ H $_{36}$ I $_2$ P $_2$ (616.28): calcd. C 42.88, H 5.89, found C 42.85, H 5.89. ^1H NMR (300.1 MHz, [D $_6$]DMSO): δ = 1.51 (d, $^2J_{\text{HP}}$ = 17.4 Hz, 3 H, PMe), 1.71 (d, $^2J_{\text{HP}}$ = 13.6 Hz, 3 H, PMe), 1.95 [d, $^{4/5}J_{\text{HP}}$ = 2.1 Hz, 3 H, C(sp 2)Me], 2.12 [s, 3 H, C(sp 2)Me], 2.37 [s, 3 H, C(sp 2)Me], 2.54 [d, $^3J_{\text{HP}}$ = 14.0 Hz, 3 H, C(sp 3)Me] ppm. ^{31}P NMR (121.5 MHz, [D $_6$]DMSO): δ = 26.6 ppm.

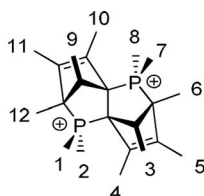
PMePh $_3$ I:^[24] Two equivalents of this phosphonium salt were obtained from the filtrate of the reaction mixture in the case of X = I by removal of the solvent in vacuo. The white solid was washed with diethyl ether (2 \times 5 mL) and *n*-pentane (2 \times 7 mL) and dried in vacuo. ESI-MS: exact mass calcd. for C $_{19}$ H $_{18}$ P $^+$: m/z = 277.1141, found m/z (%) = 277.1144 (100) [(M - I $^-$) $^+$]. I $^-$: m/z = 126.9050, found m/z (%) = 126.9052 (98) [I $^-$]. ^1H NMR (300.1 MHz, [D $_6$]DMSO): δ = 3.16 (d, $^2J_{\text{HP}}$ = 14.6 Hz, 3 H, Me), 7.74–7.89 (m, 15 H, Ph) ppm. ^{31}P NMR (121.5 MHz, [D $_6$]DMSO): δ = 21.5 ppm.

Indirect Proof for PPh $_3$ CH $_2$ Intermediate: A solution of PMe $_2$ Cp $^\#$ (**1**) was prepared following the procedure described in method A, but the reaction was downscaled to 1:10. The solvent was removed in vacuo at 0 °C to give a colourless oil, which was dissolved in acetonitrile (1.5 mL) and cooled to 0 °C. The chilled solution was added to a suspension of Ph $_3$ PCH $_2$ I $^+$ I $^-$ (0.16 g, 0.30 mmol) in acetonitrile (2 mL) at 0 °C. After 3 min sonification at 0 °C, the suspension was transferred to an NMR tube, solid material was centrifuged into the top of the NMR tube and the yellow solution was analysed by means of ^{31}P NMR spectroscopy (121.5 MHz, δ = 21.8 ppm, purity at least 80%). Addition of authentic neat PPh $_3$ CH $_2$ to the soluble part of the reaction mixture did not change the spectrum except for an increase in the intensity of the main resonance.

PMe $_2$ Cp $^\#$ (CH $_2$)I (8a, 8b): A solution of PMe $_2$ Cp $^\#$ (**1**) was prepared according to method B and its volume was reduced to 15 mL in vacuo at 0 °C. Toluene (15 mL) and diiodomethane (1.28 g, 4.78 mmol) were added and the reaction mixture was heated to 45 °C for 65 h. The product precipitated as a white, microcrystalline solid. It was separated by filtration, washed with *n*-pentane (3 \times 8 mL) and dried in vacuo. Heating the filtrate to 45 °C for additional 9 d gave another crop of the product, which was isolated as described above. The product was obtained as a mixture of the two isomers **8a** and **8b** (58:42). Combined yield 1.12 g (66%), ESI-MS: exact mass calcd. for C $_{12}$ H $_{21}$ IP $^+$: m/z = 323.0420, found m/z (%) = 323.0416 (100) [(M - I $^-$) $^+$]. C $_{12}$ H $_{21}$ I $_2$ P (450.08): calcd. C 32.02, H 4.70, found C 32.11, H 5.08. **8a:** ^1H NMR (300.1 MHz, [D $_6$]DMSO): δ = 1.18 (bd, $^4J_{\text{HP}}$ = 7.5 Hz, 3 H, 5-CpMe), 1.82 (s, 3 H, 3-CpMe), 1.93 (s, 3 H, 4-CpMe), 2.17 (d, $^2J_{\text{HP}}$ = 13.7 Hz, 3 H, PMe), 2.18 (d, $^2J_{\text{HP}}$ = 13.8 Hz, 3 H, PMe), 2.19 (s, 3 H, 2-CpMe), 3.30 (d, $^2J_{\text{HP}}$ = 6.3 Hz, 1 H, 5-CpH), 3.83 (d, $^2J_{\text{HP}}$ = 8.2 Hz, 2 H, CH $_2$ I) ppm. ^{31}P NMR (121.5 MHz, [D $_6$]DMSO): δ = 17.3 ppm. ^{13}C NMR (75.5 MHz, [D $_6$]DMSO): δ = -11.1 (d, $^1J_{\text{CP}}$ = 52.8 Hz, CH $_2$ I), 9.7 (d, $^1J_{\text{CP}}$ = 57.7 Hz, PMe), 9.8 (d, $^1J_{\text{CP}}$ = 57.9 Hz, PMe), 10.3 (s, 3-CpMe), 12.4 (d, $^4J_{\text{CP}}$ = 1.1 Hz, 4-CpMe), 14.8 (d, $^3J_{\text{CP}}$ = 3.6 Hz, 5-CpMe), 14.9 (s, 2-CpMe), 52.1 (d, $^2J_{\text{CP}}$ = 13.1 Hz, 5-Cp), 115.7 (d, $^1J_{\text{CP}}$ = 95.4 Hz, 1-Cp), 135.5 (d, $^3J_{\text{CP}}$ = 15.9 Hz, 3-Cp), 154.0 (d, $^3J_{\text{CP}}$ = 8.3 Hz, 4-Cp), 164.1 (d, $^2J_{\text{CP}}$ = 10.8 Hz, 2-Cp) ppm. **8b:** ^1H NMR (300.1 MHz, [D $_6$]DMSO): δ = 1.81 (d, $^4J_{\text{HP}}$ = 4.2 Hz, 6 H, 2,5-CpMe $_2$), 1.91 (d, $^2J_{\text{HP}}$ = 13.7 Hz, 6 H, PMe $_2$), 1.99 (s, 6 H, 3,4-CpMe $_2$), 3.57 (d, $^2J_{\text{HP}}$ = 8.4 Hz, 2 H, CH $_2$ I) 4.34 (d, $^2J_{\text{HP}}$ = 23.7 Hz, 1 H, 1-CpH) ppm. ^{31}P NMR (121.5 MHz, [D $_6$]DMSO): δ = 31.2 ppm. ^{13}C NMR (75.5 MHz, [D $_6$]DMSO): δ = -14.9 (d, $^1J_{\text{CP}}$ = 47.4 Hz, CH $_2$ I), 6.7 (d, $^1J_{\text{CP}}$ = 53.7 Hz, PMe $_2$), 11.4 (d, $^3J_{\text{CP}}$ = 1.5 Hz, 2,5-CpMe $_2$), 13.8 (s, 3,4-CpMe $_2$), 50.8 (d, $^1J_{\text{CP}}$ = 39.2 Hz, 1-Cp), 127.9 (d, $^3J_{\text{CP}}$ = 5.2 Hz, 3,4-Cp), 143.5 (d, $^2J_{\text{CP}}$ = 7.9 Hz, 2,5-Cp) ppm.

(PCp $^\#$ Me $_2$) $_2$ I $_2$ (9): A solution of PMe $_2$ Cp $^\#$ (**1**) was prepared according to method C and its volume was reduced to 12 mL in vacuo at 0 °C. In a pressure tube with teflon valve *n*-hexane (12 mL) and diiodomethane (496 mg, 1.85 mmol) were added and the reaction mixture was kept at 50 °C for 60 h, then at 70 °C for 100 h and finally at 90 °C for 66 h. A white solid had precipitated

and was separated by filtration, washed with *n*-pentane (3 × 10 mL) and dried in vacuo. Next to main product **8a,b** this salt mixture contained about 30% spectroscopic yield of **9** (¹H-, ³¹P NMR) as well as about 30% of a second by-product, presumably (CH₂(PMe₂(C₅Me₄))I₂) (¹H-, ³¹P NMR, ESI-MS). The salts were then suspended in dichloromethane (20 mL). Separation of the solid and the liquid phase was achieved by centrifugation followed by decantation. Storage of a saturated solution of the DCM insoluble solid part in methanol at 4 °C gave colourless crystals of the pure product **9**; yield 23 mg (2%), ESI-MS: exact mass calcd. for C₂₂H₃₈IP₂⁺: *m/z* = 491.1488, found *m/z* (%) = 491.1488 (100) [(M – I)⁺].



¹H NMR (300.1 MHz, [D₆]DMSO): δ = 0.94 (d, ³J_{HH} = 5.7 Hz, 6 H, Me^{3,9}), 1.42 (d, ³J_{HP} = 18.0 Hz, 6 H, Me^{6,12}), 1.70 (d, ⁴J_{HP} = 5.9 Hz, 6 H, Me^{4,10}), 1.78 (s, 6 H, Me^{5,11}), 2.19 (d, ²J_{HP} = 12.7 Hz, 6 H, Me^{1,7,2,8}), 2.22 (d, ²J_{HP} = 13.6 Hz, 6 H, Me^{2,8,11,7}), 3.08–3.11 (m, 2 H, CMe³H, CMe⁹H) ppm. ³¹P NMR (121.5 MHz, [D₆]DMSO): δ = 40.1 ppm. ¹³C NMR (125.8 MHz, [D₆]DMSO): δ = 5.3 (d, ¹J_{CP} = 46.0 Hz, Me^{1,7,2,8}), 5.7 (d, ¹J_{CP} = 42.2 Hz, Me^{2,11}), 8.3 (dd, ³J_{CP} = 4.1, ⁴J_{CP} = 3.5 Hz, Me^{3,9}), 9.0 (s, Me^{6,12}), 11.5 (s, Me^{5,11}), 15.7 (s, Me^{4,10}), 54.5 (dd, ²J_{CP} = 6.1, ³J_{CP} = 6.3 Hz, CHMe^{3,9}), 56.1 (dd, ¹J_{CP} = 47.5, ³J_{CP} = 9.9 Hz, CMe^{6,12}), 134.5 (s, CMe^{5,11}), 137.2 (dd, ²J_{CP} = 6.0, ³J_{CP} = 6.4 Hz, CMe^{4,10}) ppm.

[CH₂(PMe₂Cp⁺)]₂I₂: The data were obtained from the product mixture prior to recrystallisation from methanol. ESI-MS: exact mass calcd. for C₂₃H₃₉P₂⁺: *m/z* = 377.2522, found *m/z* (%) = 377.2522 (4) [(M – H⁺ – 2 I)⁺]. ³¹P NMR (121.5 MHz, [D₆]DMSO): δ = 16.0 ppm.

X-ray Crystallographic Studies: Crystallography: Crystal data were collected with a Stoe-IPDSII area-detector diffractometer using graphite-monochromatised Mo-K_α-radiation (λ = 71.073 pm) at 100 K. The detector was placed at a distance of 1.2 cm from the crystal. Data reduction was carried out by using the IPDS software X-Area (Stoe).^[25] The data were empirically corrected for absorption and other effects by using multiscans.^[26] The structures were solved by direct methods (Sir-97)^[27] and refined by full-matrix least-squares techniques against F_o² (SHELXL-97).^[28] The programs PLATON^[29] and PLUTON^[30] were used to check the results of the X-ray analyses. Diamond was used for structure representations.^[31]

CDC-753501 (for **3**), -753500 (for **7**) and -753502 (for **9**) contain the supplementary crystallographic data for this paper. These data can be obtained free of charge from The Cambridge Crystallographic Data Centre via www.ccdc.cam.ac.uk/data_request/cif.

Crystal Data for 3: C₁₉H₁₇Br₂P, *Mr* = 436.12, monoclinic, *P*₂₁/*n*, *a* = 10.2226(4) Å, *b* = 14.0098(5) Å, *c* = 12.4510(5) Å, *a* = 90°, *β* = 104.960(3)°, *γ* = 90°, *V* = 800.9(8) Å³, *Z* = 4, ρ(calcd.) = 1.681 g cm^{−3}, μ = 4.792 mm^{−1}, *T* = 100 K. A total of 9908 reflections were collected, of which 3034 were independent. The refinement on all data converged at *R*₁ = 2.00%, *wR*₂ = 4.44% and the goodness of fit was 0.939. Hydrogen atoms were included in idealised positions and refined with isotropic displacement parameters except that corresponding with the CH₂P group, which was found in the final density map and refined with isotropic displacement

parameters. Storage of an oversaturated solution of **3** in Pe/EtOAc/MeOH (2:1:1) for 7 d yielded colourless single crystals of this substance.

Crystal Data for 7: C₁₃H₂₄IOPS, *Mr* = 386.25, triclinic, *P*₁, *a* = 6.995(5) Å, *b* = 9.679(5) Å, *c* = 12.789(5) Å, *a* = 80.452(5)°, *β* = 75.801(5)°, *γ* = 73.601(5)°, *V* = 800.9(8) Å³, *Z* = 2, ρ(calcd.) = 1.602 g cm^{−3}, μ = 2.215 mm^{−1}, *T* = 100 K. A total of 8111 reflections were collected, of which 2825 were independent. Hydrogen atoms were included at calculated positions with fixed thermal parameters. The refinement on all data converged at *R*₁ = 2.12%, *wR*₂ = 4.48% and the goodness of fit was 0.940. In the asymmetric unit one DMSO molecule is included. Colourless single crystals of **7** were grown from a saturated solution of this bisphosphonium salt in DMSO by gas phase diffusion (Et₂O) at room temperature.

Crystal Data for 9: C_{23.50}H₄₃I₂O₂P₂, *Mr* = 673.34, triclinic, *P*₁, *a* = 10.9375(4) Å, *b* = 10.9411(4) Å, *c* = 14.1493(5) Å, *a* = 90.172(3)°, *β* = 107.398(3)°, *γ* = 119.288(3)°, *V* = 1386.36(9) Å³, *Z* = 2, ρ(calcd.) = 1.613 g cm^{−3}, μ = 2.401 mm^{−1}, *T* = 100 K. A total of 18094 reflections were collected, of which 4871 were independent. The refinement on all data converged at *R*₁ = 1.79%, *wR*₂ = 4.27% and the goodness of fit was 1.017. In the asymmetric unit two MeOH molecules are included, of which one is disordered and was modelled as two sites with 60:40 occupancy. The appropriate carbon atom of the disordered MeOH molecule resides on a crystallographic inversion center with a site-occupation factor of 0.5. The corresponding OH hydrogen atom could not be located in the difference Fourier map and was therefore fixed using the riding model, while the OH hydrogen atom at the second MeOH molecule was fixed in his located position. All other hydrogen atoms were included at calculated positions with fixed thermal parameters. Single crystals of **9** were obtained by cooling a saturated solution in MeOH to 4 °C.

- [1] a) H. Braunschweig, F. M. Breitling, *Coord. Chem. Rev.* **2006**, 250, 2691–2720; b) J. Okuda, *Dalton Trans.* **2003**, 2367–2378; c) J. Cano, K. Kunz, *J. Organomet. Chem.* **2007**, 692, 4411–4423.
- [2] a) J. A. M. Canich (Exxon), U. S. Patent, 5 096 867, **1992**; b) B. A. Harrington, G. G. Hlatkey, J. A. M. Canich, N. A. Merrill (Exxon), U. S. Patent 5 635 573, **1997**.
- [3] a) P. J. Shapiro, E. Bunel, W. P. Schaefer, J. E. Bercaw, *Organometallics* **1990**, 9, 867–869; b) J. Okuda, *Chem. Ber.* **1990**, 123, 1649–1651.
- [4] A. R. Petrov, K. A. Rufanov, B. Ziemer, P. Neubauer, V. V. Kotov, J. Sundermeyer, *Dalton Trans.* **2008**, 909–915.
- [5] K. A. Rufanov, A. R. Petrov, V. V. Kotov, F. Laquai, J. Sundermeyer, *Eur. J. Inorg. Chem.* **2005**, 3805–3807.
- [6] F. Ramirez, N. B. Desai, H. Hansen, N. McKelvie, *J. Am. Chem. Soc.* **1961**, 83, 3539–3540.
- [7] C. Zybille, G. Müller, *Organometallics* **1987**, 6, 2489–2494.
- [8] a) P. Jutzi, T. Heidemann, B. Neumann, H. G. Stammer, *Synthesis* **1992**, 1096–1098; b) S. Ford, M. Hofmann, C. P. Morley, J. L. Roberts, M. di Vaira, *Org. Biomol. Chem.* **2005**, 3, 3990–3995.
- [9] A phosphane oxide derivative has been described, see: S. Schardt, K. Hafner, *Tetrahedron Lett.* **1996**, 37, 3829–3832.
- [10] a) R. G. Pearson, *J. Am. Chem. Soc.* **1963**, 85, 3533–3539; b) R. G. Pearson, *Science* **1966**, 151, 172–177; c) R. G. Pearson in *Hard and Soft Acids and Bases* (Ed.: R. G. Pearson), Dowden, Hutchinson and Ross, Stroudsburg, PA, **1973**, vol. 1, pp. 79–84; d) R. S. Drago, G. C. Vogel, T. E. Needham, in: *Hard and Soft Acids and Bases* (Ed.: R. G. Pearson), Dowden, Hutchinson and Ross, Stroudsburg, PA, **1973**, vol. 1, pp. 267–279.
- [11] Y. Fu, H.-J. Wang, S.-S. Chong, Q.-X. Guo, L. Liu, *J. Org. Chem.* **2009**, 74, 810–819.

- [12] The dimerisation of a halophosphorane has been described previously, see: a) R. Appel, F. Knoll, H.-D. Wihler, *Angew. Chem.* **1977**, 89, 415–416; R. Appel, F. Knoll, H.-D. Wihler, *Angew. Chem. Int. Ed. Engl.* **1977**, 16, 402–403; b) J. Weiss, B. Nuber, *Z. Anorg. Allg. Chem.* **1981**, 473, 101–106.
- [13] H. Vogt, K. Lauritsen, L. Riesel, M. von Löwis, G. Reck, *Z. Naturforsch., Teil B* **1993**, 48, 1760–1766.
- [14] a) F. Ruthe, W.-W. du Mont, P. G. Jones, *Chem. Commun.* **1997**, 1947–1948; b) N. Bricklebank, S. M. Godfrey, A. G. Mackie, C. A. McAuliffe, R. G. Pritchard, *J. Chem. Soc., Chem. Commun.* **1992**, 355–356; c) S. M. Godfrey, D. G. Kelly, C. A. McAuliffe, A. G. Mackie, R. G. Pritchard, S. M. Watson, *J. Chem. Soc., Chem. Commun.* **1991**, 1163–1164; d) M. Freytag, P. G. Jones, B. Ahrens, A. K. Fischer, *New J. Chem.* **1999**, 23, 1137–1139.
- [15] A. Bondi, *J. Phys. Chem.* **1964**, 68, 441–451.
- [16] For comparison with C–Br bonds in phosphonium salts see, for example: M. ul-Haque, W. Horno, S. E. Cremer, P. W. Kremer, P. K. Kafarski, *J. Chem. Soc. Perkin Trans. 2* **1981**, 1138–1142.
- [17] G. W. Parshall, *Inorganic Syntheses*, 15, Wiley VCH, New York, **1974**, S. 191–193.
- [18] C. M. Fendrick, L. D. Schertz, V. W. Day, T. J. Marks, *Organometallics* **1988**, 7, 1828–1838.
- [19] R. Appel, W. Morbach, *Synthesis* **1977**, 699–700.
- [20] N. J. Lawrence, J. Liddle, D. Jackson, *J. Chem. Soc. Perkin Trans. 1* **2002**, 2260–2267.
- [21] J. C. Conway, P. Quayle, A. C. Regan, C. J. Urch, *Tetrahedron* **2005**, 61, 11910–11923.
- [22] H. Schmidbaur, H. Stühler, W. Vornberger, *Chem. Ber.* **1972**, 105, 1084–1086.
- [23] A synthetic approach to compound **1**, which is very similar to ours, has been reported before: M. Visseaux, A. Dormond, M. M. Kubicki, C. Moïse, D. Baudry, M. Ephritikhine, *J. Organomet. Chem.* **1992**, 433, 95–106.
- [24] For NMR spectroscopic identification of this substance, see: A. Singh, *Phosphorus Sulfur Silicon* **1990**, 49, 152–162.
- [25] Stoe & Cie GMBH, *IPDS Software*, Darmstadt, Germany, **1996**.
- [26] R. H. Blessing, *Acta Crystallogr., Sect. A* **1995**, 51, 33–38.
- [27] A. Altomare, M. C. Burla, M. Camalli, G. L. Cascarano, C. Giacovazzo, A. Guagliardi, A. G. G. Moliterni, G. Polidori, R. Spagna, *J. Appl. Crystallogr.* **1999**, 32, 115–119.
- [28] G. M. Sheldrick, *SHELXL-97*, University of Göttingen, Germany, **1993**.
- [29] A. L. Spek, *Acta Crystallogr., Sect. A* **1990**, 46, C34.
- [30] A. L. Spek, *Platon: A Multi-Purpose Crystallographic Tool*, Utrecht University, Utrecht, The Netherlands, **2001**.
- [31] K. Brandenburg, *Diamond*, release 3.0, Crystal Impact GbR, Bonn, Germany, **2004**.

Received: December 31, 2009
Published Online: June 2, 2010

Syntheses, Structures and Magnetic Properties of Trinuclear $\text{Cu}^{\text{II}}\text{M}^{\text{II}}\text{Cu}^{\text{II}}$ ($\text{M} = \text{Cu}, \text{Ni}, \text{Co}$ and Fe) and Tetranuclear $[2 \times 1 + 1 \times 2] \text{Cu}^{\text{II}}\text{Mn}^{\text{II}}-2\text{Cu}^{\text{II}}$ Complexes Derived from a Compartmental Ligand: The Schiff Base 3-Methoxysalicylaldehyde Diamine Can also Stabilize a Cocrystal

Arpita Biswas,^[a] Meenakshi Ghosh,^[b] Pascale Lemoine,^[c] Sohini Sarkar,^[a] Susanta Hazra,^[a] and Sasankasekhar Mohanta*^[a]

Keywords: Crystal engineering / Magnetic properties / Heterometallic complexes / Self-assembly / Hydrogen bonds

The present investigation describes syntheses, characterization and studies of the mononuclear compound $[\text{Cu}^{\text{II}}\text{L}(\text{H}_2\text{O})]$ (**1**), the triangular, trinuclear monophenoxido-bridged compounds $[\{\text{Cu}^{\text{II}}\text{L}\}_2\text{M}^{\text{II}}(\text{H}_2\text{O})_2](\text{ClO}_4)_2 \cdot n\text{H}_2\text{O}$ [**2** ($\text{M} = \text{Cu}$, $n = 0$), **3** ($\text{M} = \text{Ni}$, $n = 3$), **4** ($\text{M} = \text{Co}$, $n = 0$), **5** ($\text{M} = \text{Fe}$, $n = 0$)] and the tetrametallic self-assembled complex $[\{\text{Cu}^{\text{II}}\text{LMn}^{\text{II}}(\text{H}_2\text{O})_3\} - \{\text{Cu}^{\text{II}}\text{L}\}_2](\text{ClO}_4)_2 \cdot \text{H}_2\text{O}$ (**6**) derived from compartmental Schiff base ligand, H_2L , which is the $[2+1]$ condensation product of 3-methoxysalicylaldehyde and *trans*-1,2-diaminocyclohexane. Single-crystal X-ray structures of **2**, **5** and **6** were determined. Two pairs of terminal...central metal ions in the trinuclear cores in **2** and **5** are monophenoxido-bridged. Interestingly, the CuO_6 and FeO_6 environments have tetragonally compressed octahedral geometries. On the other hand, the structure of **6** reveals that it is a $[2 \times 1 + 1 \times 2]$ cocrystal of one diphenoxido-bridged dinuclear $[\text{Cu}^{\text{II}}\text{LMn}^{\text{II}}(\text{H}_2\text{O})_3]^{2+}$ dication and two mononuclear $[\text{Cu}^{\text{II}}\text{L}]$ moieties. Cocrystallization in **6**

takes place as a result of water encapsulation. The variable-temperature (2–300 K) magnetic susceptibilities of compounds **2–6** have been measured. The exchange integrals obtained are: the Cu^{II}_3 compound **2**, $J = -78.9 \text{ cm}^{-1}$; the $\text{Cu}^{\text{II}}\text{Ni}^{\text{II}}-\text{Cu}^{\text{II}}$ compound **3**, $J = -22.8 \text{ cm}^{-1}$; the $\text{Cu}^{\text{II}}\text{Co}^{\text{II}}\text{Cu}^{\text{II}}$ compound **4**, $J = -7.8 \text{ cm}^{-1}$; the $\text{Cu}^{\text{II}}\text{Fe}^{\text{II}}\text{Cu}^{\text{II}}$ compound **5**, $J = -3.0 \text{ cm}^{-1}$; the $\text{Cu}^{\text{II}}_3\text{Mn}^{\text{II}}$ compound **6**, $J = -15.1 \text{ cm}^{-1}$. The monophenoxido-bridging core in **3** and **4** has been proposed after comparison of the structures and magnetic properties of these two compounds with those of **2**, **5** and related other compounds. This paper presents rare examples of monophenoxido-bridged $\text{Cu}^{\text{II}}\text{M}^{\text{II}}\text{Cu}^{\text{II}}$ ($\text{M} = \text{Cu}, \text{Ni}, \text{Co}$ and Fe) compounds, provides an understanding of the structures from magnetic exchange integrals, and, most importantly, reports on the first example of a cocrystal derived from a 3-methoxysalicylaldehyde diamine compartmental ligand.

Introduction

Molecular magnetism has been a frontier research area.^[1–10] Several magneto–structural correlations have been established over the last few decades, and the derived ideas in discrete systems have been utilized to develop molecule-based magnetic materials.^[1–10] However, investigations of the magnetic properties of systems containing new or less-explored bridging cores is important for further enlightenment of the intimate relationship of spin coupling. Trinuclear complexes, in particular, deserve attention because of the possibility of spin frustration in such systems.^[5]

Compartmental Schiff base ligands, which are obtained on condensing 3-methoxysalicylaldehyde and 3-ethoxysalicylaldehyde with a number of diamines, have been important ligands in coordination chemistry.^[8–21] A number of mono-, di-, oligo- and polynuclear complexes have been isolated with these ligand environments. Some of the complexes have been found to exhibit interesting magnetic properties as well.^[8–11]

In the mononuclear 3d compounds derived from the ligands 3-methoxysalicylaldehyde diamine ($\text{H}_2\text{L}^{\text{OMe}}$) and 3-ethoxysalicylaldehyde diamine ($\text{H}_2\text{L}^{\text{OEt}}$), a 3d metal ion occupies the N_2O_2 cavity. In both types of ligand systems, $\text{H}_2\text{L}^{\text{OMe}}$ and $\text{H}_2\text{L}^{\text{OEt}}$, mononuclear inclusion products that contain an encapsulated water molecule in the O_4 compartment are known.^[11,13–16,18] However, while mononuclear copper(II), nickel(II) and oxovanadium(IV) compounds^[13–17] derived from $\text{H}_2\text{L}^{\text{OEt}}$ -type ligands are dominated by inclusion products,^[13–16] the inclusion of water takes place only rarely^[18] in mononuclear compounds^[11,18,19] derived from $\text{H}_2\text{L}^{\text{OMe}}$ type ligands. Further, as in the mononuclear compounds, water encapsulation also takes place in the 3d–3d systems derived from $\text{H}_2\text{L}^{\text{OEt}}$.

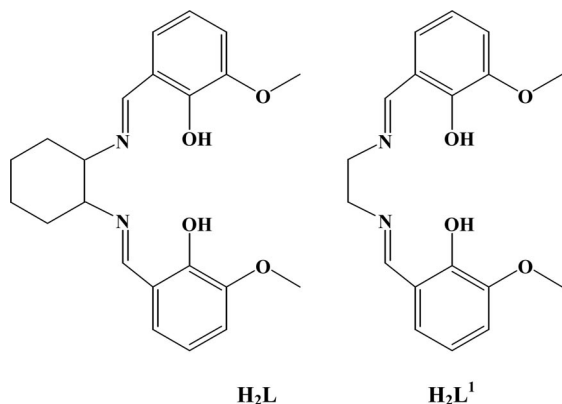
[a] Department of Chemistry, University of Calcutta, 92 A. P. C. Road, Kolkata 700009, India
Fax: +91-33-23519755

E-mail: sm_cu_chem@yahoo.co.in

[b] Department of Inorganic Chemistry, Indian Association for the Cultivation of Science, Kolkata 700032, India

[c] Université Paris Descartes, Laboratoire de Cristallographie et RMN biologiques UMR 8015, Faculté de Pharmacie, 4 avenue de l'Observatoire, 75006 Paris, France

type ligands to result in the formation of interesting examples of tetrametallic^[13–15] and heptametallic^[15] self-assemblies consisting of cocrystallized dinuclear and mononuclear units. In these dinuclear–mononuclear cocrystals, the second metal centre in the dinuclear core is coordinated to three water molecules, two of which are encapsulated in two different mononuclear $[\text{Cu}^{\text{II}}/\text{Ni}^{\text{II}}\text{L}^{\text{OEt}}]$ moieties to result in the generation of the self-assembly products. On the other hand, although there are several 3d–3d compounds derived from $\text{H}_2\text{L}^{\text{OMe}}$ -type ligands, cocrystallization does not take place in any case.^[11,21] In fact, the second metal centre in most of the 3d–3d complexes derived from $\text{H}_2\text{L}^{\text{OMe}}$ is not even coordinated to a water molecule. We anticipated that if the second metal centre in the 3d–3d complexes derived from $\text{H}_2\text{L}^{\text{OMe}}$ is coordinated to a water molecule, cocrystallization might occur. With this aim, we reacted $[\text{Cu}^{\text{II}}\text{L}^1(\text{H}_2\text{O})]$ [$\text{H}_2\text{L}^1 = N,N'$ -ethylenebis(3-methoxysalicylaldehyde)]; Scheme 1] with perchlorate salts of 3d metal ions. Although the second metal centres in the monophenoxido-bridged trinuclear products obtained therefrom are coordinated to two water molecules, cocrystallization also does not take place in these cases.^[12] The fact is that cocrystals are still not produced in the $\text{H}_2\text{L}^{\text{OMe}}$ ligand system, while the $\text{H}_2\text{L}^{\text{OEt}}$ ligand system is dominated by a number of cocrystals.^[13–15,20] The significant difference between the two closely related ligand environments is surprising, and we would like to explore this area further. We were particularly interested in the 3d–3d complexes derived from new or unexplored $\text{H}_2\text{L}^{\text{OMe}}$ ligands, which can be obtained by changing the diamine functionality, to investigate whether cocrystallization is really not possible in the $\text{H}_2\text{L}^{\text{OMe}}$ -type ligands. Accordingly, we report here the copper(II) and copper(II)– $\text{M}_{3\text{d}}$ ($\text{M}_{3\text{d}} = \text{Cu}^{\text{II}}, \text{Ni}^{\text{II}}, \text{Co}^{\text{II}}, \text{Fe}^{\text{II}}$ and Mn^{II}) complexes derived from H_2L (Scheme 1), which is the [2+1] condensation product of 3-methoxysalicylaldehyde and *trans*-1,2-diaminocyclohexane.



Scheme 1. Chemical structure of H_2L and H_2L^1 .

Results and Discussion

Description of the Structures of $[\{\text{Cu}^{\text{II}}\text{L}\}_2\text{Cu}^{\text{II}}(\text{H}_2\text{O})_2](\text{ClO}_4)_2$ (**2**) and $[\{\text{Cu}^{\text{II}}\text{L}\}_2\text{Fe}^{\text{II}}(\text{H}_2\text{O})_2](\text{ClO}_4)_2$ (**5**)

Crystal structures of **2** and **5** are shown in Figures 1 and 2, respectively, while selected bond lengths and angles of these

two compounds are listed in Tables 1 and 2, respectively. These two compounds are isostructural; both crystallize in the $C2/c$ space group with almost identical unit cell parameters. One half of both the structures is symmetry related to the other half because of the presence of a crystallographic twofold axis. The structures reveal that compounds **2** and **5** consist of the triangular, trinuclear $\text{Cu}^{\text{II}}\text{--M}^{\text{II}}\text{Cu}^{\text{II}}$ dication, $[\{\text{Cu}^{\text{II}}\text{L}\}_2\text{M}^{\text{II}}(\text{H}_2\text{O})_2]^{2+}$ [$\text{M} = \text{Cu}$ (**2**) and Fe (**5**)], and two perchlorate anions. In each of the trinuclear dications, a central metal ion, Cu^{II} or Fe^{II} , is coordinated to one phenoxido oxygen atom and one methoxy oxygen atom of each of the two symmetry-related $[\text{Cu}^{\text{II}}\text{L}]$ moieties, $[\text{Cu}^{\text{II}}(1)\text{L}]$ and $[\text{Cu}^{\text{II}}(1\text{C})\text{L}]$. In the $[\text{Cu}^{\text{II}}\text{L}]$ moieties, obviously, the metal centre is coordinated to two imine nitrogen atoms and two phenoxido oxygen atoms of the N_2O_2 compartment of $[\text{L}]^{2-}$. On the other hand, the central metal ion is hexacoordinated; in addition to two bridging phenoxido and two methoxy oxygen atoms, two water molecules are coordinated to this metal centre. Two pairs of metal ions, $\text{Cu}(1)\cdots\text{Cu}(2)/\text{Fe}(1)$ and $\text{Cu}(1\text{C})\cdots\text{Cu}(2)/\text{Fe}(1)$, in the trinuclear cores are monophenoxido-bridged, while the

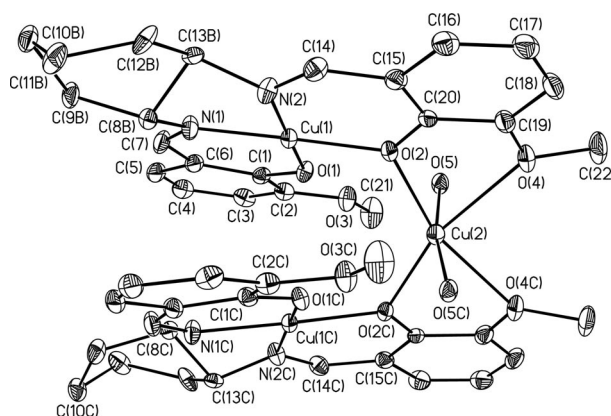


Figure 1. Crystal structure of $[\{\text{Cu}^{\text{II}}\text{L}\}_2\text{Cu}^{\text{II}}(\text{H}_2\text{O})_2](\text{ClO}_4)_2$ (**2**). Perchlorate anions and hydrogen atoms are omitted for clarity. Of the two disordered positions of the six carbon atoms of the cyclohexane ring, one is shown. Symmetry code: C, $-1 - x, y, 0.5 - z$.

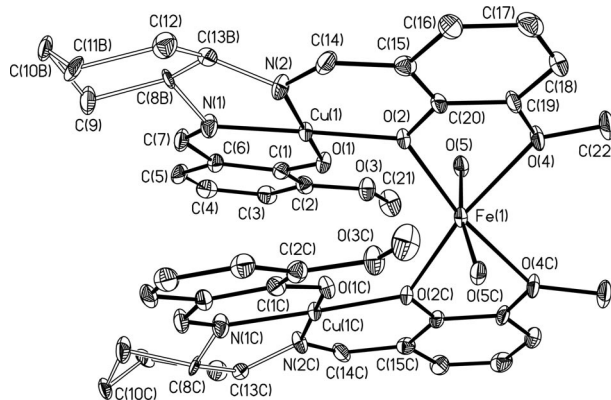


Figure 2. Crystal structure of $[\{\text{Cu}^{\text{II}}\text{L}\}_2\text{Fe}^{\text{II}}(\text{H}_2\text{O})_2](\text{ClO}_4)_2$ (**5**). Perchlorate anions and hydrogen atoms are omitted for clarity. Of the two disordered positions of the four carbon atoms of the cyclohexane ring, one is shown. Symmetry code: C, $2 - x, y, 0.5 - z$.

metal centres Cu(1) and Cu(1C) are not interlinked by any bridge. Clearly, in the trinuclear arrangement, Cu(2)/Fe(1) can be considered as the central metal ion, whereas Cu(1) and Cu(1C) can be considered as terminal metal ions. In **2**, the Cu(1)···Cu(2), Cu(1C)···Cu(2) and Cu(1)···Cu(1C) distances are 3.42, 3.42 and 3.82 Å, respectively, while the Cu(1)···Cu(2)···Cu(1C), Cu(1)···Cu(1C)···Cu(2) and Cu(1C)···Cu(1)···Cu(2) angles are 67.8, 56.1 and 56.1°, respectively. In **5**, The Cu(1)···Fe(1), Cu(1C)···Fe(1) and Cu(1)···Cu(1C) distances are 3.53, 3.53 and 3.76 Å, respectively, while the Cu(1)···Fe(1)···Cu(1C), Cu(1)···Cu(1C)···Fe(1) and Cu(1C)···Cu(1)···Fe(1) angles are 64.2, 57.9 and 57.9°, respectively. Evidently, the trinuclear arrangement of the three metal ions in **2** and **5** is triangular, and the Cu^{II}₃ and Cu^{II}Fe^{II}Cu^{II} triangles may be considered as approximately equilateral.

Table 1. Selected bond lengths [Å] and bond angles [°] in the coordination environment of the copper(II) centres in [$\{\text{Cu}^{\text{II}}\text{L}\}_2\text{Cu}^{\text{II}}(\text{H}_2\text{O})_2](\text{ClO}_4)_2$ (**2**). Symmetry code: C, $-x, y, 0.5 - z$.

Bond lengths		Bond angles	
Cu(1)–O(1)	1.902(4)	O(1)–Cu(1)–N(2)	174.0(2)
Cu(1)–O(2)	1.944(3)	N(1)–Cu(1)–O(2)	175.96(19)
Cu(1)–N(1)	1.926(5)	O(1)–Cu(1)–N(1)	94.14(18)
Cu(1)–N(2)	1.939(5)	O(1)–Cu(1)–O(2)	89.23(14)
Cu(2)–O(2)	2.070(4)	O(2)–Cu(1)–N(2)	93.56(17)
Cu(2)–O(4)	2.360(4)	N(1)–Cu(1)–N(2)	83.3(2)
Cu(2)–O(5)	1.909(4)	O(5)–Cu(2)–O(5C)	170.2(3)
		O(2)–Cu(2)–O(4C)	162.80(15)
		O(2)–Cu(2)–O(2C)	126.0(2)
		O(2)–Cu(2)–O(4)	71.20(15)
		O(2)–Cu(2)–O(5)	92.12(17)
		O(2)–Cu(2)–O(5C)	92.32(17)
		O(4)–Cu(2)–O(4C)	91.6(2)
		O(4)–Cu(2)–O(5)	85.57(18)
		O(4)–Cu(2)–O(5C)	87.61(18)
		Cu(1)–O(2)–Cu(2)	117.11(18)

Table 2. Selected bond lengths [Å] and bond angles [°] in the coordination environment of the metal(II) centres in [$\{\text{Cu}^{\text{II}}\text{L}\}_2\text{Fe}^{\text{II}}(\text{H}_2\text{O})_2](\text{ClO}_4)_2$ (**5**). Symmetry code: C, $2 - x, y, 0.5 - z$.

Bond lengths		Bond angles	
Cu(1)–O(1)	1.889(7)	O(1)–Cu(1)–N(2)	173.5(3)
Cu(1)–O(2)	1.935(6)	N(1)–Cu(1)–O(2)	175.6(3)
Cu(1)–N(1)	1.917(9)	O(1)–Cu(1)–N(1)	94.6(3)
Cu(1)–N(2)	1.919(8)	O(1)–Cu(1)–O(2)	89.3(3)
Fe(1)–O(2)	2.130(6)	O(2)–Cu(1)–N(2)	94.2(3)
Fe(1)–O(4)	2.252(6)	N(1)–Cu(1)–N(2)	82.1(4)
Fe(1)–O(5)	2.052(7)	O(2)–Fe(1)–O(4C)	170.3(2)
		O(5)–Fe(1)–O(5C)	170.7(4)
		O(2)–Fe(1)–O(2C)	117.5(3)
		O(2)–Fe(1)–O(4)	72.2(2)
		O(2)–Fe(1)–O(5)	93.1(2)
		O(2)–Fe(1)–O(5C)	91.8(2)
		O(4)–Fe(1)–O(4C)	98.1(4)
		O(4)–Fe(1)–O(5)	87.0(3)
		O(4)–Fe(1)–O(5C)	86.9(3)
		Cu(1)–O(2)–Fe(1)	120.6(3)

In the salen type N₂O₂ compartment, the two Cu–N bond lengths in both compounds are almost identical [Cu(1)–N(1) = 1.926(5) Å and Cu(1)–N(2) = 1.939(5) Å in

2, Cu(1)–N(1) = 1.917(9) Å and Cu(1)–N(2) = 1.919(8) Å in **5**]. Of the two Cu–O(phenoxido) bonds, that involving the bridging phenoxido oxygen atom [Cu(1)–O(2) = 1.944(3) Å in **2**, Cu(1)–O(2) = 1.935(6) Å in **5**] is slightly longer than that involving the monodentate phenoxido oxygen atom [Cu(1)–O(1) = 1.902(4) Å in **2**, Cu(1)–O(1) = 1.889(7) Å in **5**]. The ranges of the *cisoid* [83.3(2)–94.14(18)° in **2**, 82.1(4)–94.6(3)° in **5**] and *transoid* [174.0(2)–175.96(19)° in **2**, 173.5(3)–175.6(3)° in **5**] angles deviate only slightly from the ideal values. Both the average deviation (0.065 Å in both) of the donor centres and the displacement (0.024 Å in **2** and 0.026 Å in **5**) of the metal ion from the least-squares N₂O₂ plane are very small. All these structural parameters indicate that the environment of Cu(1) in **2** and **5** is only slightly distorted from an ideal square-planar geometry.

As already mentioned, the central metal ion, M [M = Cu(2) in **2** and Fe(1) in **5**], is hexacoordinated to two bridging phenoxido, two methoxy and two water oxygen atoms. The three types of bond lengths are significantly different; the order of bond lengths are M–O(methoxy) [Cu(2)–O(4) 2.360(4) Å, Fe(1)–O(4) 2.252(6) Å] > M–O(phenoxido) [Cu(2)–O(2) 2.070(4) Å, Fe(1)–O(2) 2.130(6) Å] > M–O(water) [Cu(2)–O(5) 1.909(4) Å, Fe(1)–O(5) 2.052(7) Å]. The wide range in the bond lengths [1.909(4)–2.360(4) Å in **2**, 2.052(7)–2.252(6) Å in **5**] as well as much of the deviation of both the *transoid* angles [162.80(15) and 170.2(3)° in **2**, 170.3(2) and 170.7(4)° in **5**] and the *cisoid* angles [71.20(15)–126.0(2)° in **2**, 72.2(2)–117.5(3)° in **5**] from the ideal values are indicative that the coordination environments of the central metal ion are significantly distorted from ideal octahedral geometry. However, comparatively the smaller ranges in the *cisoid* angles and the bond lengths for Fe(1) indicate that the environment of this metal centre in **5** is slightly less distorted than that of Cu(2) in **2**. The two donor centres [O(4) and O(4C)], which involve longer metal–ligand bond lengths, occupy two *cis* positions, and therefore the coordination environments of Cu(2) in **2** and Fe(1) in **5** are not tetragonally elongated octahedra, as usually observed. Of the three possible O₄ basal planes, O(2)O(2C)O(4)O(4C) is the best and the right choice because the average deviation of the four oxygen atoms (0.021 Å for **2** and 0.011 Å for **5**) and the displacement of the metal centre from the least-squares O₄ plane (0.000 Å for both) is either very small or zero; from the two other possible basal planes, the values of both the average deviation of the four oxygen atoms (0.100 Å for **2** and 0.025 Å for **5**) and the displacement of the metal ion (0.230 Å for **2** and 0.159 Å for **5**) are significantly greater. Clearly, two water oxygen atoms [O(5) and O(5C)], occupy the axial positions, while two bridging phenoxido [O(2) and O(2C)] and two methoxy [O(4) and O(4C)] oxygen atoms occupy the equatorial positions. Interestingly, the axial bond lengths [1.909(4) Å for **2** and 2.052(7) Å for **5**] are much shorter than the basal bond lengths [2.070(4)–2.360(4) Å for **2** and 2.130(6)–2.252(6) Å for **5**], and therefore, the coordination environments of Cu(2) and Fe(1) are tetragonally compressed octahedrals, instead of the frequently observed tetragonally elongated

octahedral geometry. However, the tetragonally compressed octahedral environment is not unusual.^[22]

As the terminal metal ions, Cu(1) and Cu(1C) are symmetry related, the two pairs of monophenoxido-bridging cores are identical. In **2**, the values of the Cu–phenoxido–Cu bridge angle, the Cu(terminal)⋯Cu(central) distance, and the dihedral angle (δ) between the basal plane of the central metal ion and the square plane of the terminal metal ion are 117.11(18)°, 3.42 Å, and 39.9°, respectively, while the corresponding parameters for **5** are 120.6(3)°, 3.53 Å, and 32.3°, respectively. As the δ values are 39.9° for **2** and 32.3° for **5**, the monophenoxido-bridging cores in both the compounds are significantly twisted.

It is relevant to compare the structure of **2** and **5** with those of the related compounds $[\{\text{Cu}^{\text{II}}\text{L}\}_2\text{Cu}^{\text{II}}(\text{H}_2\text{O})_2](\text{ClO}_4)_2 \cdot \text{H}_2\text{O}$ (**7**) and $[\{\text{Cu}^{\text{II}}\text{L}\}_2\text{Fe}^{\text{II}}(\text{H}_2\text{O})_2](\text{ClO}_4)_2 \cdot \text{H}_2\text{O}$ (**8**) derived from *N,N'*-ethylenebis(3-methoxysalicylaldehyde) (H_2L).^[12] All of the four compounds **2**, **5**, **7** and **8** are triangular, trinuclear $\text{Cu}^{\text{II}}\text{M}^{\text{II}}\text{Cu}^{\text{II}}$ compounds ($\text{M} = \text{Cu}$ or Fe), in which the two terminal⋯central metal ion pairs are monophenoxido bridged. The coordination environments of the terminal and central metal ions consist of the same set of atoms in both the compounds as well. However, while the arrangement of the three metal ions in **2** and **5** can be approximated as an equilateral triangle, the three metal ions in **7** and **8** define an isosceles triangle. In **7** and **8**, two water molecules coordinate to the central metal ion in two *cis* positions, and therefore, the water molecules are involved in hydrogen-bonding interactions with the phenoxido and methoxy oxygen atoms. In contrast, the two coordinated water molecules in **2** and **5** occupy two *trans* positions, and therefore, these cannot interact with any oxygen atom of the O_4 compartment. In fact, no intermolecular interaction involving the water molecules and O_4 compartment takes place. Again, the coordination environment of the central metal ion in **7** and **8** is elongated octahedral, as expected because of the Jahn–Teller distortion; the long axial bonds involve two methoxy oxygen atoms. In contrast, the coordination environment of the central metal ion in **2** is a tetragonally compressed octahedral. The Cu–phenoxido–Cu bridge angle in **2** [117.11(18)°] is not very different than those in **7** [129.84(13) and 121.10(12)°]. On the other hand, the Cu–phenoxido–Fe bridge angle in **5** [120.6(3)°] can be considered as almost identical to those in **8** [121.15(16) and 122.76(16)°]. However, the trinuclear cores in all the four complexes are significantly twisted ($\delta = 39.9^\circ$ in **2**, 36.3° and 58.5° in **7**, 32.3° in **5**, 49.7–75.1° in **8**).

Description of the Structure of $[\{\text{Cu}^{\text{II}}\text{LMn}^{\text{II}}(\text{H}_2\text{O})_3\}\{\text{Cu}^{\text{II}}\text{L}\}_2](\text{ClO}_4)_2 \cdot \text{H}_2\text{O}$ (**6**)

The crystal structure of **6** is shown in Figure 3, while selected bond lengths and angles are listed in Table 3. The structure consists of one diphenoxido-bridged, dinuclear dication with a composition of $[\text{Cu}^{\text{II}}\text{LMn}^{\text{II}}(\text{H}_2\text{O})_3]^{2+}$, two mononuclear copper(II) moieties of composition $[\text{Cu}^{\text{II}}\text{L}]$, two perchlorate anions and one water molecule as solvent

of crystallization. In the two mononuclear $[\text{Cu}^{\text{II}}\text{L}]$ moieties, obviously, the metal centre is coordinated to the two imine nitrogen atoms and the two phenoxido oxygen atoms. In the dinuclear $[\text{Cu}^{\text{II}}\text{LMn}^{\text{II}}(\text{H}_2\text{O})_3]^{2+}$ moiety, copper(II) occupies the salen-type N_2O_2 compartment, while manganese(II) is present in the open and larger O_4 compartment. The manganese(II) centre is pentacoordinated; in addition to two bridging phenoxido oxygen atoms, three water molecules coordinate to this metal centre. The methoxy oxygen atoms remain uncoordinated.

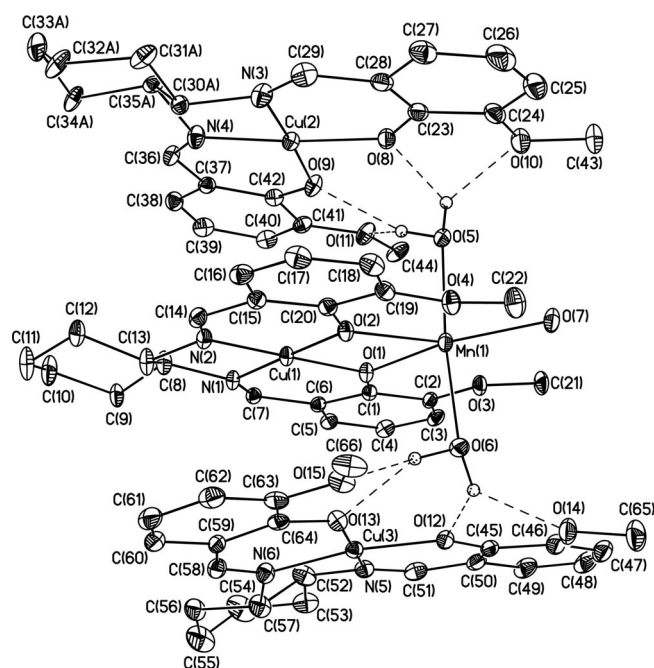


Figure 3. Crystal structure of $[\{\text{Cu}^{\text{II}}\text{LMn}^{\text{II}}(\text{H}_2\text{O})_3\}\{\text{Cu}^{\text{II}}\text{L}\}_2](\text{ClO}_4)_2 \cdot \text{H}_2\text{O}$ (**6**). Perchlorate anions, solvated water molecule and hydrogen atoms, except for those involved in hydrogen bonding, are omitted for clarity. Of the two disordered positions of the six carbon atoms of a cyclohexane ring, one is shown.

There are three copper(II) centres in the salen-type compartments. The Cu–N/O bond lengths are not very different and vary between 1.887(4) and 1.927(5) Å. However, the Cu–N bond is slightly longer than its *trans* Cu–O bond. The ranges of the *cisoid* angles in the coordination environment of the three metal ions are almost identical [82.82(16)–95.2(2)° for Cu(1), 84.5(2)–93.7(2)° for Cu(2) and 84.5(2)–93.7(2)° for Cu(3)]. However, in comparison to the *transoid* angles for Cu(1) and Cu(2) [176.0(2)–178.0(2)°], those for Cu(3) [171.6(2) and 173.7(2)°] are slightly more deviated from the ideal value. The displacements of the metal ion from the corresponding least-squares N_2O_2 planes are very small (0.000–0.043 Å) for all three cases. However, from the square planes, the deviation of 0.021 Å of the donor centres for Cu(3) is more than those for Cu(1) and Cu(2) (0.000–0.016 Å). Clearly, all three coordination environments are slightly distorted from ideal square-planar geometry; the distortion of the Cu(3) environment is slightly more than the two others.

As already mentioned, the manganese(II) ion, Mn(1), in the dinuclear unit adopts a five-coordinate MnO_5 coordina-

Table 3. Selected bond lengths [Å] and angles [°] in the coordination environment of the metal centres in [{Cu^{II}LMn^{II}(H₂O)₃}-{Cu^{II}L}]₂(ClO₄)₂·H₂O(6).

Bond lengths		Bond angles	
Cu(1)–O(1)	1.897(4)	O(1)–Cu(1)–N(2)	178.0(2)
Cu(1)–O(2)	1.887(4)	N(1)–Cu(1)–O(2)	177.88(18)
Cu(1)–N(1)	1.926(5)	O(1)–Cu(1)–N(1)	95.11(18)
Cu(1)–N(2)	1.909(5)	O(1)–Cu(1)–O(2)	82.82(16)
Cu(2)–N(3)	1.915(5)	O(2)–Cu(1)–N(2)	95.2(2)
Cu(2)–N(4)	1.912(5)	N(1)–Cu(1)–N(2)	86.9(2)
Cu(2)–O(8)	1.895(4)	N(3)–Cu(2)–O(9)	177.2(2)
Cu(2)–O(9)	1.899(4)	N(4)–Cu(2)–O(8)	176.0(2)
Cu(3)–N(5)	1.922(5)	N(3)–Cu(2)–O(8)	93.7(2)
Cu(3)–N(6)	1.927(5)	N(3)–Cu(2)–N(4)	84.5(2)
Cu(3)–O(12)	1.896(4)	N(4)–Cu(2)–O(9)	93.3(2)
Cu(3)–O(13)	1.900(4)	O(8)–Cu(2)–O(9)	88.61(18)
		N(5)–Cu(3)–O(13)	173.7(2)
		N(6)–Cu(3)–O(12)	171.6(2)
		N(5)–Cu(3)–O(12)	93.7(2)
		N(5)–Cu(3)–N(6)	84.5(2)
		N(6)–Cu(3)–O(13)	92.9(2)
		O(12)–Cu(3)–O(13)	89.64(18)
Mn(1)–O(1)	2.198(4)	O(5)–Mn(1)–O(6)	172.90(13)
Mn(1)–O(2)	2.188(4)	O(1)–Mn(1)–O(2)	69.59(14)
Mn(1)–O(5)	2.173(4)	O(1)–Mn(1)–O(5)	94.76(13)
Mn(1)–O(6)	2.188(4)	O(1)–Mn(1)–O(6)	92.33(14)
Mn(1)–O(7)	2.145(4)	O(1)–Mn(1)–O(7)	142.47(16)
		O(2)–Mn(1)–O(5)	89.98(14)
		O(2)–Mn(1)–O(6)	92.84(13)
		O(2)–Mn(1)–O(7)	146.87(17)
		O(5)–Mn(1)–O(7)	80.76(13)
		O(6)–Mn(1)–O(7)	93.38(14)
		Cu(1)–O(1)–Mn(1)	103.37(18)
		Cu(1)–O(2)–Mn(1)	104.12(18)

tion environment with the two bridging phenoxido oxygen atoms [O(1) and O(2)] and three water oxygen atoms [O(5), O(6) and O(7)]. Although the Mn–O(water) bonds [2.145(4)–2.188(4) Å] are slightly shorter than the Mn–O(phenoxido) bonds [2.188(4)–2.198(4) Å], the difference in the shortest and longest bonds is only ca. 0.05 Å. The τ value in the MnO₅ environment is 0.434, which indicates that coordination geometry is intermediate between square pyramidal and trigonal bipyramidal. For the square-pyramidal geometry, the phenoxido oxygen atom O(1) occupies the apical position, whereas the remaining phenoxido oxygen atom, O(2), and the three water oxygen atoms, O(5), O(6) and O(7), define the basal plane. Both the *transoid* angles [142.47(16) and 146.87(17)°] in the basal plane deviate greatly from the ideal value. Again, the range in all the *cisoid* angles is significantly wide [69.59(14)–142.47(16)°], which indicates appreciable distortion of the coordination environment. The average deviation of the four oxygen atoms and the displacement of the metal ion from the least-squares O(2)O(5)O(6)O(7) plane are 0.246 and 0.352 Å, respectively, which are in line with a large distortion. For the trigonal-bipyramidal coordination geometry, two phenoxido oxygen atoms, O(1) and O(2), and one water oxygen atom, O(7), define the triangular plane, and the other two water oxygen atoms, O(5) and O(6), are in the apical positions. Although the bond angle [172.90(13)°] involving the apical atoms does not deviate much from 180°, the O–Mn–

O angles involving the donor centres in the triangular plane vary greatly [69.59(14)–146.87(17)°], which indicates that the trigonal-bipyramidal geometry is significantly distorted. The copper(II)···manganese(II) separation in the dinuclear core is 3.218 Å, while the phenoxido bridge angles Cu(1)–O(1)–Mn(1) and Cu(1)–O(2)–Mn(1) are 103.37(18) and 104.12(18)°, respectively. Considering the square-pyramidal geometry of the manganese(II) centre, the dihedral angle between the basal O₄ plane of this environment and the square N₂O₂ plane of the Cu(1) environment is 88.7°, which indicates significant twisting of the bridging core.

Of the three coordinated water molecules, H₂O(5) and H₂O(6) are encapsulated in the O₄ compartment of two different mononuclear [Cu^{II}L] moieties, [Cu^{II}(2)L] and [Cu^{II}(3)L], by forming bifurcated hydrogen bonds with the phenoxido and methoxy oxygen atoms (Figure 3). The geometries of the hydrogen bonds are summarized in Table 4. As the donor···acceptor contacts lie in the range 2.82–3.01 Å, the hydrogen bonds can be considered as moderately strong. The oxygen atom of the encapsulated water molecules H₂O(5) and H₂O(6) are displaced by 1.00 and 1.19 Å, respectively, from the corresponding least-squares O₄ plane, which indicates that the extent of encapsulation is not strong.

Table 4. Geometries (distances in Å and angles in °) of the hydrogen bonds responsible for the encapsulation of water in [{Cu^{II}LMn^{II}(H₂O)₃}{Cu^{II}L}]₂(ClO₄)₂·H₂O (6).

D–H···A	D···A	H···A	D–H···A
O(5)–H(5A)···O(8)	2.840	2.000	104.6
O(5)–H(5A)···O(10)	2.940	2.098	141.3
O(5)–H(5B)···O(9)	2.816	2.019	137.5
O(5)–H(5B)···O(11)	2.846	2.012	142.2
O(6)–H(6A)···O(12)	2.789	1.899	141.0
O(6)–H(6A)···O(14)	3.009	2.176	135.2
O(6)–H(6B)···O(13)	2.844	2.174	123.9
O(6)–H(6B)···O(15)	3.009	2.072	158.3

Clearly, compound **6** is a [2×1+1×2] cocrystal of one dinuclear and two mononuclear units. Two other similar Cu^{II}₃Mn^{II} compounds, [{Cu^{II}L²Mn^{II}(H₂O)₃}{Cu^{II}L²}]₂-(ClO₄)₂ (**9**)^[13] and [{Cu^{II}L³Mn^{II}(H₂O)₃}{Cu^{II}L³}]₂(ClO₄)₂·H₂O·CH₃COCH₃ (**10**)^[15] derived from *N,N'*-ethylenebis(3-ethoxysalicylaldehyde) (H₂L²) and *N,N'*-o-phenylenebis(3-ethoxysalicylaldehyde) (H₂L³), respectively, have been previously reported. It may be mentioned that all the structural parameters of the coordination environments and bridging core in **6** are almost identical to those in compounds **9** and **10**.

Syntheses, Characterization, Composition and Proposed Structures

Reactions of [Cu^{II}L] with perchlorate salts of copper(II), nickel(II), cobalt(II) and iron(II) produce trinuclear compounds [{Cu^{II}L}₂M^{II}(H₂O)₂](ClO₄)₂·*n*H₂O [**2** (M = Cu, *n* = 0), **3** (M = Ni, *n* = 3), **4** (M = Co, *n* = 0), **5** (M = Fe, *n* = 0)]. It has been possible to determine the single-crystal X-ray structure of compounds **2** and **5**, which have mono-

phenoxido-bridged, trinuclear, triangular arrangement of the three metal ions. Elemental analyses of compound **2** and **5** as well as of compounds **3** and **4** are well matched with those of trinuclear systems with the composition $[\{\text{Cu}^{\text{II}}\text{L}\}_2\text{Cu}^{\text{II}}(\text{H}_2\text{O})_2](\text{ClO}_4)_2 \cdot n\text{H}_2\text{O}$ ($n = 0$ or 3), which indicates a similar type of trinuclear composition for all of these four compounds. The variable-temperature magnetic susceptibility data also fit well to data produced by using trinuclear models (vide infra). It may be mentioned that the composition of the products obtained on reacting $[\text{Cu}^{\text{II}}\text{L}^1]$ with perchlorate salts of copper(II), nickel(II), cobalt(II) and iron(II) are also similar, with the composition $[\{\text{Cu}^{\text{II}}\text{L}^1\}_2\text{M}^{\text{II}}(\text{H}_2\text{O})_2](\text{ClO}_4)_2 \cdot n\text{H}_2\text{O}$ [**7** ($\text{M} = \text{Cu}$, $n = 1$), **8** ($\text{M} = \text{Fe}$, $n = 0$), **11** ($\text{M} = \text{Ni}$, $n = 0$), **12** ($\text{M} = \text{Co}$, $n = 0$)].^[12] As already discussed, although both the Cu^{II}_3 compounds **2** and **7** and both the $\text{Cu}^{\text{II}}\text{Fe}^{\text{II}}\text{Cu}^{\text{II}}$ compounds **5** and **8** have monophenoxido-bridged trinuclear cores, two water molecules in **2** and **5**, derived from H_2L , and in **7** and **8**, derived from H_2L^1 , coordinate in the *trans* and *cis* positions, respectively, of the central metal ion. The $\text{Cu}^{\text{II}}\text{M}^{\text{II}}\text{Cu}^{\text{II}}$ compounds **11** [$\text{M} = \text{Ni}$], and **12** [$\text{M} = \text{Co}$] also have monophenoxido-bridged trinuclear cores with two water molecules coordinated in the *cis* positions of the central metal ion. As the structures of the compounds **2** and **5** and those of compounds **7**, **8**, **11** and **12** have monophenoxido-bridged cores, it will be a logical assumption that the trinuclear cores in the $\text{Cu}^{\text{II}}\text{M}^{\text{II}}\text{Cu}^{\text{II}}$ compounds **3** [$\text{M} = \text{Ni}$] and **4** [$\text{M} = \text{Co}$] are also monophenoxido-bridged. However, with regard to the coordination of the two water molecules in either *cis* or *trans* positions of the central metal ion in **3** and **4**, no assumption should be made.

The composition of the reaction product obtained on reacting H_2L with $\text{Mn}(\text{ClO}_4)_2 \cdot 6\text{H}_2\text{O}$ is different to the trinuclear composition of the compounds obtained on reacting either H_2L or H_2L^1 with perchlorate salts of copper(II), nickel(II), cobalt(II) and iron(II). The elemental analyses of this copper(II)–manganese(II) compound are well matched with the composition $[\{\text{Cu}^{\text{II}}\text{LMn}^{\text{II}}(\text{H}_2\text{O})_3\}\{\text{Cu}^{\text{II}}\text{L}\}_2](\text{ClO}_4)_2 \cdot \text{H}_2\text{O}$ (**6**), which has been verified from its single-crystal X-ray structure. On the other hand, it has not yet been possible to isolate an analytically pure copper(II)–manganese(II) compound derived from H_2L^1 .

The mononuclear compound $[\text{Cu}^{\text{II}}\text{LC}(\text{H}_2\text{O})]$ (**1**) exhibits two medium intensity bands at 3537 and 3502 cm^{-1} , which can be assigned to the asymmetric and symmetric stretching of the water molecule. As the two stretching bands are separated, it seems that the water molecule in this compound is encapsulated in the O_4 compartment by forming hydrogen bonds with the phenoxido and methoxy oxygen atoms.^[13] The stretching bands of the water molecules in **2–6** appear as a medium intensity broad bands centred at 3355, 3386, 3406, 3362 and 3385 cm^{-1} , respectively. Four medium or weak intensity bands in the range 2853–3051 cm^{-1} in the spectrum of **1** and three medium or weak intensity signals in the range 2837–3067 cm^{-1} in the spectra of **2–6** can be assigned to C–H vibrations. The characteristic strong C=N stretching in **1–6** vary between 1625 and 1631 cm^{-1} . The presence of perchlorate groups in **2–6** is indicated by the

appearance of two strong intensity bands in the ranges 1064–1084 cm^{-1} and 1087–1118 cm^{-1} and a weak intensity band in the range 623–627 cm^{-1} .

Magnetic Properties

Variable-temperature (2–290 K) $\chi_{\text{M}}T$ vs. T plots for compounds **2–6** are shown in Figure 4. For the Cu^{II}_3 (**2**) and $\text{Cu}^{\text{II}}_3\text{Mn}^{\text{II}}$ (**6**) compounds, the observed $\chi_{\text{M}}T$ values at 290 K (0.98 and 5.20 $\text{cm}^3\text{mol}^{-1}\text{K}$, respectively) is less than the theoretical $\chi_{\text{M}}T$ values expected for isolated paramagnetic centres (1.13 and 5.50 $\text{cm}^3\text{mol}^{-1}\text{K}$, respectively). In contrast, in the cases of the $\text{Cu}^{\text{II}}\text{Ni}^{\text{II}}\text{Cu}^{\text{II}}$ (**3**), $\text{Cu}^{\text{II}}\text{Co}^{\text{II}}\text{Cu}^{\text{II}}$ (**4**) and $\text{Cu}^{\text{II}}\text{Fe}^{\text{II}}\text{Cu}^{\text{II}}$ (**5**) compounds, the observed $\chi_{\text{M}}T$ values at 290 K (1.96, 3.63 and 4.26 $\text{cm}^3\text{mol}^{-1}\text{K}$, respectively) are greater than the theoretical $\chi_{\text{M}}T$ values expected for isolated paramagnetic centres (1.75, 2.63 and 3.75 $\text{cm}^3\text{mol}^{-1}\text{K}$, respectively). On lowering the temperature from 290 K, the $\chi_{\text{M}}T$ value for all five complexes **2–6** decreases to 0.38, 0.01, 0.36, 1.12 and 3.21 $\text{cm}^3\text{mol}^{-1}\text{K}$, respectively, at 2 K. The $\chi_{\text{M}}T$ vs. T profiles of **2–6** indicate the existence of weak antiferromagnetic interactions in these systems.

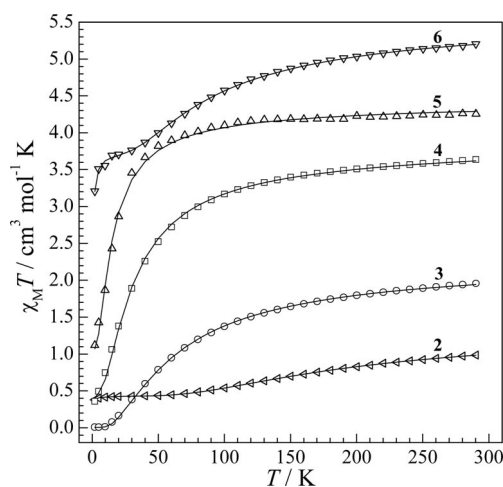


Figure 4. $\chi_{\text{M}}T$ vs. T plots for the compounds Cu^{II}_3 (**2**), $\text{Cu}^{\text{II}}\text{Ni}^{\text{II}}\text{Cu}^{\text{II}}$ (**3**), $\text{Cu}^{\text{II}}\text{Co}^{\text{II}}\text{Cu}^{\text{II}}$ (**4**), $\text{Cu}^{\text{II}}\text{Fe}^{\text{II}}\text{Cu}^{\text{II}}$ (**5**) and $\text{Cu}^{\text{II}}_3\text{Mn}^{\text{II}}$ (**6**). The solid lines represent the corresponding simulated curves.

As already discussed, the two pairs of terminal–central metal ions in the Cu^{II}_3 (**2**) and $\text{Cu}^{\text{II}}\text{Fe}^{\text{II}}\text{Cu}^{\text{II}}$ (**5**) compounds are monophenoxido-bridged with identical metrical parameters for both terminal–central pairs in both compounds, while the two terminal metal ions are not interlinked by any bridge. Therefore, the magnetic exchange interaction between the two pairs of terminal and central metal ions in **2** and **5** should be identical, while the interaction between the two terminal ions may be considered as negligible. It has also already been discussed that the trinuclear cores in the $\text{Cu}^{\text{II}}\text{Ni}^{\text{II}}\text{Cu}^{\text{II}}$ (**3**) and $\text{Cu}^{\text{II}}\text{Co}^{\text{II}}\text{Cu}^{\text{II}}$ (**4**) compounds may be approximated as being similar to those in **2** and **5**. Therefore, the exchange pathways in **3** and **4** may be considered as being similar to those in **2** and **5**. Clearly, the magnetic behaviour of the Cu^{II}_3 (**2**) compound can be modelled by the Hamiltonian Equation (Equation 1). On the other

hand, by considering the single-ion zero-field effect of Ni^{II}, Co^{II} and Fe^{II}, the magnetic behaviour of the Cu^{II}M^{II}Cu^{II} (3–5) compounds can be modelled by the Hamiltonian Equation (Equation 2).

$$H = -2J(S_1 \cdot S_2 + S_2 \cdot S_3) \quad (1)$$

$$H = -2J(S_1 \cdot S_2 + S_2 \cdot S_3) + D(S_{Z,2}^2) - 1/3[S_2(S_2 + 1)] \quad (2)$$

With these models, the susceptibility data were fitted by using the program JULX.^[23] A fixed value for the temperature-independent paramagnetism (*TIP*) for a particular complex was used in the simulations. Again, as required, the Weiss constant (θ) parameter was used in the case of the Cu^{II}₃ (2) compound. As shown by the solid lines in Figure 4, the susceptibility data are well simulated with the following sets of converging parameters: Cu^{II}₃ (2) $J = -78.9 \text{ cm}^{-1}$, $g = 2.13$, $\theta = -0.186 \text{ K}$, $TIP = 180 \times 10^{-6} \text{ cm}^3 \text{ mol}^{-1}$; Cu^{II}Ni^{II}Cu^{II} (3) $J = -22.8 \text{ cm}^{-1}$, $g = 2.227$, $|D| = 0.053 \text{ cm}^{-1}$, $TIP = 220 \times 10^{-6} \text{ cm}^3 \text{ mol}^{-1}$; Cu^{II}Co^{II}Cu^{II} (4) $J = -7.9 \text{ cm}^{-1}$, $g = 2.459$, $|D| = 8.199 \text{ cm}^{-1}$, $TIP = 220 \times 10^{-6} \text{ cm}^3 \text{ mol}^{-1}$; Cu^{II}Fe^{II}Cu^{II} (5) $J = -3.0 \text{ cm}^{-1}$, $g = 2.156$, $|D| = 0.002 \text{ cm}^{-1}$, $TIP = 120 \times 10^{-6} \text{ cm}^3 \text{ mol}^{-1}$. It may be mentioned that if D in 4 and θ in 2 are not considered in the simulations, the values of J and g remain almost identical, but the calculated profiles deviate from the observed data in the lower-temperature region, below 10 K for 4 and below 60 K for 2.

In the case of the Cu^{II}₃Mn^{II} (6) compound, although the copper(II) and manganese(II) ions in the dinuclear core should be coupled, the magnetic exchange interactions between the manganese(II) ion in the dinuclear core and the copper(II) ions in the two mononuclear moieties should either be negligible or weak because these metal ions are separated, Cu(mononuclear)–O(phenoxido)–H–O(water)–Mn(dinuclear), and the Mn(dinuclear)–H–O(water)–Cu(mononuclear) separations are significantly longer, 4.08 and 5.01 Å. By considering a molecular field approximation (zJ') for the possible weak Cu(mononuclear)–O(phenoxido)–H–O(water)–Mn(dinuclear) interaction and the same value for the magnetic moment (μ_{Cu}) of the copper(II) centres in the mononuclear fragments, the theoretical expression for the molar magnetic susceptibility (χ_M) of a system with one exchange-coupled Cu^{II}Mn^{II} ($H = -2JS_1 \cdot S_2$) and two mononuclear copper(II) moieties can be derived as Equation (3).^[13,15]

$$\chi_M = \frac{\chi_M^1}{1 - 2zJ'\chi_M^1 / N\beta^2 g^2} \quad (3)$$

where

$$\chi_M^1 = \frac{7.997\chi_D T + 2\mu_{\text{Cu}}^2}{7.997T}$$

and

$$\chi_D = \frac{N\beta^2 g^2}{kT} \frac{10 + 28e^{6J/kT}}{5 + 7e^{6J/kT}}$$

As shown by the solid lines in Figure 4, the observed susceptibility data of compound 6 fit well to Equation (3)

and result in $J = -15.2 \text{ cm}^{-1}$, $g = 2.000$, $zJ' = -0.05 \text{ cm}^{-1}$, $\mu_{\text{Cu}} = 1.73 \text{ B.M. (fixed)}$ and $TIP = 180 \times 10^{-6} \text{ cm}^3 \text{ mol}^{-1}$ (fixed). It may be mentioned that if zJ' is not considered in the simulation, the values of J and g change slightly to -12.8 cm^{-1} and 1.97, respectively. However, the matching of the observed and calculated data in the lower-temperature region, below 15 K, is poor in the simulation that does not take zJ' into account.

To the best of our awareness, both the single-crystal X-ray structures and the magnetic properties of the three monophenoxido-bridged Cu^{II}₃ compounds have been reported previously.^[12,24] Of these three, the structure of [$\{\text{Cu}^{\text{II}}\text{L}^1\}_2\text{Cu}^{\text{II}}(\text{H}_2\text{O})_2\}(\text{ClO}_4)_2 \cdot \text{H}_2\text{O}$ (7) is comparable to that of [$\{\text{Cu}^{\text{II}}\text{L}\}_2\text{Cu}^{\text{II}}(\text{H}_2\text{O})_2\}(\text{ClO}_4)_2$ (2); as already discussed, the bridging cores of both are twisted by an almost identical extent.^[12] In 7, the two J values of -97.6 cm^{-1} and -89.5 cm^{-1} correspond to the bridge angles $129.84(13)$ and $121.10(12)^\circ$, respectively. The Cu–O(phenoxido)–Cu bridge angle [$117.11(18)^\circ$] in the two symmetry-related exchange-coupled pairs in 2 is slightly less than those in 7, and therefore the slightly weaker antiferromagnetic interactions in 2 ($J = -78.9 \text{ cm}^{-1}$) than those in 7 are in excellent agreement with the dependency of the exchange integral on the bridge angle for systems with identically twisted bridging moieties.

As already discussed, in spite of the *cis* vs. *trans* coordination modes of the two water molecules, both the phenoxido bridge angles (θ) and the dihedral angles (δ) between the square plane of the terminal metal ion and the basal plane of the central metal ion are not very different in the two Cu^{II}₃ compounds 2 and 7 derived from H₂L and H₂L¹, respectively.^[12] It has also already been discussed that the phenoxido bridge angles in the two Cu^{II}Fe^{II}Cu^{II} compounds 5 and 8, derived from H₂L and H₂L¹, respectively, are almost identical. Again, the trinuclear cores in both 5 and 8 are significantly twisted. Moreover, the phenoxido bridge angle and the twisting of the bridging cores in all the structurally characterized monophenoxido-bridged trinuclear compounds derived from H₂L and H₂L¹ are comparable: 2 (Cu^{II}₃) $\theta = 117.11(18)^\circ$, $\delta = 39.9^\circ$; 7 (Cu^{II}₃) $\theta = 129.84(13)^\circ$ and $121.10(12)^\circ$, $\delta = 36.3^\circ$ and 58.5° ; 5 (Cu^{II}–Fe^{II}–Cu^{II}) $\theta = 120.6(3)^\circ$, $\delta = 32.3^\circ$; 8 (Cu^{II}–Fe^{II}–Cu^{II}) $\theta = 121.15(16)$ and $122.76(16)^\circ$, $\delta = 49.7$ – 75.1° ; 11 (Cu^{II}–Ni^{II}–Cu^{II}) $\theta = 123.18(12)$ and $125.72(12)^\circ$, $\delta = 47.6$ – 58.5° ; 12 (Cu^{II}–Co^{II}–Cu^{II}) $\theta = 122.02(16)$ and $124.20(16)^\circ$, $\delta = 48.4$ – 58.8° .^[12] Because of all these structural similarities, it seems that the bridge angles and extent of twisting in the Cu^{II}–Ni^{II}–Cu^{II} (3) and Cu^{II}–Co^{II}–Cu^{II} (4) compounds derived from H₂L should be very close to those in the corresponding compounds 11 and 12, respectively, derived from H₂L¹.^[12] This structural similarity actually exists because the values of the exchange integral for the two structurally characterized Cu^{II}Fe^{II}Cu^{II} compounds (5 and 8) as well as for the corresponding Cu^{II}M^{II}Cu^{II} compounds (M = Ni and Co) derived from the two ligands are very close ($J = -22.8 \text{ cm}^{-1}$ for 3 and -25.4 cm^{-1} for 11; $J = -7.8 \text{ cm}^{-1}$ for 4 and -9.0 cm^{-1} for 12; $J = -3.0 \text{ cm}^{-1}$ for 5 and -6.5 cm^{-1} for 8).^[12] In both the series, as expected from the symmetry of the magnetic orbitals, the order of the magnitude of the antifer-

romagnetic interactions is $\text{Cu}^{\text{II}}_3 > \text{Cu}^{\text{II}}\text{Ni}^{\text{II}}\text{Cu}^{\text{II}} > \text{Cu}^{\text{II}}\text{Co}^{\text{II}}\text{Cu}^{\text{II}} > \text{Cu}^{\text{II}}\text{Fe}^{\text{II}}\text{Cu}^{\text{II}}$ and can be explained on the basis of magnetic orbitals.^[12] On the other hand, the J value of -15.1 cm^{-1} in the dinuclear $\text{Cu}^{\text{II}}\text{Mn}^{\text{II}}$ core in the self-assembled $\text{Cu}^{\text{II}}_3\text{Mn}^{\text{II}}$ (**6**) compound does not fit, in the order of the exchange integrals of the trinuclear compounds because of the difference in the structures. However, the nature and extent of interactions in **6** are almost identical with those in the similar two previously published $[2 \times 1 + 1 \times 2]$ compounds, $[\{\text{Cu}^{\text{II}}\text{L}^2\text{Mn}^{\text{II}}(\text{H}_2\text{O})_3\}\{\text{Cu}^{\text{II}}\text{L}^2\}_2](\text{ClO}_4)_2$ (**9**) and $[\{\text{Cu}^{\text{II}}\text{L}^3\text{Mn}^{\text{II}}(\text{H}_2\text{O})_3\}\{\text{Cu}^{\text{II}}\text{L}^3\}_2](\text{ClO}_4)_2 \cdot \text{H}_2\text{O} \cdot \text{CH}_3\text{COCH}_3$ (**10**), derived from $\text{H}_2\text{L}^{\text{OEt}}$ -type ligands.^[13,15]

Conclusions

As far as we know, compound **2** is among a few rare examples of monophenoxido-bridged tricopper(II) compounds. On the other hand, the monophenoxido-bridged $\text{Cu}^{\text{II}}\text{M}^{\text{II}}\text{Cu}^{\text{II}}$ compounds **3–5** are only the second examples of such systems. All these four compounds **2–5** exhibit weak or moderate antiferromagnetic interactions. Although the crystal quality of **5** was not good, the structure determined is unambiguous. Again, although it has not been possible to get diffraction quality crystals of **3** and **4**, their structures have been qualitatively understood from comparison of the structures and magnetic behaviour of related compounds. A qualitative understanding of the structure of **5** could also be made in a similar way. While magneto-structural correlations are mainly focused to correlate exchange integrals with structural parameters, the trinuclear series derived from H_2L and H_2L^1 demonstrate nice examples for correlating the structures, at least the bridging cores, and the magnetic properties.

The main objective of the present investigation was to explore the 3d–3d dimetallic compounds derived from 3-methoxysalicylaldehyde diamine Schiff base ligands with an aim to explore whether, similar to that in complexes derived from 3-ethoxysalicylaldehyde diamine ligands, the second metal ion could be coordinated to a water molecule, which, in turn, may interact with the phenoxido and methoxy oxygen atoms to result in the formation of dinuclear–mononuclear cocrystals. Although the second metal centres in all of the compounds **2–6** contain coordinated water molecules, compounds **2–5** are not cocrystals but discrete trinuclear systems. On the other hand, the $\text{Cu}^{\text{II}}_3\text{Mn}^{\text{II}}$ compound **6** is a $[2 \times 1 + 1 \times 2]$ cocrystal of one dinuclear and two mononuclear units. Although several cocrystals have been stabilized in the $\text{H}_2\text{L}^{\text{OEt}}$ ligand environment, compound **6** represents the sole example of a cocrystal with the $\text{H}_2\text{L}^{\text{OMe}}$ ligand system, which is the major outcome of the present investigation. It may be mentioned that, in contrast to a large number of organic cocrystals, cocrystals of metal complexes are only a few.^[13–15] Further, the design of cocrystals of metal complexes is not an easy task,^[13–15] and, therefore, stabilization of the first cocrystal (**6**) in a $\text{H}_2\text{L}^{\text{OMe}}$ ligand system is an important observation. More complexes derived from H_2L are being explored in our laboratory, which will be published elsewhere.

Experimental Section

Materials and Physical Methods: All reagents and solvents were purchased from commercial sources and used as received. The Schiff base ligand H_2L was prepared by a 2:1 condensation of 3-methoxysalicylaldehyde and *trans*-1,2-diaminocyclohexane in methanol. Elemental (C, H, and N) analyses were performed on a Perkin–Elmer 2400 II analyzer. IR spectra were recorded in the region $400\text{--}4000\text{ cm}^{-1}$ on a Bruker-Optics Alpha-T spectrophotometer with samples as KBr disks. Magnetic susceptibility measurements of **2–6** at 300 K were carried out with a Quantum Design MPMS SQUID magnetometer. Diamagnetic corrections were estimated from Pascal's constant.

Syntheses

[Cu^{II}L(H₂O)] (1): To a stirred suspension of the ligand H_2L (1.91 g, 5 mmol) in methanol (25 mL) was added dropwise an aqueous solution (10 mL) of $\text{Cu}(\text{OAc})_2 \cdot \text{H}_2\text{O}$ (1.0 g, 5 mmol). During the addition, an ash-coloured product began to deposit. After the mixture was stirred for 1 h, the solid was collected by filtration and washed with methanol. The compound was dissolved in a minimum volume of *N,N'*-dimethylformamide. After filtration, the deep-green filtrate was kept at room temperature for slow evaporation. After a few days, the ash-coloured powdered mass that deposited was collected by filtration and washed with methanol. Yield: 2.19 g (95%). $\text{C}_{22}\text{H}_{26}\text{CuN}_2\text{O}_5$ (462.00): calcd. C 57.19, H 5.67, N 6.06; found C 57.32, H 5.55, N 5.98. IR (KBr): $\tilde{\nu} = 3537$ (m) [$\nu_{\text{as}}(\text{H}_2\text{O})$], 3502 (m) [$\nu_{\text{s}}(\text{H}_2\text{O})$], 3051 (w), 2994 (w), 2931 (m), 2853 (w) [$\nu(\text{C–H})$], 1627 (s) [$\nu(\text{C=N})$] cm^{-1} .

[{Cu^{II}L₂Cu^{II}(H₂O)₂}(ClO₄)₂] (2): To a suspension of $[\text{Cu}^{\text{II}}\text{L}(\text{H}_2\text{O})]$ (0.231 g, 0.5 mmol) in acetone (10 mL) was added dropwise whilst stirring an acetone solution (5 mL) of $\text{Cu}(\text{ClO}_4)_2 \cdot 6\text{H}_2\text{O}$ (0.186 g, 0.5 mmol). Immediately, a red solution formed, which was filtered after 0.5 h to remove any suspended particles. The filtrate was then kept at room temperature for slow evaporation. After 24 h, a brown crystalline compound containing diffraction-quality single crystals that deposited was collected and washed with acetone. Yield: 0.255 g (86%). $\text{C}_{44}\text{H}_{52}\text{Cl}_2\text{Cu}_3\text{N}_4\text{O}_{18}$ (1186.46): calcd. C 44.54, H 4.42, N 4.72; found C 44.43, H 4.51, N 4.78. IR (KBr): $\tilde{\nu} = 3355$ (m) [$\nu(\text{H}_2\text{O})$], 3065 (w), 2941 (m), 2850 (w) [$\nu(\text{C–H})$], 1630 (s) [$\nu(\text{C=N})$], 1087 (s), 1064 (s), 623 (w) [$\nu(\text{ClO}_4)$] cm^{-1} .

[{Cu^{II}L₂Ni^{II}(H₂O)₂}(ClO₄)₂·3H₂O] (3): To a stirred suspension of $[\text{Cu}^{\text{II}}\text{L}(\text{H}_2\text{O})]$ (0.1 g, 0.22 mmol) in methanol (10 mL) was added a methanol solution (5 mL) of $\text{Ni}(\text{ClO}_4)_2 \cdot 6\text{H}_2\text{O}$ (0.081 g, 0.22 mmol). The colour of the solution changed to green. The solution was filtered in a long tube, and diethyl ether was diffused slowly into the green filtrate. The container was closed with a stopper and kept at room temperature. After a few days, a green crystalline compound deposited. The upper ether layer was taken out with a dropper, and the lower mixture was then filtered to collect the green crystalline compound. Yield: 0.085 g (59%). $\text{C}_{44}\text{H}_{58}\text{Cl}_2\text{Cu}_2\text{NiN}_4\text{O}_{21}$ (1235.66): calcd. C 42.77, H 4.73, N 4.53; found C 42.66, H 4.86, N 4.60. IR (KBr): $\tilde{\nu} = 3386$ (m) [$\nu(\text{H}_2\text{O})$], 3055 (w), 2941 (m), 2857 (w) [$\nu(\text{C–H})$], 1631 (s) [$\nu(\text{C=N})$], 1115 (s), 1083 (s), 624 (w) [$\nu(\text{ClO}_4)$] cm^{-1} .

[{Cu^{II}L₂Co^{II}(H₂O)₂}(ClO₄)₂] (4): This compound was synthesized following the same procedure as mentioned above for $[\text{Cu}^{\text{II}}\text{L}_2\text{Ni}^{\text{II}}(\text{H}_2\text{O})_2](\text{ClO}_4)_2 \cdot 3\text{H}_2\text{O}$ (**3**). Colour: green. Yield: 0.070 g (54%). $\text{C}_{44}\text{H}_{52}\text{Cl}_2\text{CoCu}_2\text{N}_4\text{O}_{18}$ (1181.61): calcd. C 44.72, H 4.44, N 4.74; found C 44.63, H 4.35, N 4.66. IR (KBr): $\tilde{\nu} = 3406$ (m) [$\nu(\text{H}_2\text{O})$], 3055 (w), 2940 (m), 2850 (w) [$\nu(\text{C–H})$], 1631 (s) [$\nu(\text{C=N})$], 1118 (s), 1083 (s), 624 (w) [$\nu(\text{ClO}_4)$] cm^{-1} .

Table 5. Crystallographic data for the compounds **2**, **5** and **6**.

	2	5	6
Formula	C ₄₄ H ₅₂ Cl ₂ Cu ₃ N ₄ O ₁₈	C ₄₄ H ₅₂ Cl ₂ Cu ₂ FeN ₄ O ₁₈	C ₆₆ H ₈₀ Cl ₂ Cu ₃ MnN ₆ O ₂₄
Formula weight	1186.46	1178.73	1657.82
Crystal colour	brown	grey	brown
Crystal system	monoclinic	monoclinic	triclinic
Space group	<i>C2/c</i>	<i>C2/c</i>	<i>Pi</i>
<i>a</i> [Å]	25.487(5)	25.684(5)	14.114(5)
<i>b</i> [Å]	13.363(4)	13.469(5)	15.816(5)
<i>c</i> [Å]	15.549(5)	15.490(5)	17.701(5)
α [°]	90.00	90.00	87.760(5)
β [°]	117.436(14)	117.97(5)	77.010(5)
γ [°]	90.00	90.00	65.500(5)
<i>V</i> [Å ³]	4700(2)	4733(3)	3497.0(19)
<i>Z</i>	4	4	2
Temperature [K]	293(2)	293(2)	293(2)
2θ [°]	4.04–56.00	5.12–42.32	4.44–46.42
μ [mm ^{−1}]	1.540	1.387	1.237
<i>D</i> _{calcd.} [g cm ^{−3}]	1.677	1.654	1.574
<i>F</i> (000)	2436	2424	1712
Absorption correction	none	none	none
Index ranges	−33 ≤ <i>h</i> ≤ 33 −17 ≤ <i>k</i> ≤ 17 −20 ≤ <i>l</i> ≤ 20	−25 ≤ <i>h</i> ≤ 25 −13 ≤ <i>k</i> ≤ 13 −15 ≤ <i>l</i> ≤ 15	−15 ≤ <i>h</i> ≤ 15 −17 ≤ <i>k</i> ≤ 17 −19 ≤ <i>l</i> ≤ 19
Reflections collected	22054	4922	17742
Independent reflections/ <i>R</i> _{int}	5675/0.2499	2536/0.0485	9962/0.0473
<i>R</i> ₁ ^[a] / <i>wR</i> ₂ ^[b] [<i>I</i> > 2σ(<i>I</i>)]	0.0540/0.1096	0.0820/0.1971	0.0527/0.1167
<i>R</i> ₁ ^[a] / <i>wR</i> ₂ ^[b] (for all <i>F</i> o ²)	0.2001/0.1521	0.1092/0.2236	0.0983/0.1384

[a] $R_1 = [\sum |F_o| - |F_c|]/\sum |F_o|$. [b] $wR_2 = [\sum w(F_o^2 - F_c^2)^2/\sum w(F_o^2)^2]^{1/2}$.

[{Cu^{II}L₂Fe^{II}(H₂O)₂}(ClO₄)₂ (5**):** This compound was synthesized following the same procedure as mentioned above for [{Cu^{II}L₂Cu^{II}(H₂O)₂}(ClO₄)₂ (**2**). Colour: grey. Yield: 0.255 g (86%). C₄₄H₅₂Cl₂Cu₂FeN₄O₁₈ (1178.76): calcd. C 44.83, H 4.45, N 4.75; found C 44.88, H 4.37, N 4.65. IR (KBr): $\tilde{\nu}$ = 3362 (m) [ν (H₂O)], 3067 (w), 2943 (m), 2850 (w) [ν (C–H)], 1631 (s) [ν (C=N)], 1116 (s), 1084 (s), 625 (w) [ν (ClO₄)] cm^{−1}.

[{Cu^{II}LMn^{II}(H₂O)₃}{Cu^{II}L₂}(ClO₄)₂·H₂O (6**):** To a stirred suspension of [Cu^{II}L(H₂O)] (0.231 g, 0.5 mmol) in acetone (15 mL) was added a methanol (15 mL) solution of Mn(ClO₄)₂·6H₂O (0.181 g, 0.5 mmol). The colour of the solution changed to brown. After stirring for few minutes, the solution was filtered to remove any suspended particles, and the brown filtrate was kept at room temperature for slow evaporation. After a few days, a brown crystalline compound containing diffraction-quality single crystals that deposited was collected and washed with acetone. Yield: 0.246 g (89%). C₆₆H₈₀Cl₂Cu₃MnN₆O₂₄ (1657.88): calcd. C 47.82, H 4.86, N 5.07; found C 47.71, H 4.92, N 5.18. IR (KBr): $\tilde{\nu}$ = 3385 (m) [ν (H₂O)], 3053 (w), 2940 (m), 2847 (w) [ν (C–H)], 1625 (s) [ν (C=N)], 1108 (s), 1082 (s), 624 (w) [ν (ClO₄)] cm^{−1}.

Crystal Structure Determination of **2, **5** and **6**:** The crystallographic data of these three compounds are summarized in Table 5. An Enraf–Nonius CAD4 diffractometer was used to collect data for **2**, while the data for **5** and **6** were collected on a Kappa CCD diffractometer. The data were collected at 293 K. For **2**, data collection and reduction were performed with a CAD4 Express Enraf–Nonius programs package and XCAD4, respectively. In the cases of **5** and **6**, the data collection and cell refinement were carried out with COLLECT and SCALEPACK, respectively, while DENZO and SCALEPACK were used for data reduction. All data were corrected for Lorentz-polarisation effects. The three structures were solved by direct methods by using SIR92 and refined by least-squares methods on *F*² with SHELXL-97.^[25] Six carbon atoms of the cyclohexane ring in **2**, four carbon atoms of the cyclohexane

ring in **5** and six carbon atoms of a cyclohexane ring in **6** are disordered over two sites with occupancies of 0.5 for each site. The hydrogen atoms of the water molecules were first located from a difference Fourier map and then refined with constraints. All other hydrogen atoms were inserted at calculated positions with isotropic thermal parameters constrained to be 1.2 times the U_{eq} of the carrier atoms (1.5 times for hydrogen atoms of methyl groups) and refined. The final least-squares refinements (*R*₁) based on *I* > 2σ(*I*) converged to 0.0540, 0.0820 and 0.0527 for **2**, **5** and **6**, respectively. It may be mentioned that the *R*₁ value and 2θ range for the data collection for **5** are not good because of the poor quality of the single crystal; it has not been possible to get a better quality crystal in spite of many efforts. However, as discussed above, the determined structure is obvious. For **2**, as usual, *R*₁ (0.0540) is less than *wR*₂ (0.1096) for the *I* > 2σ(*I*) data. However, it is unusual that *R*₁ (0.2001) is greater than *wR*₂ (0.1521) for all data. It is difficult to explain these unusual values because the weighting scheme is usual in SHELXTL. These unusual values are probably related to many bad intensity data, which can be evidenced from the following values: total reflections 22054; independent reflections 5675; *I* > 2σ(*I*) reflections 2183; *R*_{int}, 0.2499. It should also be mentioned that the structure of **2** can also be solved in the space group *I2/a*, for which *R*₁ (all data) is also greater than *wR*₂ (all data). CCDC-760117 (**2**), 762263 (**5**) and 760118 (**6**) contains the supplementary crystallographic data for this paper. These data can be obtained free of charge from The Cambridge Crystallographic Data Centre via www.ccdc.cam.ac.uk/data_request/cif.

Acknowledgments

Financial support from the Department of Science and Technology, the Government of India (SR/S1/IC-12/2008) is gratefully acknowledged. S. S. thanks the U.G.C., Government of India and S. H. thanks the C.S.I.R., Government of India, for providing fel-

lowships. P. L. thanks the Université Paris Descartes, Laboratoire de Cristallographie et RMN biologiques UMR 8015, Faculté de Pharmacie for X-ray data collection of the single crystals.

- [1] a) O. Kahn, *Molecular Magnetism*, VCH Publications, New York, **1993**; b) R. D. Willet, D. Gatteschi, O. Kahn (Eds.), *Magneto-Structural Correlations in Exchange Coupled Systems*, D. Reidel, Dordrecht, The Netherlands, **1985**; c) C. J. O'Connor (Ed.), *Research Frontiers in Magnetochemistry*, World Scientific, Singapore, **1993**.
- [2] a) R. Winpenny (Ed.), *Single-Molecule Magnets and Related Phenomena*, Springer, **2006**; b) D. Gatteschi, O. Kahn, J. S. Miller and F. Palacio (Eds.), *Magnetic Molecular Materials*, Kluwer Academic Publishers, Dordrecht, **1991**; c) D. B. Amabilino, J. Veciana in *Magnetism: Molecules to Materials II* (Eds.: J. S. Miller, M. Drillon), pp. 1–60, Wiley-VCH, Weinheim, **2001**; d) H. Iwamura, K. Inoue in *Magnetism: Molecules to Materials II* (Eds.: J. S. Miller, M. Drillon), pp. 61–108, Wiley-VCH, Weinheim, **2001**.
- [3] a) J. Ribas, A. Escuer, M. Monfort, R. Vicente, R. Cortés, L. Loam, T. Rojo, *Coord. Chem. Rev.* **1999**, 193–195, 1027–1068; b) M. Verdager, A. Bleu zen, V. Marvaud, J. Vaissermann, M. Seuleiman, C. Desplanches, A. Scuiller, C. Train, R. Garde, G. Galley, C. Lomenech, I. Rosenman, P. Veillet, C. Cartier, F. Vilains, *Coord. Chem. Rev.* **1999**, 190–192, 1023–1047.
- [4] a) S. Fernández-Armas, J. L. Mesa, J. L. Pizarro, J. M. Clemente-Juan, E. Coronado, M. I. Arriortua, T. Rojo, *Inorg. Chem.* **2006**, 45, 3240–3248; b) E. C. Sañudo, T. Cauchy, E. Ruiz, R. H. Laye, O. Roubeau, S. J. Teat, G. Aromí, *Inorg. Chem.* **2007**, 46, 9045–9047; c) K. Suzuki, J. Haines, P. Rabu, K. Inoue, M. Drillon, *J. Phys. Chem. C* **2008**, 112, 19147–19150; d) P. Alborès, E. R. P. Alborès, E. Rentschler, *Inorg. Chem.* **2008**, 47, 7960–7962.
- [5] a) Y.-Z. Zheng, M.-L. Tong, W.-X. Zhang, X.-M. Chen, *Chem. Commun.* **2006**, 165–167; b) G. Seeber, P. Kögerler, B. M. Kar-iuki, L. Cronin, *Chem. Commun.* **2004**, 1580–1581; c) F. E. Sowrey, C. Tilford, S. Wocadlo, C. E. Anson, A. K. Powell, S. M. Bennington, W. Montfroi, U. A. Jayasooriya, R. D. Cannon, *J. Chem. Soc., Dalton Trans.* **2001**, 862–866.
- [6] a) R. Koner, S. Hazra, M. Fleck, A. Jana, C. R. Lucas, S. Mohanta, *Eur. J. Inorg. Chem.* **2009**, 4982–4988; b) Y.-C. Chou, S.-F. Huang, R. Koner, G.-H. Lee, Y. Wang, S. Mohanta, H.-H. Wei, *Inorg. Chem.* **2004**, 43, 2759–2761; c) S. Mohanta, K. K. Nanda, L. K. Thompson, U. Flörke, K. Nag, *Inorg. Chem.* **1998**, 37, 1465–1472.
- [7] J. Manzur, H. Mora, A. Vega, E. Spodine, D. Venegas-Yazigi, M. T. Garland, M. S. E. Fallah, A. Escuer, *Inorg. Chem.* **2007**, 46, 6924–6932.
- [8] a) R. E. P. Winpenny, *Chem. Soc. Rev.* **1998**, 27, 447–452; b) M. Sakamoto, K. Manseki, H. Ōkawa, *Coord. Chem. Rev.* **2001**, 219–221, 379–414.
- [9] a) R. Koner, H.-H. Lin, H.-H. Wei, S. Mohanta, *Inorg. Chem.* **2005**, 44, 3524–3536; b) R. Koner, G.-H. Lee, Y. Wang, H.-H. Wei, S. Mohanta, *Eur. J. Inorg. Chem.* **2005**, 1500–1505.
- [10] J.-P. Costes, F. Dahan, A. Dupuis, *Inorg. Chem.* **2000**, 39, 165–168.
- [11] M. Andruh, D. G. Branzea, R. Gheorghe, A. M. Madalan, *Cryst. Eng. Commun.* **2009**, 11, 2571–2584.
- [12] S. Majumder, R. Koner, P. Lemoine, M. Nayak, M. Ghosh, S. Hazra, C. R. Lucas, S. Mohanta, *Eur. J. Inorg. Chem.* **2009**, 3447–3457.
- [13] M. Nayak, R. Koner, H.-H. Lin, U. Flörke, H.-H. Wei, S. Mohanta, *Inorg. Chem.* **2006**, 45, 10764–10773 and references cited therein.
- [14] S. Sarkar, M. Nayak, M. Fleck, S. Dutta, U. Flörke, R. Koner, S. Mohanta, *Eur. J. Inorg. Chem.* **2010**, 735–743 and references cited therein.
- [15] M. Nayak, S. Hazra, P. Lemoine, R. Koner, C. R. Lucas, S. Mohanta, *Polyhedron* **2008**, 27, 1201–1213 and references cited therein.
- [16] S. Hazra, R. Koner, M. Nayak, H. A. Sparkes, J. A. K. Howard, S. Dutta, S. Mohanta, *Eur. J. Inorg. Chem.* **2009**, 4887–4894.
- [17] a) G. Hoshina, S. Ohba, K. Nakajima, H. Ishida, M. Kojima, M. Tsuchimoto, *Bull. Chem. Soc. Jpn.* **1999**, 72, 1037–1041; b) G. Hoshina, M. Tsuchimoto, S. Ohba, K. Nakajima, H. Vekusa, Y. Ohashi, H. Ishida, M. Kojima, *Inorg. Chem.* **1998**, 37, 142–145; c) R. Kasahara, M. Tsuchimoto, S. Ohba, K. Nakajima, H. Ishida, M. Kojima, *Inorg. Chem.* **1996**, 35, 7661–7665; d) J. R. Zamian, E. R. Dockal, G. Castellano, G. Olive, *Polyhedron* **1995**, 14, 2411–2418.
- [18] a) B. Jing, L. Li, D. Wang, T. Xu, X. Guo, *Acta Cryst.* **2005**, E 61, m2244–m2246; b) H. Schmidt, D. Rehder, *Inorg. Chim. Acta* **1998**, 267, 229–238.
- [19] a) S. Akine, T. Taniguchi, T. Nabeshima, *Chem. Lett.* **2001**, 682–683; b) A. M. Madalan, N. Avarvari, M. Andruh, *New J. Chem.* **2006**, 30, 521–523; c) G. Hoshina, M. Tsuchimoto, S. Ohba, *Bull. Chem. Soc. Jpn.* **2000**, 73, 369–374.
- [20] a) S. Hazra, R. Koner, M. Nayak, H. A. Sparkes, J. A. K. Howard, S. Mohanta, *Cryst. Growth Des.* **2009**, 9, 3603–3608; b) S. Hazra, S. Sasmal, M. Nayak, H. A. Sparkes, J. A. K. Howard, S. Mohanta, *Cryst. Eng. Commun.* **2010**, 12, 470–477; c) M. Nayak, S. Sarkar, P. Lemoine, S. Sasmal, R. Koner, H. A. Sparkes, J. A. K. Howard, S. Mohanta, *Eur. J. Inorg. Chem.* **2010**, 744–752.
- [21] a) S. Akine, T. Taniguchi, T. Nabeshima, *Inorg. Chem.* **2004**, 43, 6142–6144; b) H.-P. Jia, W. Li, Z.-F. Ju, J. Zhang, *Inorg. Chem. Commun.* **2007**, 10, 397–400; c) D. Cunningham, J. F. Gallagher, T. Higgins, P. McArdle, J. McGinley, D. Sheerin, *Chem. Commun.* **1990**, 959–961; d) W.-K. Lo, W.-K. Wong, W.-Y. Wong, J. Guo, *Eur. J. Inorg. Chem.* **2005**, 3950–3954; e) D. G. Branzea, A. Guerri, O. Fabelo, C. Ruiz-Pérez, L.-M. Chamoreau, C. Sangregorio, A. Caneschi, M. Andruh, *Cryst. Growth Des.* **2008**, 8, 941–949.
- [22] a) N. Atkinson, A. J. Blake, M. G. B. Drew, G. Forsyth, R. O. Gould, A. J. Lavery, G. Reid, M. Schröder, *J. Chem. Soc., Dalton Trans.* **1992**, 2993–3002; b) A. J. Bridgeman, M. A. Halcrow, M. Jones, E. Krausz, N. K. Solanki, *Chem. Phys. Lett.* **1999**, 314, 176–181; c) M. Atanasov, M. A. Hitchman, R. Hoppe, K. S. Murray, B. Moubaraki, D. Reinen, H. Strate-meier, *Inorg. Chem.* **1993**, 32, 3397–3401.
- [23] E. Bill, *JULX 1.4: A Program for Simulation of Molecular Magnetic Data*, Mülheim/Ruhr26, Germany, **2008**.
- [24] M. C. Aragoni, M. Arca, A. Bencini, A. J. Blake, C. Caltagirone, G. D. Filippo, F. A. Devillanova, A. Garau, T. Gelbrich, M. B. Hursthouse, F. Isaia, V. Lippolis, M. Mameli, P. Mariani, B. Valtancoli, C. Wilson, *Inorg. Chem.* **2007**, 46, 4548–4559.
- [25] a) A. Altomare, G. Cascarano, C. Giacovazzo, A. Guagliardi, M. C. Burla, G. Polidori, M. Camalli, *J. Appl. Cryst.* **1994**, 27, 435–436; b) G. M. Sheldrick, *SHELXL-97: A Program for Crystal Structure Refinement*, University of Göttingen, Germany, **1997**.

Received: January 20, 2010
Published Online: May 27, 2010

Examination of Water Oxidation by Catalysts Containing Cofacial Metal Sites

Derek J. Wasylenko,^[a] Chelladurai Ganesamoorthy,^[a] Bryan D. Koivisto,^[a] and
Curtis P. Berlinguette^{*[a]}

Keywords: Homogenous catalysis / Water splitting / Ruthenium / Energy conversion / Kinetics

A series of bimetallic complexes were developed to examine how the distance between two juxtaposed $\{\text{Ru}(\text{tpy})(\text{bpy})\text{Cl}\}^{1+}$ (**2**; tpy = 2,2',6',2''-terpyridine; bpy = 2,2'-bipyridine) units affect catalytic behavior in the context of water oxidation. The directionality imposed by the organic backbone for each of these "Pacman" complexes elicits idealized M...M distances of ca. 5, 10, and 12 Å for **4–6**, respectively. Cyclic voltammetry indicates that intramolecular electronic communication occurs between the metal sites of **4**, while the metal fragments are essentially electrochemically isolated for **5** and **6**. Despite the disparate distances between the metal sites, each of these complexes are shown to mediate the Ce^{IV} -driven oxidation of water in acidic media. Dioxygen evolution was monitored with an optical probe in the headspace of the reaction vessel, and independently verified by the detection of appropriate ratios of ^{18}O - ^{18}O , ^{18}O - ^{16}O , and ^{16}O - ^{16}O in GC-MS experiments using ^{18}O -labeled water. A fitting of the dioxygen evolution data indicates catalytic behavior that

is first-order with respect to catalyst concentration in all cases. This finding rules out the possibility that dioxygen formation occurs independently at each metal site simultaneously, and leaves open the possibility that O–O bond formation occurs by either both metal sites acting cooperatively, or at one metal site independent of the other. Taking into account the significant electrostatic repulsion between the two metal fragments in higher oxidation levels, we contend that the latter mechanism is the more likely scenario. Notwithstanding, complex **4** generates the largest k_{obs} values among the bimetallic series, which suggests that the close proximity of another metal may benefit catalysis. A comparison of k_{obs} and catalytic turnover numbers (TONs) of the bimetallic systems to the mononuclear complex **2**, however, does not indicate an improvement in catalytic behavior. This is an important observation in the collective pursuit of efficient water oxidation catalysts.

Introduction

The oxidation of water is a thermodynamically demanding process ($E^\circ = +1.23$ V at pH = 0) that requires a number of bond-breaking/making steps involving multiple electrons and protons.^[1,2] Drawing from the observation that the oxygen-evolving complex (OEC) within the photosynthetic apparatus is able to negotiate this process efficiently with four Mn centres,^[3] the vast majority of documented synthetic water oxidation catalysts have been designed to contain multiple metal centres,^[4–14] including the extensively studied "blue dimer" *cis,cis*- $[(\text{bpy})_2(\text{H}_2\text{O})\text{Ru}^{\text{III}}\text{ORu}^{\text{III}}(\text{OH}_2)(\text{bpy})_2]^{4+}$ (**1**; Figure 1).^[15,16] This singular approach has, however, been refuted in recent studies that have demonstrated that two metal centres are not necessary to mediate dioxygen formation.^[17–21] Indeed, there is a rapidly growing number of reports of mononuclear catalysts of various metal identities.^[22] A particularly noteworthy result is the recent finding that the simple coordination complex $[\text{Ru}(\text{tpy})(\text{bpy})\text{Cl}]^{1+}$ (**2**) is an effective water

oxidation catalyst in acidic media.^[19] Although it was subsequently shown that the catalytically active form of **2** is $[\text{Ru}(\text{tpy})(\text{bpy})(\text{OH}_2)]^{2+}$ (**3**) in aqueous media,^[17,18] this finding represents an important advancement because the efficiency and stability of the catalyst can be systematically manipulated to gain insight into mechanistic and decomposition pathways.^[17,23]

The recognition that mononuclear complexes **2** and **3** are capable of catalytically oxidizing water raises an important question: Does a second proximate metal centre benefit the activity and/or stability of the catalyst? To help resolve this issue, we report herein a set of related bimetallic systems with juxtaposed units of **2**. Our strategy relies on the set of ligand frameworks 2,7-di-*tert*-butyl-9,9-dimethyl-4,5-diterpyridinylxanthene (DTX), 4,6-diterpyridinyl-dibenzofuran (DTD), and 4,6-bis(diethynylterpyridinyl)dibenzofuran (DETD), which juxtapose $\{\text{Ru}(\text{tpy})(\text{bpy})\text{Cl}\}^{1+}$ units to afford complexes **4–6**, respectively (Figure 1). Inspired by the "Pacman" architectures developed by Nocera^[24,26] and others,^[10,27,28] each ligand elicits progressively larger M...M distances for the series (M...M \approx 5, 10, and 12 Å for **4–6**, respectively;^[29] Figure 2) within the flexible molecular cleft, which accommodates substrate binding, activation and release. Note that **4** bears a structural resemblance to the

[a] Department of Chemistry, University of Calgary
2500 University Drive NW, Canada
Fax: +1-403-289-9488
E-mail: cberling@ucalgary.ca

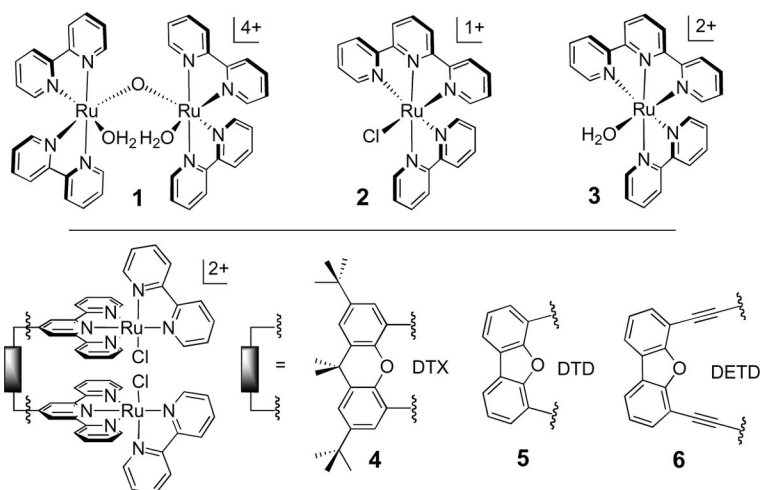


Figure 1. Representations of the molecular systems under investigation (counterion is ClO_4^- for **1**, PF_6^- for **2–6**^[24,25]).

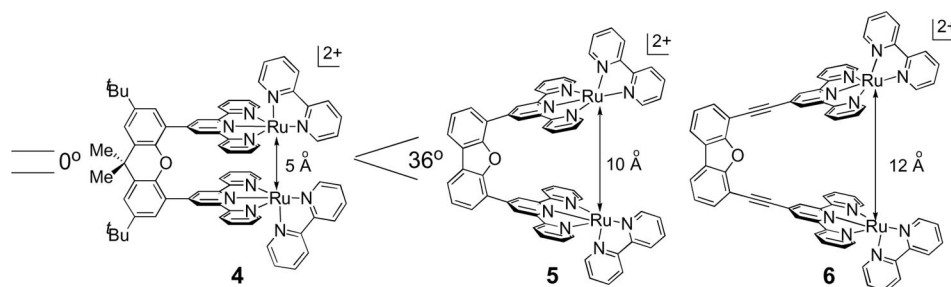
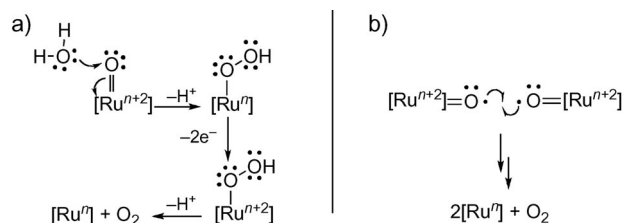


Figure 2. Depiction of approximate Ru...Ru distances in complexes **4–6** modeled using idealized geometries.

water oxidation catalyst reported by Tanaka et al., which contains a semiquinone ligand in place of the bpy ligand;^[30,31] compound **5** was subsequently reported by Nocera et al. to evolve dioxygen.^[24]

While we show herein that each of these complexes are competent water oxidation catalysts, the primary goal of this study is to gain insight into how reaction rates and TONs are affected by intramolecular metal proximity while holding the electronic structure nearly constant. We are also interested in determining whether the requisite O–O bond formation for systems of this type occurs via a nucleophile/electrophile (NE) mechanism (Scheme 1), or by the direct coupling of M=O units (e.g., radical coupling).^[24,32] The NE mechanism, which involves nucleophilic attack of a high-valent M=O unit by an incoming water molecule, has been shown by Meyer et al. to be the dominant reaction pathway in a series of mononuclear complexes related to **3**.^[20,23] In the realm of bimetallic catalysis, there is evidence by Llobet et al. that the direct interaction of M=O fragments promotes the formation of an O–O bond.^[32,33] While the ligand system in the Llobet catalyst appears to accommodate this scenario by forcing the appropriate geometric constraints on the M=O vectors to be in close proximity, it remains an open question whether the antiparallel M=O vectors of **4–6** are amenable to the same mechanism. This study attempts to unravel these two possibilities, and to as-

sess whether a second metal in close proximity actually benefits catalysis. These findings provide some important insight for the rational design of water oxidation catalysts.

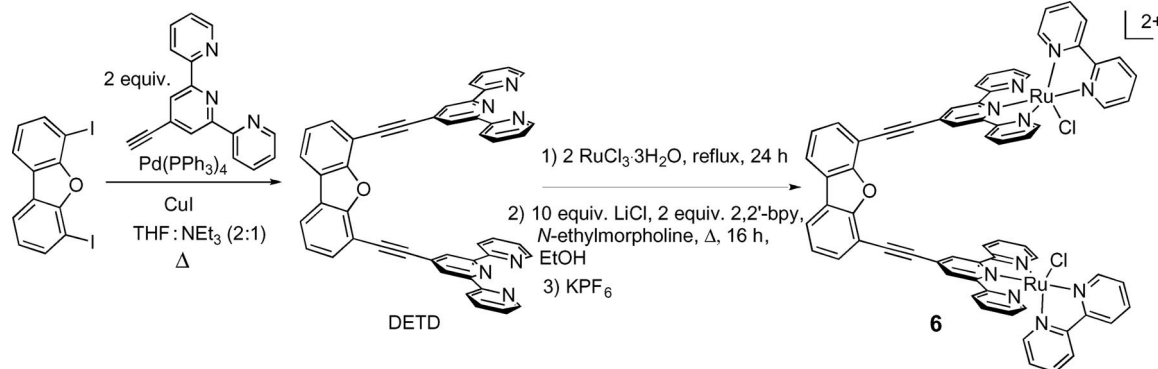


Scheme 1. Proposed mechanistic pathways summarizing dioxygen formation via (a) a nucleophile/electrophile (NE) mechanism, or (b) the direct coupling of Ru=O units.^[24,32]

Results and Discussion

Synthesis and Characterization

As part of our effort to increase the activity and long-term viability of **2**, and to gain further insight into the mechanism of water oxidation, we isolated a set of ligand frameworks DTX, DTD, and DETD that situate {Ru(tpy)-(bpy)Cl}¹⁺ units opposite to each other to afford complexes **4–6**, respectively (see Figures 1 and 2). The synthesis of the



Scheme 2. Reaction scheme summarizing the preparation of **6**.

DTX ligand follows a convergent synthetic approach documented by Tanaka et al.,^[4] while a similar Suzuki–Miyaura cross-coupling scheme furnishes the organic framework DTD. An analogous Pd-mediated Hagihara–Sonogashira approach involving 4'-ethynylterpyridine and diiododibenzofuran renders the DETD ligand in high yield (Scheme 2). The corresponding metal complexes **4–6** were isolated after the stepwise treatment of the respective organic framework with the successive addition of two equivalents of RuCl_3 and bpy. Each of the complexes were purified by column chromatographic techniques.

The structural identities of all complexes were confirmed by ^1H NMR spectroscopy and high-resolution mass spectrometry (HR-MS). Complex **4** adopts C_{2v} symmetry on the basis of the ^1H -NMR spectrum, while molecular modeling studies on this compound indicate opposed Ru–Cl vectors – an arrangement that minimizes steric congestion between the bpy capping ligands. Steric hindrance between the tpy components serve to minimize rotation of the $\{\text{Ru}(\text{tpy})(\text{bpy})\text{Cl}\}^{1+}$ units to yield a scaffold poised for a cooperative interaction of the two metal sites with the incoming substrate(s) upon displacement of the halide ligands. The same cofacial geometry is assumed for **5**, while the flexible alkyne spacers of **6** may facilitate multiple conformations.

Cyclic voltammograms (CVs) of **2** and **4–6** were recorded in MeCN to investigate the electronic communication between metal centres in the absence of aquation (Figure 3). The monometallic chloride derivative **2** shows a reversible one-electron oxidation of Ru^{II} at ca. +1.0 V vs. NHE.^[17] Compounds **5** and **6** do not appear to exhibit a significant level of intramolecular electronic coupling between the metal centres on the basis that they exhibit a similar CV profile to that of **2**. The CVs for **5** and **6**, however, each reveal two overlapping reversible metal-based oxidation processes (i.e., $\text{Ru}^{\text{II/III}}\text{–Cl}/\text{Ru}^{\text{III/III}}\text{–Cl}$) at a modestly higher potential (i.e., ca. 1.1 V) relative to **2**. There is an additional reversible metal-based oxidation process at about +1.5 V assigned to a $\text{Ru}^{\text{II/III}}\text{–MeCN}/\text{Ru}^{\text{III/III}}\text{–MeCN}$ oxidation process that occurs following the displacement of the halide ligand by coordinating solvent. The $\text{Ru}^{\text{II}}/\text{Ru}^{\text{III}}$ redox couple of the solvated analogue **2** (i.e., Ru–MeCN) occurs at roughly this same potential; however, this oxidation step is

more apparent in the bimetallic systems due to the enhanced lability of the halide ligand resulting from the substituent at the 4'-position of the tpy ligand.^[17]

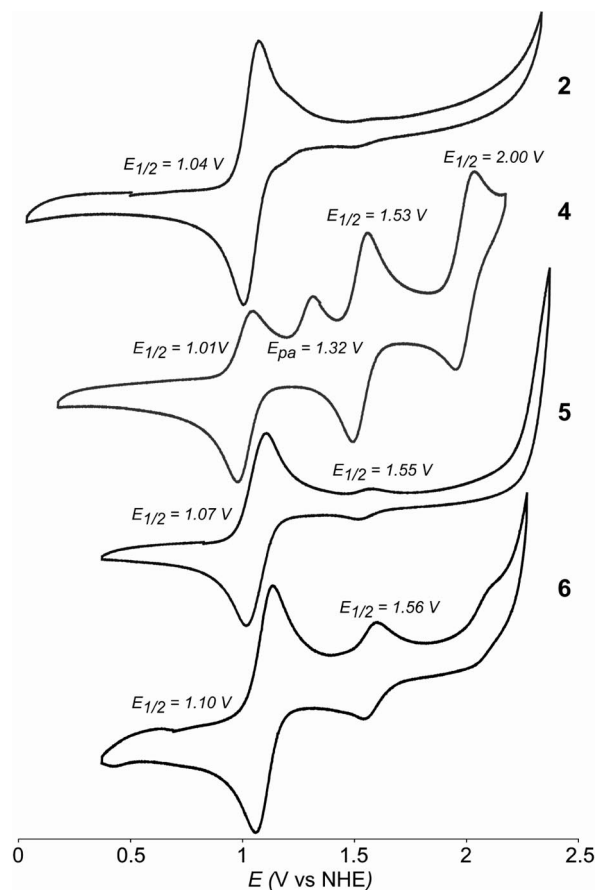


Figure 3. Cyclic voltammograms for **2** and **4–6**. Data collected using 0.1 M $(\text{NBu}_4)(\text{BF}_4)$ MeCN solutions at 100 mV/s and referenced to a $[\text{Fc}]/[\text{Fc}]^+$ internal standard followed by conversion to NHE ($[\text{Fc}]/[\text{Fc}]^+$ vs. NHE: 640 mV);^[35] $V_{\text{oc}} = 0.5\text{--}0.7$ V in all cases.

There appears to be an enhancement of intramolecular communication between the redox active metal for **4**. The CV for **4** reveals a single reversible metal-based oxidation process at ca. +1.0 V vs. NHE. While this process occurs at the same potential as the two-electron oxidation of **5** and **6**, a comparison of peak currents indicates that this oxidation

involves one-electron for **4** (i.e., $\text{Ru}^{\text{II/II}}\text{-Cl/Ru}^{\text{III/II}}\text{-Cl}$). Further divergent electrochemical behavior for **4** is revealed by an irreversible oxidation process that is ascribed to the oxidation of the Cl^- ligands (i.e., $2\text{Cl}^- \rightarrow \text{Cl}_2 + 2\text{e}^-$). This feature is rationalized by taking into account that $\text{Cl}_{2(\text{g})}$ is characterized by a standard reduction potential of ca. +1.4 V^[34] and noting that the geometric constraints of the ligand backbone of **4** could promote this irreversible process by forcing the halide ligands to be in close proximity. Following the loss of $\text{Cl}_{2(\text{g})}$, MeCN binds to the metal leading to a second reversible metal-based oxidation wave at ca. +1.5 V that is assigned to the oxidation of a single Ru centre (i.e., $\text{Ru}^{\text{II/II}}\text{-MeCN/Ru}^{\text{III/II}}\text{-MeCN}$). The accessibility of a third reversible metal-based oxidation process (i.e., $\text{Ru}^{\text{III/II}}\text{-MeCN/Ru}^{\text{IV/III}}\text{-MeCN}$) at ca. +2.0 V is a consequence of the electronic coupling between the two metal centres for **4**. Displacement by solvent is also observed for **5** and **6** on the basis of the observation of oxidation processes at $E_{1/2} > +1.5$ V. Collectively, this redox behavior indicates that **2**, **5** and **6** have similar electronic environments at the metal sites, while the close proximity between the metal sites of **4** generates divergent behavior.

Dioxygen Evolution Studies

Catalytic water oxidation studies were carried out on complexes **1–6** using conditions similar to those outlined elsewhere^[19] namely, a relatively small volume of an MeCN solution containing the catalyst was injected into a 1 M $\text{HClO}_{4(\text{aq})}$ solution containing excess Ce^{IV} as the sacrificial oxidant. A summary of catalytic parameters is listed in Table 1. The onset of dioxygen evolution following the introduction of the catalyst to the aqueous Ce^{IV} solution indicates that the bimetallic systems **4–6** are capable of oxidizing water catalytically. Detection of appropriate relative quantities of ^{18}O - ^{18}O , ^{18}O - ^{16}O , and ^{16}O - ^{16}O in the headspace of the reaction flask using an isotopically-labelled aqueous medium provides verification that the evolved dioxygen is, indeed, derived from water (Figure 4). The possible formation of RuO_2 (a potential decomposition product) was ruled out experimentally^[17] although this species is not expected to exist at the Ru/Ce ratio used in our experiments.^[36,37]

Table 1. Catalytic dioxygen evolution data for **1–6**.^[a]

Catalyst	$k_{\text{obs}}^{[\text{b}]} \times 10^{-4} \text{ s}^{-1}$	TON ^[c]
1	7.7 ^[d]	38
2	3.7	290
3	5.1	320
4	3.6	270
5	2.6	250
6	2.4	240

[a] [catalyst] = $6.7 \times 10^{-5} \text{ M}$; terminal oxidant is $(\text{NH}_4)_2[\text{Ce}(\text{NO}_3)_6]$ (0.33 M in 3 mL of 1 M $\text{HClO}_{4(\text{aq})}$); **2** and **4–6** were first dissolved in a minimum amount of MeCN. [b] Pseudo first-order rate constant obtained by an exponential fitting of the time-dependent dioxygen evolution traces [Equation (1)]. [c] TON: catalytic turnovers after 5 h; defined as mol O_2 generated per mol of catalyst. [d] Initial first-order behaviour for up to 1 h, followed by zero-order behavior for 20 h.^[38]

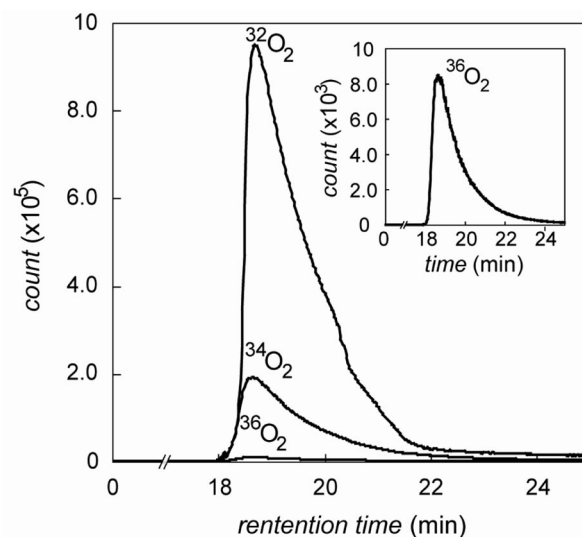


Figure 4. Isotopic distribution of dioxygen formed in the headspace after 3 h with catalyst **6**. The 1 M HClO_4 solution was prepared with ca. 10% ^{18}O -labeled water.

The mononuclear systems **2** and **3** both exhibit kinetic behavior that is first-order with respect to catalyst concentration. Dimeric complexes **4–6** also exhibit first-order behavior with respect to catalyst concentration – or half-order with respect to each Ru site. It is important to note that there is a lag in the onset of dioxygen evolution in the case of **2** because displacement of the halide ligand by a water substrate is required prior to catalysis.^[17] This same lag effect is observed for **4–6**, thereby indicating that the Cl^- ligands are displaced in solution. The k_{obs} values for **3**, which are higher than **2**, demonstrate how halide ligands can suppress catalysis. Thus, the time-dependent dioxygen evolution data was fit to the region following the catalyst induction period. As a consequence, the catalytic parameters in Table 1 are lower than what would be expected for the aqua-substituted analogues.

We note that an accurate determination of the catalytic behavior for **4–6** is made difficult by the limited concentration range that can be used for data collection (represented by horizontal lines in Figure 5). Indeed, the catalysts had to be dissolved in a minimal volume of MeCN prior to addition to the acidic medium. (Note that the presence of this coordinating solvent can suppress activity and lead to artificially low k_{obs} values.) In the case of **4**, the rate of dioxygen evolved as a function of catalyst concentration shows an increasing linear trend consistent with first-order behavior up to ca. 20 μM . Beyond this concentration, the rate of dioxygen evolution is independent of catalyst concentration, which suggests that no further amount of catalyst can be drawn into solution. The k_{obs} values were then extracted by fitting each of the time-dependent dioxygen evolution traces below the saturation point to a first-order exponential Equation (1).^[11]

$$y = y_0[1 - \exp(-kx)] \quad (1)$$

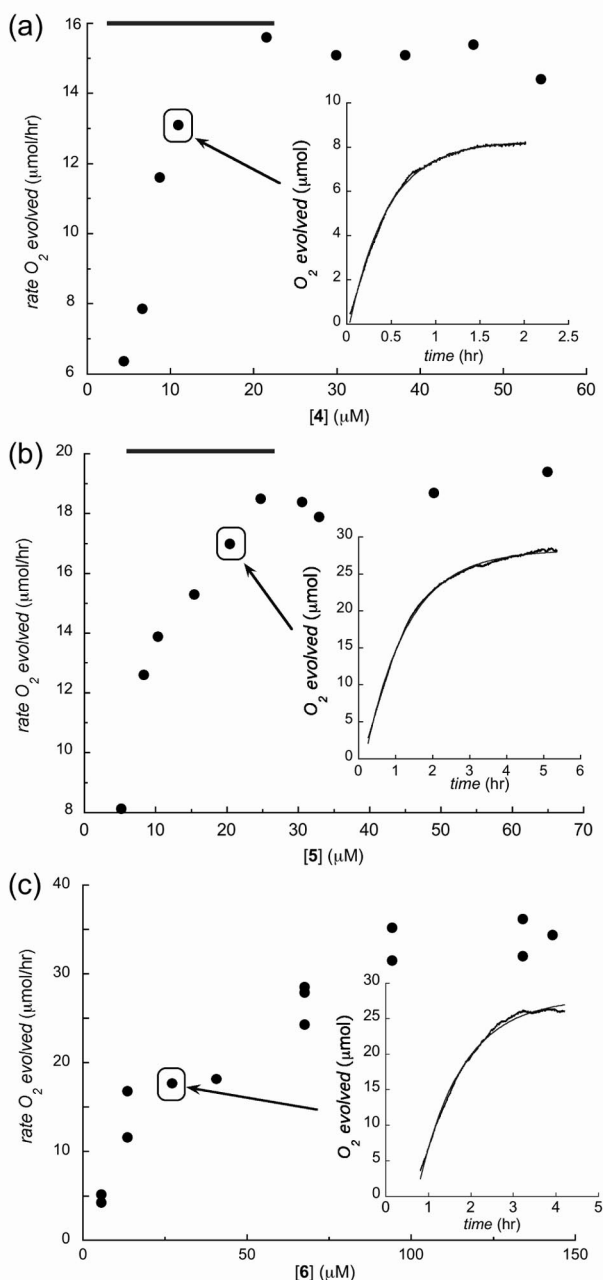


Figure 5. Dependence of initial rates of dioxygen evolution as a function of catalyst concentration for (a) **4**, (b) **5**, and (c) **6**. Horizontal bars indicate concentration range used to determine reaction order for **4** and **5**. *Inset*: Time-dependent dioxygen evolution data for a representative data set (indicated by arrow). The solid line represents a fitting of the trace according to Equation (1).

The calculated k_{obs} values were all within a margin of error of 10%; the fittings all correspond to a first-order exponential with $R^2 > 0.99$. Representative fittings of the data sets are provided in the insets of Figure 5 (a, solid line). A similar treatment was carried out for **5** (Figure 5, b); however, the data point corresponding to the lowest concentration did not produce a reasonable k_{obs} value. Consequently, only the data points within the horizontal bars in Figure 5 (b) gave similar k_{obs} values (Table 1). Data for

6 was anomalous to **4** and **5** in that a fitting of the rate of dioxygen evolved vs. **[6]** did not plateau at higher concentrations. The trend in this data does not follow a strictly linear relationship making it difficult to resolve half- or first-order behavior unambiguously. Notwithstanding, the fitting of the time-dependent dioxygen evolution data below 50 μM clearly indicates first-order behavior. We therefore conclude that solubility remains an issue for **6** despite being more soluble than both **4** and **5**.

There are multiple interpretations of these results, but the observed first-order behavior conclusively rules out both metal centres acting independently in a concomitant fashion. Elimination of this scenario leaves open two other possibilities: (i) a direct coupling of the $\text{M}=\text{O}$ units to form the $\text{O}-\text{O}$ bond; or (ii) $\text{O}-\text{O}$ bond formation occurring at a single metal site via the NE mechanism (Scheme 1). Although the kinetic data does not resolve this point, geometry optimization of **4–6** by DFT suggests that there is significant electrostatic repulsion between the metal sites at higher oxidation levels (Figure 6). Consequently, theory would suggest that the $\text{M}\cdots\text{M}$ distances are too extreme to mediate the direct coupling of the $\text{M}=\text{O}$ units, but extensive calculations by other groups have yet to clearly resolve this issue.^[24,31] Taking into account that similar catalytic parameters are observed for **5** and **6** despite a difference in metal proximity of ca. 2 Å lends support to the notion that the NE mechanism is operative in both cases.

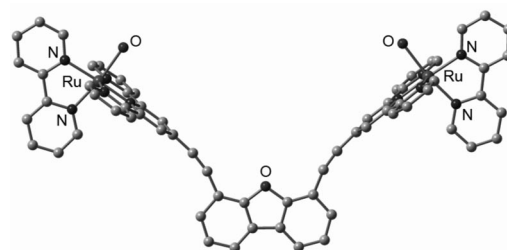


Figure 6. Gas-phase DFT-minimized structure for **6**; $\text{M}\cdots\text{M}$ distance is measured to be ca. 17 Å (H atoms are removed for clarity).

Considering that the reaction rates are all first-order with respect to catalyst concentration but that a direct interaction of the $\text{M}=\text{O}$ units is possible for **4**, the higher k_{obs} value observed for **4** relative to **5** and **6** suggests that one metal site may position an incoming water substrate appropriately relative to the neighboring $\text{Ru}=\text{O}$ unit to minimize electrostatic repulsion. While we postulate that dioxygen formation occurs at a single metal site, we do not rule out the possibility of the adjacent metal undergoing changes in both redox levels.

While the dioxygen evolution reaches a plateau within ca. 2 h for the mononuclear systems, the bimetallic systems continue to generate dioxygen over a period of several hours – albeit at a much slower rate than at $t < 2$ h. Consequently, the bimetallic systems exhibit higher catalytic turnovers over longer time periods (i.e., > 8 h). We postulate that steric congestion suppresses the initial rate of dioxygen evolution (i.e., inhibits substrate binding), but the con-

straints imposed by the organic framework suppress deactivation pathway(s) that exist for the mononuclear systems. Thus, the presence of an adjacent metal fragment may not lead to superior dioxygen evolution rates, but may be beneficial in generating more stable catalysts.

Conclusions

This investigation offers insight into the role of metal proximity for a related series of water oxidation catalysts. While these results seem to suggest that a NE mechanism is operative for catalysts containing cofacial high-valent Ru=O motifs, these principles do not necessarily apply to rigid dimeric Ru catalysts that orient the Ru–O vectors towards each other. A higher initial rate of catalytic activity for **2** endorses the claim that “one site is enough”,^[20] but the bimetallic systems appear to shunt deactivation pathways that exist for the single site catalysts. The development of catalysts optimizing the NE pathway is currently underway.

Experimental Section

Materials: Dry acetonitrile (MeCN), chloroform (CHCl₃), dichloromethane (CH₂Cl₂), *N,N*-dimethylformamide (DMF), methanol (MeOH), and tetrahydrofuran (THF) were obtained after passing these solvents through activated alumina columns on an MBraun solvent purification system (Stratham, NH). All reagents were purchased from Aldrich, except for RuCl₃·3H₂O (Pressure Chemical Company). Column chromatography was carried out using silica (Silicycle: ultrapure flash silica) or basic alumina (Fluka). Analytical thin-layer chromatography (TLC) was performed on aluminum-backed sheets pre-coated with silica 60 F254 adsorbent (0.25 mm thick, Merck, Germany), or with plastic-backed sheets pre-coated with basic alumina 200 F254 adsorbent (0.25 mm thick, Selecto Scientific: Georgia, USA) and visualized under UV light. All NMR spectra were recorded in dry deuterated solvents at ambient temperatures on a Bruker DRY 400 MHz spectrometer operating at 400 MHz. Chemical shifts were reported relative to SiMe₄ (¹H) standard; ¹H peak assignments were unequivocally made by ¹H-¹H COSY 2D experiments. ¹H NMR labels are provided in Figure 7 and a representative ¹H NMR has been provided in Figure 8. Molecular compounds [(bpy)₂(HO₂Ru(μ₂-O)Ru(OH₂)(bpy)₂](ClO₄)₄ (**1**);^[39] [Ru(tpy)(bpy)Cl](PF₆) (**2**), [Ru(tpy)(bpy)(OH₂)](PF₆) (**3**);^[40] 2,7-di-*tert*-butyl-9,9-dimethyl-4,5-bis(2,2':6',2''-

terpyridinyl)xanthene (DTX, **L4**);^[10] 4,6-dibenzofurandiylbis-(boronic acid);^[41] 4'-bromo-2,2':6',2''-terpyridine;^[42] 4,6-diiododibenzofuran;^[43] and 4'-ethynyl-2,2':6',2''-terpyridine^[44] were prepared following existing literature procedures.

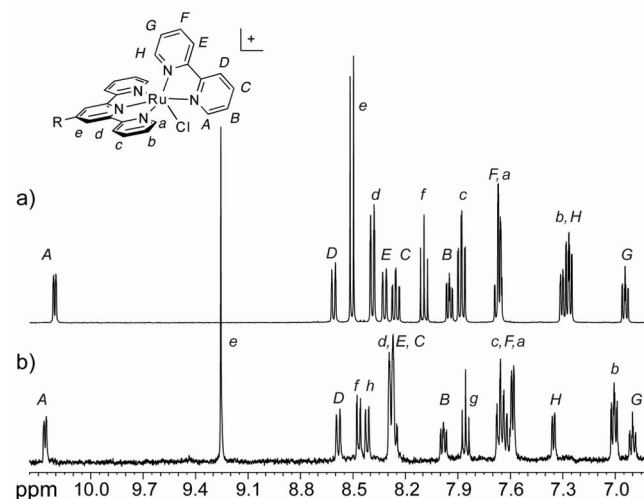


Figure 8. ¹H NMR spectra for a) **2** and b) **5** in CD₃CN.

[DTX-(RuCl₃)₂] (**P4**): DTX (**L4**) (0.50 g, 0.64 mmol) and RuCl₃·3H₂O (0.34 g, 1.3 mmol) were refluxed in absolute ethanol (100 mL) for 24 h. The mixture was cooled to room temperature, filtered, washed with ethanol and diethyl ether and air-dried to afford **P4** as a red-brown powder; yield 0.70 g, 92%. ESI-MS: *m/z* = 1094.9 [(MH – 3Cl)⁺] (calcd. for C₅₃H₄₉Cl₃N₆ORu₂⁺: *m/z* = 1094.5).

[DTX-{Ru(bpy)Cl}₂](PF₆)₂ (**4**): **P4** (0.21 g, 0.18 mmol), bpy (0.055 g, 0.35 mmol), LiCl (0.19 g, 4.4 mmol) and *N*-ethylmorpholine (0.3 mL) were refluxed for 4 h in an ethanol/water (3:1) mixture (60 mL). The reaction mixture was then cooled to room temperature, concentrated under reduced pressure, and then treated with satd. aq. KPF₆ (5 mL) to afford a dark purple precipitate. The solid was collected by filtration, washed with water and then dried to give the crude product **4**. The compound was purified via column chromatography using silica gel with CH₂Cl₂ and satd. KPF₆ in acetone (4:1) as the eluent; yield 0.23 g, 78%. ¹H NMR (CD₃OH, 400 MHz): δ = 10.27 (d, ³*J* = 5.3 Hz, 2 H, *H_A*), 8.73 (d, ³*J* = 8.0 Hz, 2 H, *H_D*), 8.62 (s, 4 H, *H_E*), 8.40 (t, ³*J* = 7.8 Hz, 2 H, *H_C*), 8.48 (d, ³*J* = 6.7 Hz, 2 H, *H_E*), 8.28 (d, ³*J* = 8.1 Hz, 4 H, *H_d*), 8.23 (t, ³*J* = 6.2 Hz, 2 H, *H_B*), 7.87 (d, ⁴*J* = 2.0 Hz, 2 H, *H_f*), 7.81 (t, ³*J* = 7.8 Hz, 4 H, *H_c*), 7.73 (d, ⁴*J* = 2.2 Hz, 2 H, *H_g*), 7.67 (t, ³*J*

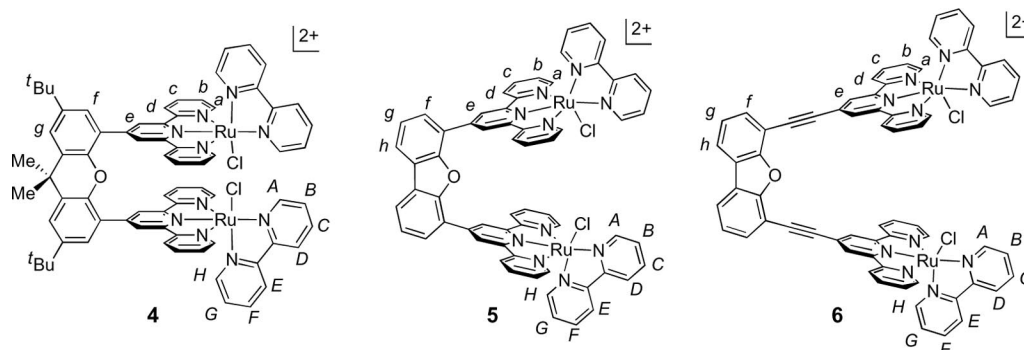


Figure 7. Labeling Scheme for ¹H NMR spectral signals. Assignments for the free ligands follow the same labeling Scheme.

= 7.5 Hz, 2 H, H_F), 7.58 (d, $^3J = 5.2$ Hz, 4 H, H_a), 7.14 (t, $^3J = 8.3$ Hz, 4 H, H_b), 7.00 (t, $^3J = 6.1$ Hz, 2 H, H_G), 6.83 (d, $^3J = 5.5$ Hz, 2 H, H_H), 1.99 (s, 6 H, Me), 1.52 (s, 18 H, tBu) ppm. HR-ESI-MS: $m/z = 685.1374$ [(M - 2PF₆)²⁺] (calcd. for C₇₃H₆₄Cl₂N₁₀ORu₂²⁺: $m/z = 685.1365$).

4,6-(Diterpyridine)dibenzofuran (DTD) (L5): 4,6-dibenzofurandiyl-bis(boronic acid) (0.25 g, 0.96 mmol), 4'-bromo-2,2':6',2''-terpyridine (0.60 g, 1.9 mmol), potassium carbonate (0.53 g, 3.8 mmol) and Pd(PPh₃)₄ (0.11 g, 0.096 mmol) were heated at 110 °C in DMF (60 mL) for 24 h. The solution was then filtered after being cooled to room temperature, followed by the removal of solvent under reduced pressure. The resultant solid was extracted using CH₂Cl₂ (50 mL), and then purified on a basic alumina column to remove residual 4'-bromo-2,2':6',2''-terpyridine and triphenylphosphane using CH₂Cl₂ as the eluent. This step was followed by a mixture of ethyl acetate and CH₂Cl₂ (1:4) as the eluent to afford **L5** as a white solid; yield 0.25 g, 40%. ¹H NMR (CDCl₃, 400 MHz): $\delta = 9.10$ (s, 4 H, H_e), 8.45 (d, $^3J = 7.9$ Hz, 4 H, H_a), 8.41 (dd, $^3J = 4.7$, $^4J = 0.8$ Hz, 4 H, H_d), 8.05 (d, $^3J = 7.6$ Hz, 2 H, H_f), 8.01 (d, $^3J = 8.0$ Hz, 2 H, H_h), 7.68 (td, $^3J = 7.9$, $^4J = 1.7$ Hz, 4 H, H_b), 7.51 (t, $^3J = 7.6$ Hz, 2 H, H_g), 7.16 (td, $^3J = 7.3$, $^4J = 1.0$ Hz, 4 H, H_c) ppm. ¹³C NMR (CDCl₃, 100 MHz): $\delta = 156.3$, 156.0, 153.8, 149.1, 145.6, 136.6, 127.0, 125.1, 123.8, 123.6, 121.7, 121.0, 120.6 ppm. ESI-HRMS: $m/z = 630.2164$ [M⁺] (calcd. for C₄₂H₂₆N₆O⁺: $m/z = 630.2168$).

[DTD-(RuCl₃)₂] (P5): **L5** (0.18 g, 0.28 mmol) and RuCl₃·3H₂O (0.15 g, 0.57 mmol) were refluxed in absolute ethanol (50 mL) for 12 h and then cooled to room temperature. The solid was isolated by filtration, and then washed with ethanol and diethyl ether, and then air-dried to afford **P5** as a red-brown powder; yield 0.27 g, 91%. ESI-MS: $m/z = 1010.3$ [(M - Cl)⁺] (calcd. for C₄₂H₂₆Cl₆N₆ORu₂⁺: $m/z = 1010.1$).

[DTD-{Ru(bpy)Cl₂}(PF₆)₂] (5): **P5** (0.10 g, 0.096 mmol), bpy (0.030 g, 0.19 mmol), LiCl (0.10 g, 2.4 mmol) and *N*-ethylmorpholine (0.3 mL) were refluxed for 6 h in a ethanol/water (3:1) solution (50 mL). The solution was then cooled to room temperature followed by the removal of solvent under reduced pressure. The resultant solid was dissolved in water and then treated with a satd. aq. KPF₆ solution (5 mL) to render a dark purple precipitate that was collected by filtration. The solid was purified using column chromatography (silica) using an acetone/satd. aqueous KPF₆ solution (99:1) as the eluent; yield 0.12 g, 83%. ¹H NMR (CD₃CN, 400 MHz): $\delta = 10.28$ (d, $^3J = 5.6$ Hz, 2 H, H_d), 9.27 (s, 4 H, H_e), 8.60 (d, $^3J = 8.0$ Hz, 2 H, H_D), 8.49 (d, $^3J = 8.9$ Hz, 2 H, H_f), 8.44 (d, $^3J = 7.6$ Hz, 2 H, H_h), 8.29 (m, 8 H, $H_{d,e,c}$), 8.00 (dd, $^3J = 6.2$, $^4J = 1.2$ Hz, 2 H, H_B), 7.87 (t, $^3J = 7.7$ Hz, 2 H, H_g), 7.67 (t, $^3J = 7.6$ Hz, 4 H, H_C), 7.65 (t, $^3J = 7.6$ Hz, 2 H, H_F), 7.60 (d, $^3J = 5.6$ Hz, 4 H, H_a), 7.37 (d, $^3J = 4.5$ Hz, 2 H, H_H), 7.02 (td, $^3J = 5.6$, $^4J = 1.2$ Hz, 4 H, H_b), 6.92 (dd, $^3J = 6.6$, $^4J = 1.2$ Hz, 2 H, H_G) ppm. HR-MALDI-MS: $m/z = 1361.0602$ [(M - PF₆)⁺] (calcd. for C₆₂H₄₂Cl₂F₆N₁₀OPRu₂⁺: $m/z = 1361.0662$).

4,6-(Diethynylterpyridine)dibenzofuran (DETD) (L6): 4,6-diiododibenzofuran (0.047 g, 0.11 mmol), 4'-ethynyl-2,2':6',2''-terpyridine (0.10 g, 0.27 mmol), [Pd(PPh₃)₄] (0.022 g, 10 mol-%) and CuI (7 mg, 20 mol-%) were combined with degassed THF (30 mL) and Et₃N (15 mL) and refluxed for 12 h. The solid in the resultant suspension was removed by filtration and then immersed in a stirred CHCl₃ solution (100 mL). The dark brown solid that formed was removed by filtration to afford a yellow solution that produced a yellow powder upon removal of solvent under reduced pressure; yield 75 mg, 85%. ¹H NMR (CDCl₃, 400 MHz): $\delta = 8.66$ (s, 4 H, H_e), 8.45 (d, $^3J = 8$ Hz, 4 H, H_a), 8.42 (d, $^3J = 5$ Hz, 4 H, H_d),

7.97 (d, $^3J = 8$ Hz, 2 H, H_h), 7.73 (ddd, $^3J = 8$, $^4J = 2$ Hz, 4 H, H_b), 7.68 (d, $^3J = 8$ Hz, 2 H, H_f), 7.39 (t, $^3J = 7$ Hz, 2 H, H_g), 7.68 (dd, $^3J = 8$, 5 Hz, 4 H, H_c) ppm. ¹³C NMR (CDCl₃, 100 MHz): $\delta = 156.2$, 155.6, 155.4, 149.0, 136.5, 133.2, 131.3, 124.3, 123.7, 123.2, 123.1, 121.7, 121.7, 120.9, 107.7, 87.9 ppm. ESI-MS: $m/z = 679.4$ [MH⁺] (calcd. for C₄₆H₂₇N₆O: $m/z = 679.2$).

[DETD(RuCl₃)₂] (P6): **L6** (0.11 g, 0.16 mmol) and RuCl₃·3H₂O (0.085 g, 0.41 mmol) were refluxed in absolute ethanol (50 mL) for 24 h. The mixture was cooled to room temperature, filtered, and washed with ethanol and diethyl ether and air-dried to afford **P6** as a black-purple solid; yield 0.16 g, 91%. ESI-MS: $m/z = 1058.1$ [(M - Cl)⁺] (calcd. for C₄₆H₂₆Cl₃N₆ORu₂⁺: $m/z = 1057.9$).

[DETD{Ru(bpy)Cl₂}(PF₆)₂] (6): **P6** (0.16 g, 0.14 mmol), bpy (0.050 g, 0.35 mmol), LiCl (0.060 g, 1.4 mmol), *N*-ethylmorpholine (1 mL) and absolute ethanol (50 mL) were refluxed for 16 h to afford a deep red-purple solution. The reaction mixture was cooled, and the volume reduced to approximately 25 mL by a rotary evaporator. A satd. aq. KPF₆ solution (5 mL) was added to the solution to precipitate a dark red-purple solid. Purification was carried out by passing the crude product through silica using acetone and satd. aq. KPF₆ (100:1) as the eluent to yield **6**; yield 0.15 g, 69%. ¹H NMR ([D₆]DMSO, 400 MHz): $\delta = 10.10$ (d, $^3J = 5$ Hz, 2 H, H_d), 9.17 (s, 4 H, H_e), 8.91 (d, $^3J = 8$ Hz, 2 H, H_D), 8.69 (d, $^3J = 8$ Hz, 4 H, H_d), 8.60 (d, $^3J = 8$ Hz, 2 H, H_f), 8.48 (d, $^3J = 8$ Hz, 2 H, H_h), 8.38 (t, $^3J = 8$ Hz, 2 H, H_B), 8.09 (t, $^3J = 7$ Hz, 2 H, H_g), 8.02 (d, $^3J = 8$ Hz, 2 H, H_E), 7.72 (t, $^3J = 8$ Hz, 4 H, H_c), 7.63 (t, $^3J = 8$ Hz, 2 H, H_g), 7.59-7.52 (m, 6 H, H_F , H_a), 7.35 (d, $^3J = 6$ Hz, 2 H, H_H), 7.19 (t, $^3J = 6$ Hz, 4 H, H_b), 6.90 (t, $^3J = 6$ Hz, 2 H, H_G) ppm. HR-MALDI-MS: $m/z = 1409.0659$ [(M - PF₆)⁺] (calcd. for C₆₆H₄₂Cl₂F₆N₁₀OPRu₂⁺: $m/z = 1409.0663$).

Physical Measurements: Fast atom bombardment (FAB), electrospray ionization (ESI) high-resolution matrix-assisted laser desorption/ionization (MALDI) and high-resolution electron impact (EI) mass spectrometry were carried out by the University of Calgary analytical services. Electrochemical measurements were performed under anaerobic conditions using a Princeton Applied Research VersaStat 3 potentiostat using dry solvents, a Pt working electrode, an Ag reference electrode, and a 0.1 M (Bu₄N)(BF₄) supporting electrolyte. Potentials were initially referenced to an internal ferrocene (Fc) standard; however, potentials reported herein are referenced to a normal hydrogen electrode (NHE) on the premise that the (Fc/Fc⁺) couple occurs at +0.640 V vs. NHE in MeCN.^[35]

DFT Calculations: Density functional theory (DFT) calculations were carried out using B3LYP [Becke's three-parameter exchange functional (B3) and the Lee-Yang-Parr correlation functional (LYP)] and the LanL2DZ basis set. All geometries were fully optimized in the ground states (closed-shell singlet S₀). Time-dependent density functional theory (TD-DFT) calculations were performed with a spin-restricted formalism to examine low-energy excitations at the ground-state geometry. All calculations were carried out with the Gaussian 03W software package.

Dioxygen Evolution Studies: The custom-built apparatus consists of a 10-mL round-bottom flask equipped with a septum and a three-armed side-arm for inserting the probe; total working volume is 16.8 mL. The flask was charged with a solution of (NH₄)₂Ce(NO₃)₆ (0.33 M) in 1 M HClO₄ (3.0 mL) under an inert dinitrogen atmosphere. A deaerated solution of catalyst (5.0 × 10⁻⁸ to 5 × 10⁻⁷ mol in Ru) was injected through a rubber septum, and then stirred at ambient temperatures (24 ± 2 °C) for the duration of the experiment. Oxygen evolution was monitored every ten seconds with an optical probe (Ocean Optics FOXY-OR125-AFMG) and a multifrequency phase fluorimeter (Ocean Optics MFPF-100). Raw

data from the sensor was collected by the TauTheta Host Program and then converted into the appropriate calibrated oxygen sensor readings in % O₂ by the OOI Sensors application.

¹⁸OH₂ Labeling Studies: The same procedure as above was followed except that the 1 M HClO₄ solution was prepared with enriched ¹⁸OH₂ (10 atom-%) purchased from Cambridge Isotope Laboratories. After 6 h, an aliquot of the headspace was drawn into a 50 µL microsyringe through the rubber septum and injected into a Varian 431-210 GC-MS system with a gas separation column. The isotope distribution of ¹⁶O₂, ¹⁶O-¹⁸O₂ and ¹⁸O₂ was monitored.

Acknowledgments

We are grateful to Canada Research Chairs, Alberta Ingenuity, Natural Science and Engineering Research Council (Canada), Canada Foundation for Innovation, and The Institute for Sustainable Energy, Environment & Economy for financial support.

- [1] R. Eisenberg, H. B. Gray, *Inorg. Chem.* **2008**, *47*, 1697–1699.
- [2] L. Hammarstrom, S. Hammes-Schiffer, *Acc. Chem. Res.* **2009**, *42*, 1859–1860.
- [3] J. Barber, *Inorg. Chem.* **2008**, *47*, 1700–1710.
- [4] T. Wada, K. Tsuge, K. Tanaka, *Angew. Chem. Int. Ed.* **2000**, *39*, 1479–1482.
- [5] Y. V. Geletii, B. Botar, P. Kögerler, D. A. Hillesheim, D. G. Musaev, D. L. Hill, *Angew. Chem. Int. Ed.* **2008**, *47*, 3896–3899.
- [6] R. Zong, R. Thummel, *J. Am. Chem. Soc.* **2005**, *127*, 12802–12803.
- [7] C. Sens, I. Romero, M. Rodriguez, A. Llobet, T. Parella, J. Benet-Buchholz, *J. Am. Chem. Soc.* **2004**, *126*, 7798–7799.
- [8] J. Limburg, J. S. Vrettos, L. M. Liable-Sands, A. L. Rheingold, R. H. Crabtree, G. W. Brudvig, *Science* **1999**, *283*, 1524–1527.
- [9] M. Yagi, M. Kaneko, *Chem. Rev.* **2001**, *101*, 21–35.
- [10] R. Okamura, T. Wada, K. Aikawa, T. Nagata, K. Tanaka, *Inorg. Chem.* **2004**, *43*, 7210–7217.
- [11] Y. H. Xu, T. Akermark, V. Gyollai, D. P. Zou, L. Eriksson, L. L. Duan, R. Zhang, B. Akermark, L. C. Sun, *Inorg. Chem.* **2009**, *48*, 2717–2719.
- [12] M. Yagi, K. V. Wolf, P. J. Baesjou, S. L. Bernasek, G. C. Dismukes, *Angew. Chem. Int. Ed.* **2001**, *40*, 2925–2928.
- [13] W. Ruettinger, G. C. Dismukes, *Chem. Rev.* **1997**, *97*, 1–24.
- [14] G. C. Dismukes, R. Brimblecombe, G. A. N. Felton, R. S. Pryadun, J. E. Sheats, L. Spiccia, G. F. Swiegers, *Acc. Chem. Res.* **2009**, *42*, 1935–1943.
- [15] J. K. Hurst, J. L. Cape, A. E. Clark, S. Das, C. Qin, *Inorg. Chem.* **2008**, *47*, 1753–1764.
- [16] F. Liu, J. J. Concepcion, J. W. Jurss, T. Cardolaccia, J. L. Templeton, T. J. Meyer, *Inorg. Chem.* **2008**, *47*, 1727–1752.
- [17] D. J. Wasylenko, C. Ganesamoorthy, B. D. Koivisto, M. A. Henderson, C. P. Berlinguette, *Inorg. Chem.* **2010**, *49*, 2202–2209.
- [18] S. Masaoka, K. Sakai, *Chem. Lett.* **2009**, *38*, 182–183.
- [19] H. Tseng, R. Zong, J. T. Muckerman, R. Thummel, *Inorg. Chem.* **2008**, *47*, 11763–11773.
- [20] J. J. Concepcion, J. W. Jurss, J. L. Templeton, T. J. Meyer, *J. Am. Chem. Soc.* **2008**, *130*, 16462–16463.
- [21] N. D. McDaniel, F. J. Coughlin, L. L. Tinker, S. Bernhard, *J. Am. Chem. Soc.* **2008**, *130*, 210–217.
- [22] J. J. Concepcion, J. W. Jurss, M. K. Brennaman, P. G. Hoertz, A. O. T. Patrocinio, N. Y. Murakami Iha, J. L. Templeton, T. J. Meyer, *Acc. Chem. Res.* **2009**, *42*, 1954–1965.
- [23] Z. Chen, J. J. Concepcion, J. W. Jurss, T. J. Meyer, *J. Am. Chem. Soc.* **2009**, *131*, 15580–15581.
- [24] T. A. Betley, Q. Wu, T. Van Voorhis, D. G. Nocera, *Inorg. Chem.* **2008**, *47*, 1849–1861.
- [25] Ref. [24] provides preliminary evidence that **5** is a water oxidation catalyst.
- [26] C. J. Chang, Z. H. Loh, C. Shi, F. C. Anson, D. G. Nocera, *J. Am. Chem. Soc.* **2004**, *126*, 10013–10020.
- [27] C. K. Chang, I. Abdalmuhdi, *J. Org. Chem.* **1983**, *48*, 5388–5390.
- [28] J. P. Collman, P. S. Wagenknecht, J. E. Hutchison, *Angew. Chem. Int. Ed. Engl.* **1994**, *33*, 1620–1639.
- [29] Intermetallic values are calculated from an idealized model of a rigid organic framework.
- [30] T. Wada, K. Tsuge, K. Tanaka, *Inorg. Chem.* **2001**, *40*, 329–337.
- [31] T. Muckerman James, E. Polyansky Dmitry, T. Wada, K. Tanaka, E. Fujita, *Inorg. Chem.* **2008**, *47*, 1787–1802.
- [32] S. Romain, L. Vigara, A. Llobet, *Acc. Chem. Res.* **2009**, *42*, 1944–1953.
- [33] F. Bozoglian, S. Romain, M. Z. Ertem, T. K. Todorova, C. Sens, J. Mola, M. Rodriguez, I. Romero, J. Benet-Buchholz, X. Fontrodona, C. J. Cramer, L. Gagliardi, A. Llobet, *J. Am. Chem. Soc.* **2009**, *131*, 15176–15187.
- [34] D. C. Harris, *Quantitative Chemical Analysis*, 6th ed., W. H. Freeman and Company, New York, **2004**.
- [35] V. V. Pavlishchuk, A. W. Addison, *Inorg. Chim. Acta* **2000**, *298*, 97–102.
- [36] J. Kiwi, M. Gratzel, G. Blondeel, *J. Chem. Soc., Dalton Trans.* **1983**, 2215–2216.
- [37] A. Mills, *J. Chem. Soc., Dalton Trans.* **1982**, 1213–1216.
- [38] R. A. Binstead, C. W. Chronister, J. Ni, C. M. Hartshorn, T. J. Meyer, *J. Am. Chem. Soc.* **2000**, *122*, 8464–8473.
- [39] J. A. Gilbert, D. S. Eggleston, J. Murphy, W. A. D. A. Geselowitz, S. W. Gersten, D. J. Hodgson, T. J. Meyer, *J. Am. Chem. Soc.* **1985**, *107*, 3855–3864.
- [40] K. J. Takeuchi, M. S. Thopson, D. W. Pipes, T. J. Meyer, *Inorg. Chem.* **1984**, *23*, 1845–1851.
- [41] E. B. Schwartz, C. B. Knobler, D. J. Cram, *J. Am. Chem. Soc.* **1992**, *114*, 10775–10784.
- [42] M. L. Muro, F. N. Castellano, *Dalton Trans.* **2007**, 4659–4665.
- [43] H. Gilman, S. Avakian, *J. Am. Chem. Soc.* **1945**, *67*, 349–351.
- [44] V. Grosshenny, F. M. Romero, R. Ziessel, *J. Org. Chem.* **1997**, *62*, 1491–1500.

Received: January 30, 2010
Published Online: May 27, 2010

Dinuclear Complexes of the N₂O₂ Oxime Chelate Ligand with Zinc(II)–Lanthanide(III) as a Selective Sensitization System for Sm³⁺

Shigehisa Akine,^[a] Fumihiko Utsuno,^[a] Takanori Taniguchi,^[a] and Tatsuya Nabeshima^{*[a]}

Keywords: Zinc / Lanthanides / Heterometallic complexes / N,O ligands / Luminescence

A series of zinc(II)–lanthanide(III) dimetallic complexes have been synthesized by the one-pot reaction of the oxime-based N₂O₂ chelate ligand H₂L with zinc(II) acetate and lanthanide(III) salts. The heavier lanthanides (Sm–Lu) produced heterodinuclear complexes [LZnLn]³⁺ (Ln = Sm–Lu) in which the zinc(II) ion occupies the N₂O₂ chelate site of H₂L and the lanthanide(III) ion is located in the semicircular O₄ site. In contrast, the trinuclear complex [(LZn)₂La]³⁺ was obtained by the reaction of H₂L with zinc(II) and lanthanum(III) salts. The heterometallic complexes [LZnLn]³⁺ and [(LZn)₂La]³⁺ were also formed by the reaction of [L₂Zn₃]²⁺ with the heavier lanthanides (Sm³⁺–Lu³⁺) and La³⁺, respectively. The dinuclear

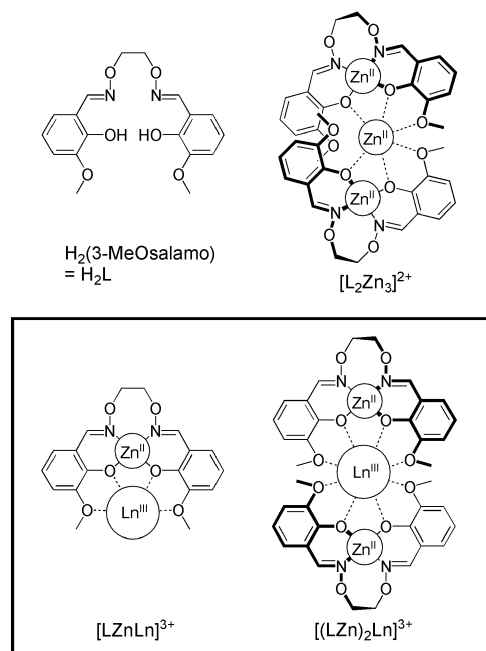
complex [LZnSm(OAc)₃] exhibited a relatively intense red emission due to Sm³⁺, whereas [LZnEu(OAc)₃] gave no detectable emission. The corresponding complexes containing other lanthanides showed only a weak blue emission due to the ligand moiety. Therefore the ligand L^{2–} can selectively sensitize Sm³⁺ from among Sm³⁺, Eu³⁺, Tb³⁺, and Dy³⁺, although these complexes would often exhibit f–f luminescence. The deep-red luminescence from samarium(III) at around 650 nm is potentially useful for a full-color display. In addition, [LZnYb(OAc)₃] exhibited near-infrared luminescence.

Introduction

Metal complexes of salen-type ligands are good precursors for the synthesis of oligometallic complexes^[1,2] due to the high coordination ability of the phenoxo moiety which can bridge two metal centers in a μ₂-M–O–M fashion. A number of homo- and heterometallic complexes have been derived from salen^[1] and analogous ligands.^[2] In particular, salen–metal complexes with alkoxy groups at the 3-position are useful for obtaining the oligonuclear 3d–4f heterometallic system.^[3,4] These 3d–4f metal complexes have been extensively studied because some of them exhibit interesting magnetic^[3] and photophysical^[4] properties. In particular, the zinc–lanthanide complexes are of interest because of the visible and near-infrared luminescence resulting from lanthanide f–f transitions.^[4] In general, such 3d–4f complexes are prepared via mononuclear d-block metal complexes, which are isolated in advance or formed in situ.

We recently developed a new series of oxime-based tetradentate ligands, “salamo”, which are stable against C=N bond recombination.^[5–8] The complexation of the ligand H₂(3-MeOsalamo) (H₂L hereafter, Scheme 1) with zinc(II) acetate did not give the mononuclear complex [LZn] but

the trinuclear complex [L₂Zn₃]²⁺ in a cooperative fashion.^[6] Heterometallic complexes [LZnLn]³⁺ and [(LZn)₂La]³⁺ were formed from the homometallic complex [L₂Zn₃]²⁺.^[7]



Scheme 1. Ligand H₂L in the heterometallic zinc(II)–lanthanide(III) complexes.

We now report the synthesis, X-ray crystal structures, and luminescence properties of a series of dinuclear zinc(II)–lanthanide(III) complexes of the ligand H₂L. The [LZn]

[a] Graduate School of Pure and Applied Sciences, University of Tsukuba, Tsukuba Ibaraki 305-8571, Japan
Fax: +81-29-853-4507
E-mail: nabesima@chem.tsukuba.ac.jp

Supporting information for this article is available on the WWW under <http://dx.doi.org/10.1002/ejic.200901243>.

moiety was found to selectively sensitize Sm^{3+} , that is, the zinc(II)–samarium(III) complex exhibits a characteristic red luminescence due to Sm^{3+} f–f transitions, whereas most of the other complexes, such as europium(III) or terbium(III), showed no emission or weak blue fluorescence of the organic ligand.

Results and Discussion

Synthesis and Structures of the Metal Complexes

The heterodinuclear complexes $[\text{LZnLn}(\text{OAc})_3]$ ($\text{Ln} = \text{Sm, Eu, Gd, Tb, Dy, Ho, Er, Tm, Yb, Lu}$) were synthesized by the one-pot reaction of H_2L with zinc(II) acetate (1 equiv.) and lanthanide(III) acetate (1 equiv.) in yields of 53–88%. X-ray-quality single crystals were obtained by the vapor phase diffusion of diethyl ether into a solution of each complex in methanol/chloroform. The dinuclear complexes $[\text{LZnLn}(\text{OAc})_3]$ ($\text{Ln} = \text{Sm–Ho}$) crystallized in the orthorhombic $P2_12_12_1$ space group with a solvated diethyl ether molecule. These crystals contain two crystallographically independent molecules that adopt a similar conformation. $[\text{LZnLn}(\text{OAc})_3]$ ($\text{Ln} = \text{Dy–Lu}$) form unsolvated crystals in the monoclinic $P2_1/a$ space group. Both types of the crystals were obtained for Dy and Ho.

X-ray crystallographic analysis revealed that all the dinuclear complexes $[\text{LZnLn}(\text{OAc})_3]$ ($\text{Ln} = \text{Sm–Lu}$) have similar structural features (see Figure 1 for $\text{Ln} = \text{Sm, Lu}$ and also Figures S1–S12). The N_2O_2 site of the ligand L^{2-} is occupied by the zinc(II) ion. The two phenoxo oxygen atoms (O1, O5) as well as the two methoxy oxygen atoms (O2, O6) form a semicircular O_4 site to accommodate the lanthanide(III) ion. One acetato ligand (O7, O8) bridges the zinc(II) and lanthanide(III) ions in a μ_2 fashion, whereas the other two acetato ligands (O9, O10 and O11, O12) coordinate to the lanthanide(III) ion in an η_2 fashion. As a result, the lanthanide(III) and zinc(II) ions are in a nona- and pentacoordinate environment, respectively.

The coordination environment around the lanthanide(III) ions in the complexes $[\text{LZnLn}(\text{OAc})_3]$ ($\text{Ln} = \text{Sm–Lu}$) are very similar. The nine oxygen atoms formed a coordination polyhedron, which can be best described as a triaugmented triangular prism (tricapped trigonal prism), as shown in Scheme 2. The average distances of the Ln–O coordination bonds almost decrease monotonically from Sm to Lu (phenoxo–Ln, 2.406–2.278 Å; methoxy–Ln, 2.607–2.487 Å; acetato–Ln, 2.439–2.348 Å) due to lanthanide contraction (Table 1). In relation to the changes in the bond lengths, the sum of the three O–Ln–O angles of the O_4 donor of $[\text{LZn}]$ increase from 189 to 197° and the Zn–Ln separation changes from 3.446 (Sm) to 3.356 Å (Lu).

The dinuclear complexes $[\text{LZnLn}(\text{OAc})_3]$ contain a pentacoordinate zinc(II) ion, the geometry of which changes depending on the type of crystal. The trigonality indices $\tau^{[9]}$ for the zinc(II) ions in $[\text{LZnLn}(\text{OAc})_3]$ with $\text{Ln} = \text{Sm–Ho}$, which crystallize in the orthorhombic crystal system, are in the range of 0.428–0.438, which indicates an intermediate geometry between square pyramidal and trigo-

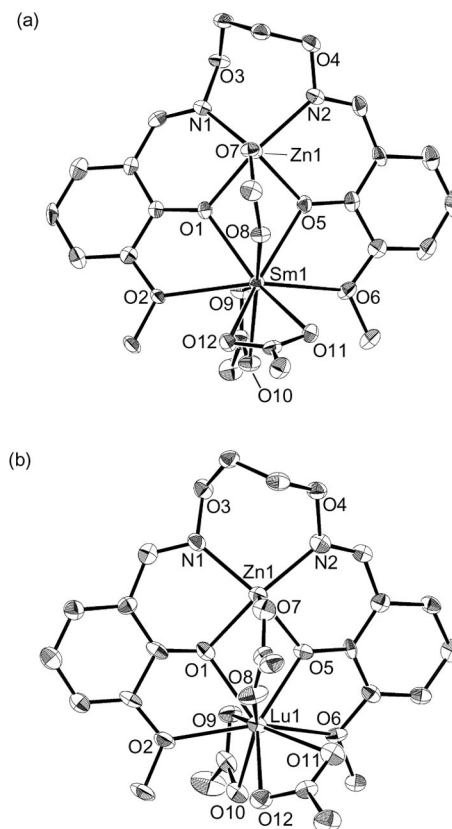
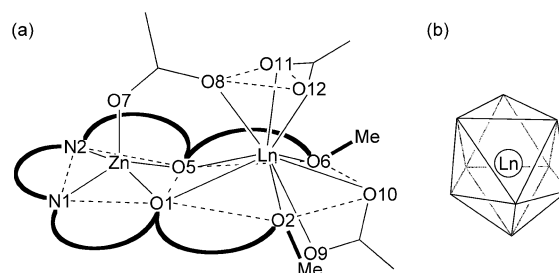


Figure 1. X-ray crystal structures of the dinuclear complexes (a) $[\text{LZnSm}(\text{OAc})_3]$ (only one of the crystallographically independent molecules is shown) and (b) $[\text{LZnLu}(\text{OAc})_3]$ (disordered atoms have been omitted for clarity) with thermal ellipsoids drawn at the 50% probability level.



Scheme 2. (a) Schematic drawing of the coordination sphere of the zinc and lanthanide atoms in $[\text{LZnLn}(\text{OAc})_3]$ ($\text{Ln} = \text{Sm–Lu}$). (b) Triaugmented triangular prism coordination polyhedron of the Ln atom.

nal bipyramidal. On the other hand, the zinc(II) ions in $[\text{LZnLn}(\text{OAc})_3]$ with $\text{Ln} = \text{Dy–Lu}$, which crystallize in the monoclinic system, have a zinc(II) ion with an almost ideal square pyramidal geometry ($\tau = 0.088–0.121$). This difference in the geometry of the zinc(II) ion is probably a result of differences in the crystal packing of the two types of crystals.

When lighter lanthanides, that is, La, Ce, Pr, and Nd, were used, the corresponding dinuclear complexes $[\text{LZnLn}(\text{OAc})_3]$ were not isolated under the same condi-

Table 1. Structural parameters of [LZnLn(OAc)₃].

Ln	Type	Distance [Å]				θ (Ln) ^[c] [°]	τ (Zn) ^[d]
		Zn–Ln	ArO–Ln	MeO–Ln	AcO–Ln		
Sm	O ^[a]	3.4458	2.406	2.607	2.439	188.7	0.438
Eu	O ^[a]	3.4440	2.407	2.596	2.429	189.7	0.430
Gd	O ^[a]	3.4349	2.387	2.586	2.421	190.4	0.433
Tb	O ^[a]	3.4144	2.366	2.586	2.403	190.9	0.432
Dy	O ^[a]	3.4119	2.359	2.580	2.394	191.4	0.428
Ho	O ^[a]	3.4037	2.348	2.572	2.385	192.0	0.431
Dy	M ^[b]	3.4209	2.354	2.535	2.409	193.8	0.121
Ho	M ^[b]	3.4140	2.341	2.524	2.400	194.7	0.112
Er	M ^[b]	3.4041	2.327	2.517	2.387	195.4	0.105
Tm	M ^[b]	3.3962	2.319	2.525	2.375	195.7	0.112
Yb	M ^[b]	3.3817	2.306	2.506	2.364	196.6	0.093
Lu	M ^[b]	3.356	2.278	2.487	2.348	196.8	0.088

[a] Orthorhombic crystal. Averaged values for the two crystallographically independent molecules are shown. [b] Monoclinic crystal. [c] Angle θ is defined as the sum of the three O–Ln–O angles (O1–Ln1–O2, O1–Ln1–O5, O5–Ln1–O6). [d] τ values are calculated according to ref.^[9].

tions. However, ESI-MS analysis indicated the formation of mixtures of the trinuclear complex [(LZn)₂Ln]³⁺ and the dinuclear complex [LZnLn]³⁺ (see below).

In the case of lanthanum, the trinuclear complex [(LZn)₂La(OAc)₂](NO₃) was obtained in 97% yield by the reaction of H₂L with lanthanum(III) nitrate (0.5 equiv.) and zinc(II) acetate (1.5 equiv.). In the crystal structure, the zinc(II) ions are located in the N₂O₂ site of each ligand L^{2–} to form the [LZn] unit (Figure 2). The two zinc(II) ions are pentacoordinate with a geometry intermediate between square pyramidal and trigonal bipyramidal (τ = 0.556, 0.620). The two

[LZn] units act as a semicircular tetradentate O₄ chelate ligand for the decacoordinate lanthanum(III) ion. The two acetato ligands complete the coordination sphere of the lanthanum(III) ion bridging the zinc(II) and lanthanum(III) ions (Zn1–La1 and Zn2–La1) in a μ_2 fashion. The distances between the O donors and the lanthanum(III) ion in [(LZn)₂La(OAc)₂]⁺ (ArO–La, 2.516 Å; MeO–La, 2.760 Å) are longer than those in the dinuclear complexes [LZnLn(OAc)₃] (Ln = Sm–Lu; ArO–Ln, 2.406–2.278 Å; MeO–Ln, 2.607–2.487 Å). The larger ionic radius of the lanthanum(III) ion allows the second [LZn] unit access to the coordination sphere to give [(LZn)₂La(OAc)₂]⁺.

The cationic [(LZn)₂La(OAc)₂]⁺ unit possesses an approximate two-fold axis passing through the lanthanum(III) ion. The two [LZn] units of the complex [(LZn)₂La(OAc)₂]⁺ cross each other in a double helical fashion. The two μ -acetato ligands coordinate to the trinuclear Zn–La–Zn core from the same side of the complex. Consequently, the two salicylaldoxime moieties of each [LZn] unit are not equivalent; one is close to the acetato ligands and the other is further away. A significant C–H \cdots O contact was found between the acetato oxygen and one of the methylene protons of the *O*-alkyloxime moiety. The distances (H10 \cdots O14, 2.322 Å; H28 \cdots O16, 2.333 Å) were significantly shorter than the sum of the van der Waals radii of these elements (O, 1.52 Å; H, 1.20 Å). The counter-anion NO₃[–] did not coordinate to any metal ion.

Conversion of [L₂Zn₃]²⁺ into [LZnLn]³⁺ or [(LZn)₂Ln]³⁺

As described above, the one-pot complexation of H₂L with zinc(II) and lanthanide(III) gave the heterodinuclear complexes [LZnLn]³⁺ (Ln = Sm–Lu) or trinuclear complex [(LZn)₂La]³⁺. The mononuclear complex [LZn] would be a good precursor of these heteronuclear complexes, but complexation between H₂L and zinc(II) gave homotrimeric complex [L₂Zn₃]²⁺ (Scheme 3, a).^[6] If the complexation with zinc(II) and lanthanide(III) is under thermodynamic control, this homotrimeric complex [L₂Zn₃]²⁺ can also act as a precursor of the zinc(II)–lanthanide(III) heteronuclear complexes (see parts b, c in Scheme 3). Therefore we investigated the complexation process with the two kinds of metals by ¹H NMR titration experiments using the diamagnetic lanthanum(III) and lutetium(III).

The zinc(II) trimeric complex [L₂Zn₃]²⁺ was almost quantitatively formed in situ by mixing H₂L with 2 equiv. of zinc(II) acetate in CDCl₃/CD₃OD (1:1). When Lu³⁺ was added to the solution of [L₂Zn₃]²⁺, a new set of signals appeared in the ¹H NMR spectrum (Figure 3, a). About 80% of [L₂Zn₃]²⁺ was converted into a new species in the presence of 2 equiv. of Lu³⁺ and the addition of 6 equiv. of Lu³⁺ resulted in almost complete conversion (>97%). The titration curve showed a 1:2 [L₂Zn₃]²⁺/Lu³⁺ stoichiometry, which is consistent with the dinuclear species [LZnLu]³⁺ having a 1:1 [LZn]/Lu³⁺ ratio (Figure 3, b and Scheme 3, b). The dinuclear species [LZnLu]³⁺ was exclusively formed with no other complexes with a different stoichiometry being detected in the NMR spectra.

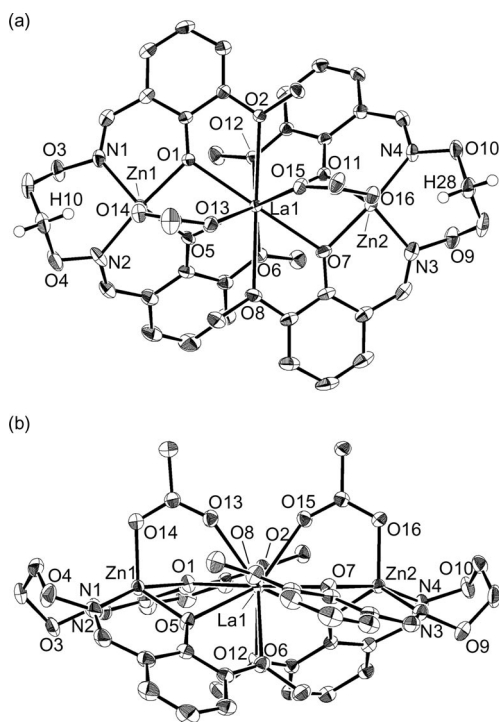
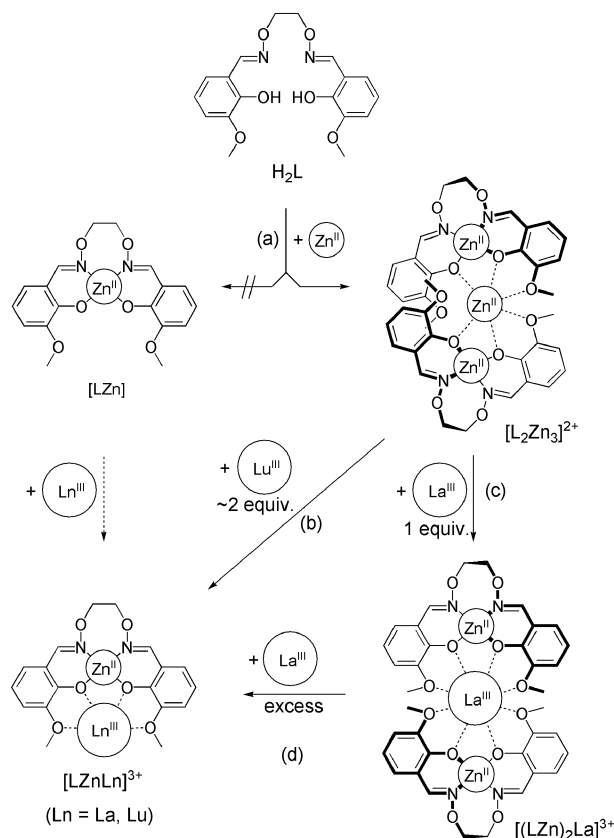


Figure 2. Crystal structure of [(LZn)₂La(OAc)₂]⁺ with thermal ellipsoids drawn at the 50% probability level. (a) Top view (along the approximate two-fold axis). (b) Side view.



Scheme 3. Complexation of H_2L with zinc(II) and lanthanide(III) ions.

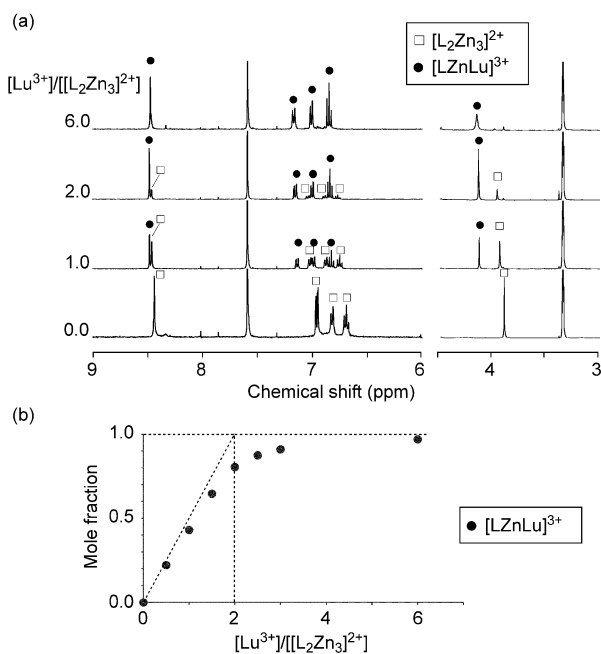


Figure 3. (a) 1H NMR spectra of $[L_2Zn_3]^{2+}$ (400 MHz, 2.0 mM) in the presence of $Lu(NO_3)_3$ in $CDCl_3/CD_3OD$ (1:1). (b) Mole fraction of $[LZnLu]^{3+}$ vs. $[Lu^{3+}]/[L_2Zn_3]^{2+}$.

In contrast, the complexation of $[L_2Zn_3]^{2+}$ with La^{3+} led to the formation of a different type of complex. In this case, the addition of La^{3+} (1.0 equiv.) resulted in the quantitative conversion of $[L_2Zn_3]^{2+}$ into $[(LZn)_2La]^{3+}$ (Figure 4, a and Scheme 3, c). The 1:1 $La^{3+}/[L_2Zn_3]^{2+}$ stoichiometry found in the 1H NMR titration is consistent with the presence in the new complex of $[LZn]$ and La^{3+} in a 2:1 ratio. In the 1H NMR spectra, two sets of signals were observed for the methoxy, oxime, and aromatic protons. Note that four protons of the methylene moiety were observed as nonequivalent diastereotopic pairs. The structure of the trinuclear complex in solution is essentially the same as that in the crystalline state because the nonequivalent 1H NMR spectral pattern is consistent with the unsymmetrical feature found in the crystalline state. The significant upfield shift of the methoxy protons ($\delta = 3.38$ and 3.40 ppm) can be explained by a structure in which the methoxy group is close to the benzene ring of the other $[LZn]$ moiety. In addition, the considerable downfield shift of one of the OCH_2CH_2O protons ($\delta = 5.55$ ppm) has been attributed to the $C-H\cdots O$ contact between the proton and the acetato oxygen found in the crystal structure.^[10]

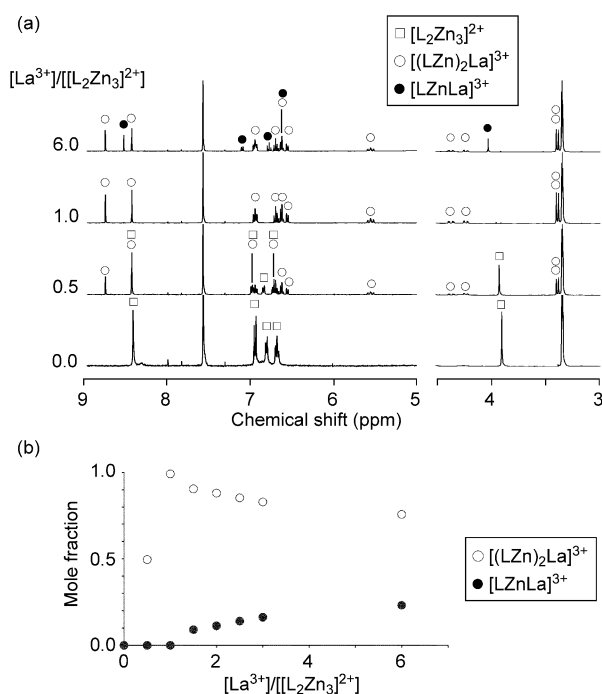


Figure 4. (a) 1H NMR spectra of $[L_2Zn_3]^{2+}$ (400 MHz, 2.0 mM) in the presence of $La(NO_3)_3$ in $CDCl_3/CD_3OD$ (1:1). (b) Mole fractions of $[(LZn)_2La]^{3+}$ and $[LZnLa]^{3+}$ vs. $[La^{3+}]/[L_2Zn_3]^{2+}$.

When an excess amount of La^{3+} ($[La^{3+}]/[L_2Zn_3]^{2+} > 1$) was added, another new set of signals appeared in the 1H NMR spectra (Figure 4, a). This complex has been assigned to the heterodinuclear complex $[LZnLa]^{3+}$, which has a symmetrical 1H NMR spectral pattern similar to that of the lutetium complex $[LZnLu]^{3+}$. However, the dinuclear complex was formed with low efficiency. The mole fraction of $[LZnLa]^{3+}$ was 23% even in the presence of 6 equiv. of La^{3+} (Figure 4, b and Scheme 3, d). That only a small

amount of $[(\text{LZn})_2\text{La}]^{2+}$ was converted into the dinuclear complex $[\text{LZnLa}]^{3+}$ in the presence of an excess amount of La^{3+} shows that the trinuclear complex $[(\text{LZn})_2\text{La}]^{3+}$ is thermodynamically more stable.

During the formation of $[(\text{LZn})_2\text{La}]^{3+}$, the central zinc(II) ion of $[\text{L}_2\text{Zn}_3]^{2+}$, which occupies the semicircular O₄ site of each $[\text{LZn}]$ unit, was exchanged for La^{3+} . When 1 equiv. of La^{3+} was added, the central zinc(II) ion was simply replaced by the La^{3+} to give the heterotrinuclear complex $[(\text{LZn})_2\text{La}]^{3+}$ (Scheme 3, c). On the other hand, when Lu^{3+} or excess La^{3+} was added, $[\text{L}_2\text{Zn}_3]^{2+}$ dissociates to give $[\text{LZnLn}]^{3+}$ (Ln = La, Lu; Scheme 3, b and d).

The transformation of $[\text{L}_2\text{Zn}_3]^{2+}$ into $[(\text{LZn})_2\text{La}]^{3+}$ or $[\text{LZnLu}]^{3+}$ may be driven by the strong interaction between the $[\text{LZn}]$ moiety and the lanthanide(III) ions, which arises because the size of the semicircular O₄ donor set (two phenoxo and two methoxy donors) is suitable for the lanthanide(III) ion but not for the zinc(II) ion. Crystallographic analysis showed that the O₄ donor set of the $[\text{LZn}]$ moiety can form four coordination bonds to the lanthanide(III) ions, but only three bonds to the zinc(II) ion. In addition, the strength of each of the coordination bonds to the lanthanide(III) ion must be stronger than that to the zinc(II) ion because of the larger positive charge.

The difference between the complexation behavior of La^{3+} and Lu^{3+} should result from the difference in their ionic radii. Because the ionic radius of La^{3+} is larger, it can accommodate two $[\text{LZn}]$ units. The two μ_2 -bridging acetato ligands also contribute to the stabilization of the trinuclear structure. In contrast, Lu^{3+} is too small to accommodate two $[\text{LZn}]$ units. Consequently, $[\text{L}_2\text{Zn}_3]^{2+}$ was directly converted into the dinuclear complex $[\text{LZnLu}]^{3+}$ upon reaction with Lu^{3+} without forming $[(\text{LZn})_2\text{Lu}]^{3+}$.

The complexation of H_2L with zinc(II) and lanthanide(III) ions was also investigated by ESI mass spectrometry (Figure 5; see also Figure S13). The mass spectrum of a mixture containing H_2L , Zn^{2+} , and Lu^{3+} (1:2:1) exhibited intense peaks at $m/z = 328.0$ and 715.0 , which have been assigned to $[\text{LZnLu}(\text{OAc})]^{2+}$ and $[\text{LZnLu}(\text{OAc})_2]^+$, respectively (Figure 5, d). No peak from the trinuclear complex $[(\text{LZn})_2\text{Lu}]^{3+}$ was detected. This is consistent with the exclusive formation of the dinuclear complex $[\text{LZnLu}]^{3+}$ observed in the ^1H NMR spectra. Other heavier lanthanides (Ln = Sm–Yb) also efficiently produced the corresponding dinuclear complexes $[\text{LZnLn}]^{3+}$. Peaks from the trinuclear complexes $[(\text{LZn})_2\text{Ln}]^{3+}$ were very weak or not detected (Figure 5, c; Ln = Sm).

However, when the lighter lanthanides La^{3+} , Ce^{3+} , Pr^{3+} , and Nd^{3+} were used, the existence of both $[(\text{LZn})_2\text{Ln}]^{3+}$ and $[\text{LZnLn}]^{3+}$ were indicated (Figure 5, a and b). This is evident from the observation of the molecular peak of $[(\text{LZn})_2\text{Ln}(\text{OAc})_2]^+$ in addition to those of $[\text{LZnLn}(\text{OAc})]^{2+}$ and $[\text{LZnLn}(\text{OAc})_2]^+$. In particular, $[(\text{LZn})_2\text{La}]^{3+}$ was formed very efficiently, as evidenced from the ^1H NMR investigation. An intense peak at $m/z = 1103.1$ from the heterotrinuclear species $[(\text{LZn})_2\text{La}(\text{OAc})_2]^+$ was observed (Figure 5, a). Peaks assigned to $[\text{LZnLa}(\text{OAc})]^{2+}$ ($m/z = 310.0$) and $[\text{LZnLa}(\text{OAc})_2]^+$ ($m/z = 679.0$) were rather weak.

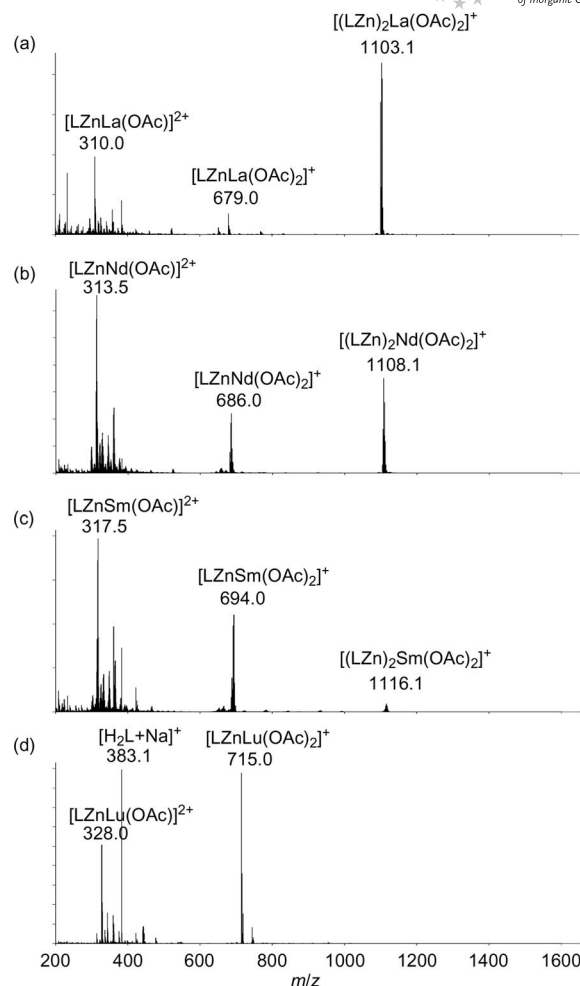


Figure 5. ESI mass spectra of H_2L in the presence of zinc(II) and lanthanide(III). (a) Ln = La; (b) Ln = Nd, (c) Ln = Sm, and (d) Ln = Lu.

We have already reported that a trinuclear zinc(II) complex of bis(salamo) ligands, in which two salamo moieties share a benzene ring, undergoes site-selective metal exchange by lanthanide(III) ions irrespective of the ionic radius.^[11,12] For the mono(salamo) ligand H_2L reported herein, the tendency to form the heteronuclear complexes $[(\text{LZn})_2\text{Ln}]^{3+}$ and $[\text{LZnLn}]^{3+}$ depends on the ionic radius of the lanthanide(III) ions. When $[\text{L}_2\text{Zn}_3]^{2+}$ reacts with La^{3+} , metal exchange takes place to efficiently give $[(\text{LZn})_2\text{La}]^{3+}$. On the other hand, the reaction of $[\text{L}_2\text{Zn}_3]^{2+}$ with the heavier lanthanide(III) ions causes dissociation of $[\text{L}_2\text{Zn}_3]^{2+}$ to give $[\text{LZnLn}]^{3+}$.

Luminescence Properties of the Dinuclear Complexes $[\text{LZnLn}(\text{OAc})_3]$

The luminescence properties of lanthanide(III) complexes are of considerable interest because of their potential applications in photochemical bioassays and materials science.^[13] Various complexes of europium(III) and terbium(III), which emit a strong visible luminescence, have been extensively studied. Several zinc(II)–lanthanide(III) heterometallic complexes of salen and analogous ligands

have also recently been reported to exhibit a visible or near-infrared luminescence.^[4,14,15] Thus, we investigated the optical properties of a series of heterodinuclear complexes [LZnLn(OAc)₃] (Ln = Sm–Lu; Table 2).

Table 2. Summary of the emission from [LZnLn(OAc)₃].^[a]

Complex	λ [nm] (intensity [a.u.])	
	Emission from L ²⁻	Emission from Ln ³⁺
[LZnSm(OAc) ₃]	466 (120)	560 (480), 597 (1670), 644 (2920), 704 (170), 789 (30), 951 (160)
[LZnEu(OAc) ₃]	n.d. ^[b]	613 (30)
[LZnGd(OAc) ₃]	466 (630)	
[LZnTb(OAc) ₃]	465 (80)	
[LZnDy(OAc) ₃]	468 (200)	
[LZnHo(OAc) ₃]	470 (20) ^[c]	
[LZnEr(OAc) ₃]	470 (40) ^[c]	
[LZnTm(OAc) ₃]	467 (240)	
[LZnYb(OAc) ₃]	468 (340)	976 (940)
[LZnLu(OAc) ₃]	464 (1050)	

[a] At room temperature, excitation at 350 nm in air-equilibrated chloroform solution (0.020 mM). [b] No detectable emission. [c] Emission maximum wavelength was not accurately determined due to weak intensity.

The absorption spectra of all the dinuclear complexes [LZnLn(OAc)₃] are similar, exhibiting a π – π^* band at around 350 nm; see part a of Figure 6 for the spectrum of [LZnSm(OAc)₃]. The luminescence spectrum of [LZnSm(OAc)₃] under excitation at 350 nm showed four narrow emission peaks at 560, 597, 644, and 704 nm (Figure 6, b). These peaks have been assigned to the $^4G_{5/2} \rightarrow ^6H_J$ ($J = 5/2, 7/2, 9/2, 11/2$) transitions typical of Sm³⁺. In addition, the spectrum showed a weak and broad peak at 466 nm, which has been assigned to the intraligand fluorescent emission of L²⁻. The excitation spectrum of [LZnSm(OAc)₃] monitored at 644 nm exhibited a broad maximum at 354 nm, which matches well the corresponding absorption spectrum (Figure 6, a). Thus, Sm³⁺ is excited not by direct metal excitation but by efficient sensitization by the [LZn] unit. The very weak ligand emission at 466 nm also confirms the efficient energy transfer from the ligand to Sm³⁺.

The quantum yield for the luminescence of [LZnSm(OAc)₃] was determined to be 0.89%. This value is much lower than those of the bright europium(III) and terbium(III) complexes reported previously.^[13e,16] However, samarium(III) complexes generally show relatively weak f–f emission and those exhibiting quantum yields of more than around 1% are quite rare.^[17] This weak emission is explained by nonradiative losses mainly attributed to multiphonon relaxation.^[18] Considering these facts, the ligand moiety of the dinuclear complex [LZnSm(OAc)₃] can effectively sensitize Sm³⁺. Although multiphonon relaxation probably still dominates, strong coordination of the [LZn] moiety and acetate ions to Sm³⁺ may prevent solvent molecules from accessing Sm³⁺ thereby suppressing the nonradiative losses due to solvent coordination.

Note also that the electric dipole transition at 644 nm ($^4G_{5/2} \rightarrow ^6H_{9/2}$) is the strongest among the observed transi-

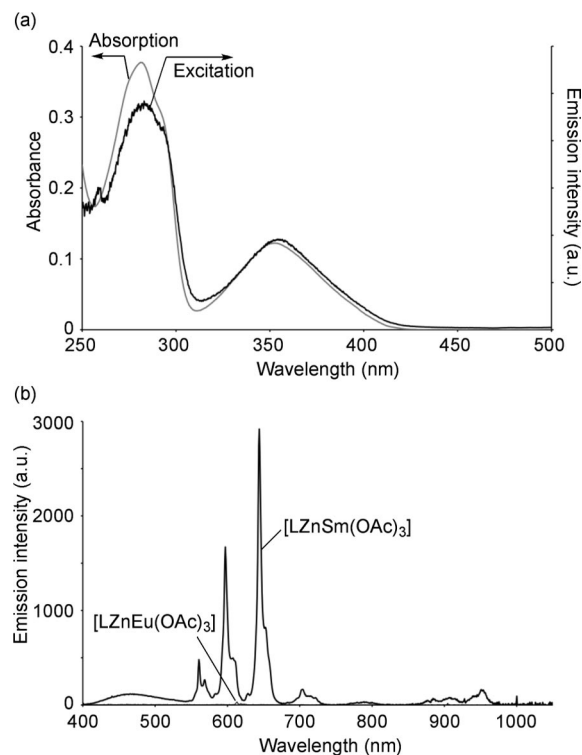


Figure 6. (a) Absorption spectrum of 0.020 mM [LZnSm(OAc)₃] in chloroform and excitation spectrum of 5.0 μ M [LZnSm(OAc)₃] in chloroform monitored at 644 nm. (b) Luminescence spectra of 0.020 mM [LZnSm(OAc)₃] and [LZnEu(OAc)₃] in chloroform upon excitation at 350 nm.

tions. This transition is known to be sensitive to the coordination environment of Sm³⁺ and its intensity increases as the symmetry of the environment decreases.^[17,19] Sm³⁺ in [LZnSm(OAc)₃] adopts a triaugmented triangular prism geometry, that is, it deviates significantly from a centrosymmetric coordination environment. This low-symmetrical structure may also contribute to the relatively efficient emission.

In general, the luminescence of europium(III) complexes is much more intense than that of the corresponding samarium(III) complexes. Thus, [LZnEu(OAc)₃] was expected to show a more intense luminescence due to the f–f transition of Eu³⁺. However, the emission from [LZnEu(OAc)₃] was almost quenched. Only a very weak emission at 613 nm due to the $^5D_0 \rightarrow ^7F_2$ transition of Eu³⁺ was observed. In this case the intraligand fluorescence is also very weak. The weak f–f emission may be due to thermal quenching of the 5D_0 level of Eu³⁺ by an intramolecular ligand-to-metal charge-transfer (LMCT) process.^[20,21] This LMCT process is probably a result of the electron-rich character of the phenoxo moieties and the strong tendency of Eu³⁺ to be reduced to Eu²⁺.

In the luminescence spectra of [LZnLn(OAc)₃] (Ln = Tb, Dy), only a weak broad band at around 465 nm due to intraligand fluorescence was observed instead of the f–f emission expected for Tb³⁺ and Dy³⁺. In these complexes, energy transfer from the ligand to the metal is not efficient, probably because the energy levels of the excited states of

these ions lie higher than that of the excited state of the [LZn] moiety. Hence, the ligand L²⁻ can selectively sensitize Sm³⁺ from among Sm³⁺, Eu³⁺, Tb³⁺, and Dy³⁺, although these complexes would often exhibit f–f luminescence.

In the emission spectra of [LZnLn(OAc)₃] (Ln = Gd, Lu), a relatively intense emission at around 465 nm due to intraligand fluorescence was observed (Figure 7). Note also that [LZnYb(OAc)₃] exhibits emission in the near-infrared region at 976 nm, which has been assigned to the ²F_{5/2} → ²F_{7/2} transition. Complexes with such a near-infrared emission are of interest because they have potential as chemosensors and in fluoroimmuno assay applications.^[22,23]

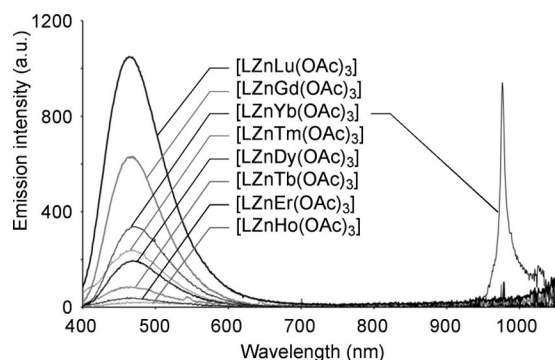


Figure 7. Luminescence spectra of 0.020 mM [LZnLn(OAc)₃] (Ln = Gd, Tb, Dy, Ho, Er, Tm, Yb, Lu) in chloroform upon excitation at 350 nm.

Conclusions

A series of zinc(II)–lanthanide(III) dimetallic complexes have been synthesized by the one-pot reaction of the oxime-based N₂O₂ chelate ligand H₂L with zinc(II) acetate and lanthanide(III) salts. The heavier lanthanides Sm–Lu produced heterodinuclear complexes [LZnLn(OAc)₃] (Ln = Sm–Lu) in which the zinc(II) ion occupies the N₂O₂ chelate site of H₂L with the lanthanide(III) ion located in the semi-circular O₄ site. In contrast, the trinuclear complex [(LZn)₂–La(OAc)₂](NO₃) was obtained by the reaction of H₂L with zinc(II) and lanthanum(III) salts. The difference in the stoichiometries of the complexes has mainly been attributed to the large ionic radius of La³⁺, which can accommodate two [LZn] units. The heterometallic complexes [LZnLn]³⁺ and [(LZn)₂La]³⁺ were also formed by the reaction of [L₂Zn₃]²⁺ with the heavier lanthanide ions (Ln = Sm–Lu) and La³⁺, respectively. The dinuclear complex [LZnSm(OAc)₃] exhibited a relatively intense red emission due to Sm³⁺, whereas [LZnEu(OAc)₃] gave no detectable emission. The corresponding complexes containing other lanthanides showed only a weak blue emission due to the ligand moiety. Therefore the ligand L²⁻ can selectively sensitize Sm³⁺ from among Sm³⁺, Eu³⁺, Tb³⁺, and Dy³⁺, although these complexes would often exhibit f–f luminescence. The deep-red luminescence from Sm³⁺ at around 650 nm is potentially useful for a full-color display. In addition, [LZnYb(OAc)₃] exhibited a near-infrared luminescence, which is potentially

useful as a chemosensor and in fluoroimmuno assay applications. The framework of the oxime chelate ligand H₂L has been utilized as a building block for various metallo-architectures such as helical complexes. The findings in this study could be useful for the development of photoluminescent metallo-architectures based on zinc(II)–lanthanide(III) systems.

Experimental Section

General: All experiments were carried out in air unless otherwise noted. Commercial chloroform, methanol, and diethyl ether were used without further purification. ¹H NMR spectra were recorded with a Bruker ARX 400 spectrometer (400 MHz) in CDCl₃/CD₃OD (1:1).

General Procedure for the Synthesis of [LZnLn(OAc)₃] (Ln = Sm–Lu): A solution of H₂(3-MeOsalamo) (H₂L;^[5] 9.0 mg, 0.025 mmol) in chloroform/methanol (1:1, 1 mL) was added to a solution of zinc(II) acetate dihydrate (5.5 mg, 0.025 mmol) and Ln(OAc)₃·*n*H₂O (0.025 mmol) in H₂O (ca. 0.2 mL) and methanol (2 mL) at room temperature. After removing the solvent under reduced pressure, the residue was dissolved in chloroform/methanol. Vapor phase diffusion of diethyl ether into this solution afforded pale-yellow crystals of [LZnLn(OAc)₃].

[LZnSm(OAc)₃]·0.5Et₂O: Yield 17.0 mg (86%). C₂₆H₃₂N₂O_{12.5}SmZn (788.31): calcd. C 39.61, H 4.09, N 3.55; found C 39.32, H 3.85, N 3.40.

[LZnEu(OAc)₃]: Yield 9.6 mg (53%). C₂₄H₂₇EuN₂O₁₂Zn (752.85): calcd. C 38.29, H 3.61, N 3.72; found C 37.91, H 3.62, N 3.59.

[LZnGd(OAc)₃]·0.25Et₂O: Yield 16.3 mg (84%). C₂₅H_{29.5}GdN₂O_{12.25}Zn (776.67): calcd. C 38.66, H 3.83, N 3.61; found C 38.65, H 3.92, N 3.42.

[LZnTb(OAc)₃]·0.25Et₂O: Yield 12.0 mg (62%). C₂₅H_{29.5}N₂O_{12.25}TbZn (778.34): calcd. C 38.58, H 3.82, N 3.60; found C 38.51, H 3.87, N 3.43.

[LZnDy(OAc)₃]: Yield 14.0 mg (73%). C₂₄H₂₇DyN₂O₁₂Zn (763.39): calcd. C 37.76, H 3.56, N 3.67; found C 37.51, H 3.49, N 3.59.

[LZnHo(OAc)₃]: Yield 16.8 mg (88%). C₂₄H₂₇HoN₂O₁₂Zn (765.82): calcd. C 37.64, H 3.55, N 3.66; found C 37.74, H 3.68, N 3.41.

[LZnEr(OAc)₃]: Yield 14.6 mg (76%). C₂₄H₂₇ErN₂O₁₂Zn (768.15): calcd. C 37.53, H 3.54, N 3.65; found C 37.12, H 3.38, N 3.51.

[LZnTm(OAc)₃]: Yield 15.4 mg (80%). C₂₄H₂₇N₂O₁₂TmZn (769.82): calcd. C 37.44, H 3.54, N 3.64; found C 37.35, H 3.46, N 3.56.

[LZnYb(OAc)₃]: Yield 12.3 mg (64%). C₂₄H₂₇N₂O₁₂YbZn (773.93): calcd. C 37.25, H 3.52, N 3.62; found C 37.22, H 3.44, N 3.50.

[LZnLu(OAc)₃]: Yield 11.2 mg (58%). ¹H NMR (400 MHz, CDCl₃/CD₃OD, 1:1, 298 K): δ = 2.00 (s, 9 H, OAc), 4.16 (s, 6 H, OMe), 4.65 (s, 4 H, CH₂), 6.85 (t, *J* = 8.0 Hz, 2 H, ArH), 7.01 (dd, *J* = 8.0, 1.3 Hz, 2 H, ArH), 7.17 (dd, *J* = 8.0, 1.3 Hz, 2 H, ArH), 8.47 (s, 2 H, CH=N) ppm. C₂₄H₂₇LuN₂O₁₂Zn (775.83): calcd. C 37.15, H 3.51, N 3.61; found C 37.17, H 3.39, N 3.48.

Synthesis of [(LZn)₂La(OAc)₂](NO₃): A solution of zinc(II) acetate dihydrate (17.0 mg, 0.077 mmol) in methanol (1 mL) and a solution

of lanthanum(III) nitrate hexahydrate (11.0 mg, 0.025 mmol) in methanol (1 mL) were added to a solution of H_2L (18.0 mg, 0.050 mmol) in methanol (1 mL). After removal of the solvent, the residue was dissolved in ethanol and vapor phase diffusion of hexane into this solution afforded pale-yellow crystals of $[(\text{LZn})_2\text{La}(\text{OAc})_2](\text{NO}_3)$ (29.4 mg, yield 97%). ^1H NMR (400 MHz, $\text{CDCl}_3/\text{CD}_3\text{OD}$, 1:1, 298 K): δ = 2.10 (s, 6 H, OAc), 3.38, (s, 6 H, OMe), 3.40 (s, 6 H, OMe), 4.23 (dd, J = 12.8, 2.2 Hz, 2 H, CH_2), 4.36 (dd, J = 15.7, 4.3 Hz, 2 H, CH_2), 4.55 (td, J = 12.8, 4.3 Hz, 2 H, CH_2), 5.55 (ddd, J = 15.7, 12.8, 2.2 Hz, 2 H, CH_2), 6.57 (dd, J = 8.1, 1.3 Hz, 2 H, ArH), 6.63 (dd, J = 7.9, 2.3 Hz, 2 H, ArH), 6.65 (t, J = 7.9 Hz, 2 H, ArH), 6.71 (t, J = 8.1 Hz, 2 H, ArH), 6.95 (dd, J = 7.9, 2.3 Hz, 2 H, ArH), 6.97 (dd, J = 8.1, 1.3 Hz, 2 H, ArH), 8.45 (s, 2 H, $\text{CH}=\text{N}$), 8.77 (s, 2 H, $\text{CH}=\text{N}$) ppm. $\text{C}_{40}\text{H}_{42}\text{LaN}_5\text{O}_{19}\text{Zn}_2\cdot 2\text{H}_2\text{O}$ (1202.54): calcd. C 39.95, H 3.86, N 5.82; found C 39.85, H 4.11, N 5.57.

X-ray Crystallographic Analysis: Intensity data were collected with a Rigaku R-Axis Rapid or Mercury CCD diffractometer with Mo-K_α radiation (λ = 0.71069 Å). Reflection data were corrected for Lorentzian and polarization effects and for absorption using the multiscan method. The structure was solved by direct methods (SHELXS 97^[24]) or Patterson methods (DIRDIF 99^[25]) and re-

finied by full-matrix least-squares on F^2 using SHELXL 97.^[26] The non-hydrogen atoms were refined anisotropically except for the disordered counter-anions or solvent molecules of the crystal of $[(\text{LZn})_2\text{La}(\text{OAc})_2](\text{NO}_3)$. Hydrogen atoms were included at idealized positions and refined by use of riding models. The crystallographic data are summarized in Table 3 and Table 4.

CCDC-759173 (for $[\text{LZnSm}(\text{OAc})_3]\cdot 0.5\text{Et}_2\text{O}$), -759174 (for $[\text{LZnEu}(\text{OAc})_3]\cdot 0.5\text{Et}_2\text{O}$), -759175 (for $[\text{LZnGd}(\text{OAc})_3]\cdot 0.5\text{Et}_2\text{O}$), -759176 (for $[\text{LZnTb}(\text{OAc})_3]\cdot 0.5\text{Et}_2\text{O}$), -759177 (for $[\text{LZnDy}(\text{OAc})_3]\cdot 0.5\text{Et}_2\text{O}$), -759178 (for $[\text{LZnHo}(\text{OAc})_3]\cdot 0.5\text{Et}_2\text{O}$), -759179 (for $[\text{LZnDy}(\text{OAc})_3]$), -759180 (for $[\text{LZnHo}(\text{OAc})_3]$), -759181 (for $[\text{LZnEr}(\text{OAc})_3]$), -759182 (for $[\text{LZnTm}(\text{OAc})_3]$), -759183 (for $[\text{LZnYb}(\text{OAc})_3]$), -759216 (for $[\text{LZnLu}(\text{OAc})_3]$), and -293013 (for $[(\text{LZn})_2\text{La}(\text{OAc})_2](\text{NO}_3)\cdot 2\text{H}_2\text{O}\cdot \text{EtOH}\cdot 0.5\text{hexane}$) contain the supplementary crystallographic data for this paper. These data can be obtained free of charge from The Cambridge Crystallographic Data Center via www.ccdc.cam.ac.uk/data_request/cif.

NMR Titrations: Sample solutions containing H_2L (4.0 mM), zinc(II) acetate dihydrate (8.0 mM), and varying amounts of Ln- $(\text{NO}_3)_3\cdot n\text{H}_2\text{O}$ (Ln = La, Lu; 0–12.0 mM) in $\text{CDCl}_3/\text{CD}_3\text{OD}$ (1:1) were prepared. The ^1H NMR spectra (400 MHz) were recorded with a Bruker ARX 400 spectrometer.

Table 3. Crystallographic data for the zinc(II)–lanthanide(III) complexes.

	$[\text{LZnSm}(\text{OAc})_3]\cdot 0.5\text{Et}_2\text{O}$	$[\text{LZnEu}(\text{OAc})_3]\cdot 0.5\text{Et}_2\text{O}$	$[\text{LZnGd}(\text{OAc})_3]\cdot 0.5\text{Et}_2\text{O}$	$[\text{LZnTb}(\text{OAc})_3]\cdot 0.5\text{Et}_2\text{O}$	$[\text{LZnDy}(\text{OAc})_3]\cdot 0.5\text{Et}_2\text{O}$	$[\text{LZnHo}(\text{OAc})_3]\cdot 0.5\text{Et}_2\text{O}$	$[\text{LZnDy}(\text{OAc})_3]$
Formula	$\text{C}_{26}\text{H}_{32}\text{N}_2\text{O}_{12.5}\text{SmZn}$	$\text{C}_{26}\text{H}_{32}\text{EuN}_2\text{O}_{12.5}\text{Zn}$	$\text{C}_{26}\text{H}_{32}\text{GdN}_2\text{O}_{12.5}\text{Zn}$	$\text{C}_{26}\text{H}_{32}\text{N}_2\text{O}_{12.5}\text{TbZn}$	$\text{C}_{26}\text{H}_{32}\text{DyN}_2\text{O}_{12.5}\text{Zn}$	$\text{C}_{26}\text{H}_{32}\text{HoN}_2\text{O}_{12.5}\text{Zn}$	$\text{C}_{24}\text{H}_{27}\text{DyN}_2\text{O}_{12}\text{Zn}$
Crystal system	orthorhombic	orthorhombic	orthorhombic	orthorhombic	orthorhombic	orthorhombic	monoclinic
Space group	$P2_12_12_1$	$P2_12_12_1$	$P2_12_12_1$	$P2_12_12_1$	$P2_12_12_1$	$P2_12_12_1$	$P2_1/a$
a [Å]	15.678(2)	15.693(5)	15.6927(4)	15.702(3)	15.6786(4)	15.6755(3)	16.0952(13)
b [Å]	16.504(2)	16.493(5)	16.4773(4)	16.478(3)	16.4834(4)	16.4604(4)	11.3653(7)
c [Å]	22.185(3)	22.160(7)	22.1678(6)	22.129(4)	22.1629(6)	22.1862(4)	16.2990(10)
α [°]							
β [°]							115.5292(15)
γ [°]							
V [Å ³]	5740.4(14)	5735(3)	5732.0(3)	5725.4(17)	5727.7(3)	5724.6(2)	2690.4(3)
Z	8	8	8	8	8	8	4
D_{calcd}	1.824	1.830	1.843	1.849	1.856	1.863	1.885
$R1$ [$I > 2\sigma(I)$] ^[a]	0.0324	0.0387	0.0246	0.0297	0.0254	0.0209	0.0459
$wR2$ (all data)	0.0677	0.0960	0.0564	0.0638	0.0569	0.0500	0.1077

[a] $R1 = \Sigma||F_o| - |F_c||/\Sigma|F_o|$; $wR2 = \{\Sigma w(F_o^2 - F_c^2)^2/\Sigma[w(F_o^2)^2]\}^{1/2}$.

Table 4. Crystallographic data for zinc(II)–lanthanide(III) complexes.

	$[\text{LZnHo}(\text{OAc})_3]$	$[\text{LZnEr}(\text{OAc})_3]$	$[\text{LZnTm}(\text{OAc})_3]$	$[\text{LZnYb}(\text{OAc})_3]$	$[\text{LZnLu}(\text{OAc})_3]$	$[(\text{LZn})_2\text{La}(\text{OAc})_2](\text{NO}_3)\cdot 2\text{H}_2\text{O}\cdot \text{EtOH}\cdot 0.5\text{hexane}$
Formula	$\text{C}_{24}\text{H}_{27}\text{HoN}_2\text{O}_{12}\text{Zn}$	$\text{C}_{24}\text{H}_{27}\text{ErN}_2\text{O}_{12}\text{Zn}$	$\text{C}_{24}\text{H}_{27}\text{N}_2\text{O}_{12}\text{TmZn}$	$\text{C}_{24}\text{H}_{27}\text{N}_2\text{O}_{12}\text{YbZn}$	$\text{C}_{24}\text{H}_{27}\text{LuN}_2\text{O}_{12}\text{Zn}$	$\text{C}_{45}\text{H}_{59}\text{LaN}_5\text{O}_{22}\text{Zn}_2$
Crystal system	monoclinic	monoclinic	monoclinic	monoclinic	monoclinic	triclinic
Space group	$P2_1/a$	$P2_1/a$	$P2_1/a$	$P2_1/a$	$P2_1/a$	$P\bar{1}$
a [Å]	16.0629(5)	16.0486(4)	16.0128(4)	15.958(5)	15.865(19)	12.0194(7)
b [Å]	11.3656(3)	11.3486(4)	11.3673(4)	11.355(3)	11.310(12)	14.5924(13)
c [Å]	16.2790(4)	16.2518(4)	16.2331(5)	16.157(5)	16.048(19)	16.5166(14)
α [°]						98.913(4)
β [°]	115.4962(10)	115.3335(7)	115.1438(10)	114.910(13)	114.652(16)	101.5164(13)
γ [°]						108.1109(9)
V [Å ³]	2682.54(13)	2675.28(13)	2674.80(14)	2655.3(14)	2617(5)	2623.7(4)
Z	4	4	4	4	4	2
D_{calcd}	1.896	1.907	1.912	1.936	1.969	1.635
$R1$ [$I > 2\sigma(I)$] ^[a]	0.0227	0.0255	0.0252	0.0271	0.0685	0.0382
$wR2$ (all data) ^[a]	0.0542	0.0643	0.0625	0.0570	0.1657	0.1215

[a] $R1 = \Sigma||F_o| - |F_c||/\Sigma|F_o|$; $wR2 = \{\Sigma w(F_o^2 - F_c^2)^2/\Sigma[w(F_o^2)^2]\}^{1/2}$.

MS Measurements: Sample solutions containing H₂L (0.020 mM), zinc(II) acetate dihydrate (0.040 mM), and Ln(NO₃)₃·nH₂O (Ln = La–Lu; 0.020 mM) in methanol were prepared. The mass spectra (ESI, positive mode) were recorded with an Applied Biosystems QStar Pulsar i spectrometer.

Optical Measurements: UV/Vis absorption spectra were recorded at room temperature with a JASCO V-660 spectrophotometer using a 10 mm pathlength quartz cell. Visible/near-infrared emission spectra in the range of 350–1100 nm were recorded at room temperature with a Hamamatsu Photonics PMA-12 Multichannel Analyzer using an air-equilibrated solution of [LnLn(OAc)₃] (Ln = Sm–Lu; 0.020 mM) in chloroform with an excitation wavelength of 350 nm. The excitation spectrum of 5.0 μM [LnSm(OAc)₃] in chloroform monitored at 644 nm was recorded with a Hitachi F4500 fluorescence spectrophotometer. The absolute quantum yield of [LnLn(OAc)₃] was determined by using an integration sphere equipped with a Hamamatsu photonics PMA-12 Multichannel Analyzer.

Supporting Information (see also the footnote on the first page of this article): X-ray crystallographic data for complexes [LnLn(OAc)₃] (Ln = Sm, Eu, Gd, Tb, Dy, Ho, Er, Tm, Yb, Lu) and ESI mass spectra of H₂L in the presence of zinc(II) acetate and lanthanide(III) nitrate.

Acknowledgments

The work was supported by Grants-in-Aid for Scientific Research from the Ministry of Education, Culture, Sports, Science and Technology, Japan.

- [1] a) S. J. Gruber, C. M. Harris, E. Sinn, *J. Inorg. Nucl. Chem.* **1968**, *30*, 1805–1830; b) C. A. Bear, J. M. Waters, T. N. Waters, *J. Chem. Soc., Dalton Trans.* **1974**, 1059–1062; c) J. M. Epstein, B. N. Figgis, A. H. White, A. C. Willis, *J. Chem. Soc., Dalton Trans.* **1974**, 1954–1961; d) I. Cacelli, L. Carbonaro, P. La Pegna, *Eur. J. Inorg. Chem.* **2002**, 1703–1710.
- [2] a) C. Fukuhara, E. Asato, T. Shimoji, K. Katsura, M. Mori, K. Matsumoto, S. Ooi, *J. Chem. Soc., Dalton Trans.* **1987**, 1305–1311; b) C. Fukuhara, K. Tsuneyoshi, K. Katsura, N. Matsumoto, S. Kida, M. Mori, *Bull. Chem. Soc. Jpn.* **1989**, *62*, 3939–3943; c) A. Gerli, K. S. Hagen, L. G. Marzilli, *Inorg. Chem.* **1991**, *30*, 4673–4676; d) D. Ülkü, F. Ercan, O. Atakol, F. N. Dinçer, *Acta Crystallogr., Sect. C* **1997**, *53*, 1056–1057; e) O. Atakol, C. Arici, F. Ercan, D. Ülkü, *Acta Crystallogr., Sect. C* **1999**, *55*, 511–513; f) O. Atakol, M. Aksu, F. Ercan, C. Arici, M. N. Tahir, D. Ülkü, *Acta Crystallogr., Sect. C* **1999**, *55*, 1072–1075; g) J. Reglinski, S. Morris, D. E. Stevenson, *Polyhedron* **2002**, *21*, 2167–2174.
- [3] a) J.-P. Costes, F. Dahan, A. Dupuis, J.-P. Laurent, *Inorg. Chem.* **1996**, *35*, 2400–2402; b) J.-P. Costes, F. Dahan, A. Dupuis, J.-P. Laurent, *Inorg. Chem.* **1997**, *36*, 3429–3433; c) J.-P. Costes, F. Dahan, A. Dupuis, J.-P. Laurent, *Inorg. Chem.* **1997**, *36*, 4284–4286; d) J.-P. Costes, F. Dahan, A. Dupuis, J.-P. Laurent, *New J. Chem.* **1998**, *22*, 1525–1529; e) J.-P. Costes, F. Dahan, A. Dupuis, J.-P. Laurent, *Chem. Eur. J.* **1998**, *4*, 1616–1620; f) J.-P. Costes, F. Dahan, A. Dupuis, *Inorg. Chem.* **2000**, *39*, 165–168; g) J.-P. Costes, F. Dahan, B. Donnadieu, J. Garcia-Tojal, J.-P. Laurent, *Eur. J. Inorg. Chem.* **2001**, 363–365; h) J.-P. Costes, J. M. Clemente-Juan, F. Dahan, F. Dumestre, J.-P. Tuchagues, *Inorg. Chem.* **2002**, *41*, 2886–2891; i) R. Gheorghe, M. Andruh, J.-P. Costes, B. Donnadieu, *Chem. Commun.* **2003**, 2778–2779; j) R. Koner, H.-H. Lin, H.-H. Wei, S. Mohanta, *Inorg. Chem.* **2005**, *44*, 3524–3536; k) T. Kajiwaru, M. Nakano, S. Takaishi, M. Yamashita, *Inorg. Chem.* **2008**, *47*, 8604–8606.
- [4] a) W.-K. Wong, H. Liang, W.-Y. Wong, Z. Cai, K.-F. Li, K.-W. Cheah, *New J. Chem.* **2002**, *26*, 275–278; b) O. Margeat, P. G. Lacroix, J.-P. Costes, B. Donnadieu, C. Lepetit, K. Nakatani, *Inorg. Chem.* **2004**, *43*, 4743–4750; c) W.-K. Lo, W.-K. Wong, J. Guo, W.-Y. Wong, K.-F. Li, K.-W. Cheah, *Inorg. Chim. Acta* **2004**, *357*, 4510–4521; d) X. Yang, R. A. Jones, V. Lynch, M. M. Oye, A. L. Holmes, *Dalton Trans.* **2005**, 849–851.
- [5] H₂salamo = 1,2-bis(salicylideneaminoxyl)ethane, see: a) S. Akine, T. Taniguchi, T. Nabeshima, *Chem. Lett.* **2001**, 682–683; b) S. Akine, T. Taniguchi, W. Dong, S. Masubuchi, T. Nabeshima, *J. Org. Chem.* **2005**, *70*, 1704–1711.
- [6] S. Akine, T. Taniguchi, T. Nabeshima, *Inorg. Chem.* **2004**, *43*, 6142–6144.
- [7] S. Akine, T. Taniguchi, T. Nabeshima, *Chem. Lett.* **2006**, *35*, 604–605.
- [8] For related complexes, see: a) S. Akine, T. Nabeshima, *Inorg. Chem.* **2005**, *44*, 1205–1207; b) S. Akine, T. Matsumoto, T. Taniguchi, T. Nabeshima, *Inorg. Chem.* **2005**, *44*, 3270–3274; c) S. Akine, W. Dong, T. Nabeshima, *Inorg. Chem.* **2006**, *45*, 4677–4684; d) S. Akine, A. Akimoto, T. Shiga, H. Oshio, T. Nabeshima, *Inorg. Chem.* **2008**, *47*, 875–885.
- [9] The trigonality index τ ($\tau = 0$ denotes ideal square pyramidal; $\tau = 1$ denotes ideal trigonal bipyramidal) was calculated according to the literature, see: A. W. Addison, T. N. Rao, J. Reedijk, J. van Rijn, G. C. Verschoor, *J. Chem. Soc., Dalton Trans.* **1984**, 1349–1356.
- [10] The intramolecular C–H···O contact causes a significant downfield shift of the ¹H NMR signal, see: S. A. Bourne, X. Y. Mbianda, H. Wan, T. A. Modro, *J. Mol. Struct.* **1999**, *475*, 161–165.
- [11] S. Akine, T. Nabeshima, *Dalton Trans.* **2009**, 10395–10408.
- [12] For bis- and tris(salamo) complexes, see: a) S. Akine, T. Taniguchi, T. Nabeshima, *Angew. Chem. Int. Ed.* **2002**, *41*, 4670–4673; b) S. Akine, T. Taniguchi, T. Saiki, T. Nabeshima, *J. Am. Chem. Soc.* **2005**, *127*, 540–541; c) S. Akine, T. Taniguchi, T. Nabeshima, *Tetrahedron Lett.* **2006**, *47*, 8419–8422; d) S. Akine, T. Taniguchi, T. Nabeshima, *J. Am. Chem. Soc.* **2006**, *128*, 15765–15774; e) S. Akine, T. Taniguchi, T. Matsumoto, T. Nabeshima, *Chem. Commun.* **2006**, 4961–4963; f) S. Akine, S. Sunaga, T. Taniguchi, H. Miyazaki, T. Nabeshima, *Inorg. Chem.* **2007**, *46*, 2959–2961; g) S. Akine, S. Kagiya, T. Nabeshima, *Inorg. Chem.* **2007**, *46*, 9525–9527; h) S. Akine, T. Taniguchi, T. Nabeshima, *Inorg. Chem.* **2008**, *47*, 3255–3264; i) S. Akine, S. Kagiya, T. Nabeshima, *Inorg. Chem.* **2010**, *49*, 2141–2152.
- [13] a) G. R. Choppin, D. R. Peterman, *Coord. Chem. Rev.* **1998**, *174*, 283–299; b) H. Tsukube, S. Shinoda, *Chem. Rev.* **2002**, *102*, 2389–2403; c) D. Parker, *Coord. Chem. Rev.* **2000**, *205*, 109–130; d) K. Binnemans, *Chem. Rev.* **2009**, *109*, 4283–4374; e) J.-C. G. Bünzli, *Chem. Rev.* **2010**, *110*, 2729–2755.
- [14] For the luminescence of zinc(II)–lanthanide(III) dinuclear complexes of salen-type ligands, see: a) W.-K. Wong, X. Yang, R. A. Jones, J. H. Rivers, V. Lynch, W.-K. Lo, D. Xiao, M. M. Oye, A. L. Holmes, *Inorg. Chem.* **2006**, *45*, 4340–4345; b) W.-K. Lo, W.-K. Wong, W.-Y. Wong, J. Guo, K.-T. Yeung, Y.-K. Cheng, X. Yang, R. A. Jones, *Inorg. Chem.* **2006**, *45*, 9315–9325; c) X. Yang, R. A. Jones, Q. Wu, M. M. Oye, W.-K. Lo, W.-K. Wong, A. L. Holmes, *Polyhedron* **2006**, *25*, 271–278; d) X.-P. Yang, R. A. Jones, W.-K. Wong, V. Lynch, M. M. Oye, A. L. Holmes, *Chem. Commun.* **2006**, 1836–1838; e) X. Lü, W. Bi, W. Chai, J. Song, J. Meng, W.-Y. Wong, W.-K. Wong, R. A. Jones, *New J. Chem.* **2008**, *32*, 127–131; f) W.-Y. Bi, X.-Q. Lü, W.-L. Chai, J.-R. Song, W.-K. Wong, X.-P. Yang, R. A. Jones, *Z. Anorg. Allg. Chem.* **2008**, *634*, 1795–1800; g) W.-Y. Bi, X.-Q. Lü, W.-L. Chai, J.-R. Song, W.-Y. Wong, W.-K. Wong, R. A. Jones, *J. Mol. Struct.* **2008**, *891*, 450–455; h) X. Lü, W. Bi, W. Chai, J. Song, J. Meng, W.-Y. Wong, W.-K. Wong, X. Yang, R. A. Jones, *Polyhedron* **2009**, *28*, 27–32.
- [15] For the luminescence of zinc(II)–lanthanide(III) trinuclear complexes of related bis(salamo) ligands, see: a) S. Akine, F. Utsuno, T. Nabeshima, *IOP Conf. Ser.: Mater. Sci. Eng.* **2009**,

- J.*, 012009; b) S. Akine, Y. Morita, F. Utsuno, T. Nabeshima, *Inorg. Chem.* **2009**, *48*, 10670–10678.
- [16] E. G. Moore, A. P. S. Samuel, K. N. Raymond, *Acc. Chem. Res.* **2009**, *42*, 542–552.
- [17] Y. Hasegawa, S.-i. Tsuruoka, T. Yoshida, H. Kawai, T. Kawai, *J. Phys. Chem. A* **2008**, *112*, 803–807.
- [18] a) N. Sabbatini, S. Dellonte, G. Blasse, *Chem. Phys. Lett.* **1986**, *129*, 541–545; b) A. P. Bassett, S. W. Magennis, P. B. Glover, D. J. Lewis, N. Spencer, S. Parsons, R. M. Williams, L. De Cola, Z. Pikramenou, *J. Am. Chem. Soc.* **2004**, *126*, 9413–9424.
- [19] a) P. S. May, M. F. Reid, F. S. Richardson, *Mol. Phys.* **1987**, *61*, 1471–1485; b) P. S. May, D. H. Metcalf, F. S. Richardson, R. C. Carter, C. E. Miller, R. A. Palmer, *J. Lumin.* **1992**, *51*, 249–268; c) X. Cunjin, *J. Rare Earths* **2006**, *24*, 429–433.
- [20] a) S. Petoud, J.-C. G. Bünzli, T. Glanzman, C. Piguet, Q. Xiang, R. P. Thummel, *J. Lumin.* **1999**, *82*, 69–79; b) M. D. Regulacio, M. H. Pablico, J. A. Vasquez, P. N. Myers, S. Gentry, M. Prushan, S.-W. Tam-Chang, S. L. Stoll, *Inorg. Chem.* **2008**, *47*, 1512–1523.
- [21] Similar quenching of the f–f emission of a Schiff base Zn–Eu complex by LMCT has recently been reported, see: T. D. Pasatoiu, A. M. Madalan, M. U. Kumke, C. Tiseanu, M. Andruh, *Inorg. Chem.* **2010**, *49*, 2310–2315.
- [22] M. D. Ward, *Coord. Chem. Rev.* **2007**, *251*, 1663–1677.
- [23] a) S. Faulkner, S. J. A. Pope, *J. Am. Chem. Soc.* **2003**, *125*, 10526–10527; b) S. Quici, M. Cavazzini, G. Marzanni, G. Accorsi, N. Armaroli, B. Ventura, F. Barigelli, *Inorg. Chem.* **2005**, *44*, 529–537; c) D. Imbert, S. Comby, A.-S. Chauvin, J.-C. G. Bünzli, *Chem. Commun.* **2005**, 1432–1434; d) R. F. Ziesel, G. Ulrich, L. Charbonnière, D. Imbert, R. Scopelliti, J.-C. G. Bünzli, *Chem. Eur. J.* **2006**, *12*, 5060–5067; e) H. Tsukube, Y. Suzuki, D. Paul, Y. Kataoka, S. Shinoda, *Chem. Commun.* **2007**, 2533–2535.
- [24] G. M. Sheldrick, *SHELXS 97, Program for crystal structure solution*, University of Göttingen, Göttingen, Germany, **1997**.
- [25] P. T. Beurskens, G. Beurskens, R. de Gelder, S. Garcia-Granda, R. O. Gould, R. Israel, J. M. M. Smits, *The DIRDIF 99 program system*, Crystallography Laboratory, University of Nijmegen, Nijmegen, The Netherlands, **1999**.
- [26] G. M. Sheldrick, *SHELXL 97, Program for crystal structure refinement*, University of Göttingen, Göttingen, Germany, **1997**.

Received: December 24, 2009
Published Online: May 26, 2010

Linear Tetranickel String Complexes with Mixed Supported Ligands and Mixed-Valence Units $[\text{Ni}_2]^{3+}$: Synthesis, Crystal Structure, and Magnetic Studies

Che-Wei Yeh,^[a] Isiah Po-Chun Liu,^{[a,b]‡} Rui-Ren Wang,^[a] Chen-Yu Yeh,^[c] Gene-Hsiang Lee,^[a] and Shie-Ming Peng^{*[a,b]}

Keywords: Molecular wire / Mixed-valent compounds / Magnetic properties / Nickel / Ligand effects

The synthesis, crystal structures, and magnetic properties of linear tetranickel string complexes supported by mixed 2-(α -pyridylamino)-1,8-naphthyridine (Hpyany) and *N*-(*p*-tolylsulfonyl)dipyridyldiamine (H_2tsdpda) ligands are reported. In comparing the crystal structure of $[\text{Ni}_4(\text{pyany})_2(\text{tsdpda})_2\text{Cl}](\text{PF}_6)$ (**1**) with that of $[\text{Ni}_4(\text{pyany})_2(\text{tsdpda})_2\text{Cl}(\text{H}_2\text{O})](\text{PF}_6)$ (**2**), the one-electron-reduced compound **1** displays shorter Ni(3)–Ni(4) (ca. 2.28 Å) and longer Ni(3)–N (ca. 2.02 Å) bond lengths. Similar trends have also been observed for axial NCS[–]-substituted derivatives $[\text{Ni}_4(\text{pyany})_2(\text{tsdpda})_2(\text{NCS})]$

(**3**) and $[\text{Ni}_4(\text{pyany})_2(\text{tsdpda})_2(\text{NCS})_2]$ (**4**). These structural variations indicate the formation of a mixed-valence $[\text{Ni}_2]^{3+}$ unit and a three-electron, two-center Ni(4)–Ni(3) σ bond. Magnetic measurements of **2** and **4** show that both terminal Ni(1) and Ni(4) ions are in the high-spin states ($S = 1$) and are antiferromagnetically coupled. The one-electron-reduced complexes **1** and **3**, however, exhibit a delocalized mixed-valence $[\text{Ni}_2]^{3+}$ unit ($S = 3/2$), which is antiferromagnetically coupled with the terminal high-spin Ni^{II} ion.

Introduction

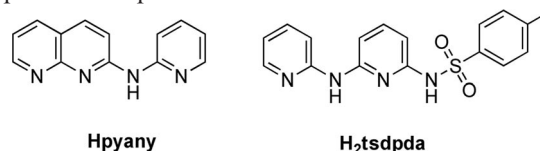
Metal string complexes mimic the electric wires in our macroscopic world down to the atomic scale, and are expected to serve as molecular wires in the fabrication of future nanoelectronic devices.^[1] Because of this potential application, numerous metal string complexes have been synthesized and characterized in the past two decades.^[2] The general approach to synthesize the metal string complexes is to utilize oligo- α -pyridylamido ligands. These ligands contain numerous amido and pyridino groups, which can stabilize the cationic 1D linear transition-metal backbone.

Recently, oligo-(α -pyridylamido) ligands have been modified by insertion of naphthyridino and anilino groups. Interestingly, the resulting metal string complexes exhibit novel physical properties. For instance, the bis(naphthyridylamido) (bna^-) ligand is less anionic than the tripyridyldiamido (tpda^{2-}) ligand. The resulting pentanickel string complex $[\text{Ni}_5(\text{bna})_4(\text{NCS})_2] \cdot (\text{NCS})_2$ has a reduced metal framework and greater electronic mobility, which shows about 40% conductance enhancement relative to that of the $[\text{Ni}_5(\text{tpda})_4(\text{NCS})_2]$ complex.^[3] This result suggests that the modification of supporting organic ligands is a suitable

method to fine-tune the properties of metal string complexes.^[2d]

In addition to the crystal structures, the physical properties of metal string complexes may also be modulated by utilizing mixed ligands. In our previous report, trinickel string complexes with various mixed ligands exhibited various spin states because of the different interactions between the axial ligands and metal ions.^[4] It suggested that a novel metal string complex may be synthesized by carefully designing its surrounding ligands, since the coordinated ability and steric hindrance of these ligands are quite different, and these can modulate the physical properties of the linear metal framework.

Based on the above ideas, new tetranickel string complexes with mixed 2-(α -pyridylamino)-1,8-naphthyridine (Hpyany) and *N*-(*p*-tolylsulfonyl)dipyridyldiamine (H_2tsdpda) ligands (Scheme 1) have been synthesized and isolated. The crystal structures, and magnetic properties of these tetranickel string complexes are reported and discussed in this work.



Scheme 1. Hpyany and H_2tsdpda ligands.

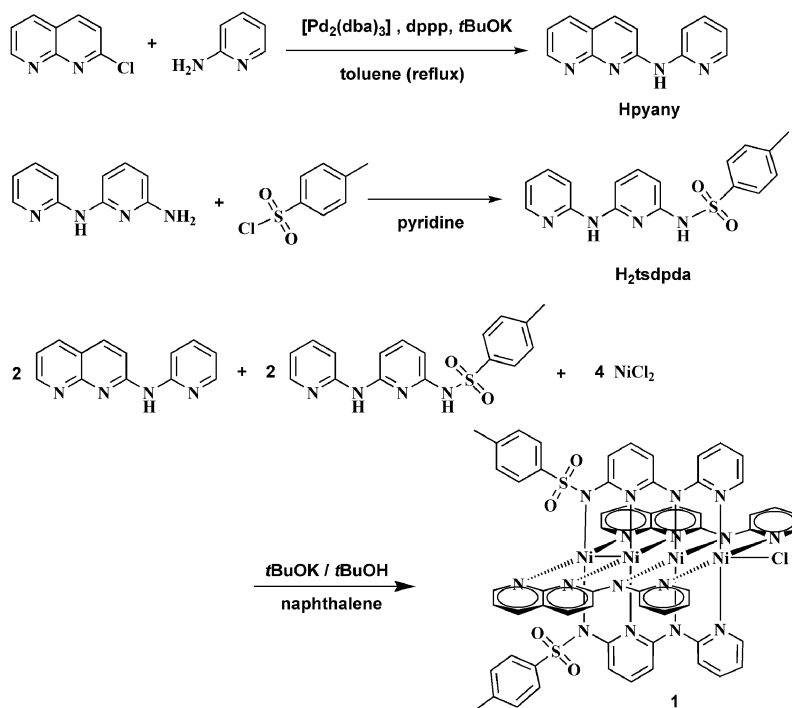
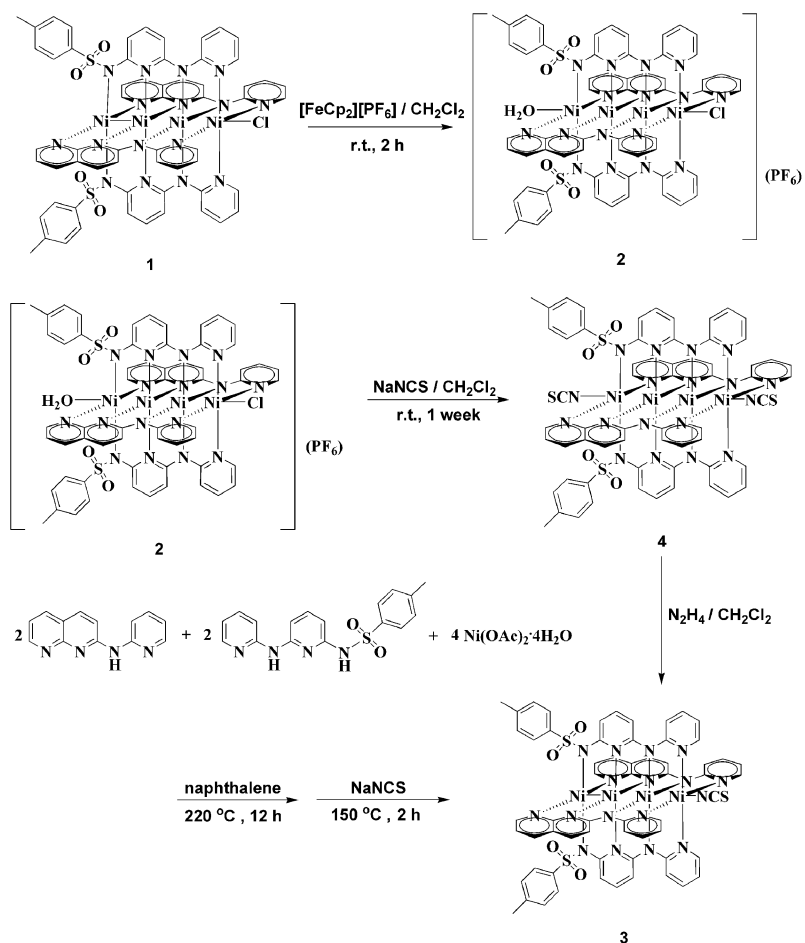
For clarity, the tetranickel string complexes presented in this paper are as follows: $[\text{Ni}_4(\text{pyany})_2(\text{tsdpda})_2\text{Cl}](\text{PF}_6)$ (**1**), $[\text{Ni}_4(\text{pyany})_2(\text{tsdpda})_2\text{Cl}(\text{H}_2\text{O})](\text{PF}_6)$ (**2**), $[\text{Ni}_4(\text{pyany})_2(\text{tsdpda})_2(\text{NCS})]$ (**3**), and $[\text{Ni}_4(\text{pyany})_2(\text{tsdpda})_2(\text{NCS})_2]$ (**4**).

[a] Department of Chemistry, National Taiwan University, Taipei, Taiwan

[b] Institute of Chemistry, Academia Sinica, Taipei, Taiwan

[c] Department of Chemistry, National Chung Hsing University, Taichung, Taiwan

[‡] Current address: Institut für Anorganische Chemie, Universität Bonn, Bonn, Germany

Scheme 2. Synthesis of complex **1** [dba = dibenzylideneacetone; dppp = 1,3-bis(diphenylphosphanyl)propane].Scheme 3. Synthesis of complexes **2**, **3**, and **4**.

Results and Discussion

Synthesis and Characterization

The overall synthetic routes to the Hpyany and H₂tsdpda ligands, and then to complexes **1–4** are summarized in Schemes 2 and 3. The Hpyany ligand was prepared by reaction of 2-chloro-1,8-naphthyridine and 2-aminopyridine with palladium catalyst. The H₂tsdpda ligand was prepared by reaction of dipyridyldiamine (H₃dpda) with *p*-toluenesulfonyl chloride (*p*TsCl) in pyridine. Treatment of Hpyany and H₂tsdpda with NiCl₂ in the presence of *t*BuOK generated compound **1**. The one-electron-oxidized compound **2** was obtained by treating **1** with [FeCp₂][PF₆] (Cp = cyclopentadienyl) in CH₂Cl₂. The axial ligand exchange of compound **2** to generate compound **4** was achieved by stirring **2** with an excess amount of NaNCS in CH₂Cl₂. The one-electron-reduced compound **3** was obtained by treatment of **4** with N₂H₄ in CH₂Cl₂ or by reaction of Hpyany and H₂tsdpda with Ni(OAc)₂ in naphthalene heated at reflux followed by ligand exchange.

X-ray Analysis

The crystallographic data for **1–4** are listed in Table 1. The labeled ORTEP plots excluding solvent molecules and selected bond lengths for all complexes are reported in Figures 1, 2 <yigr2 pos="x1">, 3, 4, and 5. The core structures of **1–4** reveal a tetranickel framework, which are helically wrapped by two pyany[−] and two tsdpda^{2−} ligands. These ligands adopt a (2,2)-*trans* arrangement, which causes these compounds to exhibit an approximate C₂ symmetry. Crystallographically, compounds **1–4** all exhibit one independent metal string in an asymmetric unit.

The tetranickel cores of **2** and **4** are [Ni₄]⁸⁺, in which the coordination environment of the terminal Ni(1) and Ni(4) atoms is square pyramidal, whereas that of Ni(2) and Ni(3) is square planar. The outmost Ni(1)–N and Ni(4)–N bond lengths are around 2.10 Å, thereby suggesting a high-spin nickel(II) (*S* = 1) character.^[5] The inner Ni(2) and Ni(3)

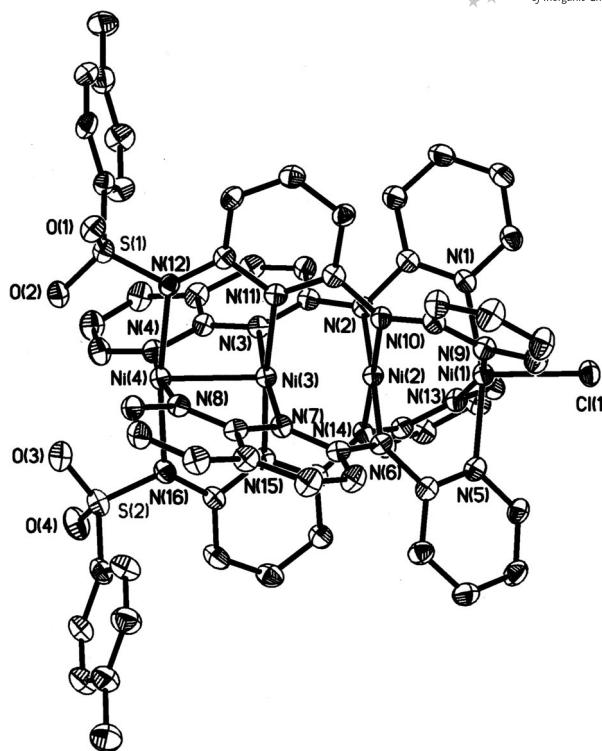


Figure 1. Molecular structure of complex **1**. Ellipsoids are drawn at 30% probability levels. Hydrogen atoms and interstitial solvent molecules have been omitted for clarity.

are of a low-spin nickel(II) electronic configuration (*S* = 0) judging by their short Ni–N bond lengths (ca. 1.90 Å).^[6] The axial ligands at the terminal Ni^{II} ions of **2** and **4** are different. The large PF₆[−] ion of **2** does not bond to the Ni(4) ion due to the steric interaction with the two tolylsulfonyl groups. Instead of the PF₆[−] ion, a neutral H₂O molecule occupies the axial position. Hydrogen bonds were observed between the hydrogen atoms of H₂O and oxygen atom of two tolylsulfonyl groups. The small NCS[−] ligand, however, does not show steric interaction with the tolylsulfonyl groups. Compound **4** has two axial NCS[−] ligands and is suitable for conductivity measurement.^[3]

Table 1. X-ray crystallographic data for **1**, **2**, **3**, and **4**.

	1 ·3.5CH ₂ Cl ₂ ·C ₆ H ₁₄	2 ·2CH ₂ Cl ₂ ·Et ₂ O	3 ·4CH ₂ Cl ₂ ·0.5EtOH	4 ·3.5CH ₂ Cl ₂
Formula	C _{69.5} H ₆₇ Cl ₈ N ₁₆ Ni ₄ O ₄ S ₂	C ₆₆ H ₆₂ Cl ₅ F ₆ N ₁₆ Ni ₄ O ₆ PS ₂	C ₆₆ H ₅₇ Cl ₈ N ₁₇ Ni ₄ O _{4.5} S ₃	C _{65.5} H ₅₃ Cl ₇ N ₁₈ Ni ₄ O ₄ S ₄
<i>M_r</i>	1815.41	1796.5	1806.95	1783.51
Crystal system	triclinic	triclinic	triclinic	monoclinic
Space group	<i>P</i> 1̄	<i>P</i> 1̄	<i>P</i> 1̄	<i>C</i> 2/ <i>c</i>
<i>a</i> [Å]	15.0592(5)	14.3336(2)	14.9080(4)	39.7482(9)
<i>b</i> [Å]	15.9191(6)	14.8998(2)	15.6760(4)	16.0945(5)
<i>c</i> [Å]	17.8018(6)	18.7954(3)	17.6095(5)	25.8662(6)
<i>α</i> [°]	81.483(2)	75.8719(8)	81.8419(17)	90
<i>β</i> [°]	74.805(2)	87.4940(7)	75.5677(18)	118.1843(14)
<i>γ</i> [°]	68.839(2)	68.2975(9)	70.4780(18)	90
<i>V</i> [Å ³]	3833.9(2)	3611.92(9)	3748.57(17)	14585.3(7)
<i>Z</i>	2	2	2	8
<i>T</i> [K]	150(2)	150(2)	150(2)	293(2)
<i>ρ</i> _{calcd.} [g cm ^{−3}]	1.573	1.652	1.601	1.624
<i>R</i> 1 ^[a] / <i>wR</i> 2 ^[b] [<i>I</i> > 2σ(<i>I</i>)]	0.0755/0.2061	0.0759/0.2297	0.0738/0.1981	0.0711/0.1936
<i>R</i> 1 ^[a] / <i>wR</i> 2 ^[b] (all data)	0.1039/0.2331	0.1179/0.2614	0.1141/0.2330	0.1380/0.2300

[a] *R*1 = Σ||*F*_o − |*F*_c||/Σ|*F*_o|. [b] *wR*2 = {Σ[*w*(*F*_o² − *F*_c²)²]/Σ[*w*(*F*_o²)²]}^{1/2}, in which *w* = 1/σ²(*F*_o²) + (*aP*)² + *bP*, *P* = (*F*_o² + 2*F*_c²)/3.

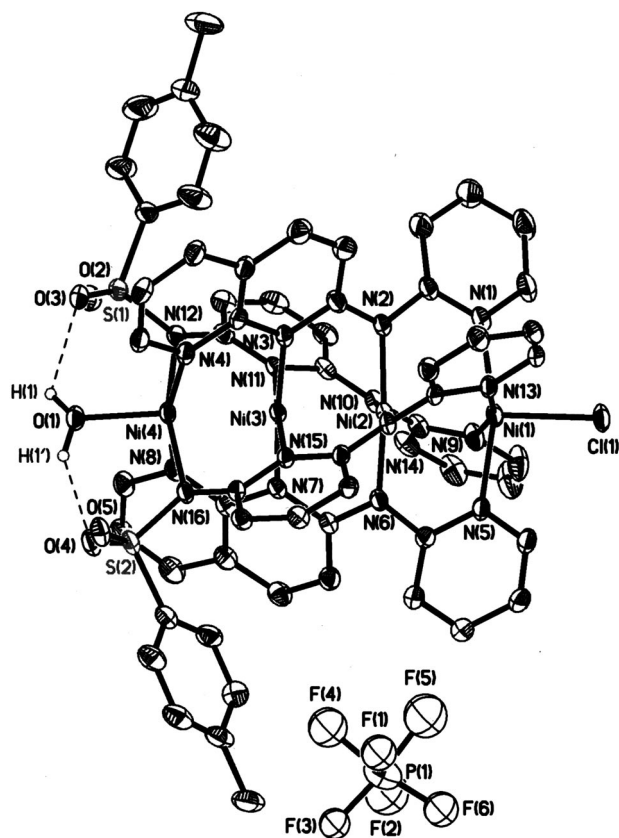


Figure 2. Molecular structure of complex **2**. Ellipsoids are drawn at 30% probability levels. Hydrogen atoms and interstitial solvent molecules have been omitted for clarity.

The one-electron-reduced compounds **1** and **3** possess a $[\text{Ni}_4]^{7+}$ core. Compounds **1** and **3** display a significantly shorter Ni(4)–Ni(3) bond length (ca. 2.28 Å) and a longer

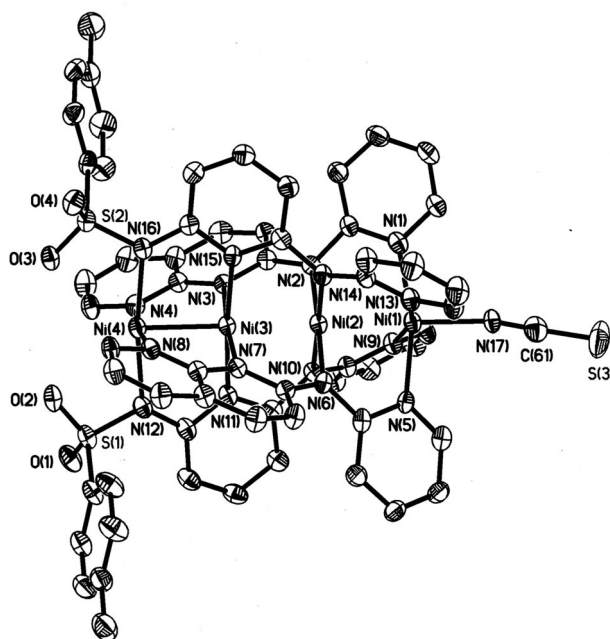


Figure 3. Molecular structure of complex **3**. Ellipsoids are drawn at 30% probability levels. Hydrogen atoms and interstitial solvent molecules have been omitted for clarity.

Ni(3)–N bond length (ca. 2.00 Å) than **2** and **4**. These structural variations indicate that an extra electron occupies the $d_{x^2-y^2}$ orbital of Ni(3), which results in the formation of a three-electron, two-center Ni(4)–Ni(3) σ bond and the $S = 3/2$ mixed-valence $[\text{Ni}_2]^{3+}$ unit.^[3,7] The Ni(1)–N and Ni(2)–N bond lengths of **1** and **3** are around 2.09 and around 1.90 Å, respectively. Considering these Ni–N bond lengths and the coordination spheres of Ni(1) (square pyramidal)

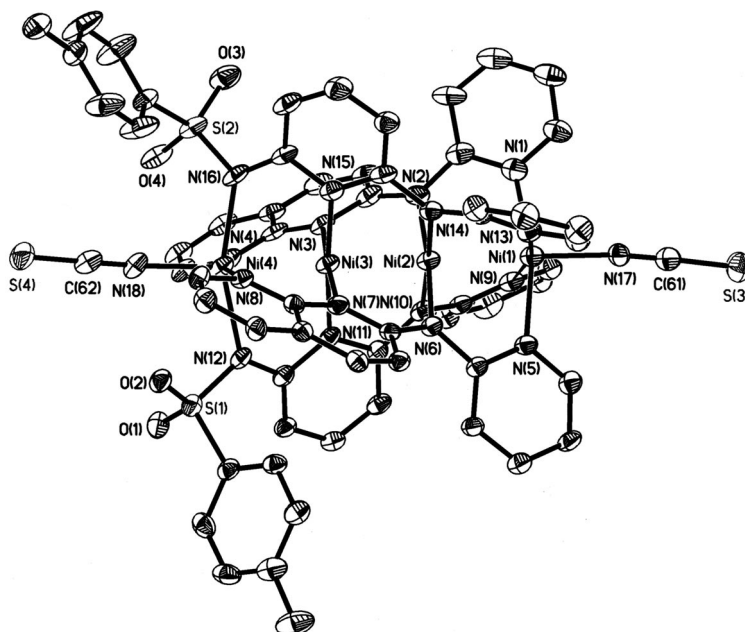


Figure 4. Molecular structure of complex **4**. Ellipsoids are drawn at 30% probability levels. Hydrogen atoms and interstitial solvent molecules have been omitted for clarity.

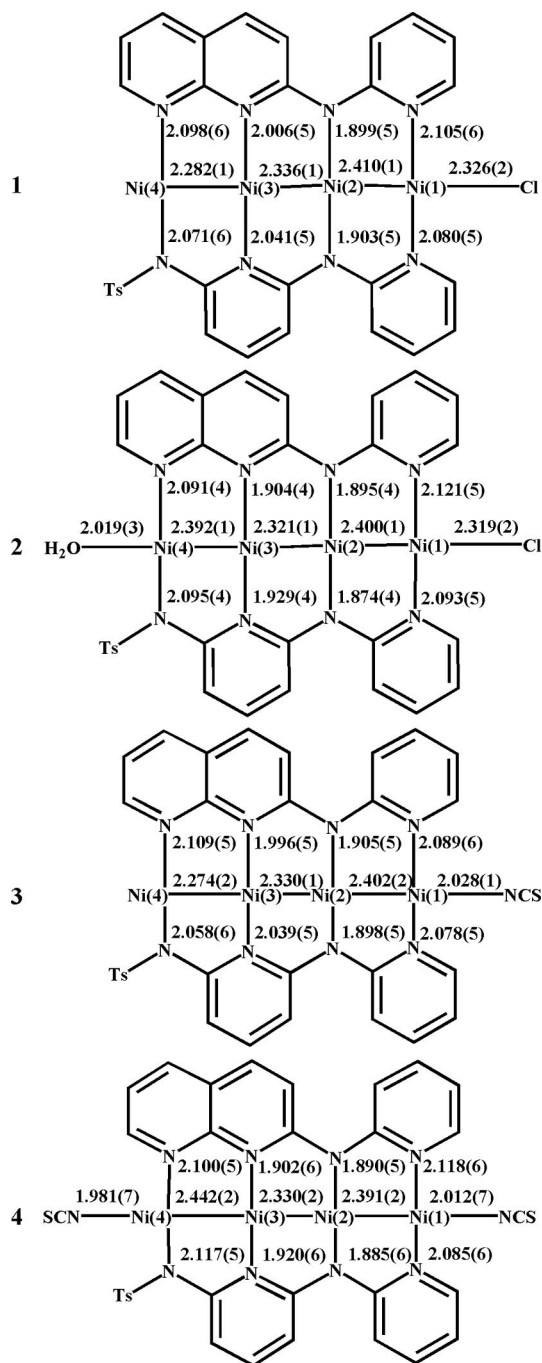
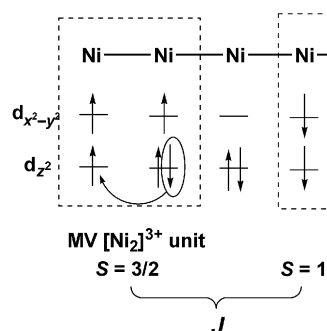


Figure 5. Selected interatomic distances [Å] observed for complexes 1–4.

and Ni(2) (square planar), the Ni(1) and Ni(2) ions were assigned to high-spin ($S = 1$) and low-spin ($S = 0$) nickel(II) ions, respectively.^[5,6]

In our previous reports, the mixed-valence (MV) $[\text{Ni}_2]^{3+}$ unit (Scheme 4) was found to be stabilized by four less anionic naphthyridyl groups.^[3,7] The crystal structural analysis of **1** and **3**, however, suggests that the $[\text{Ni}_2]^{3+}$ unit can be stabilized by only two instead of four naphthyridyl groups, which might allow us to modulate the physical properties of metal string complexes by modifying the other two ligands.



Scheme 4. Coupling scheme for complexes **1** ($X = \text{Cl}$) and **3** ($X = \text{NCS}$).

Magnetism

Magnetic susceptibility measurements for compounds **1**–**4** were made on polycrystalline samples in the temperature range of 4–300 K (Figure 6). The $\chi_M T$ product values ($\text{cm}^3 \text{mol}^{-1} \text{K}$) of compounds **2** and **4** at 300 K are 2.03 and 1.81, respectively. These values are similar to that obtained from complexes with two uncoupled high-spin Ni^{II} ($S = 1$) ions (ca. 2).^[3,6] The $\chi_M T$ values of **2** and **4** decrease gradually with decreasing temperature, which clearly indicates that an antiferromagnetic coupling is operating. To study the coupling constant of **2** and **4**, an isotropic Heisenberg–Dirac–van Vleck (HDvV) Hamiltonian – see Equation (1) – with $S_1 = S_2 = 1$ was used.^[8]

$$H = -JS_1S_2 + g\beta SH \quad (1)$$

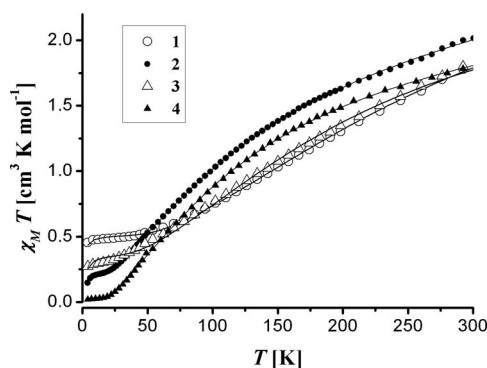


Figure 6. Plot of $\chi_M T$ versus T for complexes **1**–**4**. The solid line represents the best theoretical fit.

The best-fit parameters obtained were $J = -70.7 \text{ cm}^{-1}$ and $g = 2.04$ for **2**; $J = -68.8 \text{ cm}^{-1}$ and $g = 1.98$ for **4**. The coupling constant J is in agreement with the moderate antiferromagnetic interaction.

According to the X-ray structural analysis and our previous studies, the spin centers of **1** and **3** can be assigned to $S = 3/2$ and $S = 1$ (Scheme 4). The $\chi_M T$ product values ($\text{cm}^3 \text{mol}^{-1} \text{K}$) of compounds **1** and **3** at 300 K are 1.81 and 1.83, respectively, which are significantly lower than the theoretical expected value for two uncoupled $S = 3/2$ and S

= 1 magnetic centers (ca. 2.88), thus indicating a relative strong antiferromagnetic interaction.^[9] Upon cooling, the χ_{MT} product values of **1** and **3** decrease rapidly to reach a value of 0.46 and 0.28, respectively, at 4 K. This pattern suggests the presence of an antiferromagnetic coupling between $S = 3/2$ and $S = 1$ centers and a $S = 1/2$ ground state. By means of the appropriate HDvV Hamiltonian [see Equation (1), $S_1 = 3/2$, $S_2 = 1$], the experimental susceptibility curve could be well reproduced with the set of parameter $J = -121 \text{ cm}^{-1}$ and $g = 2.12$ for **1**; $J = -89.3 \text{ cm}^{-1}$ and $g = 1.97$ for **3**, which shows a relative stronger antiferromagnetic interaction.

Conclusion

Four linear tetranickel string complexes supported by mixed pyany[−] and tsdpda^{2−} ligands were synthesized and studied. An X-ray crystal structural analysis and the magnetic properties of compounds **1** and **3** indicate the formation of a mixed-valence $S = 3/2$ $[\text{Ni}_2]^{3+}$ unit. It was found that the $[\text{Ni}_2]^{3+}$ unit can be stabilized by two naphthyridyl-containing ligands and the remaining two surrounding ligands can be modified. It is noteworthy that even-numbered metal strings exhibit structural and magnetic behavior that is different from odd-numbered ones.^[10] The physical properties of even-numbered metal string complexes, could thus be tentatively fine-tuned by utilizing various sets of mixed ligands, which introduces a new approach to the development of future metal string complexes.

Experimental Section

Materials: All reagents and solvents were purchased from commercial sources and were used as received unless otherwise noted. The precursor 2-chloro-1,8-naphthyridine and the ligand *N*-(*p*-tolylsulfonyl)dipyridyldiamine (H_2tsdpda) were prepared according to the literature procedures.^[3,10]

2-(α -Pyridylamino)-1,8-naphthyridine (Hpyany): 2-Chloro-1,8-naphthyridine (4.95 g, 30.2 mmol), *t*BuOK (4.37 g, 39.0 mmol), $[\text{Pd}_2(\text{dba})_3]$ (0.820 mg, 0.895 mmol), and dppp (0.740 mg, 1.80 mmol) were placed in a flame-dried flask under argon. The mixture was stirred and heated at reflux in toluene (150 mL) for 72 h. The solvent was removed under reduced pressure. The mixture was purified by column chromatography over silica gel (Hpyany/silica gel = 0.9 wt. %) with $\text{CH}_2\text{Cl}_2/\text{acetone}$ (1:4), then the yellow powder of the Hpyany was obtained. Yield: 60%. ¹H NMR (400 MHz, $[\text{D}]\text{DMSO}$): δ = 10.3 (s, 1 H), 8.81 (dd, J = 4.0, 4.8 Hz, 1 H), 8.58 (d, J = 8.8 Hz, 1 H), 8.29 (dd, J = 3.6, 4.8 Hz, 1 H), 8.19 (t, J = 19.2 Hz, 1 H), 8.18 (t, J = 16.8 Hz, 1 H), 7.80 (tt, J = 15.6, 16.0 Hz, 1 H), 7.60 (d, J = 9.2 Hz, 1 H), 7.33 (dd, J = 7.6, 8 Hz, 1 H), 6.99 (tt, J = 12.0, 12.4 Hz, 1 H) ppm. MS (FAB): m/z = 223.1 $[\text{C}_{13}\text{H}_4\text{N}_{10} + \text{H}]^+$. $\text{C}_{13}\text{H}_4\text{N}_{10}$ (222.25): calcd. C 70.26, H 4.54, N 25.21; found C 70.27, H 4.66, N 25.55.

$[\text{Ni}_4(\text{pyany})_2(\text{tsdpda})_2\text{Cl}]$ (1**):** A mixture of Hpyany (150 mg, 0.675 mmol), H_2tsdpda (230 mg, 0.675 mmol), naphthalene (30 g), and NiCl_2 (230 mg, 1.77 mmol) was placed in an Erlenmeyer flask. After stirring the mixture at 200 °C for 12 h, *t*BuOK (240 mg, 2.14 mmol) in *t*BuOH (3 mL) was added dropwise. The solution then turned dark green and was stirred for an additional 8 h. After

cooling the mixture to 70 °C, hexane was added and the resulting precipitate was filtered out. The solid (yield 314 mg, 67%) was extracted with CH_2Cl_2 and layered with hexane. After one week, deep green crystals were obtained; yield 23.4 mg, 5%. MS (MALDI): m/z = 1390 $[\text{Ni}_4(\text{pyany})_2(\text{tsdpda})_2\text{Cl} + \text{H}]^+$. $\text{C}_{125}\text{H}_{106}\text{Cl}_4\text{N}_{32}\text{Ni}_8\text{O}_{10}\text{S}_4$ (2956.01): calcd. C 50.79, H 3.61, N 15.16; found C 50.46, H 3.60, N 15.28.

$[\text{Ni}_4(\text{pyany})_2(\text{tsdpda})_2\text{Cl}(\text{H}_2\text{O})](\text{PF}_6)$ (2**):** The complex **1** (20.0 mg, 0.0144 mmol) was dissolved in CH_2Cl_2 (50 mL) and treated with $[\text{FeCp}_2][\text{PF}_6]$ (5.30 mg, 0.0170 mmol). The resulting solution was stirred for 2 h and dried under vacuum. The powder was extracted with $\text{CH}_2\text{Cl}_2/\text{diethyl ether}$ (1:1) to get rid of the FeCp_2 . The solvent was removed under vacuum. The residue was dissolved in CH_2Cl_2 . Brown crystals were obtained by slow diffusion of diethyl ether into this solution; yield 16.2 mg, 70%. MS (FAB): m/z = 1389 $[\text{Ni}_4(\text{pyany})_2(\text{tsdpda})_2\text{Cl}]^+$. $\text{C}_{121}\text{H}_{98}\text{Cl}_4\text{F}_{12}\text{N}_{32}\text{Ni}_8\text{O}_{10}\text{P}_2\text{S}_4$ (3189.82): calcd. C 45.56, H 3.10, N 14.05; found C 45.67, H 3.15, N 13.98.

$[\text{Ni}_4(\text{pyany})_2(\text{tsdpda})_2(\text{NCS})]$ (3**):** A mixture of Hpyany (150 mg, 0.675 mmol), H_2tsdpda (230 mg, 0.675 mmol), naphthalene (30 g), and $\text{Ni}(\text{OAc})_2 \cdot 4\text{H}_2\text{O}$ (400 mg, 1.61 mmol) was placed in an Erlenmeyer flask. After stirring the mixture at 200 °C for 18 h, the mixture was cooled to 150 °C and NaNCS (270 mg, 3.33 mmol) was added. The solution then was stirred for an additional 2 h. After cooling the mixture to 70 °C, hexane was added and the resulting precipitate was filtered out. The solid (yield 353 mg, 74%) was extracted with CH_2Cl_2 and layered with hexane. After one week, deep green crystals were obtained; yield 47.7 mg, 10%. MS (FAB): m/z = 1413 $[\text{Ni}_4(\text{pyany})_2(\text{tsdpda})_2\text{NCS} + \text{H}]^+$. $\text{C}_{63}\text{H}_{50}\text{Cl}_4\text{N}_{17}\text{Ni}_4\text{O}_4\text{S}_3$ (1581.96): calcd. C 47.83, H 3.19, N 15.05; found C 47.52, H 3.35, N 15.96.

$[\text{Ni}_4(\text{pyany})_2(\text{tsdpda})_2(\text{NCS})_2]$ (4**):** Complex **2** (20.0 mg, 0.0124 mmol) was dissolved in CH_2Cl_2 (50 mL) and treated with NaNCS (10.0 mg, 0.123 mmol). The resulting solution was stirred for a week and dried under vacuum. The solid was extracted with CH_2Cl_2 and layered with hexane. After one week, deep brown crystals were obtained; yield 12.8 mg, 70%. MS (FAB): m/z = 1413 $[\text{Ni}_4(\text{pyany})_2(\text{tsdpda})_2\text{NCS} + \text{H}]^+$. $\text{C}_{64}\text{H}_{50}\text{Cl}_4\text{N}_{18}\text{Ni}_4\text{O}_4\text{S}_3$ (1640.05): calcd. C 46.87, H 3.07, N 15.37; found C 46.51, H 3.41, N 15.70.

Physical Measurements: FAB mass spectra were recorded with a JEOL HX-110 HF double-focusing spectrometer operating in the positive-ion detection mode. The MALDI spectra were performed with a MALDI-TOF mass spectrometer Voyager DE-STR. ¹H NMR spectra were recorded in DMSO with a Bruker AMX 400 MHz spectrometer. Magnetic susceptibility data were collected with a Quantum external magnetic field 3000 G instrument.

X-ray Structure Determinations: Crystallographic data were collected at 150(1) K with a NONIUS Kappa CCD diffractometer with graphite-monochromatized Mo- K_α radiation ($\lambda = 0.71073 \text{ \AA}$). Cell parameters were retrieved and refined with DENZO-SMN software on all observed reflections. Data reduction was performed with the DENZO-SMN software.^[11] An empirical absorption was based on the symmetry-equivalent reflection, and absorption corrections were applied with the SORTAV program.^[12] All the structures were solved and refined with the SHELX-97 programs.^[5] The hydrogen atoms were included in calculated positions and refined with a riding mode.

CCDC-763548 (for **1**), -763680 (for **2**), -763682 (for **3**), and -763681 (for **4**) contain the supplementary crystallographic data for this paper. These data can be obtained free of charge from The Cambridge Crystallographic Data Centre via www.ccdc.cam.ac.uk/data_request/cif.

Acknowledgments

The authors would like to acknowledge financial support from the National Science Council and the Ministry of Education of Taiwan.

- [1] a) C. Joachim, S. Roth, *Atomic and Molecular Wires*, NATO Applied Science, Kluwer, Boston, **1997**, vol. 341; b) A. Aviram, M. Ratner, *Molecular Electronics: Science and Technology*, in: *Annals of the New York Academy of Sciences*, **1998**, vol. 852; c) M. C. Petty, M. R. Bryce, D. Bloor, *Introduction to Molecular Electronics*, Oxford University Press, New York, **1995**; d) *Molecular Wires: From Design to Perspectives*, in: *Top. Curr. Chem.* (Ed.: L. De Cola), **2005**, vol. 257; e) K. Krogmann, *Angew. Chem. Int. Ed. Engl.* **1969**, *81*, 10–17; f) J. M. Williams, *Adv. Inorg. Chem. Radiochem.* **1983**, *26*, 235–268; g) J. R. Ferraro, J. M. Williams, *Introduction to Synthetic Electrical Conductors*, Academic Press, San Diego, **1987**, chapter 4; h) J. K. Bera, K. R. Dunbar, *Angew. Chem. Int. Ed.* **2002**, *41*, 4453–4457; i) S. Roth, *One-Dimensional Metals*, Wiley-VCH, New York, **1995**; j) J. S. Miller, *Extended Linear Chain Compounds*, Plenum, New York, **1982**, vols. 1–3.
- [2] a) J. F. Berry, F. A. Cotton, P. Lei, T. Lu, C. A. Murillo, *Inorg. Chem.* **2003**, *42*, 3534–3539; b) L.-G. Zhu, S.-M. Peng, *Wuji Huaxue Xuebao* **2002**, *18*, 117–124; c) C.-Y. Yeh, C.-C. Wang, C.-h. Chen, S.-M. Peng, in *Nano Redox Sites: Nano-Space Control and its Applications* (Ed.: T. Hirao), Springer, Berlin, **2006**, Chapter 5, pp. 85–117; d) I. P.-C. Liu, W.-Z. Wang, S.-M. Peng, *Chem. Commun.* **2009**, 4323–4331; e) I. P.-C. Liu, G.-H. Lee, S.-M. Peng, M. Bénard, M.-M. Rohmer, *Inorg. Chem.* **2007**, *46*, 9602–9608; f) G.-C. Huang, M. Bénard, M.-M. Rohmer, L.-A. Li, M.-J. Chiu, C.-Y. Yeh, G.-H. Lee, S.-M. Peng, *Eur. J. Inorg. Chem.* **2008**, 1767–1777; g) M. Nippe, J. F. Berry, *J. Am. Chem. Soc.* **2007**, *129*, 12684–12685; h) M. Nippe, E. Victor, J. F. Berry, *Eur. J. Inorg. Chem.* **2008**, 5569–5572; i) I. P.-C. Liu, C.-H. Chen, C.-F. Chen, G.-H. Lee, S.-M. Peng, *Chem. Commun.* **2009**, 577–579.
- [3] I. P.-C. Liu, M. Bénard, H. Hasanov, I.-W. P. Chen, W.-H. Tseng, M.-D. Fu, M.-M. Rohmer, C.-h. Chen, G.-H. Lee, S.-M. Peng, *Chem. Eur. J.* **2007**, *13*, 8667–8677.
- [4] M.-Y. Huang, C.-Y. Yeh, G.-H. Lee, S.-M. Peng, *Dalton Trans.* **2006**, 5683–5690.
- [5] a) G. M. Sheldrick, *Acta Crystallogr., Sect. A* **1990**, *46*, 467–473; b) G. M. Sheldrick, *SHELXL-97, Program for the Solution and Refinement of Crystal Structures*, University of Göttingen, Germany, **1997**.
- [6] a) S.-J. Shieh, C.-C. Chou, G.-H. Lee, C.-C. Wang, S.-M. Peng, *Angew. Chem. Int. Ed. Engl.* **1997**, *36*, 56–59; b) C.-C. Wang, W.-C. Lo, C.-C. Chou, G.-H. Lee, J.-M. Chen, S.-M. Peng, *Inorg. Chem.* **1998**, *37*, 4059–4065.
- [7] I. P.-C. Liu, C.-F. Chen, S.-A. Hua, C.-H. Chen, H.-T. Wang, G.-H. Lee, S.-M. Peng, *Dalton Trans.* **2009**, 3571–3573.
- [8] a) P. A. M. Dirac, *Proc. R. Soc. London Ser. A* **1926**, *112*, 661–677; P. A. M. Dirac, *Proc. R. Soc. London Ser. A* **1929**, *123*, 714–733; b) W. Heisenberg, *Z. Phys.* **1926**, *38*, 411–426; c) J. H. Van Vleck, *Theory of Electric and Magnetic Susceptibilities*, Oxford University Press, London, **1932**.
- [9] a) R. Clérac, F. A. Cotton, K. R. Dunbar, C. A. Murillo, I. Pascual, X. Wang, *Inorg. Chem.* **1999**, *38*, 2655–2657; b) J. F. Berry, F. A. Cotton, T. Lu, C. A. Murillo, X. Wang, *Inorg. Chem.* **2003**, *42*, 3595–3601.
- [10] a) X. López, M.-Y. Huang, G.-C. Huang, S.-M. Peng, F.-Y. Li, M. Bénard, M.-M. Rohmer, *Inorg. Chem.* **2006**, *45*, 9075–9084; b) S. Y. Lai, T.-W. Lin, Y.-H. Chen, C.-C. Wang, G.-H. Lee, M.-h. Yang, M.-k. Leung, S.-M. Peng, *J. Am. Chem. Soc.* **1999**, *121*, 250.
- [11] Z. Otwinowski, W. Minor, *Methods Enzymol.* **1997**, *276*, 307–326.
- [12] R. H. Blessing, *Acta Crystallogr., Sect. A* **1995**, *51*, 33–38.

Received: February 5, 2010
Published Online: June 2, 2010

Unusual Anion Effects in the Iron-Catalyzed Formation of 3-Hydroxyacrylates from Aromatic Aldehydes and Ethyl Diazoacetate

Luis Gonalo Alves,^[a] Georg Dazinger,^[a] Luis F. Veiros,^[b] and Karl Kirchner*^[a]

Dedicated to Professor Kurt Mereiter on the occasion of his 65th birthday

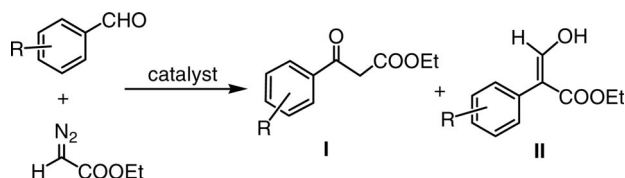
Keywords: Iron / Pincer complexes / Aminophosphanes / C-C coupling / Anions / Density functional calculations

Due to the lability of one of the CO ligands in *trans*-[Fe(PNP)(CO)₂Cl]⁺ this compound is an efficient catalyst for the coupling of a series of aromatic aldehydes with ethyl diazoacetate (EDA), which give, in most cases, selectively 3-hydroxyacrylates rather than β -oxo esters. This reaction is strongly dependent on the nature of the counterion. Whereas with BF₄[−] the reaction proceeds with conversions up to 90 %, in

the case of the counterions NO₃[−], CF₃COO[−], CF₃SO₃[−], SbF₆[−], and BAr'₄[−] [Ar' = 3,5-(CF₃)₂C₆H₃] no reaction took place. In the case of PF₆[−] only up to 20 % conversion was achieved. A conceivable mechanism for the coupling of aromatic aldehydes with EDA was established by means of DFT/B3LYP calculations, which allowed the rationalization of both the chemoselectivity and the role of the counterions.

Introduction

Aromatic aldehydes are known to react with ethyl diazoacetate (EDA) in the presence of Lewis acids such as BF₃, ZnCl₂, AlCl₃, GeCl₂, and SnCl₄ to give mainly ethyl 3-aryl-3-oxopropanoates (β -oxo esters) **I** in high yields (Scheme 1).^[1–3] Hossain and co-workers have found that the dicarbonyl(cyclopentadienyl) complex [FeCp(CO)₂(thf)]·BF₄ is an excellent catalyst for the coupling of aromatic aldehydes with EDA to afford ethyl 2-aryl-3-hydroxyacrylates (3-hydroxyacrylates) **II** as the main product (Scheme 1).^[4] They applied this methodology to the synthesis of the Naproxen precursor 2-(6-methoxy-2-naphthyl)propenoic acid and other related compounds.^[4b] Later on the same authors also showed^[5] that even the simple Brønsted acid HBF₄·Et₂O is an active catalyst for the preparation of **I** and **II**.



Scheme 1.

[a] Institute of Applied Synthetic Chemistry, Vienna University of Technology, Getreidemarkt 9, 1060 Vienna, Austria
Fax: +43-1-58801-16399
E-mail: kkirchner@mail.zserv.tuwien.ac.at

[b] Centro de Química Estrutural, Instituto Superior Técnico, 1049-001 Lisboa, Portugal

Likewise, Kanemasa et al. also reported the synthesis of **I** and **II** using ZnCl₂ in the presence of chlorotrimethylsilane as catalyst.^[6] Very recently, Pérez and co-workers have reported the use of N-heterocyclic carbene based gold complexes, which are capable of mediating this reaction with low catalyst loadings and high reaction rates.^[7] In all these examples, however, a major problem is the selectivity since typically mixtures of **I** and **II** are obtained. In this context we have shown^[8] that cationic iron pincer complexes of the types [Fe(PNP)(CH₃CN)₃](BF₄)₂ and [Fe(PNP)(CO)(CH₃CN)₂](BF₄)₂ (PNP are various tridentate pincer-type ligands based on 2,6-diaminopyridine), which contain labile CH₃CN ligands, are active catalysts for the coupling of aromatic aldehydes with EDA to selectively form **I**.^[9] The formation of **II** is typically below 3%.

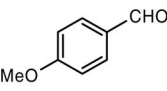
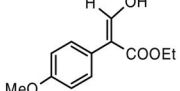
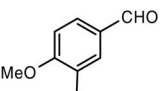
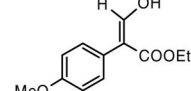
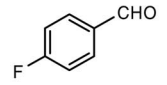
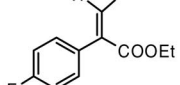
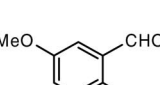
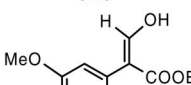
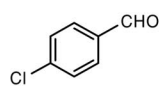
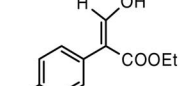

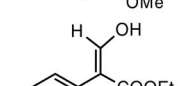
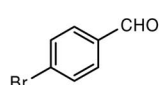
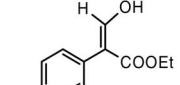
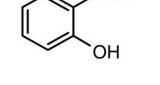
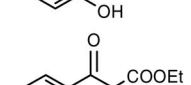
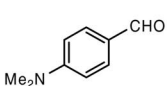
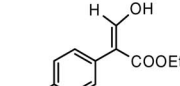

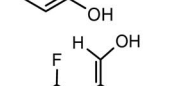
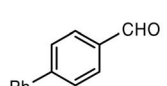
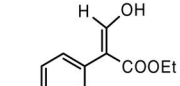
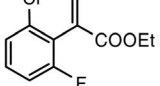
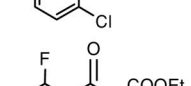
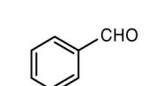
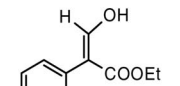

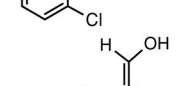
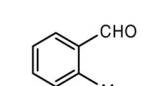
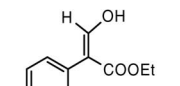
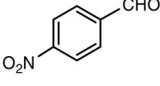
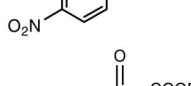
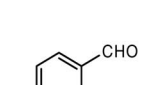
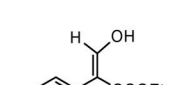

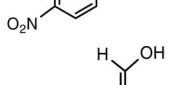
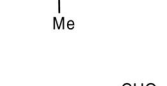
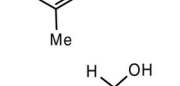
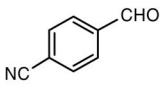
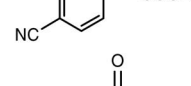
As part of our ongoing research on the synthesis and reactivity of iron(II) pincer complexes^[10] we have recently prepared cationic pincer complexes^[11] of the types *trans*-[Fe(PNP)(CO)₂Cl]⁺.^[11] These complexes are unusual as they feature two CO ligands in a mutual *trans* position making one of them comparatively labile, which may thus be replaced by other potential ligands. Accordingly, *trans*-[Fe(PNP)(CO)₂Cl]⁺ complexes may be promising candidates as precatalysts for Lewis acid catalyzed reactions. Here we report on our investigations on the catalytic activity of the iron pincer complex *trans*-[Fe(PNP-*i*Pr)(CO)₂Cl]X with X = NO₃[−], CF₃COO[−], CF₃SO₃[−], BF₄[−], PF₆[−], SbF₆[−], BAr'₄[−] [Ar' = 3,5-(CF₃)₂C₆H₃] in the coupling of aromatic aldehydes with EDA. Mechanistic aspects of this reaction will be supported by DFT/B3LYP calculations.

Results and Discussion

In the present study complexes of the type *trans*-[Fe(PNP-*i*Pr)(CO)₂Cl]X (**1**·X) with X[−] = NO₃[−], CF₃COO[−], CF₃SO₃[−], BF₄[−], PF₆[−], SbF₆[−], and BAR'₄[−] were used as pre-catalysts. They were prepared by treating [Fe(PNP-*i*Pr)Cl₂] with 1 equiv. of the respective silver or sodium salts in the presence of CO. It has to be noted that the synthesis of the corresponding *cis* isomer, *cis*-[Fe(PNP-Ph)(CO)₂Br]BPh₄, has been described recently and was found to be catalytically inactive for the coupling of aromatic aldehydes and EDA.^[9] In order to evaluate the scope and limitations of

these compounds we first focused on **1**·BF₄ as pre-catalyst for the coupling of various aromatic aldehydes and EDA. The results of this study are provided in Table 1. Operationally, EDA and aldehyde were mixed in a 1:1 ratio together with 10 mol-% of **1**·BF₄ in CH₃NO₂ as the solvent, and the solution was stirred at room temperature for 16 h. Although the catalytic reactions were routinely performed under argon, admission of air did not affect the yields. In most cases 3-hydroxyacrylates **II**, as judged from the ¹H NMR spectra of the crude reaction mixture, were formed selectively. The formation of β-oxo esters **I** is typically

Table 1. Yields of 3-hydroxyacrylates from the reactions of aromatic aldehydes with EDA catalyzed by *trans*-[Fe(PNP-*i*Pr)(CO)₂Cl]-BF₄ (**1**·BF₄).^[a, b]

Entry	Aldehyde	3-Hydroxyacrylate	Yield (%)	Entry	Aldehyde	3-Hydroxyacrylate	Yield (%)
1			88	11			45
2			71	12			48
3			90				48
4			68	13			13
5			43				34
6			84	14			19
7			76				35
8			63	15			13
9			68				35
10			69	16			11

[a] Reaction conditions: 1 equiv. aldehyde, 1 equiv. EDA, 10 mol-% catalyst, CH₃NO₂ as solvent, room temp., reaction time 16 h; yields represent isolated yields (average of at least three experiments). [b] The yield of β-oxo ester is < 3% unless indicated.

< 3%, whereas the formation of epoxides was not observed in any of these reactions. The yields of 3-hydroxyacrylates are in the range of 34–90%. The catalytic effect of the iron complexes was confirmed by running the reaction of *p*-anisaldehyde and EDA without catalyst. No product was formed, and only starting materials were isolated from the reaction mixture.

In Lewis acid catalyzed transformations the nature of the counterion sometimes has a strong effect on reaction rates, yields, and even product distribution.^[12–15] Therefore, we also investigated the influence of the counterion on the coupling of aromatic aldehydes with EDA by using *trans*-[Fe(PNP-*i*Pr)(CO)₂Cl]X (**1**·X) complexes as catalyst precursors (containing the counterions X[−] = NO₃[−], CF₃COO[−], CF₃SO₃[−], PF₆[−], SbF₆[−], BAR'₄[−]) and *p*-anisaldehyde as model substrate. Complexes **1**·X bearing the coordinating anions NO₃[−], CF₃COO[−] or CF₃SO₃[−] turned out to be completely inefficient and no conversion was observed (Figure 1). This may be explained by competition of the anion and the substrate for the Lewis acid site.^[11] If this is the case for all counterions, one would expect the activity of the precatalyst to increase in the order NO₃[−] < CF₃COO[−] < CF₃SO₃[−] < BF₄[−] < PF₆[−] < SbF₆[−] < BAR'₄[−]. Surprisingly, this is not the case. In fact, complexes **1**·X bearing the non-coordinating anion BAR'₄[−] or the poorly coordinating anion SbF₆[−] turned out to be completely inefficient, whereas in the case of **1**·X with PF₆[−] as weakly coordinating counterion the conversion was merely 20%. In order to explain this phenomenon we propose that the weakly coordinating anions interact simultaneously with either catalyst, coordinated aldehyde and/or EDA by hydrogen-bonding interactions, which must be highly sensitive to the nature of the anion. This observation is in strong contrast to the reaction of aromatic aldehydes and EDA catalyzed by both [Fe(PNP)(CH₃CN)₃](BF₄)₂ and [Fe(PNP)(CO)(CH₃CN)₂](BF₄)₂, where no anion dependence was observed.^[9]

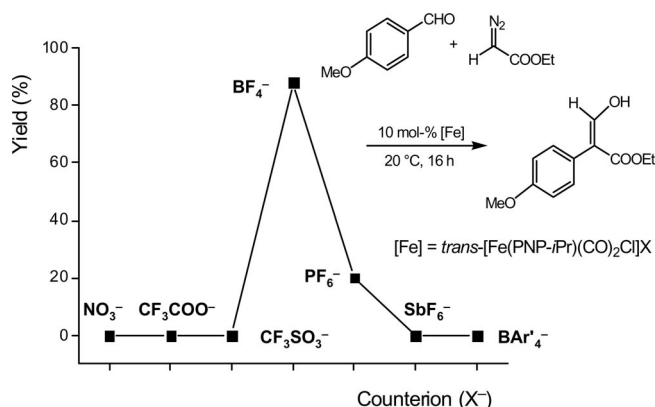
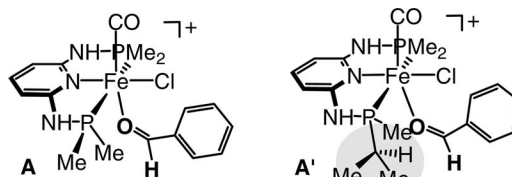


Figure 1. Plot of yield vs. counterion (X[−]) of the coupling of EDA with *p*-anisaldehyde catalyzed by *trans*-[Fe(PNP-*i*Pr)(CO)₂Cl]X.

In order to gain insight into the mechanism of this catalytic process and the subtle and unusual anion effect, DFT calculations were performed. As model systems [Fe(PNP-Me)(CO)(Cl){κ¹(O)-benzaldehyde}]⁺ (**A**), [Fe(PNP-Me,*i*Pr)(CO)(Cl){κ¹(O)-benzaldehyde}]⁺ (**A'**) (see

Scheme 2), and methyl diazoacetate (MDA) were chosen. A mechanistic proposal for the coupling of aromatic aldehydes with MDA catalyzed by **A** with no counterion interactions considered – as would be the case for BAR'₄[−] and possibly also SbF₆[−] – is depicted in Scheme 3 and Figure 2.

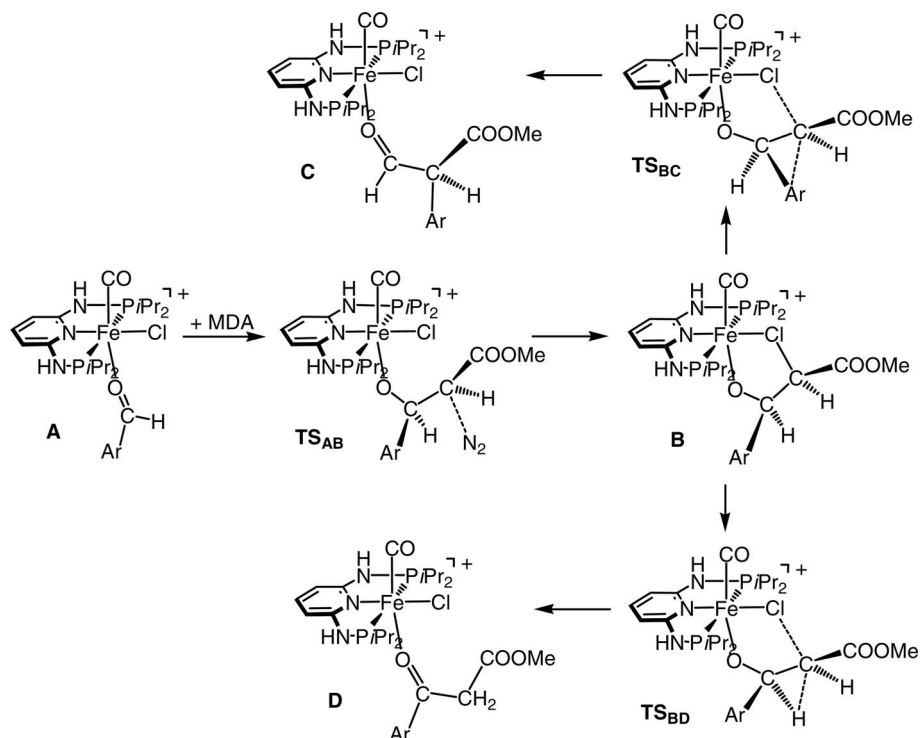


Scheme 2.

Since CO exhibits a strong *trans* effect (and *trans* influence) one of the two CO ligands is substitutionally labile.^[11] Accordingly, facile dissociation of one CO ligand and subsequent addition of an aldehyde molecule (which is present in large excess under catalytic conditions, benzaldehyde in the calculations) affords [Fe(PNP-Me)(CO)(Cl){κ¹(O)-benzaldehyde}]⁺ (**A**).

Nucleophilic attack of MDA to the coordinated aldehyde yields, via transition state **TS_{AB}**, intermediate **B**. Upon N₂ loss the carbenium ion is stabilized by a comparatively strong C⋯Cl (1.87 Å) interaction. Once **TS_{AB}** is reached the changes associated with this step are already visible. The new C–C bond formed is 1.57 Å, while at the same time N₂ is moving away from the original MDA molecule with a C–N separation of 1.77 Å. Despite the fact that a new C–C bond is formed and N₂ is liberated, the activation barrier for this process is as high as 41.4 kcal/mol. Consequently, despite the exergonicity (−3.2 kcal/mol), the kinetic barrier for the formation of **B** is prohibitively high and thus an unlikely scenario. Nevertheless, preferential migration of the aryl substituent (energy of activation is 13.9 kcal/mol) over hydride migration (energy of activation is 27.4 kcal/mol) leads eventually to **C** featuring a κ¹(O)-coordinated aldehyde–ester ligand, going over **TS_{BC}**, while hydrogen migration affords **D** featuring a κ¹(O)-coordinated β-oxo ester ligand, passing through **TS_{BD}**. The structures of all transition states are intermediate between the minima involved in each path. Thus, in **TS_{BD}** the transferring hydride is bridging the two C atoms with distances of 1.16 and 1.73 Å, while in **TS_{BC}** the migrating phenyl group exhibits C–C_{Ph} distances of 1.64 and 1.96 Å. After liberation of the ester–aldehyde in **C** by coordination of incoming aldehyde substrate, that molecule rapidly tautomerizes to yield the corresponding thermodynamically more stable 3-hydroxyacrylates. This mechanism may explain why the reaction is not proceeding in the case of non- and very weakly coordinating counteranions, i.e., BAR'₄[−] and SbF₆[−], since it was calculated in the absence of the counterion, and the energy barrier involved is too high for a feasible reaction given the experimental conditions (room temperature, 16 h).

The possible participation of the counterion (BF₄[−]) in the reaction was also investigated computationally, and the results are presented in Figure 3. The pathway obtained for



Scheme 3.

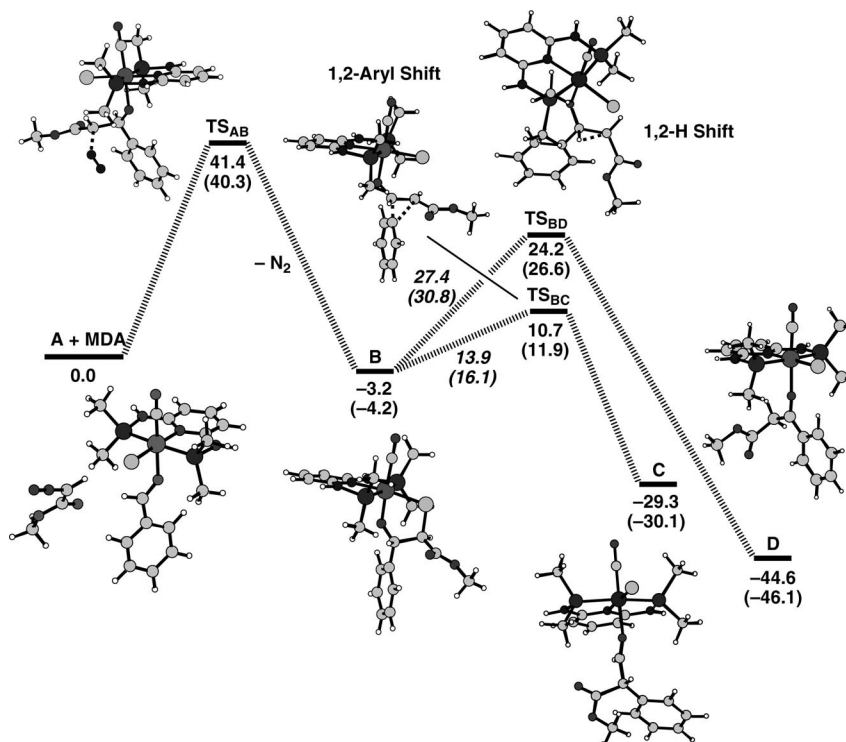


Figure 2. Energy profile for the coupling of $[\text{Fe}(\text{PNP-Me})(\text{CO})(\text{Cl})\{\kappa^1(\text{O})\text{-benzaldehyde}\}]^+$ (**A**) and methyl diazoacetate (MDA) in the absence of the counterion BF_4^- (energies in kcal/mol, numbers in parentheses are solvent-corrected energies; solvent: CH_3NO_2).

the formation of $\kappa^1(\text{O})$ -coordinated β -oxo ester **B^H** is represented on the left-hand side of Figure 2. In the reagent **A^H** there is a network of hydrogen bonds connecting the counterion BF_4^- with the complex and the MDA molecule

in a cyclic arrangement: complex(NH)··· BF_4^- ···MDA···coordinated benzaldehyde. From **A^H** the reaction follows a single-step mechanism to the formation of the final product **B^H** showing that the overall process is slightly facilitated

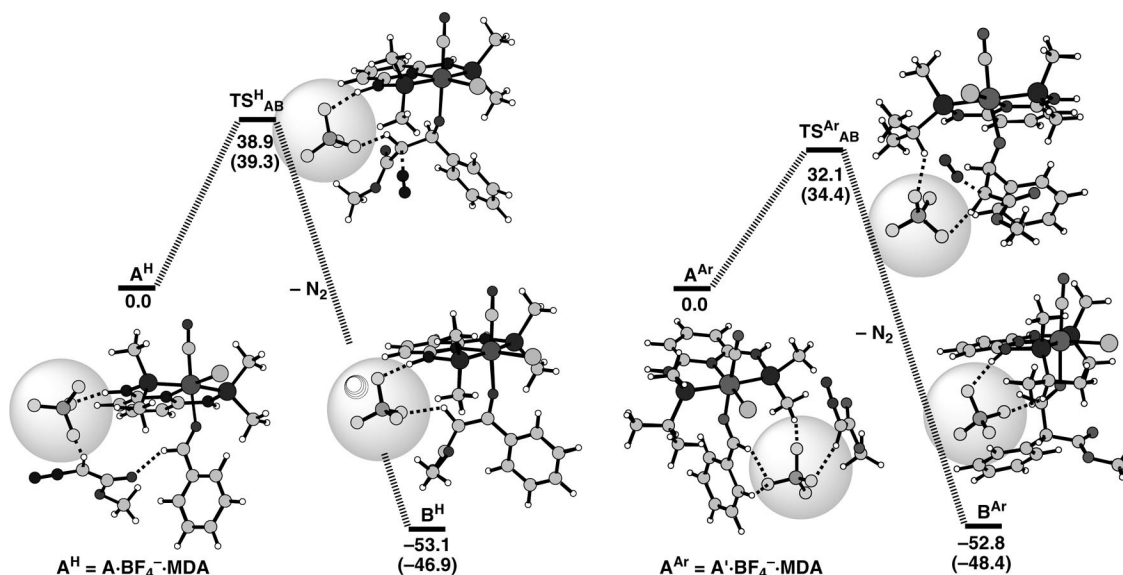


Figure 3. Energy profile for the coupling of [Fe(PNP-Me,iPr)(CO)(Cl){κ¹(O)-benzaldehyde}]⁺ (A') and methyl diazoacetate (MDA) involving the counterion BF₄⁻ through hydrogen bonding (Aᴴ and Aᴳ). Left-hand side: hydrogen migration; right-hand side: phenyl migration (energies in kcal/mol, numbers in parentheses are solvent-corrected energies; solvent: CH₃NO₂).

with respect to the mechanism calculated without anion that requires two steps to accomplish the reaction (Figure 2). In the transition state TSᴴ_{AB} the new C–C bond is already formed (1.51 Å), while loss of N₂ is underway ($d_{\text{C-N}} = 1.93$ Å). At the same time, the shifting hydrogen atom is starting to move from the carbonyl carbon atom ($d_{\text{C-H}} = 1.13$ Å) towards the adjacent carbon atom ($d_{\text{C-H}} = 1.93$ Å). The activation energy calculated for this path (38.9 kcal/mol) is lower than the one obtained for the “anion-free” reaction (41.4 kcal/mol).

The energy profile calculated for the formation of the κ¹(O)-coordinated aldehyde Bᴳ, resulting from aryl migration with participation of the BF₄⁻ anion is represented on the right-hand side of Figure 2. It should be noted that this pathway was calculated with the model complex *trans*-[Fe(PNP-Me,iPr)(CO)₂Cl]⁺ (A', see Scheme 2) where one of the four *P*-methyl substituents is replaced by a bulkier isopropyl group. This is a more realistic model, closer to the real system, and its use was necessary in order to prevent BF₄⁻ to form a strong hydrogen bond to the acidic N–H proton of the PNP ligand in the transition state, thereby promoting aryl migration rather than hydrogen migration. Computational limitations prevent us from using the real complex (with four isopropyl groups) due to the size of the system. The calculated path starts from the aggregate of the three species: the Fe complex, the BF₄⁻ anion, and the MDA molecule held together by means of hydrogen interactions (Aᴳ). From here, the reaction is accomplished in one single step through transition state TSᴳ_{AB}. In TSᴳ_{AB} the new C–C bond is already formed (1.52 Å), and loss of one N₂ molecule is still proceeding ($d_{\text{C-N}} = 1.83$ Å), while at the same time the phenyl group starts to migrate between the two adjacent carbon atoms [$d_{\text{C-C(Ph)}} = 1.58$ and 2.29 Å]. The activation energy associated with this path is 32.1 kcal/mol and thus lower than the one obtained for the formation

of the β-oxo ester complex Bᴴ (38.9 kcal/mol) indicating that the aldehyde should be the product formed in the reaction, in agreement with the experimental observations.

It should be added that the effect of PF₆⁻ as counterion was also investigated. However, we were unable to locate any transition states, which may have led to experimentally observed products. In addition, solvation effects were evaluated with the polarized continuum model (PCM), leading to similar results with only 2–4 kcal/mol differences (see Figures 2 and 3, numbers in parentheses refer to solvent-corrected energies, solvent = CH₃NO₂).

Conclusion

We have shown that the *trans*-dicarbonyl complex *trans*-[Fe(PNP-*i*Pr)(CO)₂Cl]X with X = BF₄⁻ is an efficient precatalyst for the coupling of aromatic aldehydes with ethyl diazoacetate. A general and efficient protocol for this process has been developed and various aromatic aldehydes have been used as substrates. In most cases, 3-hydroxyacrylates rather than β-oxo esters are selectively obtained. The catalyst is part of a new generation of air-stable, well-defined iron PNP pincer-type systems. However, this reaction turned out to be strongly dependent on the nature of the counterion. Whereas with BF₄⁻ the reaction proceeds with conversions up to 90%, in the case of NO₃⁻, CF₃COO⁻, CF₃SO₃⁻, SbF₆⁻, and BAR'₄⁻ no reaction took place. With PF₆⁻ about 20% conversion was observed. A conceivable mechanism for the coupling of aromatic aldehydes with EDA was established by means of DFT/B3LYP calculations, rationalizing both the chemoselectivity and the role of the counterions. The calculated mechanism indicates that the selective formation of 3-hydroxyacrylates II over β-oxo esters I, as experimentally observed, results from a

lower energy barrier and, thus, a more favorable reaction pathway that is stabilized by means of hydrogen-bond formation with the BF_4^- anion.

Experimental Section

General: All manipulations were performed under argon by using Schlenk techniques. Solvents were purified according to standard procedures.^[16] NaBAR'_4 was prepared according to the literature.^[17] Deuterated solvents were purchased from Aldrich and dried with molecular sieves (4 Å). ^1H , $^{13}\text{C}\{^1\text{H}\}$, and $^{31}\text{P}\{^1\text{H}\}$ NMR spectra were recorded with a Bruker Avance-250 spectrometer and were referenced to SiMe_4 (^1H , ^{13}C) and H_3PO_4 (85%) (^{31}P).

trans-[Fe(PNP-*i*Pr)(CO)₂Cl]BF₄ (1·BF₄): Carbon monoxide was bubbled through a solution of $\text{Fe(PNP-}i\text{Pr)Cl}_2$ (1.18 g, 2.52 mmol) in CH_3NO_2 (60 mL) at room temperature, whereupon the brownish solution turned into a blue suspension. After 2 min, AgBF_4 (0.494 g, 2.54 mmol) was added. The bubbling was continued for additional 10 min allowing the bluish suspension to turn into a red suspension. After filtration through a syringe filter, the solvent was removed under reduced pressure to afford a red solid, which was washed with diethyl ether and dried under vacuum. Yield: 1.12 g (77%). $\text{C}_{19}\text{H}_{33}\text{ClF}_4\text{FeN}_3\text{O}_2\text{P}_2$ (564.73): calcd. C 39.65, H 5.78, N 7.30; found C 39.60, H 5.81, N 7.27. ^1H NMR (CD_3NO_2 , 20 °C): δ = 7.29 (t, J = 7.8 Hz, 1 H, py^4), 6.63 (s, 2 H, NH), 6.21 (d, J = 7.8 Hz, 2 H, $\text{py}^{3,5}$), 3.25 [m, J = 6.7 Hz, 4 H, $\text{CH}(\text{CH}_3)_2$], 1.56 [s, 12 H, $\text{CH}(\text{CH}_3)_2$], 1.53 [s, 12 H, $\text{CH}(\text{CH}_3)_2$] ppm. $^{13}\text{C}\{^1\text{H}\}$ NMR (CD_3NO_2 , 20 °C): δ = 211.6 (t, J = 24.4 Hz, CO), 161.4 (t, J = 6.2 Hz, $\text{py}^{2,6}$), 141.2 (py^4), 100.0 (t, J = 3.0 Hz, $\text{py}^{3,5}$), 31.7 [vt, J = 12.2 Hz, $\text{CH}(\text{CH}_3)_2$], 16.9 [d, J = 3.7 Hz, $\text{CH}(\text{CH}_3)_2$] ppm. $^{31}\text{P}\{^1\text{H}\}$ NMR (CD_3NO_2 , 20 °C): δ = 119.2 ppm. IR [ATR (attenuated total reflection)]: $\tilde{\nu}$ = 2020 ($\nu_{\text{C=O}}$) cm^{-1} .

trans-[Fe(PNP-*i*Pr)(CO)₂Cl]CF₃SO₃ (1·CF₃SO₃): This complex was prepared analogously to 1·BF₄ with $\text{Fe(PNP-}i\text{Pr)Cl}_2$ (354 mg, 0.76 mmol) and AgCF_3SO_3 (198 mg, 0.77 mmol) as the starting materials. Yield: 288 mg (60%). IR (ATR): $\tilde{\nu}$ = 2015 ($\nu_{\text{C=O}}$) cm^{-1} .

trans-[Fe(PNP-*i*Pr)(CO)₂Cl]CF₃COO (1·CF₃COO): This complex was prepared analogously to 1·BF₄ with $\text{Fe(PNP-}i\text{Pr)Cl}_2$ (318 mg, 0.68 mmol) and AgCF_3COO (153 mg, 0.69 mmol) as starting materials. Yield: 137 mg (34%). $\text{C}_{21}\text{H}_{33}\text{ClF}_3\text{FeN}_3\text{O}_4\text{P}_2$ (601.75): calcd. C 41.92, H 5.53, N 6.98; found C 41.80, H 5.41, N 6.87. IR (ATR): $\tilde{\nu}$ = 2012 ($\nu_{\text{C=O}}$) cm^{-1} .

trans-[Fe(PNP-*i*Pr)(CO)₂Cl]NO₃ (1·NO₃): This complex was prepared analogously to 1·BF₄ with $\text{Fe(PNP-}i\text{Pr)Cl}_2$ (212 mg, 0.45 mmol) and AgNO_3 (80 mg, 0.47 mmol) as the starting materials. Yield: 152 mg (61%). IR (ATR): $\tilde{\nu}$ = 2005 ($\nu_{\text{C=O}}$) cm^{-1} .

trans-[Fe(PNP-*i*Pr)(CO)₂Cl]PF₆ (1·PF₆): This complex was prepared analogously to 1·BF₄ with $\text{Fe(PNP-}i\text{Pr)Cl}_2$ (219 mg, 0.47 mmol) and AgPF_6 (123 mg, 0.49 mmol) as the starting materials. Yield: 219 mg (74%). IR (ATR): $\tilde{\nu}$ = 2020 ($\nu_{\text{C=O}}$) cm^{-1} .

trans-[Fe(PNP-*i*Pr)(CO)₂Cl]SbF₆ (1·SbF₆): This complex was prepared analogously to 1·BF₄ with $\text{Fe(PNP-}i\text{Pr)Cl}_2$ (300 mg, 0.64 mmol) and AgSbF_6 (230 mg, 0.67 mmol) as the starting materials. Yield: 324 mg (70%). IR (ATR): $\tilde{\nu}$ = 2016 ($\nu_{\text{C=O}}$) cm^{-1} .

trans-[Fe(PNP-*i*Pr)(CO)₂Cl]BAR'₄ (1·BAR'₄): NaBAR'_4 was added to a suspension of 1·BF₄ (156 mg, 0.27 mmol) in toluene (40 mL) at room temperature and was stirred for 2 h, whereupon the solution turned red, and a precipitate was formed. Then, the mixture was filtered through a syringe filter, and the solvent was evaporated under reduced pressure to afford a red oil. Washing with *n*-pentane

afforded a red solid, which was dried under vacuum. Yield: 164 mg (45%). IR (ATR): $\tilde{\nu}$ = 2012 ($\nu_{\text{C=O}}$) cm^{-1} .

General Procedure for the Iron(II)-Catalyzed Synthesis of 3-Hydroxyacrylates: In a typical experiment, aldehyde (ca. 3–5 mmol, 1 equiv.) and ethyl diazoacetate (ca. 3–5 mmol, 1 equiv.) were added to a solution of the catalyst (ca. 0.3–0.5 mmol, 10 mol-%) in CH_3NO_2 (5 mL), and the mixture was stirred at room temperature for 16 h. The mixture was then filtered through a plug of silica to remove the catalyst, and the product was purified by flash chromatography (silica, CH_2Cl_2). In the case of *p*-(dimethylamino)-benzaldehyde, CH_3CN was used as eluent.

Computational Details: Calculations were performed by using the Gaussian 03 software package,^[18] and the B3LYP functional^[19] without symmetry constraints. The optimized geometries were obtained with the Stuttgart/Dresden ECP (SDD) basis set^[20] to describe the electrons of the iron atom. For all other atoms the 6-31g** basis set was employed.^[21] Frequency calculations were performed to confirm the nature of the stationary points, yielding one imaginary frequency for the transition states and none for the minima. Each transition state was further confirmed by following its vibrational mode downhill on both sides, and obtaining the minima presented on the energy profiles. Solvent effects (CH_3NO_2) were considered through single-point energy calculations with the optimized geometries by using the Polarizable Continuum Model (PCM) initially devised by Tomasi and co-workers^[22] as implemented in Gaussian 03.^[23,24] The molecular cavity was based on the united atom topological model applied on UAHF radii, optimized for the HF/6-31G(d) level.

Acknowledgments

The support by COST Action D24 (“Sustainable Chemical Processes: Stereoselective Transition Metal Catalyzed Reactions”) is kindly acknowledged.

- [1] a) C. R. Holmquist, E. J. Roskamp, *J. Org. Chem.* **1989**, *54*, 3258; b) C. R. Holmquist, E. J. Roskamp, *Tetrahedron Lett.* **1992**, *33*, 1131.
- [2] a) A. Padwa, S. F. Hornbuckle, Z. Zhang, L. Zhi, *J. Org. Chem.* **1990**, *55*, 5297; b) S. G. Sudrik, B. S. Balaji, A. P. Singh, R. B. Mitra, H. R. Sonawane, *Synlett* **1996**, 369.
- [3] K. Nomura, T. Lida, K. Hori, E. Yoshii, *J. Org. Chem.* **1994**, *59*, 488.
- [4] a) S. J. Mahmood, M. M. Hossain, *J. Org. Chem.* **1998**, *63*, 3333; b) S. J. Mahmood, C. Brennan, M. M. Hossain, *Synthesis* **2002**, 1807.
- [5] M. E. Dudley, M. M. Morshed, C. L. Brennan, M. S. Islam, M. S. Ahmad, M.-R. Atuu, B. Branstetter, M. M. Hossain, *J. Org. Chem.* **2004**, *69*, 7599.
- [6] S. Kanemasa, T. Kanai, T. Araki, E. Wada, *Tetrahedron Lett.* **1999**, *40*, 5055.
- [7] M. R. Frutos, M. M. Diaz-Requejo, P. Perez, *J. Chem. Commun.* **2009**, *34*, 5153.
- [8] D. Benito-Garagorri, E. Becker, J. Wiedermann, W. Lackner, M. Pollak, K. Mereiter, J. Kisala, K. Kirchner, *Organometallics* **2006**, *25*, 1900.
- [9] D. Benito-Garagorri, J. Wiedermann, M. Pollak, K. Mereiter, K. Kirchner, *Organometallics* **2007**, *26*, 217.
- [10] a) D. Benito-Garagorri, L. G. Alves, M. Puchberger, L. F. Veios, M. J. Calhorda, M. D. Carvalho, L. P. Ferreira, M. Godinho, K. Mereiter, K. Kirchner, *Organometallics* **2009**, *28*, 6902; b) D. Benito-Garagorri, M. Puchberger, K. Mereiter, K. Kirchner, *Angew. Chem. Int. Ed.* **2008**, *47*, 9142; c) D. Benito-Garagorri, K. Kirchner, *Acc. Chem. Res.* **2008**, *41*, 201.

- [11] D. Benito-Garagorri, L. G. Alves, C. M. Standfest-Hauser, S. Tanaka, L. F. Veiros, K. Mereiter, K. Kirchner, *Organometallics*, DOI: 10.1021/om1001638.
- [12] E. P. Kündig, C. M. Saudan, G. Bernardinelli, *Angew. Chem. Int. Ed.* **1999**, *38*, 1219.
- [13] D. A. Evans, J. A. Murry, P. von Matt, R. D. Norcross, S. J. Miller, *Angew. Chem. Int. Ed. Engl.* **1995**, *34*, 798.
- [14] For reviews concerning anion effects, see: a) A. Macchioni, *Chem. Rev.* **2005**, *105*, 2039; b) J. Lacour, V. Hebbe-Viton, *Chem. Soc. Rev.* **2003**, *32*, 373–382, and references therein.
- [15] For specific examples of anion effects, see: a) L.-N. Appelhans, D. Zuccaccia, A. Kovacevic, A. R. Chianese, J. R. Miecznikowski, A. Macchioni, E. Clot, O. Eisenstein, R. H. Crabtree, *J. Am. Chem. Soc.* **2005**, *127*, 16299; b) M. G. Basallote, M. Besora, J. Durán, M. J. Fernández-Trujillo, A. Lleós, M. A. Máñez, F. Maseras, *J. Am. Chem. Soc.* **2004**, *126*, 2320; c) A. Pfaltz, J. Blankenstein, R. Hilgraf, E. Hörmann, S. McIntyre, F. Menges, M. Schönleber, S. P. Smidt, B. Wüstenberg, N. Zimmermann, *Adv. Synth. Catal.* **2003**, *345*, 33; d) D. B. Llewellyn, D. Adamson, B. A. Arndtsen, *Org. Lett.* **2000**, *2*, 4165; e) A. Macchioni, C. Zuccaccia, E. Clot, K. Gruet, R. H. Crabtree, *Organometallics* **2001**, *20*, 2367; f) J. R. Miecznikowski, S. Gründemann, M. Albrecht, C. Mégret, E. Clot, J. Faller, O. Eisenstein, R. H. Crabtree, *Dalton Trans.* **2003**, 831; g) A. Macchioni, *Eur. J. Inorg. Chem.* **2003**, 195; h) A. Macchioni, G. Bellachioma, G. Cardaci, V. Gramlich, H. Rüegger, S. Terenzi, L. M. Venzani, *Organometallics* **1997**, *16*, 2139; i) G. Bellachioma, G. Cardaci, A. Macchioni, G. Reichenbach, S. Terenzi, *Organometallics* **1996**, *15*, 4349.
- [16] D. D. Perrin, W. L. F. Armarego, *Purification of Laboratory Chemicals*, 3rd ed., Pergamon, New York, **1988**.
- [17] M. Brookhart, B. Grant, J. Volpe, *Organometallics* **1992**, *11*, 3920.
- [18] M. J. Frisch, G. W. Trucks, H. B. Schlegel, G. E. Scuseria, M. A. Robb, J. R. Cheeseman, J. A. Montgomery Jr., T. Vreven, K. N. Kudin, J. C. Burant, J. M. Millam, S. S. Iyengar, J. Tomasi, V. Barone, B. Mennucci, M. Cossi, G. Scalmani, N. Rega, G. A. Petersson, H. Nakatsuji, M. Hada, M. Ehara, K. Toyota, R. Fukuda, J. Hasegawa, M. Ishida, T. Nakajima, Y. Honda, O. Kitao, H. Nakai, M. Klene, X. Li, J. E. Knox, H. P. Hratchian, J. B. Cross, V. Bakken, C. Adamo, J. Jaramillo, R. Gomperts, R. E. Stratmann, O. Yazyev, A. J. Austin, R. Cammi, C. Pomelli, J. W. Ochterski, P. Y. Ayala, K. Morokuma, G. A. Voth, P. Salvador, J. J. Dannenberg, V. G. Zakrzewski, S. Dapprich, A. D. Daniels, M. C. Strain, O. Farkas, D. K. Malick, A. D. Rabuck, K. Raghavachari, J. B. Foresman, J. V. Ortiz, Q. Cui, A. G. Baboul, S. Clifford, J. Cioslowski, B. B. Stefanov, G. Liu, A. Liashenko, P. Piskorz, I. Komaromi, R. L. Martin, D. J. Fox, T. Keith, M. A. Al-Laham, C. Y. Peng, A. Nanayakkara, M. Challacombe, P. M. W. Gill, B. Johnson, W. Chen, M. W. Wong, C. Gonzalez, J. A. Pople, *Gaussian 03*, Revision D.01, Gaussian, Inc., Wallingford CT, **2004**.
- [19] a) A. D. Becke, *J. Chem. Phys.* **1993**, *98*, 5648; b) B. Miehlich, A. Savin, H. Stoll, H. Preuss, *Chem. Phys. Lett.* **1989**, *157*, 200; c) C. Lee, W. Yang, G. Parr, *Phys. Rev. B* **1988**, *37*, 785.
- [20] a) U. Haeusermann, M. Dolg, H. Stoll, H. Preuss, P. J. Schwerfeger, R. M. Pitzer, *Mol. Phys.* **1993**, *78*, 1211; b) W. Kuechle, M. Dolg, H. Stoll, H. Preuss, *J. Chem. Phys.* **1994**, *100*, 7535; c) T. Leininger, A. Nicklass, H. Stoll, M. Dolg, P. Schwerdfeger, *J. Chem. Phys.* **1996**, *105*, 1052.
- [21] a) A. D. McLean, G. S. Chandler, *J. Chem. Phys.* **1980**, *72*, 5639; b) R. Krishnan, J. S. Binkley, R. Seeger, J. A. Pople, *J. Chem. Phys.* **1980**, *72*, 650; c) A. J. H. Wachters, *Chem. Phys.* **1970**, *52*, 1033; d) P. J. Hay, *J. Chem. Phys.* **1977**, *66*, 4377; e) K. Raghavachari, G. W. Trucks, *J. Chem. Phys.* **1989**, *91*, 1062; f) R. C. Binning, L. A. Curtiss, *J. Comput. Chem.* **1995**, *103*, 6104; g) M. P. McGrath, L. Radom, *J. Chem. Phys.* **1991**, *94*, 511.
- [22] a) M. T. Cancès, B. Mennucci, J. Tomasi, *J. Chem. Phys.* **1997**, *107*, 3032; b) M. Cossi, V. Barone, B. Mennucci, J. Tomasi, *Chem. Phys. Lett.* **1998**, *286*, 253; c) B. Mennucci, J. Tomasi, *J. Chem. Phys.* **1997**, *106*, 5151.
- [23] J. Tomasi, B. Mennucci, R. Cammi, *Chem. Rev.* **2005**, *105*, 2999.
- [24] M. Cossi, G. Scalmani, N. Rega, V. Barone, *J. Chem. Phys.* **2002**, *117*, 43.

Received: February 28, 2010

Published Online: May 21, 2010

Dehydrogenation of Hydrido- β -diketones in Methanol: The Selective Formation of Mono- and Dinuclear Acyl Complexes

Roberto Ciganda,^[a] María A. Garralda,^{*,[a]} Lourdes Ibarlucea,^[a] Claudio Mendicute,^[a] Elena Pinilla,^[b] and M. Rosario Torres^[b]

Keywords: Iridium complexes / Acyl bridging ligands / Dehydrogenation

The hydrido- β -diketone $[\text{IrH}(\text{PPh}_2(o\text{-C}_6\text{H}_4\text{CO}))_2\text{H}]\text{Cl}$ (**1**) reacts with diimines (NN) or with pyridine (py) in refluxing methanol to undergo dehydrogenation. The reactions afford selectively the *cis*-acyl, *trans*-phosphane isomers of the cationic $[\text{Ir}(\text{PPh}_2(o\text{-C}_6\text{H}_4\text{CO}))_2(\text{NN})]^+$ [NN = 2,2'-bipyridine (**2**); R–N=C(CH₃)–C(CH₃)=N–R' [R = R' = NH₂ (**3**); R = R' = OH (**4**); R = OH, R' = NH₂ (**5**)] or neutral $[\text{IrCl}(\text{PPh}_2(o\text{-C}_6\text{H}_4\text{CO}))_2(\text{py})]$ (**6**) derivatives. The reactions are faster for ligands containing amino substituents. Refluxing **1** in MeOH affords the formation of an equimolar mixture of dimer

cationic species $[\text{Ir}_2(\mu\text{-Cl})(\mu\text{-PPh}_2(o\text{-C}_6\text{H}_4\text{CO}))_2(\text{PPh}_2(o\text{-C}_6\text{H}_4\text{CO}))_2]^+$ (**7a** and **7b**) containing two acyls and a chloride as bridging groups. The isomers could be separated by fractional precipitation. Compound **3**Cl, containing amino substituents in the imino functionalities, catalyses the hydrogen transfer from 2-propanol to cyclohexanone to afford cyclohexanol. All the complexes were fully characterised spectroscopically. Single crystal X-ray diffraction analysis was performed on complexes **6** and **7b**ClO₄.

Introduction

Hydrido- β -diketones can be easily prepared by activation of aldehydes, tethered to N- or P-ligands, by hydridoacyliridium complexes.^[1] Metalla- β -diketones, also described as acylhydroxycarbene complexes, are rather stable due to the formation of a strong intramolecular hydrogen bond between the acyl and the hydroxycarbene moieties. Recently it has been reported that this hydrogen bond is stronger than that in acetylacetone, an organic β -diketone.^[2] The hydrido- β -diketone complex $[\text{IrH}\{\text{PPh}_2(o\text{-C}_6\text{H}_4\text{CO}))_2\text{H}\}\text{Cl}$ (**1**) being an electronically saturated species is remarkably stable. In solvents of low polarity, **1** is unreactive toward σ -donors such as pyridine or triphenylphosphane. It requires the abstraction of chloride to afford cationic mononuclear $[\text{IrH}\{\text{PPh}_2(o\text{-C}_6\text{H}_4\text{CO}))_2\text{H}\}(\text{L})][\text{ClO}_4]$ complexes, or the dinuclear species $[\text{Ir}_2\text{H}(\text{PPh}_2(o\text{-C}_6\text{H}_4\text{CO}))\{\mu\text{-PPh}_2(o\text{-C}_6\text{H}_4\text{CO}))_3\}\text{BF}_4$, containing three acylphosphane bridging ligands and a single terminal hydride, in a reversible process.^[3] In methanol the reaction of **1** with bases such as KOH or Et₃N, at room temperature, led to dehydrodechlorination and afforded the acyl-bridged hydrido iridium derivative $[\text{Ir}_2\text{H}_2(\text{PPh}_2(o\text{-C}_6\text{H}_4\text{CO}))_2(\mu\text{-PPh}_2(o\text{-C}_6\text{H}_4\text{CO}))_2]$. When the reaction was performed in refluxing methanol, KOH led to a novel di-

hydrido- β -diketone $[\text{IrH}_2\{\text{PPh}_2(o\text{-C}_6\text{H}_4\text{CO}))_2\text{H}\}]$ while Et₃N gave $[\text{Ir}_2(\mu\text{-H})\{\mu\text{-PPh}_2(o\text{-C}_6\text{H}_4\text{CO}))_2\}(\text{PPh}_2(o\text{-C}_6\text{H}_4\text{CO}))_2]\text{Cl}$, with two acylphosphane chelate-bridging ligands and a bridging hydride.^[4] In some of these reactions dehydrogenation reactions also occurred. We report now on the reactivity of **1** in methanol in the presence or absence of N-donor ligands such as diimines: 2,2'-bipyridine (bipy), R–N=C(CH₃)–C(CH₃)=N–R' [dihydrazone, R = R' = NH₂ (bdh); dioxime, R = R' = OH (dmg); oxime hydrazone, R = OH, R' = NH₂ (boh)] or pyridine (py). In all cases dehydrogenation occurs to afford mono- or dinuclear diacyl complexes.

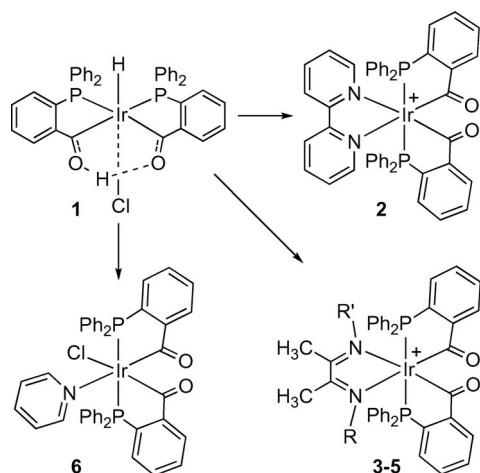
Results and Discussion

Complex **1** reacts with diimines in refluxing methanol, to undergo dehydrogenation affording the cationic diacyl derivatives $[\text{Ir}(\text{PPh}_2(o\text{-C}_6\text{H}_4\text{CO}))_2(\text{NN})]^+$ (NN = bipy, **2**; bdh, **3**; dmg, **4**; boh, **5**) shown in Scheme 1. The reactions are slow and require reaction times in a 90 min–9 h range to reach completion. The corresponding complexes have been isolated as perchlorate compounds by addition of sodium perchlorate (see Exp. Sect.). High stereochemical selectivity is observed in these reactions that afford a single isomer. The obtained complexes show the expected features in their IR spectra, their FAB spectra show the parent peaks and they behave as 1:1 electrolytes in acetone solution.^[5] For complexes containing symmetric diimines, **2–4**, the diimine ligand shows one set of resonances due to equivalent imino fragments, their ³¹P{¹H} NMR spectra contain only one singlet in the 27–33 ppm range, indicating equivalent P-

[a] Facultad de Química de San Sebastián, Universidad del País Vasco, Apdo. 1072, 20080 San Sebastián, Spain

[b] Departamento de Química Inorgánica, Laboratorio de Difracción de Rayos X, Facultad de Ciencias Químicas, Universidad Complutense, 28040 Madrid, Spain

atoms and the $^{13}\text{C}\{^1\text{H}\}$ NMR spectra show also only one singlet in the 216–224 ppm range, corresponding to equivalent acyl groups. According to these data two isomers are possible for these complexes, the *cis*-acyl, *trans*-phosphane species or the *trans*-acyl, *cis*-phosphane compound. Taking into account electronic considerations, the most stable isomer would be the *cis*-acyl, *trans*-phosphane isomer, with the acyl groups *trans* to the imino groups, since acyls, having the largest *trans* influence and being the best σ -donors, would prefer to be *trans* to the imino group with the lowest *trans* influence, being the weakest σ -donor, when compared to phosphanes.^[6] This is confirmed by the reaction of **1** with boh, containing nonsymmetrical imino groups, which shows that the stereochemistry of **5** corresponds to that shown in Scheme 1. The oxime hydrazone ligand shows two sets of resonances due to nonequivalent imino fragments, the $^{31}\text{P}\{^1\text{H}\}$ NMR spectrum shows two doublets (AB pattern) at $\delta = 37.3$ and 26.7 ppm corresponding to two nonequivalent phosphanes mutually *trans* [$J(\text{P,P}) = 323$ Hz] and the $^{13}\text{C}\{^1\text{H}\}$ NMR spectrum contains two acyl resonances at $\delta = 233.9$ and 214.6 ppm.



Scheme 1. NN = bipy, **2**; bdh ($\text{R} = \text{R}' = \text{NH}_2$), **3**; dmgl ($\text{R} = \text{R}' = \text{OH}$) **4**; boh, ($\text{R} = \text{NH}_2$, $\text{R}' = \text{OH}$), **5**.

Complex **1** contains a hydride, which may behave as a proton acceptor, and an alcoholic $\text{O}\cdots\text{H}\cdots\text{O}$ proton. In $\text{CDCl}_3/\text{CD}_3\text{OD}$ solution H/D exchange of this proton is observed. We believe that the dehydrogenation reaction most likely occurs by interaction of H^- and H^+ . Because of the low rate of our reactions we were unable to observe any hydrogen evolution by NMR during the dehydrogenation reaction. Nevertheless, the interaction between late transition-metal hydrides and alcoholic or hydroxycarbene protons that may result in hydrogen formation is documented.^[7] Furthermore, we observe some relation between the reaction rate and the type of ligand. The slowest reaction occurs for the dioxime ligand containing OH groups (ca. 9 h), the reaction with a good “proton acceptor” ligand such as bipyridine is faster (ca. 150 min) and the reaction with ligands containing amino groups, bdh or boh, are the fastest (ca. 90 min). Recent studies on a reversible reaction involving dehydrogenation of $[\text{Ru}(\text{H})_2(\text{PMe}_3)\{\text{HN}(\text{CH}_2-$

$\text{CH}_2\text{P}(\text{Pr}_2)_2\}$] and hydrogenation of $[\text{RuH}(\text{PMe}_3)\{\text{N}(\text{CH}_2\text{CH}_2\text{P}(\text{Pr}_2)_2)\}]$, via heterolytic splitting of hydrogen, suggest that the barrier for the hydrogen splitting may be lowered by hydrogen bond formation with added water.^[8] In the present case the different dehydrogenation rates may be related to initial hydrogen bond formation between the hydroxycarbene proton and the free N-donor ligand which may lead to the proton being closer to the hydride thus allowing for easier formation of hydrogen when better proton acceptor ligands are available. X-ray diffraction studies on hydrido-irida- β -diketones have shown that the iridacycle comprising the acyl(hydroxycarbene) group is essentially planar.^[3a] In these reactions complete dehydrogenation occurs while previously we have observed that the reaction of **1** with Et_3N in refluxing methanol led only to partial dehydrogenation.^[4] We believe that this different behaviour may be related to the better coordinating ability of diimines, when compared to Et_3N , which may favour the removal of the hydride in the present case.

The reaction of $[\text{IrHCl}\{\text{P}(\text{Ph}_2)(o\text{-C}_6\text{H}_4\text{CO})_2\text{H}\}]$ (**1**) with pyridine in refluxing methanol also leads to dehydrogenation to afford the neutral diacyl $[\text{IrCl}(\text{P}(\text{Ph}_2)(o\text{-C}_6\text{H}_4\text{CO})_2)_2(\text{py})]$ (**6**). Its IR spectrum contains the band due to coordinated acyl groups at 1624 cm^{-1} and the FAB spectrum shows the peak due to pyridine loss. The $^{31}\text{P}\{^1\text{H}\}$ NMR spectrum contains an AB spin pattern due to *trans* phosphorus atoms [$J(\text{P,P}) = 347$ Hz] and the $^{13}\text{C}\{^1\text{H}\}$ NMR spectrum contains two resonances in the 210 ppm region, attributed to two acyl groups bonded to iridium. These spectral features indicate *trans* P-atoms and *cis*-acyl groups *trans* to chloride and to pyridine, which are the groups with lower *trans* influence, as shown in Scheme 1.

Complex **6** could be characterised by single-crystal X-ray diffraction, which confirms the spectroscopic findings. Complex **6** crystallises in the $P2_1/c$ monoclinic group. Figure 1 shows an ORTEP view of complex **6**. Selected bond lengths and angles are listed in Table 1. The coordinative environment of the rhodium atom is distorted octahedral, with four positions occupied by the phosphorus and carbon atoms of the two bidentate ligands, and the other two positions are occupied by the nitrogen atom of the pyridine and by chloride. As also proposed for complexes **2–5**, the phosphorus atoms are mutually *trans*, and the acyl groups are mutually *cis*. A similar feature has also been observed in a related rhodium complex.^[7d] The bond lengths in **6** are in the expected ranges.^[9] The Ir–P distances are similar and the Ir–N1 [2.229(4) Å] and Ir–Cl [2.515(1) Å] distances are rather long, because of the high *trans* influence of the acyl groups.

Attempts to obtain a diacyl complex similar to **6** using more sterically demanding ligands such as 2-methylpyridine proved unsuccessful. Instead, the formation of an equimolar mixture of dimer cationic species $[\text{Ir}_2(\mu\text{-Cl})(\mu\text{-P}(\text{Ph}_2)(o\text{-C}_6\text{H}_4\text{CO}))_2(\text{P}(\text{Ph}_2)(o\text{-C}_6\text{H}_4\text{CO}))_2]^+$ (**7a** and **7b**) occurred (see Scheme 2). Refluxing **1** in MeOH affords also the formation of **7**. The two isomers could be separated by addition of NaClO_4 . The precipitation of $[\text{7a}]\text{ClO}_4$ was quantitative and from the remaining solution $[\text{7b}]\text{ClO}_4$

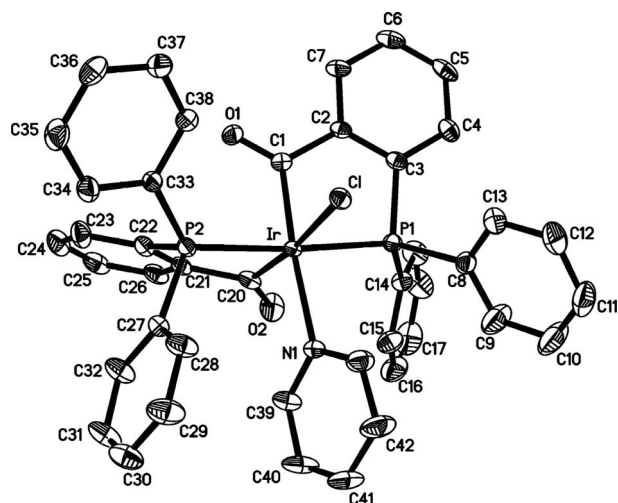
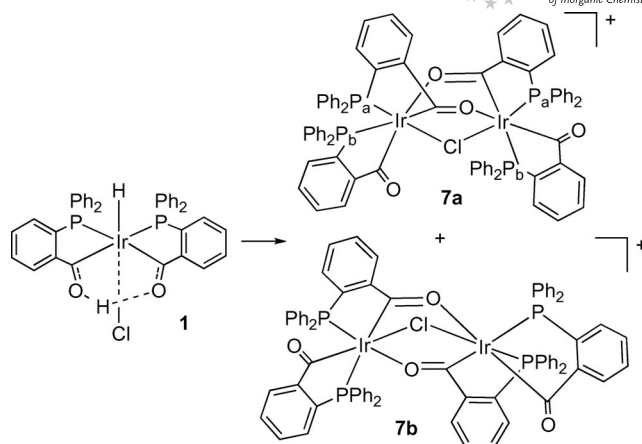


Figure 1. ORTEP view of compound **6** showing the atomic numbering (20% probability ellipsoids). The hydrogen atoms and some carbon atoms have been omitted for clarity.

Table 1. Selected bond lengths [Å] and angles [°] for **6** and [**7b**]ClO₄.

6		[7b]ClO ₄			
Ir–P1	2.342(1)	Ir1–P1	2.373(3)	Ir2–P3	2.382(3)
Ir–P2	2.321(1)	Ir1–P2	2.270(2)	Ir2–P4	2.258(3)
Ir–C20	2.020(6)	Ir1–C20	2.02(1)	Ir2–C58	2.04(1)
Ir–Cl	2.029(5)	Ir1–Cl1	2.00(1)	Ir2–C39	2.01(1)
Ir–N1	2.229(4)	Ir1–Cl1	2.418(4)	Ir2–Cl1	2.496(4)
Ir–Cl	2.515(1)	Ir1–O4	2.267(7)	Ir2–O2	2.126(7)
C20–O2	1.210(6)	C20–O2	1.27(1)	C58–O4	1.24(1)
Cl–O1	1.214(6)	Cl1–O1	1.23(1)	C39–O3	1.22(1)
		Ir1–Ir2	3.564(1)		
P1–Ir–P2	175.01(5)	P1–Ir1–P2	99.1(1)	P3–Ir2–P4	101.4(1)
P1–Ir–C20	96.4(2)	P1–Ir1–C20	177.0(3)	P3–Ir2–C58	175.3(3)
P1–Ir–Cl	89.1(5)	P1–Ir1–Cl1	88.8(1)	P3–Ir2–O2	85.5(2)
P1–Ir–Cl	84.3(2)	P1–Ir1–Cl1	83.8(3)	P3–Ir2–Cl1	99.4(1)
P1–Ir–N1	91.0(1)	P1–Ir1–O4	95.9(2)	P3–Ir2–C39	83.6(3)
P2–Ir–C20	82.4(2)	P2–Ir1–C20	82.0(2)	P4–Ir2–C58	81.7(3)
P2–Ir–Cl	91.9(1)	P2–Ir1–Cl1	168.6(1)	P4–Ir2–O2	169.5(2)
P2–Ir–Cl	90.8(2)	P2–Ir1–Cl1	84.9(3)	P4–Ir2–Cl1	101.2(1)
P2–Ir–N1	93.9(1)	P2–Ir1–O4	104.0(2)	P4–Ir2–C39	89.9(3)
C20–Ir–Cl	173.3(2)	C20–Ir1–Cl1	89.7(3)	C58–Ir2–O2	90.9(3)
C20–Ir–Cl	86.1(2)	C20–Ir1–Cl1	93.6(4)	C58–Ir2–Cl1	84.4(3)
C20–Ir–N1	94.6(2)	C20–Ir1–O4	86.4(3)	C58–Ir2–C39	92.9(4)
Cl–Ir–Cl	90.6(2)	Cl1–Ir1–Cl1	87.8(3)	O2–Ir2–Cl1	85.3(2)
N1–Ir–Cl	89.1(1)	Cl1–Ir1–O4	171.0(3)	O2–Ir2–C39	82.9(3)
Cl–Ir–N1	175.3(2)	Cl1–Ir1–O4	83.2(2)	Cl1–Ir2–C39	167.6(3)
		Ir1–Cl1–Ir2	93.0(2)		
		Ir1–Cl1–O1	122.3(8)	Ir2–C39–O3	123.4(8)
		Ir1–C20–O2	124.0(7)	Ir2–C58–O4	125.4(8)
		Ir1–O4–C58	119.5(7)	Ir2–O2–C20	123.0(6)

could be obtained. Both compounds behave as 1:1 electrolytes in acetone solution and the FAB spectra show the [M]⁺ peak at 1577 as expected for such dinuclear species. Their IR spectra show stretches at 1633 cm^{−1} due to the terminal acyl groups and a strong stretch at 1515 cm^{−1} that can be assigned to bridging acyl groups.



Scheme 2.

The ¹³C{¹H} NMR spectrum of **7a** contains two doublets due to acyl groups. In both resonances the coupling to one of the phosphorus atoms is observed while the coupling to the other phosphorus is unobservable. The resonance at lower field is due to acyl groups with carbon atoms *trans* to phosphorus atoms [*J*(P,C) = 99 Hz]. The chemical shift, 264.9 ppm, is in the upper end of the range 274–240 ppm, reported for bridging acyl groups between iridium atoms in dinuclear complexes,^[3b,4,10] and is similar to that of the related rhodium [Rh₂(μ-Cl)(μ-PPh₂(*o*-C₆H₄CO))₂-(PPh₂(*o*-C₆H₄CO))₂]⁺ complex.^[6d] The resonance at higher field, 197.6 ppm, is attributed to terminal acyl groups and appears at higher field than that of the related rhodium derivative, 219.0 ppm. The ³¹P{¹H} NMR spectrum contains two doublets consistent with an AX pattern. For this isomer we propose the structure depicted in Scheme 2, with two equivalent iridium fragments, and with phosphorus atoms *trans* to acyl and to chlorine. It contains the weakest σ-donor oxygen atoms *trans* to the strongest σ-donor acyl groups, which represents the most electronically favourable geometry. Nevertheless, a disposition with phosphorus atoms being *trans* to acyl and to oxygen cannot be excluded. For **7b**, the spectra are due to the presence of four nonequivalent acyl-phosphane fragments, two per iridium atom. In the ¹³C{¹H} NMR spectrum two close doublets due to terminal acyl groups [ca. 198.9 ppm, *J*(P,C) = 8 Hz] and two close doublets due to bridging acyl groups [ca. 264 ppm, *J*(P,C) = 102 Hz] are observed. The ³¹P{¹H} NMR spectrum consists of four doublets. The *J*(P,P) coupling constants agree with both phosphorus atoms bonded to the same iridium atom being mutually *cis*.

It is noteworthy that by refluxing **1** in MeOH in the presence of NEt₃, partial dehydrochlorination and partial dehydrogenation occurred, thus yielding the dinuclear [Ir₂(μ-H)(μ-PPh₂(*o*-C₆H₄CO))₂(PPh₂(*o*-C₆H₄CO))₂]Cl, with a hydride and two acyl groups bridging the two iridium atoms.^[4] An isomer, [Ir₂H(PPh₂(*o*-C₆H₄CO))₂(μ-PPh₂(*o*-C₆H₄CO))₃]BF₄, containing three acylphosphane bridging ligands and a single terminal hydride, could be obtained by complete halide abstraction and partial dehydrogenation of **1** promoted by halide abstractors.^[3] In the present case, complete

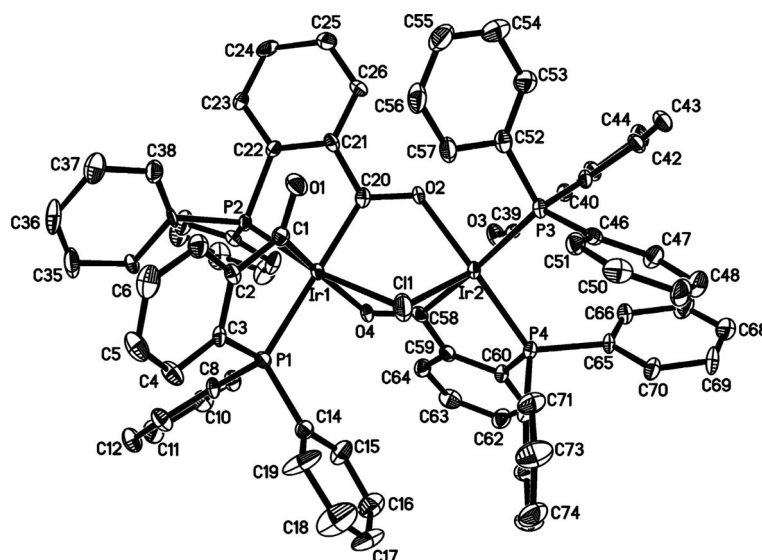


Figure 2. ORTEP view of the cation in compound **[7b]**ClO₄ showing the atomic numbering (20% probability ellipsoids). The hydrogen atoms and some carbon atoms have been omitted for clarity.

dehydrogenation leads the chloride to occupy a bridging position in **7**. The formation of these triply bridged iridium dimers appears easy. In all cases two of the bridging groups between the two iridium atoms are acyls and the nature of the third bridge appears to depend markedly on the reaction conditions.

We succeeded in isolating compound **[7b]**ClO₄ as single crystals suitable for X-ray diffraction. This compound crystallises in the *P*2₁/*n* monoclinic group. The asymmetric unit consists of a dinuclear cation and a ClO₄[−] anion. Figure 2 shows an ORTEP view of the cation. Selected bond lengths and angles are listed in Table 1. Two acyl groups in a head-to-tail arrangement and a chloride bridge the Ir atoms. The geometry around each Ir atom is pseudo-octahedral with the chloro ligand *trans* to a phosphorus atom through the Ir1 atom and *trans* to the carbon atom of a terminal acyl group through the Ir2 atom. The bridging Ir2–Cl1 distance [2.496(4) Å] is longer than the Ir1–Cl1 distance [2.418(4) Å] reflecting the higher *trans* influence of the acyl group.^[11] The bridging Ir2–Cl1 distance is slightly shorter than that observed in the mononuclear complex **6** [2.515(1) Å], and is similar to that reported for complexes containing a bridging chloride *trans* to vinyl [2.495(6) and 2.464(6) Å].^[10] The Ir1–Ir2 distance [3.564(1) Å] and the Ir1–Cl1–Ir2 angle [93.0(2)°] exclude any Ir–Ir interaction. As in other dinuclear species,^[12] the Ir1–Ir2 distance in **7b** is longer than that in the related [Ir₂(μ-H)(μ-PPh₂(*o*-C₆H₄CO))₂(PPh₂(*o*-C₆H₄CO))₂]⁺ [2.9629(4) Å] containing hydride instead of chloride as the bridge. The Ir–C and the C–O distances of the bridging and terminal acyl groups are practically equal. The average Ir–C and C–O bond lengths, 2.02(1) Å and 1.24(1) Å respectively are as expected for coordinated acyl groups with low carbene-like character.^[10] The Ir–P distances also reflect the decreasing *trans* influence in the series: acyl [Ir1–P1 2.373(3) and Ir2–P3 2.382(4) Å] >> chlorine [Ir1–P2 2.270(2) Å] > oxygen [Ir2–P4 2.258(3) Å].

It is well known that metal hydrides may catalyse the transfer hydrogenation of ketones.^[13] Chelated Ir^{III} bis-carbene complexes, proposed to involve a monohydride active species, or hemilabile pincer-type hydride Ir^{III} derivatives have been reported to promote the transfer hydrogenation of cyclohexanone, reaching TOF values higher than 1000 mol/h.^[14] We have recently shown that in methanol and in the presence of strong bases iridium acylhydrides,^[4] and that the presence of P- and N-donor ligands, instead of only P-donor ligands, make the corresponding iridium hydrides more useful for transfer hydrogenation reactions of ketones.^[1c] We have tested the catalytic activity of complexes **2–7** in the transfer hydrogenation of cyclohexanone in *i*PrOH, in the presence of a strong base. From the transfer hydrogenation data it is apparent that compound **[3]Cl**, containing amino substituents in both the imino functionalities shows the highest activity reaching 88% conversion to cyclohexanol after 180 min (TOF^[15] of 134 after 10 min). The dimer compound **[7]Cl** reaches 59% conversion after 180 min (TOF^[15] of 85 after 10 min) and the pyridine complex **6** shows lower activity, reaching 44% conversion after 180 min. For compounds **[2]Cl**, **[4]Cl** and **[5]Cl** less than 10% conversion was attained after 180 min. The corresponding perchlorate compounds show a lower activity than the chloride compounds, probably due to their low solubility. Compound **[3]Cl** shows a comparable catalytic activity to that of Cp*Ir^{III} complexes containing functionalised carbenes.^[16]

Conclusions

The hydrido-irida-β-diketone [IrH{(PPh₂(*o*-C₆H₄CO))₂-H}Cl] (**1**) undergoes dehydrogenation in protic solvents to afford dimer complexes with bridging acyl and chloride groups. The presence of N-donors makes the dehydrogena-

tion reaction faster, suggesting hydrogen bond formation favouring the dehydrogenation reaction, affording selectively cationic or neutral diacyl complexes of the *cis*-acyl, *trans*-phosphane type. The dihydrazone-containing complex can be used as a pre-catalyst for transfer hydrogenation of ketones.

Experimental Section

General Procedures: The preparation of the metal complexes was carried out at room temperature under nitrogen using standard Schlenk techniques. $[\text{IrH}\{\text{P}(\text{Ph}_2(o\text{-C}_6\text{H}_4\text{CO}))_2\text{H}\}\text{Cl}]$ (**1**) was prepared as previously reported.^[1a] Microanalyses were carried out with a Leco CHNS-932 microanalyser. Conductivities were measured in acetone solution with a Metrohm 712 conductimeter. IR spectra were recorded with a Nicolet FTIR 510 spectrophotometer in the range 4000–400 cm^{-1} using KBr pellets. NMR spectra were recorded with Bruker Avance DPX 300 or Bruker Avance 500 spectrometers, ^1H and $^{13}\text{C}\{^1\text{H}\}$ (TMS internal standard), $^{31}\text{P}\{^1\text{H}\}$ (H_3PO_4 external standard), were measured from CDCl_3 solutions. Mass spectra were recorded with a VG Autospec, by liquid secondary ion (LSI) MS using nitrobenzyl alcohol as matrix and a caesium gun (Universidad de Zaragoza).

$[\text{Ir}(\text{P}(\text{Ph}_2(o\text{-C}_6\text{H}_4\text{CO}))_2(\text{bipy}))\text{ClO}_4$ (2**):** To a methanol suspension of $[\text{IrH}\{\text{P}(\text{Ph}_2(o\text{-C}_6\text{H}_4\text{CO}))_2\text{H}\}\text{Cl}]$ (**1**) (50 mg, 0.062 mmol) was added 2,2'-bipyridine (bipy) (9.7 mg, 0.062 mmol). The suspension was refluxed for 150 min whereupon a yellow solution was formed. The solution was cooled and a methanol solution of $\text{NaClO}_4 \cdot \text{H}_2\text{O}$ (8.7 mg, 0.062 mmol) was added to afford a yellow solid that was decanted, washed with methanol and dried under vacuum. Yield 50.3 mg, 79%. IR (KBr): $\tilde{\nu} = 1627$ (s) ($\text{C}=\text{O}$) cm^{-1} . A_M ($\text{ohm}^{-1}\text{cm}^2\text{mol}^{-1}$): 128 (acetone). $^{31}\text{P}\{^1\text{H}\}$ NMR (CDCl_3): $\delta = 27.2$ (s) ppm. $^{13}\text{C}\{^1\text{H}\}$ NMR (CDCl_3): $\delta = 216.0$ (s) ppm. $\text{C}_{48}\text{H}_{36}\text{ClIrN}_2\text{O}_6\text{P}_2$ (1026.14): calcd. C 56.17, H 3.53, N 2.73; found C 55.79, H 3.16, N 2.71.

$[\text{Ir}(\text{P}(\text{Ph}_2(o\text{-C}_6\text{H}_4\text{CO}))_2(\text{bdh}))\text{ClO}_4$ (3**):** To a methanol suspension of $[\text{IrH}\{\text{P}(\text{Ph}_2(o\text{-C}_6\text{H}_4\text{CO}))_2\text{H}\}\text{Cl}]$ (**1**) (50 mg, 0.062 mmol) was added bisacetylhydrazine (bdh) (7.1 mg, 0.062 mmol). The suspension was refluxed for 90 min whereupon a yellow solution was formed. The solution was cooled and a methanol solution of $\text{NaClO}_4 \cdot \text{H}_2\text{O}$ (8.7 mg, 0.062 mmol) was added to afford a yellow solid that was decanted, washed with methanol and dried under vacuum. Yield 45.2 mg, 74%. IR (KBr): $\tilde{\nu} = 3398$ (m) (OH), 3299 (m), 3201 (m) (NH_2), 1597 (s) ($\text{C}=\text{O}$) cm^{-1} . A_M ($\text{ohm}^{-1}\text{cm}^2\text{mol}^{-1}$): 134 (acetone). ^1H NMR (CDCl_3): $\delta = 5.68$ (s, 4 H, NH), 1.57 (s, 3 H, CH_3) ppm. $^{31}\text{P}\{^1\text{H}\}$ NMR (CDCl_3): $\delta = 31.4$ (s) ppm. $^{13}\text{C}\{^1\text{H}\}$ NMR (CDCl_3): $\delta = 218.3$ (s, IrCO); 15.1 (s, CH_3) ppm. FAB-MS: calcd. for $\text{C}_{42}\text{H}_{38}\text{IrN}_4\text{O}_4\text{P}_2$, 885; obsd. 885 [M^+]. $\text{C}_{42}\text{H}_{38}\text{ClIrN}_4\text{O}_6\text{P}_2 \cdot \text{CH}_3\text{OH}$ (1016.18): calcd. C 50.81, H 4.17, N 5.51; found C 50.62, H 4.18, N 5.78.

$[\text{Ir}(\text{P}(\text{Ph}_2(o\text{-C}_6\text{H}_4\text{CO}))_2(\text{dmg}))\text{ClO}_4$ (4**):** To a methanol suspension of $[\text{IrH}\{\text{P}(\text{Ph}_2(o\text{-C}_6\text{H}_4\text{CO}))_2\text{H}\}\text{Cl}]$ (**1**) (50 mg, 0.062 mmol) was added dimethylglyoxime (dmg) (8.7 mg, 0.062 mmol). The suspension was refluxed for 9 h whereupon a yellow solution was formed. The solution was cooled and a methanol solution of $\text{NaClO}_4 \cdot \text{H}_2\text{O}$ (7.6 mg, 0.062 mmol) was added to afford a yellow solid that was decanted, washed with methanol and dried under vacuum. Yield 29.4 mg, 48%. IR (KBr): $\tilde{\nu} = 3611$ (m) (OH), 1624 (s) ($\text{C}=\text{O}$) cm^{-1} . A_M ($\text{ohm}^{-1}\text{cm}^2\text{mol}^{-1}$): 140 (acetone). ^1H NMR (CDCl_3): $\delta = 1.73$ (s, 3 H, CH_3) ppm. $^{31}\text{P}\{^1\text{H}\}$ NMR (CDCl_3): $\delta = 32.8$ (s) ppm. $^{13}\text{C}\{^1\text{H}\}$ NMR (CDCl_3): $\delta = 224.6$ (s, IrCO); 14.7 (s, CH_3) ppm.

$\text{C}_{42}\text{H}_{36}\text{ClIrN}_2\text{O}_8\text{P}_2 \cdot \text{CH}_3\text{OH}$ (1018.16): calcd. C 50.71, H 3.96, N 2.75; found C 50.57, H 4.10, N 2.94.

$[\text{Ir}(\text{P}(\text{Ph}_2(o\text{-C}_6\text{H}_4\text{CO}))_2(\text{boh}))\text{ClO}_4$ (5**):** To a methanol suspension of $[\text{IrH}\{\text{P}(\text{Ph}_2(o\text{-C}_6\text{H}_4\text{CO}))_2\text{H}\}\text{Cl}]$ (**1**) (50 mg, 0.062 mmol) was added biacetylloxime hydrazone (boh) (8.7 mg, 0.062 mmol). The suspension was refluxed for 90 min whereupon a yellow solution was formed. The solution was cooled and a methanol solution of $\text{NaClO}_4 \cdot \text{H}_2\text{O}$ (7.6 mg, 0.062 mmol) was added to afford a yellow solid that was decanted, washed with methanol and dried under vacuum. Yield 37.3 mg, 61%. IR (KBr): $\tilde{\nu} = 3341$ (w) (OH), 3395 (w), 3201 (w) (NH), 1607 (s) ($\text{C}=\text{O}$) cm^{-1} . A_M ($\text{ohm}^{-1}\text{cm}^2\text{mol}^{-1}$): 94 (acetone). ^1H NMR (CDCl_3): $\delta = 10.6$ (s, 1 H, OH); 6.17 (s, 2 H, NH); 1.72 (s, 3 H, CH_3); 1.56 (s, 3 H, CH_3) ppm. $^{31}\text{P}\{^1\text{H}\}$ NMR (CDCl_3): $\delta = 37.3$ (d) and 26.7 (d) [$J(\text{P,P}) = 273$ Hz] ppm. $^{13}\text{C}\{^1\text{H}\}$ NMR (CDCl_3): $\delta = 233.9$ [d, $J(\text{P,CO}) = 4$ Hz, IrCO]; 214.6 [d, $J(\text{P,CO}) = 4$ Hz, IrCO]; 13.6 (s, CH_3); 13.2 (s, CH_3) ppm. $\text{C}_{42}\text{H}_{37}\text{ClIrN}_3\text{O}_7\text{P}_2 \cdot \text{CH}_3\text{OH}$ (1017.17): calcd. C 50.76, H 4.06, N 4.13; found C 50.40, H 4.01, N 4.02.

$[\text{IrCl}(\text{P}(\text{Ph}_2(o\text{-C}_6\text{H}_4\text{CO}))_2(\text{py}))]$ (6**):** To a methanol suspension of $[\text{IrH}\{\text{P}(\text{Ph}_2(o\text{-C}_6\text{H}_4\text{CO}))_2\text{H}\}\text{Cl}]$ (**1**) (50 mg, 0.062 mmol) was added pyridine (py) (5 μL , 0.062 mmol). The suspension was refluxed for 3 h whereupon a yellow solution was formed. The solution was cooled and evaporation of the methanol solution under vacuum afforded a yellow solid that was decanted, washed with methanol and dried under vacuum. Yield 31.8 mg, 58%. IR (KBr): $\tilde{\nu} = 1624$ (s) ($\text{C}=\text{O}$) cm^{-1} . $^{31}\text{P}\{^1\text{H}\}$ NMR (CDCl_3): $\delta = 33.5$ (d) and 29.0 (d) [$J(\text{P,P}) = 347$ Hz] ppm. $^{13}\text{C}\{^1\text{H}\}$ NMR (CDCl_3): $\delta = 211.4$ [d, $J(\text{P,C}) = 2$ Hz, IrCO]; 209.8 [d, $J(\text{P,C}) = 4$ Hz, IrCO] ppm. FAB-MS: calcd. for $\text{C}_{43}\text{H}_{33}\text{ClIrNO}_2\text{P}_2$, 885; obsd. 806 [$\text{M} - \text{py}^+$]. $\text{C}_{43}\text{H}_{33}\text{ClIrNO}_2\text{P}_2 \cdot \text{CH}_3\text{OH}$ (917.16): calcd. C 57.61, H 4.07, N 1.53; found C 57.30, H 3.95, N 1.84.

Reaction of 1 with 2-Methylpyridine. Formation of $[\text{Ir}_2(\mu\text{-Cl})(\mu\text{-P}(\text{Ph}_2(o\text{-C}_6\text{H}_4\text{CO}))_2(\text{P}(\text{Ph}_2(o\text{-C}_6\text{H}_4\text{CO}))_2\text{H})\text{Cl}]$ (7a**)** **Cl**: To a methanol suspension of $[\text{IrH}\{\text{P}(\text{Ph}_2(o\text{-C}_6\text{H}_4\text{CO}))_2\text{H}\}\text{Cl}]$ (**1**) (30 mg, 0.037 mmol) was added 2-methylpyridine (3.7 μL , 0.037 mmol). The suspension was refluxed for 90 min whereupon a yellow solution was formed. The solution was cooled and evaporation of the methanol solution under vacuum afforded an equimolar mixture of **[7a]Cl** and **[7b]Cl** that was identified by NMR spectroscopy.

$[\text{Ir}_2(\mu\text{-Cl})(\mu\text{-P}(\text{Ph}_2(o\text{-C}_6\text{H}_4\text{CO}))_2(\text{P}(\text{Ph}_2(o\text{-C}_6\text{H}_4\text{CO}))_2\text{H})\text{ClO}_4$ (7a**)** **ClO₄** and **[7b]ClO₄**: A methanol suspension of $[\text{IrH}\{\text{P}(\text{Ph}_2(o\text{-C}_6\text{H}_4\text{CO}))_2\text{H}\}\text{Cl}]$ (**1**) (50 mg, 0.062 mmol) was refluxed for 10 h whereupon a yellow solution was formed. The solution was cooled and a methanol solution of $\text{NaClO}_4 \cdot \text{H}_2\text{O}$ (1.8 mg, 0.031 mmol) was added to afford a yellow solid, **[7a]ClO₄**, which was decanted, washed with methanol and dried under vacuum. Yield 24.9 mg, 48%. To the remaining solution a methanol solution of $\text{NaClO}_4 \cdot \text{H}_2\text{O}$ (1.8 mg, 0.031 mmol) was added to afford a yellow solid, **[7b]ClO₄**, which was decanted, washed with methanol and dried under vacuum. Yield 15.6 mg, 30%. Data for **[7a]ClO₄**. IR (KBr): $\tilde{\nu} = 1638$ (s) ($\text{C}=\text{O}$)_t, 1516 (s) ($\text{C}=\text{O}$)_b cm^{-1} . A_M ($\text{ohm}^{-1}\text{cm}^2\text{mol}^{-1}$): 137 (acetone). $^{31}\text{P}\{^1\text{H}\}$ NMR (CDCl_3): $\delta = 21.9$ [d, $J(\text{P,P}) = 3$ Hz, P_a]; 9.9 (d, P_b) ppm. $^{13}\text{C}\{^1\text{H}\}$ NMR (CDCl_3): $\delta = 264.9$ [d, $J(\text{P,C}) = 99$ Hz, IrC_aO]; 197.6 [d, $J(\text{P,C}) = 6$ Hz, IrC_bO] ppm. FAB-MS: calcd. for $\text{C}_{76}\text{H}_{56}\text{ClIr}_2\text{O}_4\text{P}_4$, 1577; obsd. 1577 [M^+]. $\text{C}_{76}\text{H}_{56}\text{Cl}_2\text{Ir}_2\text{O}_8\text{P}_4 \cdot 2\text{CH}_3\text{OH}$ (1740.22): calcd. C 53.82, H 3.71; found C 53.49, H 3.55. Data for **[7b]ClO₄**. IR (KBr): $\tilde{\nu} = 1633$ (s) ($\text{C}=\text{O}$)_t, 1515 (s) ($\text{C}=\text{O}$)_b cm^{-1} . A_M ($\text{ohm}^{-1}\text{cm}^2\text{mol}^{-1}$): 95 (acetone). $^{31}\text{P}\{^1\text{H}\}$ NMR (CDCl_3): $\delta = 20.2$ (d) and 17.4 (d) [$J(\text{P,P}) = 9$ Hz]; 17.8 (d) and 13.4 (d) [$J(\text{P,P}) = 6$ Hz] ppm. $^{13}\text{C}\{^1\text{H}\}$ NMR (CDCl_3): $\delta = 263.8$ [d, $J(\text{P,C}) = 102$ Hz]; 263.1 [d, $J(\text{P,C}) = 102$ Hz]; 198.9 [d, $J(\text{P,C}) = 8$ Hz] and 195.7 (m) for IrCO ppm. FAB-MS: calcd. for $\text{C}_{76}\text{H}_{56}\text{Cl}$

$\text{Ir}_2\text{O}_4\text{P}_4$, 1577; obsd. 1577 $[\text{M}^+]$. $\text{C}_{76}\text{H}_{56}\text{Cl}_2\text{Ir}_2\text{O}_8\text{P}_4$ (1676.16): calcd. C 54.45, H 3.37; found C 54.46, H 3.71.

Catalytic Reactions: The transfer hydrogenation reactions were carried out under nitrogen in refluxing 2-propanol with magnetic stirring. The equipment consisted of a 100-mL round-bottomed flask, fitted with a condenser and provided with a septum cap. The catalysts, as chloride compounds, were prepared "in situ" by refluxing equimolar amounts (0.02 mmol) of **1** and the corresponding ligand in MeOH to obtain solutions. After cooling, the methanol was eliminated under vacuum. The solid residue was dissolved in 30 mL of 2-propanol and 0.2 mmol of potassium hydroxide in 10 mL of 2-propanol were added. The resulting solutions were heated to 83 °C and 4 mmol of the substrate was injected. The analysis of the catalytic reactions was carried out with a Shimadzu GC-14A chromatograph, connected to a Shimadzu C-R6A calculation integrator.

X-ray Structure Determination of **6 and **[7b]ClO₄**:** Prismatic yellow crystals of $[\text{C}_{43}\text{H}_{33}\text{Cl}_1\text{N}_1\text{O}_2\text{P}_2\text{Ir}]$ and $[\text{C}_{76}\text{H}_{56}\text{Cl}_1\text{O}_4\text{P}_4\text{Ir}_2]\text{ClO}_4$ suitable for X-ray experiments were obtained by slow diffusion of diethyl ether into chloroform solutions of **6** or **[7b]ClO₄**. A summary of the fundamental crystal and refinement data are given in Table 2. The crystals were resin epoxy coated and mounted on a Bruker Smart CCD diffractometer, with graphite-monochromated Mo- K_α ($\lambda = 0.71073$) radiation, operating at 50 kV and 20 mA. Data were collected over a hemisphere of the reciprocal space by combination of three exposure sets. Each frame exposure time was of 20 s, covering 0.3° in ω . The cell parameters were determined and

Table 2. Crystal data and structure refinement for compounds **6** and **[7b]ClO₄**.

Crystal data	6	[7b]ClO₄
Empirical formula	$[\text{C}_{43}\text{H}_{33}\text{Cl}_1\text{IrN}_1\text{O}_2\text{P}_2]$	$[\text{C}_{76}\text{H}_{56}\text{Cl}_1\text{Ir}_2\text{O}_4\text{P}_4]\text{ClO}_4$
Formula weight	885.29	1676.39
Crystal system	monoclinic	monoclinic
Space group	$P2_1/c$	$P2_1/n$
a [Å]	12.0866(5)	20.471(1)
b [Å]	17.2053(7)	11.864(1)
c [Å]	17.7139(7)	28.438(2)
β [°]	99.837(1)	99.352(1)
Volume [Å ³]	3629.5(3)	6814.5(8)
Z	4	4
$D(\text{calcd.})$ [g cm ⁻³]	1.620	1.634
Absorption coefficient [mm ⁻¹]	3.879	4.130
Scan technique	ω and ϕ	ω and ϕ
$F(000)$	1752	3296
Range for data collection [°]	1.66 to 25.00	1.14 to 25.00
Index ranges	-14, -20, -20 to 13, 19, 20	-21, -14, -33 to 24, 14, 22
Reflections collected	25701	34851
Independent reflections	6091 $[R(\text{int}) = 0.0450]$	12015 $[R(\text{int}) = 0.065]$
Completeness to theta	95.2%	100.0%
Data / restraints / parameters	6091 / 0 / 451	12015 / 0 / 805
Goodness-of-fit on F^2	1.063	1.082
$R^{[\text{a}]}$ (refl. obsd.)		
$[I > 2\sigma(I)]$	0.0303 (4490)	0.0516 (7132)
$R_w^{[\text{b}]}$ (all data)	0.0698	0.1463
Largest diff. peak and hole	0.922 and -0.649 e Å ⁻³	1.329 and -1.181 e Å ⁻³

[a] $\Sigma |F_o| - |F_c| / \Sigma |F_o|$. [b] $\{\Sigma [w(F_o^2 - F_c^2)^2] / \Sigma [w(F_o^2)^2]\}^{1/2}$.

refined by a least-squares fit of all reflections collected. The first 100 frames were recollected at the end of the data collection to monitor crystal decay, and no appreciable decay was observed. In both cases a semi-empirical absorption correction was applied. The structures were solved by direct methods and conventional Fourier techniques and refined by applying full-matrix least-squares on F^2 with anisotropic thermal parameters for the non-hydrogen atoms, with the exception of the oxygen atoms of the perchlorate anions of **7b**, which were refined isotropically. The hydrogen atoms were included at their calculated positions determined by molecular geometry and refined riding on the corresponding bonded atom. All the calculations were carried out with SHELX-97.^[17]

CCDC-767995 (for **6**) and -767996 (for **7b**) contain the supplementary crystallographic data for this paper. These data can be obtained free of charge from The Cambridge Crystallographic Data Centre via www.ccdc.cam.ac.uk/datarequest/cif.

Acknowledgments

Financial support by Ministerio de Ciencia e Innovación (MCINN) (CTQ2008-2967/BQU), Universidad del País Vasco, and Diputación Foral de Guipuzcoa is gratefully acknowledged.

- a) M. A. Garralda, R. Hernández, L. Ibarlucea, E. Pinilla, M. R. Torres, *Organometallics* **2003**, *22*, 3600–3603; b) M. A. Garralda, *Dalton Trans.* **2009**, 3635–3645; c) R. Ciganda, M. A. Garralda, L. Ibarlucea, E. Pinilla, M. R. Torres, *Dalton Trans.* **2009**, 4227–4235.
- a) C. M. Lukehart, *Acc. Chem. Res.* **1981**, *14*, 109–116; b) C. M. Lukehart, *Adv. Organomet. Chem.* **1986**, *25*, 45–71; c) D. Steinborn, *Dalton Trans.* **2005**, 2664–2671; d) D. Steinborn, S. Schwieger, *Chem. Eur. J.* **2007**, *13*, 9668–9678.
- a) F. Acha, M. A. Garralda, L. Ibarlucea, E. Pinilla, M. R. Torres, *Inorg. Chem.* **2005**, *44*, 9084–9091; b) F. Acha, M. A. Garralda, R. Hernández, L. Ibarlucea, E. Pinilla, M. R. Torres, M. Zarandona, *Eur. J. Inorg. Chem.* **2006**, 3893–3900.
- F. Acha, R. Ciganda, M. A. Garralda, R. Hernández, L. Ibarlucea, E. Pinilla, M. R. Torres, *Dalton Trans.* **2008**, 4602–4611.
- W. J. Geary, *Coord. Chem. Rev.* **1971**, *7*, 81–122.
- a) T. G. Appleton, H. C. Clark, L. E. Manzer, *Coord. Chem. Rev.* **1973**, *10*, 335–422; b) O. Blum, R. Carmielli, J. M. L. Martín, D. Milstein, *Organometallics* **2000**, *19*, 4608–4612; c) M. A. Garralda, R. Hernández, L. Ibarlucea, E. Pinilla, M. R. Torres, M. Zarandona, *Organometallics* **2007**, *26*, 5369–5376; d) M. A. Garralda, R. Hernández, E. Pinilla, M. R. Torres, M. Zarandona, *Dalton Trans.* **2009**, 9860–9869.
- a) J. N. Coalter III, J. C. Huffman, K. G. Caulton, *Organometallics* **2000**, *19*, 3569–3578; b) W. Yao, R. H. Crabtree, *Inorg. Chem.* **1996**, *35*, 3007–3011; c) L. M. Epstein, E. S. Shubina, *Coord. Chem. Rev.* **2002**, *231*, 165–181; d) M. A. Garralda, R. Hernández, L. Ibarlucea, E. Pinilla, M. R. Torres, M. Zarandona, *Organometallics* **2007**, *26*, 1031–1038.
- A. Friedrich, M. Drees, J. Schmedt auf der Gönne, S. Schneider, *J. Am. Chem. Soc.* **2009**, *131*, 17552–17553.
- a) G. R. Clark, T. R. Greene, W. R. Roper, *J. Organomet. Chem.* **1985**, *293*, C25–C28; b) M. V. Jiménez, E. Sola, A. P. Martínez, F. J. Lahoz, L. A. Oro, *Organometallics* **1999**, *18*, 1125–1136; c) S. N. Paisner, P. Burger, R. G. Bergman, *Organometallics* **2000**, *19*, 2073–2083.
- J. M. O'Connor, R. Merwin, A. L. Rheingold, M. L. Adams, *Organometallics* **1995**, *14*, 2102–2105.
- A. Albinati, H. Lehner, L. M. Venanzi, *Inorg. Chem.* **1985**, *24*, 1483–1488.
- a) A. Musco, R. Naegeli, L. M. Venanzi, A. Albinati, *J. Organomet. Chem.* **1982**, *228*, C15–C18; b) H. Lehner, D. Matt, A. Togni, R. Thouvenot, L. M. Venanzi, A. Albinati, *Inorg. Chem.* **1984**, *23*, 4254–4261.

- [13] a) J. E. Bäckvall, *J. Organomet. Chem.* **2002**, 652, 105–111; b) S. E. Clapham, A. Hadzovic, R. H. Morris, *Coord. Chem. Rev.* **2004**, 248, 2201–2237; c) J. S. M. Samec, J. E. Bäckvall, P. G. Andersson, P. Brandt, *Chem. Soc. Rev.* **2006**, 35, 237–248; d) S. Gladiali, E. Alberico, *Chem. Soc. Rev.* **2006**, 35, 226–236.
- [14] a) M. Albrecht, J. R. Miecznikowski, A. Samuel, J. W. Faller, R. H. Crabtree, *Organometallics* **2002**, 21, 3596–3604; b) A. Choualeb, A. J. Lough, D. G. Gusev, *Organometallics* **2007**, 26, 5224–5229.
- [15] TOF calculated after 10 min and expressed in mol of product/ (mol of pre-catalyst \times h).
- [16] A. Pontes da Costa, M. Viciano, M. Sanaú, S. Merino, J. Tejada, E. Peris, B. Royo, *Organometallics* **2008**, 27, 1305–1309.
- [17] G. M. Sheldrick, *SHELX-97, Program for Crystal Structure Determination*, University of Göttingen, Göttingen, Germany, **1997**.

Received: March 2, 2010
Published Online: May 28, 2010

Low-Temperature Synthesis of Meshy Boron Nitride with a Large Surface Area

Xiang-Lin Meng,^[a] Ning Lun,^[a] Yong-Qiu Qi,^[b] Jian-Qiang Bi,^[a] Yong-Xin Qi,^[a] Hui-Ling Zhu,^[a] Fu-Dong Han,^[a] Yu-Jun Bai,^{*[a]} Long-Wei Yin,^{*[a]} and Run-Hua Fan^[a]

Keywords: Boron nitride / Luminescence / Density functional calculations / Nanostructures

Meshy boron nitride (BN) was synthesized by the reaction of NaBH_4 and $\text{CS}(\text{NH}_2)_2$ at 550 °C for 10 h. X-ray diffraction indicates the formation of hexagonal boron nitride (h-BN) with lattice constants $a = 2.501$ and $c = 6.724$ Å. Observations by TEM show that the BN obtained has a meshy structure with a quantity of pores distributing on each mesh. The nitrogen adsorption-desorption test gives a high surface area of

$220 \text{ m}^2 \text{ g}^{-1}$ for the meshy BN. The cathode-luminescence spectrum exhibits a strong peak at 354 nm in the ultraviolet range. Thermogravimetric analysis proves that the meshy BN has good thermal stability and oxidation resistance up to 800 °C. The formation of meshy BN is due to the promotion of sulfur-containing compounds for the cross-linking of borazine and subsequent pyrolysis.

Introduction

Hexagonal boron nitride (h-BN) attracts more and more attention because of its excellent solid lubricative properties, high thermal conductivity, high thermal stability, chemical inertness, good electrical insulation properties, and low density (2.27 g cm^{-3}).^[1,2] It is interesting to note that BN may exhibit various morphologies, such as one-dimensional nanostructures,^[3–5] hollow spheres,^[6] nanocapsules,^[7] nanocages,^[8] porous structures,^[9] micromesh,^[10] and nanomesh structures.^[11,12] Porous BN has recently attracted a lot of attention due to its unique properties and potential applications. For example, porous or micromesh BN with a large specific surface area can be used as a catalyst support under harsh operating conditions.^[13]

Meshy BN is a kind of two-dimensional film with porous structure and large surface area, yet it has been rarely reported. Wang et al. prepared h-BN micromeshes by using B_2O_3 , Mg, and NaN_3 as starting materials.^[10] These micromeshes might have various potential applications, such as supports for catalysts, chemical filtration, and separations under severe operating conditions. A highly regular nanomesh of h-BN was formed by self-assembly through thermal decomposition of borazine (HBNH_3) at about 800 °C on a transition-metal surface, such as $\text{Rh}(111)$ ^[11] or $\text{Ru}(0001)$.^[12] The insulating BN nanomesh can be exposed

to air^[14] or liquid^[15] without losing its unique properties. The nanomesh may serve as a template for the deposition of electrochemically active molecules^[16] and metal clusters,^[17–20] or as an ideal playground for studying the electronic properties of adsorbates electronically decoupled from the substrate.^[19] So it is of great significance to explore a simple route to prepare meshy BN with a large surface area.

The wide band gap of h-BN makes it a promising candidate for deep-blue and UV applications.^[21] The optical properties of h-BN nanostructures with different morphologies has recently been studied. Chen et al. fabricated novel BN hollow nanoribbons that exhibit an extraordinary ultraviolet cathode-luminescence (CL) emission at 5.33 eV and are applicable to blue lasing and light-emitting diodes.^[22] Gao et al. synthesized BN nanosheets with strong ultraviolet CL emission between 3.79 and 3.96 eV.^[23] Chen et al. reported that the direct band gap of multiwall BN nanotubes is 5.75 eV from photoluminescence spectra.^[24] However, to the best of our knowledge, little is known about the CL properties of meshy BN.

Herein, we provide a facile approach to prepare meshy BN at 550 °C by using $\text{CS}(\text{NH}_2)_2$ and NaBH_4 as raw materials. The meshy BN obtained exhibits a large specific surface area of $220 \text{ m}^2 \text{ g}^{-1}$, a strong luminescence peak at 354 nm, good thermal stability, and oxidation resistance up to 800 °C. The formation mechanism of the meshes was proposed based on detailed investigations and the vulcanization behavior of $\text{CS}(\text{NH}_2)_2$.

Results and Discussion

Figure 1 shows the XRD pattern of the resulting product prepared by the reaction of NaBH_4 and $\text{CS}(\text{NH}_2)_2$ at

[a] Key Laboratory for Liquid-Solid Structural Evolution and Processing of Materials (Ministry of Education), Shandong University, Jinan 250061, P. R. China
Fax: +86-531-88392315
E-mail: byj97@126.com
yinlw@sdu.edu.cn

[b] Laiwu Advanced Technical School, Laiwu 271100, Shandong Province, P. R. China
Supporting information for this article is available on the WWW under <http://dx.doi.org/10.1002/ejic.201000260>.

550 °C for 10 h. Two diffraction peaks at $2\theta=26$ and 41° can be indexed to the (002) and (100) planes of h-BN with lattice constants $a=2.501$ and $c=6.724$ Å, which agree well with those in JCPDS 34-0421. The intense diffraction peaks denote the high crystallinity of the BN obtained.

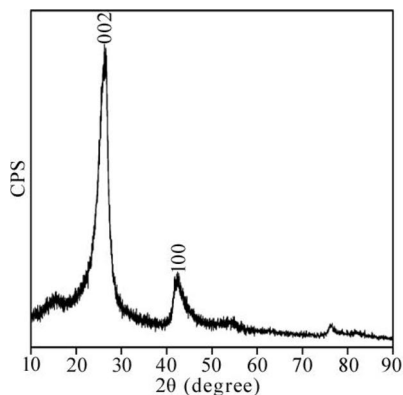


Figure 1. XRD pattern of the resulting product.

The morphology of the product was examined by TEM and HRTEM. Large quantities of two-dimensional thin films with a spider-web-like structure can be observed. The films are uniform and transparent under TEM and HRTEM, indicative of their thickness in the nanometer scale because the penetrable thickness of TEM in the accelerating voltage range of 100–200 kV is 50–100 nm and the appropriate thickness for HRTEM is thinner than 15 nm. Figure 2 (a) is a typical low-magnification TEM image of a single piece of the film, clearly exhibiting the weblike structure. The inset in Figure 2 (a) is the corresponding electron diffraction pattern (EDP); two clear diffraction rings correspond to the (002) and (100) planes of h-BN. Based on the detailed TEM examinations, the areas of the films are from about $1\text{ }\mu\text{m}^2$ to 3 mm^2 . Figure 2 (b) is the higher-magnification TEM image of the films, clearly displaying the pilot-axitic textures. When the film is further magnified a number of pores with sizes from several nanometers to 30 nm can be observed in the webs, as shown in Figure 2 (c). So the spider-web-like films microscopically have a meshy structure, and the dark-contrast weblike region is the edge of the mesh domains. By comparison with the pore sizes, it can be estimated that the thickness of the film is 30 nm or so. Figure 2 (d–f) are the HRTEM images of the product. From Figure 2 (d), the webs consist of a lot of meshes with various sizes, and each mesh is comprised of some small pores. Additionally, the supporting copper microgrid can be clearly observed, further confirming the good transparency and the small thickness of the film. Figure 2 (e) shows the edges of several neighboring meshes, clearly implying that the meshes are cross-linked into webs by some ribbonlike structures. The inset in Figure 2 (e) is the HRTEM lattice fringe image of the edge; the lattice spacing of 0.34 nm is close to that between two adjacent (002) planes of h-BN. Figure 2 (f) displays the inner structure of one mesh, the

pores are interlaced together to form a weblike structure. It is obvious from the TEM observations that the meshy BN is related to the cross-linking of molecules.

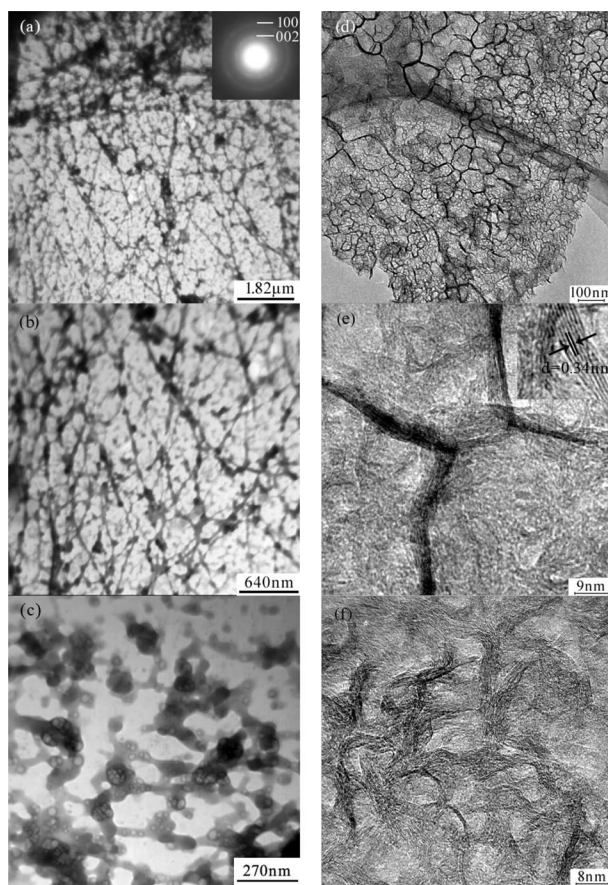


Figure 2. TEM (a, b, c) and HRTEM images (d, e, f) of the resulting product. The inset in (a) is the corresponding EDP, and that in (e) is the lattice fringe image of the meshy BN edge.

Nitrogen adsorption–desorption isotherms were conducted to determine the surface area of the meshy BN. From Figure 3 (a), the isotherms are a characteristic of type IV isotherms with a hysteresis loop at a relative pressure between 0.4 and 1.0, which indicates the presence of mesopores in the product.^[25] Calculation with the BET model gives a large specific surface area of $220\text{ m}^2\text{ g}^{-1}$ and a pore volume of $0.269\text{ cm}^3\text{ g}^{-1}$. The surface area of the meshy BN is much larger than that of the h-BN micromesh.^[10] The DFT method was employed to evaluate the pore-size distribution. From Figure 3 (b), the pore diameters of the meshy BN are around 5 nm, which is also larger than that of the h-BN micromesh.^[10]

For a better understanding the optical properties of meshy BN, CL spectra were measured by thermal field emission SEM (FESEM; see Figure 4). A strong peak at 354 nm in the ultraviolet range corresponds to the energy of 3.5 eV. The strong ultraviolet CL emission from the meshy BN can be ascribed to the deep-level emissions associated with defect-related centers.

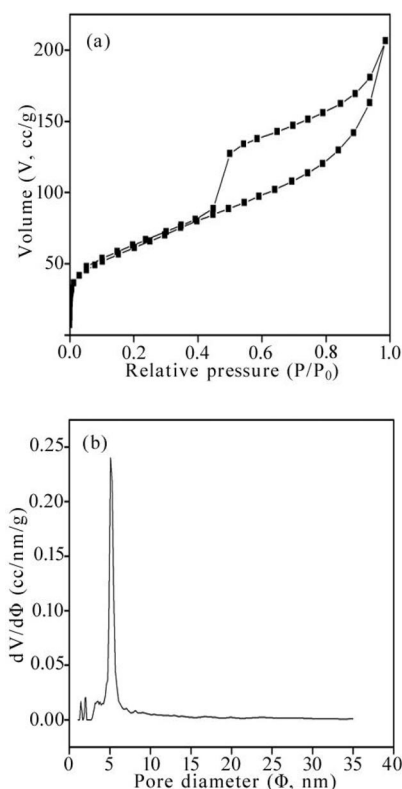


Figure 3. Nitrogen adsorption-desorption isotherms (a) and DFT pore-size distribution curve (b).

Thermal stability and oxidation resistance are important properties for the application of meshy BN, so a combined differential thermal analysis-thermogravimetric analysis (DTA-TGA) test was performed. Figure 5 shows the TGA-DTA curves of the meshy BN between room temperature and 1200 °C under flowing air. A slight weight loss occurs below 800 °C due to the desorption of H₂O (below 200 °C) and the oxidation (300–600 °C) of a small amount of carbon in the product; however, when the temperature is above 800 °C, the weight increases rapidly. Associated with the DTA analysis, the weight gain between 800 and 1000 °C is owing to the gradual oxidation of BN into B₂O₃, which is about 19% from 800 to 1000 °C, and is less than the theoretical weight gain (41.4%) by the thorough oxidation of BN into B₂O₃, because the oxidation of BN is accompanied by the evaporation of B₂O₃ at around 1000 °C.^[26,27] The evaporation of B₂O₃ is greater than the oxidation of BN beyond 1000 °C, thus this results in a gradual weight loss. From the DTA-TGA result, it can be seen that meshy BN has good thermal stability and oxidation resistance up to 800 °C.

A possible reaction mechanism for our approach to meshy BN is proposed. Based on a series of comparative experiments it was found the reaction temperature and time play important roles in the reaction between NaBH₄ and CS(NH₂)₂. If the temperature is below 400 °C, no BN could be obtained. When the temperature is above 600 °C, the yield of the product hardly increases. The optimum reaction temperature is about 550 °C. At 550 °C, the reaction time

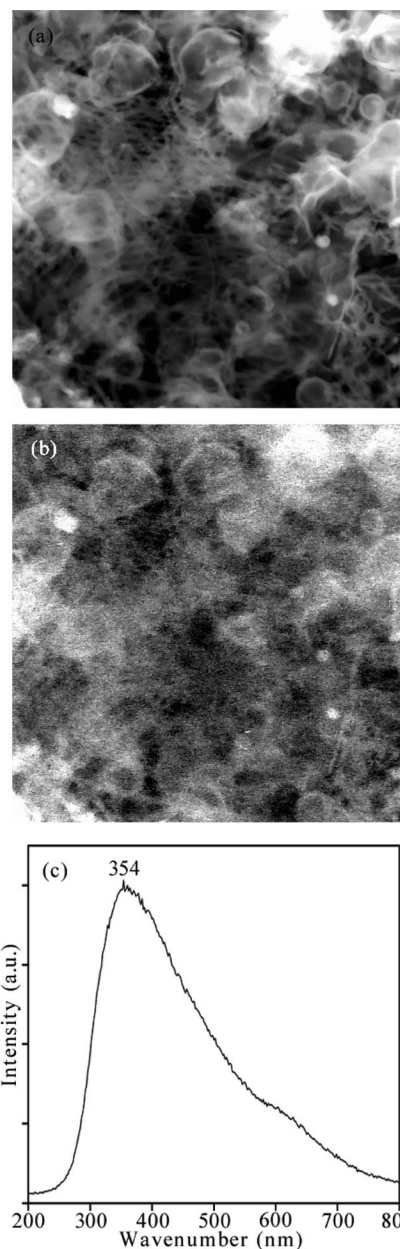


Figure 4. FESEM image (a), corresponding CL-SEM image (b), and CL spectrum (c) of the meshy BN.

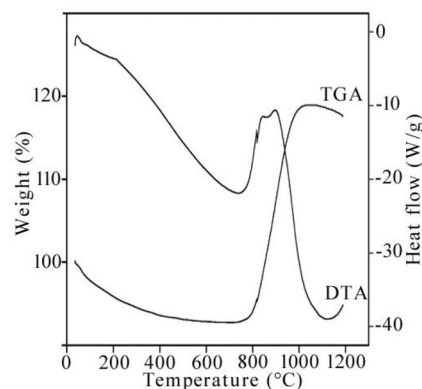
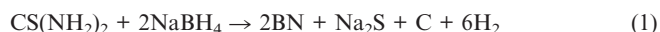


Figure 5. TGA and DTA curves of meshy BN.

in the range of 5–10 h does not significantly affect the yield and the structure. However, if the time is shorter than 2 h, the reaction becomes very incomplete and the crystallinity of the product is poor.

According to the XRD pattern of the as-prepared product without any washing treatments (see the Supporting Information), besides BN, Na₂S is the dominant phase in the as-prepared product. In addition, when the autoclaves were opened after the reaction, some gases were given off, which may have been NH₃, H₂, and etc. In the combined TGA–DTA curves shown in Figure 5, the slight weight loss between 300–600 °C is a result of the oxidation of carbon in the product. So the possible reaction equation can be expressed as follows [Equation (1)].



If the reactant of CS(NH₂)₂ is substituted by other ammonium salts, such as NH₄Cl and CO(NH₂)₂, the only product is porous BN, other than novel meshy BN. So CS(NH₂)₂ is critical for the formation of meshy BN. Associated with the TEM observations and the vulcanization of natural rubber latex promoted by CS(NH₂)₂^[28,29] it is reasonably considered that CS(NH₂)₂ also promotes the cross-linking among molecules during the formation of meshy BN. With the rise of temperature beyond 400 °C, CS(NH₂)₂ begins to decompose and produce H₂S and NH₃. Then H₂S reacts with NaBH₄ to yield borane, and borane combines with NH₃ to form borazine.^[2] With the help of the sulfur-containing compounds, the cross-linking occurs among the borazine molecules. Under the autogenic pressure and the reaction temperature of 550 °C or so, the cross-linked borazine pyrolyzes into the BN with a meshy structure as shown in Figure 2.

Conclusions

In summary, meshy BN with a large specific area of 220 m² g^{−1} and a strong CL peak at 354 nm was synthesized by the reaction between NaBH₄ and CS(NH₂)₂ at 550 °C for 10 h without using any templates. The vulcanization behavior of CS(NH₂)₂ for the cross-linking among borazine molecules is critical for the formation of meshy BN. The cheap reactants, CO(NH₂)₂ and NaBH₄, and the simple operation make this convenient route applicable in the large-scale synthesis of meshy BN.

Experimental Section

General: The raw materials used in this work are analytically pure CS(NH₂)₂ and NaBH₄ (produced from Zhanyun Chemical Co. Ltd., Shanghai, China). In a typical procedure, NaBH₄ (1.6 g, 0.021 mol) and CS(NH₂)₂ (1.5 g, 0.019 mol) were placed into a stainless steel autoclave of 30 mL capacity. Then the autoclave was sealed and heated in a furnace to 550 °C and the temperature maintained for 10 h. When the autoclave was cooled to ambient temperature naturally, the products in the autoclave were collected and washed successively with anhydrous ethanol, dilute hydrochloric acid, and deionized water several times to remove the residual re-

agents and the byproduct. Then, the final product was dried at 60 °C for 10 h and white powders were ultimately obtained. The yield of the resulting product was about 80 wt.-% based on the starting material of NaBH₄.

XRD patterns were obtained on a Rigaku Dmax-rc diffractometer with Ni-filtered Cu-K_α radiation (*V* = 50 kV, *I* = 80 mA) at a scanning rate of 4 °C/min. The morphology of the products was examined by using a Hitachi H-800 transmission electron microscope at an accelerating voltage of 150 kV and a Tecnai 20U-Twin high-resolution transmission electron microscope with a point-to-point resolution of 0.19 nm operating at 200 kV. Combined DTA–TGA analysis was conducted in a SDT Q600 (TA Instruments Ltd., New Castle, Delaware) thermal-microbalance apparatus at a heating rate of 10 °C/min in an air atmosphere by using Al₂O₃ sample pans. A CL spectrophotometer attached to a SU-70-type thermal field emission scanning electron microscope (FESEM) was used to investigate the optical properties of the meshy BN.

Nitrogen adsorption–desorption isotherms were carried out at 77.3 K on a Quadrasorb SI sorption analyzer. The samples were outgassed for 8 h at 250 °C under a vacuum in the degas port of the analyzer. The specific surface area was calculated with the Brunauer–Emmett–Teller (BET) model. Pore-size distribution was calculated from the adsorption–desorption data by using the DFT method.

Supporting Information (see also the footnote on the first page of this article): FTIR spectra of the resulting product and XRD pattern of the as-prepared product without any washing treatments.

Acknowledgments

This work was supported by the National Natural Science Foundation of China (no. 50972076, 50872072, and 50772061), the Shandong Provincial Natural Science Foundation, China (Y2008F26 and Y2008F40), the Science and Technology Development Project of Shandong Province (2009GG10003001, 2009GG10003003), and Special Fund for Postdoctoral Innovative Project of Shandong Province (200702024).

- [1] S. Rudolph, *Am. Ceram. Soc. Bull.* **1994**, 73, 89–90.
- [2] R. T. Paine, C. K. Narula, *Chem. Rev.* **1990**, 90, 73–91.
- [3] W. Mickelson, S. Aloni, W. Q. Han, J. Cumings, A. Zettl, *Science* **2003**, 300, 467–470.
- [4] F. L. Deepak, C. P. Vinod, K. Mukhopadhyay, A. Govindaraj, C. N. R. Rao, *Chem. Phys. Lett.* **2002**, 353, 345–352.
- [5] P. Dibandjo, F. Chassagneux, L. Bois, C. Sigala, P. Miele, *Micropor. Mesopor. Mater.* **2006**, 92, 286–291.
- [6] L. Y. Chen, Y. L. Gu, L. Shi, Z. H. Yang, J. H. Ma, Y. T. Qian, *Solid State Commun.* **2004**, 130, 537–540.
- [7] T. Oku, M. Kuno, H. Kitahara, I. Narita, *Int. J. Inorg. Mater.* **2001**, 3, 597–612.
- [8] Y. Pan, K. F. Huo, Y. M. Hu, J. J. Fu, Y. N. Lu, Z. D. Dai, Z. Hu, Y. Chen, *Small* **2005**, 1, 1199–1203.
- [9] A. Vinu, M. Terrones, D. Golberg, S. Hishita, K. Ariga, T. Mori, *Chem. Mater.* **2005**, 17, 5887–5890.
- [10] L. C. Wang, L. Q. Xu, C. H. Sun, Y. T. Qian, *J. Mater. Chem.* **2009**, 19, 1989–1994.
- [11] M. Corso, W. Auwarter, M. Muntwiler, A. Tamai, T. Greber, J. Osterwalder, *Science* **2004**, 303, 217–220.
- [12] A. Goriachko, Y. He, M. Knapp, H. Over, *Langmuir* **2007**, 23, 2928–2931.
- [13] G. Postole, A. Gervasini, M. Caldararu, B. Bonnetot, A. Auroux, *Appl. Catal. A* **2007**, 325, 227–236.
- [14] S. Berner, M. Corso, R. Widmer, O. Groening, R. Laskowski, P. Blaha, K. Schwarz, A. Goriachko, H. Over, S. Gsell, M.

- Schreck, H. Sachdev, T. Greber, J. Osterwalder, *Angew. Chem. Int. Ed.* **2007**, *46*, 5115–5119.
- [15] O. Bunk, M. Corso, D. Martoccia, R. Herger, P. R. Willmott, B. D. Patterson, J. Osterwalder, J. F. van der Veen, T. Greber, *Surf. Sci.* **2007**, *601*, L7–L10.
- [16] A. Goriachko, A. A. Zakharov, H. Over, *J. Phys. Chem. C* **2008**, *112*, 10423–10427.
- [17] M. L. Ng, A. B. Preobrajenski, A. S. Vinogradov, N. Martensson, *Surf. Sci.* **2008**, *602*, 1250–1255.
- [18] A. Goriachko, Y. B. He, H. Over, *J. Phys. Chem. C* **2008**, *112*, 8147–8152.
- [19] I. Brihuega, C. H. Michaelis, J. Zhang, S. Bose, V. Sessi, J. Honolka, M. A. Schneider, A. Enders, K. Kern, *Surf. Sci.* **2008**, *602*, L95–L99.
- [20] J. Zhang, V. Sessi, C. H. Michaelis, I. Brihuega, J. Honolka, K. Kern, *Phys. Rev. B* **2008**, *78*, 165430-1–165430-5.
- [21] K. Watanabe, T. Taniguchi, H. Kanda, *Nat. Mater.* **2004**, *3*, 404.
- [22] Z. G. Chen, J. Zou, G. Liu, F. Li, Y. Wang, L. Z. Wang, X. L. Yuan, T. Sekiguchi, H. M. Cheng, G. Q. Lu, *ACS Nano* **2008**, *2*, 2183–2191.
- [23] R. Gao, L. W. Yin, C. X. Wang, Y. X. Qi, N. Lun, L. Y. Zhang, Y. X. Liu, L. Kang, X. F. Wang, *J. Phys. Chem. C* **2009**, *113*, 15160–15165.
- [24] H. Chen, Y. Chen, Y. Liu, C. N. Xu, J. S. Williams, *Optical Materials* **2007**, *29*, 1295–1298.
- [25] K. S. W. Singh, D. H. Everett, R. A. W. Haul, W. Haul, L. Moscou, R. A. Pierotti, J. Rouquerol, T. Siemieniowska, *Pure Appl. Chem.* **1985**, *57*, 603–619.
- [26] J. H. Ma, J. Li, G. X. Li, Y. G. Tian, J. Zhang, J. F. Wu, J. Y. Zheng, H. M. Zhuang, T. H. Pan, *Mater. Res. Bull.* **2007**, *42*, 982–988.
- [27] A. Tampieri, A. Bellosi, *J. Mater. Sci.* **1993**, *28*, 649–653.
- [28] A. P. Susamma, T. Varghese, M. Elizabeth, A. P. Kuriakose, *J. Appl. Polym. Sci.* **2001**, *79*, 1–8.
- [29] C. V. Marykutty, G. Mathew, E. J. Mathew, S. Thomas, *J. Appl. Polym. Sci.* **2003**, *90*, 173–3182.

Received: March 7, 2010

Published Online: May 19, 2010

A New Cobalt(II)-Layered Network Based on Phenyl(carboxymethyl) Phosphinate

Ferdinando Costantino,^[a,b] Andrea Ienco,^{*,[b]} Stefano Midollini,^[b] Annabella Orlandini,^[b] Andrea Rossin,^[b] and Lorenzo Sorace^[c,d]

Dedicated to the memory of Professor Mario Ciampolini

Keywords: Metal–organic frameworks / Layered compounds / Magnetic properties

In the presence of 4,4'-bipyridine (4,4'-bipy) and Co^{II} metal ions, a bifunctional phosphinate-carboxylate ligand, phenyl-(carboxymethyl) phosphinate (pcc), forms a new polymeric metal-organic framework (MOF), $[[\text{Co}(\text{pcc})(4,4'\text{-bipy})(\text{H}_2\text{O})](\text{H}_2\text{O})_{1.5}]_n$ (**1**). The structure consists of 2D slabs connected by solvent water molecules with cobalt metal atoms in two different coordination environments. The temperature-de-

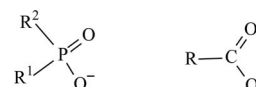
pendent X-ray powder diffraction analysis of **1** shows the formation of dehydrated phases in the range 120–180 °C. The dehydration–rehydration process is reversible. The overall magnetic behaviour of complex **1** is dominated by single ion effects with only weak exchange coupling interactions, due to the *syn/anti* conformation of the Co–O–C–O–Co path.

Introduction

The chemistry of MOFs is developing at an extraordinary rate.^[1] These unique materials show a vast range of structure types and have potential applications in areas such as gas storage, catalysis, separation and exchange reactions and magnetic materials.^[2]

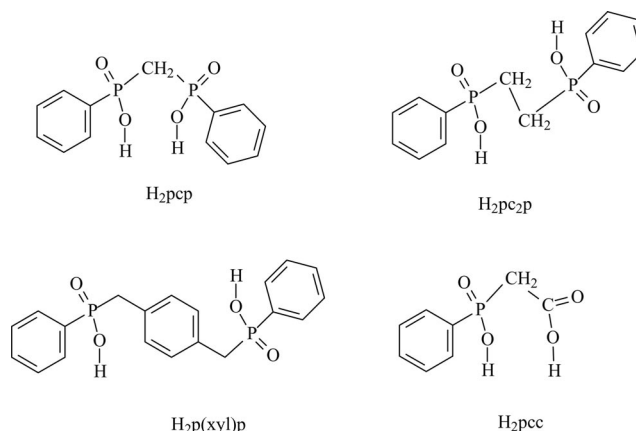
In the broad family of MOFs, networks based on phosphinate ligands have been scarcely studied,^[3] despite the fact that the possible coordination modes of phosphinate ($\text{R}^1\text{R}^2\text{PO}_2$), unlike those of phosphonate (R-PO_3), are formally analogous to those of carboxylate as shown in Scheme 1. The electronic and steric properties of the phosphinate ligand can be easily tuned by changing the two organic groups R^1 and R^2 attached to phosphorus.

In the last decade our group has reported the synthesis and characterization of a series of metal(II) coordination polymers based on the anions *P,P'*-diphenylmethylenediphosphinate (pcp), *P,P'*-diphenylethylenediphosphinate (pc₂p) and *P,P'*-diphenyl-*p*-xylenediphosphinate [p(xyl)p]



Scheme 1.

(Scheme 2). These networks, whose dimensionality ranges from 1D to 3D, present a variety of structural architectures, where the basic building unit is constituted of a robust chain of metal ions alternating with bridging diphosphinates.^[4–13]



Scheme 2.

Now we are extending our investigations to the anion phenyl(carboxymethyl) phosphinate (pcc, Scheme 2). From a structural point of view, there is a general interest in

[a] Dipartimento di Chimica e CEMIN, Università di Perugia, Via Elce di Sotto 8, 06123 Perugia, Italy

[b] Istituto di Chimica dei Composti Organometallici, Consiglio Nazionale delle Ricerche, Via Madonna del Piano 10, 50019 Sesto Fiorentino, Firenze, Italy

E-mail: andrea.ienco@iccom.cnr.it

[c] UdR INSTM, Università di Firenze, Via della Lastruccia 3, 50019 Sesto Fiorentino, Firenze, Italy

[d] Dipartimento di Chimica, Università di Firenze, Via della Lastruccia 3, 50019 Sesto Fiorentino, Firenze, Italy

Supporting information for this article is available on the WWW under <http://dx.doi.org/10.1002/ejic.201000276>.

multifunctional ligands because of their ability to bind either to chemically different metals or to the same metal with different coordination geometries; pcc contains both carboxylate and phosphinate coordinating groups. To date, $[[\text{Co}_2(\text{pcc})_2(\text{H}_2\text{O})_2]\cdot\text{H}_2\text{O}]_n$ is the only complex of this type reported.^[14]

Herein we present our results on a new derivative of the formula $[[\text{Co}(\text{pcc})(4,4'\text{-bipy})(\text{H}_2\text{O})](\text{H}_2\text{O})_{1.5}]_n$ (**1**). **1** was prepared by the reaction of $\text{CoCl}_2\cdot 4\text{H}_2\text{O}$ with K_2pcc in the presence of the 4,4'-bipy auxiliary ligand. The polymer has been characterized through single-crystal X-ray diffraction, DG-TD thermal analysis and temperature-dependent X-ray powder diffraction analysis. Its magnetic behaviour has also been examined for completeness.

Results and Discussion

Synthesis and Structure

Complex **1** was precipitated by mixing a water solution of K_2pcc salt with a solution of cobalt(II) chloride and 4,4'-bipy at approximately 90 °C. The bronze crystals obtained were characterized by X-ray single crystal analysis at −100 °C. The structure of $[[\text{Co}(\text{pcc})(4,4'\text{-bipy})(\text{H}_2\text{O})](\text{H}_2\text{O})_{1.5}]_n$ (**1**) consists of two rectangular 2D slabs connected by solvent water molecules as shown in Figure 1. Selected bond lengths and distances are reported in Table 1.

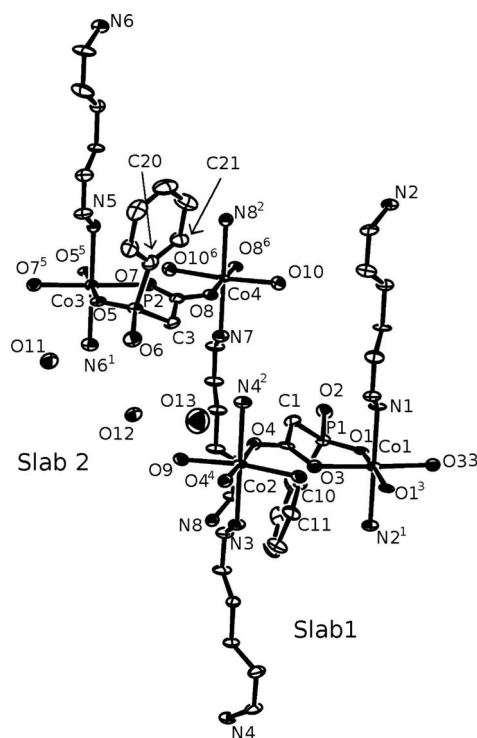


Figure 1. Portion of the structure of **1** showing the coordination environment of the cobalt atoms and the coordination of the pcc ligand. All hydrogen atoms are omitted for clarity. Symmetry transformations used to generate equivalent atoms: #1: $x, y + 1, z$; #2: $x, y - 1, z$; #3: $-x, y, -z - 1$; #4: $-x - 1, y, -z - 1$; #5: $-x - 1, y, -z$; #6: $-x, y, -z$.

Table 1. Selected bond lengths and O–O distances [Å] for **1**^[a].

Slab 1	Bond length (Å)	Slab 2	Bond length (Å)
Co(1)–O(1)	2.049(4)	Co(3)–O(5)	2.057(4)
Co(1)–O(3)	2.086(4)	Co(3)–O(7)	2.045(4)
Co(1)–N(1)	2.176(8)	Co(3)–N(5)	2.157(9)
Co(1)–N(2)#1	2.154(9)	Co(3)–N(6)#1	2.178(9)
Co(2)–O(4)	2.111(4)	Co(4)–O(10)	2.080(4)
Co(2)–O(9)	2.097(5)	Co(4)–O(8)	2.133(4)
Co(2)–N(3)	2.162(9)	Co(4)–N(7)	2.171(9)
Co(2)–N(4)#2	2.176(8)	Co(4)–N(8)#2	2.175(9)
O–O distances	Distance (Å)	Distance (Å)	Distance (Å)
O(2)#3...O(11)	2.779(8)	O(6)...O(12)	2.720(7)
O(2)#3...O(12)	2.788(7)	O(9)...O(12)	2.704(6)
O(4)...O(13)	2.923(7)	O(10)#4...O(11)	2.720(6)
O(6)...O(11)	2.937(7)	O(12)...O(13)	2.923(8)

[a] Symmetry transformations used to generate equivalent atoms: #1: $x, y + 1, z$; #2: $x, y - 1, z$; #3: $-x - 1, y, z$; #4: $-x - 1, y, -z$.

The cobalt atoms form the corners of a rectangle and are linked by 4,4'-bipy along the b axis and pcc along the a axis (Figure 2, top). The two slabs have the same chemical composition but they differ in the orientation of the pyridine rings of the 4,4'-bipy and the phenyl rings of the pcc as seen in Figure 2. The relative orientations of the pyridine rings (the calculated torsion angles between the pyridine rings) are 23.2(5), 28.8(4), 7.9(6) and 46.2(5)° for 4,4'-bipy with N1–N2 and N3–N4 nitrogen atoms in slab 1 and N5–N6 and N7–N8 nitrogen atoms in slab 2, respectively. The torsion angles C1–P1–C10–C11 and C3–P2–C20–C21 are 126.4(6) and 165.2(7)° for slabs 1 and 2, respectively. In each slab, two nonequivalent cobalt atoms present octahedral geometries with different coordination environments as shown in Figure 1.

Both the metal atoms and the 4,4'-bipy sit on a two-fold axis. Co1 (in slab 1) and Co3 (in slab 2) are surrounded by four oxygen atoms from two pcc ligands and two nitrogen atoms from two 4,4'-bipy ligands, whereas Co2 (in slab 1) and Co4 (in slab 2) are bound by two carboxyl oxygen atoms from two pcc ligands, two nitrogen donors from two 4,4'-bipy ligands and two water molecules. Each pcc ligand utilizes one phosphinate oxygen and one carboxylate oxygen atom to embrace the first metal centre, and the second carboxylate oxygen links to the other metal centre. The second phosphinate oxygen, that is not metal bonded, engages in hydrogen bonding interactions with the solvent water molecules.

In Figure 3 the complete packing diagrams are shown, and the hydrogen bonding interactions are highlighted. The O–O distances involved in hydrogen bonding are reported in Table 1. The solvent water molecules do not form chains and are found in cavities between the slabs. The pillaring of the pcc phenyl rings in different layers is evident in Figure 3. Such phenyl stacking strengthens the connection between the sheets and, together with the hydrogen bonding interactions, contributes to the increased dimensionality of **1**.

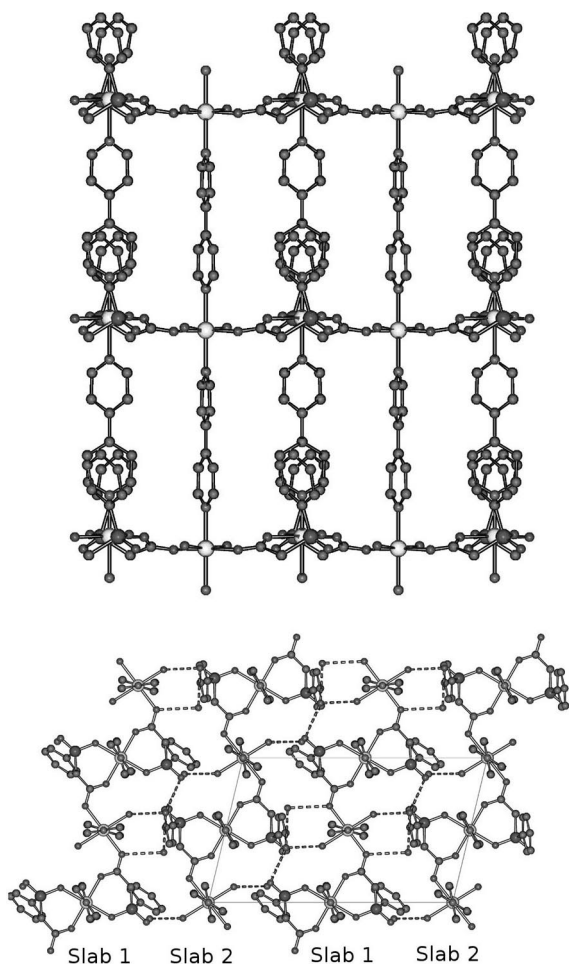


Figure 2. View of a portion of slab 1 normal to [001] (top) and of the slab 1/slab 2 sequence normal to [010] (bottom).

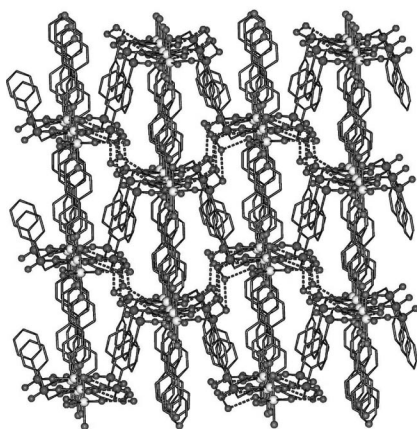


Figure 3. Packing diagram of **1** with the view almost normal to [100]. The interaction between two adjacent layers through some important hydrogen bonds (dashed bonds) and the π - π interactions of the phenyl groups (superimposed head to tail with distance of approximately 5.0 Å) are highlighted.

The same structural motif and ligand coordination was found for a nickel(II) phosphonopropionate and 4,4'-bipy network.^[15] In this complex, one of the oxygen atoms is

protonated and forms strong hydrogen bonds. To the best of our knowledge this is the first evidence of the formation of comparable architectures for structurally analogous phosphinate and phosphonate ligands.

The reaction of the related diphosphinate ligand system, pcp, with 4,4'-bipy and cobalt(II) ions led to the isolation of two structural isomers of formula $[\text{Co}(\text{pcp})(4,4'\text{-bipy})_{0.5}(\text{H}_2\text{O})_2]_n$ ^[11] with different structural features (an undulating 2D layer and a monodimensional strand). These compounds do not contain Co-bipy infinite lines as only one nitrogen atom is coordinated to the metal. On the other hand, 2D structural arrangements similar to that of **1** were found in $[[\text{Cu}(\text{pc}_2\text{p})4,4'\text{-bipy}(\text{H}_2\text{O})]\cdot 3(\text{H}_2\text{O})]_n$ ^[12] and $[[\text{Cu}(\text{p}(\text{xy})\text{p})4,4'\text{-bipy}(\text{H}_2\text{O})_2]\cdot 2(\text{H}_2\text{O})]_n$ ^[13] polymers.

Thermal Analysis and Phase Transitions

The thermal behaviour of **1** was studied by coupling thermogravimetric (Figure 4) and temperature-dependent X-ray powder diffraction analyses (Figure 5). At the beginning of the analysis the weight remained stable until 110 °C, corresponding to the phase stability evidenced from the first three thermal diffraction patterns of Figure 5.

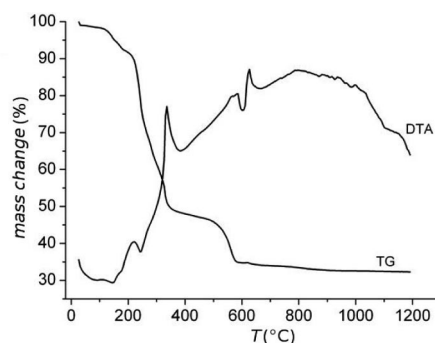


Figure 4. Coupled TG-TDA curve for complex **1**.

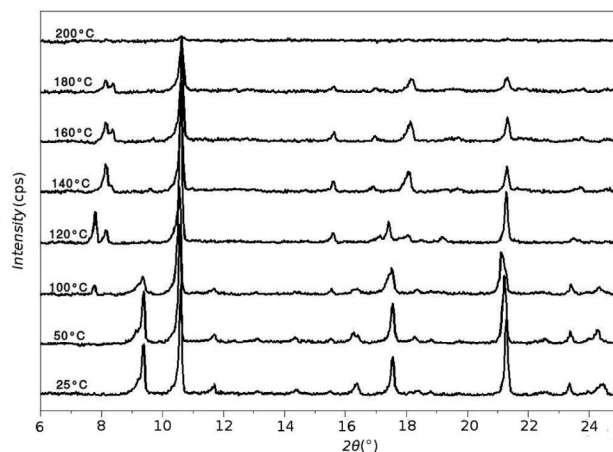


Figure 5. Temperature-dependent X-ray powder diffraction pattern recorded up to 200 °C.

Between 120 and 200 °C a weight loss of about 6.4% was measured which corresponds to the loss of the noncoordinated water molecules (5.9% calcd.). The corresponding thermal diffraction patterns show the disappearance of the original phase and the formation of two different dehydrated phases. We have observed that when compound **1** is heated at 150 °C for two hours and then cooled to room temperature the original hydrated phase is partially recovered in minutes. The process can be accelerated by introducing water to the powder. Between 200 °C and 300 °C the compound appears to be amorphous whereas the TG curve shows a second weight loss of about 46.5%.

The thermal diffraction patterns at 300, 400 and 450 °C (see Supporting Information) show the presence of three peaks at 5.9, 11.8 and 17.8° which can be attributed to the anhydrous cobalt(II) phenylphosphonate phase.^[16] Then the second loss of material is most likely due to the elimination of the coordinated water, 4,4'-bipy and a CH₂CO fragment (calcd. 46.9%). The last weight loss of about 15.0% (calcd. 16.8%), in the 520–600 °C temperature range, may be ascribed to the combustion of the phenyl ring which is suggested by the presence of an exothermal peak in the DTA curve. The pcc moiety appears to be less stable in comparison with the related diphosphinate ligand. The pcc decomposition starts at 200 °C, whereas the Cu and Co pcp anhydrous networks are stable up to 340 °C.^[12–14]

Magnetic Proprieties of **1**

The temperature dependence of the magnetic susceptibility (Figure 6) of complex **1** follows the Curie–Weiss law down to 100 K, with a Curie constant of $C = 3.4 \text{ cm}^3 \text{ K mol}^{-1}$ and an antiferromagnetic correction term, $\theta = 77 \text{ K}$. A clear deviation from the linear behaviour is evident below 50 K, and the value obtained for C falls within the range reported for similar polymeric carboxylate and phosphinate complexes. At the same time, the high value of the Weiss temperature should not be considered as a signature of strong antiferromagnetic interaction as it is well known that the same effect usually occurs in mononuclear Co^{II} complexes due to local magnetic anisotropies.^[17] The corresponding χT vs. T plot (Figure 6) evidences a marked and continuous decrease of the χT value with decreasing temperature to reach $1.25 \text{ cm}^3 \text{ K mol}^{-1}$ at 5 K, below which the value weakly increases again to reach $1.33 \text{ cm}^3 \text{ K mol}^{-1}$ at 1.9 K (Figure 6 inset). This behaviour can be qualitatively explained by attributing the decrease observed in the 300–5 K range to the depopulation of the excited levels arising from the splitting of the $^4\text{T}_{1g}$ ground state of the Co^{II} ions due to the combined effect of low symmetry distortions and spin-orbit coupling.^[18]

In this framework the low temperature increase is attributed to weak intrachain ferromagnetic exchange-coupling interactions. This is most likely transmitted by the carboxylate ligand, since the Co ions bridged by the 4,4'-bipy ligands are far apart from each other ($\text{Co}\cdots\text{Co} \approx 11.43 \text{ \AA}$) and such ligands are unable to transmit any significant cou-

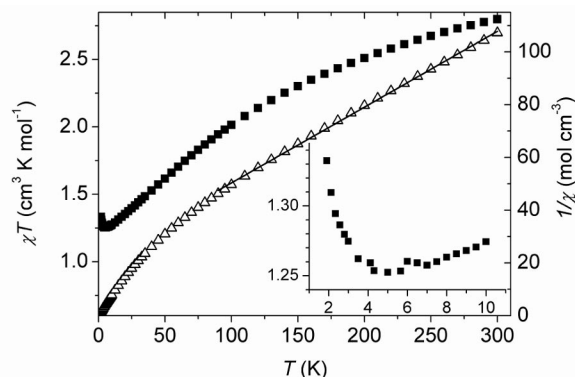


Figure 6. Plot of χT vs. T and $1/\chi$ vs. T for compound **1**. In the inset a detailed view of the low temperature region of χT vs. T plot is shown.

pling.^[19] In agreement with the weak ferromagnetic coupling, the isothermal magnetization curve at different temperatures, when plotted vs. H/T , rescale on a single curve (Figure 7 inset). Accordingly, the M vs. H plots could be easily fitted by assuming a Brillouin law for an $S_{\text{eff}} = 1/2$ with $g = 4.18 \pm 0.02$ and taking into account a Van Vleck paramagnetic contribution of $\chi_{\text{VV}} = (2 \pm 0.5) \times 10^{-3} \text{ cm}^{-1}$.

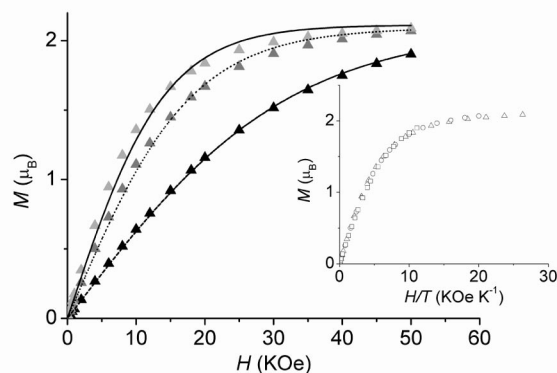


Figure 7. Isothermal magnetization curves at 1.9 K (light grey triangles), 2.5 K (dark grey triangles), 4.5 K (black triangles) and best fit curves obtained by the model described in the text. In the inset the same curves reported vs. H/T are reported, showing an almost perfect superposition.

A model of the system which takes into account both single ion effects (strength of the ligand field, reduction of the orbital contribution due to covalency and spin-orbit coupling) and the exchange coupling between cobalt(II) centres would have to be considered to go beyond this simple qualitative analysis. However, such a detailed approach, which has been recently implemented by Lloret and co-workers,^[20] is outside the scope of this manuscript. We note that the overall magnetic behaviour of complex **1**, dominated by single ion effects, is substantially different to that reported for the parent pcc derivative.^[14] The magnetic behaviour of the latter is due to moderate intrachain ferromagnetic coupling and correspondingly increased dipolar interactions, that result in the complex undergoing a long-

range magnetic (antiferromagnetic) transition around 2 K. On the contrary both zero field cooling/field cooling measurements and AC measurements excluded the existence of long-range magnetic order in **1**. The difference in the magnetic behaviour between the two compounds is not surprising however, as, in the case of the pcc derivative, the coupling was transmitted by a Co–O–Co bridge, whereas in complex **1** the exchange involves a Co–O–C–O–Co path in *syn/anti* conformation. On the basis of literature data the latter is expected to give rise to much weaker exchange coupling interactions, of the order of 1 cm^{−1} or less,^[21] which can be ferro- or antiferromagnetic.

Conclusions

We obtained a 2D polymer with cobalt metal atoms with two different coordination environments using 4,4'-bipy and a bifunctional carboxylate-phosphinate ligand. The replacement of a phosphinate with a carboxylate group in pcp affects the metal–ligand coordination modes and the network topologies. In this respect, the behaviour of pcc is between diphosphinates with longer carbon chains as pc₂p and p(xyl)p and the related pcp. While pcc is able to chelate a metal in the same way as pcp, the 2D slabs formed connecting metal-4,4'-bipy pillars with a secondary ligand is a characteristic of pc₂p and p(xyl)p ligands. In comparison with other diphosphinate ligands, the pcc ligand is itself less stable during the thermal treatment as it decomposes at around 200 °C. Finally, the possibility of having different coordination sites in the same ligand is an intriguing feature of the carboxylate-phosphinate ligand and gives the possibility of building ordered materials with potentially interesting physical properties and functionalities.

Experimental Section

Materials and Methods: All reagents were analytical-grade commercial products and were used without further purification. K₂pcc was prepared as described previously.^[14] Elemental analyses (C, H, N) were performed with an EA 1108 CHNS-O automatic analyzer. XRD data of complex **1** was collected with an X'Pert PRO diffractometer with Cu–K_α radiation ($\lambda = 1.5418$). Thermogravimetric analysis were performed under air with an Anton Paar HTK 1200N hot chamber. Coupled thermogravimetric and differential thermal analysis measurements were performed using a Netzsch STA490C thermoanalyser under a 20 mL min^{−1} air flux with a heating rate of 10 °C min^{−1}.

Magnetic Measurements: Temperature (2–300 K) and field dependent (0–5 T) magnetization of a microcrystalline powder sample of **1** were investigated with a Quantum design MPMS SQUID magnetometer. At low temperature (2–20 K), measurements were performed with applied fields of 50 Oe and 1 kOe to check for possible effects of the magnetic field on the susceptibility, obtained as the ratio between the magnetization and the applied field. AC measurements were performed in the range 2–10 K with an oscillating field of 3 Oe and zero DC field using the same instrument. The powder was pressed into a pellet to avoid preferential orientation of the microcrystallites. Data were corrected for the diamagnetism of the sample holder, measured in the same range of field and temperature

and for the intrinsic diamagnetic contribution for the sample estimated through Pascal's constants.

Synthesis of {[Co(pcc)(4,4'-bipy)(H₂O)](H₂O)_{1.5}}_n: To a solution of K₂pcc (60 mg, 0.21 mmol) and 4,4'-bipy (33 mg, 0.21 mmol) in 60 mL of H₂O was added a solution of CoCl₂·6H₂O (51 mg, 0.21 mmol) in 15 mL of H₂O. The resulting solution was evaporated in air at ca. 80–90 °C until thin bronze-coloured crystals precipitated. The compound was filtered, washed with water and dried in air at room temperature; yield 71 mg, 73%. C₁₈H₂₂CoN₂O_{6.5}P (455.24): calcd. C 46.97, H 4.82, N 6.09; found C 47.10, H 4.95, N 6.04.

X-ray Structure Determination: A summary of the crystal data are given in Table 2. The data collection was performed at 173 K with an Oxford Diffraction Excibur 3 diffractometer equipped with Cu–K_α radiation and CCD area detector. Data collection was performed with the program CrysAlis CCD^[22] and data reductions were carried out with the program CrysAlis RED.^[23] Absorption correction was applied through the program ABSPACK.^[23] The structure was solved by direct methods using Sir97^[24] and refined on *F*² by full-matrix least-squares techniques with the SHELXL program.^[25] The crystal used for the data collection was selected after a long screening process. A merohedral twinning was present and the twin component was found to be 0.591(5). It was not possible to locate the hydrogen atoms of the noncoordinated water molecules from the Fourier map. All nonhydrogen atoms were refined anisotropically. The hydrogen atoms of the coordinated water were found in the Fourier map and refined with distance restraints. The hydrogen atoms bonded to carbon atoms were introduced in calculated positions.

Table 2. Crystal data and structure refinement details for **1**.

Empirical formula	C ₃₆ H ₃₄ Co ₂ N ₄ O ₁₃ P ₂
Formula weight	910.47
Temperature [K]	173(2)
Wavelength [Å]	1.54184
Crystal system	monoclinic
Space group	<i>P</i> 2
Unit cell dimensions	
<i>a</i> [Å]	10.36280(10)
<i>b</i> [Å]	11.43110(10)
<i>c</i> [Å]	16.9994(2)
β [°]	103.4460(10)°
<i>V</i> [Å ³]	1958.52(3)
<i>Z</i> ; calculated density [Mg/m ³]	2; 1.544
Absorption coefficient [mm ^{−1}]	8.012
<i>F</i> (000)	932
Crystal size [mm]	0.2 × 0.1 × 0.05
θ range for data collection	4.39 to 62.07°
Index ranges	−11 ≤ <i>h</i> ≤ 11, −13 ≤ <i>k</i> ≤ 13, −19 ≤ <i>l</i> ≤ 19
Reflections collected	27933
Data/restraints/parameters	6062/5/511
Goodness-of-fit on <i>F</i> ²	1.09
Final <i>R</i> indices [<i>I</i> > 2σ(<i>I</i>)]	<i>R</i> ₁ = 0.0568, <i>wR</i> ₂ = 0.1428
<i>R</i> indices (all data)	<i>R</i> ₁ = 0.0718, <i>wR</i> ₂ = 0.1571
Absolute structure parameter	0.591(5)

CCDC-768237 contains the supplementary crystallographic data for compound **1**. These data can be obtained free of charge from the Cambridge Crystallographic Data Centre via www.ccdc.cam.ac.uk/data_request/cif.

Supporting Information (see also the footnote on the first page of this article): Additional XRD patterns are given in Figures S1 and S2.

Acknowledgments

We thank the FIRENZE HYDROLAB project sponsored by Ente Cassa di Risparmio di Firenze for funding. This work was supported by Ministero dell'Istruzione, dell'Università e della Ricerca (MIUR) through the "Progetti di Rilevante Interesse Nazionale" (PRIN) project 2007X2RLL2: "Nuove strategie per il controllo delle reazioni metallo assistite: interazioni non convenzionali di frammenti molecolari".

- [1] J. R. Long, O. M. Yaghi, *Chem. Soc. Rev.* **2009**, *38*, 1213–1214; S. Horike, S. Shimomura, S. Kitagawa, *Nature Chem.* **2009**, *1*, 695–704.
- [2] O. M. Yaghi, M. O'Keeffe, N. W. Ockwig, H. Chae, M. Edaudi, J. Kim, *Nature* **2003**, *423*, 705–714; S. Kitagawa, R. Kitaura, I. S. Noro, *Angew. Chem. Int. Ed.* **2004**, *43*, 2334; G. Ferey, *Chem. Soc. Rev.* **2008**, *37*, 191–214.
- [3] A. Vioux, J. Le Bideau, P.-H. Mutin, D. Leclercq, in: *Topics in Current Chemistry*, Springer, Heidelberg, **2004**, p. 145.
- [4] E. Berti, F. Cecconi, C. A. Ghilardi, S. Midollini, A. Orlandini, E. Pitzalis, *Inorg. Chem. Commun.* **2002**, *5*, 1041–1043.
- [5] F. Cecconi, D. Dakternieks, A. Duthie, C. A. Ghilardi, P. Gili, P. Lorenzo-Luis, S. Midollini, A. Orlandini, *J. Solid State Chem.* **2004**, *177*, 786–792.
- [6] S. Ciattini, F. Costantino, P. Lorenzo-Luis, S. Midollini, A. Orlandini, A. Vacca, *Inorg. Chem.* **2005**, *44*, 4008–4016.
- [7] J. Beckmann, F. Costantino, D. Dakternieks, A. Duthie, A. Ienco, S. Midollini, C. Mitchell, A. Orlandini, L. Sorace, *Inorg. Chem.* **2005**, *44*, 9416–9423.
- [8] S. Midollini, P. Lorenzo-Luis, A. Orlandini, *Inorg. Chim. Acta* **2006**, *359*, 3275–3282.
- [9] F. Costantino, S. Midollini, A. Orlandini, L. Sorace, *Inorg. Chem. Commun.* **2006**, *9*, 591–594.
- [10] T. Bataille, F. Costantino, P. Lorenzo-Luis, S. Midollini, A. Orlandini, *Inorg. Chim. Acta* **2008**, *361*, 327–334.
- [11] F. Costantino, S. Midollini, A. Orlandini, *Inorg. Chim. Acta* **2008**, *361*, 327–334.
- [12] T. Bataille, F. Costantino, A. Ienco, A. Guerri, F. Marmottini, S. Midollini, *Chem. Commun.* **2008**, 6381–6383.
- [13] F. Costantino, A. Ienco, S. Midollini, *Cryst. Growth Des.* **2010**, *10*, 7–10.
- [14] S. Midollini, A. Orlandini, P. Rosa, L. Sorace, *Inorg. Chem.* **2005**, *44*, 2060–2066.
- [15] Z. Chen, L. Weng, D. Zhao, *Inorg. Chem. Commun.* **2007**, *10*, 447–450.
- [16] T. O. Salami, X. Fan, P. Y. Zavalij, S. R. J. Oliver, *Dalton Trans.* **2006**, 1574–1578.
- [17] K. S. Gavrilenko, O. Cadot, K. Bernot, P. Rosa, R. Sessoli, S. Golhen, V. V. Pavlishchuk, L. Ouahab, *Chem. Eur. J.* **2008**, *14*, 2034–2043.
- [18] A. Bencini, A. Beni, F. Costantino, A. Dei, D. Gatteschi, L. Sorace, *Dalton Trans.* **2006**, 722–729.
- [19] S. Chandra Manna, S. Konar, E. Zangrando, K. Okamoto, J. Ribas, N. Ray Chaudhuri, *Eur. J. Inorg. Chem.* **2005**, 4646–4654.
- [20] F. Lloret, M. Julve, J. Cano, R. Ruiz-García, E. Pardo, *Inorg. Chim. Acta* **2008**, *361*, 3432–3445.
- [21] a) J.-M. Rueff, N. Masciocchi, P. Rabu, A. Sironi, A. Skoulios, *Eur. J. Inorg. Chem.* **2001**, 2843–2848; b) J.-M. Rueff, N. Masciocchi, P. Rabu, A. Sironi, A. Skoulios, *Chem. Eur. J.* **2002**, *8*, 1813–1820; c) F. S. Delgado, J. Sanchiz, C. Ruiz-Perez, F. Lloret, M. Julve, *CrystEngComm* **2003**, *5*, 280–284; d) A. Beghidja, P. Rabu, G. Rogez, R. Welter, *Chem. Eur. J.* **2006**, *12*, 7627–7638; e) O. Fabelo, J. Pasan, L. Canadillas-Delgado, F. S. Delgado, F. Lloret, M. Julve, C. Ruiz-Perez, *Inorg. Chem.* **2009**, *48*, 6086–6095.
- [22] *CrysAlisCCD*, Oxford Diffraction Ltd., version 1.171.31.2 (release 07-07-2006 CrysAlis171.NET).
- [23] *CrysAlis RED*, Oxford Diffraction Ltd., version 1.171.31.2 (release 07-07-2006 CrysAlis171.NET).
- [24] A. Altomare, M. C. Burla, M. Cavalli, G. L. Cascarano, C. Giacovazzo, A. Gagliardi, A. G. G. Moliterni, G. Polidori, R. Spagna, *J. Appl. Crystallogr.* **1999**, *32*, 115–119.
- [25] G. M. Sheldrick, *Acta Crystallogr., Sect. A* **2008**, *64*, 112–122.

Received: March 10, 2010
Published Online: May 27, 2010

The Preparation and Structure of $[\text{Pt}(\text{S}_2\text{N}_2)\{\text{P}(\text{OR})_n\text{R}'_{3-n}\}_2]$ and $[\text{Pt}(\text{SeSN}_2)\{\text{P}(\text{OMe})_n\text{Ph}_{3-n}\}_2]$ ($n = 0-3$)

Paul G. Waddell,^[a] Alexandra M. Z. Slawin,^[a] Nicolas Sieffert,^[a] Michael Bühl,^[a] and J. Derek Woollins^{*[a]}

Keywords: Sulfur / Selenium / Platinum / DFT calculations

Dissolution of $[\text{S}_4\text{N}_3]\text{Cl}$ in liquid ammonia produces a reactive solution which on treatment with *cis*- $[\text{PtCl}_2(\text{PR}_3)_2]$ gives $[\text{S}_2\text{N}_2]^{2-}$ complexes in 32–76 % yields. Similarly, SeCl_4 and $[\text{S}_4\text{N}_3]\text{Cl}$ in a ratio of 5:1 react cleanly with *cis*- $[\text{PtCl}_2\{\text{P}(\text{OMe})_n\text{Ph}_{3-n}\}]$ to give the desired selenosulfur dinitrido, $[\text{SeSN}_2]^{2-}$ complexes with no phosphorus containing starting material evident by ^{31}P NMR spectroscopy. The new complexes were characterised by IR, ^{31}P NMR, microanalysis and X-ray crys-

tallography with nine crystal structures being reported. In ^{31}P nmr the 1J PtP coupling constants are influenced by the oxygen content of their phosphorus ligands. In the mixed chalcogen complexes the Pt–N bond lengths appear to follow a simple trend as a consequence of the electronic properties of the phosphorus ligand and these trends can be interpreted empirically by examination of the LUMO but are not well supported by DFT calculations.

Introduction

The discovery of the unusual electrical properties of $(\text{SN})_x$ polymer in 1973 led to sustained interest in this area though M–S–N chemistry has been of interest since the 1950s^[1] and examples are shown in Figure 1. The disulfur dinitride dianion is not known in simple salts but can be isolated in metal complexes and as fragments in heterocycles.^[2–7] These complexes may be protonated at the metal-coordinated nitrogen and we have previously commented on the structural consequences of this protonation.^[8,9] M–S–N complexes may be prepared by a variety of routes, e.g. oxidative addition of S_4N_4 or $\text{S}_4\text{N}_4\text{H}_4$ with $[\text{Pt}(\text{PPh})_4]$, reaction of $\text{Na}[\text{S}_3\text{N}_3]$ with $[\text{PtCl}_2(\text{PR}_3)_2]$ or transmetallation

using $[\text{Me}_2\text{SnS}_2\text{N}_2]_2$ or $[\text{nBu}_2\text{SnS}_2\text{N}_2]_2$. We have also shown the value of the use of $[\text{S}_4\text{N}_3]\text{Cl}$ in liquid ammonia as a solvent in these reaction but have not established it for the synthesis of $\text{M}(\text{S}_2\text{N}_2)$ systems.^[10,11]

Surprisingly there is some ambiguity about the bond length pattern in some $[\text{Pt}(\text{S}_2\text{N}_2)(\text{PR}_3)_2]$ complexes^[14] and there is only one example of a $[\text{Pt}(\text{S}_2\text{N}_2)\{\text{P}(\text{OR})_3\}_2]$ complex whose formulation was proposed using only IR spectroscopy and microanalysis data.^[15] The formulation of this complex remains doubtful.

In addition to $[\text{S}_2\text{N}_2]^{2-}$ complexes, some selenium-substituted analogues have been investigated.^[16–21] As yet only one $[\text{SeSN}_2]^{2-}$ containing complex $[\text{Pt}(\text{SeSN}_2)(\text{PMe}_2\text{Ph})_2]$ has been analysed using X-ray crystallography and this ex-

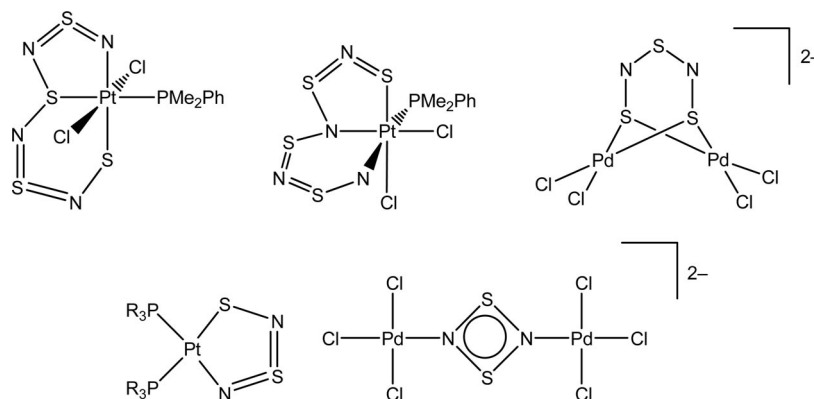


Figure 1. Examples of fully characterised M–S–N species.^[12,13]

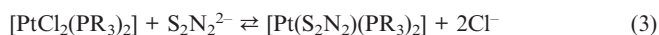
[a] School of Chemistry, University of St Andrews, St Andrews, Scotland, KY16 9ST
E-mail: jdw3@st-and.ac.uk

ample was found to exhibit a twofold disorder about the ring. Given the need to develop routes in liquid ammonia, the lack of crystal data for selenium-substituted analogues

of these complexes, bond length ambiguity mentioned above and the poor understanding of the bonding in these types of molecules we have studied the synthesis, structure and spectroscopic properties of simple $[\text{Pt}(\text{S}_2\text{N}_2)\{\text{P}(\text{OR})_n\text{R}'_{3-n}\}_2]$ and $[\text{Pt}(\text{SeSN}_2)\{\text{P}(\text{OMe})_n\text{Ph}_{3-n}\}_2]$ complexes. Here we report the synthesis of several of these $[\text{Pt}(\text{S}_2\text{N}_2)\{\text{P}(\text{OR})_n\text{R}'_{3-n}\}_2]$ and $[\text{Pt}(\text{SeSN}_2)\{\text{P}(\text{OMe})_n\text{Ph}_{3-n}\}_2]$ complexes which have been characterised by IR spectroscopy, ^{31}P NMR spectroscopy, elemental analysis and X-ray crystallography.

Results and Discussion

There are a number of possible routes to $[\text{Pt}(\text{S}_2\text{N}_2)\{\text{P}(\text{OR})_3\}_2]$ complexes. Use of S_4N_4 or $[\text{S}_3\text{N}_3]^-$ salts are best avoided because of explosion hazard. We chose to generate the appropriate anion in situ using $[\text{S}_4\text{N}_3]\text{Cl}$ in liquid ammonia which reacted cleanly with *cis*- $[\text{PtCl}_2(\text{PR}_3)]$ to give the desired disulfur dinitrido complexes with no phosphorus containing starting material evident by ^{31}P NMR spectroscopy. Though the mechanism and its stoichiometry are complex and are not completely understood to date, the stoichiometry of 14 equiv. of $[\text{S}_4\text{N}_3]\text{Cl}$ to 9 equiv. of *cis*- $[\text{PtCl}_2(\text{PR}_3)]$ is in accord with previously suggested equilibria; see Equations (1)–(3).^[23,24]



The new complexes **1**, $\text{PR}_3 = \text{P}(\text{OEt})_3$; **2**, $\text{PR}_3 = \text{P}(\text{OnBu})_3$; **3**, $\text{PR}_3 = \text{P}(\text{OPh})_3$; **4**, $\text{PR}_3 = \text{P}(\text{OMe})_3$; **5**, $\text{PR}_3 = \text{P}(\text{OMe})_2\text{Ph}$; **6**, $\text{PR}_3 = \text{P}(\text{OMe})_2\text{Ph}$ were characterised by ^{31}P NMR (Table 1), IR, microanalysis (Table 2) and X-ray crystallography. In their IR spectra the important ν_{SN} vibrations were assigned by analogy with previously reported $[\text{Pt}(\text{S}_2\text{N}_2)(\text{PR}_3)_2]$ complexes.^[2] However, the presence of the $\nu_{(\text{P}-\text{O}-\text{alkyl})}$ vibration (1050–1030 cm^{-1}) obscures one of the ν_{SN} vibrations, which is normally observed around 1050 cm^{-1} for **1** and **4** though the band at around 680 cm^{-1} is not obscured. The intensity of the $\nu_{(\text{P}-\text{O}-\text{alkyl})}$ vibration (1050–1030 cm^{-1}) increases with the oxygen content as would be expected. Distinct vibrations due to the P-Ph group (approx. 1440 cm^{-1}) were also observed for **5** and **6**.

Mixed-chalcogen compounds containing the $[\text{SeSN}_2]^{2-}$ fragment have been synthesised using $[\text{Se}_2\text{SN}_2]_2\text{Cl}_2$ or a combination of SeCl_4 and $[\text{S}_4\text{N}_3]\text{Cl}$ in liquid ammonia. The nature of the species in the liquid ammonia solution has not been determined. As dissolution of $[\text{S}_4\text{N}_3]\text{Cl}$ in liquid ammonia results in formation of $[\text{S}_3\text{N}_3]^-$ it is possible that this species is in equilibrium with a range of change SN anions which can undergo chalcogen exchange to give mixed SeSN anions. The formation of the PtSeSN_2 rings with selenium always platinum-bound may suggest that the SeSN anions have terminal selenium atoms. Certainly we would expect that SeNSN would be a more stable isomer than SNSN. Furthermore SeNSN could be readily formed by chain lengthening of the well know $[\text{NSN}]^{2-}$ dianion.^[25] After a number of trials we employed SeCl_4 and $[\text{S}_4\text{N}_3]\text{Cl}$ in a ratio of 5:1 which reacted cleanly with *cis*- $[\text{PtCl}_2(\text{P}(\text{OMe})_n\text{Ph}_{3-n})]$ to give the desired selenosulfur dinitrido complexes with no phosphorus containing starting material evident by ^{31}P NMR spectroscopy however trace amounts of the disulfur analogue were observed.

The new complexes $[\text{Pt}(\text{SeSN}_2)\{\text{P}(\text{OMe})_n\text{Ph}_{3-n}\}_2]$ (**7**, $n = 3$, **8**, $n = 2$, **9**, $n = 1$) were characterised by ^{31}P NMR, IR, microanalysis (Table 1, 2) and X-ray crystallography. The X-ray of the previously reported complex **10** ($n = 0$) was also determined. In their IR spectra the vibrations due characteristic of the $[\text{SeSN}_2]^{2-}$ fragment were assigned by analogy with previously reported $[\text{Pt}(\text{SeSN}_2)(\text{PR}_3)_2]$ complexes.^[21] In the case of **9** the ν_{SN} vibration typically observed at ca. 1070 cm^{-1} was slightly lower than expected (1059 cm^{-1}). The corresponding stretch observed in $[\text{S}_2\text{N}_2]^{2-}$ complexes is observed at ca. 1045 cm^{-1} . Vibrations indicative of ν_{PtSe} were not observed and are likely to be very low in frequency compared to the ν_{PtS} stretch in $[\text{S}_2\text{N}_2]^{2-}$ complexes (ca. 350 cm^{-1}) due to the larger mass of selenium compared to sulfur. The intensity of the $\nu_{(\text{P}-\text{O}-\text{alkyl})}$ vibration (1050–1030 cm^{-1}) increases with the oxygen content as would be expected. Distinct vibrations due to the P-Ph group (approx. 1440 cm^{-1}) were also observed for **8** and **9**.

The ^{31}P NMR of **1**–**10** exhibit AX doublets (Table 1, see Figure 2 for labelling and Figure 3 for a typical spectrum) with $^2J_{\text{P,P}}$ couplings together with satellites due to $^1J_{\text{Pt,P}}$ couplings. **7**–**10** also exhibit $^2J_{\text{P-Se(trans)}}$ couplings^[26] though $^2J_{\text{P-Se(cis)}}$ couplings were not observed. These couplings en-

Table 1. ^{31}P NMR chemical shifts (ppm) and coupling constants (Hz) for **1**–**10** and $[\text{Pt}(\text{S}_2\text{N}_2)(\text{PPh}_3)_2]$.

	δ_{A}	δ_{X}	$^1J_{\text{A}}$	$^1J_{\text{X}}$	$^2J_{\text{P-P}}$	$^2J_{\text{P-Se(trans)}}$
$[\text{Pt}(\text{S}_2\text{N}_2)\{\text{P}(\text{OEt})_3\}_2]$ (1)	98.5	105.5	4498	4415	49.3	
$[\text{Pt}(\text{S}_2\text{N}_2)\{\text{P}(\text{OnBu})_3\}_2]$ (2)	102.8	109.0	4470	4334	49.3	
$[\text{Pt}(\text{S}_2\text{N}_2)\{\text{P}(\text{OPh})_3\}_2]$ (3)	89.6	96.7	4634	4503	54.0	
$[\text{Pt}(\text{S}_2\text{N}_2)\{\text{P}(\text{OMe})_3\}_2]$ (4)	105.3	110.9	4502	4395	51.0	
$[\text{Pt}(\text{S}_2\text{N}_2)\{\text{P}(\text{OMe})_2\text{Ph}\}_2]$ (5)	120.4	126.2	3864	3761	37.6	
$[\text{Pt}(\text{S}_2\text{N}_2)\{\text{P}(\text{OMe})\text{Ph}_2\}_2]$ (6)	91.8	104.1	3287	3249	28.2	
$[\text{Pt}(\text{S}_2\text{N}_2)(\text{PPh}_3)_2]$	11.4	23.6	2994	2827	22	
$[\text{Pt}(\text{SeSN}_2)\{\text{P}(\text{OMe})_3\}_2]$ (7)	106.0	108.1	4530	4571	49	94
$[\text{Pt}(\text{SeSN}_2)\{\text{P}(\text{OMe})_2\text{Ph}\}_2]$ (8)	122.9	124.8	3868	3900	33	75
$[\text{Pt}(\text{SeSN}_2)\{\text{P}(\text{OMe})\text{Ph}_2\}_2]$ (9)	89.3	103.1	3309	3391	26	66
$[\text{Pt}(\text{SeSN}_2)\{\text{P}(\text{Ph})_3\}_2]$ (10)	7.2	22.6	2995	2956	21	54

Table 2. Microanalyses, yields, melting points and selected IR absorptions with tentative assignments [cm⁻¹] for **1** and **3–9**.^[a]

	$\tilde{\nu}_{\text{SN}}$	$\nu_{\text{SN/SeN}}$	ν_{PtN}	δ_{SN}	ν_{PtS}	% C (calcd.)	% H (calcd.)	Yield (%)	M.p. (°C)
[Pt(S ₂ N ₂){P(OEt) ₃ }] ₂ (1)	686 s ^[b]	618 m	469 m	370 m	354 m	23.25 (23.26)	4.78 (4.88)	47	138– 142
[Pt(S ₂ N ₂){P(OPh) ₃ }] ₂ ·0.5CH ₂ Cl ₂ (3)	687 s ^[b]	618 m	491 s	380 w	357 w	45.90 (46.13)	3.12 (3.28)	32	117– 120
[Pt(S ₂ N ₂){P(OMe) ₃ }] ₂ (4)	682 s ^[b]	614 w	467 w	372 m	354 w	13.23 (13.46)	3.08 (3.39)	58	123– 125
	1094(17) 727(10)	648(3) ^[c]	492(2) ^[d]	366(2) ^[e]	362(1)				
[Pt(S ₂ N ₂){P(OMe) ₂ Ph}] ₂ ·0.5CH ₂ Cl ₂ (5)	1047 s 684 m	613 m	467 m	371 m	355 m	29.74 (29.58)	3.38 (3.46)	62	139– 142
[Pt(S ₂ N ₂){P(OMe)Ph ₂ }] ₂ (6)	1042 s 680 m	615 w	462 m	360 w	349 w	43.22 (43.39)	3.79 (3.64)	60	160– 163
[Pt(SeSN ₂){P(OMe) ₃ }] ₂ (7)	1068s 633m	541 m	401 w	357 w		12.76 (12.37)	2.70 (3.12)	76	132– 134
	1110(10) 659(7) ^[f]	580(3) ^[g]	428(1) [d]	360(2) [e]	246(1) ^[g]				
[Pt(SeSN ₂){P(OMe) ₂ Ph}] ₂ ·0.5CH ₂ Cl ₂ (8)	1071 s 634 m	556 s	402 m	357 m		27.38 (27.64)	2.82 (3.23)	51	184– 187
[Pt(SeSN ₂){P(OMe)Ph ₂ }] ₂ ·0.5CH ₂ Cl ₂ (9)	1059 s 634 m	542 s	402 w	355 w		39.42 (39.34)	2.96 (3.36)	63	146– 149

[a] Printed in *italics*: PBE0/ECP1 computed harmonic frequencies (in parentheses: intensities in 104 M/mol; maximum absorption around 60.104 M/mol). [b] Band obscured by P–O–alkyl absorption. [c] Combination with δ_{NSN} and δ_{PtNS} . [d] Combination with δ_{SNS} . [e] SN2 out-of-plane. [f] Combination of ν_{sym} , PtN/SeN and δ_{NSN} . [g] ν_{asym} , PtN/SeN. *h*_v, PtSe.

abled assignment of the individual phosphorus resonances. By analogy with phosphane complexes, the largest $^1J(^{195}\text{Pt}-^{31}\text{P})$ coupling constant in [S₂N₂]²⁻ complexes is assigned to the phosphorus *trans* to the nitrogen (δ_{A}) as this platinum–phosphorus bond is generally the shorter of the two and the shorter distance can be associated with the larger coupling constant. The smaller of the two $^1J_{\text{Pt,P}}$ values is assigned to the phosphorus *trans* to sulfur (δ_{X}). In [SeSN₂]²⁻ complexes similar $^1J_{\text{A}}$ values are observed to those in [S₂N₂]²⁻ complexes however in the case the $^1J_{\text{X}}$ (the phosphorus *trans* to selenium is the larger value).

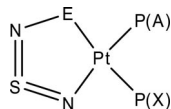


Figure 2. Labelling of the phosphorus atoms (E = S or Se).

As expected the coupling constants for **1** to **10** are influenced by the phosphorus ligands. The effect of replacing phenyl groups of the phosphanes with methyl groups in [S₂N₂]²⁻ complexes has been previously reported,^[2] with $^1J_{\text{Pt-P}}$ being observed to decrease in the order PPh₃ > PMePh₂ > PMe₂Ph > PMe₃. The effect of replacing phenyl groups in the phosphorus ligand with methoxy groups has the opposite effect in both [S₂N₂]²⁻ and [SeSN₂]²⁻ complexes with the coupling constants increasing in the order PPh₃ < P(OMe)Ph₂ < P(OMe)₂Ph < P(OMe)₃ (Table 1, Figures 4 and 5).

Comparing $^1J_{\text{Pt,P}}$ values observed for [S₂N₂]²⁻ and [SeSN₂]²⁻ complexes with the same phosphorus ligand with those of their dichloride starting materials gives some indi-

cation as to the *trans*-influence^[27,28] of the chalcogen–nitrogen fragments. From the coupling constants we can see that the *trans* influence of the [S₂N₂]²⁻ fragment is greater than that of the chlorine atoms as the coupling constants are seen to decrease by over 20% for both P_A and P_X indicating weaker Pt–P bonds in both cases. When compared with [SeSN₂]²⁻ complexes, the $^1J_{\text{A}}$ values are observed to be of a similar magnitude and $^1J_{\text{A}}$ is seen to be ca. 100–200 Hz greater than that observed in [S₂N₂]²⁻ complexes. The *trans* influence of selenium in the [SeSN₂]²⁻ fragment can hence be said to be less than that of the sulfur in the [S₂N₂]²⁻ fragment.

The co-ordination shifts of the [Pt(S₂N₂)(PR₃)] (R = alkyl, aryl) relative to their [PtCl₂(PR₃)₂] starting materials are about –8 ppm for δ_{A} and about +7 ppm for δ_{X} .² For the phosphite-containing complexes the chemical shifts also exhibit a relatively constant co-ordination shift compared to their starting materials: δ_{A} is shifted by ca. +31 ppm and δ_{X} by ca. +37 ppm for all the phosphite systems. The chemical shifts for **7–10** were found to be similar to their [S₂N₂]²⁻ analogues.

The $^2J_{\text{P,P}}$ coupling constants increase in the order PPh₃ < P(OMe)Ph₂ < P(OMe)₂Ph < P(OMe)₃ from ca. 22 Hz to ca. 49 Hz presumably reflecting the relative Pt–P bond strengths in this series. Similarly $^2J_{\text{P-Se(trans)}}$ for **7–10** decreases from 94 to 60 Hz. No *cis*-selenium satellites were observed and given the small magnitudes of previously reported $^2J_{\text{P-Se(cis)}}$ values this is understandable.^[26]

The structures of the [S₂N₂]²⁻ complexes **1** and **3–6** (Table 3, Figures 6 and 7) exhibit square-planar geometry about platinum. The Pt–P distances (Table 3, Figure 8) lie in the range 2.217(3) Å and 2.256(2) Å. One might antici-

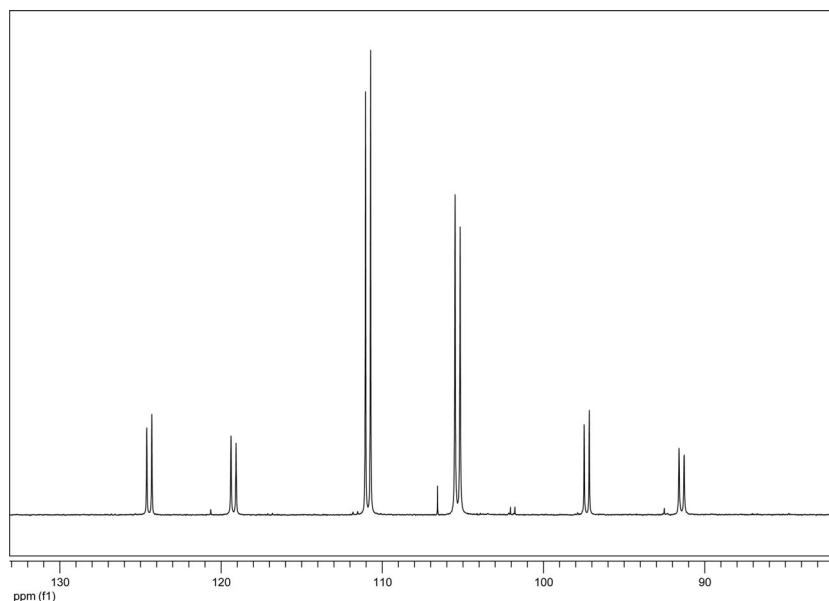


Figure 3. $^{31}\text{P}\{^1\text{H}\}$ NMR spectrum (109 MHz, CH_2Cl_2 solution) of **4**.

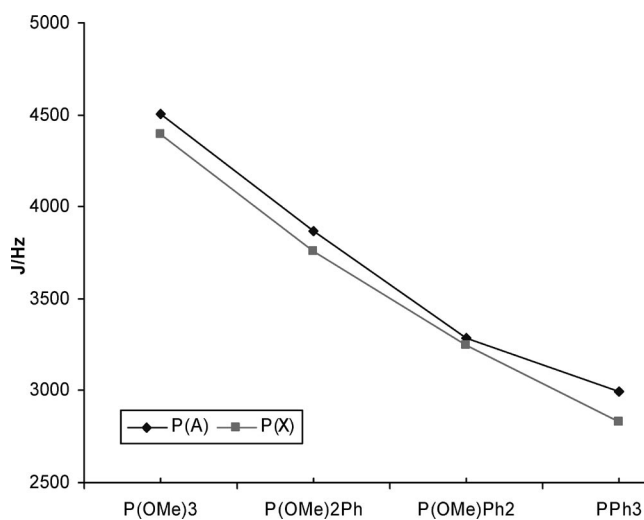


Figure 4. Variation of 1J_A and 1J_X in $[\text{Pt}(\text{S}_2\text{N}_2)\{\text{P}(\text{OMe})_n\text{Ph}_{3-n}\}_2]$ complexes.

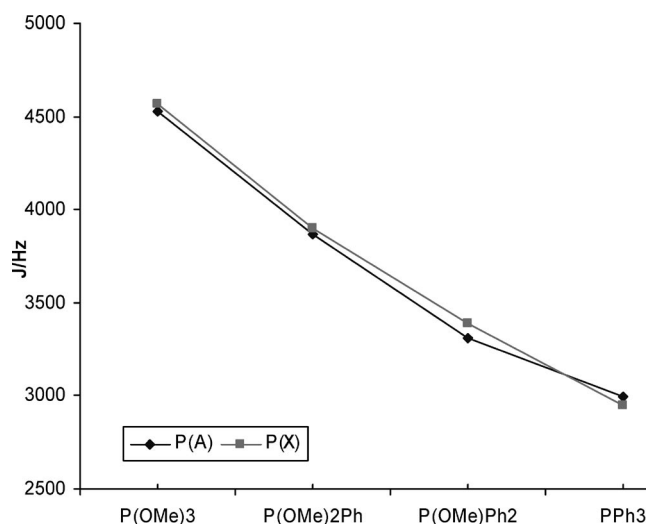


Figure 5. Variation of 1J_A and 1J_X in $[\text{Pt}(\text{SeSN}_2)\{\text{P}(\text{OMe})_n\text{Ph}_{3-n}\}_2]$ complexes.

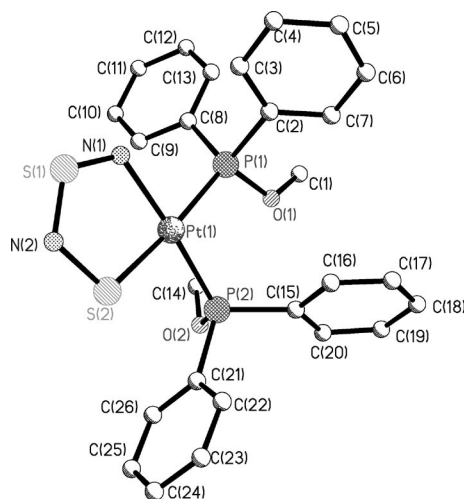
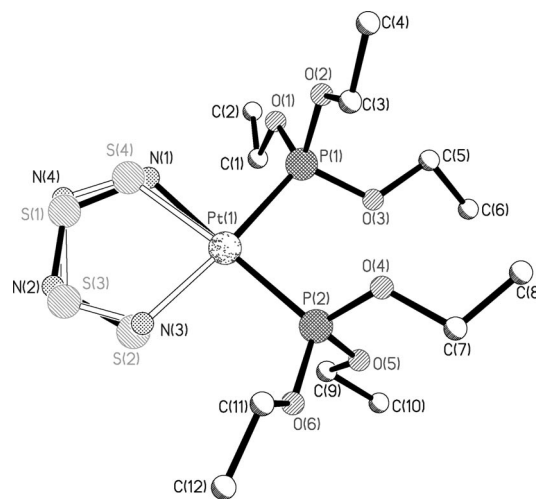
pate a difference in Pt–P bond length *trans* to sulfur versus *trans* to nitrogen and there does appear to be a trend suggesting that Pt–P(2) (*trans* to nitrogen) is usually shorter [i.e. for those where there is a structurally relevant difference, Pt–P(2) is shorter than Pt–P(1)]. In general all of the Pt–P distances observed for **1** and **3–6** are longer than for the chloride complexes. The Pt–N bond lengths are in the range 2.016(4)–2.070(7) Å and the Pt–S bond lengths are in the range 2.289(2)–2.295(3) Å. The Pt–N distance appears more sensitive to the nature of the phosphane/phosphite though we cannot see any direct trends.

As changing the phosphorus ligands gave rise to trends in coupling constants in ^{31}P NMR we wondered if we might see an effect on the geometry of the metal sulfur–nitrogen ring complexes. On the whole however this effect was not

measurable crystallographically. The bond lengths and angles are comparable to equivalent complexes with phosphane ligands with two short sulfur–nitrogen bonds, which are slightly longer than a typical sulfur–nitrogen double bond (1.45 Å) ranging from 1.515(8)–1.590(9) Å and one long sulfur–nitrogen bond, which corresponds to the length of a typical sulfur–nitrogen single bond (1.69 Å) ranging from 1.673(9)–1.709(11) Å. There is a small departure from this trend in the case of **6** for which there is one short, one long and one medium intermediate length bond indicating some degree of electron delocalisation. If the S–N bond lengths in **1** are discounted (since this structure contains significant disorder) then the average bond lengths for the remaining structures are N(1)–S(1) 1.54(2), S(1)–N(2) 1.58(2) and S(2)–N(2) 1.69(2) Å. Bond angles within the

Table 3. Selected bond lengths [Å] and angles [°] for **1**, **3–6** and [Pt(S₂N₂)(PPh₃)₂]. Values printed in *italics* are DFT-calculated parameters (asterisks * denote two-fold disorder).

	1	3	4	5	6	[Pt(S ₂ N ₂)(PPh ₃) ₂]-4CH ₂ Cl ₂ ^[7]	[Pt(S ₂ N ₂)(PPh ₃) ₂]-C ₇ H ₈ ^[4]
Pt–N(1)	2.050(17)	2.057(11)	2.064(8)	2.016(4)	2.070(7)	2.018(4)	2.093(13)
			<i>2.019</i>			<i>2.017</i>	<i>2.017</i>
Pt–S(2)	2.293(9)	2.291(3)	2.295(3)	2.2923(15)	2.289(2)	2.288(5)	2.294(6)
			<i>2.315</i>			<i>2.308</i>	<i>2.308</i>
Pt–P(1)	2.237(2)	2.234(3)	2.246(3)	2.2407(15)	2.256(2)	2.317(4)	2.308(5)
			<i>2.257</i>			<i>2.334</i>	<i>2.334</i>
Pt–P(2)	2.239(2)	2.221(3)	2.217(3)	2.2175(15)	2.250(2)	2.263(4)	2.259(3)
			<i>2.244</i>			<i>2.299</i>	<i>2.299</i>
N(1)–S(1)	1.69(2)*	1.541(11)	1.544(13)	1.572(5)	1.515(8)	1.546(16)	1.499(16)
			<i>1.567</i>			<i>1.563</i>	<i>1.563</i>
S(1)–N(2)	1.46(2)*	1.589(13)	1.554(13)	1.568(5)	1.590(9)	1.567(19)	1.702(15)
			<i>1.570</i>			<i>1.571</i>	<i>1.571</i>
N(2)–S(2)	1.763(17)*	1.689(12)	1.709(11)	1.702(5)	1.673(9)	1.682(16)	1.548(12)
			<i>1.682</i>			<i>1.687</i>	<i>1.687</i>
P(1)–Pt–P(2)	93.57(7)	96.18(11)	93.89(15)	95.12(6)	96.14(7)	98.4(1)	97.8(1)
			<i>96.2</i>			<i>100.2</i>	<i>100.2</i>
N(1)–Pt–S(2)	90.5(5)	88.5(3)	87.8(4)	88.78(15)	87.0(2)	87.6(5)	86.8(4)
Pt–N(1)–S(1)	109.5(10)	114.6(6)	115.0(7)	115.1(3)	115.6(4)	116.2(9)	113.5(7)
N(1)–S(1)–N(2)	120.6(12)	116.9(6)	117.2(6)	116.7(3)	117.0(4)	116.0(9)	117.5(7)
S(1)–N(2)–S(2)	115.2(14)	116.3(6)	116.6(7)	115.8(3)	115.6(5)	116.1(11)	113.7(8)
N(2)–S(2)–Pt	103.3(9)	103.6(4)	103.4(4)	103.60(18)	104.9(3)	104.0(7)	108.4(7)


 Figure 6. X-ray crystal structure of **6**. The structures of **3–5** are not illustrated as they are similar.

 Figure 7. X-ray crystal structure of **1** showing twofold disorder about the [S₂N₂]^{2–} fragment.

ring were fairly consistent throughout and were comparable to previously reported examples. When compared to the starting materials the bond angle P(1)–Pt–P(2) was observed to be smaller with a range of 96.18(11)–93.57(7) Å.

The structures of the [SeSN₂]^{2–} complexes **7–10** (Table 4, Figure 9) also exhibit square-planar geometry about platinum. Unlike the previously reported structure, none of the structures exhibit detectable disorder. Only **9** was observed to be isomorphous (ie similar unit cell and crystal system) to its [S₂N₂]^{2–} analogue. Of the bonds within the ring those involving N(1) are most sensitive to the nature of the phosphorus ligand. The Pt–N(1) bond lengths increases from 2.041(9)–2.095(4) Å as the OMe groups are successively replaced by Ph groups ie the phosphane complex has the longest Pt–N(1) bond length. Concurrently, the N(1)–S(1)

bond length decreases from 1.532(9)–1.480(7) Å with the PPh₃ complex having the shortest N(1)–S(1) distance. Interestingly, and perhaps counter-intuitively, the Pt–P distances in **7–10** [in the range 2.214(2) Å and 2.3069(17) Å] also increase as OMe is replaced by Ph for both Pt–P(1) and Pt–P(2) (Figure 10).

In order to understand these apparent trends in bond lengths we performed DFT calculations on a range of complexes. For compounds **4** and **7**, the DFT-computed IR data are included in Table 2 for comparison. The computed harmonic frequencies are systematically larger than the observed fundamentals (by typically 30–40 cm^{–1}), but overall the observed patterns assigned to the metallacycle are reasonably well reproduced computationally. Since the [S₂N₂]^{2–} ligand often appears to be disordered we included

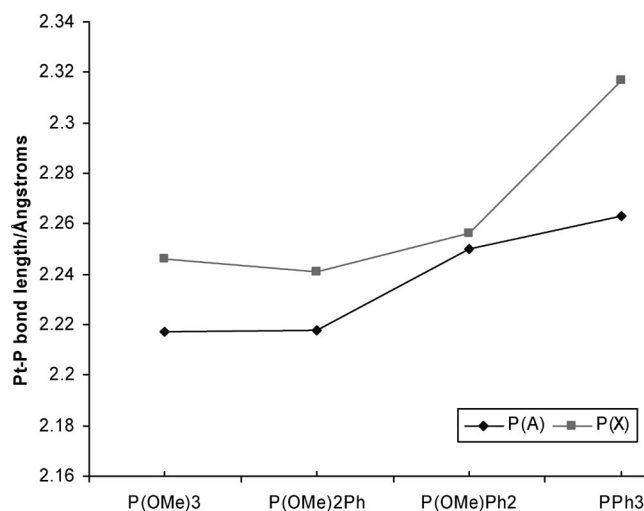


Figure 8. Variation of Pt–P(A) and Pt–P(X) bond lengths in $[\text{Pt}(\text{S}_2\text{N}_2)\{\text{P}(\text{OMe})_n\text{Ph}_{3-n}\}_2]$ complexes.

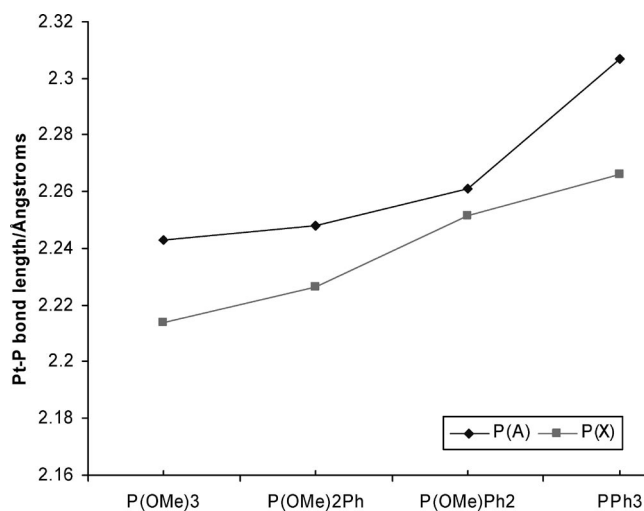


Figure 10. Variation of Pt–P(A) and Pt–P(X) bond lengths in $[\text{Pt}(\text{SeSN}_2)\{\text{P}(\text{OMe})_n\text{Ph}_{3-n}\}_2]$ complexes.

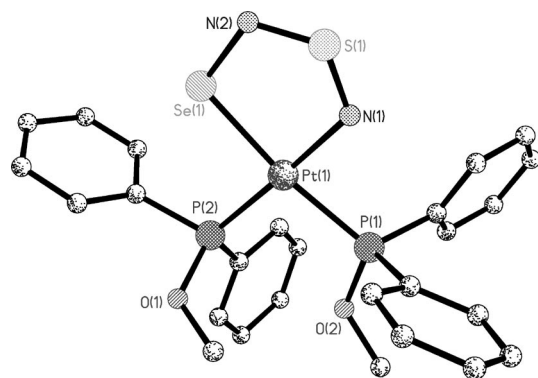


Figure 9. X-ray crystal structure of **9**. The structures of **7**, **8** and **10** are not illustrated as they are similar.

an example of the protonated system which appears more well-behaved crystallographically. The results of the DFT calculations are shown in Tables 3 and 4. It is striking that these calculations, whilst fitting the protonated structures well, do not mirror the observed trends in Pt–N and S–N bond lengths. The DFT calculations suggest that the Pt–N bond length is not significantly influenced by the nature of the *trans* ligand in the compounds studied here. Quite unusually, the DFT-optimised Pt–N distances are noticeably shorter than most of the X-ray data. For the model system $[\text{Pt}(\text{S}_2\text{N}_2)(\text{PH}_3)_2]$, PBE0-optimised distances agree well with those obtained at the CCST(T) level, the “gold standard” of ab initio quantum chemistry. There is thus no evidence for a particular DFT problem with this kind of bond.^[29]

Table 4. Selected bond lengths [Å] and angles [°] for **7–10**. Values printed in *italics* are DFT-calculated parameters.

	7	8	9	10
Pt–N(1)	2.041(9) <i>2.025</i>	2.065(4)	2.074(13)	2.095(4) <i>2.022</i>
Pt–Se(1)	2.3874(11) <i>2.423</i>	2.4099(5)	2.3987(16)	2.3818(9) <i>2.421</i>
Pt–P(1)	2.214(2) <i>2.240</i>	2.2266(13)	2.2517(18)	2.2664(12) <i>2.295</i>
Pt–P(2)	2.243(2) <i>2.263</i>	2.2480(14)	2.2609(16)	2.3069(17) <i>2.338</i>
N(1)–S(1)	1.532(9) <i>1.562</i>	1.523(4)	1.496(15)	1.480(7) <i>1.557</i>
S(1)–N(2)	1.571(7) <i>1.564</i>	1.564(5)	1.547(16)	1.572(6) <i>1.565</i>
N(2)–Se(1)	1.826(9) <i>1.838</i>	1.858(4)	1.858(15)	1.819(5) <i>1.843</i>
P(1)–Pt–P(2)	94.83(9) <i>96.9</i>	94.94(5)	96.29(14)	97.84(5) <i>100.5</i>
P(2)–Pt–Se(1)	174.37(3)	173.45(7)	172.49(4)	170.74(3)
P(1)–Pt–N(1)	179.4(2)	173.80(11)	175.32(16)	176.85(18)
N(1)–Pt–Se(1)	88.0(2)	87.87(12)	86.7(3)	86.31(18)
Pt–N(1)–S(1)	117.9(4)	117.8(2)	119.1(7)	118.5(2)
N(1)–S(1)–N(2)	118.4(4)	119.5(2)	118.8(7)	118.9(2)
S(1)–N(2)–Se(1)	115.0(5)	114.8(2)	115.1(8)	114.8(4)
N(2)–Se(1)–Pt	100.7(2)	100.01(15)	100.2(4)	101.5(2)

We considered that even a small component of disorder in eg the $[\text{SeSN}_2]^{2-}$ could cause apparent lengthening of the Pt–N bond length and re-examined our crystal structures carefully for residual electron density peaks as well as looking carefully at the thermal parameters. We do not see any evidence of disorder.

The HOMO and LUMO of the $\text{Pt}(\text{SSeN}_2)$ fragment were examined (Figures 11 and 12). On going from phosphane to phosphite ligands, the weaker σ -donor capability should result in shorter Pt–N and longer N(1)–S(1) bonds (as less electron density is donated into this LUMO). On the other hand, the HOMO has antibonding character for both bonds. The stronger π -acceptor capability of phosphites over phosphanes should thus produce shorter bonds (as more electron density is removed from the HOMO).^[30] While no clear trend can be predicted for the N(1)–S(1) distance on these grounds, the Pt–N bond should contract with an increasing number of phosphites, in good apparent agreement with the observed trend. So overall we can see that the trends in bond lengths are not well supported by the DFT calculations though empirical arguments based on the LUMO may be used to rationalise the trends. We cannot judge if the difficulties here are a consequence of experimental or computational difficulties.

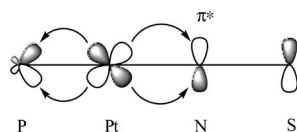


Figure 11. Backbonding from Pt to the π^* orbital on N in the metallacycles studied here.

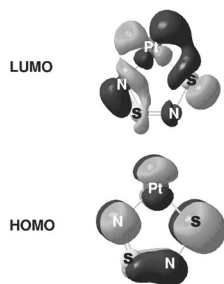


Figure 12. Frontier molecular orbitals of the $\text{Pt}(\text{S}_2\text{N}_2)$ fragment (in the geometry of the PMe_3 complex, PBE0/ECPI level).

The variation in Pt–P bond length can be correlated with the decreasing magnitude of $^1J_{\text{Pt,P}}$ which is itself a crude measure of bond strength. The remaining three bonds in the metallacycle appear less sensitive to the phosphorus ligand and do not exhibit any distinguishable trend [S(1)–N(2) range 1.547(16)–1.572(6) Å and N(2)–Se(1) range 1.819(5)–1.858(15) Å]. The Pt–Se bond lengths are in the range 2.3818(9)–2.4099(5) Å.

When compared to the $[\text{S}_2\text{N}_2]^{2-}$ analogues the P(1)–Pt–P(2) bond angles in the mixed-chalcogen complexes are observed to be similar and influenced by the steric bulk of the

phosphorus ligand with a range of 94.83(9)° to 97.84(5)° increasing in the order $7 < 8 < 9 < 10$. Similarly the N(1)–Pt–Se angles [which are comparable to the N(1)–Pt–S(2) angles of $[\text{Pt}(\text{S}_2\text{N}_2)\{\text{P}(\text{OMe})_n\text{Ph}_{3-n}\}_2$] complexes with a range of 86.31(18)° to 88.0(2)°] increase as the P(1)–Pt–P(2) bond angle decreases, again reflecting the increasing steric bulk of the phosphorus ligands. At the PBE0 level, P–Pt–P bond angles tend to be overestimated by up to ca. 2°, which for $[\text{Pt}(\text{S}_2\text{N}_2)(\text{PPh}_3)_2]$ is remedied at the dispersion-corrected B97-D level, where a P–Pt–P angle of 97.5° is obtained, in excellent agreement with experiment.

Conclusions

We have synthesised the series of complexes $[\text{Pt}(\text{S}_2\text{N}_2)\{\text{P}(\text{OR})_n\text{R}'_{3-n}\}_2]$ and $[\text{Pt}(\text{SeSN}_2)\{\text{P}(\text{OMe})_n\text{Ph}_{3-n}\}_2]$ ($n = 0$ –3) by straightforward and relatively low-hazard routes in liquid ammonia. In common with other S/Se–N systems the bonding in these complexes proves to be difficult to rationalise in detail. Whilst there appear to be structural trends, particularly in the selenium containing systems, these are not well modelled by the DFT calculations and further detailed work may be needed to understand the differences between experiment and calculations in these systems.

Experimental Section

General: Unless otherwise stated all manipulations were performed under an oxygen-free nitrogen atmosphere, using standard Schlenk techniques and glassware. Solvents were dried and stored according to common procedures. Reagents were obtained from Aldrich and used without further purification. Solution state NMR spectra were recorded using a JEOL GSX Delta 270. Microanalyses were performed by the University of St. Andrews microanalysis service. The compound $[\text{S}_4\text{N}_3]\text{Cl}$ was prepared by standard methods.^[31] *cis*- $[\text{PtCl}_2\{\text{P}(\text{OR})_n\text{R}'_{3-n}\}_2]$ ($\{\text{P}(\text{OR})_n\text{R}'_{3-n}\}_2 = \text{P}(\text{OPh})_3$, $\text{P}(\text{ONBu})_3$, $\text{P}(\text{OEt})_3$, $\text{P}(\text{OMe})_3$, $\text{P}(\text{OMe})_2\text{Ph}$ or $\text{P}(\text{OMe})\text{Ph}_2$) were prepared from $[\text{PtCl}_2(\text{cyclo-octa-1,5-diene})]$ ^[32] and two equivalents of the phosphite, phosphonite or phosphinite in dichloromethane. *cis*- $[\text{PtCl}_2(\text{PPh}_3)_2]$ was prepared via reaction of $\text{K}_2[\text{PtCl}_4]$ in water and with PPh_3 in ethanol.^[33] All compounds were characterised using ^{31}P NMR spectroscopy. Low solubility and sample size prevented measurement of ^{77}Se NMR spectroscopy.

CAUTION: Reactions involving S–N compounds may generate explosive S_4N_4 . S_4N_4 explodes upon mechanical or heat shock. Its explosiveness increases with the purity of the substance. Kevlar gloves and visor should be used when manipulating S_4N_4 . Residues of S_4N_4 were disposed of by decomposition with aqueous NaOH.

Preparation of Disulfur Dinitrido Complexes $[\text{Pt}(\text{S}_2\text{N}_2)\{\text{P}(\text{OR})_n\text{R}'_{3-n}\}_2]$ $\{\text{PR}_3 = \text{P}(\text{OMe})_3$, $\text{P}(\text{OMe})_2\text{Ph}$, $\text{P}(\text{OMe})\text{Ph}_2$, $\text{P}(\text{OPh})_3$, $\text{P}(\text{ONBu})_3$ or $\text{P}(\text{OEt})_3\}$: In a typical reaction, liquid ammonia (30 mL) was condensed using a condenser filled with dry ice and acetone into a Schlenk tube in a dry ice/acetone bath. To this $[\text{S}_4\text{N}_3]\text{Cl}$ (0.78 mmol) was added to produce a dark red solution. After stirring for 30 min $[\text{PtCl}_2\{\text{P}(\text{OR})_n\text{R}'_{3-n}\}_2]$ (0.5 mmol) was added. Over the course of one hour the solution lightened to a pale orange colour. After stirring the reaction mixture at -78°C for 3 h the

solution was warmed to room temp. and the ammonia was evaporated under a stream of nitrogen. The resulting pale orange residue was dried in vacuo then dissolved in dichloromethane (10 mL) and filtered through celite. The product was precipitated via slow addition of hexane. Isolated yields were 30–65%. Attempts to isolate $[\text{Pt}(\text{S}_2\text{N}_2)\{\text{P}(\text{OMe})_n\text{Ph}_{3-n}\}_2]$ gave only oils. Crystals suitable for X-ray crystallography were grown by slow diffusion of hexane into a solution of the complex in dichloromethane.

Preparation of Monoselenium Monosulfur Dinitrido Complexes $[\text{Pt}(\text{SeSN}_2)\{\text{P}(\text{OMe})_n\text{Ph}_{3-n}\}_2]$ ($n = 0\text{--}3$): In a typical reaction liquid ammonia (30 mL) was condensed using a condenser filled with dry ice and acetone into a Schlenk tube in a dry ice/acetone bath. To this $[\text{S}_4\text{N}_3]\text{Cl}$ (0.78 mmol) and SeCl_4 (3.9 mmol) were added to produce a dark red solution. Over the course of 30 min the solution became pale orange in colour. $[\text{PtCl}_2\{\text{P}(\text{OMe})_n\text{Ph}_{3-n}\}_2]$ (0.5 mmol) was then added. After stirring the reaction mixture at -78°C for 3 h the solution was warmed to room temp. and the ammonia was evaporated under a stream of nitrogen. The resulting dark brown

residue was dried in vacuo then dissolved in dichloromethane (10 mL) and filtered through celite. The product was precipitated via slow addition of hexane; isolated yields were 50–75%.

Crystals suitable for X-ray crystallography were grown by slow diffusion of hexane into a solution of the complex in dichloromethane.

Crystallography

Crystal structure data were collected for **1**, **4**, **5** and **6** at 93 K on a Rigaku MM007 confocal optics/Saturn CCD diffractometer using Mo- K_α radiation ($\lambda = 0.71073\text{ \AA}$), for **3**, **7**, **8**, **9** and **10** at 125 K using a Rigaku SCX-Mini. All data was corrected for absorption. The structures were solved by direct methods and refined by full-matrix least-squares methods on F^2 values of all data.^[34] Refinements were performed using SHELXL.^[35]

CCDC-755579 (for **1**), -755580 (for **3**), -755581 (for **4**), -755582 (for **5**), -755583 (for **6**, Table 5), -766913 (for **7**), -766914 (for **8**), -766915 (for **9**), -766916 (for **10**, Table 6) contain the supplementary crystal-

Table 5. Experimental and refinement details for the X-ray structures of **1** and **3–6**.

	1	3	4	5	6
<i>F</i> _w	$[\text{C}_{12}\text{H}_{18}\text{N}_2\text{O}_6\text{P}_2\text{PtS}_2]$	$[\text{C}_{36}\text{H}_{30}\text{N}_2\text{O}_6\text{P}_2\text{PtS}_2]$	$[\text{C}_6\text{H}_{18}\text{N}_2\text{O}_6\text{P}_2\text{PtS}_2]$	$[\text{C}_{16}\text{H}_{22}\text{N}_2\text{O}_4\text{P}_2\text{PtS}_2]$	$[\text{C}_{26}\text{H}_{26}\text{N}_2\text{O}_2\text{P}_2\text{PtS}_2]$
<i>M</i>	619.54	907.77	535.37	627.51	719.64
Temperature /K	93	125	93	93	93
Crystal system	monoclinic	triclinic	monoclinic	monoclinic	orthorhombic
Space group	$P2_1/c$	$P\bar{1}$	$P2(1)$	$P2_1/c$	$P2(1)2(1)2(1)$
<i>a</i> /Å	8.900(4)	10.8476(13)	8.299(4)	19.622(2)	10.2231(11)
<i>b</i> /Å	13.719(10)	13.2659(15)	6.783(3)	13.4726(11)	14.6259(16)
<i>c</i> /Å	18.519(13)	13.4783(16)	14.587(6)	18.8268	17.7113(19)
α /°	90	78.290(3)	90	90	90
β /°	101.345(11)	78.106(3)	101.864	117.33(3)	90
γ /°	90	67.963(3)	90	90	90
<i>V</i> /Å ³	2217(3)	1742.3(4)	803.7(6)	4421.6(14)	2648.2(5)
<i>Z</i>	4	2	2	8	4
$\mu(\text{Mo-}K_\alpha)$ /mm ⁻¹	6.689	4.288	9.207	6.704	5.604
<i>D</i> _c /Mg m ⁻³	1.856	1.730	2.212	1.885	1.805
Independent reflections (<i>R</i> _{int})	4006 (0.1219)	6341 (0.1000)	2882 (0.0490)	8052 (0.0455)	4803 (0.1261)
Max. and min. transmission	0.792, 1.000	0.414, 1.000	0.740, 1.000	0.696, 1.000	0.971, 1.000
Final <i>R</i> , <i>R'</i>	0.0449, 0.1024	0.0783, 0.1748	0.0418, 0.0997	0.0353, 0.0842	0.0442, 0.1105
Largest difference peak/hole /e Å ⁻³	2.591/−1.418	3.091/−2.635	2.049/−1.099	3.854/−1.439	1.394/−1.725

Table 6. Experimental and refinement details for the X-ray structures of **7–10**.

	7	8	9	10·2H₂O
<i>F</i> _w	$[\text{C}_6\text{H}_{18}\text{N}_2\text{O}_6\text{P}_2\text{SSePt}]$	$[\text{C}_{16}\text{H}_{22}\text{N}_2\text{O}_4\text{P}_2\text{SSePt}]$	$[\text{C}_{26}\text{H}_{26}\text{N}_2\text{O}_2\text{P}_2\text{SSePt}]$	$[\text{C}_{36}\text{H}_{32}\text{N}_2\text{O}_2\text{P}_2\text{SSePt}]$
<i>M</i>	582.28	674.42	766.56	894.73
Temperature /K	125	125	125	125
Crystal system	monoclinic	monoclinic	orthorhombic	triclinic
Space group	$P2_1/c$	$P2_1/n$	$P2(1)2(1)2(1)$	$P\bar{1}$
<i>a</i> /Å	15.1888(8)	9.0315(3)	10.1701(4)	11.3630(4)
<i>b</i> /Å	6.8320(4)	17.8064(5)	14.7525(5)	12.1702(5)
<i>c</i> /Å	16.4967(9)	13.5320(4)	18.0251(6)	16.5588(7)
α /°	90	90	90	93.4760(10)
β /°	109.6816(13)	102.6458(9)	90	108.3000(10)
γ /°	90	90	90	113.4650(10)
<i>V</i> /Å ³	1611.85(15)	2123.41(11)	2704.39(17)	1948.47(13)
<i>Z</i>	4	4	4	2
$\mu(\text{Mo-}K_\alpha)$ /mm ⁻¹	11.276	8.569	6.736	4.687
<i>D</i> _c /Mg m ⁻³	2.399	2.109	1.883	1.525
Independent reflections (<i>R</i> _{int})	13159 (0.102)	22112 (0.063)	23268 (0.064)	16900 (0.043)
Max. and min. transmission	0.2353, 0.0930	0.4253, 0.1895	0.3451, 0.1636	0.4111, 0.2066
Final <i>R</i> , <i>R'</i>	0.0416, 0.1062	0.0326, 0.0619	0.0311, 0.0648	0.0502, 0.1545
Largest difference peak/hole /e Å ⁻³	3.32/−2.19	1.51/−1.24	1.50/−0.74	2.76/−1.27

lographic data for this paper. These data can be obtained free of charge from The Cambridge Crystallographic Data Centre via www.ccdc.cam.ac.uk/data_request/cif.

Computational Details

Geometries were fully optimised at the PBE0/ECP1 level, i.e. employing the hybrid variant of the PBE functional,^[36] the Stuttgart–Dresden relativistic effective core potential (SDD ECP) along with its [6s5p3d] valence basis on Pt,^[37] Binning and Curtiss' 962(d) basis on Se,^[38] and 6-31G* basis^[39] elsewhere. This combination of functional and basis sets has performed very well for the description of bond lengths between third-row transition metals and their ligands.^[40] For [Pt(S₂N₂)(PMe₃)₂], reoptimisation with the larger TZVP basis^[41] (including the 6s4p3d1f valence basis^[42] for the SDD ECP) afforded only minor changes in the Pt ligand and S–N bond lengths (typically less than 1 pm). [Pt(S₂N₂)(PH₃)₂] was reoptimised at the CCSD(T)/TZVP level, imposing C_s symmetry (the minimum character of which had been confirmed by a frequency calculation at the PBE0/ECP1 level). Finally, some exploratory calculations were performed for [Pt(S₂N₂)(PPh₃)₂] at the B97-D/ECP1 level, i.e. including empirical dispersion corrections^[43] that had been shown to be beneficial for the description of metal-phosphane binding energies.^[44] All computations employed the Gaussian 09^[45] suite of programs.

Acknowledgments

We wish to thank Engineering and Physical Sciences Research Council (EaStCHEM) for support and access to the EaStCHEM Research Computing Facility maintained by Dr. H. Früchtl.

- [1] P. F. Kelly, J. D. Woollins, *Polyhedron* **1986**, *5*, 607–632.
- [2] P. A. Bates, M. B. Hursthouse, P. F. Kelly, J. D. Woollins, *J. Chem. Soc., Dalton Trans.* **1986**, 2367–2370.
- [3] P. S. Belton, I. P. Parkin, D. J. Williams, J. D. Woollins, *J. Chem. Soc., Chem. Commun.* **1988**, 1479–1480.
- [4] T. Chivers, F. Edelmann, U. Behrens, R. Drews, *Inorg. Chim. Acta* **1986**, *116*, 145–151.
- [5] R. Jones, P. F. Kelly, C. P. Warrens, D. J. Williams, J. D. Woollins, *J. Chem. Soc., Chem. Commun.* **1986**, 711–713.
- [6] R. Jones, P. F. Kelly, D. J. Williams, J. D. Woollins, *J. Chem. Soc., Chem. Commun.* **1985**, 1325–1326.
- [7] R. Jones, P. F. Kelly, D. J. Williams, J. D. Woollins, *Polyhedron* **1985**, *4*, 1947–1950.
- [8] R. Jones, P. F. Kelly, D. J. Williams, J. D. Woollins, *J. Chem. Soc., Dalton Trans.* **1988**, 803–807.
- [9] R. Jones, C. P. Warrens, D. J. Williams, J. D. Woollins, *J. Chem. Soc., Dalton Trans.* **1987**, 907–910.
- [10] S. M. Aucott, P. Bhattacharyya, H. L. Milton, A. M. Z. Slawin, J. D. Woollins, *New J. Chem.* **2003**, *27*, 1466–1469.
- [11] S. M. Aucott, A. M. Z. Slawin, J. D. Woollins, *Can. J. Chem.* **2002**, *80*, 1481–1487.
- [12] M. B. Hursthouse, M. Motevalli, P. F. Kelly, J. D. Woollins, *Polyhedron* **1989**, *8*, 997.
- [13] P. F. Kelly, A. M. Z. Slawin, D. J. Williams, J. D. Woollins, *Polyhedron* **1991**, *10*, 2337.
- [14] B. D. Read, A. M. Z. Slawin, J. D. Woollins, *Acta Crystallogr., Sect. E* **2007**, *63*, m751–m752.
- [15] A. A. Bhattacharyya, J. A. McLean Jr., A. G. Turner, *Inorg. Chim. Acta* **1979**, *34*, 199.
- [16] P. F. Kelly, I. P. Parkin, A. M. Z. Slawin, D. J. Williams, J. D. Woollins, *Angew. Chem. Int. Ed. Engl.* **1989**, *28*, 1047.
- [17] P. F. Kelly, A. M. Z. Slawin, D. J. Williams, J. D. Woollins, *Polyhedron* **1990**, *9*, 1567.
- [18] P. F. Kelly, J. D. Woollins, *Polyhedron* **1993**, *12*, 1129–1134.
- [19] V. C. Ginn, P. F. Kelly, J. D. Woollins, *Polyhedron* **1994**, *13*, 1501–1506.
- [20] C. A. O'Mahoney, I. P. Parkin, D. J. Williams, J. D. Woollins, *Polyhedron* **1989**, *8*, 2215–2220.
- [21] I. P. Parkin, J. D. Woollins, *J. Chem. Soc., Dalton Trans.* **1990**, 925–930.
- [22] P. F. Kelly, J. D. Woollins, *J. Chem. Soc., Dalton Trans.* **1988**, 1053–1058.
- [23] I. P. Parkin, J. D. Woollins, P. S. Belton, *J. Chem. Soc., Dalton Trans.* **1990**, 511–517.
- [24] T. Chivers, K. J. Schmidt, *J. Chem. Soc., Chem. Commun.* **1990**, 1342–1344.
- [25] M. Herberhold, W. Ehrenreich, *Angew. Chem.* **1982**, *94*, 637–638.
- [26] P. F. Kelly, I. P. Parkin, R. N. Sheppard, J. D. Woollins, *Heteroat. Chem.* **1991**, *2*, 301–3015.
- [27] F. H. Allen, A. Pidcock, C. R. Waterhouse, *J. Chem. Soc. A* **1970**, 2087–2093.
- [28] L. J. Manojlović-Muir, K. W. Muir, *Inorg. Chim. Acta* **1974**, *10*, 47–55.
- [29] Also, for a closely related system, [Pt(N=S=O)₂(PMe₃)₂], the mean Pt–N distances at the PBE0/ECP1 level, 2.047 Å, are in excellent agreement with the X-ray data (2.049 Å for the PPh₃ derivative: R. Short, M. B. Hursthouse, T. G. Purcell, J. D. Woollins, *J. Chem. Soc., Chem. Commun.* **1987**, 407).
- [30] It should be noted, however, that these arguments based on a covalent σ-bonding and π-back-bonding model can be masked by more subtle electrostatic effects, see: G. Frenking, K. Wichmann, N. Fröhlich, C. Loschen, M. Lein, J. Frunzke, V. M. Rayon, *Coord. Chem. Rev.* **2003**, *238–239*, 55–82.
- [31] W. L. Jolly, M. Becke-Goering, *Inorg. Chem.* **1962**, *1*, 76–78.
- [32] J. C. Bailar, H. Itatani, *Inorg. Chem.* **1965**, *4*, 1618–1620.
- [33] F. J. Ramos-Lima, A. G. Quiroga, J. M. Pérez, M. Font-Bardía, X. Solans, C. Navarro-Ranninger, *Eur. J. Inorg. Chem.* **2003**, *8*, 1591–1598.
- [34] Rigaku, *Crystal Structure*, version 3.8 (2006), Single Crystal Structure Analysis Software, Rigaku/MS, 9009 TX, USA 77381-5209. Rigaku, Tokyo 196-8666, Japan.
- [35] G. M. Sheldrick, *Acta Crystallogr., Sect. A* **2008**, *64*, 112–122.
- [36] a) J. P. Perdew, K. Burke, M. Ernzerhof, *Phys. Rev. Lett.* **1996**, *77*, 3865–3868; b) C. Adamo, V. Barone, *J. Chem. Phys.* **1999**, *110*, 6158–6170.
- [37] M. Dolg, U. Wedig, H. Stoll, H. Preuss, *J. Chem. Phys.* **1987**, *86*, 866–872.
- [38] R. C. Binning, L. A. Curtiss, *J. Comput. Chem.* **1990**, *11*, 1206.
- [39] a) W. J. Hehre, R. Ditchfield, J. A. Pople, *J. Chem. Phys.* **1972**, *56*, 2257–2261; b) P. C. Hariharan, J. A. Pople, *Theor. Chim. Acta* **1973**, *28*, 213–222.
- [40] M. Bühl, C. Reimann, D. A. Pantazis, T. Bredow, F. Neese, *J. Chem. Theory Comput.* **2008**, *4*, 1449–1459.
- [41] A. Schäfer, C. Huber, R. Ahlrichs, *J. Chem. Phys.* **1994**, *100*, 5829–5835.
- [42] F. Weigend, R. Ahlrichs, *Phys. Chem. Chem. Phys.* **2005**, *7*, 3297–3305.
- [43] a) S. J. Grimme, *Comput. Chem.* **2004**, *25*, 1463; b) S. J. Grimme, *Comput. Chem.* **2006**, *27*, 1787. C₆ parameters for Pt are not available and have been set to zero.
- [44] a) N. Sieffert, M. Bühl, *Inorg. Chem.* **2009**, *48*, 4622; b) Y. Minenkov, G. Occhipinti, V. R. Jensen, *J. Phys. Chem. A* **2009**, *113*, 11833.
- [45] M. J. Frisch, G. W. Trucks, H. B. Schlegel, G. E. Scuseria, M. A. Robb, J. R. Cheeseman, J. A. Montgomery Jr., T. Vreven, K. N. Kudin, J. C. Burant, J. M. Millam, S. S. Iyengar, J. Tomasi, V. Barone, B. Mennucci, M. Cossi, G. Scalmani, N. Rega, G. A. Petersson, H. Nakatsuji, M. Hada, M. Ehara, K. Toyota, R. Fukuda, J. Hasegawa, M. Ishida, T. Nakajima, Y. Honda, O. Kitao, H. Nakai, M. Klene, X. Li, J. E. Knox, H. P. Hratchian, J. B. Cross, V. Bakken, C. Adamo, J. Jaramillo, R. Gomperts, R. E. Stratmann, O. Yazyev, A. J. Austin, R. Cammi, C. Pomelli, J. W. Ochterski, P. Y. Ayala, K. Morok-

uma, G. A. Voth, P. Salvador, J. J. Dannenberg, V. G. Zakrzewski, S. Dapprich, A. D. Daniels, M. C. Strain, O. Farkas, D. K. Malick, A. D. Rabuck, K. Raghavachari, J. B. Foresman, J. V. Ortiz, Q. Cui, A. G. Baboul, S. Clifford, J. Cioslowski, B. B. Stefanov, G. Liu, A. Liashenko, P. Piskorz, I. Komaromi, R. L. Martin, D. J. Fox, T. Keith, M. A. Al-Laham, C. Y. Peng, A.

Nanayakkara, M. Challacombe, P. M. W. Gill, B. Johnson, W. Chen, M. W. Wong, C. Gonzalez, and J. A. Pople, *Gaussian 03*, Revision E.01, Gaussian, Inc., Wallingford CT, **2004**.

Received: March 24, 2010
Published Online: May 31, 2010

Unique Supramolecular Assembly of Wheel-Shaped Nanoscale Polyanions with a Hydrophobic Core

Jie Zhang,^[a] Tianbo Liu,^{*[a]} Sib Sankar Mal,^[b] and Ulrich Kortz^[b]

Keywords: Polyoxometalates / Amphiphiles / Self-assembly / Vesicles / Hydrophobic effect

The unique self-assembly behavior of the amphiphilic wheel-shaped polyanion $[\{K(H_2O)\}_3\{Ru(p\text{-cymene})(H_2O)\}_4P_8W_{49}O_{186}(H_2O)_2\}]^{27-}$ (**1**) in binary mixed solvents of water and various organic solvents is reported. Polyanion **1** does not undergo supramolecular assembly formation in water/acetone solutions with acetone contents below 55 vol.-%. However, in solutions with acetone contents of 55–80 vol.-%, vesicle-like structures were observed by light scattering and further confirmed by transmission electron microscopy. The average size of the vesicles decreases with increasing acetone contents. Similar results were found in water/THF and

water/acetonitrile binary solvents. This relation between assembly size and solvent composition contradicts the self-assembly of all other polyanions reported to date, which all follow the charge-regulation mechanism. However, for various binary solvents containing 75 vol.-% organic solvents (acetonitrile, ethanol, 2-propanol, THF, dioxane), the assembly sizes of **1** decrease with increasing dielectric constants of the solvents, which is again consistent with the charge-regulation mechanism. This unique solution behavior of **1** could be partially due to possible involvement of the hydrophobic organic *p*-cymene ligands in the self-assembly process.

Introduction

Incorporation of functional building blocks into amphiphilic molecules can result in the formation of assemblies with particular properties.^[1] Polyoxometalates (POMs), a class of large, molecular transition metal oxide clusters with well-defined structures, are promising functional materials based on their redox, catalytic, photochemical, and magnetic properties.^[2,3] Fabrication of amphiphilic POM-containing inorganic–organic hybrids can be achieved by tethering organic ligands to the POM surface through covalent bonding.^[4] These hybrids are more stable than those complexes formed by electrostatic interaction between cationic surfactants and polyanions.^[5] The self-assembly of POM-containing hybrid amphiphiles can improve the compatibility and processibility of POM materials in organic media while maintaining the functional properties of the POMs.^[4]

Recently, we demonstrated the amphiphilic nature of such hybrids by reporting the solution behavior of two POM-containing hybrid amphiphiles $[nBu_4N]_3[MnMo_6O_{18}\{(OCH_2)_3\text{-CNHCO}\text{-}(CH_2)_{n-2}CH_3\}_2]$ ($\{Mn\text{-Anderson-}C_n\}$, $n = 6, 16$).^[6a] These amphiphiles, with two hydrophobic alkyl tails and one hydrophilic POM polar head, have typical structures of surfactants. Similarly, a dumbbell-shaped

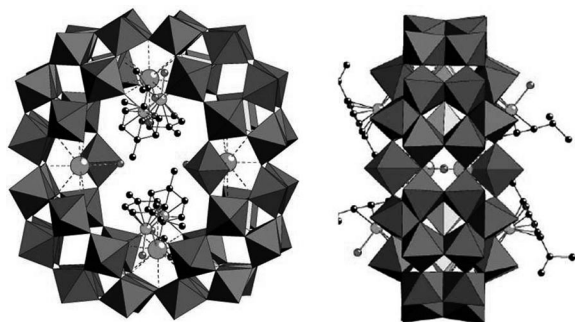
hybrid with two POM groups connected by an organic linker also forms amphiphilic vesicular structures in selective solvents.^[6b] Compared to conventional surfactants, the hybrid surfactants have much larger inorganic polar head groups, which affect the packing of the surfactants in their assemblies. These hybrid surfactants can slowly self-assemble into vesicles in water/CH₃CN or water/acetone mixed solvents mainly due to hydrophobic interactions.

The wheel-shaped polyanion $[\{K(H_2O)\}_3\{Ru(p\text{-cymene})(H_2O)\}_4P_8W_{49}O_{186}(H_2O)_2\}]^{27-}$ (**1**, see Scheme 1)^[7] also contains hydrophobic components (*p*-cymene), which are located in the center of the molecule. Polyanion **1** has four $\{Ru(p\text{-cymene})(H_2O)\}^{2+}$ fragments and an extra WO_6 group grafted onto the cyclic $[H_7P_8W_{48}O_{184}]^{33-}$ (P_8W_{48}) precursor, resulting in an unprecedented $\{P_8W_{49}\}$ assembly with a dimension of about $1 \times 2 \times 2$ nm³. Polyanion **1** is structurally related to the wheel-shaped Cu₂₀-containing derivative $[Cu_{20}Cl(OH)_{24}(H_2O)_{12}(P_8W_{48}O_{184})]^{25-}$ (**2**),^[8] but the former carries slightly more negative charges and has a hydrophobic center. The four organoruthenium(II) units in **1** are grafted on the rim of the central cavity, with the hydrophobic *p*-cymene groups sticking out of the “wheel”, generating a possible amphiphilic property of the polyanion.^[7]

More interestingly, the large polyanion “wheel” **1** belongs to an important class of ions-hydrophilic macroions. As we have shown previously, this class is represented by various large polyanions and some metal–organic cationic nanocages, which all have in common that they self-assemble into single-layered, vesicle-like “blackberry” or “shell” structures, with the driving force of formation most

[a] Department of Chemistry, Lehigh University, Bethlehem, Pennsylvania 18015, U.S.A
Fax: +1-610-758-6536
E-mail: liu@lehigh.edu

[b] School of Engineering and Science, Jacobs University, P. O. Box 750 561, 28725 Bremen, Germany
Fax: +49-421-200-3229
E-mail: u.kortz@jacobs-university.de



Scheme 1. Combined polyhedral/ball-and-stick representation of the wheel-shaped polyanion $[\{K(H_2O)\}_3\{Ru(p\text{-cymene})(H_2O)\}_4P_8W_{49}O_{186}(H_2O)_2\}]^{27-}$ (**1**). Left: top view; right: side view.

likely being counterion-mediated attractions and hydrogen bonds.^[9–13] The cyclic analogue **2** alone also shows such behavior in aqueous solution, and in fact its size approaches the lower limit of macroions needed for this type of self-assembly.^[8] The blackberry size can be accurately and reversibly adjusted by changing solvent, macroion charge density, or pH in some cases.^[10–13]

It is evident that the supramolecular self-assemblies of “inorganic–hydrophilic” POMs (such as **2**) versus “inorganic–organic amphiphilic” POMs (e.g., $\{Mn\text{-Anderson-}C_{16}\}$) are fundamentally different. Polyanion **1** is extremely interesting in this regard, as it lies exactly in between the two extremes described above: it obviously has organic groups (unlike **2**), but they are not very exposed and accessible (unlike $\{Mn\text{-Anderson-}C_{16}\}$). In **1**, the four aromatic rings are bound through the Ru ions in the center of the P_8W_{48} wheel, and hence, the hydrophilic as well as the hydrophobic regions of the polyanions are rather close in space. Also, the inorganic component in **1** is significantly larger than in $\{Mn\text{-Anderson-}C_{16}\}$.

All these are good reasons to explore the solution behavior of **1** and to compare it with hydrophilic **2**, and amphiphilic hybrids such as $\{Mn\text{-Anderson-}C_{16}\}$. This work could significantly advance our understanding on the interactions of complex macromolecules in general, and particularly of charged molecular clusters.

Results and Discussion

The major difference between **1** and **2** is that the former possesses a hydrophobic domain near the center of the polyanion. On the other hand, the Mn-Anderson hybrid species has long and “soft” alkyl tails, whereas the hydrophobic part of **1** is rather rigid and its hydrophilic-inorganic unit has a significantly higher negative charge (27- vs. 3- for $\{Mn\text{-Anderson-}C_n\}$). Polyanion **1** is soluble in water and stays as discrete polyanions without any association to larger assemblies for a long period of time, mostly due to its high charge density. The effective charge density of the polyanions can be easily tuned by changing the type of solvent, which could induce the self-assembly of **1**, as also seen for many other types of POMs.^[10,11]

A series of dilute solutions of **1** in mixed acetone/water solvents with different acetone contents was prepared for static and dynamic light scattering (SLS and DLS) studies. Polyanion **1** is still quite soluble in such solvents {up to 80 vol.-% acetone at 0.10 mg/mL of the mixed potassium–lithium salt $K_{16}Li_{11}[\{K(H_2O)\}_3\{Ru(p\text{-cymene})(H_2O)\}_4P_8W_{49}O_{186}(H_2O)_2\} \cdot 87H_2O$ (**1a**)}. The total scattered intensities of freshly prepared solutions were very low in SLS measurements, indicating that there was no large assembly present in such solutions, hence suggesting polyanions **1** homogeneously distributed as discrete ions. The solutions were kept at different temperatures and monitored by SLS frequently. For solutions with acetone content below 50%, there was no obvious increase in scattered intensity after several months. In solutions containing 55–80 vol.-% acetone, a slow self-association process was observed, similar to our previous studies on the self-assembly behavior of hydrophilic POMs.^[8–10] For example, for the solution with 60 vol.-% acetone, the scattered intensity remained unchanged for the first four days and then started to increase continuously from 41 Kcps to 2000 Kcps over a month (Figure 1), indicating the formation of supramolecular structures. During this slow self-association process, the average hydrodynamic radius R_h of the assemblies, as obtained by CONTIN analysis of the DLS studies, increased slightly from 15.7 to 22.9 nm. Neither the scattered intensity nor the R_h value of this clear solution changed any more after 40 days, indicating that equilibrium between discrete **1** and large assemblies had been reached. The final R_h value for the assemblies at a scattering angle of 90° is $\approx 22.9 \pm 0.6$ nm with a narrow size distribution (Figure 2). The R_h value does not show any angular dependence, implying a spherical morphology of the assemblies. Additionally, the average radius of gyration (R_g) of the supramolecular structures from the SLS measurement is 24 ± 1 nm; that is, the ratio R_g/R_h is very close to 1.0. It is known that for a solid sphere $R_g/R_h \approx 0.778$, whereas R_g/R_h approaches 1.0 for a hollow sphere. Consequently, we can conclude that the assemblies of **1** have a hollow, vesicle-like structure, very likely being of the blackberry-type. The solutions with different contents of acetone show similar, slow self-association behavior.

Similar results were obtained in various different polar solvents, such as the mixed solvents of water with acetonitrile, ethanol, 2-propanol, THF, dioxane, and so on. Interestingly, the relation between the average R_h values of the blackberries and the solvent content (in dielectric constant) seems to be similar to our previous observations in other self-assembly processes of polyanions (mostly) in mixed water/acetone solvents with different acetone contents.^[10] For example, the average R_h of **1**-based blackberries in mixed aqueous/organic solvents containing 75 vol.-% organic components (DMSO, acetonitrile, acetone, ethanol, 2-propanol, THF, or dioxane) increases with increasing inverse dielectric constants of the solvents (Figure 3), indicating that blackberry formation is a charge-regulated process.^[12] The counterion-mediated attraction between polyanions might be the driving force for the self-association of

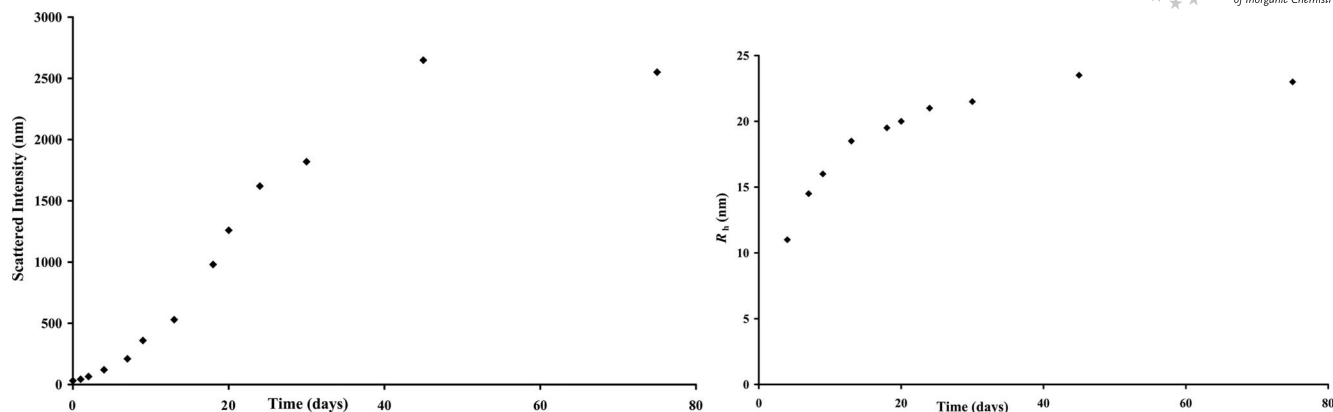


Figure 1. Change of the scattered intensity and average hydrodynamic radius (R_h) as a function of time in a solution of **1** with 60 vol.-% acetone.

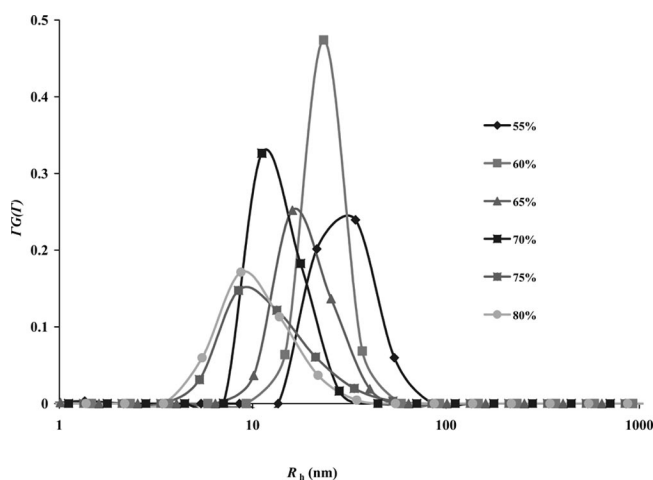


Figure 2. CONTIN analysis of DLS study on 0.1 mg **1a**/mL solutions in water/acetone mixed solvents containing 55–80 vol.-% acetone. The measurements were performed at $\approx 90^\circ$ scattering angle at 25°C .

1. No blackberry formation was observed in mixed water/DMSO solvent containing 75 vol.-% DMSO. Consequently, in Figure 3 this data point is assigned as $R_h = 0$. The obvi-

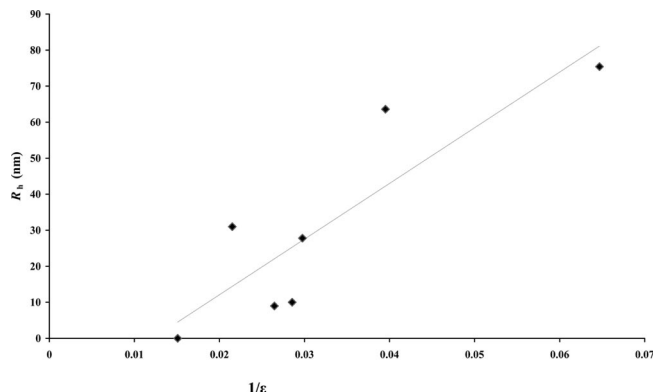


Figure 3. Plot of average hydrodynamic radii (R_h) of the blackberries formed by **1** as a function of the inverse relative dielectric constants of various mixed solvents. Dielectric constants were varied by using organic solvent/water mixtures (75 vol.-%): DMSO, acetonitrile, acetone, ethanol, 2-propanol, THF, dioxane.

ous trend shown in Figure 3 strongly suggests that the self-assembly processes in different solvents follow very similar mechanisms and can be directly compared quantitatively. This conclusion is consistent with our earlier observations for other polyanion solutions.

However, unexpected results were obtained when studying the self-assembly in the same binary solvent systems with different volume fractions. Increasing acetone contents in the solutions (i.e., decreasing dielectric constant) resulted in the formation of smaller blackberries; for example, the average blackberry size decreased from ≈ 23 to ≈ 11 nm when the acetone content was increased from 55 to 75 vol.-% (Figure 4). The hollow shells formed in different solvents have relatively narrow size distributions (Figure 2).

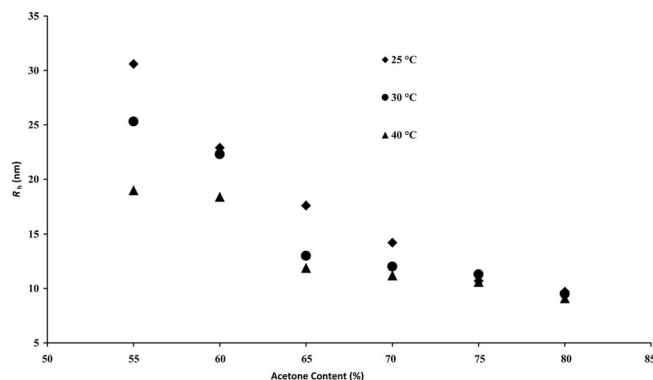


Figure 4. Average hydrodynamic radii (R_h) of **1**-based blackberries in mixed water/acetone solvents measured by DLS at different temperatures.

TEM studies were performed to further clarify the nature of the assemblies. Under high vacuum, large and spherical burst structures with an average radius of ≈ 25 nm were observed (Figure 5), further confirming that the assemblies are hollow blackberry structures. These sizes are consistent with the DLS studies ($R_h \approx 23$ nm in the solution containing 55 vol.-% acetone). Additionally, the burst assemblies had a uniform wall thickness of ≈ 7.5 nm, which could be due to the wrinkle structures after burst or even multilayer shells.

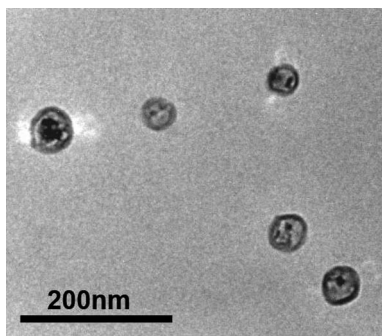


Figure 5. A typical TEM image of blackberry structure formed in 0.1 mg **1a**/mL mixed water/acetone solvent containing 55 vol.-% acetone.

To exclude the possibility of chemical reactions between the amphiphilic **1** and organic solvent molecules (i.e., ligand exchange) that might contribute to the formation of **1**-based assemblies, additional experiments were performed in other binary solvents. In those solvents, **1** demonstrated very similar self-assembly behavior to that in the acetone/water system. Polyanion **1** assembles to vesicle-like structures in mixed solvents of water and 60–80 vol.-% acetonitrile or THF. A similar relation between R_h and the solvent composition was also obtained in water/acetonitrile and water/THF mixtures, as shown in Figure 6. Increasing the organic component always decreases the size of the supramolecular assemblies. These results indicate that the self-assembly of amphiphilic **1** to blackberries is highly dependent on the solvent composition and their size is tunable.

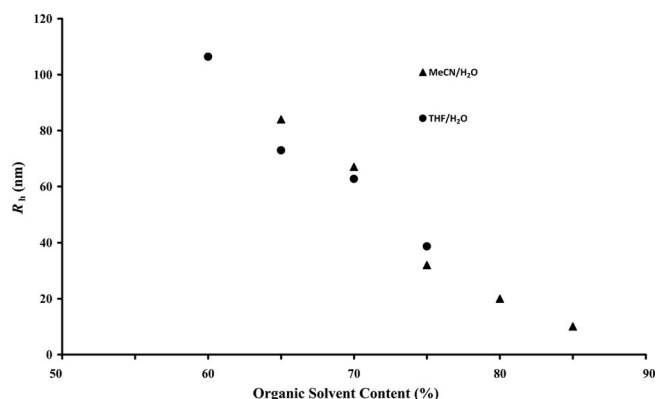


Figure 6. Average hydrodynamic radius (R_h) of **1**-based vesicles in mixed water/THF or water/CH₃CN solvents.

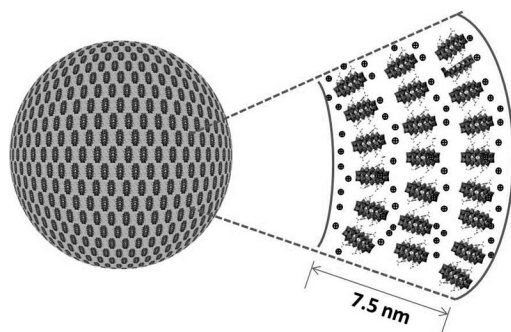
The relation between the assembly size and the solvent composition shows an unexpected, contradicting “dual effect” that follows the charge-regulation mechanism in different solvents,^[10,13] but is completely against it for different volume fractions of a binary solvent mixture. In our previously studied POM solutions (e.g., {Mo₁₃₂} in mixed water/acetone solvents^[10]), no blackberry formation occurred at low acetone contents when the polyanion carried too many charges; the blackberry size decreased with increasing dielectric constant of the solvent, suggesting that the self-assembly processes are charge regulated.^[12] How-

ever, in the present work on **1**, the size of the assemblies decreased with increasing percentage of the organic solvent. The reason for this unusual phenomenon is still unclear, but the hydrophobic domains on **1** could play an important role. Acetone is a good solvent for the organic, hydrophobic *p*-cymene, whereas water is not. Therefore, the hydrophobic interaction between the *p*-cymene groups of neighboring polyanions could be stronger at low acetone fractions, consequently leading to larger assemblies. In other words, the hydrophobic interaction becomes a more dominant driving force in relatively polar solvents for the intermolecular self-assembly of **1**.

Considering that for **1** there is no vesicle formation in mixed water/acetone solvents at low acetone contents (0–50 vol.-%), the electrostatic repulsion between the hydrophilic metal-oxide portion undoubtedly plays an important role in balancing the hydrophobic interaction between the *p*-cymene group. In the aqueous solution of **1**, each polyanion theoretically carries 27 negative charges, a charge density that is even higher than that of the hydrophilic **2**.^[8] Under these circumstances, the strong electrostatic repulsion would hinder the self-assembly of **1**, which in turn would be favored by various factors such as the hydrophobic interaction of the *p*-cymene groups and the counterion-mediated attractions. As the solvent composition is changed by increasing the acetone percentage, **1** becomes less negatively charged and the hydrophobic interaction between the *p*-cymene groups is also weakened. The balance between attractive hydrophobic interaction and electrostatic repulsion would make the self-assembly possible after passing a critical organic solvent concentration (\approx 55 vol.-% acetone). The hydrophobic interaction becomes weaker with acetone contents above 55% and consequently the vesicles become smaller. Overall, the unique solution behavior of amphiphilic **1** might be attributed to a subtle balance between repulsive electrostatic and attractive hydrophobic interactions. A similar competition between those two interactions can also be seen in protein assembly.^[14,15] For example, the polyomavirus capsid protein can assemble into a variety of single-layer hollow capsids under certain conditions, such as low pH, addition of Ca²⁺ ions, or high ionic strength. Even though the hydrophobic interaction as the dominant driving force is responsible for capsid formation, negatively charged carboxylate pairs of this protein pentamer provide a sensitive electrostatic switch that controls the assembly. The capsid protein stays as unassembled capsomeres in alkaline solution with low ionic strength. Binding of Ca²⁺ cations, or protons, or increasing the salt concentration shields the electrostatic repulsion between the terminal carboxylate pairs and promotes the assembly by burying the hydrophobic surface of the protein subunits into the capsids.^[14]

A good way of confirming the contribution from hydrophobic interactions to the assembly is to study the effect of temperature. As shown in Figure 4, in mixed water/acetone solvents, the assembly size shows weak temperature dependence in solutions containing 55–65 vol.-% acetone in the range 25–40 °C with larger assemblies formed at lower tem-

peratures. Furthermore, the effect of temperature becomes more significant in solvents with lower acetone content. This is reasonable because the solvophobic groups become more soluble in solvents with low polarity, that is, weaker hydrophobic interactions at higher acetone contents. Compared to Mn-Anderson-POM-based hybrid vesicles with long, “soft” hydrophobic alkyl tails,^[6a] the *p*-cymene groups in **1** are relatively small and rigid. Consequently, no bending of the *p*-cymene groups is possible during the vesicle assembly process. The amphiphilic **1** must pack in the vesicles in a different way compared to the Mn-Anderson-POMs. A possible packing model of **1** in the assemblies is proposed in Scheme 2. To bury these rigid, hydrophobic *p*-cymene groups protruding away from each side of the nanowheel plane, the polyanions **1** might adopt an ordered suprastructure with their molecular main plane perpendicular to the vesicle surface. This resembles the organic discotic liquid-crystal mesogen, which has a structure similar to that of **1**, and self-organizes into columnar liquid crystalline structures.^[16,17] The *p*-cymene groups between neighboring polyanions associate with each other, driven by hydrophobic attraction. According to TEM images the vesicle shell thickness is ≈ 7.5 nm, suggesting that up to three layers of polyanions might be distributed laterally in the shell. This specific blackberry packing model is also different from that of **2**, where the polyanions might be homogeneously distributed on the surface of the hollow shell with their molecular isotropic plane parallel to the surface.



Scheme 2. Schematic representation of the packing model of wheel-shaped **1**: A face-on model with orientational packing of the polyanions in the blackberries/shells with their isotropic plane perpendicular to the surface.

Another possible reason for the unexpected R_h -solvent composition relationship for **1** is that in the presence of a large fraction of organic solvent, the self-assembly mechanism changes. In some cases (e.g., mixed water/acetone solvent containing 80 vol.-% acetone), the assemblies had an average R_h value of ≈ 10 nm, even smaller than the smallest blackberries we observed before. We speculate that such small assemblies might not be blackberry or any self-assembled structures. No TEM study is available and the SLS technique becomes less accurate for R_g measurements of such small species. Instead, they might just be minicrystals formed as a result of poor solubility.

Conclusions

In summary, we report the self-assembly behavior of the amphiphilic wheel-shaped **1** with hydrophobic *p*-cymene groups in binary mixed solvents of water and various organic solvents. Polyanion **1** is unique because its behavior is different from that of fully hydrophilic POMs (such as **2**) and inorganic-organic POM hybrids containing long alkyl chains (such as {Mn-Anderson-C₁₆}). No formation of large assembled structures occurred in water/acetone solutions with acetone contents below 55 vol.-% due to the high charge density on **1**. By adjusting the solvent content, **1** becomes less negatively charged, which leads to the formation of (possibly multilayered) vesicle-like structures, perhaps partially due to hydrophobic interaction of the organic *p*-cymene ligands. The size of the assemblies constantly decreases with increasing acetone contents (55–80 vol.-%), contradicting the trend reported before for the self-assembly of polyanions controlled by the charge-regulation mechanism. However, at the same time the assembly sizes decrease with increasing dielectric constants of the organic solvents for various aqueous water/organic binary solvents (e.g., containing 75 vol.-% organic solvent). This mysterious inconsistency is not fully understood yet but it could be due to an interpolyanion hydrophobic interaction in the self-assembly process.

Experimental Section

Sample Preparation: The mixed potassium-lithium salt of polyanion **1**, $K_{16}Li_{11}[\{K(H_2O)\}_3\{Ru(p\text{-cymene})(H_2O)\}_4P_8W_{49}O_{186}(H_2O)_2\} \cdot 87H_2O$ (**1a**) was synthesized according to a published procedure.^[7] A series of 0.1 mg **1a**/mL solutions in mixed solvents of water and organic solvents (acetone, acetonitrile and THF) were prepared. Compound **1a** is quite soluble in such mixed media (up to 85 vol.-% organic solvents at 0.10 mg/mL). After all solutions were filtered into dust-free cells through Millipore filters with a 0.20 μ m pore size, the self-assembly process was monitored by using static and dynamic light scattering techniques (SLS and DLS).

Static and Dynamic Light Scattering Measurements: The BIZPM laser-light-scattering spectrometer (Brookhaven Instruments) equipped with a coherent radiation 200 mW diode-pumped solid-state (DPSS 532) laser operating at a wavelength of 532 nm and a BI-9000 correlator was used for SLS and DLS measurements. DLS measured the intensity-intensity time correlation functions at scattering angles of 30–90° at 25 °C. The correlation functions from DLS were analyzed by the CONTIN method.^[18] SLS measurements were performed over a scattering angle range of 30–150°. The data analysis of SLS is based on the Rayleigh-Gans-Debye equation.^[9]

Transmission Electron Microscopy (TEM): Transmission electron microscopy experiments were performed with a JEOL-2000FX TEM operating at an acceleration voltage of 200 kV. A drop of a solution of **1** containing supramolecular assemblies was deposited onto a carbon-coated copper EM grid and dried in air.

Acknowledgments

T. L. gratefully acknowledges support of this work by the National Science Foundation (CHE-0545983), Alfred P. Sloan Foundation,

and Lehigh University and valuable discussions with Dr. W. Kegel at Utrecht University. U. K. acknowledges support from the German Science Foundation (DFG KO-2288/3-2), the Fonds der Chemischen Industrie, and Jacobs University.

- [1] a) J. M. Lehn, *Proc. Natl. Acad. Sci. USA* **2002**, *99*, 4763–4768; b) G. M. Whitesides, M. Boncheva, *Proc. Natl. Acad. Sci. USA* **2002**, *99*, 4769–4774.
- [2] a) A. Müller, P. Kögerler, A. W. M. Dress, *Coord. Chem. Rev.* **2001**, *222*, 193–218; b) C. L. Hill, *Chem. Rev.* **1998**, *98*, 1–2 and the entire issue.
- [3] a) D. L. Long, E. Burkholder, L. Cronin, *Chem. Soc. Rev.* **2007**, *36*, 105–121; b) Y. V. Geletti, B. Botar, P. Kögerler, D. A. Hille-sheim, D. G. Musaev, C. L. Hill, *Angew. Chem. Int. Ed.* **2008**, *47*, 3896–3899.
- [4] a) Z. H. Peng, *Angew. Chem. Int. Ed.* **2004**, *43*, 930–935; b) Q. Li, Y. G. Wei, J. Hao, Y. Zhu, L. Wang, *J. Am. Chem. Soc.* **2007**, *129*, 5810–5811; c) Y. F. Song, D. L. Long, L. Cronin, *Angew. Chem. Int. Ed.* **2007**, *46*, 3900–3904.
- [5] a) D. G. Kurth, P. Lehmann, D. Volkmer, H. Cölfen, M. J. Koop, A. Müller, A. Du Chesne, *Chem. Eur. J.* **2000**, *6*, 385–393; b) H. Li, H. Sun, W. Qi, M. Xu, L. Wu, *Angew. Chem. Int. Ed.* **2007**, *46*, 1300–1303.
- [6] a) J. Zhang, Y. F. Song, L. Cronin, T. B. Liu, *J. Am. Chem. Soc.* **2008**, *130*, 14408–14409; b) C. P. Chullikkattil, P. Pradeep, M. F. Misdrahi, F. Y. Li, J. Zhang, L. Xu, D. L. Long, T. B. Liu, L. Cronin, *Angew. Chem. Int. Ed.* **2009**, *48*, 8309–8313.
- [7] S. S. Mal, N. H. Nsouli, M. H. Dickman, U. Kortz, *Dalton Trans.* **2007**, 2627–2630.
- [8] G. Liu, T. B. Liu, S. S. Mal, U. Kortz, *J. Am. Chem. Soc.* **2006**, *128*, 10103–10110.
- [9] T. B. Liu, *J. Am. Chem. Soc.* **2003**, *125*, 312–313.
- [10] M. L. Kistler, A. Bhatt, G. Liu, D. Casa, T. B. Liu, *J. Am. Chem. Soc.* **2007**, *129*, 6453–6460.
- [11] P. P. Mishra, J. Jing, L. C. Francesconi, T. B. Liu, *Langmuir* **2008**, *24*, 9308–9313.
- [12] A. A. Verhoeff, M. L. Kistler, A. Bhatt, J. Pigga, J. Gronewold, M. Klokkenburg, S. Veen, S. Roy, T. B. Liu, W. K. Kegel, *Phys. Rev. Lett.* **2007**, *99*, 066104-1–066104-4.
- [13] D. Li, J. Zhang, K. Landskron, T. B. Liu, *J. Am. Chem. Soc.* **2008**, *130*, 4226–4227.
- [14] D. M. Salunke, D. L. D. Caspar, R. L. Garcea, *Biophys. J.* **1989**, *56*, 887–900.
- [15] W. K. Kegel, P. van der Schoot, *Biophys. J.* **2004**, *86*, 3905–3913.
- [16] L. Schmidt-Mende, A. Fechtenkötter, K. Müllen, E. Moons, R. H. Friend, J. D. MacKenzie, *Science* **2001**, *293*, 1119–1122.
- [17] S. Polarz, B. Smarsly, M. Antonietti, *ChemPhysChem* **2001**, *2*, 457–461.
- [18] S. W. Provencher, *Biophys. J.* **1976**, *16*, 29–41.

Received: April 9, 2010

Published Online: June 8, 2010

Preparation of New Ligand-Deficient Thiocyanato Compounds with Cooperative Magnetic Phenomena by Thermal Decomposition of Their Ligand-Rich Precursors

Mario Wriedt^[a] and Christian Näther^{*[a]}

Keywords: Organic–inorganic hybrid composites / N ligands / Nickel / Manganese / Cobalt / Magnetic properties

The reaction of nickel thiocyanate with bipy (4,4'-bipyridine) in water at room temperature leads to the formation of the ligand-rich 1:2 (1:2 ratio between metal salt and organic ligand) hydrate $[\{\text{Ni}(\text{NCS})_2(\text{bipy})(\text{H}_2\text{O})_2\} \cdot (\text{bipy})]_n$ (**1-Ni**), which is isotypic to its analogues **1-Mn** and **1-Co** reported recently. In their crystal structure, the metal cations are coordinated by two terminal N-bonded thiocyanato anions, two water molecules, and two bridging bipy ligands in an octahedral coordination mode. These building blocks elongate in linear M–bipy–M chains, which are further connected by hydrogen bonds between H_2O and noncoordinated bipy ligands into layers. On heating these precursor compounds, two-step decomposition is observed: New ligand-rich 1:2 anhydrous compounds $[\text{M}(\text{NCS})_2(\text{bipy})_2]_n$ [M = Mn (**2-Mn**), Co (**2-Co**), and Ni (**2-Ni**)] could be identified as intermediates in the first heating step, and new ligand-deficient 1:1 compounds

$[\text{M}(\text{NCS})_2(\text{bipy})]_n$ [M = Mn (**3-Mn**), Co (**3-Co**), and Ni (**3-Ni**)] could be identified as intermediates in the second heating step. A smooth reaction pathway in their crystal structures is observed: First, water is removed, leading to directly coordinating bipy ligands, and second, half of the bipy ligands are removed, leading to μ -1,3-bridging thiocyanato anions. This structural transformation is accompanied by a dramatic change in their magnetic properties: Whereas the ligand-rich 1:2 hydrates and anhydrous compounds show only Curie–Weiss paramagnetism, the ligand-deficient 1:1 intermediates show either Curie–Weiss paramagnetism or antiferromagnetic ordering at lower temperatures, mediated by the bridging thiocyanato anions. These results are qualitatively compared with those of the related ligand-rich and ligand-deficient compounds with pyrazine and pyrimidine.

Introduction

Enormous efforts have recently been focused on the synthesis and investigations of new coordination polymers and inorganic–organic hybrid compounds.^[1] The combination of organic and inorganic components in these compounds has created a new dimension in searching for functional materials. Especially new compounds with interesting magnetic properties, such as cooperative magnetic phenomena, for example, antiferro- or ferromagnetism, are of interest.^[2]

In this context, we are interested in thermal decomposition reactions of ligand-rich precursor compounds to obtain new ligand-deficient intermediates with interesting magnetic properties. We could prove that thermal decomposition of ligand-rich precursors, which consist of paramagnetic transition metals and not bridging potential magnetic active ligands, leads in most cases to the formation of new ligand-deficient intermediates with a more condensed crystal structure.^[3–6] In comparison with their pristine crystal structures, the magnetic active ligands become bridging;

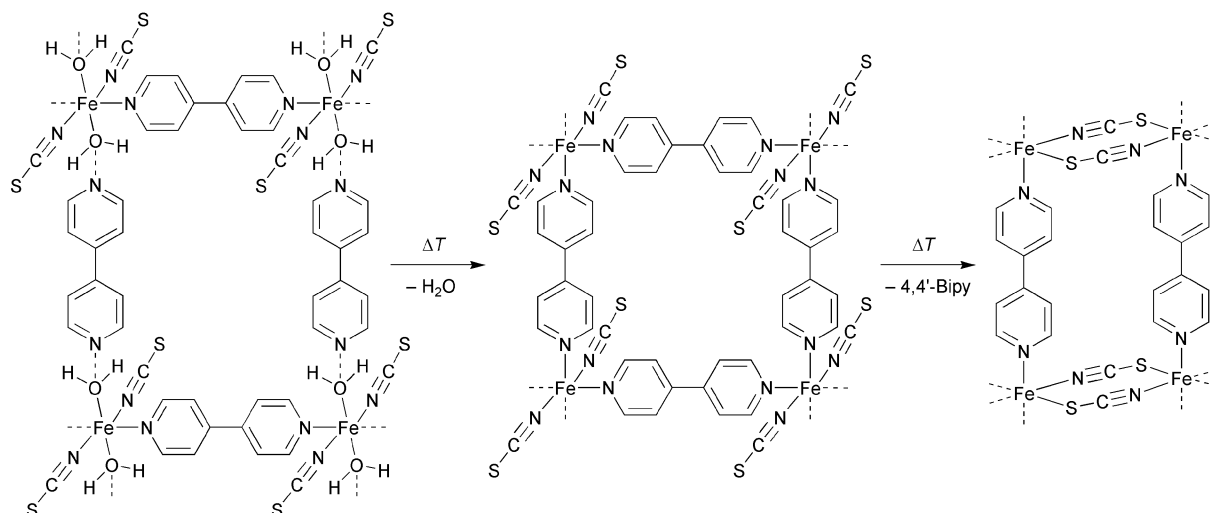
and therefore, cooperative magnetic phenomena were observed. It must be noted that these ligand-deficient compounds are mostly not accessible by reaction of their starting materials in solution, but they can always be prepared phase pure by thermal decomposition of their ligand-rich precursors.

Recently, we reported on the thermal decomposition of the ligand-rich 1:2 hydrate $[\{\text{Fe}(\text{NCS})_2(\text{bipy})(\text{H}_2\text{O})_2\} \cdot (\text{bipy})]_n$ (1:2 ratio between metal salt and organic ligand; bipy = 4,4'-bipyridine; **1-Fe**).^[3] On heating, two-step decomposition was found to occur, in which first the solvent-free 1:2 intermediate $[\text{Fe}(\text{NCS})_2(\text{bipy})_2]_n$ (**2-Fe**) and second the ligand-deficient 1:1 intermediate $[\text{Fe}(\text{NCS})_2(\text{bipy})]_n$ (**3-Fe**) could be isolated (Scheme 1). Due to the bridging thiocyanato anions only the latter exhibits an antiferromagnetic ordering state at lower temperatures and the other compounds show only Curie–Weiss behavior.

Similar thermal behavior was also reported for the ligand-rich 1:2 analogues **1-Mn**^[7,8] and **1-Co**,^[9] but none of their intermediates were structurally characterized and investigated for their magnetic properties. In the course of systematic investigations on magnetostructural correlations we prepared the analogous ligand-rich 1:2 hydrates **1-Mn**, **1-Co**, and **1-Ni** to obtain their ligand-deficient intermediates by thermal decomposition. Furthermore, for a more

[a] Institut für Anorganische Chemie, Universität zu Kiel, Max-Eyth-Straße 2, 24098 Kiel, Germany
Fax: +49-431-8801520
E-mail: cnaether@ac.uni-kiel.de

Supporting information for this article is available on the WWW under <http://dx.doi.org/10.1002/ejic.201000155>.



Scheme 1. Schematic representation of the thermal decomposition reaction of the ligand-rich 1:2 hydrate $[\{\text{Fe}(\text{NCS})_2(\text{bipy})(\text{H}_2\text{O})_2\} \cdot (\text{bipy})_n] (\mathbf{1}\text{-Fe})$.

extensive investigation of the magnetostructural correlations, we prepared the ligand-deficient 1:1 Cu compound $[\text{Cu}(\text{NCS})_2(\text{bipy})]_n (\mathbf{3}\text{-Cu})$, of which no ligand-rich analogue exists, and only its structure was reported recently.^[10] Here we report on these investigations.

Results and Discussion

Crystal Structures

The ligand-rich 1:2 hydrate $[\{\text{Ni}(\text{NCS})_2(\text{bipy})(\text{H}_2\text{O})_2\} \cdot (\text{bipy})]_n (\mathbf{1}\text{-Ni})$ is isotypic to its analogues $\mathbf{1}\text{-Mn}$,^[7,8] $\mathbf{1}\text{-Fe}$,^[11] and $\mathbf{1}\text{-Co}$ ^[9] and crystallizes in the centrosymmetric triclinic space group $P\bar{1}$ with one formula unit in the unit cell (Table 8). The crystal structure was refined by the Rietveld method with the structure model of its analogue $\mathbf{1}\text{-Co}$ as the starting structure model. In the crystal structure the metal cations are coordinated by two terminal *N*-bonded thiocyanato anions, two water molecules, and two bridging *N*-bonded bipy ligands in a slightly distorted octahedral coordination mode (Figure 1, top). These building blocks elongate in linear Ni–bipy–Ni chains, which are further connected by hydrogen bonds between H_2O and noncoordinated bipy ligands into layers (Figure 1, bottom).

The metal–metal separation through the coordinating bipy ligands is 11.3393(2) Å, and the metal–metal separation through noncoordinated bipy ligands is 15.4722(3) Å, whereas the shortest interlayer separation of two adjacent metal cations is 7.4686(2) Å. Further distances and angles around the metal center are given in Table 1 and are comparable with those found in its analogues $\mathbf{1}\text{-Mn}$, $\mathbf{1}\text{-Fe}$, and $\mathbf{1}\text{-Co}$.

The ligand-rich 1:2 anhydrous compound $[\text{Co}(\text{NCS})_2(\text{bipy})_2]_n (\mathbf{2}\text{-Co})$ is isotypic to its analogues $\mathbf{2}\text{-Ni}$ ^[12] and $\mathbf{2}\text{-Fe}$ ^[13] and crystallizes in the centrosymmetric monoclinic space group $C2/c$ with four formula units in the unit cell (Table 8). The crystal structure was refined by the Rietveld method with the structure model of its analogue $\mathbf{2}\text{-Ni}$ as the

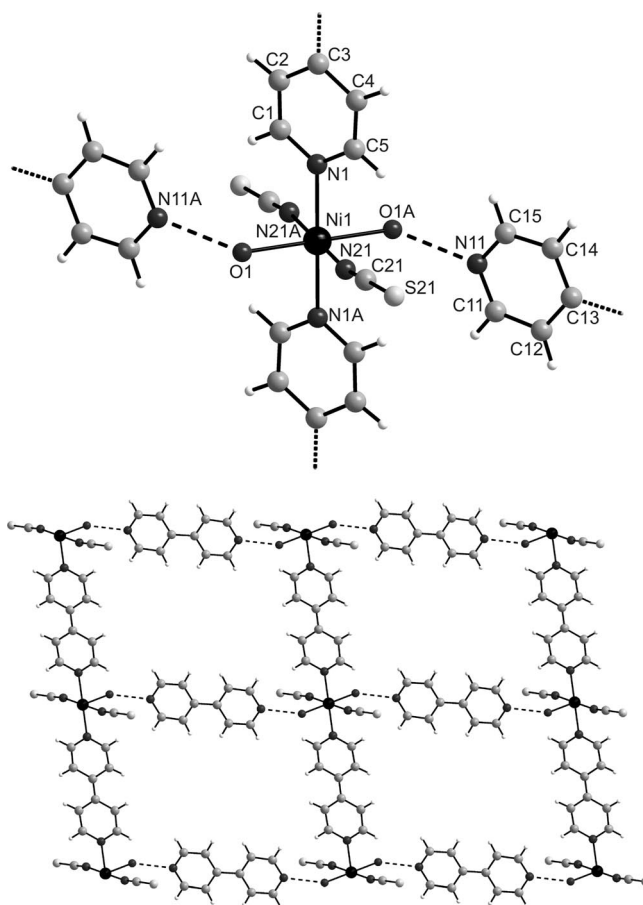


Figure 1. Crystal structure of $[\{\text{Ni}(\text{NCS})_2(\text{bipy})(\text{H}_2\text{O})_2\} \cdot (\text{bipy})]_n (\mathbf{1}\text{-Ni})$ with view of the coordination sphere of the Ni^{2+} cation with labeling (top) and with view of a single layer along the crystallographic *a* axis (bottom). The dashed lines indicate expected hydrogen bonding as it was found in the single-crystal structure of its isotypic analogues $\mathbf{1}\text{-Mn}$, $\mathbf{1}\text{-Fe}$, and $\mathbf{1}\text{-Co}$. Symmetry code A: $-x, -y, -z$.

starting structure model. In the crystal structure the metal cations are coordinated by two terminal *N*-bonded thiocy-

Table 1. Selected bond lengths [Å] and angles [°] for compound **1-Ni**.^[a]

Ni1–N1	2.196(4)	N1–Ni1–N21A	86.3(2)
Ni1–N21	2.150(5)	N1–Ni1–O1	92.0(2)
Ni1–O1	2.094(5)	N1–Ni1–O1A	88.0(2)
N1–Ni1–N21	93.7(2)	N21–Ni1–O1	90.0(2)
N21–Ni1–N21A	180	N21–Ni1–O1A	90.0(2)
N1–Ni1–N1A	180	N11–O1–Ni1	121.4(3)
O1–Ni1–O1A	180		

[a] Symmetry code A: $-x, -y, -z$.

anato anions and four bridging *N*-bonded bipy ligands in a slightly distorted octahedral coordination mode (Figure 2, left). In context to the pristine hydrate crystal structure, the metal centers in the linear Co–bipy–Co chains are now further directly connected by those bipy ligands into layers, which were not involved in metal coordination in the hydrate structure (Figure 2, right). The metal–metal separation through the bipy ligands is 11.42(2) and 11.491(4) Å, whereas the shortest interlayer separation of two adjacent metal cations is 8.374(9) Å. Further distances and angles around the metal center are given in Table 2 and are comparable to those found in its analogue **2-Ni**.

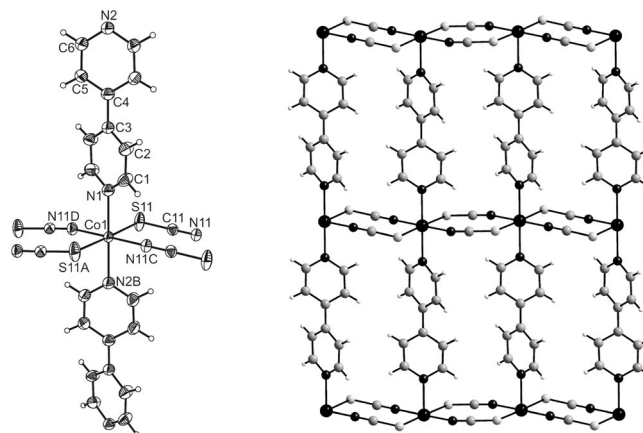
Table 2. Selected bond lengths [Å] and angles [°] for compound **2-Co**.^[a]

Co1–N1	2.11(2)	N1–Co1–N11	95.23(5)
Co1–N2	2.19(2)	N1–Co1–N21	91.13(5)
Co1–N11	2.249(9)	N2–Co1–N11	84.77(5)
Co1–N21	2.022(8)	N2–Co1–N21	88.87(5)
N1–Co1–N2	180	N11–Co1–N21	88.6(1)
N11–Co1–N11A	169.5(1)	N11–Co1–N21A	91.2(1)
N21–Co1–N21A	177.74(9)		

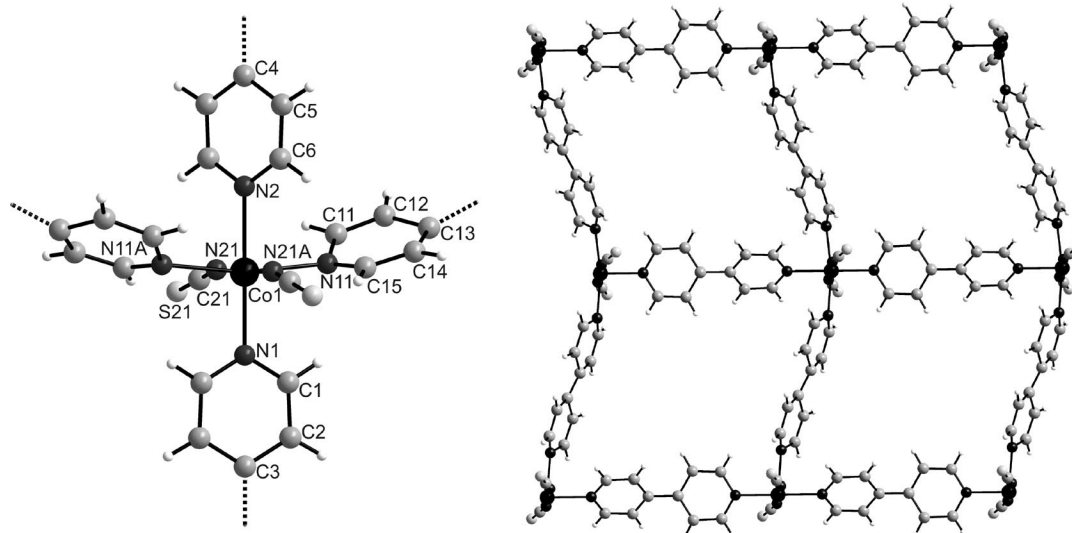
[a] Symmetry code A: $-x + 1, y, 0.5 - z$.

The ligand-deficient 1:1 compound $[\text{Co}(\text{NCS})_2(\text{bipy})]_n$ (**3-Co**) is isotypic to its analogue **3-Fe**^[13] and crystallizes in the centrosymmetric monoclinic space group $C2/c$ with four formula units in the unit cell (Table 9). In the crystal struc-

ture, the metal cations are coordinated by two bridging bipy ligands and two S and two N atoms of four bridging thiocyanato anions in a slightly distorted octahedral coordination mode (Figure 3, left). The cobalt(II) cations are *N,N'*-bridged by the bipy ligands, forming chains, which are fur-

Figure 3. Crystal structure of $[\text{Co}(\text{NCS})_2(\text{bipy})]_n$ (**3-Co**) with view of the coordination sphere of the Co^{2+} cation with labeling and displacement ellipsoids drawn at the 50% probability level (left) and with view of a single layer approximately along the crystallographic *a* axis (right). Symmetry codes A: $-x + 1, y, -z + 3/2$; B: $x, y - 1, z$; C: $-x + 1, -y, -z + 1$; D: $x, -y, z + 1/2$.Table 3. Selected bond lengths [Å] and angles [°] for compound **3-Co**.^[a]

Co1–N1	2.171(2)	N11C–Co1–S11	92.67(5)
Co1–N2B	2.190(2)	N2B–Co1–S11	90.85(2)
Co1–N11C	2.0666(16)	N11C–Co1–N1	90.18(5)
Co1–S11	2.5759(6)	N11C–Co1–N2B	89.82(5)
N1–Co1–N2B	180	N1–Co1–S11	89.15(2)
N11D–Co1–N11C	179.64(9)	N11D–Co1–S11	87.33(5)
S11A–Co1–S11	178.30(4)	C11–S11–Co1	101.88(7)

[a] Symmetry codes A: $-x + 1, y, -z + 3/2$; B: $x, y - 1, z$; C: $-x + 1, -y, -z + 1$; D: $x, -y, z + 1/2$.Figure 2. Crystal structure of $[\text{Co}(\text{NCS})_2(\text{bipy})_2]_n$ (**2-Co**) with view of the coordination sphere of the Co^{2+} cation with labeling (left) and with view of a single layer (right). Symmetry code: A: $-x + 1, y, 0.5 - z$.

ther connected by μ -1,3-bridging thiocyanato anions into layers (Figure 3, right). Selected bond lengths and angles for compound **3-Co** are summarized in Table 3.

Investigations on the Thermal Decomposition Reactions

All ligand-rich 1:2 hydrates **1-Mn**, **1-Co**, and **1-Ni** can be prepared by the facile reaction of their starting materials in solution (see Experimental Section). Because of their extended crystal structure they seem to be good candidates as precursor compounds for thermal decomposition reactions with a view to obtain new ligand-deficient compounds.

For the ligand-rich 1:2 hydrate $[\{\text{Ni}(\text{NCS})_2(\text{bipy})(\text{H}_2\text{O})_2\} \cdot (\text{bipy})]_n$ (**1-Ni**), upon heating in a thermobalance to 500 °C, three mass steps are observed in the TG curve that are accompanied with endothermic events in the DTA curve. From the MS trend scan curve, it is proven that only water ($m/z = 18$) is emitted during the first mass step and bipy ($m/z = 156$) during the second and third mass step. The DTG curve shows that these events are well separated (Figure 4). The experimental mass losses of 6.4% for the release of water in the first step and 29.4% for the release of bipy in the second step are in good agreement with that calculated $[\Delta m_{\text{theo}}(-2\text{H}_2\text{O}) = 6.9\%; \Delta m_{\text{theo}}(-\text{bipy}) = 29.9\%]$. Similar thermal behavior is also found for its analogues **1-Mn** and **1-Co**, comparable with that found in the literature (Figure S17, Supporting Information).^[8,9]

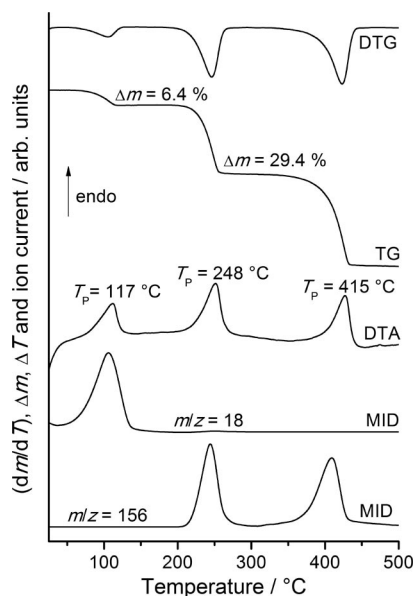


Figure 4. DTG, TG, DTA, and MS trend scan curves for $[\{\text{Ni}(\text{NCS})_2(\text{bipy})(\text{H}_2\text{O})_2\} \cdot (\text{bipy})]_n$ as a representative for the ligand-rich 1:2 hydrates **1-Mn**, **2-Co**, and **1-Ni**. Heating rate: 4 °C min⁻¹; $m/z = 18$ (water) and 156 (bipy); given are the mass changes [%] and the peak temperatures T_p [°C].

On the basis of the experimental mass losses, it can be assumed that in the first heating step the solvent-free 1:2 compounds of composition $[\text{M}(\text{NCS})_2(\text{bipy})_2]_n$ with $\text{M} = \text{Mn}$ (**2-Mn**), **Co** (**2-Co**), and **Ni** (**2-Ni**) and in the second step the ligand-deficient 1:1 compounds of composition

$[\text{M}(\text{NCS})_2(\text{bipy})]_n$ with $\text{M} = \text{Mn}$ (**3-Mn**), **Co** (**3-Co**), and **Ni** (**3-Ni**) are formed. On further heating, the remaining ligands are emitted, leading to the formation of $\text{M}(\text{NCS})_2$, which decompose on further heating.

To investigate the intermediates formed in the thermal decomposition reaction of compounds **1-Mn**, **1-Co**, and **1-Ni**, additional TG measurements were performed and stopped after the first and second TG step. The residues obtained were identified by elemental analysis (see Experimental Section), X-ray powder diffraction (Figures 5 and 6), and infrared spectroscopy. These investigations clearly prove that the intermediates obtained in the first TG step concern to ligand-rich 1:2 anhydrous compounds $[\text{M}(\text{NCS})_2(\text{bipy})_2]_n$, and the intermediates obtained in the second TG step concern to ligand-deficient 1:1 compounds $[\text{M}(\text{NCS})_2(\text{bipy})]_n$.

Regarding the XRPD patterns of the ligand-rich 1:2 anhydrous compounds **2-Mn**, **2-Co**, and **2-Ni**, it can be assumed that the structures of all compounds are very similar (Figure 5) and that compound **2-Co** is probably isotypic to compound **2-Ni** (Figure 5, compare B with C/D). The structure of compound **2-Ni** was determined by single-crystal analysis recently,^[12] and therefore, the crystal structure of compound **2-Co** was refined by the Rietveld method with the structure model of compound **2-Ni** as the starting model (see the section on Crystal Structures). All attempts to retrieve structural information on compound **2-Mn** were unsuccessful due to extreme broadening of the XRPD reflections (Figure 5, A).

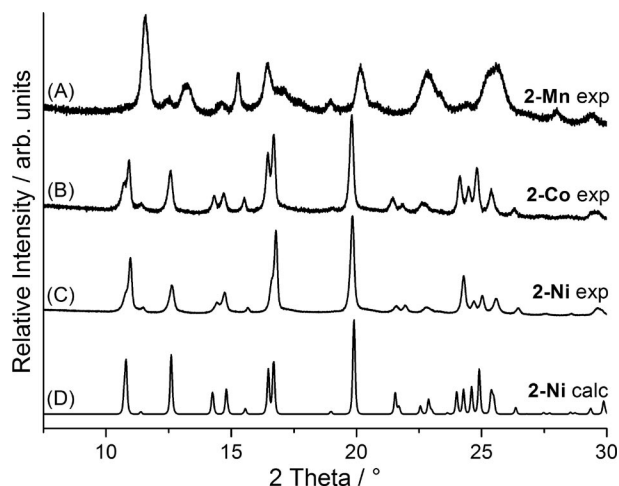


Figure 5. Experimental XRPD patterns of the ligand-rich 1:2 anhydrous compounds $[\text{M}(\text{NCS})_2(\text{bipy})_2]_n$ with $\text{M} = \text{Mn}$ (**2-Mn**; A), **Co** (**2-Co**; B), and **Ni** (**2-Ni**; C) obtained in the first TG step in the thermal decomposition reaction of their ligand-rich 1:2 hydrates as well as XRPD pattern calculated from single-crystal analysis^[12] for $[\text{Ni}(\text{NCS})_2(\text{bipy})_2]_n$ (**2-Ni**; D).

However, the coordination mode of the thiocyanato anion (terminal or bridging) can be determined by infrared spectroscopy. In the case of terminally *N*-bonded thiocyanato anions the very strong asymmetric N–C stretching vibration is observed at about 2050 cm⁻¹, whereas for the μ -1,3-bridging mode this vibration is located around

2100 cm^{-1} .^[14] For compounds **2-Co** and **2-Ni** values of 2063 and 2073 cm^{-1} are found, which shows that the anions are terminally *N*-bonded (Figure S5 and S6, Supporting Information). In contrast, for **2-Mn** two bands at 2049 and 2083 cm^{-1} are observed, indicating two kinds of terminally *N*-bonded thiocyanato anions with the latter related to the presence of the hydrate precursor (Figure S4, Supporting Information). We really have no explanation for this, because this additional band is always present independent of the temperature at which **2-Mn** is isolated in the first TG step. Therefore, it is unlikely that it belongs to contamination with **1-Mn**.

The XRPD patterns of the ligand-deficient 1:1 compounds **3-Mn**, **3-Co**, and **3-Ni** obtained by thermal decomposition show similarities, indicating that all structures are related. However, if the patterns of **3-Mn** and **3-Ni** are compared with those calculated for **3-Co** and **3-Fe** (Figure 6, compare A, C vs. D; Figure S18 and S19, Supporting Information, compare B vs. C). However, regardless of the temperature at which the intermediates were isolated in the second TG step, these reflections are always present, and for all the isolated samples elemental analysis clearly shows that they are pure and that the composition exactly matches that for the corresponding 1:1 compounds. Therefore, contaminations with the ligand-rich precursor compounds can definitely be excluded. To investigate this phenomenon in more detail, temperature-dependent XRPD measurements were performed starting with **1-Mn** and **1-Ni**. Interestingly, at higher temperatures the additional reflections disappear and the pattern clearly shows that these compounds are isotypic to **3-Fe** and **3-Co** at higher temperatures (Figures S18 and S19, Supporting Information, compare A vs. C). On cooling, the additional reflections appear again, which indicate that a structural phase transformation occurs. The powder pattern can be indexed on the basis of a triclinic unit cell that is related to the monoclinic unit cell found for

3-Co and **3-Fe**, but we were not able to solve the structure. In this context, it must be mentioned that **3-Mn** cannot be prepared in solution, but if $\text{Ni}(\text{SCN})_2$ is treated with bipy in water a residue is isolated, whose X-ray powder pattern is a perfect match to that of the intermediate obtained by thermal decomposition (Figure S20, Supporting Information). Therefore, it is proven that **3-Mn** and **3-Ni** are phase pure, which is in agreement with all other investigation.

For compounds **3-Mn** and **3-Ni** a similar coordination topology is expected, which was confirmed by IR spectroscopic data. Explicit shifting of the very strong asymmetric N–C stretching vibration of the thiocyanato anion to higher values in comparison to their precursors (2092 cm^{-1} for **3-Mn**, 2105 cm^{-1} for **3-Co**, and 2117 cm^{-1} for **3-Ni**) proves μ -1,3-bridging thiocyanato anions (Figures S7–S9, Supporting Information).

Magnetic Investigations

To investigate all compounds for magnetostructural correlations, the temperature dependence of their susceptibility was investigated by applying a magnetic field of $H = 0.1$ and 1 T in the temperature range of 300–2 K (Figure 7). It must be noted that magnetic measurements were already reported for compound **1-Mn**, but for comparison this compound was also investigated. However, these results are in accordance with that found in the literature.^[8]

In all compounds the metal centers are separated by eight atoms of the bipy ligand, and therefore, no significant magnetic exchange interactions mediated by this ligand can be expected. Thus, cooperative magnetic phenomena can only be observed in those compounds for which the metal centers are bridged by the thiocyanato anions, which is the case in the ligand-deficient 1:1 intermediates **3-Mn**, **3-Co**, and **3-Ni** and for literature known 1:1 compound **3-Cu**.^[10]

For the ligand-rich 1:2 hydrates **1-Mn**, **1-Co**, and **1-Ni** and the ligand-rich 1:2 anhydrous intermediates **2-Mn**, **2-Co**, and **2-Ni** only Curie–Weiss paramagnetism is found (Figure 7, A and C). Just the negative Weiss constant θ for compounds **1-Co** (–5.25 K), **2-Mn** (–4.78 K), and **2-Co** (–0.76 K) as well as the positive Weiss constant for compounds **1-Mn** (0.18 K), **1-Ni** (17.69 K), and **2-Ni** (5.97 K) reveal weak net antiferro- or rather ferromagnetic interactions (Tables 4 and 5). Above approximately 25 K, the decrease in the values of $\chi_M T$ upon cooling indicates consistent weak antiferromagnetic interactions between adjacent metal centers in compounds **1-Mn**, **1-Co**, and **1-Ni** (Figure 7, B and D). The effective magnetic moments μ_{eff} for compounds **1-Mn** (5.95 μ_B) and **2-Mn** (5.81 μ_B) as well as for compounds **1-Ni** (2.80 μ_B) and **2-Ni** (2.78 μ_B) are in good agreement with their spin-only values for their high-spin states ($S = 5/2$ for Mn^{2+} and 1 for Ni^{2+} , $g = 2.00$). In contrast, for compounds **1-Co** (4.84 μ_B) and **2-Co** (4.93 μ_B), μ_{eff} is much larger than the spin-only value (3.87 μ_B) for a high-spin Co^{2+} ion ($S = 3/2$, $g = 2.00$; Tables 4 and 5). However, it is well documented that a significant spin-orbit cou-

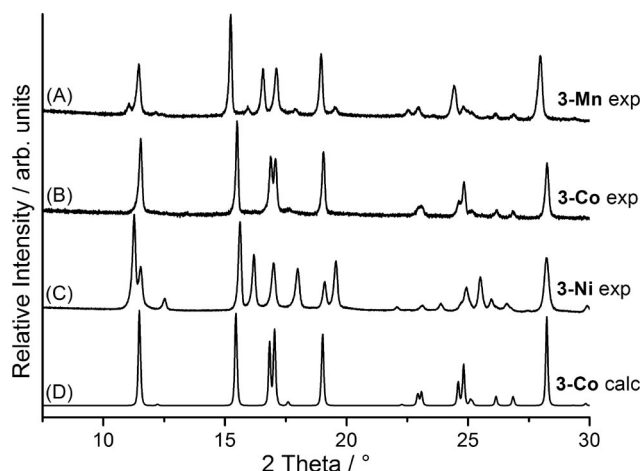


Figure 6. Experimental XRPD patterns of the ligand-deficient 1:1 compounds $[\text{M}(\text{NCS})_2(\text{bipy})]_n$ with (A) $\text{M} = \text{Mn}$ (**3-Mn**), (B) Co (**3-Co**), and (C) Ni (**3-Ni**) obtained in the second TG step in the thermal decomposition reaction of their ligand-rich 1:2 hydrates as well as (D) XRPD pattern calculated from single-crystal analysis of $[\text{Co}(\text{NCS})_2(\text{bipy})]_n$ (**3-Co**).

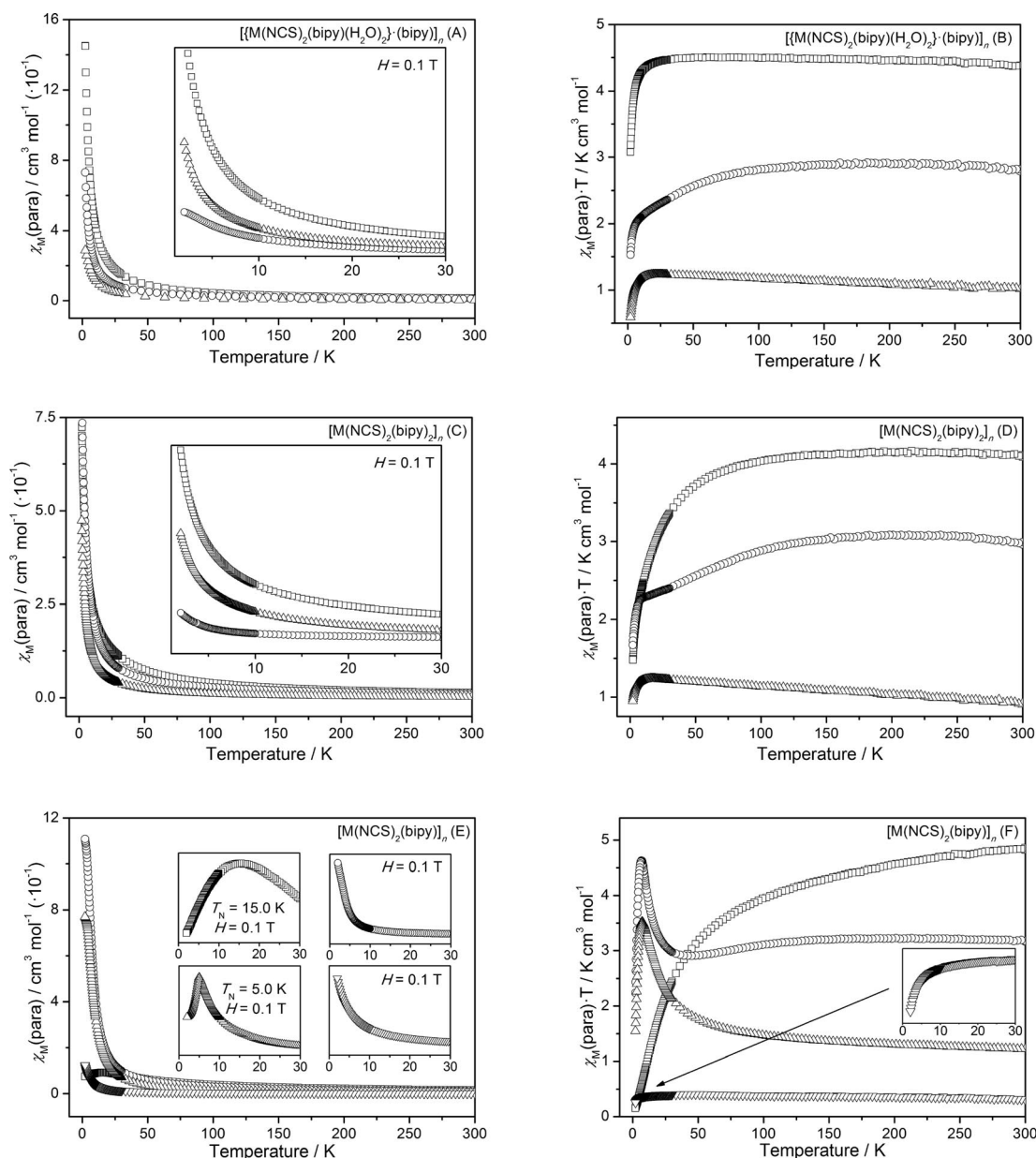


Figure 7. Paramagnetic susceptibility (A, C, E) and $\chi_M T$ (B, D, F) as a function of temperature at $H = 1$ T for the ligand-rich 1:2 hydrates **1-Mn**, **1-Co**, and **1-Ni** (A, B), the anhydrous 1:2 intermediates **2-Mn**, **2-Co**, and **2-Ni** (C, D), and the ligand-deficient 1:1 intermediates **3-Mn**, **3-Co**, **3-Ni**, and **3-Cu** (E, F) (\square = Mn; \circ = Co, \triangle = Ni, ∇ = Cu). The insets in the graphs on the left show measurements at a lower magnetic field of $H = 0.1$ T in the low-temperature ranges.

pling/zero-field splitting with g values strongly deviating from 2.00 yields effective magnetic moments between 4.3 and $5.2 \mu_B$.^[15]

Table 4. Results of the fits of the magnetic susceptibility data with the Curie–Weiss law for the ligand-rich 1:2 hydrates.

	[M(NCS) ₂ (bipy)(H ₂ O) ₂ (bipy)] _n		
	1-Mn	1-Co	1-Ni
$C / \text{cm}^3 \text{K mol}^{-1}$	4.43	2.93	0.98
θ / K	0.18	−5.25	17.69
$\mu_{\text{eff}} (\text{exp.}) / \mu_B$	5.95	4.84	2.80
$\mu_{\text{eff}} (\text{calcd.})^{[15]} / \mu_B$	5.92	3.87	2.83
Fit / K	2–300	20–300	60–300

For the ligand-deficient 1:1 compounds **3-Mn**, **3-Co**, **3-Ni**, and **3-Cu**, no consistent magnetic behavior is found. Only compounds **3-Mn** and **3-Ni** show a long-range antiferromagnetic ordering at lower temperatures ($T_N = 15.0$ K for **3-Mn** and 5.0 K for **3-Ni**), which must be mediated by the bridging thiocyanato anions. This is obvious by a sharp maximum in the χ_M vs. T curves (Figure 7, E). For compound **3-Mn**, the negative Weiss constant (-38.17 K) and the decrease in the values of $\chi_M T$ upon cooling (Figure 7, F) confirm the antiferromagnetic behavior, whereas for compound **3-Ni** net ferromagnetic interactions are found, which is obvious from the positive Weiss constant (21.85 K) and increasing values of $\chi_M T$ upon cooling to 7.2 K (Fig-

Table 5. Results of the fits of the magnetic susceptibility data with the Curie–Weiss law for the ligand-rich 1:2 anhydrous intermediates.

	[M(NCS) ₂ (bipy) ₂] _n		
	2-Mn	2-Co	2-Ni
$C / \text{cm}^3 \text{K mol}^{-1}$	4.22	3.05	0.97
θ / K	−4.78	−0.76	5.97
$\mu_{\text{eff}} (\text{exp.}) / \mu_{\text{B}}$	5.81	4.93	2.78
$\mu_{\text{eff}} (\text{calcd.})^{[15]} / \mu_{\text{B}}$	5.92	3.87	2.83
Fit / K	30–300	100–300	100–300

ure 7, F). Above this temperature, antiferromagnetic interactions are present. The effective moments are consistent with their calculated spin-only values (Table 6).

Table 6. Results of the fits of the magnetic susceptibility data with the Curie–Weiss law for the ligand-deficient 1:1 compounds.

	[M(NCS) ₂ (bipy)] _n			3-Cu
	3-Mn	3-Co	3-Ni	
$C / \text{cm}^3 \text{K mol}^{-1}$	5.45	3.26	1.15	0.37
θ / K	−38.17	−4.26	21.85	0.96
$\mu_{\text{eff}} (\text{exp.}) / \mu_{\text{B}}$	5.95	5.11	3.03	1.72
$\mu_{\text{eff}} (\text{calcd.})^{[15]} / \mu_{\text{B}}$	5.92	3.87	2.83	1.73
T_{N} / K	15.0	—	5.0	—
Fit / K	50–300	50–300	50–300	2–200

For the ligand-deficient 1:1 compounds **3-Co** and **3-Cu**, only Curie–Weiss paramagnetism is found (Figure 7, E). The values of the Weiss constant for compounds **3-Co** (−4.62 K) and **3-Cu** (0.96 K) indicate weak net antiferro- or ferromagnetic interactions, respectively (Table 6). The χ_{MT} values upon cooling are consistent with those interactions (Figure 7, F). For compound **3-Co**, in the temperature range 300–45 K, a smooth decrease is observed, reaching a sharp maximum at 7.6 K. For compound **3-Cu**, in the temperature range 300–48 K, a smooth increase is observed with a following smooth decrease. The effective magnetic moment for compound **3-Co** (5.11 μ_{B}) is much higher than the spin-only value for a high-spin Co^{2+} ion (see above), whereas μ_{eff} for compound **3-Cu** (1.72 μ_{B}) corresponds to the spin-only value (1.73 μ_{B}) for a single Cu^{2+} ion ($S = 1/2$, $g = 2.00$).

In this context it is of special interest to compare the magnetic properties of all compounds with those of the related compounds with pyrazine and pyrimidine as organic spacer ligands, for which also 1:2 and 1:1 compounds exist.^[5,6,13,16–20] In all the ligand-rich 1:2 compounds the metal centers are connected by organic spacer ligands into layers and the thiocyanato anions are only terminally *N*-bonded. In contrast, in the corresponding ligand-deficient 1:1 compounds the metal centers are connected through the organic spacer ligands into chains, which are further connected by the thiocyanato anions into layers. Thus, the coordination topology is always the same for compounds of identical stoichiometry. In the present work we have used bipy as an organic spacer ligand, which cannot mediate magnetic exchange interactions. Consequently, in the ligand-rich 1:2 compounds, in which the thiocyanato anions do not bridge the metal centers, only Curie–Weiss paramag-

netism is found. However, the thiocyanato anions act as μ -1,3-bridging ligands in the ligand-deficient 1:1 compounds, which leads to antiferromagnetic ordering in compounds **3-Mn**, **3-Fe**, and **3-Ni** (Table 7).

Table 7. Magnetic properties of related ligand-rich 1:2 and ligand-deficient 1:1 compounds on the basis of different organic spacer ligands, but with same coordination topology.

	4,4'-Bipyridine		Pyrazine		Pyrimidine	
	1:2	1:1	1:2	1:1	1:2	1:1
Mn	CW ^[a] ^[8]	T_{N} ^[a]	CW ^[17,19]	T_{N} ^[19]	T_{N} ^[5,17]	T_{N} ^[5]
Fe	CW ^[13]	T_{N} ^[13]	T_{N} ^[16,17,20]	CW ^[16]	T_{N} ^[5,17]	T_{N} ^[5]
Co	CW ^[a]	CW ^[a]	CW ^[16–18]	CW ^[16]	T_{C} ^[6,17,18]	T_{N} ^[6]
Ni	CW ^[a]	T_{N} ^[a]	CW ^[16,17]	CW ^[16]	T_{C} ^[6,17]	T_{N} ^[6]

[a] This work; T_{N} represents antiferromagnetic, T_{C} ferromagnetic ordering, and CW Curie–Weiss behavior.

This situation changes dramatically if pyrazine is used as an organic spacer ligand, which can propagate magnetic exchange interactions. In this case, an antiferromagnetic ordering is already observed in the ligand-rich 1:2 Fe compound, whereas Mn, Co, and Ni still show only Curie–Weiss behavior. Surprisingly, in the corresponding ligand-deficient 1:1 compounds antiferromagnetic ordering is only observed in the Mn compound (Table 7).

Moreover, if pyrazine is exchanged by pyrimidine the influence of the organic spacer ligands become obvious. In this case, only three atoms participate in magnetic exchange interactions. Therefore, a completely different behavior is found so that for all ligand-rich 1:2 and ligand-deficient 1:1 compounds cooperative magnetic phenomena are found and two of the four ligand-rich 1:2 compounds show ferromagnetism (Table 7).

Even if such systematic work on structure–property relationships is really needed, it shows that the overall situation is much more complex. However, in these considerations, only the influence of the ligands is discussed, which is admittedly too simple, because the influence of the magneto-orbitals of the cations should not be neglected; the geometrical changes around the metal centers must also be taken into account.

Conclusion

In this contribution, investigations on the thermal and magnetic properties of several coordination polymers based on metal thiocyanates and 4,4'-bipyridine as an organic spacer ligand were reported. Starting with the synthesis of the ligand-rich 1:2 hydrates **1-Mn**, **1-Co**, and **1-Ni** in solution, the corresponding ligand-rich 1:2 anhydrous compounds **2-Mn**, **2-Co**, and **2-Ni** and the ligand-deficient 1:1 compounds **3-Mn**, **3-Co**, and **3-Ni** were prepared by thermal decomposition. It must be pointed out that compounds **3-Co** and **3-Ni** can only be prepared if a large excess of metal salt is used and that compounds **2-Mn**, **2-Co**, **2-Ni**, and **3-Mn** cannot be prepared if the synthesis is performed in solution. This is completely different if thermal decomposition reactions are used, in which all compounds are easily obtained phase-pure and in quantitative yield. In this

context, it must be mentioned that the use of thermal decomposition reactions for the preparation of coordination polymers provides additional advantageous in order that compounds are obtained, in which the coordination networks are much more condensed in comparison to those in the precursor compounds. This is especially useful if precursors were decomposed that contain small anionic ligands, which are only terminally bonded to the metal cations. Dependent on the complexity of the precursors a number of intermediates of different connectivity are formed by thermal treatment, which finally must lead to compounds in which the metal centers are now bridged by the anionic ligands. It is absolutely clear that amongst others, exactly such compounds are of special interest in the context of magnetic exchange interactions. In addition, systematic investigations on such systems like those presented in this work allow investigation of structure–property relationships, because compounds with simple and predictable coordination topologies are obtained, which is always the same for compounds of identical stoichiometry.

However, even for simple systems it is markedly difficult to find at least simple rules for the correlations between structure and property, which is obvious if the magnetic properties of the bipy compounds presented in this work are compared with those of the analogous coordination polymers with pyrazine and pyrimidine reported recently.

Experimental Section

Synthesis: MnCl_2 , $\text{Co(NCS)}_2 \cdot \text{H}_2\text{O}$, Ni(NCS)_2 , and 4,4'-bipyridine were obtained from Alfa Aesar and KNCS was obtained from Fluka. Cu(NCS)_2 was prepared by the reaction of equimolar amounts of KNCS and CuSO_4 in water. The black precipitate was filtered off immediately and washed with water. The residue was dried with concentrated H_2SO_4 .

Catena[bis(isothiocyanato-*N*)diaqua(μ_2 -4,4'-bipy-*N,N'*)manganese(II) 4,4'-bipy Solvate] (1-Mn): Light-yellow crystalline powder was prepared by the reaction of MnCl_2 (125.8 mg, 1.0 mmol), KNCS (194.4 mg, 2 mmol), and 4,4'-bipyridine (312.4 mg, 2.0 mmol) in water (5 mL). After stirring this mixture for 3 d at room temperature, the obtained residue was filtered, washed with water, ethanol, and ethyl ether, and dried in air. Yield based on the metal salt: 240.1 mg (46.2%). The purity was checked by XRPD (Figure S11, Supporting Information). $\text{C}_{22}\text{H}_{20}\text{MnN}_6\text{O}_2\text{S}_2$ (519.5): calcd. C 50.86, H 3.88, N 16.18, S 12.34; found C 51.02, H 3.92, N 16.38, S 12.49. IR (KBr): $\tilde{\nu}$ = 3418 (m), 2839 (br.), 2081 (vs), 1942 (w), 1679 (w), 1605 (s), 1595 (s), 1537 (m), 1490 (w), 1410 (m), 1320 (w), 1244 (m), 1060 (m), 1001 (w), 808 (s), 730 (w), 622 (s), 531 (w), 460 (w) cm^{-1} (Figure S1, Supporting Information).

Catena[bis(isothiocyanato-*N*)diaqua(μ_2 -4,4'-bipy-*N,N'*)cobalt(II) 4,4'-bipy Solvate] (1-Co): Light-pink crystalline powder was prepared by the reaction of $\text{Co(NCS)}_2 \cdot \text{H}_2\text{O}$ (179.6 mg, 0.93 mmol) and 4,4'-bipyridine (312.4 mg, 2.0 mmol) in ethanol (6 mL). After stirring this mixture for 3 d at room temperature, the obtained residue was filtered, washed with water, ethanol, and ethyl ether, and dried in air. Yield based on the metal salt: 397.8 mg (81.7%). The purity was checked by XRPD (Figure S12, Supporting Information). $\text{C}_{22}\text{H}_{20}\text{CoN}_6\text{O}_2\text{S}_2$ (523.5): calcd. C 50.48, H 3.85, N 16.05, S 12.25; found C 50.36, H 3.75, N 15.96, S 12.22. IR (KBr): $\tilde{\nu}$ =

3409 (m), 3066 (w), 2895 (br.), 2103 (vs), 1607 (s), 1536 (m), 1489 (w), 1406 (m), 1320 (w), 1214 (m), 1068 (m), 1000 (w), 808 (s), 730 (w), 632 (m), 470 (w) cm^{-1} (Figure S2, Supporting Information).

Catena[bis(isothiocyanato-*N*)diaqua(μ_2 -4,4'-bipy-*N,N'*)nickel(II) 4,4'-bipy Solvate] (1-Ni): Light-blue crystalline powder was prepared by the reaction of Ni(NCS)_2 (162.6 mg, 0.93 mmol) and 4,4'-bipyridine (312.4 mg, 2.0 mmol) in ethanol (6 mL). After stirring this mixture for 3 d at room temperature, the obtained residue was filtered, washed with water, ethanol, and ethyl ether, and dried in air. Yield based on the metal salt: 415.1 mg (85.3%). $\text{C}_{22}\text{H}_{20}\text{NiN}_6\text{O}_2\text{S}_2$ (523.3): calcd. C 50.50, H 3.85, N 16.06, S 12.26; found C 50.79, H 3.79, N 16.02, S 12.31. IR (KBr): $\tilde{\nu}$ = 3421 (m), 3068 (w), 2883 (br.), 2106 (vs), 1942 (w), 1609 (s), 1536 (m), 1491 (w), 1405 (m), 1319 (w), 1214 (m), 1070 (m), 1002 (w), 807 (s), 730 (w), 622 (m), 475 (w) cm^{-1} (Figure S3, Supporting Information).

Poly[bis(isothiocyanato-*N*)bis(μ_2 -4,4'-bipy-*N,N'*)manganese(II)] (2-Mn): This compound cannot be prepared in solution. However, a light-yellow crystalline powder of 2-Mn was obtained as a residue in the first TG step of the thermal decomposition reaction of 1-Mn. $\text{C}_{22}\text{H}_{16}\text{MnN}_6\text{S}_2$ (483.5): calcd. C 54.65, H 3.34, N 17.38, S 13.26; found C 54.40, H 3.52, N 17.25, S 13.26. IR (KBr): $\tilde{\nu}$ = 3398 (br.), 3043 (w), 2084 (s), 2049 (vs), 1604 (s), 1533 (m), 1486 (w), 1406 (m), 1320 (w), 1219 (m), 1067 (w), 1045 (w), 1006 (w), 807 (s), 732 (w), 627 (m), 477 (w) cm^{-1} (Figure S4, Supporting Information).

Poly[bis(isothiocyanato-*N*)bis(μ_2 -4,4'-bipy-*N,N'*)cobalt(II)] (2-Co): This compound cannot be prepared in solution. However, a light-pink crystalline powder of 2-Co was obtained as a residue in the first TG step of the thermal decomposition reaction of 1-Co. $\text{C}_{22}\text{H}_{16}\text{CoN}_6\text{S}_2$ (488.5): calcd. C 54.21, H 3.31, N 17.24, S 13.16; found C 54.25, H 3.35, N 17.18, S 13.17. IR (KBr): $\tilde{\nu}$ = 3424 (br.), 3040 (w), 2063 (vs), 1605 (s), 1534 (m), 1487 (w), 1410 (m), 1320 (w), 1219 (m), 1070 (w), 1008 (w), 804 (m), 731 (w), 627 (m), 575 (w), 476 (w) cm^{-1} (Figure S5, Supporting Information).

Poly[bis(isothiocyanato-*N*)bis(μ_2 -4,4'-bipy-*N,N'*)nickel(II)] (2-Ni): This compound cannot be prepared in solution. However, a light-blue crystalline powder of 2-Ni was obtained as a residue in the first TG step of the thermal decomposition reaction of 1-Ni. $\text{C}_{22}\text{H}_{16}\text{NiN}_6\text{S}_2$ (487.2): calcd. C 54.23, H 3.31, N 17.25, S 13.16; found C 54.12, H 3.24, N 17.34, S 13.23. IR (KBr): $\tilde{\nu}$ = 3451 (br.), 3040 (w), 2877 (w), 2077 (vs), 1606 (s), 1535 (m), 1487 (m), 1410 (m), 1321 (w), 1217 (s), 1072 (m), 1009 (w), 804 (s), 731 (w), 629 (m), 576 (w), 540 (w), 485 (w) cm^{-1} (Figure S6, Supporting Information).

Poly[bis(μ_2 -thiocyanato-*N,S*)(μ_2 -4,4'-bipy-*N,N'*)manganese(II)] (3-Mn): This compound cannot be prepared in solution. However, a white crystalline powder of 3-Mn was obtained as a residue in the second TG step of the thermal decomposition reaction of 1-Mn. $\text{C}_{12}\text{H}_8\text{MnN}_4\text{S}_2$ (327.8): calcd. C 44.04, H 2.46, N 17.12, S 19.59; found C 43.94, H 2.59, N 17.15, S 19.61. IR (KBr): $\tilde{\nu}$ = 3430 (br.), 3064 (w), 2861 (w), 2092 (vs), 1986 (w), 1606 (m), 1532 (w), 1490 (w), 1412 (m), 1320 (w), 1201 (m), 1071 (w), 1007 (w), 859 (w), 815 (m), 717 (w), 630 (m), 573 (w), 475 (w) cm^{-1} (Figure S7, Supporting Information).

Poly[bis(μ_2 -thiocyanato-*N,S*)(μ_2 -4,4'-bipy-*N,N'*)cobalt(II)] (3-Co): Light-purple crystalline powder was prepared by the reaction of $\text{Co(NCS)}_2 \cdot \text{H}_2\text{O}$ (772.5 mg, 4.0 mmol) and 4,4'-bipyridine (156.2 mg, 1.0 mmol) in water (7 mL). After stirring this mixture for 3 d at room temperature, the obtained residue was filtered, washed with water, ethanol, and ethyl ether, and dried in air. Yield based on 4,4'-bipyridine: 305.8 mg (92.3%). The purity was

checked by XRPD (Figure S13, Supporting Information). $\text{C}_{12}\text{H}_8\text{CoN}_4\text{S}_2$ (331.3): calcd. C 43.51, H 2.43, N 16.91, S 19.36; found C 43.44, H 2.42, N 16.96, S 19.44. IR (KBr): $\tilde{\nu}$ = 3432 (br.), 3053 (w), 2105 (vs), 1948 (w), 1605 (s), 1533 (m), 1490 (w), 1411 (m), 1330 (w), 1221 (m), 1071 (w), 1009 (w), 859 (w), 808 (m), 632 (m), 573 (w), 503 (w), 463 (w) cm^{-1} (Figure S13, Supporting Information). Compound **3-Co** can also be prepared by thermal decomposition of compound **1-Co** in quantitative yield. Purple block-shaped single crystals suitable for X-ray structure determination were grown in a snap vial at room temperature without stirring by reaction of $\text{Co}(\text{NCS})_2 \cdot \text{H}_2\text{O}$ (38.6 mg, 0.2 mmol) and 4,4'-bipyridine (15.6 mg, 0.1 mmol) in water (2 mL).

Poly[bis(μ_2 -thiocyanato-*N,S*)(μ_2 -4,4'-bipy-*N,N'*)nickel(II)] (3-Ni): Light-green crystalline powder was prepared by the reaction of $\text{Ni}(\text{NCS})_2$ (699.4 mg, 4.0 mmol) and 4,4'-bipyridine (156.2 mg, 1.0 mmol) in water (7 mL). After stirring this mixture for 3 d at room temperature, the obtained residue was filtered, washed with water, ethanol, and ethyl ether, and dried in air. Yield based on 4,4'-bipyridine: 295.3 mg (89.2%). $\text{C}_{12}\text{H}_8\text{NiS}_2$ (331.0): calcd. C 43.54, H 2.44, N 16.92, S 19.37; found C 43.60, H 2.45, N 16.92, S 19.32. IR (KBr): $\tilde{\nu}$ = 3071 (w), 2901 (w), 2117 (vs), 1606 (m), 1533 (w), 1490 (w), 1416 (w), 1319 (w), 1220 (m), 1069 (w), 1010 (w), 859 (w), 809 (m), 633 (m), 573 (w), 507 (w), 475 (w) cm^{-1} (Figure S9, Supporting Information). Compound **3-Ni** can also be prepared by thermal decomposition of compound **1-Ni** in quantitative yield.

Poly[bis(μ_2 -thiocyanato-*N,S*)(μ_2 -4,4'-bipy-*N,N'*)copper(II)] (3-Cu): Green crystalline powder was prepared by the reaction of $\text{Cu}(\text{NCS})_2$ (89.9 mg, 0.5 mmol) and 4,4'-bipyridine (320.4 mg, 4.0 mmol) in a mixture of water (2 mL) and ethanol (2 mL). After stirring this mixture for 3 d at room temperature, the obtained residue was filtered, washed with water, ethanol and ethyl ether, and dried in air. Yield based on the metal salt: 141.1 mg (84.0%). The purity was checked by XRPD (Figure S14, Supporting Information). $\text{C}_{12}\text{H}_8\text{CuN}_4\text{S}_2$ (335.9): calcd. C 42.91, H 2.40, N 16.68, S 19.09; found C 42.48, H 2.24, N 16.21, S 18.88. IR (KBr): $\tilde{\nu}$ = 3431 (br.), 3073 (w), 2918 (w), 2107 (vs), 1609 (m), 1534 (w), 1491 (w), 1413 (w), 1319 (w), 1229 (m), 1072 (w), 1015 (w), 809 (m), 727 (w), 643 (w), 582 (w), 505 (w), 471 (w) cm^{-1} (Figure S10, Supporting Information).

Rietveld Refinements: The Rietveld refinements of compounds **1-Ni** and **2-Co** were performed by using Fullprof2k with the Winplotr software package.^[21] The cell parameters were refined with the WinXPOW Software package.^[22] After the initial refinements of the scale factors, unit-cell parameters, and profile parameters, the organic parts were refined by using constraints for the bipy and thiocyanato ligands. All atoms were refined isotropically, and the H atoms were not considered. Details of the structure refinements are given in Table 8. For difference plots of the Rietveld refinements see Figures S15 and S16 (Supporting Information).

Single-Crystal Structure Analysis: The investigation was performed with an imaging plate diffraction system (IPDS-2) with $\text{Mo-}K_\alpha$ radiation from STOE & CIE. The crystal structure of compound **3-Co** was refined with the crystal data of its isotypic analogue **3-Fe**^[3] as initial structure model. These refinements were performed against $|F|^2$ by using SHELXL-97.^[23] A numerical absorption correction was applied by using X-Red Version 1.31 and X-Shape Version 2.11 of the Program Package X-Area.^[24] All non-hydrogen atoms were refined with anisotropic displacement parameters. All hydrogen atoms were positioned with idealized geometry and were refined with fixed isotropic displacement parameters [$U_{\text{eq}}(\text{H}) = -1.2U_{\text{eq}}(\text{C})$] by using a riding model with $d_{\text{C-H}} = 0.93 \text{ \AA}$. Details

Table 8. Selected crystal data and details on the structure refinement from powder data for $[\{\text{Ni}(\text{NCS})_2(\text{bipy})(\text{H}_2\text{O})_2\} \cdot (\text{bipy})]_n$ (**1-Ni**) and $[\text{Co}(\text{NCS})_2(\text{bipy})_2]_n$ (**2-Co**).

	1-Ni	2-Co
Formula	$\text{C}_{22}\text{H}_{20}\text{NiN}_6\text{O}_2\text{S}_2$	$\text{C}_{22}\text{H}_{16}\text{CoN}_6\text{S}_2$
MW / g mol^{-1}	523.26	487.47
Crystal system	triclinic	monoclinic
Space group	$P\bar{1}$	$C2/c$
$a / \text{\AA}$	7.4686(2)	12.246(1)
$b / \text{\AA}$	8.8864(2)	11.424(1)
$c / \text{\AA}$	10.2169(3)	16.555(1)
$\alpha / ^\circ$	107.974(1)	90
$\beta / ^\circ$	103.629(1)	100.174(2)
$\gamma / ^\circ$	98.037(1)	90
$V / \text{\AA}^3$	610.04(3)	2279.6(3)
Z	1	4
2θ range / $^\circ$	5–54	4–48
Number of reflections	294	206
Number of parameters	29	27
R_p , R_{wp}	0.199, 0.210	0.256, 0.173
GOF / χ^2	0.1520	0.0335
R_{Bragg}	0.1120	0.1100
R_F	0.1080	0.1200

of the structure determination are given in Table 9. CCDC-767578 (for **1-Ni**), -767579 (for **2-Co**), and -767580 (for **3-Co**) contain the supplementary crystallographic data for this paper. These data can be obtained free of charge from The Cambridge Crystallographic Data Centre via www.ccdc.cam.ac.uk/data_request/cif.

Table 9. Selected crystal data and details on the structure determinations from single-crystal data for $[\text{Co}(\text{NCS})_2(\text{bipy})]_n$ (**3-Co**).

	3-Co
Formula	$\text{C}_{12}\text{H}_8\text{CoN}_4\text{S}_2$
MW / g mol^{-1}	331.27
Crystal system	monoclinic
Space group	$C2/c$
$a / \text{\AA}$	11.1982(8)
$b / \text{\AA}$	11.4580(6)
$c / \text{\AA}$	11.3321(8)
$\beta / ^\circ$	111.798(5)
$V / \text{\AA}^3$	1350.05(15)
T / K	293(2)
Z	4
$D_{\text{calcd.}} / \text{g cm}^{-3}$	1.630
μ / mm^{-1}	1.569
Min./max. transmission	0.7455/0.8331
$\theta_{\text{max}} / ^\circ$	29.25
Measured reflections	8843
Unique reflections	1814
Reflections $[F_o > 4\sigma(F_o)]$	1521
Parameters	89
R_{int}	0.0416
$R_1^{[a]} [F_o > 4\sigma(F_o)]$	0.0377
$wR_2^{[b]} [\text{all data}]$	0.0728
GOF	1.136
$\Delta\rho_{\text{max}}, \Delta\rho_{\text{min}} / \text{e \AA}^{-3}$	0.278, -0.360

[a] $R_1 = \sum |F_o| - |F_c| / \sum |F_o|$. [b] $wR_2 = \{\sum [w(F_o^2 - F_c^2)^2] / \sum [w(F_o^2)^2]\}^{1/2}$.

X-ray Powder Diffraction (XRPD): XRPD experiments were performed by using a Stoe Transmission Powder Diffraction System (STADI P) with $\text{Cu-}K_\alpha$ radiation ($\lambda = 154.0598 \text{ pm}$) that was equipped with a linear position-sensitive detector (Delta 2 θ : 6.5–7° simultaneous; scan range overall: 2–130°) from STOE & CIE.

Differential Thermal Analysis, Thermogravimetry, and Mass Spectroscopy (DTA-TG-MS): The DTA-TG measurements were performed under a nitrogen atmosphere (purity: 5.0) in Al_2O_3 crucibles by using a STA-409CD instrument from Netzsch. The DTA-TG-MS measurements were performed with the same instrument, which was connected to a quadrupole mass spectrometer from Balzers via Skimmer coupling from Netzsch. The MS measurements were performed in analogue and trend scan mode in Al_2O_3 crucibles under a dynamic nitrogen atmosphere (purity: 5.0) by using heating rates of 4°C min^{-1} . All measurements were performed with a flow rate of 75 mL min^{-1} . The instrument was calibrated by using standard reference materials.

Elemental Analysis: CHNS analyses were performed with a EURO EA elemental analyzer, fabricated by EURO VECTOR Instruments and Software.

Spectroscopy: Fourier transform IR spectra were recorded with a Genesis series FTIR spectrometer, by ATI Mattson, in KBr pellets.

Magnetic Measurement: Magnetic measurements were performed by using a Physical Property Measuring System (PPMS) from Quantum Design, which was equipped with a 9 T magnet. The data were corrected for core diamagnetism.^[25]

Supporting Information (see also the footnote on the first page of this article): IR spectroscopic data of all compounds; experimental and calculated XRPD patterns of compounds **1-Mn**, **2-Co**, **3-Co**, and **3-Cu**; difference plots of the Rietveld refinements of compounds **1-Ni** and **2-Co**; thermal investigations (DTG, TG, DTA, and MS trend scan curves) of compounds **1-Mn** and **1-Co**.

Acknowledgments

M.W. thanks the Stiftung Stipendien-Fonds des Verbandes der Chemischen Industrie and the Studienstiftung des deutschen Volkes for a PhD scholarship. We gratefully acknowledge financial support of the State of Schleswig-Holstein, and we thank Professor Dr. Wolfgang Bensch for the opportunity to use his experimental facility. Special thanks to Inke Jeß for her support in the single-crystal measurements and to Sina Sellmer for her laboratory work.

- [1] C. Janiak, *Dalton Trans.* **2003**, 2781–2804; D. Maspoch, D. Ruiz-Molina, J. Veciana, *J. Mater. Chem.* **2004**, *14*, 2713–2723; D. Maspoch, D. Ruiz-Molina, J. Veciana, *Chem. Soc. Rev.* **2007**, *36*, 770–818; S. L. James, *Chem. Soc. Rev.* **2003**, *32*, 276–288; A. N. Khlobystov, A. J. Blake, N. R. Champness, D. A. Lemenovskii, A. G. Majouga, N. V. Zyk, M. Schröder, *Coord. Chem. Rev.* **2001**, *222*, 155–192; S. Kitagawa, R. Matsuda, *Coord. Chem. Rev.* **2007**, *251*, 2490–2509; S. Kitagawa, K. Uemura, *Chem. Soc. Rev.* **2005**, *34*, 109–119; B. Moulton, M. J. Zaworotko, *Chem. Rev.* **2001**, *101*, 1629–1658; R. J. Puddphatt, *Coord. Chem. Rev.* **2001**, *216–217*, 313–332; A. Y. Robin, K. M. Fromm, *Coord. Chem. Rev.* **2006**, *250*, 2127–2157; S. R. Batten, K. S. Murray, *Coord. Chem. Rev.* **2003**, *246*, 103–130; A. J. Blake, N. R. Brooks, N. R. Champness, M. Crew, D. H. Gregory, P. Hubberstey, M. Schröder, A. Deveson, D. Fenske, L. R. Hanton, *Chem. Commun.* **2001**, 1432–1433; A. J. Blake, N. R. Champness, P. Hubberstey, W.-S. Li, M. A. Withersby, M. Schröder, *Coord. Chem. Rev.* **1999**, *183*, 117–138; C. Janiak, L. Uehlin, H.-P. Wu, P. Klüfers, H. Piotrowski, T. G. Scharmann, *J. Chem. Soc., Dalton Trans.* **1999**, 3121–3131.
- [2] E. Pardo, R. Ruiz-Garcia, J. Cano, X. Ottenwaelder, R. Lescouezec, Y. Journaux, F. Lloret, M. Julve, *Dalton Trans.* **2008**, 2780–2805; M. L. Liu, W. Shi, H. B. Song, P. Cheng, D. Z. Liao, S. P. Yan, *CrystEngComm* **2009**, *11*, 102–108; M. A. M. Abu-Youssef, A. Escuer, F. A. Mautner, L. Ohrstrom, *Dalton Trans.* **2008**, 3553–3558; H. A. Habib, J. Sanchiz, C. Janiak, *Dalton Trans.* **2008**, 4877–4884; K. Drabent, Z. Ciunik, A. Ozarowski, *Inorg. Chem.* **2008**, *47*, 3358–3365; H. A. Habib, J. Sanchiz, C. Janiak, *Dalton Trans.* **2008**, 1734–1744; K. S. Gavrilenko, O. Cador, K. Bernot, P. Rosa, R. Sessoli, S. Golhen, V. V. Pavlishchuk, L. Ouahab, *Chem. Eur. J.* **2008**, *14*, 2034–2043; A. J. E. Joel, S. Miller, *Angew. Chem.* **1994**, *106*, 399–432; W. Li, H.-P. Jia, Z.-F. Ju, J. Zhang, *Dalton Trans.* **2008**, 5350–5357; H. Miyasaka, M. Yamashita, *Dalton Trans.* **2007**, 399–406; A. Prescimone, J. Wolowska, G. Rajaraman, S. Parsons, W. Wernsdorfer, M. Murugesu, G. Christou, S. Piligkos, E. J. L. McInnes, E. K. Brechin, *Dalton Trans.* **2007**, 5282–5289; L. M. Toma, R. Lescouezec, J. Pasan, C. Ruiz-Perez, J. Vaissermann, J. Cano, R. Carrasco, W. Wernsdorfer, F. Lloret, M. Julve, *J. Am. Chem. Soc.* **2006**, *128*, 4842–4853; M. Verdaguer, A. Bleuzen, C. Train, R. Garde, F. F. d. Biani, C. Desplanches, *Philos. Trans. R. Soc. London, Ser. A* **1999**, *357*, 2959–2976; X.-Y. Wang, Z.-M. Wang, S. Gao, *Chem. Commun.* **2008**, 281–294; W. X. Zhang, W. Xue, J. B. Lin, Y. Z. Zheng, X. M. Chen, *CrystEngComm* **2008**, *10*, 1770–1776.
- [3] M. Wriedt, S. Sellmer, C. Näther, *Dalton Trans.* **2009**, 7975–7984.
- [4] M. Wriedt, I. Jeß, C. Näther, *Eur. J. Inorg. Chem.* **2009**, 1406–1413; M. Wriedt, C. Näther, *Z. Anorg. Allg. Chem.* **2009**, 635, 2459–2464; M. Wriedt, C. Näther, *Dalton Trans.* **2009**, 10192–10198.
- [5] M. Wriedt, C. Näther, *Z. Anorg. Allg. Chem.* **2010**, *636*, 569–575.
- [6] M. Wriedt, S. Sellmer, C. Näther, *Inorg. Chem.* **2009**, *48*, 6896–6903.
- [7] I. S. Ahuja, R. Singh, C. L. Yadava, *J. Mol. Struct.* **1981**, *74*, 143–151; A. Anagnostopoulos, *Inorg. Nucl. Chem. Lett.* **1976**, *12*, 225–234; H. Hou, Y. Wei, Y. Fan, C. Du, Y. Zhu, Y. Song, Y. Niu, X. Xin, *Inorg. Chim. Acta* **2001**, *319*, 212–218; R. E. Marsh, *Acta Crystallogr., Sect. B* **1999**, *55*, 931–936.
- [8] M.-X. Li, G.-Y. Xie, Y.-D. Gu, J. Chen, P.-J. Zheng, *Polyhedron* **1995**, *14*, 1235–1239.
- [9] J. Lu, T. Paliwala, S. C. Lim, C. Yu, T. Niu, A. J. Jacobson, *Inorg. Chem.* **1997**, *36*, 923–929.
- [10] W.-X. Luo, M.-M. Yu, L. Zheng, A.-L. Cui, H.-Z. Kou, *Acta Crystallogr., Sect. E* **2006**, *62*, m2532–m2534.
- [11] N. Moliner, M. C. Muñoz, J. A. Real, *Inorg. Chem. Commun.* **1999**, *2*, 25–27; S.-i. Noro, M. Kondo, T. Ishii, S. Kitagawa, H. Matsuzaka, *J. Chem. Soc., Dalton Trans.* **1999**, 1569–1574.
- [12] Y. Zhang, L. Jianmin, M. Nishiura, T. Imamoto, *J. Mol. Struct.* **2000**, *519*, 219–224; Y. Zhang, L. Jianmin, D. Wei, M. Nishiura, T. Imamoto, *Chem. Lett.* **1999**, 195.
- [13] M. Wriedt, S. Sellmer, C. Näther, *Dalton Trans.* **2009**, 7975–7984.
- [14] R. A. Bailey, S. L. Kozak, T. W. Michelsen, W. N. Mills, *Coord. Chem. Rev.* **1971**, *6*, 407–445.
- [15] A. F. Holleman, E. Wiberg, *Lehrbuch der Anorganischen Chemie*, vol. 101, de Gruyter, Berlin, **1995**.
- [16] M. Wriedt, I. Jeß, C. Näther, *Eur. J. Inorg. Chem.* **2009**, 1406–1413.
- [17] F. Lloret, M. Julve, J. Cano, G. D. Munno, *Mol. Cryst. Liq. Cryst.* **1999**, *334*, 569–585.
- [18] F. Lloret, G. D. Munno, M. Julve, J. Cano, R. Ruiz, A. Caneschi, *Angew. Chem. Int. Ed.* **1998**, *37*, 135–138.
- [19] C. Näther, J. Greve, *J. Solid State Chem.* **2003**, *176*, 259–265.
- [20] J. A. Real, G. D. Munno, M. C. Munoz, M. Julve, *Inorg. Chem.* **1991**, *30*, 2701–2704; J. S. Haynes, A. Kostikas, J. R. Sams, A. Simopoulos, R. C. Thompson, *Inorg. Chem.* **1987**, *26*, 2630–2637; B. N. Figgis, J. Lewis, F. E. Mabbs, G. A. Webb, *J. Chem. Soc. A* **1967**, 442–447.
- [21] T. Roisnel, J. Rodriguez-Carvajal in *Proceedings of the Seventh European Powder Diffraction Conference (EPDIC 7)* (Eds.: R.

- Delhez, E. J. Mittenmeijer), **2000**, pp. 118–123; J. Rodriguez-Carvajal, *Phys. Rev. B: Condens. Matter* **1993**, 192, 55.
- [22] *WinXPOW*, version 2.23, STOE & CIE GmbH, Darmstadt, Germany, **2003**.
- [23] G. M. Sheldrick, *Acta Crystallogr., Sect. A* **2008**, 64, 112–122.
- [24] *X-Area, Program Package for Single Crystal Measurements*, version 1.44, STOE & CIE GmbH, Darmstadt, Germany, **2008**.
- [25] G. A. Bain, J. F. Berry, *J. Chem. Educ.* **2008**, 85, 532–536.

Received: February 8, 2010
Published Online: May 26, 2010

Cubane-Like Bismuth-Iron Cluster: Synthesis, X-ray Crystal Structure and Theoretical Characterization of the $[\text{Bi}_4\text{Fe}_8(\text{CO})_{28}]^{4-}$ Anion

Kirill Yu. Monakhov,^[a] Thomas Zessin,^[a] and Gerald Linti*^[a]

Keywords: Bismuth / Iron / Cluster compounds / Aromaticity / Density functional calculations

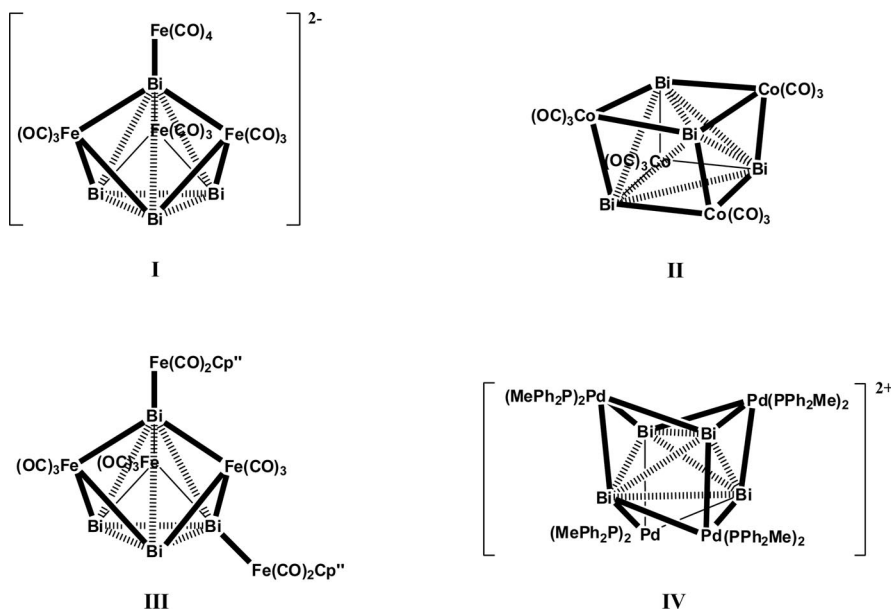
The reaction of *cyclo*- $\text{Bi}_4[\text{Si}(\text{SiMe}_3)_3]_4$ (**1**) with $\text{Na}_2[\text{Fe}(\text{CO})_4]$ in the presence of $n\text{Bu}_4\text{NCl}$ leads to the formation of the cage compound $[n\text{Bu}_4\text{N}]_4[\text{Bi}_4\text{Fe}_8(\text{CO})_{28}]$ (**2**). According to X-ray single-crystal structure analysis, the faces of the tetrahedral Bi_4 core are capped by $\text{Fe}(\text{CO})_3$ moieties in a μ_3 fashion to give a cubanoid Bi_4Fe_4 framework. The four $\text{Fe}(\text{CO})_4$ fragments are μ_1 -coordinated to bismuth, each. With 12 skeletal electron pairs the $[\text{Bi}_4\text{Fe}_8(\text{CO})_{28}]^{4-}$ anion (**2a**) is a Bi_4Fe_4 cubane. The negative charge is localized within cluster **2a** ac-

cording to the NBO analysis of its derivatives. The strength of metal–ligand interactions $\text{Bi}-\mu_3\text{-Fe}(\text{CO})_3$ is responsible for the size of the cluster's cubic core. NICS computations at the cage centers of considered molecules show that **2a** has paratropic character, whereas removal of four $\mu_1\text{-Fe}(\text{CO})_4$ fragments from latter causes spherical aromaticity of the modified clusters $[\text{Bi}_4\text{Fe}_4(\text{CO})_{12}]^{4-}$ (**2aa**) and $[\text{Bi}_4\text{Fe}_4(\text{CO})_{12}]^{2+}$ (**2ab**), mediated by a Bi_4 cluster π orbital.

Introduction

The tetrahedral cluster Bi_4 is a high-temperature modification, which exists only in the liquid or in the gas phase. Matrix isolation studies^[1] and quantum-chemical calcu-

tions^[2] are available. Tetrahedral Bi_4 is stabilized in the solid state by using transition metal fragments. The hybrid Zintl-metal carbonyl cluster anion $[\text{Bi}_4\text{Fe}_4(\text{CO})_{13}]^{2-}$ has been discovered by Whitmire et al.^[3] Other examples of such



Scheme 1. Survey of I–IV bismuth-transition-metal clusters displaying Bi_4 core.

[a] Anorganisch-Chemisches Institut, Universität Heidelberg, Im Neuenheimer Feld 270, 69120 Heidelberg, Germany
Fax: +49-6221-546617,
E-mail: gerald.linti@aci.uni-heidelberg.de

Supporting information for this article is available on the WWW under <http://dx.doi.org/10.1002/ejic.201000215>.

bismuth–transition-metal (Bi-TM) clusters are rare, up to now. The structural and electronic features of this class of molecules as well as the synthetic pathways to these are an interesting area and target of chemistry. The Bi-TM heteronuclear cluster systems (Scheme 1) could be obtained

by different synthetic strategies: (a) carbonylation of $[n\text{Bu}_4\text{N}][\text{BiFe}_3(\text{CO})_{10}]$ to form **I**,^[3] (b) pyrolysis of $[\text{Bi}\{\text{Co}(\text{CO})_4\}_3]$ or photolysis of $[\text{Bi}\{\text{Co}(\text{CO})_4\}_2\text{Fe}(\text{CO})_2\text{Cp}]$ to form **II**,^[4,5] (c) conversion of $[\{\text{Cp}''(\text{CO})_2\text{Fe}\}\text{BiCl}_2]$ ($\text{Cp}'' = \eta^5\text{-C}_5\text{H}_3\text{tBu}_2$) with $\text{Na}_2[\text{Fe}(\text{CO})_4]$ to form **III**,^[5] (d) conversion of $\text{Pd}(\text{PPh}_2\text{Me})_4$ with Ph_2BiBr to form **IV**.^[6] The question of whether the Bi_4 cores in these compounds, taking in account different molecular symmetry, have bonding Bi–Bi interactions ($d_{\text{Bi–Bi}} = 314\text{--}353\text{ pm}$) was a subject of intensive discussions. For example, polyhedral bismuth polycations like trigonal bipyramidal Bi_5^{3+} and square pyramidal Bi_5^+ clusters as well as the distorted Bi_6^{2+} octahedron, square-antiprismatic Bi_8^{2+} , tricapped trigonal prismatic Bi_9^{5+} and pentagonal-antiprismatic Bi_{10}^{4+} clusters were isolated in intermetallic phases as naked units with the closest Bi–Bi contacts.^[7] An example of a Bi_4N_4 cubane cluster core with significant longer Bi···Bi separations ($d_{\text{Bi–Bi}} = 344\text{--}364\text{ pm}$) is also known.^[8]

In this article we present an unusual synthetic method of the formation of the bismuth–iron metal complex $[n\text{Bu}_4\text{N}]_4[\text{Bi}_4\text{Fe}_8(\text{CO})_{28}]$ (**2**), displaying a cuboid cluster shape, where eight carbonyl iron fragments are involved in bonding to a Bi_4 cluster core. In addition, DFT quantum chemical calculations were performed for the anionic moiety **2a** of the complex **2** and its derivatives to get an insight into the geometric and electronic structures, the chemical bonding as well as into stability and aromaticity of these species.

Results and Discussion

Synthesis

The reaction of $\text{Bi}_4[\text{Si}(\text{SiMe}_3)_3]_4$ ^[9] (**1**) with eight equivalents of $\text{Na}_2[\text{Fe}(\text{CO})_4]$ and an excess of $n\text{Bu}_4\text{NCl}$ in the solvent thf leads to a redox process under the applied conditions (warming up from -78°C to room temp. during the reaction), resulting in compound $[n\text{Bu}_4\text{N}]_4[\text{Bi}_4\text{Fe}_8(\text{CO})_{28}]$ (**2**) [see Equation (1)]. During the reaction a gradual deepening of the dark-red color of the solution was observed. Workup allows isolation of **2** as thf soluble black crystals. The anion portion $[\text{Bi}_4\text{Fe}_8(\text{CO})_{28}]^{4-}$ (**2a**) of **2** is the largest cluster of the bismuth–iron family. The reaction does not take place without the addition of the ammonium salt, which means activation of $[\text{Fe}(\text{CO})_4]^{2-}$ via exchange of the cation. The bismuth–silicon bonds are cleaved with formation of $[\text{Si}(\text{SiMe}_3)_3]_2$ and other products.

X-ray Crystal Structure

2 crystallizes together with six thf molecules in the orthorhombic space group *Pba2*. Four $[n\text{Bu}_4\text{N}]^+$ cations are the counterions for the tetraanionic **2a** molecule. The C_2 -symmetric cluster core of **2a** (Figure 1) is a distorted Bi_4Fe_4 cube. The building Bi_4 tetrahedron is nearly ideal [$d_{\text{Bi–Bi}} = 342.8\text{--}343.8\text{ pm}$]. The neutral bismuth–cobalt complex **II** has a similar cluster core with shorter Bi–Bi distances [$d_{\text{Bi–Bi}} = 331.6\text{--}337.6\text{ pm}$].^[4,5] Three other examples, **I**, **III** and **IV**, display more distorted Bi_4 tetrahedra. The Bi–Bi

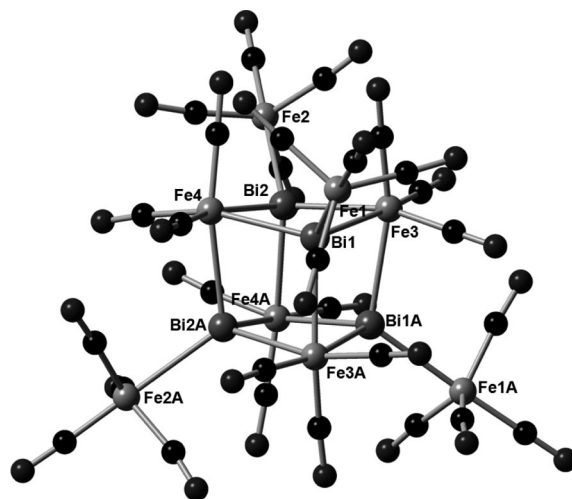
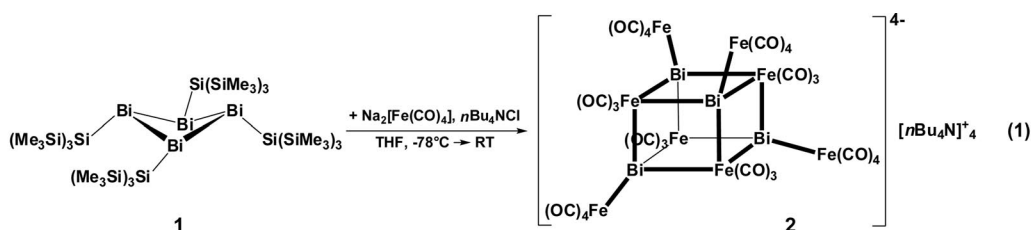


Figure 1. View of cluster molecule **2a**. Selected bond lengths [pm] and angles $^\circ$: Bi(1)–Bi(1A) 343.46(8), Bi(1)–Bi(2) 343.84(8), Bi(1)–Bi(2A) 343.68(8), Bi(2)–Bi(1A) 343.68(8), Bi(2)–Bi(2A) 342.76(9), Bi(1A)–Bi(2A) 343.84(8), Bi(1)–Fe(1) 271.92(20), Bi(2)–Fe(2) 272.37(20), Bi(1A)–Fe(1A) 271.92(20), Bi(2A)–Fe(2A) 272.37(20), Bi(1)–Fe(3) 271.82(16), Bi(1)–Fe(3A) 270.83(15), Bi(1)–Fe(4) 272.68(12), Bi(2)–Fe(3) 271.56(23), Bi(2)–Fe(4A) 272.13(15), Bi(2)–Fe(4) 270.63(16), Bi(1A)–Fe(3) 270.83(15), Bi(1A)–Fe(3A) 271.82(16), Bi(1A)–Fe(4A) 272.68(21), Bi(2A)–Fe(4) 272.13(15), Bi(2A)–Fe(3A) 271.56(23), Bi(2A)–Fe(4A) 270.63(16), Bi(1)–Fe(4)–Bi(2) 78.522(48), Bi(2)–Fe(3)–Bi(1) 78.511(49), Bi(1A)–Fe(3A)–Bi(2A) 78.511(49), Bi(2A)–Fe(4A)–Bi(1A) 78.522(48), Bi(1A)–Fe(3A)–Bi(1) 78.533(43), Bi(1)–Fe(3)–Bi(1A) 78.533(43), Bi(1)–Fe(3A)–Bi(2A) 78.640(48), Bi(2A)–Fe(4)–Bi(1) 78.222(46), Bi(2A)–Fe(4)–Bi(2) 78.322(39), Bi(2)–Fe(4A)–Bi(2A) 78.322(39), Bi(2)–Fe(3)–Bi(1A) 78.640(48), Bi(1A)–Fe(4A)–Bi(2) 78.222(46), Fe(3)–Bi(1)–Fe(4) 100.082(56), Fe(4)–Bi(2)–Fe(3) 100.668(54), Fe(3A)–Bi(2A)–Fe(4A) 100.668(54), Fe(4A)–Bi(1A)–Fe(3A) 100.082(56), Fe(3A)–Bi(1)–Fe(3) 100.439(44), Fe(3)–Bi(1A)–Fe(3A) 100.439(44), Fe(3A)–Bi(2A)–Fe(4) 100.482(53), Fe(4)–Bi(1)–Fe(3A) 100.528(55), Fe(4)–Bi(2)–Fe(4A) 100.554(47), Fe(4A)–Bi(2A)–Fe(4) 100.554(47), Fe(4A)–Bi(2)–Fe(3) 100.482(53), Fe(3)–Bi(1A)–Fe(4A) 100.528(55).



distances are lying in the regions 313.9–347.3,^[3] 308.9–353.0^[5] and 320.1–350.9^[6] pm, respectively. All of these Bi–Bi distances lie in an interval comparable with the closest Bi–Bi contacts of 307.1–352.9 pm in the pure crystalline element.^[10] The four tetrahedral Bi₄ faces of **2a** and **II** are capped by Fe(CO)₃ and Co(CO)₃ moieties in a μ_3 fashion, respectively. The Bi–Fe bond lengths in **2a** [$d_{\text{Bi-Fe}} = 270.6$ – 272.7 pm] are slightly shorter than the Bi–Co bonds in **II** [$d_{\text{Bi-Co}} = 274.2$ – 276.3 pm].^[4,5] The special structural feature of **2a** are the four Fe(CO)₄ fragments coordinated in a μ_1 fashion to four Bi atoms. The Bi–Fe bond lengths [$d_{\text{Bi-Fe}} = 271.9$ – 272.4 pm] are nearly equal to the bridging ones. This is, on the first glance, unexpected, but indicates a low basicity of the bismuth atoms via the lone pair. This is in line with the ligand behavior of P₄.^[11] In **I**^[3] the terminal Bi–Fe-bond [$d_{\text{Bi-Fe}} = 275.2$ pm] is even longer than in **2a**, whilst the bridging ones are in a similar range [$d_{\text{Bi-Fe}} = 269.9$ – 275.3 pm]. In complex **II** these four bismuth tops are left bare. The Bi–Fe–Bi bond angles [approx. 78°] in **2a** are smaller than the 90° angles of a cube, whereas the Fe–Bi–Fe bond angles [approx. 100°] are larger.

Theoretical Characterization

DFT quantum chemical calculations (see Tables 1, 2, and 3) were performed for **2a** as well as {Bi₄[μ_3 -Fe(CO)₃]₄}⁴⁻ (**2aa**) and {Bi₄[μ_3 -Fe(CO)₃]₄}²⁺ (*closo-2ab*, *arachno-2ab*). The last two species were used as model compounds for the cluster system **2a**. The four μ_1 -coordinated Fe(CO)₄ fragments were removed either as neutral fragment, isolobal to an oxygen atom or partially negatively in order to obtain models with negative or positive charge in the remaining Bi₄Fe₄ cores (Scheme 2). Skeletal electron counts (SEC) for **2a** and **2aa** show that the clusters belong to cubane classes on the basis of the isolobality principle. Thus, **2a** and **2aa**

providing 12 skeletal electron pairs are structural analogs to cubane C₈H₈. {Bi₄[μ_3 -Fe(CO)₃]₄}²⁺ providing only 9 skeletal electron pairs should adopt a structure analogously to *closo*-borane B₈H₈²⁻.^[12] Really, a cubane-like cluster structure (*arachno-2ab*) of {Bi₄[μ_3 -Fe(CO)₃]₄}²⁺ is slightly less energetically favored by 21 kJ/mol in comparison to *closo-2ab*.^[13a,13b] Such insignificant energy difference between these two structures may be related to that that stella quadrangula structure^[13c] (tetracapped tetrahedron; *arachno-2ab*) is allowed to be on the basis that the t₁ set on the Bi₄ tetrahedron is well able to stabilize the capping Fe₄ t₁ set.^[13a] For example, the cubane-like [Bi₄Pd₄(PPh₂-Me)₈]²⁺ cluster^[6] and the *closo*-deltahedron [Bi₄Ni₄(CO)₆]²⁻ bisdisphenoid,^[14] isoelectronic with these two **2ab** clusters, were synthesized and described.

Table 3. Stretching vibrations of the carbonyl groups of cluster anion **2a** and its simplified derivatives, anionic **2aa** and cationic *arachno-2ab* calculated at the LSDA/BS-I level; selected energy values and GIAO-NICS values from MW1PW91/BS-II computations for closed-shell **2a**, **2aa**, *arachno-2ab* and **2ac**.

Parameter	[Bi ₄ Fe ₈ (CO) ₂₈] ⁴⁻ , 2a	[Bi ₄ Fe ₄ (CO) ₁₂] ⁴⁻ , 2aa	[Bi ₄ Fe ₄ (CO) ₁₂] ²⁺ , <i>arachno-2ab</i>	Bi ₄ , 2ac
$\tilde{\nu}_{\text{CO}}$ ^[a]	2074, 2053, 2022, 2017, 1993, 1988	1954, 1912	2168, 2131	
HLG ^[b]	2.86	1.96	2.92	4.44
NICS ^[c]	+23.7	-12.3	-19.4	-37.4

[a] Stretching vibrations [cm⁻¹] of the carbonyl groups. [b] Energy of the HOMO–LUMO gap [eV]. [c] NICS value [ppm] at the cage center of cluster.

The DFT-optimized geometry of **2a** is very close to the experimental one of **2** (Table 1). The calculated Bi–Fe–Bi and Fe–Bi–Fe bond angles for **2aa** and *arachno-2ab* demonstrate more distorted cubic structures in comparison to **2a** (Figure 2). This fact can be well correlated with the electrostatic repulsions and attractions within these clusters on the

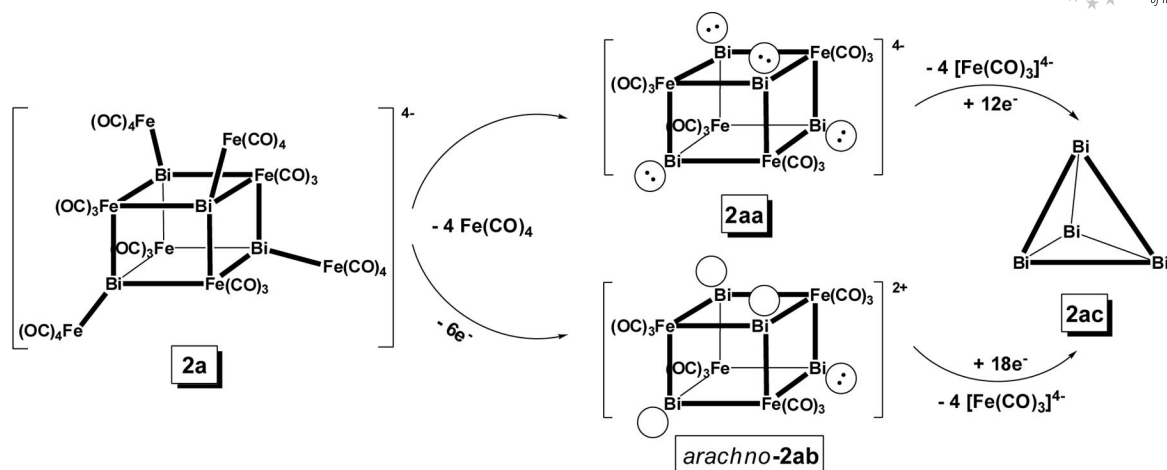
Table 1. Selected theoretical structural parameters (LSDA/BS-I level; bond lengths in pm and bond angles in degrees) for closed-shell cluster anion **2a** and its simplified derivatives, anionic **2aa**, cationic *arachno-2ab* and neutral **2ac**. Structural data of **2a**, obtained from X-ray crystal structure analysis of **2** are given for comparison.

Parameter	[Bi ₄ Fe ₈ (CO) ₂₈] ⁴⁻ , 2a	[Bi ₄ Fe ₄ (CO) ₁₂] ⁴⁻ , 2aa	[Bi ₄ Fe ₄ (CO) ₁₂] ²⁺ , <i>arachno-2ab</i>	Bi ₄ , 2ac	Experimental data for 2
Bi–Bi	341.2–341.6	332.4–332.7	319.6–320.2	297.3	342.8–343.8
Bi– μ_3 -Fe	268.7–269.1	276.9–277.1	267.5–267.7		270.6–272.7
Bi– μ_1 -Fe	269.2–269.3				271.9–272.4
Bi–Fe–Bi	78.7–78.9	73.7–73.8	73.3–73.5		78.2–78.6
Fe–Bi–Fe	100.1–100.3	104.1–104.2	104.2–104.5		100.1–100.7

Table 2. Selected theoretical data obtained from the NBO analysis at the MW1PW91/BS-II level for closed-shell cluster anion **2a** and its simplified derivatives, anionic **2aa**, cationic *arachno-2ab* and neutral **2ac**.

Parameter	[Bi ₄ Fe ₈ (CO) ₂₈] ⁴⁻ , 2a	[Bi ₄ Fe ₄ (CO) ₁₂] ⁴⁻ , 2aa	[Bi ₄ Fe ₄ (CO) ₁₂] ²⁺ , <i>arachno-2ab</i>	Bi ₄ , 2ac
WBI _{Bi-Bi} ^[a]	0.112	0.233	0.272	0.992
WBI _{Bi-Fe}	0.615 (μ_3) ^[b] , 0.565 (μ_1) ^[c]	0.556	0.673	
OOV _{Bi-Bi} ^[d]	+0.213	+0.288	+0.299	+0.581
OOV _{Bi-Fe}	+0.636 (μ_3), +0.616 (μ_1)	+0.601	+0.708	
Q _{NPA} ^[e] (Bi)	+1.285	+0.926	+1.141	0
Q _{NPA} (Fe)	-2.244 (μ_3), -1.921 (μ_1)	-2.345	-2.098	

[a] Wiberg bond index. [b] For bonding between Bi and μ_3 -coordinated iron carbonyl. [c] For bonding between Bi and μ_1 -coordinated iron carbonyl. [d] Order of orbital overlapping. [e] NPA charge on the metal atom [e].



Scheme 2. Simplification of **2a** (24 SEC) into **2aa** (24 SEC), *arachno-2ab* (18 SEC) and **2ac** (12 SEC) upon elimination of μ_1 -Fe(CO)₄ and μ_3 -Fe(CO)₃ fragments.

basis of the charges on the metal atoms (Table 2), indicating a high degree of the ionic character of the Bi–Fe bonds. Thus, more positive charges on the Bi atoms and less negative charges on these of μ_3 -Fe lead to an elongation of Bi–Bi distances and to a shortening of Bi– μ_3 -Fe bonds in **2a**. Interesting, the cubes **2a** and *arachno-2ab* have smaller size

than **2aa**. While the height and the wide of **2a** are 266.6 pm, the values of these parameters for *arachno-2ab* and **2aa** are 262.6 pm and 272.0 pm, respectively. Such change of the cluster size may be related to the strength of metal–ligand interactions, i.e. for the contraction of the cubes **2a** and *arachno-2ab* the Bi– μ_3 -Fe attraction forces are responsible.

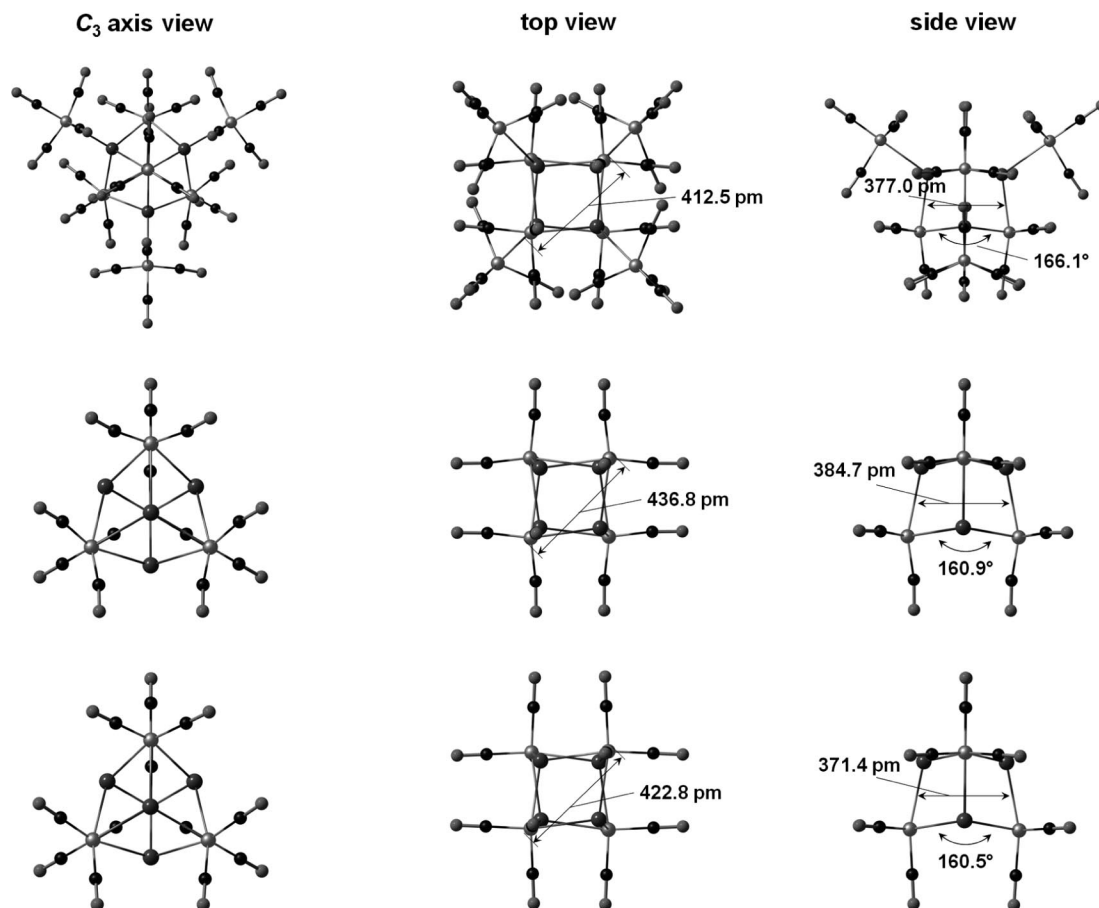


Figure 2. DFT-optimized structures of the clusters **2a** (top), **2aa** (middle) and *arachno-2ab* (bottom) representing stationary points (global minima for **2a** and **2aa** and local minimum for **2ab**) on their potential energy surfaces. The number of imaginary frequencies for all structures is 0.

First, the Bi– μ_3 -Fe distances in **2a** and *arachno-2ab* clusters are very close to each other and shorter than these in **2aa** (Table 1) where the Bi– μ_3 -Fe repulsion forces prevail. Secondly, computed WBI values and overlap populations for the Bi– μ_3 -Fe bonds exhibit stronger bonding character of these for **2a** and *arachno-2ab* species than for **2aa** (Table 2), as consequence. This interesting observation lies in line with this one, pointed out by Sarasa et al. for M_4X_4 structures in transition metal chemistry ($M = \text{Ti, V}$; $X = \text{N, P, As}$).^[15] The Bi– μ_1 -Fe bonds in **2a** are slightly more elongate with regard to the Bi– μ_3 -Fe bonds and consequently weaker. The bonding to four μ_1 -Fe(CO)₄ fragments in **2a** is carried out via lone pairs of Bi. The lone pair of electrons on each Bi atom in **2aa** possesses 79.4% and 81.5% s character according to the NBO and NLMO analysis, respectively. Four μ_1 -Fe(CO)₄ groups are involved in 2c–2e bonding to three-valent Bi atoms, here. As a consequence, the negative charge is localized within cluster **2a**. The NBO analysis for *arachno-2ab* finds one nonbonded lone pair (LP) orbital on Bi (s 63.2%; s 80.6% according to the NLMO) and three unfilled nonbonded lone pair (LP*) orbitals of s type. This may result in the Jahn–Teller-type distortion of the cube as has been discussed by Whitmire, Saillard et al.^[6]

Formally, removal of four μ_3 -coordinated iron carbonyl fragments from **2aa** and *arachno-2ab* leads to the neutral Bi₄ tetrahedron (6 skeletal electron pairs) (**2ac**) as a building block of all represented species (Scheme 2). Monotonous shortening of Bi–Bi distances, observed in direction of **2a** → **2aa** → *arachno-2ab* → **2ac** (Table 1), is accompanied by an increase in the Bi–Bi bonding strength according to the WBI values and order of orbital overlapping (Table 2). These bonding characteristics indicate that the bonding along the edges of Bi₄ tetrahedron is very weak or completely absent in **2a** (about 85% of ionic character).

The relatively large value of the HOMO–LUMO gap computed for **2a** predicts higher stability for the latter than for its derivative **2aa** where four Bi tops are left bare (Table 3). For the cationic cluster *arachno-2ab* the HOMO–LUMO gap is comparable to that of **2a**. This is in line with the higher positive charge on the bismuth atoms in **2a** and *arachno-2ab*. In spite of this, the charge reconstruction by an elimination of four Fe(CO)₄ groups from the cluster **2a** to give *arachno-2ab* is energetically ungained ($\Delta E_{\text{rel}} = +3102$ kJ/mol), whereas the μ_1 coordination of iron carbonyl fragments to *arachno-2ab* is vice versa. Analogically, the elimination process of four Fe(CO)₄ groups from **2a** to give its derivative **2aa** is endothermic ($\Delta E_{\text{rel}} = +1638$ kJ/mol). The charge reconstruction of **2aa** toward *arachno-2ab* is endothermic ($\Delta E_{\text{rel}} = +1465$ kJ/mol), too.

The infrared (IR) spectra of **2** in thf solution and in solid state as well as the IR spectra computed for the gas-phase structures of the clusters **2a**, **2aa** and *arachno-2ab* are a precedent for the discussions. Thus, the IR spectrum of the saturated thf solution of **2** displays six bands of different strength for the CO vibrations (2004 w, 1977 s, 1957 s, 1934 m, 1919 m, 1899 m cm^{−1}). The same number of stretching vibrations of the carbonyl groups (2008 w, 1994 w, 1976 m, 1915 s, 1895 s, 1878 s cm^{−1}) was observed for solid state of

2. The computed IR spectrum for the cluster anion **2a** predicts three bands of stretching vibrations of the Fe(CO)₃ carbonyl groups at 2074, 2022 and 1917 cm^{−1} and three these ones of the Fe(CO)₄ fragments at 2053, 1993 and 1988 cm^{−1}. The computed spectra of **2aa** and *arachno-2ab* show two bands of these vibrations, only (Table 3). The stretching modes of the CO groups for cationic *arachno-2ab* are shifted to higher wave numbers in comparison to anionic clusters **2a** and **2aa**.

According to the nucleus-independent chemical shifts (NICS) computations, the “naked” Bi₄ cage [$d(\text{Bi–Bi})_{\text{theor}} = 297.3$ pm (**a**)] demonstrates spherical aromaticity (NICS ca. −37 ppm), as is well-known.^[2b,16] For a swollen up tetrahedron with fixed Bi–Bi distances similar to those in **2a** [$d(\text{Bi–Bi}) = 342.8$ – 343.8 pm (**b**)] no significant decrease of aromaticity (NICS −32.3 at the cage center) is expected. The Bi–Bi bonds are weakened only marginally by the elongation from **a** to **b** (WBI = 0.986). For this reason, one would anticipate similar diatropic character of anionic clusters **2a** and **2aa** as well as cationic cluster *arachno-2ab* containing tetracapped Bi₄ core as building block.

Thus, NICS computations (Table 3) show that **2aa** and *arachno-2ab* exhibit diatropic NICS values of −12.3 and −19.4 ppm, respectively, providing aromaticity of these species despite the fact that the WBI values for the Bi–Bi separations are here 0.233 (**2aa**) and 0.272 (*arachno-2ab*), only (Table 2). In contrast, the positive NICS value of +23.7 ppm was observed at the cage center of **2a** that is an evidence for paratropic ring current associated with antiaromaticity.

The NICS values at the cage centers of **2aa** and *arachno-2ab* are strongly reduced with regard to “naked” Bi₄ tetrahedron. Such large difference in the NICS values of these species may be related to an influence of d-electrons of μ_3 -coordinated iron carbonyl fragments and the partially ionic character of the Bi–Fe bonds on the electronic density picture within the cluster. Besides, the strength of the diatropic ring current should depend on the size of a cluster π orbital (π molecular orbital subsystem), responsible for the spherical aromaticity of the cage. To understand from which cluster π orbital (Bi₄ vs. Fe₄) this aromaticity comes and to get more insight into the different magnetic shielding behavior of **2a**, **2aa** and *arachno-2ab* clusters the molecular orbitals (MOs) of these were analyzed. Figure 3 shows the correlations between cluster π orbitals placed within the Bi₄ and Fe₄ cages of the clusters **2aa** and *arachno-2ab*. Thus, the a_1 (s, π)-orbital of Bi₄ (HOMO-9) in **2aa** is a cluster π orbital. The later is reduced compared to the size of the (d, π)-orbital (cluster π orbital) of Fe₄ (HOMO-23), whereas the share of analogical π orbitals of Bi₄ (HOMO-3) and Fe₄ (HOMO-20) in *arachno-2ab* are similar. The antiaromatic character of **2a** is shown in the tetrahedral-shaped orbital within Bi₄ tetrahedron (HOMO-17), whilst the cluster π orbital within Fe₄ cage (HOMO-39) retains its integrity (Figure 3). Such magnetic deshielding of **2a** to positive NICS value (+23.7 ppm) may be mainly related to an involving of s-type lone pairs of Bi₄ in the interactions with the μ_1 -Fe(CO)₄ fragments. This μ_1 coordination leads to the strong

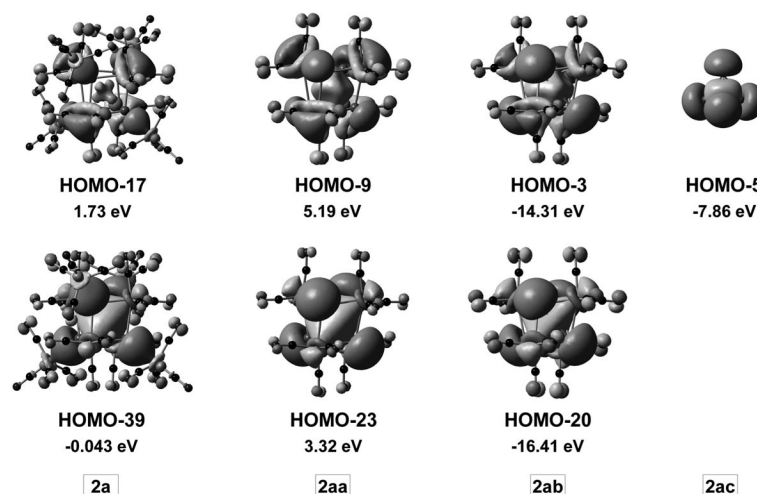


Figure 3. π Molecular orbital subsystems of Bi_4 (top) and Fe_4 (bottom) within **2a**, **2aa**, *arachno-2ab* and **2ac** species (± 0.02 isosurface value). The eigenvalues of these MOs were computed at the MPW1PW91/BS-II level (positive eigenvalues are typical for DFT calculations of highly negative charged species).

change in the electronic structure within the cluster. All of these results suggest that namely the cluster π orbitals contributed by Bi_4 tetrahedra are responsible for the aromatic character of the discussed species where the lone pairs of Bi_4 play a key role. The size of these internal-caged π orbitals also explains the difference in the degree of spherical aromaticity of **2aa** (−12.3 ppm) and *arachno-2ab* (−19.4 ppm). Finally, it is interesting to remark that *arachno-2ab* has slightly larger HOMO–LUMO gap separation in comparison to *closo-2ab* (HLG is 2.45 eV). This may be related to less aromatic character of the latter, exhibiting the NICS value of −14.0 ppm at the cage center.

Conclusions

By the reaction of **1** with $\text{Na}_2[\text{Fe}(\text{CO})_4]$ and $n\text{Bu}_4\text{NCl}$ the formation of cluster **2** was observed. The Zintl anion (**2a**) of latter is an unprecedented cluster displaying Bi–Fe cubane shape and being the largest cluster of the bismuth-iron family. Electrophilic cluster anion **2a** is antiaromatic, whereas its hypothetical derivatives, **2aa** and *arachno-2ab*, are spherically aromatic in their nature. The synthetic availability of these is a challenge in the bismuth-transition metal chemistry. In addition, cubane-like **2a** and its models might be valuable single-source molecular precursors to polycrystalline E_nTM_m materials (E = heavy group 15 element; TM = transition metal).^[6] A Bi_2Fe ion observed in thf solution of **2** by ESI mass spectrometry predicts a presence of such capability. Whether these unique compounds are really practical for synthetic applications will depend on their improved availability.

Experimental Section

General Methods: All manipulations were carried out with the use of standard Schlenk techniques under an oxygen-free and water-free argon atmosphere and in vacuo. All organic solvents were dis-

tilled, dried and degassed according to standard procedures. IR spectra of **2** in thf solution and in solid state were recorded from 4000 to 450 cm^{-1} with a Perkin–Elmer Spectrum 100 FT-IR instrument. The electrospray mass spectra (ESI-MS) was recorded on a Bruker Apex-Qe 9.4 T FT-ICR operating in the negative ion mode with full scanning in the range [200.0–2500.0]; compound **2** was supplied as dilute solutions at about 0.1 mg mL^{-1} in thf.

Crystal Structure Determination: X-ray data for single-crystals of **2** were collected on an STOE IPDS I diffractometer equipped with an image plate area detector, using a graphite monochromator Mo-K_α ($\lambda = 71.073\text{ pm}$). The structure was refined against all F^2 data by full-matrix least-squares techniques (SHELXT 5.01; PC Version, Siemens, Bruker AXS). All non-hydrogen atoms were refined with anisotropic thermal parameters. All H atoms were placed in calculated positions and refined using a riding model. A

Table 4. Crystallographic data of **2**.

2	
Empirical formula	$(\text{C}_{16}\text{H}_{36}\text{N})_4^+[\text{Bi}_4\text{Fe}_8\text{C}_{28}\text{O}_{28}]^{4-}$
Formula weight [g/mol]	3469.46
Crystal size [mm^3]	$0.52 \times 0.38 \times 0.35$
Crystal system	orthorhombic
Space group	Pba2
<i>a</i> [pm]	2184.1(4)
<i>b</i> [pm]	2269.3(5)
<i>c</i> [pm]	1513.3(3)
<i>V</i> [nm^3]	7.501(3)
<i>Z</i>	4
$D_{\text{calcd.}}$ [g cm^{-3}]	1.536
μ (Mo-K_α) [mm^{-1}]	5.49
$F(000)$	3456
θ Range for data collection [$^\circ$]	2–28
Index ranges <i>hkl</i>	$\pm 27 \pm 29 \pm 19$ to ± 11
Reflections collected	37959
Numerical absorption correction	$T_{\text{min}} = 0.151$, $T_{\text{max}} = 0.241$
Data/restraints/parameters	14007/31/748
Goodness-of-fit (<i>S</i>) on F^2	0.96
Final <i>R</i> indices [$I > 2\sigma(I)$]	$R_1 = 0.053$; $wR_2 = 0.130$
<i>R</i> indices (all data)	$R_1 = 0.075$; $wR_2 = 0.141$
Largest diff. peak and hole [$\text{e } \text{\AA}^{-3}$]	+3.40/−2.59

summary of crystal data and structure refinements for the compounds are listed in Table 4. The thf molecules have very large thermal parameters, indicating severe disorder, which was not possible to describe with simple splitting. Therefore, only averaged atom positions are used. An additional thf molecule, which is even more disordered, was not included in the refinement and is responsible for the void in the structure.

Synthesis of $[n\text{Bu}_4\text{N}]_4[\text{Bi}_4\text{Fe}_8(\text{CO})_{28}]$ (2**):** A suspension of 0.17 g (0.8 mmol) of $\text{Na}_2[\text{Fe}(\text{CO})_4]$ in 10 mL of thf was added dropwise to a stirred dark-red solution of 0.18 g (0.1 mmol) $\text{Bi}_4[\text{Si}(\text{SiMe}_3)_3]_4$ (**1**) in 15 mL of thf at -78°C . After the addition was complete, the reaction mixture was warmed for an additional 2 h to ambient temperature. 16 fold excess (ca. 1.6 mmol) of $n\text{Bu}_4\text{NCl}$ in 20 mL of thf was then introduced to the reaction mixture. After stirring for further 16 h at ambient temperature all volatile reaction components were removed in oil pump vacuum. The dark residue was extracted with 20 mL of thf. After filtration a dark-brown solution was obtained. The thf solution was removed; the dark residue was washed with some amount of hexane and re-crystallized again in 15 mL of thf. The thf solution was reduced to a volume of 5 mL and cooled to -20°C . Black crystals of **2** were obtained after some months. Yield 54 mg (18%; referring to Bi). $\text{Bi}_4\text{Fe}_8\text{C}_{92}\text{O}_{28}\text{H}_{144}\text{N}_4$ ($M = 3036.4$). IR (thf): $\tilde{\nu} = 2004$ w, 1977 s, 1957 s, 1934 m, 1919 m, 1899 m (ν_{CO}). IR (KBr): $\tilde{\nu} = 2008$ w, 1994 w, 1976 m, 1915 s, 1895 s, 1878 s (ν_{CO}). ESI-MS (thf): unspecific decomposition of the compound; m/z 349 $[\text{BiFe}(\text{CO})_3]^+$, 474 $[\text{Bi}_2\text{Fe}]^+$, 502 $[\text{Bi}_2\text{Fe}(\text{CO})]^+$, 530 $[\text{Bi}_2\text{Fe}(\text{CO})_2]^+$, 586 $[\text{Bi}_2\text{Fe}_2(\text{CO})_2]^+$, 642 $[\text{Bi}_2\text{Fe}_2(\text{CO})_4]^+$, 879 $[\text{Bi}_3\text{Fe}_2(\text{CO})_5]^+$.

Computational Methods: All of the calculations reported herein were carried out using the Gaussian 03 program package. Electron correlation for geometry optimizations was treated within the Local Spin Density Approximation denoted as LSDA.^[17] SCF convergence criterion of 10^{-7} was used. The LSDA density functional was employed with the double- ζ quality plus polarization SV(P) basis set of def2 type (Basis Set System I, which is denoted as BS-I) for all atoms.^[18,19] The vibrational frequencies were evaluated at the same level of theory on all optimized geometries of the clusters to verify their status as true global and local minima on the potential energy surfaces and to obtain zero-point corrections to the energies (ZPE). As a result of true minima, there were no imaginary vibrational frequencies (negative signs) for all optimized geometries. To evaluate nature of the chemical bonding, energies and Nucleus Independent Chemical Shifts (NICS) values of the clusters, the hybrid MW1PW91 density functional^[20] was employed with the Hay–Wadt relativistic effective core potentials (RECPs) plus LANL08 basis sets (correspond to triple- ζ valence orbital quality), augmented by adding one set of polarization d and f functions [denoted as LANL08(d)^[21] for Bi and LANL08(f)^[22] for Fe, respectively] and the split-valence basis sets 6-311G(d)^[23] for C, O and H atoms. The combination of these basis sets is denoted Basis Set System II (BS-II). Nature of the chemical bonding was analyzed by means of Natural Bond Orbital (NBO) approach. The atomic charges were computed within the Natural Population Analysis (NPA). Wiberg bond indexes (WBI) were evaluated and used as bond strength indicators. NBO analyses were performed with NBO Version 3.1^[24] incorporated in the Gaussian 03 program.^[25] NICS-computations^[26] were carried out at the cage centers of clusters on their DFT-optimized geometries.

CCDC-767166 contains the supplementary crystallographic data (excluding structure factors) for **2**. These data can be obtained free of charge from The Cambridge Crystallographic Data Centre via www.ccdc.cam.ac.uk/data_request/cif.

Supporting Information (see also the footnote on the first page of this article): Wade's electron counting for **2a** and **2aa** as well as for the cluster $\{\text{Bi}_4[\mu_3\text{-Fe}(\text{CO})_3]_4\}^{2+}$, and isolobality between given species and carbon and boron structural analogs.

Acknowledgments

We are grateful to the Graduate College 850 “Molecular Modeling” of the Deutsche Forschungsgemeinschaft (DFG) for financial support. We also thank Philipp Butzug for assistance in collecting the crystallographic data sets.

- [1] V. E. Bondybey, J. H. English, *J. Chem. Phys.* **1980**, *73*, 42–48.
- [2] a) H. Zhang, K. Balasubramanian, *J. Chem. Phys.* **1992**, *97*, 3437–3444; b) A. Hirsch, Z. Chen, H. Jiao, *Angew. Chem.* **2001**, *113*, 2916–2920; *Angew. Chem. Int. Ed.* **2001**, *40*, 2834–2838; c) I. Krossing, in: *Molecular Clusters of the Main Group Elements* (Eds.: M. Driess, H. Nöth), Wiley-VCH, Weinheim, **2004**, pp. 209–229.
- [3] a) K. H. Whitmire, M. R. Churchill, J. C. Fetting, *J. Am. Chem. Soc.* **1985**, *107*, 1056–1057; b) K. H. Whitmire, T. A. Albright, S.-K. Kang, M. R. Churchill, J. C. Fetting, *Inorg. Chem.* **1986**, *25*, 2799–2805.
- [4] G. Ciani, M. Moret, A. Fumagalli, S. Martinengo, *J. Organomet. Chem.* **1989**, *362*, 291–296.
- [5] T. Gröer, M. Scheer, *Organometallics* **2000**, *19*, 3683–3691.
- [6] J. L. Stark, B. Harms, I. Guzman-Jimenez, K. H. Whitmire, R. Gautier, J.-F. Halet, J.-Y. Saillard, *J. Am. Chem. Soc.* **1999**, *121*, 4409–4418.
- [7] a) S. Ulvenlund, K. Stahl, L. Bengtsson-Kloo, *Inorg. Chem.* **1996**, *35*, 223–230; b) M. Ruck, *Z. Anorg. Allg. Chem.* **1998**, *624*, 521–528; c) J. Beck, C. J. Brendel, L. Bengtsson-Kloo, B. Krebs, M. Mummert, A. Stankowski, S. Ulvenlund, *Chem. Ber.* **1996**, *129*, 1219–1226; d) A. Hershaft, J. D. Corbett, *Inorg. Chem.* **1963**, *2*, 979–985; e) M. Ruck, V. Dubenskyy, T. Söhnel, *Angew. Chem.* **2003**, *115*, 3086; *Angew. Chem. Int. Ed.* **2003**, *42*, 2978–2982.
- [8] J. F. Bickley, A. D. Bond, F. Garcia, K. Jantos, G. T. Lawson, M. McPartlin, A. Steiner, D. S. Wright, *J. Chem. Soc., Dalton Trans.* **2002**, 4629–4633.
- [9] G. Linti, W. Köstler, *Z. Anorg. Allg. Chem.* **2002**, *628*, 63–66.
- [10] P. Cucka, C. S. Barrett, *Acta Crystallogr.* **1962**, *15*, 865.
- [11] a) I. Krossing, L. Van Wullen, *Chem. Eur. J.* **2002**, *8*, 700–711; b) I. de Los Rios, J.-R. Hamon, P. Hamon, C. Lapinte, L. Toupet, A. Romerosa, M. Peruzzini, *Angew. Chem.* **2001**, *113*, 4028–4030; *Angew. Chem. Int. Ed.* **2001**, *40*, 3910–3912; c) M. Di Vaira, P. Frediani, S. Seniori Costantini, M. Peruzzini, P. Stoppioni, *Dalton Trans.* **2005**, 2234–2236; d) P. Barbaro, M. Di Vaira, S. Seniori Costantini, M. Peruzzini, P. Stoppioni, *Chem. Eur. J.* **2007**, *13*, 6682–6690.
- [12] a) L. J. Guggenberger, *Inorg. Chem.* **1969**, *8*, 2771–2774.
- [13] a) T. A. Albright, K. A. Yee, J.-Y. Saillard, S. Kahlal, J.-F. Halet, J. S. Leigh, K. H. Whitmire, *Inorg. Chem.* **1991**, *30*, 1179–1190; b) This work: the relative energies ($\Delta E_{\text{rel}} + \text{ZPE}$) were calculated at the LSDA/BS-I level of theory; c) C. Zheng, R. Hoffmann, D. R. Nelson, *J. Am. Chem. Soc.* **1990**, *112*, 3784–3791.
- [14] J. M. Goicoechea, M. W. Hull, S. C. Sevov, *J. Am. Chem. Soc.* **2007**, *129*, 7885–7893.
- [15] J. P. Sarasa, J. M. Poblet, M. Bénard, *Organometallics* **2000**, *19*, 2264–2272.
- [16] Z. Chen, R. B. King, *Chem. Rev.* **2005**, *105*, 3613–3642.
- [17] S. H. Vosko, L. Wilk, M. Nusair, *Can. J. Phys.* **1980**, *58*, 1200–1211.
- [18] B. Metz, H. Stoll, M. Dolg, *J. Chem. Phys.* **2000**, *113*, 2563–2569.
- [19] F. Weigend, R. Ahlrichs, *Phys. Chem. Chem. Phys.* **2005**, *7*, 118, 3297–3305.

- [20] a) J. P. Perdew, in: *Electronic Structure of Solids '91* (Eds.: P. Ziesche, H. Eschig), Akademie Verlag, Berlin, **1991**, p. 11; b) C. Adamo, V. Barone, *J. Chem. Phys.* **1998**, *108*, 664; c) B. J. Lynch, Y. Zhao, D. G. Truhlar, *J. Phys. Chem. A* **2003**, *107*, 1384.
- [21] a) P. J. Hay, W. R. Wadt, *J. Chem. Phys.* **1985**, *82*, 284; b) C. E. Check, T. O. Faust, J. M. Bailey, B. J. Wright, T. M. Gilbert, L. S. Sunderlin, *J. Phys. Chem. A* **2001**, *105*, 8111; c) L. E. Roy, P. J. Hay, R. L. Martin, *J. Chem. Theory Comput.* **2008**, *4*, 1029.
- [22] a) P. J. Hay, W. R. Wadt, *J. Chem. Phys.* **1985**, *82*, 299; b) A. W. Ehlers, M. Bohme, S. Dapprich, A. Gobbi, A. Hollwarth, V. Jonas, K. F. Kohler, R. Stegmann, A. Veldkamp, G. Frenking, *Chem. Phys. Lett.* **1993**, *208*, 111; c) L. E. Roy, P. J. Hay, R. L. Martin, *J. Chem. Theory Comput.* **2008**, *4*, 1029.
- [23] R. Krishnan, J. S. Binkley, R. Seeger, J. A. Pople, *J. Chem. Phys.* **1980**, *72*, 650.
- [24] a) E. D. Glendening, A. E. Reed, J. E. Carpenter, F. Weinhold, *NBO program*, ver. 3.1; b) A. E. Reed, L. A. Curtiss, F. Weinhold, *Chem. Rev.* **1988**, *88*, 899.
- [25] M. J. Frisch, G. W. Trucks, H. B. Schlegel, G. E. Scuseria, M. A. Robb, J. R. Cheeseman, J. A. Montgomery Jr., T. Vreven, K. N. Kudin, J. C. Burant, J. M. Millam, S. S. Iyengar, J. Tomasi, V. Barone, B. Mennucci, M. Cossi, G. Scalmani, N. Rega, G. A. Petersson, H. Nakatsuji, M. Hada, M. Ehara, K. Toyota, R. Fukuda, J. Hasegawa, M. Ishida, T. Nakajima, Y. Honda, O. Kitao, H. Nakai, M. Klene, X. Li, J. E. Knox, H. P. Hratchian, J. B. Cross, V. Bakken, C. Adamo, J. Jaramillo, R. Gomperts, R. E. Stratmann, O. Yazyev, A. J. Austin, R. Cammi, C. Pomelli, J. W. Ochterski, P. Y. Ayala, K. Morokuma, G. A. Voth, P. Salvador, J. J. Dannenberg, V. G. Zakrzewski, S. Dapprich, A. D. Daniels, M. C. Strain, O. Farkas, D. K. Malick, A. D. Rabuck, K. Raghavachari, J. B. Foresman, J. V. Ortiz, Q. Cui, A. G. Baboul, S. Clifford, J. Cioslowski, B. B. Stefanov, G. Liu, A. Liashenko, P. Piskorz, I. Komaromi, R. L. Martin, D. J. Fox, T. Keith, M. A. Al-Laham, C. Y. Peng, A. Nanayakkara, M. Challacombe, P. M. W. Gill, B. Johnson, W. Chen, M. W. Wong, C. Gonzalez, J. A. Pople, *Gaussian 03*, Revision E.01, Gaussian, Inc., Wallingford CT, **2004**.
- [26] Nucleus Independent Chemical Shifts (NICS): P. von Rague Schleyer, C. Maerker, A. Dransfeld, H. Jiao, N. J. R. van Eikema Hommes, *J. Am. Chem. Soc.* **1996**, *118*, 6317–6318.

Received: February 23, 2010
Published Online: May 31, 2010

Preparation of Cobalt-Containing Ligands with NHC- and/or P-Coordinating Sites and Their Application in Heck Reactions: The Formation of an Unexpected Cobalt-Containing Zwitterionic Complex

Chi-Shing Guo,^[a] Chia-Ming Weng,^[a] and Fung-E Hong^{*[a]}

Keywords: Zwitterions / Carbenes / Phosphanes / Cobalt / Palladium / Heck reaction

An unexpected cobalt-containing zwitterionic complex, $[(\mu\text{-PPh}_2\text{CH}_2\text{PPh}_2)\text{Co}_2(\text{CO})_4]\{\mu,\eta\text{-}(\text{R}1)\text{PC}\equiv\text{CCH}_2(\text{R}2)\}$ (**8**; $\text{R}1 = \text{Ph}_2\text{Bz}$; $\text{R}2 = 3\text{-CoBr}_3\text{-1-benzimidazole}$), has been obtained during an attempt to modify the imidazole moiety in the alkynyl-bridging dicobalt complex $[(\mu\text{-PPh}_2\text{CH}_2\text{PPh}_2)\text{Co}_2(\text{CO})_4]\{\mu,\eta\text{-Ph}_2\text{PC}\equiv\text{CCH}_2(\text{IM})\}$ (**5**; $\text{IM} = \text{benzimidazole}$) to a carbene-type substituent by reaction with benzyl bromide. As revealed in the crystal structure of **8**, it is clear that the benzyl bromide was nucleophilically attacked by the phosphane moiety of **5** with the result the addition of the benzyl moiety. This phosphane site in **8** is in a tetrahedral environment and presumably cationic in nature. In addition, an unusual anionic species CoBr_3^- was found to have attached itself to the free nitrogen site of the imidazole moiety. Thus **8** can be re-

garded as an unusual metal-containing zwitterionic complex. When the phosphane site of **5** was replaced by a non-reactive substituent, for example, $[(\mu\text{-PPh}_2\text{CH}_2\text{PPh}_2)\text{Co}_2(\text{CO})_4]\{\mu,\eta\text{-RC}\equiv\text{CCH}_2(\text{IM})\}$ (**5'**; $\text{R} = \text{H}$; **5_O**: $\text{R} = \text{Ph}_2(\text{O})\text{P}$), nucleophilic attack took place exclusively on the imidazole moiety and led to the formation of $[(\mu\text{-PPh}_2\text{CH}_2\text{PPh}_2)\text{Co}_2(\text{CO})_4]\{\mu,\eta\text{-RC}\equiv\text{CCH}_2(\text{IM}')\}^+\text{Br}^-$ [**9'**: $\text{R} = \text{H}$; **9_O**: $\text{R} = \text{Ph}_2(\text{O})\text{P}$; $\text{IM}' = 3\text{-benzyl-1H-benzimidazole}$]. Complex **9'** could act as a carbene precursor, which was demonstrated by the formation of the bis-**9'**-coordinated palladium complex $[\text{trans-}[(\mu\text{-PPh}_2\text{CH}_2\text{PPh}_2)\text{Co}_2(\text{CO})_4]\{\mu,\eta\text{-HC}\equiv\text{CCH}_2(\text{IM}')\}]_2\text{PdBr}_2]$ (**11**) on treatment with $[\text{Pd}(\text{cod})\text{Cl}_2]$. Fair-to-good efficiencies were observed in Heck reactions employing either isolated **11** or in situ **9'**/ PdCl_2 (2:1) as the catalytic precursor.

Introduction

For the past few decades metal-catalysed cross-coupling reactions have probably been the most frequently employed method for the formation of C–X ($\text{X} = \text{C}, \text{N}, \text{O}, \text{S}$) bonds in modern synthetic chemistry.^[1] Meanwhile, it has been demonstrated repeatedly that a well-chosen ligand is crucial to the success of palladium-catalysed Suzuki reactions.^[2] Therefore considerable effort has been devoted to searching for more efficient ligands for these reactions. For many years, various types of organic phosphanes and phosphane derivatives have most frequently been employed as ligands.^[1e,2,3] Nevertheless, relatively few transition-metal-containing phosphanes have been reported and examined.^[3f,3g,4] In our previous work we demonstrated that a new category of metal-containing phosphanes $[(\mu\text{-PPh}_2\text{CH}_2\text{PPh}_2)\text{Co}_2(\text{CO})_4(\mu,\eta\text{-R}^1\text{C}\equiv\text{CR}^2)]$ [$\text{R}^1, \text{R}^2 = \text{P}(t\text{Bu})_2, \text{P}(i\text{Pr})_2, \text{PCy}_2, \text{PPh}_2, \text{Ph}, \text{py}, \text{H}$] could be easily prepared by synthetic procedures reported previously (Figure 1).^[5] These complexes are essentially disubstituted alkynyl-bridged dicobalt complexes coordinated by a bidentate ligand, bis(diphenylphosphanyl)methane (dppm). This new class of phosphane naturally leads to bulky ligands, which

is clearly beneficial to the reductive elimination process of the catalytic cycle in the widely accepted Suzuki reaction mechanism. Their role as legitimate and active ligands in palladium-catalysed cross-coupling reactions has also been carefully evaluated.^[5,6]

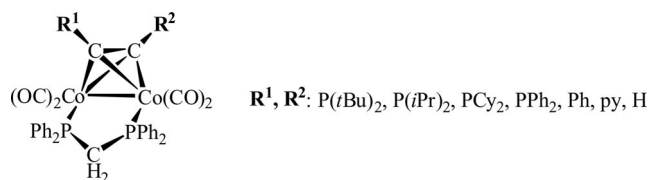


Figure 1. General structure of cobalt-containing mono- or bidentate phosphanes.

As is known, most phosphane ligands are electron-rich and are subject to ready oxidation in an oxygen-containing environment. This oxidation will naturally lead to a great reduction in its catalytic performance as a ligand. Recently, since the first report of Arduengo et al. in 1991, the versatile N-heterocyclic carbenes (NHCs) have emerged as potent alternatives.^[7] NHCs have attracted much attention because of their superb stability towards oxidation, adjustable steric factor through the modification of substituents and strong σ -donating capacity towards low-valence transition metals.^[8] Numerous applications of NHCs in catalysis have been developed.^[8c–8g,9] The advantage of combining the merits of both phosphanes and NHCs by coupling these

[a] Department of Chemistry, National Chung Hsing University, 250 Kuo-Kuang Road, Taichung 40227, Taiwan
E-mail: fehong@dragon.nchu.edu.tw

Supporting information for this article is available on the WWW under <http://dx.doi.org/10.1002/ejic.201000271>.

two distinct ligands in an organic or ferrocenyl moiety has been proposed and put into effect.^[10] In contrast, the full power of uniting an NHC and a phosphane in a dicobalt framework has yet to be realized.^[11] In this work, a new category of dicobalt-based NHCs has been explored and their role as authentic ligands has been examined.

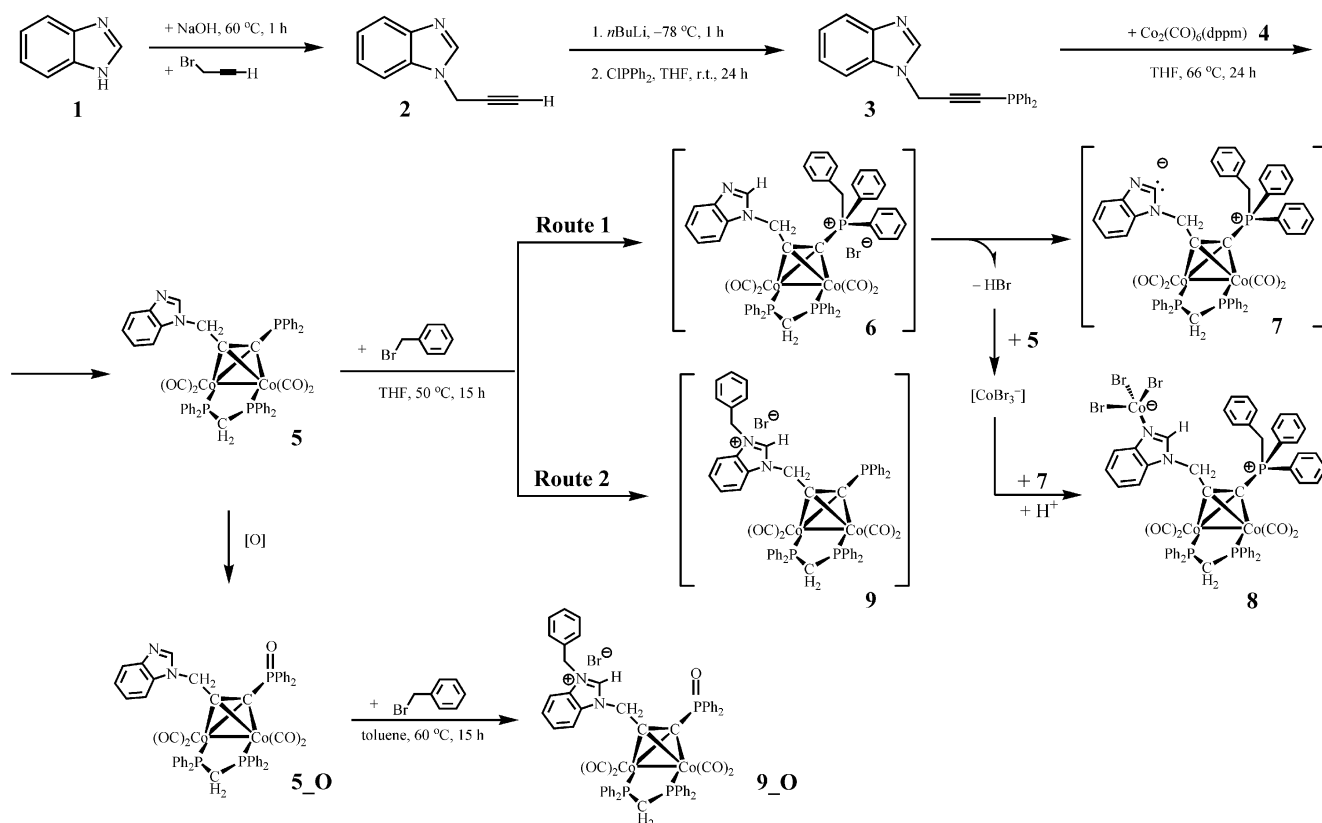
Results and Discussion

Preparation of Cobalt-Containing Mono- or Bidentate Ligands with NHC- and/or P-Coordinating Sites and Their Reactions with a Palladium Salt

A phosphanyl-benzimidazole-disubstituted alkyne-bridged dicobalt complex $[(\mu\text{-PPh}_2\text{CH}_2\text{PPh}_2)\text{Co}_2(\text{CO})_4]\{\mu,\eta\text{-Ph}_2\text{PC}\equiv\text{CCH}_2(\text{IM})\}$ (**5**; IM = 1*H*-benzimidazole) was prepared according to the procedure shown in Scheme 1. It was characterized by ¹H, ¹³C and ³¹P NMR spectroscopy. Unfortunately, the molecular structure of **5** could not be determined unambiguously by single-crystal X-ray diffraction methods due to disorder problems. However, the crystal structure of its oxidized form, $[(\mu\text{-PPh}_2\text{CH}_2\text{PPh}_2)\text{Co}_2(\text{CO})_4]\{\mu,\eta\text{-Ph}_2(\text{O})\text{PC}\equiv\text{CCH}_2(\text{IM})\}$ (**5_O**; IM = 1*H*-benzimidazole), which was prepared by the oxidation of **5** with hydrogen peroxide, was determined unequivocally by this technique.

The ORTEP diagram of **5_O** depicted in Figure 2 shows the presence of a pseudo-tetrahedral Co₂C₂ core, a typical framework of alkyne-bridged dicobalt complexes. The dppm bridges two cobalt atoms and bends away from the benzimidazole moiety to prevent steric hindrance. In addition, the two substituents, the phosphanyl and benzimidazole, on the bridging alkyne bend away from the dicobalt moiety and reside on the same side, as predicted by the Dewar–Chatt–Duncanson model.^[12] The oxidation of the phosphorus atom in **5_O** is evidenced by the formation of a P=O bond [P(3)–O(5) 1.490(4) Å]. The oxidized phosphane naturally loses its coordination capacity towards soft metals.^[13] It also indicates that the phosphanyl site on **5** is electron-rich and suitable for coordination to soft metals.

Subsequently, an attempt was made to modify the benzimidazole moiety of **5** to an NHC-type ligand by reaction with benzyl bromide. This procedure is well prescribed in the literature as a general route to the preparation of N-heterocyclic carbenes from imidazole derivatives (Routes 1 and 2, Scheme 1).^[8h,14] Nevertheless, an unexpected compound with a rather unusual conformation was formed as a bright-red precipitate (Route 1), which was characterized as $[(\mu\text{-PPh}_2\text{CH}_2\text{PPh}_2)\text{Co}_2(\text{CO})_4]\{\mu,\eta\text{-(R1)PC}\equiv\text{CCH}_2\text{-(R2)}\}$ (**8**; R1 = Ph₂Bz; R2 = 3-CoBr₃-1*H*-benzimidazole). On the other hand, the existence of the targeted compound, $[(\mu\text{-PPh}_2\text{CH}_2\text{PPh}_2)\text{Co}_2(\text{CO})_4]\{\mu,\eta\text{-Ph}_2\text{PC}\equiv\text{CCH}_2(\text{IM})\}^+\text{Br}^-$ (**9**; IM = 3-benzyl-1*H*-benzimidazole), was not certain.



Scheme 1. Preparation of cobalt-containing mono- or bidentate ligands. The existence of the complexes in brackets is speculative.

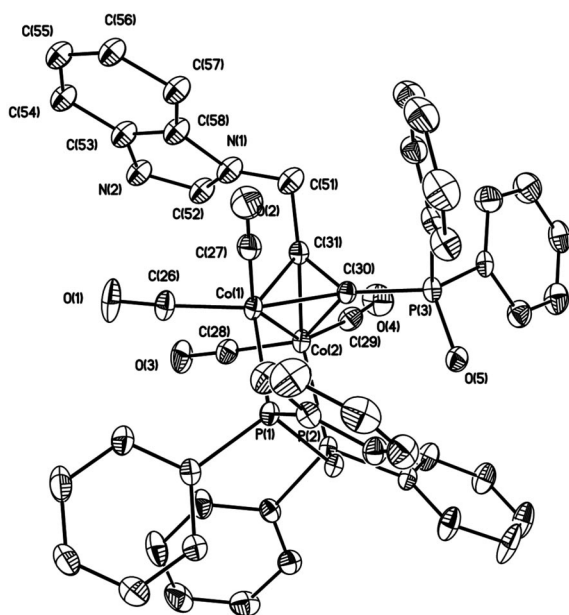


Figure 2. ORTEP drawing of **5_O**. Hydrogen atoms have been omitted for clarity.

The ^1H NMR spectrum of the crude reaction mixture shows a complicated pattern. Nevertheless, the observation of its oxidized counterpart [$\{(\mu\text{-PPh}_2\text{CH}_2\text{PPh}_2)\text{Co}_2(\text{CO})_4\}\{\mu,\eta\text{-Ph}_2\text{P(=O)C}\equiv\text{CCH}_2(\text{IM})\}^+\text{Br}^-$ (**9_O**; IM = 3-benzyl-1*H*-benzimidazole) in the reaction of **5_O** with benzyl bromide in a better-resolved ^1H NMR spectrum substantiates the possibility of the existence of **9**. Note that the oxidized phosphane site of **5_O** is not subjected to the attack of benzyl bromide. Therefore the reaction must take place at the benzimidazole site.

Complex **8** was further characterized by spectroscopic means as well as by single-crystal X-ray diffraction methods. The ^{31}P NMR spectrum exhibits two signals at $\delta = 30.5$ and 36.9 ppm, in a ratio of 1:2, corresponding to the alkylated phosphane and dppm, respectively. The significant downfield shift of the former phosphane reflects its electron-deficient nature, which is consistent with its positively charged character. As revealed in the ORTEP diagram depicted in Figure 3, a pseudo-tetrahedral core Co_2C_2 was obtained and a benzyl group is present on the original phosphane site in **5**, as evidenced by the formation of a P–C bond [P(3)–C(44) 1.829(7) Å]. The phosphane site in **8** is in a tetrahedral environment and presumably cationic in nature. It is also observed that an unusual anionic CoBr_3^- moiety is attached to the free nitrogen site of the imidazole moiety. Alternatively this can be viewed as a coordination of the imidazole unit with Co^{II} . The Co(3)–N(2) bond length is 2.041(5) Å, an indication of a genuine covalent bond yet a dative one. Although several complexes with an anionic CoBr_3^- moiety attached to a pyridine moiety are known, to the best of our knowledge this is the first example of a metal-containing species in which the benzimidazole is attached to a CoBr_3^- moiety. This cobalt atom is in a pseudo-tetrahedral environment and the nitrogen atom

attached to the CoBr_3^- moiety is in a trigonal environment and presumably anionic in nature. In a sense, complex **8** is a unique variation of a metal-containing zwitterion. Normally, zwitterions are polar with a high solubility in polar solvents. Nevertheless, **8** is soluble in organic solvents mainly due to its multiple organic substituents. For comparison, the reaction of benzyl bromide with an equimolar amount of triphenylphosphane and 1-methyl-1*H*-benzo[*d*]imidazole was carried out in a one-pot reaction. Analysis of the products revealed that the attack of benzyl bromide on triphenylphosphane and 1-methyl-1*H*-benzo[*d*]imidazole occurs in a ratio of 89:11. This indicates that the phosphane site is more vulnerable towards electrophilic attack by benzyl bromide than the benzimidazole moiety.

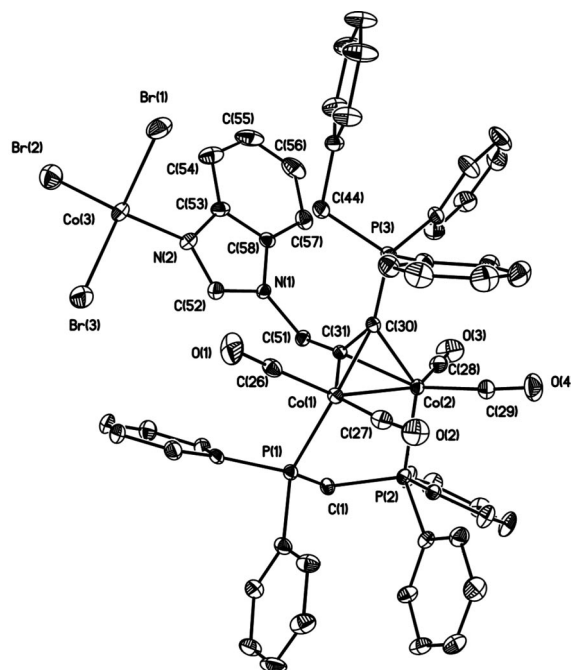
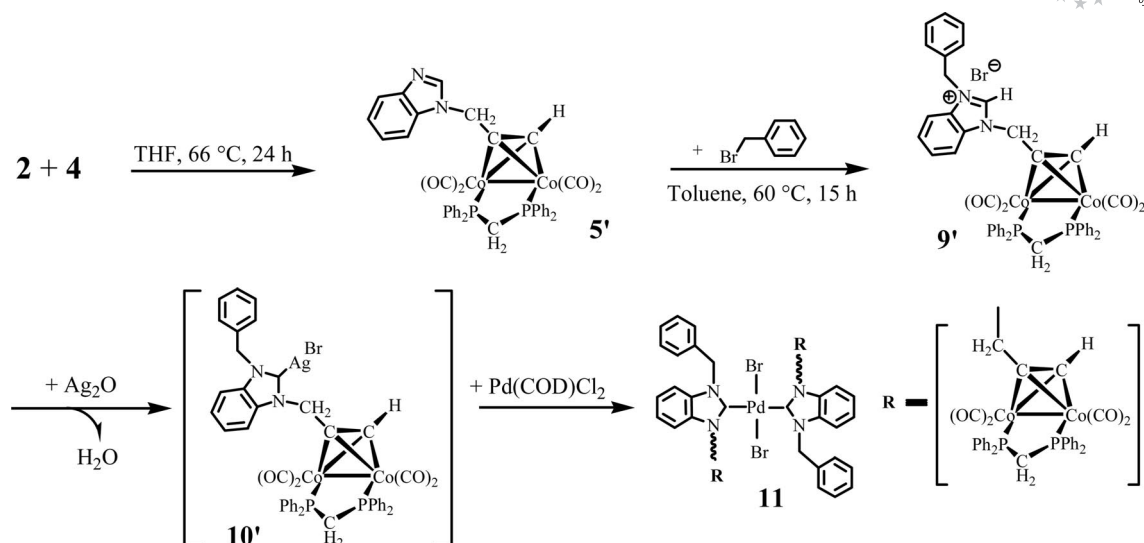


Figure 3. ORTEP drawing of **8**. Hydrogen atoms have been omitted for clarity.

In principle, the reaction path leading to the formation of an **8**-like compound should be blocked whereas the route for the attack of benzyl bromide on the phosphane site of a **5**-like compound is not available. This speculation was confirmed by the reaction of benzyl bromide with [$\{(\mu\text{-PPh}_2\text{CH}_2\text{PPh}_2)\text{Co}_2(\text{CO})_4\}\{\mu,\eta\text{-HC}\equiv\text{CCH}_2(\text{IM})\}$] (**5'**; IM = 1*H*-benzimidazole) in which the PPh_2 unit of **5** is replaced by an inert H in **5'**. Complex **5'** was prepared by the procedure shown in Scheme 2. The reaction of **5'** with benzyl bromide indeed yielded a **9**-like compound, [$\{(\mu\text{-PPh}_2\text{CH}_2\text{PPh}_2)\text{Co}_2(\text{CO})_4\}\{\mu,\eta\text{-HC}\equiv\text{CCH}_2(\text{IM}')\}^+\text{Br}^-$] (**9'**; IM' = 3-benzyl-1*H*-benzimidazole). Subsequent treatment of **9'** with Ag_2O yielded the presumed carbene precursor [$\{(\mu\text{-PPh}_2\text{CH}_2\text{PPh}_2)\text{Co}_2(\text{CO})_4\}\{\mu,\eta\text{-HC}\equiv\text{CCH}_2(\text{IM}')\}\text{-[AgBr]}(\text{10}')$].^[10a,15] The role of **10'** as carbene precursor was shown by the formation of the palladium complex [$\text{trans-}\{(\mu\text{-PPh}_2\text{CH}_2\text{PPh}_2)\text{Co}_2(\text{CO})_4\}\{\mu,\eta\text{-HC}\equiv\text{CCH}_2(\text{IM}')\}_2$]

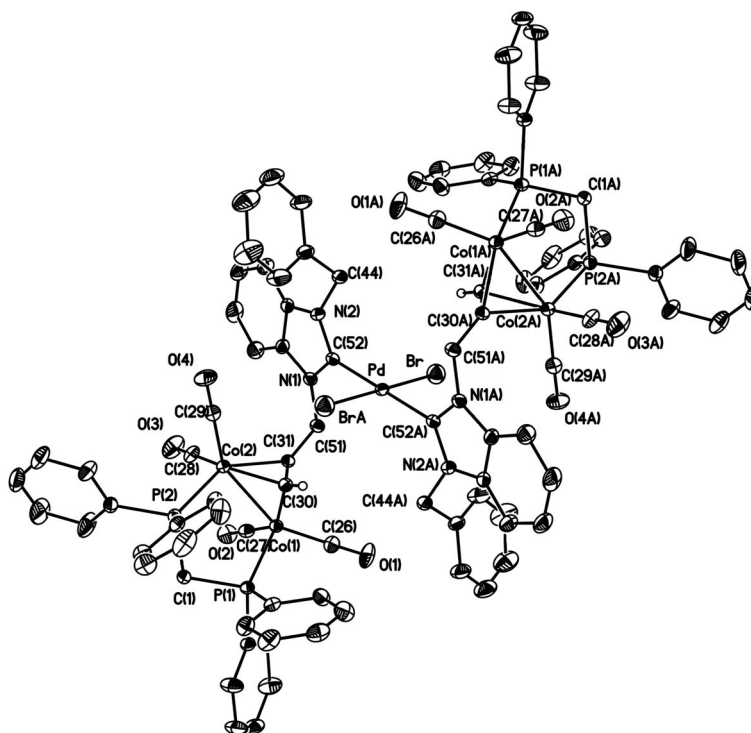


Scheme 2.

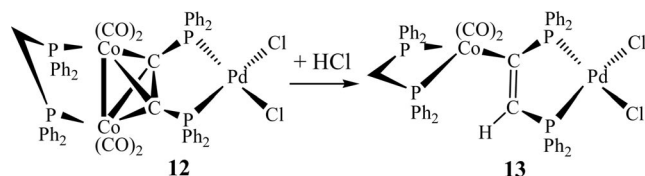
PdBr_2] (**11**) on treatment with $[\text{Pd}(\text{cod})\text{Cl}_2]$. Interestingly, the solubility of **11** is poor in commonly used solvents such as toluene, CH_2Cl_2 and DMSO but good in THF.

The identity of complex **11** was first characterized by spectroscopic means and its structure determined further by single-crystal X-ray diffraction methods. In the ^{31}P NMR spectrum, only one singlet signal at 41.5 ppm was observed, which corresponds to the cobalt-coordinated dppm. The existence of the acetylenic proton is evidenced by the multiplet signal at $\delta = 6.61$ ppm in the ^1H NMR spectrum. As

revealed in the ORTEP diagram depicted in Figure 4, the Pd^{II} is centred in a square-planar environment. The two bulky carbene ligands are arranged in *trans* positions to keep them separated. The $\text{Pd}(3)–\text{C}(52)$ bond length is 2.020(4) Å, a genuine dative bond. Interestingly, two bromides rather than chlorides are observed in **11**; it is believed that the chlorides were replaced by the excess bromide released during the formation of **11** because the formation of the side-product AgCl is thermodynamically more favourable than the formation of AgBr .

Figure 4. ORTEP drawing of **11**. Hydrogen atoms have been omitted for clarity.

Until now, the reaction pathway for the formation of the unexpected **8** remained to be ascertained. The most perplexing question that might be raised is the source of the CoBr_3^- moiety. In principle, one of the probable ways to obtain the CoBr_3^- moiety is from the reaction of the bromide released from benzyl bromide with the Co_2C_2 framework. Interestingly, our previous work revealed some clues about the depletion of the cobalt atom from the Co_2C_2 skeleton. The novel palladium complex *cis*-dichlorido[1,2-bis(diphenylphosphanyl)vinyl-*P,P'*,*C*]palladium(II)-[bis(diphenylphosphanyl)methane-*P,P'*]cobaltacarbonyl (**13**) was obtained from the treatment of $[(\mu\text{-Ph}_2\text{PCH}_2\text{PPh}_2)\text{Co}_2(\text{CO})_4] \cdot \{(\text{Ph}_2\text{PC}\equiv\text{CPh}_2)\text{PdCl}_2\}$ (**12**) with hydrochloric acid (Scheme 3). The complex **13** was characterized by spectroscopic means as well as by single-crystal X-ray diffraction methods.^[16] There are several unique features about this reaction. First, the dicobalt framework fragmented into a mono-cobalt moiety. Secondly, the bonding mode of the dppm ligand changed from bridging to chelating. Thirdly, one of the acetylenic carbon atoms became protonated. Fourthly, the palladium environment remained almost intact. Fifthly, the effective atomic number (EAN) rule was obeyed at the cobalt centre. Based on our previous work, it is assumed that the cobalt of the unusual anionic CoBr_3^- moiety, which attaches to the free nitrogen site of the imidazole moiety, might derive from the depletion of dicobalt fragment by the addition of bromide.

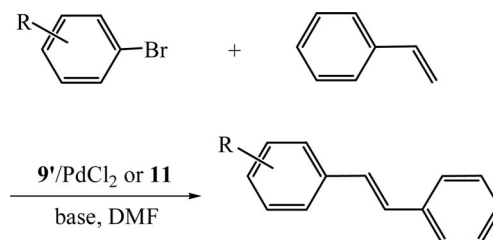


Scheme 3.

Application of **11** or In Situ **9'**/ PdCl_2 (2:1) as a Catalyst Precursor in the Heck Reaction

As has been demonstrated, the catalytic performance of a palladium-catalysed cross-coupling reaction is determined by various influences such as the type of ligand and palladium salt employed, the ratio of ligand/palladium, the temperature, solvent, and base.^[17] In principle, excellent efficiency only comes with the optimization of the most influential factors involved. Normally Heck reactions require more severe reaction conditions than Suzuki reactions.^[18] Therefore it seems appropriate to employ **11** or in situ **9'**/ PdCl_2 (2:1) as catalyst precursor in Heck reactions as this system has been proven to be more endurable at high reaction temperatures. The Heck reactions of substituted bromobenzenes with styrene were carried out at elevated temperature (Scheme 4). Because a high temperature is required, DMF, a high boiling-point solvent, was selected as the reaction media. For comparison of the catalytic efficiency with the published work of Hayashi and co-workers,^[19] a similar procedure was used for the catalytic

reactions under investigation. A suitable Schlenk tube was charged with 1.0 mmol of substituted bromobenzene, 1.0 mmol of styrene, 1.0 mL of DMF, 2.0 mmol of base, 1.0 mol-% of PdCl_2 and 1.0 mol-% of **11** (or in situ **9'**/ PdCl_2 (2:1)) as catalyst precursor. The mixture was stirred at the designated reaction temperature and time depending on the reaction executed. The mixture was then worked up. Owing to steric hindrance, the *trans* form dominated over the *cis* form as the major product.

Scheme 4. Heck reaction catalysed by **11** or in situ **9'**/ PdCl_2 (2:1).

As has been demonstrated, the type of base employed in Heck reactions is crucial to the catalytic efficiency.^[20] It is also the most unpredictable ingredient among all the factors that affect the catalytic performance.^[17b,21] The influence of the bases used in the Heck reactions catalysed by **11** or in situ **9'**/ PdCl_2 (2:1) was examined (Table 1). As shown, acceptable results were obtained with K_2CO_3 or NaOAc as the base (entries 1 and 2). Quite a poor performance was observed by using Cs_2CO_3 as the base (entry 3). The catalytic performance was also poor when the heterocyclic compound 2-bromothiophene was used as the substrate; only 32% yield was observed under the same reaction conditions as used in entry 1. Similar catalytic efficiencies were obtained by employing purified **11** as the catalyst precursor (entries 6–8). This implies that the in situ addition of 2 mol-equiv. of **9'** to PdCl_2 yields **11** quantitatively.

Table 1. Heck reactions of bromobenzenes with styrene catalysed by **11** or in situ **9'**/ PdCl_2 (2:1) employing various substituents, bases and reaction hours.^[a]

Entry	Catalyst precursor	R	Base	Time [h]	Yield [%] ^[b]
1	9' / PdCl_2 (2:1)	4-OMe	K_2CO_3	24	88 (74)
2	9' / PdCl_2 (2:1)	4-OMe	NaOAc	24	87 (79)
3	9' / PdCl_2 (2:1)	4-OMe	Cs_2CO_3	24	30 (24)
4	9' / PdCl_2 (2:1)	4-CHO	K_2CO_3	16	– (71)
5	9' / PdCl_2 (2:1)	H	K_2CO_3	24	– (85)
6	11	4-OMe	K_2CO_3	24	– (80)
7	11	4-CHO	K_2CO_3	24	<99 (81)
8	11	H	K_2CO_3	24	– (90)

[a] Reactions were conducted in DMF (1.0 mL) with base (2.0 equiv.) at 120 °C for the indicated time employing 1.0 mmol-% of **11** or in situ **9'**/ PdCl_2 (2.0 mmol/1.0 mmol). [b] Conversion. Isolated yield given in parentheses as an average of two runs.

Conclusion

We have developed a general route for the preparation of some interesting cobalt-containing mono- or bidentate ligands with NHC- and/or P-coordinating sites. The appli-

cation of the monodentate ligand **9'** in Heck reactions gave reasonable efficiencies at an elevated temperature. The formation of an unexpected cobalt-containing zwitterionic complex **8** was observed and characterized.

Experimental Section

General: All operations were performed in a nitrogen-flushed glove box or in a vacuum system. Freshly distilled solvents were used. All product separations were performed by centrifugal thin-layer chromatography (CTLC, Chromatotron, Harrison model 8924) or by column chromatography. Most of the ^1H NMR spectra were recorded with a 300 MHz Varian VXR-300S spectrometer. In addition, some routine ^1H NMR spectra were recorded either with a Gemini-200 spectrometer at 200.00 MHz or a Varian-400 spectrometer at 400.00 MHz. The chemical shifts are reported in ppm relative to CHCl_3 ($\delta = 7.26$ ppm), CH_2Cl_2 ($\delta = 5.30$ ppm) or $\text{CH}_3\text{C}(\text{O})\text{CH}_3$ ($\delta = 2.09$ ppm) as internal standards. ^{31}P and ^{13}C NMR spectra were recorded at 121.44 and 75.46 MHz, respectively. The ^{31}P and ^{13}C NMR chemical shifts are reported in ppm relative to H_3PO_4 ($\delta = 0.0$ ppm) and CHCl_3 ($\delta = 77$ ppm) or CH_2Cl_2 ($\delta = 53$ ppm), respectively, as internal standards. Mass spectra were recorded with a JEOL JMS-SX/SX 102A GC/MS/MS spectrometer. Elemental analyses were performed with a Heraeus CHN-O-S-Rapid instrument.

Synthesis and Characterization of 1-Prop-2-ynyl-1H-benzimidazole (2): A 100 mL round-bottomed flask equipped with a magnetic stirring bar was charged with 1H-benzimidazole (3.307 g, 28.00 mmol), NaOH (1.120 g, 28.00 mmol) and THF (30 mL). The resulting mixture was then stirred at 50 °C for 1 h before it was cooled to 25 °C. Subsequently, 3-bromopropyne (3.729 g, 30.80 mmol) was added and the solution was stirred for another 12 h. After filtration, the resulting solution was concentrated and the solvent removed under reduced pressure. The title compound, 1-(prop-2-ynyl)-1H-benzimidazole (**2**), was isolated in a yield of 85.0% (3.712 g, 23.80 mmol).

Selected Spectroscopic Data for 2: ^1H NMR (CDCl_3): $\delta = 8.03$ (s, 1 H, NCHN), 4.93 (s, 2 H, $\text{NCH}_2\text{C}\equiv\text{CH}$), 2.50 (s, 1 H, $\text{C}\equiv\text{CH}$), 7.26–7.84 (m, 4 H, arene) ppm. ^{13}C NMR (CDCl_3): $\delta = 143.57$ (NCHN), 141.97, 133.02, 122.86, 122.15, 120.09, 109.38, 75.74 ($\text{NCH}_2\text{C}\equiv\text{CH}$), 74.57 ($\text{NCH}_2\text{C}\equiv\text{CH}$), 34.12 ($\text{NCH}_2\text{C}\equiv\text{CH}$) ppm.

Synthesis and Characterization of 1-[3-(Diphenylphosphanyl)prop-2-ynyl]-1H-benzimidazole (3): The same sized round-bottomed flask equipped with a magnetic stirring bar was charged with 1-(prop-2-ynyl)-1H-benzimidazole (**2**; 0.234 g, 1.50 mmol) and THF (10 mL). The resulting mixture was then stirred at –78 °C before 1.1 equiv. of *n*BuLi (0.66 mL, 2.5 M in hexane) was slowly added. In a dry box, diphenylchlorophosphane (0.330 g, 1.50 mmol) was added to the solution. Subsequently, the mixture was stirred at 25 °C for another 24 h. Then the solvent was removed under reduced pressure and the title compound, 1-[(3-diphenylphosphanyl)prop-2-ynyl]-1H-benzimidazole (**3**), was isolated in a yield of 50.4% (0.275 g, 0.75 mmol).

Selected Spectroscopic Data for 3: ^1H NMR (CDCl_3): $\delta = 8.04$ (s, 1 H, NCHN), 5.13 (s, 2 H, $\text{NCH}_2\text{C}\equiv\text{C}$), 7.30–7.85 (m, 14 H, arene) ppm. ^{13}C NMR (CDCl_3): $\delta = 143.79$ (NCHN), 99.80–134.77, 87.93 ($\text{NCH}_2\text{C}\equiv\text{CH}$), 84.47 ($\text{NCH}_2\text{C}\equiv\text{CH}$), 35.68 ($\text{NCH}_2\text{C}\equiv\text{CH}$) ppm. ^{31}P NMR (CDCl_3): $\delta = -33.77$ (s, 1 P, $\text{C}\equiv\text{C}\text{PPh}_2$) ppm.

Synthesis and Characterization of [(μ-PPh₂CH₂PPh₂)Co₂(CO)₄]-{μ,η-Ph₂PC≡CCH₂(IM)}] (5; IM = 1H-benzimidazole): A 100 mL

round-bottomed flask was charged with $[\text{Co}_2(\text{CO})_8]$ (1.00 mmol, 0.342 g), dppm (1.00 mmol, 0.385 g) and toluene (10 mL). The solution was stirred at 60 °C for 6 h to give the yellow compound $[\text{Co}_2(\text{CO})_6(\mu\text{-}P\text{-}P\text{-}dppm)]$. Without further separation, the reaction flask was charged with 1 equiv. of 1-[(3-diphenylphosphanyl)prop-2-ynyl]-1H-benzimidazole (**3**; 0.340 g, 1.00 mmol) in toluene (5 mL). Subsequently the solution was stirred at 66 °C for another 24 h before the solvent was removed under reduced pressure. The residue was further separated by CTLC. A reddish-brown band was eluted with CH_2Cl_2 /ethyl acetate (10:1) and was identified as the title compound **5** in 60.0% yield (0.60 mmol, 0.570 g).

Selected Spectroscopic Data for 5: ^1H NMR (CDCl_3): $\delta = 8.06$ (s, 1 H, NCHN), 5.49 (s, 2 H, $\text{NCH}_2\text{C}\equiv\text{C}$), 3.35 (q, 1 H, dppm), 3.93 (s, 1 H, dppm), 6.97–7.82 (m, 34 H, arene) ppm. ^{13}C NMR (CDCl_3): $\delta = 204.44$ (CO), 202.89 (CO), 143.30 (NCHN), 128.26–138.90, 122.36, 121.65, 120.73, 120.23, 109.84, 49.68 ($\text{NCH}_2\text{C}\equiv\text{C}$), 35.89 (dppm) ppm. ^{31}P NMR (CDCl_3): $\delta = -3.28$ (s, 1 P, PPh_2), 38.98 (s, 2 P, dppm) ppm. $\text{C}_{52}\text{H}_{40}\text{Co}_2\text{N}_2\text{O}_5\text{P}_3$ (983.63): calcd. C 64.16, H 4.12, N 2.93; found C 60.05, H 4.23, N 2.24.

Reaction of 5 with Bromomethylbenzene: Compound **5** (0.955 g, 1.00 mmol) was placed in a 100 mL round-bottomed flask with bromomethylbenzene (1.10 mmol, 0.185 g) and THF (5 mL). The solution was stirred at 50 °C for 15 h. After filtration, the residue was washed with THF (10 mL) and diethyl ether (10 mL) before it was dried under reduced pressure. [(μ-PPh₂CH₂PPh₂)Co₂(CO)₄]-{μ,η-(R1)PC≡CCH₂(R2)}] (**8**; R1 = Ph₂Bz; R2: 3-CoBr₃-1H-benzimidazole) was isolated in a yield of 23% (0.320 g, 0.23 mmol).

Selected Spectroscopic Data for 8: ^1H NMR (CDCl_3): $\delta = 6.26$ (s, 2 H, $\text{NCH}_2\text{C}\equiv\text{C}$), 6.18 (d, $J_{\text{P-H}} = 6.8$ Hz, 2 H, $\text{PCH}_2\text{C}_6\text{H}_5$), 4.38 (q, 1 H, dppm), 3.78 (q, 1 H, dppm), 6.97–7.82 (m, 34 H, arene) ppm. ^{13}C NMR (CD_3OD): $\delta = 203.82$ (CO), 199.63 (CO), 59.04, 58.02 ppm. ^{31}P NMR (CDCl_3): $\delta = 30.52$ (s, 1 P, $\text{PCH}_2\text{Ph}(\text{Ph})_2$), 36.85 (s, 2 P, dppm) ppm. $\text{C}_{58}\text{H}_{46}\text{Br}_3\text{Co}_3\text{N}_2\text{O}_4\text{P}_3$ (1344.40): calcd. C 51.85, H 3.38, N 2.09; found C 53.43, H 4.35, N 2.00.

Synthesis and Characterization of [(μ-PPh₂CH₂PPh₂)Co₂(CO)₄]-{μ,η-HC≡CCH₂(IM)}] (5'; IM = 1H-Benzimidazole): A 100 mL round-bottomed flask equipped with a magnetic stirring bar was charged with $[\text{Co}_2(\text{CO})_8]$ (1.00 mmol, 0.342 g), dppm (1.00 mmol, 0.385 g) and THF (10 mL). The solution was stirred at 60 °C for 6 h to give the yellow compound $[\text{Co}_2(\text{CO})_6(\mu\text{-}P\text{-}P\text{-}dppm)]$ (**4**). Without further separation, the reaction flask was charged again with 1 molequiv. of 1-prop-2-ynyl-1H-benzimidazole (**2**; 0.156 g, 1.00 mmol) in THF (5 mL). Subsequently, the solution was stirred at 66 °C for another 16 h before the solvent was removed under reduced pressure. The residue was further separated by CTLC. A red band eluted with CH_2Cl_2 /ethyl acetate (3:1) was identified as the title compound **5'** in 75.0% yield (0.75 mmol, 0.557 g).

Selected Spectroscopic Data for 5': ^1H NMR (CDCl_3): $\delta = 8.13$ (s, 1 H, NCHN), 5.51 (s, 2 H, $\text{NCH}_2\text{C}\equiv\text{C}$), 5.58 (s, 1 H, $\text{C}\equiv\text{CH}$), 7.60 (s, 1 H, C_6H_4), 7.79 (s, 1 H, C_6H_4), 3.03 (m, 1 H, dppm), 3.57 (m, 1 H, dppm), 7.13–7.34 (m, 22 H, arene) ppm. ^{13}C NMR (CDCl_3): $\delta = 206.02$ (CO), 202.40 (CO), 143.02 (NCHN), 137.58–135.50, 122.57, 121.60, 120.22, 110.04 (arene), 96.03, 72.99 ($\text{C}\equiv\text{CH}$), 49.43 ($\text{NCH}_2\text{C}\equiv\text{C}$), 41.83 (dppm) ppm. ^{31}P NMR (CDCl_3): $\delta = 42.91$ (s, 2 P, dppm) ppm. $\text{C}_{39}\text{H}_{30}\text{Co}_2\text{N}_2\text{O}_4\text{P}_2$ (770.48): calcd. C 60.80, H 3.92, N 3.04; found C 60.88, H 4.24, N 2.95.

Reaction of 5' with Bromomethylbenzene: Compound **5'** (0.830 g, 1.00 mmol) was placed in a 100 mL round-bottomed flask with bromomethylbenzene (1.10 mmol, 0.185 g) and toluene (5 mL). The solution was stirred at 60 °C for 15 h. After filtration, the residue was washed with toluene (10 mL) and diethyl ether (10 mL)

before it was dried under reduced pressure. Dark-red $[(\mu\text{-PPh}_2\text{CH}_2\text{PPh}_2)\text{Co}_2(\text{CO})_4]\{\mu,\eta\text{-HC}\equiv\text{CCH}_2(\text{IM}')\}^+\text{Br}^-$ (**9'**; IM': 3-benzyl-1*H*-benzimidazole) was isolated in a yield of 85.0% (0.851 g, 0.85 mmol).

Selected Spectroscopic Data for 9': ^1H NMR (CDCl_3): δ = 11.19 (s, 1 H, NCHN), 7.86 (d, $J_{\text{H,H}}$ = 8.4 Hz, 1 H, C_6H_4), 5.77 (s, 2 H, $\text{NCH}_2\text{C}_6\text{H}_5$), 5.87 (s, 2 H, $\text{NCH}_2\text{C}\equiv\text{C}$), 5.96 (m, 1 H, $\text{C}\equiv\text{CH}$), 3.63 (m, 1 H, dppm), 3.05 (m, 1 H, dppm), 7.13–7.61 (m, 28 H, arene) ppm. ^{13}C NMR (CDCl_3): δ = 205.82 (CO), 201.69 (CO), 141.92 (NCHN), 126.54–135.96, 113.44, 75.15, 52.52 (s, 2 C, $\text{NCH}_2\text{C}\equiv\text{C}$), 51.68 (s, 2 C, $\text{NCH}_2\text{C}_6\text{H}_5$), 41.59 (s, 1 C, dppm) ppm. ^{31}P NMR (CDCl_3): δ = 42.91 (s, 2 P, dppm) ppm. $\text{C}_{46}\text{H}_{37}\text{BrCo}_2\text{N}_2\text{O}_4\text{P}_2$ (941.51): calcd. C 58.68, H 3.96, N 2.98; found C 58.43, H 3.92, N 2.63.

Conversion of 9' into a Carbene-Type Ligand and Reaction with $[\text{Pd}(\text{cod})\text{Cl}_2]$: A 100 mL round-bottomed flask was charged with **9'** (1.882 g, 2.00 mmol) and CH_2Cl_2 (15 mL). The flask was wrapped in aluminium foil to avoid exposure to light. Then Ag_2O (0.462 g, 2.00 mmol) was added and the solution was stirred at 25 °C for 12 h. The solution was then filtered through Celite and dried under reduced pressure. A reddish-brown residue, presumed to be $[(\mu\text{-PPh}_2\text{CH}_2\text{PPh}_2)\text{Co}_2(\text{CO})_4]\{\mu,\eta\text{-HC}\equiv\text{CCH}_2(\text{IM}')\}[\text{AgBr}]$ (**10'**), was collected. Compound **10'** was treated with dichloro(1,5-cyclooctadiene)palladium (0.028 g, 0.10 mmol) in THF (15 mL) at 25 °C and stirred for 12 h before filtration through Celite and drying under reduced pressure. The bright-red residue, $[\text{trans-}[(\mu\text{-PPh}_2\text{CH}_2\text{PPh}_2)\text{Co}_2(\text{CO})_4]\{\mu,\eta\text{-HC}\equiv\text{CCH}_2(\text{IM}')\}_2\text{PdBr}_2]$ (**11**), was washed with CH_2Cl_2 (10 mL). The yield of **11** was 67% (1.334 g, 0.67 mmol). Bright-red crystals suitable for X-ray crystallographic studies were obtained from THF solution.

Selected Spectroscopic Data for 11: ^1H NMR (THF): δ = 7.83 (d, $J_{\text{H,H}}$ = 12.0 Hz, 2 H, C_6H_4), 6.28 (s, 4 H, $\text{NCH}_2\text{C}_6\text{H}_5$), 6.40 (s, 4 H, $\text{NCH}_2\text{C}\equiv\text{C}$), 6.61 (m, 2 H, $\text{C}\equiv\text{CH}$), 3.44 (m, 2 H, dppm), 3.26 (m, 2 H, dppm), 6.91–7.60 (m, 56 H, arene) ppm. ^{31}P NMR (CDCl_3): δ = 41.52 (s, 2 P, dppm) ppm. ^{13}C NMR ($[\text{D}_8]\text{THF}$): δ = 208.55 (CO), 203.13 (CO), 184.19 [NC(Pd)N], 123.07–138.57, 112.59, 112.07, 77.75, 54.25, 51.03 ppm. $\text{C}_{92}\text{H}_{72}\text{Br}_2\text{Co}_4\text{N}_4\text{O}_8\text{P}_4\text{Pd}$

(1987.43): calcd. C 53.25, H 3.58, N 3.11; found C 55.45, H 4.14, N 2.25.

Preparation of 5_O and 9_O: Compound **5** (0.954 g, 1.00 mmol) dissolved in THF (5 mL) was placed in a 100 mL round-bottomed flask and H_2O_2 (3 mL) was then slowly added. The solution was stirred at 25 °C for 3 h. After filtration, the bright-red residue was washed with ethyl acetate (30 mL) before it was dried under reduced pressure. $[(\mu\text{-PPh}_2\text{CH}_2\text{PPh}_2)\text{Co}_2(\text{CO})_4]\{\mu,\eta\text{-Ph}_2\text{P(=O)-C}\equiv\text{CCH}_2(\text{IM})\}$ (**5_O**; IM = 1*H*-benzimidazole) was isolated in a yield of 95.0% (0.921 g, 0.95 mmol). Oxide **5_O** (0.921 g, 0.95 mmol) was treated with bromomethylbenzene (1.10 mmol, 0.185 g) in toluene (5 mL) at 60 °C and stirred for 15 h. After filtration, the bright-red residue was washed with toluene and diethyl ether before it was dried under reduced pressure. $[(\mu\text{-PPh}_2\text{CH}_2\text{PPh}_2)\text{Co}_2(\text{CO})_4]\{\mu,\eta\text{-Ph}_2\text{P(=O)C}\equiv\text{CCH}_2(\text{IM})\}^+\text{Br}^-$ (**9_O**; IM = 3-benzyl-1*H*-benzimidazole) was isolated in a yield of 85% (0.921 g, 0.85 mmol).

Selected Spectroscopic Data for 5_O: ^1H NMR (CDCl_3): δ = 8.10 (s, 1 H, NCHN), 7.86 (d, $J_{\text{H,H}}$ = 2.4 Hz, 1 H, C_6H_4), 5.65 (t, 2 H, $\text{NCH}_2\text{C}\equiv\text{C}$), 5.65 (m, 1 H, dppm), 3.20 (m, 1 H, dppm), 6.86–7.71 (m, 33 H, arene) ppm. ^{13}C NMR (CDCl_3): δ = 205.38 (CO), 200.27 (CO), 143.73 (NCHN), 127.82–138.00, 107.5, 122.61, 121.92, 120.49, 109.72, 50.63, 35.59 (t, 1 C, dppm) ppm. ^{31}P NMR (CDCl_3): δ = 27.99 [s, 1 P, $\text{P(=O)CH}_2\text{Ph(Ph)}_2$], 36.99 (s, 2 P, dppm) ppm.

Selected Spectroscopic Data for 9_O: ^1H NMR (CDCl_3): δ = 10.94 (s, 1 H, NCHN), 7.79 (m, 1 H, C_6H_4), 5.80 (s, 2 H, $\text{NCH}_2\text{C}_6\text{H}_5$), 6.32 (s, 2 H, $\text{NCH}_2\text{C}\equiv\text{C}$), 5.69 (m, 1 H, dppm), 3.22 (m, 1 H, dppm), 6.91–7.59 (m, 38 H, arene) ppm. ^{13}C NMR (CDCl_3): δ = 206.40 (CO), 199.18 (CO), 125.12–137.68, 113.55, 113.05, 75.07, 73.73, 54.83 ($\text{NCH}_2\text{C}\equiv\text{C}$), 54.06 ($\text{NCH}_2\text{C}_6\text{H}_5$), 35.52 (dppm) ppm. ^{31}P NMR (CDCl_3): δ = 28.07 [s, 1 P, $\text{PCH}_2\text{Ph(Ph)}_2$], 37.29 (s, 2 P, dppm) ppm. $\text{C}_{58}\text{H}_{46}\text{BrCo}_2\text{N}_2\text{O}_5\text{P}_3$ (1141.69): calcd. C 61.02, H 4.06, N 2.45; found C 61.13, H 4.05, N 2.49.

General Procedure for the Heck Reactions: Heck reactions were performed according to the following procedure. Reactants including

Table 2. Crystal data for **5_O**, **8** and **11**.

Compound	5_O	8	11
Formula	$\text{C}_{52}\text{H}_{40}\text{Co}_2\text{N}_2\text{O}_6\text{P}_3$	$\text{C}_{58}\text{H}_{46}\text{Br}_3\text{Co}_3\text{N}_2\text{O}_4\text{P}_3$	$\text{C}_{92}\text{H}_{72}\text{Br}_2\text{Co}_4\text{N}_4\text{O}_8\text{P}_4\text{Pd}\cdot 2\text{CH}_2\text{Cl}_2$
Formula mass	999.63	1344.40	2157.21
Crystal system	monoclinic	orthorhombic	monoclinic
Space group	$C2/c$	$Pbca$	$P2_1/c$
a [Å]	28.128(4)	18.187(5)	13.0513(9)
b [Å]	12.6177(18)	17.336(5)	17.9369(13)
c [Å]	29.079(4)	35.433(10)	20.3915(14)
α [°]	90	90	90
β [°]	101.008(3)	90	104.0760(10)
γ [°]	90	90	90
V [Å ³]	10131(2)	11172(5)	4630.3(6)
Z	8	8	2
D_c [Mg/m ³]	1.311	1.599	1.547
$\lambda(\text{Mo-K}\alpha)$ [Å]	0.71073	0.71073	0.71073
μ [mm ⁻¹]	0.798	3.160	1.996
θ range [°]	1.43–26.02	1.72–26.07	1.97–26.03
Observed reflections [$F > 4\sigma(F)$]	9938	11001	9095
No. of refined parameters	586	667	547
R_1 for significant reflections ^[a]	0.0778	0.0610	0.0558
wR_2 for significant reflections ^[b]	0.2563	0.1727	0.2040
GoF ^[c]	1.024	1.118	1.006

[a] $R_1 = [\Sigma(|F_o| - |F_c|)/\Sigma F_o]$. [b] $wR_2 = \{\Sigma[w(F_o^2 - F_c^2)^2]/\Sigma[w(F_o^2)^2]\}^{1/2}$ with $w = 0.1300, 0.1000$ and 0.1850 for the crystal data of **5_O**, **8** and **11**, respectively. [c] $\text{GoF} = [\Sigma w(F_o^2 - F_c^2)^2/(N_{\text{refl}} - N_{\text{params}})]^{1/2}$.

palladium(II) chloride (1.7 mg, 0.01 mmol), **9'** (18.8 mg, 0.02 mmol) and a base (2.0 mmol) were placed in a 20 mL Schlenk flask. The flask was evacuated and back-filled with nitrogen before adding DMF (1.0 mL), the aryl bromide (1.0 mmol) and styrene (0.114 mL, 1.0 mmol). The solution was stirred at the designated temperature and time. Subsequently the mixture was filtered and concentrated in vacuo. The crude material was purified by CTLC on silica gel. A similar procedure was applied in the case of catalyst precursor **11** (19.91 mg, 0.01 mmol).

X-ray Crystallographic Studies: Suitable crystals of **5_O**, **8** and **11** were sealed in thin-walled glass capillaries under nitrogen and mounted on a Bruker AXS SMART 1000 diffractometer. Intensity data were collected in 1350 frames with increasing ω (width of 0.3° per frame). The space groups were determined on the basis of the Laue symmetries and systematic absences, and confirmed by using structure solution methods. The structures were solved by direct methods using the SHELXTL package.^[22] All non-hydrogen atoms were located from successive Fourier maps and hydrogen atoms were refined by using the riding model. Anisotropic thermal parameters were used for all non-hydrogen atoms and fixed isotropic parameters were used for hydrogen atoms. The crystallographic data for **5_O**, **8** and **11** are summarized in Table 2.

CCDC-708000 (for **5_O**), -708001 (for **8**) and -708002 (for **11**) contain the supplementary crystallographic data for this paper. These data can be obtained free of charge from The Cambridge Crystallographic Data Centre via www.ccdc.cam.ac.uk/data_request/cif.

Supporting Information (see also the footnote on the first page of this article): Spectroscopic data such as ¹H, ¹³C, ³¹P NMR, and mass spectra of **5**, **8**, **9'**, **9_O** and **11**.

Acknowledgments

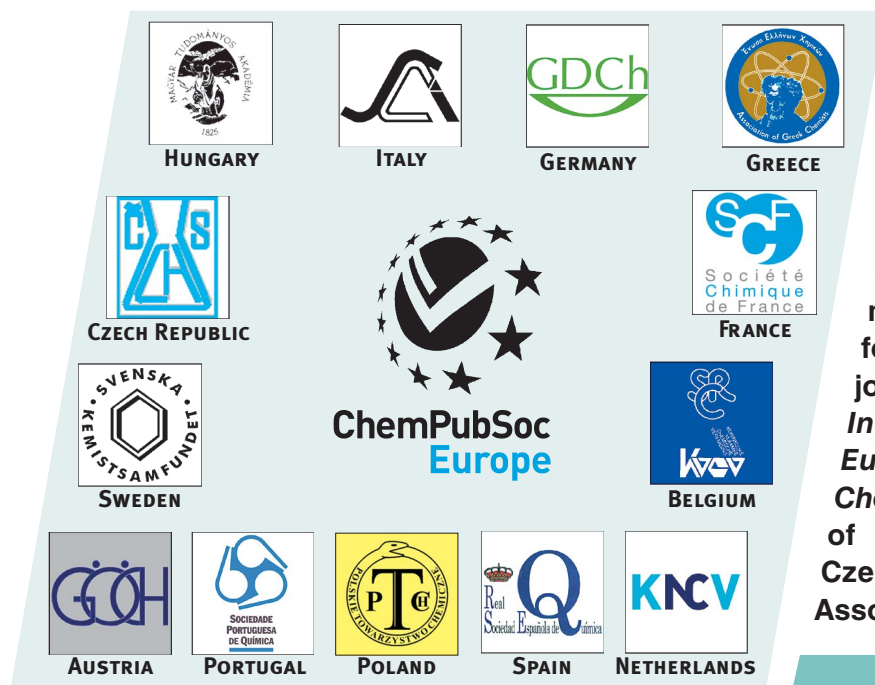
We are grateful to the National Science Council of the R.O.C. (Grant NSC 95-2113-M-005-015-MY3) for financial support.

- [1] a) S. L. Buchwald, *Acc. Chem. Res.* **2008**, *41*, 1439–1439; b) D. Alberico, M. E. Scott, M. Lautens, *Chem. Rev.* **2007**, *107*, 174–238; c) J.-P. Corbet, G. Mignani, *Chem. Rev.* **2006**, *106*, 2651–2710; d) J. Tsuji, *Palladium Reagents and Catalysts: New Perspectives for the 21st Century*, Wiley, New York, **2004**; e) J. Hassan, M. Sévignon, C. Gozzi, E. Schulz, M. Lemaire, *Chem. Rev.* **2002**, *102*, 1359–1469; f) K. N. Houk, H. Sessler, J.-M. Lehn, S. V. Ley, A. de Meijere, S. L. Schreiber, J. Thiem, B. M. Trost, F. Vögtle, H. Yamamoto (Eds.), *Cross-Coupling Reactions-A Practical Guide in Topics in Current Chemistry*, Springer, Heidelberg, **2002**, vol. 219; g) F. Diederich, P. J. Stang (Eds.), *Metal-Catalyzed Cross-coupling Reactions*, Wiley-VCH, Weinheim, **1998**.
- [2] T. E. Barder, S. D. Walker, J. R. Martinelli, S. L. Buchwald, *J. Am. Chem. Soc.* **2005**, *127*, 4685–4696.
- [3] a) W. Tang, X. Zhang, *Chem. Rev.* **2003**, *103*, 3029–3069; b) C. A. Bessel, P. Aggarwal, A. C. Marschillok, K. J. Takeuchi, *Chem. Rev.* **2001**, *101*, 1031–1066; c) S. D. Walker, T. E. Barder, J. R. Martinelli, S. L. Buchwald, *Angew. Chem. Int. Ed.* **2004**, *43*, 1871–1876; d) J. F. Hartwig, *Angew. Chem. Int. Ed.* **1998**, *37*, 2046–2067; e) G. Mann, J. F. Hartwig, *J. Am. Chem. Soc.* **1996**, *118*, 13109–13110; f) N. Kataoka, Q. Shelby, J. P. Stambuli, J. F. Hartwig, *J. Org. Chem.* **2002**, *67*, 5553–5556; g) A. F. Littke, C. Dai, G. C. Fu, *J. Am. Chem. Soc.* **2000**, *122*, 4020–4028; h) J. G. Planas, J. A. Gladysz, *Inorg. Chem.* **2002**, *41*, 6947–6949; i) Q.-S. Hu, Y. Lu, Z.-Y. Tang, H.-B. Yu, *J. Am. Chem. Soc.* **2003**, *125*, 2856–2857; j) T. E. Pickett, F. X. Roca, C. J. Richards, *J. Org. Chem.* **2003**, *68*, 2592–2599; k) Z.-Y. Tang, Y. Lu, Q.-S. Hu, *Org. Lett.* **2003**, *5*, 297–300; l) N. G. Andersen, B. A. Keay, *Chem. Rev.* **2001**, *101*, 997–1030.
- [4] a) O. Delacroix, J. A. Gladysz, *Chem. Commun.* **2003**, 665–675; b) A. Salzer, *Coord. Chem. Rev.* **2003**, *242*, 59–72; c) J. F. Jesen, M. Johannsen, *Org. Lett.* **2003**, *5*, 3025–3028; d) N. Kataoka, Q. Shelby, J. P. Stambuli, J. F. Hartwig, *J. Org. Chem.* **2002**, *67*, 5553–5556; e) A. F. Littke, C. Dai, G. C. Fu, *J. Am. Chem. Soc.* **2000**, *122*, 4020–4028; f) T. E. Pickett, F. X. Roca, C. J. Richards, *J. Org. Chem.* **2003**, *68*, 2592–2599; g) Z.-Y. Tang, Y. Lu, Q.-S. Hu, *Org. Lett.* **2003**, *5*, 297–300.
- [5] a) F.-E. Hong, Y.-C. Chang, R.-E. Chang, S.-C. Chen, B.-T. Ko, *Organometallics* **2002**, *21*, 961–967; b) Y.-C. Chang, F.-E. Hong, *Organometallics* **2005**, *24*, 5686–5695.
- [6] a) F.-E. Hong, Y.-J. Ho, Y.-C. Chang, Y.-L. Huang, *J. Organomet. Chem.* **2005**, *690*, 1249–1257; b) C.-P. Chang, Y.-L. Huang, F.-E. Hong, *Tetrahedron* **2005**, *61*, 3835–3839; c) F.-E. Hong, Y.-C. Chang, C.-P. Chang, Y.-L. Huang, *Dalton Trans.* **2004**, 157–165; d) F.-E. Hong, Y.-J. Ho, Y.-C. Chang, Y.-C. Lai, *Tetrahedron* **2004**, *60*, 2639–2645; e) F.-E. Hong, C.-P. Chang, Y.-C. Chang, *Dalton Trans.* **2003**, 3892–3897; f) F.-E. Hong, Y.-C. Lai, Y.-J. Ho, Y.-C. Chang, *J. Organomet. Chem.* **2003**, *688*, 161–167; g) J.-C. Lee, M.-G. Wang, F.-E. Hong, *Eur. J. Inorg. Chem.* **2005**, 5011–5017.
- [7] a) A. J. Arduengo III, R. L. Harlow, M. Kline, *J. Am. Chem. Soc.* **1991**, *113*, 361–363; b) A. J. Arduengo III, H. V. R. Davis, R. L. Harlow, M. Kline, *J. Am. Chem. Soc.* **1992**, *114*, 5530–5534.
- [8] a) D. Bourissou, O. Guerret, F. P. Gabbaï, G. Bertrand, *Chem. Rev.* **2000**, *100*, 39–92; b) W. A. Herrmann, M. Elison, J. Fischer, C. Köchter, G. R. J. Artus, *Angew. Chem. Int. Ed.* **1995**, *34*, 2371–2374; c) W. A. Herrmann, T. Weskamp, V. P. W. Bohm, *Adv. Organomet. Chem.* **2002**, *48*, 1–69; d) L. Jafarpour, S. P. Nolan, *Adv. Organomet. Chem.* **2001**, *46*, 181–222; e) O. Navarro, R. A. Kelly III, S. P. Nolan, *J. Am. Chem. Soc.* **2003**, *125*, 16194–16195; f) J. Yin, M. P. Rainka, X. X. Zhang, S. L. Buchwald, *J. Am. Chem. Soc.* **2002**, *124*, 1162–1163; g) J. P. Stambuli, R. Kuwano, J. F. Hartwig, *Angew. Chem. Int. Ed.* **2002**, *41*, 4746–4748; h) E. A. B. Kantchev, C. J. O'Brien, M. G. Organ, *Angew. Chem. Int. Ed.* **2007**, *46*, 2768–2813; i) F. E. Hahn, M. C. Jahnke, *Angew. Chem. Int. Ed.* **2008**, *47*, 3122–3172; j) N. Marion, S. P. Nolan, *Acc. Chem. Res.* **2008**, *41*, 1440–1449.
- [9] a) W. A. Herrmann, *Angew. Chem. Int. Ed.* **2002**, *41*, 1290–1309; b) W. A. Herrmann, C. Köcher, *Angew. Chem. Int. Ed. Engl.* **1997**, *36*, 2162–2187; c) M. S. Viciu, R. A. Kelly III, E. D. Stevens, F. Naud, M. Studer, S. P. Nolan, *Org. Lett.* **2003**, *5*, 1479–1482; d) W. D. Jones, *J. Am. Chem. Soc.* **2009**, *131*, 15075–15077; e) F. E. Hahn, L. Wittenbecher, R. Boese, D. Bläser, *Chem. Eur. J.* **1999**, *5*, 1931–1935; f) F. E. Hahn, L. Wittenbecher, D. L. Van, R. Fröhlich, *Angew. Chem. Int. Ed.* **2000**, *39*, 541–544.
- [10] a) F. Visentin, A. Togni, *Organometallics* **2007**, *26*, 3746–3754; b) F. E. Hahn, M. C. Jahnke, T. Pape, *Organometallics* **2006**, *25*, 5927–5936; c) S. Gischig, A. Togni, *Organometallics* **2004**, *23*, 2479–2487.
- [11] S. E. Gibson, C. Johnstone, J. A. Loch, J. W. Steed, A. Stevenazzi, *Organometallics* **2003**, *22*, 5374–5377.
- [12] a) M. J. S. Dewar, *Bull. Soc. Chim. Fr.* **1951**, *18*, C71–C79; b) J. Chatt, L. A. Duncanson, *J. Chem. Soc.* **1953**, 2939–2947.
- [13] a) R. G. Pearson, *J. Am. Chem. Soc.* **1963**, *85*, 3533–3539; b) R. G. Pearson (Ed.), *Hard and Soft Acids and Bases*, Dowden, Hutchinson and Ross, Stroudsburg, **1973**; c) R. G. Pearson, in: *Chemical Hardness, Structure and Bonding* (Eds.: K. D. Sen, D. M. P. Mingos), Springer, Berlin, **1993**, vol. 80, chapter 1.
- [14] a) D. S. McGuinness, K. J. Cavell, *Organometallics* **2000**, *19*, 741–748; b) F. E. Hahn, C. Holtgrewe, T. Pape, M. Martin, E. Sola, L. Oro, *Organometallics* **2005**, *24*, 2203–2209; c) F. E. Hahn, M. C. Jahnke, V. Gomez-Benitez, D. Morales-Morales, T. Pape, *Organometallics* **2005**, *24*, 6458–6463; d) C. Holtgrewe, C. Diedrich, T. Pape, S. Grimme, F. E. Hahn, *Eur. J. Org. Chem.* **2006**, 3116–3124.

- [15] a) A. W. Waltman, R. H. Grubbs, *Organometallics* **2004**, *23*, 3105–3107; b) G. A. Grasa, M. S. Viciu, J. Huang, S. P. Nolan, *J. Org. Chem.* **2001**, *66*, 7729–7737.
- [16] C.-P. Chang, F.-E. Hong, *J. Chin. Chem. Soc.* **2005**, *52*, 1105–1109.
- [17] a) E. R. Goldman, I. L. Medintz, J. L. Whitley, A. Hayhurst, A. R. Clapp, H. T. Uyeda, J. R. Deschamps, M. E. Lassman, H. Mattoussi, *J. Am. Chem. Soc.* **2005**, *127*, 6744–6751; b) A. A. C. Braga, N. H. Morgon, G. Ujaque, F. Maseras, *J. Am. Chem. Soc.* **2005**, *127*, 9298–9307.
- [18] a) N. T. S. Phan, M. van der Sluys, C. W. Jones, *Adv. Synth. Catal.* **2006**, *348*, 609–679; b) J. G. de Vries, *Dalton Trans.* **2006**, 421–429.
- [19] K. Kawamura, S. Haneda, Z. Gan, K. Eda, M. Hayashi, *Organometallics* **2008**, *27*, 3748–3752.
- [20] a) S. R. Dubbaka, P. Vogel, *Org. Lett.* **2004**, *6*, 95–98; b) G. A. Grasa, A. C. Hillier, S. P. Nolan, *Org. Lett.* **2001**, *3*, 1077–1080; c) N. Miyaura, K. Yamada, H. Sugimoto, A. Suzuki, *J. Am. Chem. Soc.* **1985**, *107*, 972–980; d) J.-I. Uenishi, J.-M. Beau, R. W. Armstrong, Y. Kishi, *J. Am. Chem. Soc.* **1987**, *109*, 4756–4758.
- [21] a) A. A. C. Braga, N. H. Morgon, G. Ujaque, A. Lledós, F. Maseras, *J. Organomet. Chem.* **2006**, *691*, 4459–4466; b) S. R. Chemler, D. Trauner, S. J. Danishefsky, *Angew. Chem. Int. Ed.* **2001**, *40*, 4544–4568.
- [22] G. M. Sheldrick, *SHELXTL PLUS User's Manual, Revision 4.1*, Nicolet XRD Corporation, Madison, WI, **1991**.

Received: March 9, 2010

Published Online: June 2, 2010

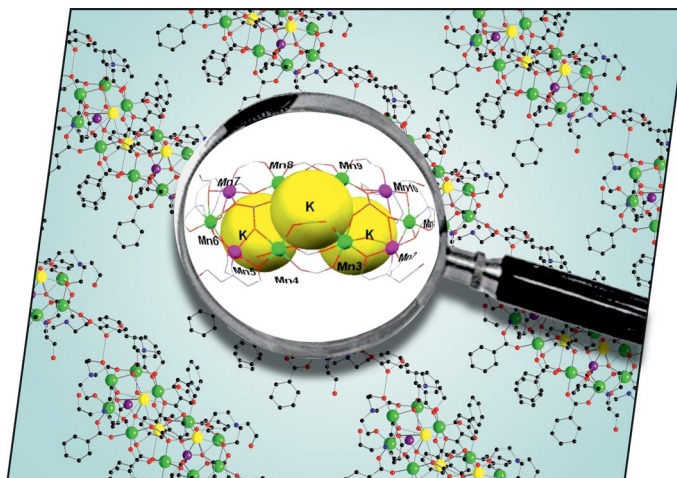


EurJIC is co-owned by 11 societies of ChemPubSoc Europe, a union of European chemical societies for the purpose of publishing high-quality science. All owners merged their national journals to form two leading chemistry journals, the *European Journal of Inorganic Chemistry* and the *European Journal of Organic Chemistry*. Three further members of ChemPubSoc Europe (Austria, Czech Republic and Sweden) are Associates of the two journals.

Other ChemPubSoc Europe journals are *Chemistry – A European Journal*, *ChemBioChem*, *ChemPhysChem*, *ChemMedChem*, *ChemSusChem* and *ChemCatChem*.

COVER PICTURE

The cover picture shows a mixed-valence $\{\text{Mn}_{10}\}$ cage, which can be regarded as an analogue of 24-metallacrown-10. The cage is a host for three potassium ions and crystallises as a cation; benzoate anions link the cages into a 1D polymer within the crystal. Details are discussed in the article by C. Dendrinou-Samara, R. E. P. Winpenny et al. on p. 3097ff. The authors thank Mrs. A. Samara for the artwork of the cover picture.



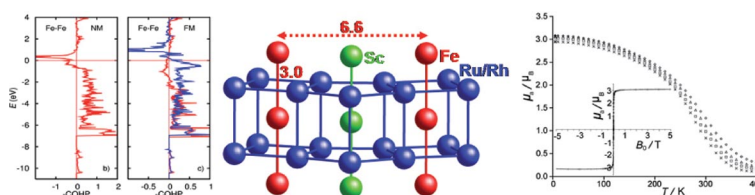
MICROREVIEW

Transition-Metal-Rich Borides

B. P. T. Fokwa* 3075–3092

Transition-Metal-Rich Borides – Fascinating Crystal Structures and Magnetic Properties

Keywords: Transition metals / Boron / Structure elucidation / Density functional calculations / Magnetic properties



Structure–property relationships, with a particular emphasis on magnetic properties of transition-metal-rich borides, have been the focus of some research in the last

decade. The figure exemplifies the study of a 3d-transition-metal boride ferromagnet found experimentally (right) and the theory that explains it (left).

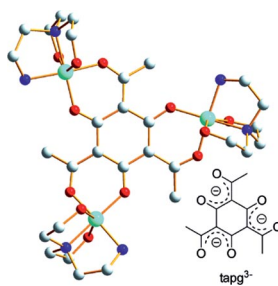
SHORT COMMUNICATION

Trinuclear Copper Complexes

E. T. Spielberg, W. Plass* 3093–3096

2,4,6-Triacetylphlorogucinol as Threefold Symmetric Bridging Ligand: Synthesis, Structure and Magnetic Properties of the Copper Complex

Keywords: Copper / Bridging ligands / Magnetic properties / Stacking interactions / Tritopic Complex



The trinuclear copper complex of the annulated threefold acetylacetone tapg^{3-} is reported. The bridging core ligand transmits ferromagnetic exchange coupling between the copper ions.

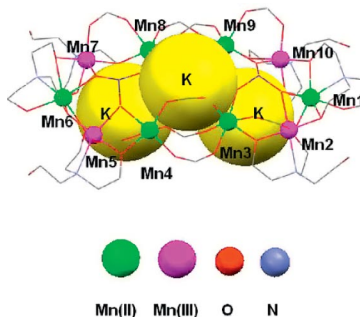
FULL PAPERS

{Mn₁₀} Cage

C. Dendrinou-Samara,* C. A. Muryn, F. Tuna, R. E. P. Winpenny* 3097–3101

Non-Oxido Mixed-Valence $\text{Mn}^{\text{II}}_6\text{Mn}^{\text{III}}_4$ Cluster with Benzoate, Triethanolamine and Phosphonate Bridging Ligands

Keywords: Manganese / Cluster compounds / Antiferromagnetic behaviour / Tripodal ligands / Mixed-valent compounds



$\{[\text{K}_3\text{Mn}_{10}(\text{PhCOO})_{10}(\text{PhPO}_3)_2(\text{Htea})_6](\text{PhCOO})_6\text{MeCN}\}_n$ (**1**) was prepared by a combination of triethanolamine and phosphonates with manganese benzoate chemistry. The resulting $\{\text{Mn}_{10}\}$ cage can be regarded as an analogue of 24-metallacrown-10, acting as a host for three potassium ions, while it crystallises as a cation; benzoate anions link the cages into a 1D polymer within the crystal. The room-temperature value of **1** is very close to the spin-only value of $38.25 \text{ cm}^3 \text{ mol}^{-1} \text{ K}$ expected for six Mn^{II} and four Mn^{III} ions.

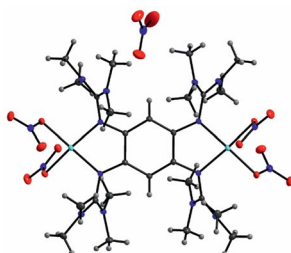
Trapped Radical Cation

C. Trumm, O. Hübner, E. Kaifer, H.-J. Himmel* 3102–3108

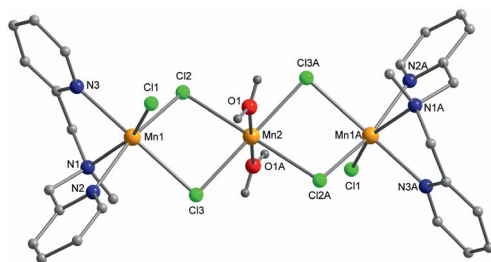


Trapped in a Complex: the 1,2,4,5-Tetrakis(tetramethylguanidino)benzene Radical Cation ($\text{ttmgb}^{+\bullet}$) with a Bisallylic Structure

Keywords: Copper / Redox chemistry / Radical ions



Isolation by Complexation: The radical cation $\text{ttmgb}^{+\bullet}$ [ttmgb = 1,2,4,5-tetrakis(tetramethylguanidino)benzene] can only be stabilized by complexation. It is formed as an intermediate in oxidation of ttmgb to ttmgb^{2+} with Cu^{II} and features a bisallyl-type structure.



A new trinuclear manganese(II) complex has been synthesized and structurally characterized by X-ray crystallography. The variable temperature-dependent sus-

ceptibility measurement (2–300 K) of **1** reveals a weak antiferromagnetic interaction between the manganese ions through the bridging dichlorido ligands.

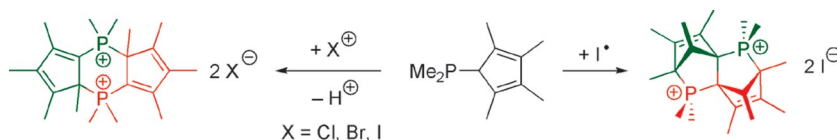
J. Qian, X.-F. Ma, H.-Z. Xu, J.-L. Tian,*
J. Shang, Y. Zhang,
S.-P. Yan* 3109–3116

Synthesis, Crystal Structure, DNA Binding, and Hydrolytic Cleavage Activity of a Manganese(II) Complex



Keywords: Manganese / Bridging ligands / Magnetic properties / DNA cleavage / Hydrolytic cleavage / Structure elucidation

Phosphacyclic Compounds



The reactions of $\text{PMe}_2(\text{C}_5\text{HMe}_4)$ (**1**) with $\text{PPh}_3\text{CH}_2\text{X}^+\text{X}^-$ ($\text{X} = \text{Cl}, \text{Br}, \text{I}$) and with CH_2I_2 were studied. The potential electrophiles act as oxidising agents initiating the

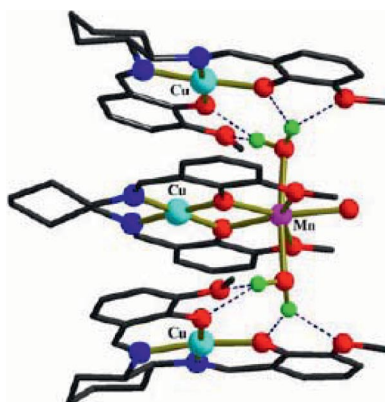
unexpected reaction pathway of oxidative dimerisations in all four cases. Single-crystal XRD analyses of two of these structurally remarkable products are reported.

C. Lichtenberg, M. Elfferding,
J. Sundermeyer* 3117–3124

Unexpected Oxidative Dimerisations of a Cyclopentadienyl-Phosphane – Formation of Unprecedented, Structurally Remarkable Phosphacyclic Compounds

Keywords: Phosphorus heterocycles / Phosphanes / Spiro compounds / Isolobal relationship / Oxidative dimerisation

The syntheses, structures and magnetic properties of the monophenoxido-bridged, trinuclear $\text{Cu}^{\text{II}}\text{M}^{\text{II}}\text{Cu}^{\text{II}}$ ($\text{M} = \text{Cu}, \text{Ni}, \text{Co}, \text{Fe}$) complexes and the tetranuclear $[2 \times 1 + 1 \times 2]$ cocrystal of the diphenoxido-bridged, dinuclear $\text{Cu}^{\text{II}}\text{Mn}^{\text{II}}$ and mononuclear Cu^{II} moieties from a compartmental ligand are described. The ligand is the $[2+1]$ condensation product of 3-methoxysalicylaldehyde and *trans*-1,2-diaminocyclohexane.

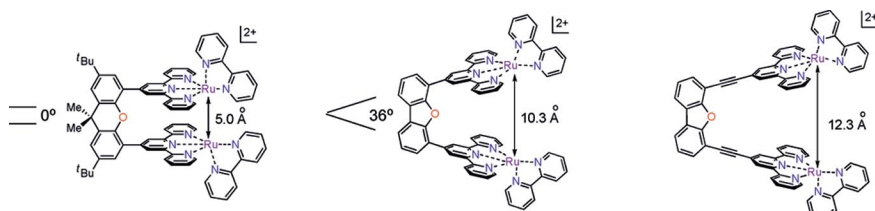


A. Biswas, M. Ghosh, P. Lemoine,
S. Sarkar, S. Hazra,
S. Mohanta* 3125–3134

Syntheses, Structures and Magnetic Properties of Trinuclear $\text{Cu}^{\text{II}}\text{M}^{\text{II}}\text{Cu}^{\text{II}}$ ($\text{M} = \text{Cu}, \text{Ni}, \text{Co}$ and Fe) and Tetranuclear $[2 \times 1 + 1 \times 2]$ $\text{Cu}^{\text{II}}\text{Mn}^{\text{II}}-2\text{Cu}^{\text{II}}$ Complexes Derived from a Compartmental Ligand: The Schiff Base 3-Methoxysalicylaldehyde Diamine Can also Stabilize a Cocrystal

Keywords: Crystal engineering / Magnetic properties / Heterometallic complexes / Self-assembly / Hydrogen bonds

Water Splitting



A series of bimetallic architectures were developed to examine how the distance between two juxtaposed $\{\text{Ru}(\text{tpy})(\text{bpy})\text{Cl}\}^{1+}$ units affect catalytic water oxidation. Despite $\text{M} \cdots \text{M}$ distances ranging from ca.

5–12 Å, each member of the series is shown to catalyze the Ce^{IV} -driven oxidation of water. This result suggests that metal co-operativity is not essential to dioxygen bond formation.

D. J. Wasylenko, C. Ganesamoorthy,
B. D. Koivisto,
C. P. Berlinguette* 3135–3142

Examination of Water Oxidation by Catalysts Containing Cofacial Metal Sites

Keywords: Homogenous catalysis / Water splitting / Ruthenium / Energy conversion / Kinetics

CONTENTS

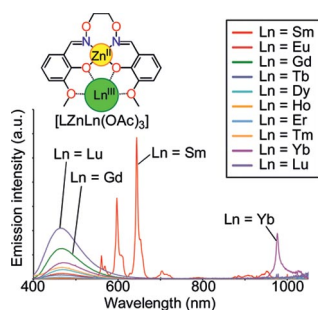
Luminescent Dinuclear Complexes

S. Akine, F. Utsuno, T. Taniguchi,
T. Nabeshima* 3143–3152



Dinuclear Complexes of the N₂O₂ Oxime Chelate Ligand with Zinc(II)–Lanthanide(III) as a Selective Sensitization System for Sm³⁺

Keywords: Zinc / Lanthanides / Hetero-metallic complexes / N,O ligands / Luminescence



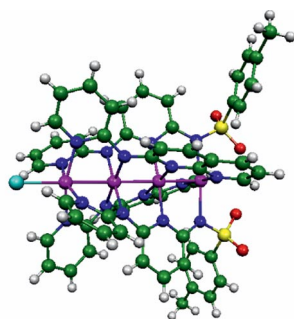
Complexation of an oxime chelate ligand H₂L with Zn^{II} and Ln^{III} afforded a series of dimetallic complexes [LZnLn(OAc)₃] (Ln = Sm–Lu). The ligand moiety selectively sensitizes the f–f emission of Sm³⁺; [LZnSm(OAc)₃] exhibits a relatively intense red luminescence due to f–f transitions, whereas the complexes [LZnLn(OAc)₃] (Ln = Eu, Tb, Dy, etc.) exhibit very weak emission.

Metal String Complexes

C.-W. Yeh, I. P.-C. Liu, R.-R. Wang,
C.-Y. Yeh, G.-H. Lee,
S.-M. Peng* 3153–3159

Linear Tetranickel String Complexes with Mixed Supported Ligands and Mixed-Valence Units [Ni₂]³⁺: Synthesis, Crystal Structure, and Magnetic Studies

Keywords: Molecular wire / Mixed-valent compounds / Magnetic properties / Nickel / Ligand effects



"Mixed-Ligands" Nickel Strings

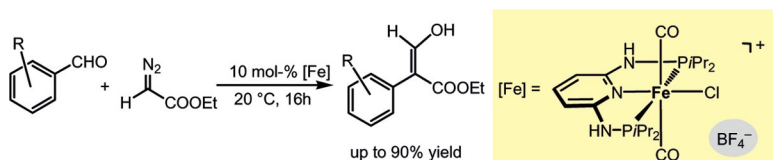
Four linear tetranickel string complexes supported by mixed ligands were synthesized and isolated. The crystal structural analysis showed that the mixed-valence [Ni₂]³⁺ unit can possibly be stabilized by only two naphthyridyl groups, which might allow us to modulate the physical properties of metal string complexes by modifying the other two ligands.

Anion Effects in C–C Coupling Reactions

L. G. Alves, G. Dazinger, L. F. Veiros,
K. Kirchner* 3160–3166

Unusual Anion Effects in the Iron-Catalyzed Formation of 3-Hydroxyacrylates from Aromatic Aldehydes and Ethyl Diazoacetate

Keywords: Iron / Pincer complexes / Aminophosphanes / C–C coupling / Anions / Density functional calculations



The complex *trans*-[Fe(PNP-*i*Pr)(CO)₂Cl]X with X = BF₄[−] is an efficient precatalyst for the coupling of aromatic aldehydes with ethyl diazoacetate to afford selectively 3-hydroxyacrylates in up to 90% yield. This reaction is strongly dependent on the na-

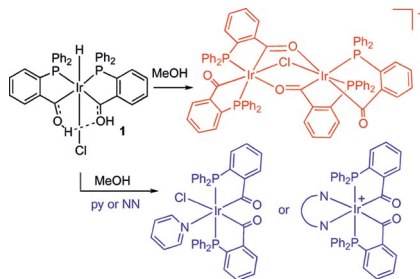
ture of the counterion. With PF₆[−] about 20% conversion is observed, whereas in the case of NO₃[−], CF₃COO[−], CF₃SO₃[−], SbF₆[−], and BAr'₄[−] no reaction takes place. A conceivable mechanism is established by means of DFT/B3LYP calculations.

Hydrido-iridium Complex Chemistry

R. Ciganda, M. A. Garraalda,*
L. Ibarlucea, C. Mendicute, E. Pinilla,
M. R. Torres 3167–3173

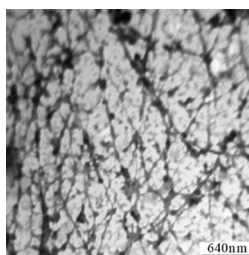
Dehydrogenation of Hydrido-irida-β-diketones in Methanol: The Selective Formation of Mono- and Dinuclear Acyl Complexes

Keywords: Iridium complexes / Acyl bridging ligands / Dehydrogenation




The hydrido-irida-β-diketone (1) undergoes dehydrogenation in protic solvents to afford dimer complexes with bridging acyl and chloride groups. In the presence of N-donors cationic or neutral *cis*-acyl, *trans*-phosphane isomers are selectively formed.

Meshy boron nitride (BN) with a large surface area of $220 \text{ m}^2 \text{ g}^{-1}$ was synthesized by the reaction of NaBH_4 and $\text{CS}(\text{NH}_2)_2$, which exhibits strong cathode-luminescence emission, good thermal stability, and oxidation resistance up to 800°C . The vulcanization behavior of $\text{CS}(\text{NH}_2)_2$ for the cross-linking among borazine molecules is critical for the formation of meshy BN.



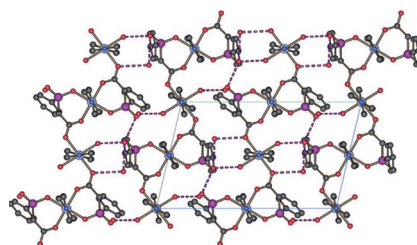
X.-L. Meng, N. Lun, Y.-Q. Qi, J.-Q. Bi,
Y.-X. Qi, H.-L. Zhu, F.-D. Han,
Y.-J. Bai,* L.-W. Yin,*
R.-H. Fan 3174–3178

Low-Temperature Synthesis of Meshy Boron Nitride with a Large Surface Area 


Keywords: Boron nitride / Luminescence / Density functional calculations / Nanostructures

Layered Coordination Polymers

A new layered cobalt coordination polymer, based on a bifunctional phosphinate-carboxylate ligand and 4,4'-bipyridine, was synthesized and characterized structurally and magnetically.



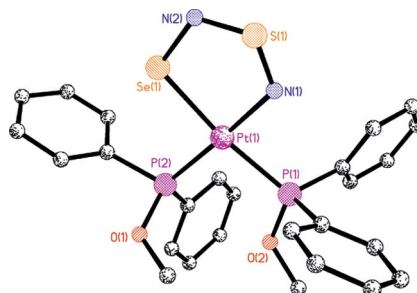
F. Costantino, A. Ienco,* S. Midollini,
A. Orlandini, A. Rossin,
L. Sorace 3179–3184

A New Cobalt(II)-Layered Network Based on Phenyl(carboxymethyl) Phosphinate 

Keywords: Metal–organic frameworks / Layered compounds / Magnetic properties

Main Group Metallacycles

M-S/Se-N complexes continue to challenge conventional bonding treatments. The new complexes described here prove difficult to model using DFT calculations.

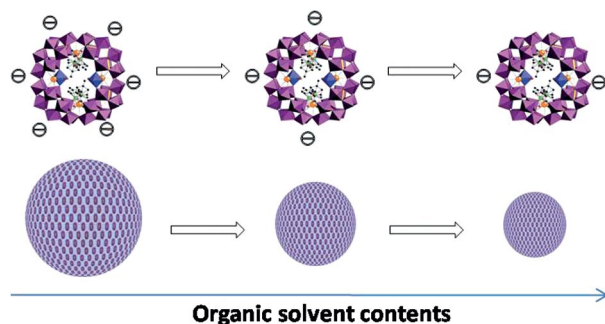


P. G. Waddell, A. M. Z. Slawin,
N. Sieffert, M. Bühl,
J. D. Woollins* 3185–3194

The Preparation and Structure of $[\text{Pt}(\text{S}_2\text{N}_2)\{\text{P}(\text{OR})_n\text{R}'_{3-n}\}_2]$ and $[\text{Pt}(\text{SeSN}_2)\{\text{P}(\text{OMe})_n\text{Ph}_{3-n}\}_2]$ ($n = 0-3$)

Keywords: Sulfur / Selenium / Platinum / DFT calculations

Assembly of Polyanions



The amphiphilic wheel-shaped polyanion $[\{\text{K}(\text{H}_2\text{O})\}_3\{\text{Ru}(p\text{-cymene})(\text{H}_2\text{O})\}_4\text{P}_8\text{W}_{49}\text{O}_{186}(\text{H}_2\text{O})_2\}^{27-}]$ (**1**) self-assembles into vesicles in binary mixed solvents of water and various organic solvents. The size of the

vesicles decreases with increasing organic solvent contents, which contradicts the self-assembly of all other polyanions reported, all following the charge–regulation mechanism.

J. Zhang, T. Liu,* S. S. Mal,
U. Kortz 3195–3200

Unique Supramolecular Assembly of Wheel-Shaped Nanoscale Polyanions with a Hydrophobic Core

Keywords: Polyoxometalates / Amphiphiles / Self-assembly / Vesicles / Hydrophobic effect

CONTENTS

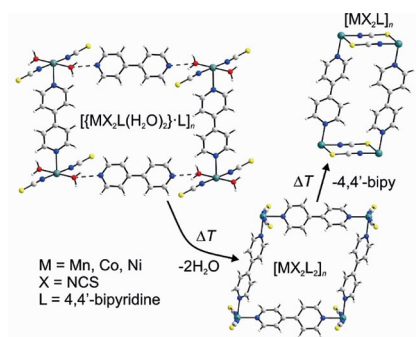
Ligand-Deficient Compounds

M. Wriedt, C. Näther* 3201–3211



Preparation of New Ligand-Deficient Thiocyanato Compounds with Cooperative Magnetic Phenomena by Thermal Decomposition of Their Ligand-Rich Precursors

Keywords: Organic–inorganic hybrid composites / N ligands / Nickel / Manganese / Cobalt / Magnetic properties



Thiocyanato metal coordination polymers with 4,4'-bipyridine as ligand were prepared and their structures and thermal and magnetic properties were investigated. On heating, the ligand-rich hydrates decompose quantitatively to give new ligand-deficient compounds. The last step of this process is accompanied with dramatic changes in their magnetic properties.

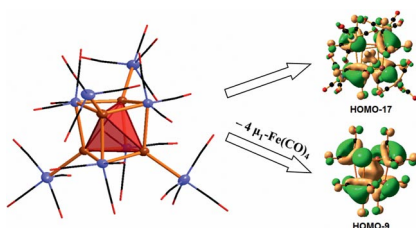
Bismuth-Iron Cluster

K. Yu. Monakhov, T. Zessin,
G. Linti* 3212–3219



Cubane-Like Bismuth-Iron Cluster: Synthesis, X-ray Crystal Structure and Theoretical Characterization of the $[\text{Bi}_4\text{Fe}_8(\text{CO})_{28}]^{4-}$ Anion

Keywords: Bismuth / Iron / Cluster compounds / Aromaticity / Density functional calculations



The anionic Zintl cluster $[\{\text{Bi}_4\text{Fe}_4(\text{CO})_{12}\}-\{\text{Fe}(\text{CO})_4\}_4]^{4-}$ shows a Bi_4Fe_4 heterocubane framework with three-dimensional aromaticity.

Metal-Containing Carbenes

C.-S. Guo, C.-M. Weng,
F.-E. Hong* 3220–3228



Preparation of Cobalt-Containing Ligands with NHC- and/or P-Coordinating Sites and Their Application in Heck Reactions: The Formation of an Unexpected Cobalt-Containing Zwitterionic Complex

Keywords: Zwitterions / Carbenes / Phosphanes / Cobalt / Palladium / Heck reaction



An unusual dicobalt-containing zwitterionic compound **8** has been obtained from the reaction of **5** with benzyl bromide.

* Author to whom correspondence should be addressed.

Supporting information on the WWW (see article for access details).